THE UNIVERSITY OF
SYDNEY

Guest-Dependence on Spin Crossover and Thermal Expansion in Nanoporous Coordination Framework Materials

Benjamin Ross Mullaney

A thesis submitted in fulfilment of the requirements for the degree of Doctor of Philosophy

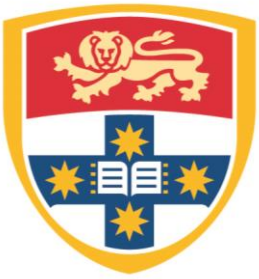

THE UNIVERSITY OF SYDNEY

School of Chemistry

University of Sydney

May 2013

Declaration of Student Contribution

I declare that unless stated below or elsewhere in the text, the work presented in this thesis is my own and has not been submitted in any form for another degree or diploma at any university or institution of tertiary education. Information derived from published or unpublished work of others has been acknowledged in the text.

The single crystal X-ray diffraction data collections, structure solutions and refinements were performed by Dr David Price. The ethanol adsorption isotherms and isobars were performed on an IGA by Dr Peter Southon, by whom the PPMS VSM sample containment method was also developed to prevent *in situ* desolvation. Dr Laurence Goux prepared and sent samples for the elemental analysis experiments, which were performed by the staff at the Campbell Elemental Analysis Facility at the University of Otago. All other data collections, including powder X-ray diffraction, magnetic susceptibility and ASAP nitrogen isotherm experiments, as well as all other calculations and analyses, were performed by myself.

Benjamin Mullaney

Abstract

Coordination framework materials have attracted much interest in modern chemistry due to the plethora of properties that they may possess. They are also attractive due to the relative ease through which systematic study of framework behaviour may be used to understand the underlying mechanisms that produce the observed properties. Through such study, coordination frameworks have the potential to eventually use rational design to create desired functionality. The frameworks described in this thesis demonstrate the properties of spin crossover, anomalous thermal expansion, and nanoporosity, which enables guest-dependent studies into the material behaviour.

The first frameworks that are described herein are the $[Fe(bpac)M(CN)_4]\cdot x(bpac)\{guest\}$ (M = Ni, Pd, Pt; bpac = 1,4-bis(4′-pyridyl)acetylene) family. These frameworks demonstrated two significant degrees of freedom in the guest occupancy, each of which affect the spin transition properties: the variable quantity of bpac guest molecules, and the quantity and type of solvent guest.

Single crystal structural analysis demonstrated that the maximum quantity of bpac guest that may reside within the lattice pores is 0.5 molecules per framework formula unit. The relative spin transitions of the $[Fe(bpac)M(CN)_4]\cdot 0.5(bpac)\{EtOH\}$ (M = Ni, Pd, Pt) series were determined to arise primarily through the internal pressure effect due to steric interactions between the occluded bpac guest molecules and the framework host. The degree by which the HS state is stabilised was then determined by the atomic radius of the framework co-metal, which affects the lattice pore dimension.

The properties of the alcohol-solvated $[Fe(bpac)Pd(CN)_4]\cdot x(bpac)$ (x = 0.4, 0.5) frameworks were studied, and the major guest influence on the resulting spin crossover behaviour was determined to be due to an internal pressure effect produced by the kinetic volume and compressibility of the guest. The $[Fe(bpac)Pd(CN)_4]\cdot 0.4(bpac)\{1\text{-}PnOH\}$ sample demonstrated spin crossover behaviour with a very large hysteresis width, and a relatively gradual, two-stage transition. While the two-stage transition is likely to arise primarily due to multiple transition behaviours in the heterogeneous sample, structural analysis of this sample by powder X-ray diffraction demonstrated the existence of multiple crystallographically independent Fe(II) sites in the framework lattice, which may also have an influence on the

SCO behaviour. The large hysteresis could be structurally explained due to the significant difference in lattice dimension between the HS and LS states, which would introduce a large energetic barrier to spin transition.

By obtaining a variety of EtOH adsorption isotherms and isobars, a Temperature-Pressure phase diagram of SCO was produced for the $[Fe(bpac)Pd(CN)_4]\cdot 0.4(bpac)\{EtOH\}$ material. This diagram demonstrated that at higher pressures, the bistability temperature range increased and the transition temperature decreased. This behaviour was attributed to an increased quantity of adsorbed EtOH with higher pressure, which would stabilise the HS state and increase bistability due to the subsequent increase in host–guest interactions.

In addition to these frameworks, the behaviour of the $[Fe(bpac)(Au(CN)_2)_2)]\cdot\{guest\}$ framework material was also investigated. This framework demonstrated unprecedented multifunctional behaviour, with a synergistic interplay between the spin crossover, lattice structure and host–guest properties. The framework lattice was exceptionally flexible, and displayed a facile 'scissor-type' motion of the $\{Fe(Au(CN)_2)_2\}$ (4,4)-grids. Due to the energetic ease by which the framework may adopt a variety of conformations, the precise grid geometry was then determined by weak inter-network and host–guest interactions.

It was shown that as the framework undergoes transition to the LS state, the lattice undergoes a significant conformational change as the $\{Fe(Au(CN)_2)_2\}$ (4,4)-grids tend closer to a more regular orthogonal conformation through scissor-type motion of the lattice nets. This primarily occurs because the coordination environment of the Fe(II) sites becomes more rigidly octahedral. The framework also demonstrated the scissor-type conformational behaviour independently of spin transition, resulting from temperature-dependence on the dynamic balance between inter-network and host–guest interactions, which influence the framework conformation.

Due to the extreme conformational flexibility of the $\{Fe(Au(CN)_2)_2\}$ (4,4)-grids of this material, the $[Fe(bpac)(Au(CN)_2)_2)]\cdot\{EtOH\}$ sample displayed colossal uniaxial thermal expansion behaviour. Below the spin transition, the *a*-parameter displayed a maximum thermal expansion coefficient of $-1070 \times 10^{-6}\ K^{-1}$, which is an order of magnitude greater than any yet reported for this quantity.

Guest-dependent studies on this framework demonstrate the strong effect of guest properties

on the conformation of the {$Fe(Au(CN)_2)_2$} (4,4)-grids, distortion of the dicyanidoaurate linkers, and distortion of the bpac linker away from an orthogonal coordination between the adjacent Fe(II) centres. In the desolvated state, the HS lattice is highly distorted with significant compression of the interpenetrated nets, but as the framework undergoes transition to the LS phase the lattice becomes more open as adjacent bpac ligands in the interpenetrated nets move further apart. It was generally observed that larger, more rigidly bulky guests produce more open framework conformations, which is attributed to an internal pressure effect from the adsorbed guest species.

The spin transition behaviour displayed a strong dependence on the lattice distortion of the framework, especially when there was a non-orthogonal coordination of the bpac pillar ligand. In cases where the lattice displayed greater distortion, the spin transition occurred more gradually. This behaviour is attributed to a decrease in the rigidity of the framework produced by lattice distortion, which decreases the strength of the long-range elastic interactions that produce cooperativity in the spin transition.

The synergistic relationship of the framework properties in conjunction with the extreme flexibility of the framework led to a great dependence of the framework behaviour on the precise sample environment and degree of solvation. It was also shown that guests which may adopt multiple conformations and solvent packing behaviour in the framework pores produced multiple spin transition stages when included in the framework.

Acknowledgments

Throughout my research for this thesis, there have been many people who have helped me survive and succeed, and to whom I owe my sincere thanks.

First and foremost, I owe the greatest debt of gratitude to my never-tiring supervisor, Prof Cameron Kepert. His advice and knowledge, encouragement and companionable nature make working for and with him a true pleasure. Dr Peter Southon has been a stalwart bastion of sense and helpfulness, he ran all the IGA measurements which took about a month of continuous instrument time, and developed the VSM sample containment method, which has been used liberally in my research. Dr David Price has been of immense value in solving all crystal structures in this thesis, and Dr Laurence Goux has been a great research ally, accompanying me in many of my adventures with the $[Fe(bpac)(Au(CN)_2)_2]$ material and helping me out with elemental analysis and other experiments while I've been away from Sydney.

For proofreading various parts of this massive work, I give my thanks to Dr Nick White, who isn't even part of the Kepert group, as well as Mr Alex Diwa, Drs Laurence Goux, David Price, Feng Li and of course, Cameron (who had the unenviable task of reading all of it…).

In the lab and office, Dr Liz Fellows has been a wonderful spin crossover buddy and sounding board for ideas and results (we got so excited about new and funky hysteresis shapes!). Drs Yue Wu, Lisa Cameron and Sam Duyker have been great cubicle-mates and put up with my excesses with patience and good humour, and I am grateful to everyone else in the Kepert group for being fantastic colleagues and workmates – it makes all the difference!

On a more personal level, my family and friends in all their different ways have helped make my life as happy as it is.

Table of Contents

Abbreviations and Symbols

°	degrees
2D	two-dimensional
Å	angstroms
a, *b*, *c*	unit cell parameters (SCXRD)
ASAP	accelerated surface area and porosimetry system
azpy	4,4′-azopyridine
bpac	1,2-bis(4′-pyridyl)ethyne
BuOH	butanol
C	Celsius
C	Curie constant (magnetism)
ca.	*circa*, about/approximately
CIF	Crystallographic information file
cm	centimetres
d	deuterated (NMR solvents)
EtBr	bromoethane
$EtBr_2$	dibromoethane
$EtCl_2$	dichloroethane
EtI	iodoethane
EtOH	ethanol
eqv	equivalent
g	grams
G	guest molecule
GOF	goodness of fit (SCXRD)
hr	hours
HS	high spin
K	Kelvin
k_B	Boltzmann constant
L_0	initial unit cell length (thermal expansion)
LS	low spin
M	mole per litre
M	metal
MeBrCl	bromochloromethane
$MeCl_2$	dichloromethane
MeCN	acetonitrile
MeOH	methanol
mg	milligrams
mL	millilitres

mm	millimetres
mmol	millimoles
NMR	nuclear magnetic resonance
MPMS	Magnetic Property Measurement System
NTE	negative thermal expansion
P	electron pairing energy
P	Pressure
P_0	saturation pressure of adsorbant
PnOH	pentanol
PPMS	Physical Property Measurement System
PrBr	bromopropane
PrCl	chloropropane
PrI	iodopropane
PrOH	propanol
PXRD	powder X-ray diffraction
R	residual (SCXRD)
S	spin number
SCO	spin crossover
SCXRD	single crystal X-ray diffraction
SQUID	Superconducting Quantum Interference Device
T	Torr (pressure)
T	Temperature
$T_{1/2}$	Temperature at which the proportion of HS and LS states involved in a transition are equal
V	unit cell volume (SCXRD)
V_0	initial unit cell volume (thermal expansion)
vs.	versus (against)
VT	variable temperature
Z	formula units per unit cell (SCXRD)
α	axial thermal expansion coefficient
β	volumetric thermal expansion coefficient
γ_{HS}/γ_{LS}	relative stoichiometric fraction
Δ	crystal field splitting energy
ΔE^0_{HL}	difference between zero point energies of HS and LS state
ΔG	change in Gibbs free energy
ΔH	change in enthalpy
Δr_{HL}	difference in the ligand–metal bond length between the HS and LS states
ΔS	change in entropy
θ	angle (diffraction)
λ	wavelength

μ	absorption coefficient (SCXRD)
μ_B	Bohr magneton
μ_{eff}	effective magnetic moment
ρ	density
σ_{oct}	Octahedral distortion parameter
χ_M	molar magnetic susceptibility
§	section
≈	approximately equal to

List of Figures

List of Tables

Chapter 1: Introduction

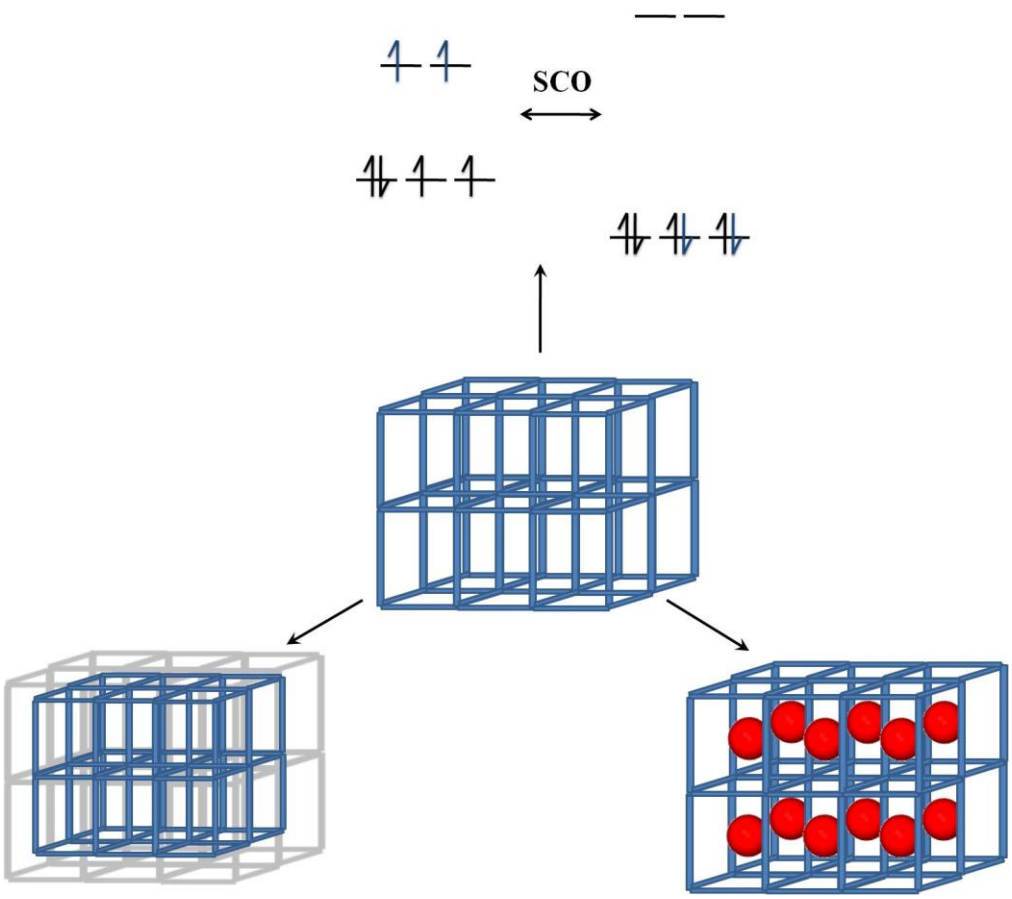

Coordination frameworks may exhibit many different functional properties, such as spin crossover (SCO), porosity for guest adsorption, and negative thermal expansion.

1.1 *Overview*

The ability to design molecular materials for specific applications is a major goal in modern chemistry.[1-4] Coordination frameworks offer a versatile path toward this goal, with seemingly limitless structural and behavioural possibilities.[5-9] The focus of the work presented in this thesis is on the development and characterisation of framework materials that display the properties of spin crossover, nanoporosity and negative thermal expansion.

Spin crossover is an attractive property of certain transition metal coordination complexes and coordination frameworks, and involves their reversibly switching between high spin and low spin states.[10] This is accompanied by a significant change in many of the chemical and physical properties, most notably including magnetic, electronic, absorption and structural behaviour.[10-12] Combining spin crossover with nanoporosity can lead to guest-dependent behaviour.[13] This not only has the practical benefit of increasing the tunability of properties, but also enables a more fundamental study of structure–property relationships, arising from systematic perturbations of the structure through guest exchange. Furthermore, the introduction of a solvent effect on the spin crossover behaviour could in principle lead to molecular sensing devices.[9]

Thermal expansion properties are an important consideration in materials engineering, especially in the design of devices that work at a variety of temperatures.[14,15] Most materials display positive thermal expansion, which can generate stress at high temperatures, or create inaccuracies in high precision devices that rely on dimension. Thus, the study of materials that display negative thermal expansion, or other unusual thermal expansion behaviour, is important in developing strategies to counteract, or eliminate this effect.

1.2 *Coordination Frameworks*

Coordination frameworks, also known as coordination polymers or metal-organic frameworks, are the subject of intense interest in modern chemistry, due to the potential to use rational design in order to fine-tune their properties,[1] and the variety of applicable behaviours that they offer.[7,16] Coordination frameworks display a range of properties including catalysis, porosity, fluorescence, conductivity, chirality, negative thermal expansion, host–guest interactions and spin crossover.[7,17,18] These behaviours could lead to commercial use with potential application as sensors, semiconductors, switches, small

molecule storage and separation, data storage and non-linear optics.[3,7,18]

The chemical construction of coordination frameworks, as with supermolecules, was best expressed by Lehn in his 1987 Nobel lecture: "One may say that supermolecules are to molecules and the intermolecular bond what molecules are to atoms and the covalent bond".[19] It is through labile interactions that coordination frameworks are assembled and stabilised. Such directional interactions as ligand–metal bonds, aromatic interactions and hydrogen bonding drive the formation of framework architectures.

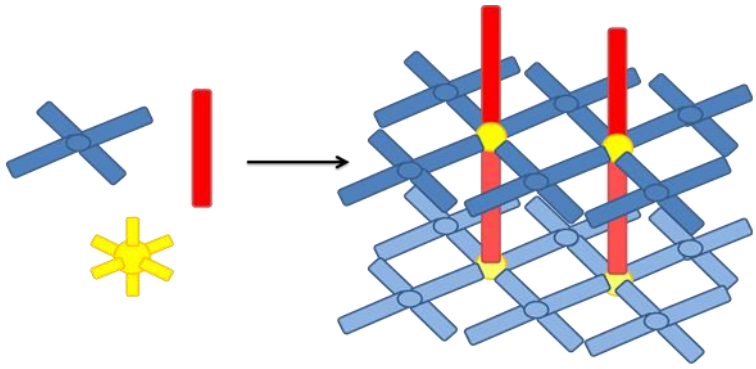

Figure 1-1: Through design of the geometry and connectivity of the building blocks, crystal structures with specific topologies are formed.

In the design of coordination frameworks, the constituent components can be described as building blocks with well-defined connectivity within the crystal structure. Nodes, such as transition metal centres, are joined together through non-covalent bonds with organic ligand 'linkers'. The coordination properties of the metal node and the properties of the ligand, including structure, denticity and rigidity, contribute to the determination of the precise topology of the resulting framework structure (**Figure 1-1**).[16,17]

As the assembly of coordination frameworks is driven by relatively weak interactions and labile bonds, this provides an inbuilt 'error correction' in the growth of the framework in solution, as its components are in an equilibrium with their dissolved state. The product is then a balance between enthalpic and entropic processes, including those of crystallite nucleation.[16] Crystallisation conditions are important in the self-assembly of frameworks, with solvent, temperature, time, concentration, pH, and counterions contributing to the energetics of the system, thus affecting the precise structure of the framework. Furthermore, it is often the case that multiple phases of the same building blocks have similar energies, and

crystal polymorphs can form, which may in turn display different properties.

Due to the large array of influences driving formation of the framework structure, many different structural topologies can arise, often from the same building blocks. 1D chains, 2D sheets or 3D lattices can all be produced, depending on the number of node connections and the interaction energetics within the framework.[17] **Figure 1-2** gives examples in which different node connectivities can often produce many distinct framework structures.

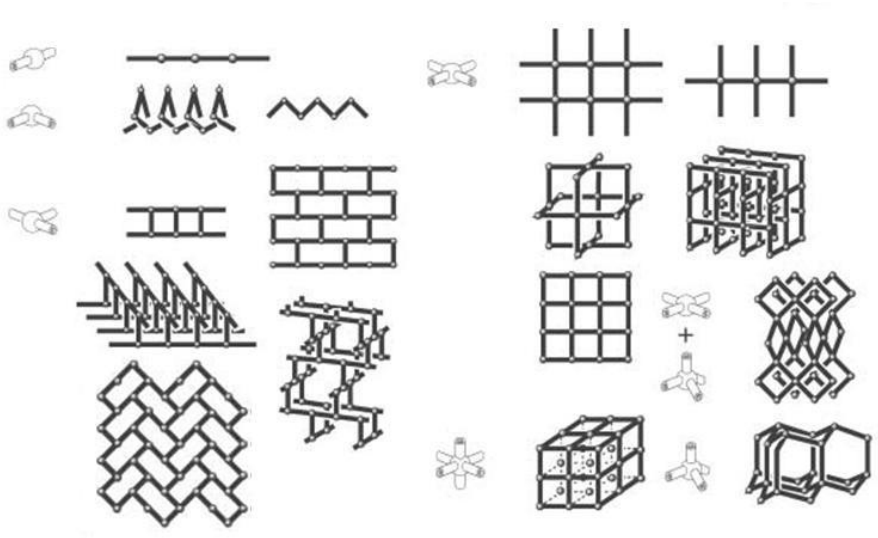

Figure 1-2: Different connectivity behaviour gives rise to different framework topologies. Often, a single connection geometry can also produce multiple different topologies, the relative stabilities of which are influenced by the energetics of interactions between the constituent molecules within the framework. Reproduced from Kitagawa *et al*.[17]

Often, a given framework topology will result in voids within the structural net. To avoid the entropic penalty of guest inclusion within these void spaces, framework layers may exhibit interdigitation, self-penetration, and/or multiple interpenetrated nets can form.[20-25] The latter case is demonstrated in the doubly interpenetrated 3,5-connected 3D nets of the [Ag(tcm)(pyz)] (tcm = tricyanomethanide; pyz = pyrazine) framework, as shown in **Figure 1-3**.[26]

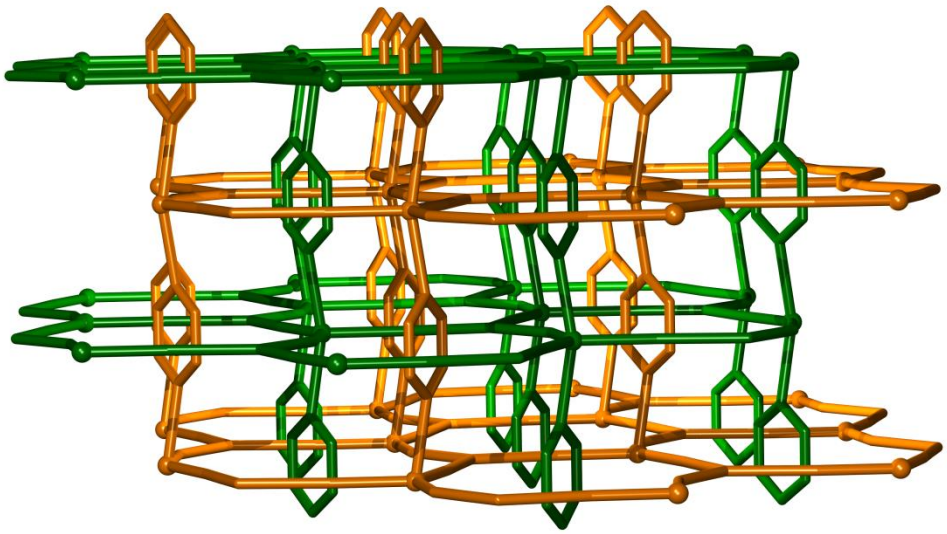

Figure 1-3: The structure of [Ag(tcm)(pyz)], which is an example of an interpenetrated framework material.[26]

Research into the synthesis and characterisation of coordination polymers has grown significantly in recent years, due to their structural and behavioural diversity and the ease with which they can be systematically altered to obtain different properties.[27,28] Through careful study of the structure–property relationships of these materials, it is anticipated that it will be possible to utilise rational design of such materials to exhibit desired behaviour for specific applications.[18,28-30]

1.3 *Porosity*

Porous materials are of significant commercial interest, and their development has become an important goal for many crystal engineers and material scientists.[17] Porous materials are classified according to the width of their structural pores: a width of < 2 nm is termed microporous, 2–50 nm mesoporous, and > 50 nm macroporous.[31] The word ‘nanoporous’ is also often used as a more general term to describe materials with a porous dimension on the scale of nanometers. It is possible for porous materials to have an internal surface area that is greater than their external surface area, leading to significant interest in these materials for functionalisation toward making efficient catalysts, and for molecular separation.[1,17,32]

Among the longest standing and most explored of nanoporous materials are porous aluminosilicates, known as zeolites, which have been used extensively both industrially and for domestic applications, due to their efficacy in storage, separations, sensing, catalysis and

ion exchange.[33,34] Coordination polymers are an alternative family of nanoporous materials, with added potential benefits including an increased selectivity in their sorption properties due to organic functional groups and metal sites, which can alter host–guest interactions.[4,17,35,36]

Space in a coordination framework that is not occupied by framework atoms is known as *void volume*. This volume can be in the form of zero-dimensional cavities (discrete nano-spaces), one-dimensional channels, two-dimensional layers, or three-dimensional intersecting channels. These voids are typically filled with solvent molecules, counterions and/or unbound ligand, which can act as a template in the construction and stabilisation of the framework. Coordination frameworks are most commonly not stable to removal of these guest molecules, and they undergo structural collapse. However, recent years have seen a rapid growth in the number of frameworks which are stable to guest removal.[1,17] In order to have functional porosity, the framework must be stable and robust, so that structural integrity is retained after the removal of guest molecules.[35]

1.3.1 *Guest-Exchange*

The ability of a framework to reversibly store and release guest molecules is highly desired, both as a property in itself, and in conjunction with other framework behaviours. There is much ongoing research into nanoporous materials for use as low-pressure storage and transport media for gaseous fuels, such as methane and hydrogen.[36-38] They are also being investigated for their potential to adsorb CO_2 for separation and sequestration.[39,40] Coordination frameworks are very promising for use in gas and vapour storage due to their low density, chemical inertness, and versatility for modification.[36,41-46]

Porosity and guest-exchange can be measured by the adsorption of gases, which tests the effective porosity and surface area of frameworks; and by the sorption of liquids and vapours, to analyse guest uptake and behavioural effects. Important information regarding pore size and shape can be determined through analysis of adsorption behaviour. There are six general types of behaviour displayed in physisorption isotherms upon adsorption and desorption of guest species (see **Figure 1-4**).[31]

Type I isotherms are characterised by a steep adsorption curve at low pressure followed by an adsorption plateau, and are produced by microporous solids with relatively small external

surface areas. The limiting uptake is determined by the accessible micropore volume, rather than the internal surface area. *Type II* isotherms begin with a small amount of abrupt adsorption at low pressure, which levels out slightly before becoming steep again at higher pressure. This is the normal isotherm behaviour for a non-porous or macroporous material, and is due to unrestricted monolayer-multilayer adsorption.

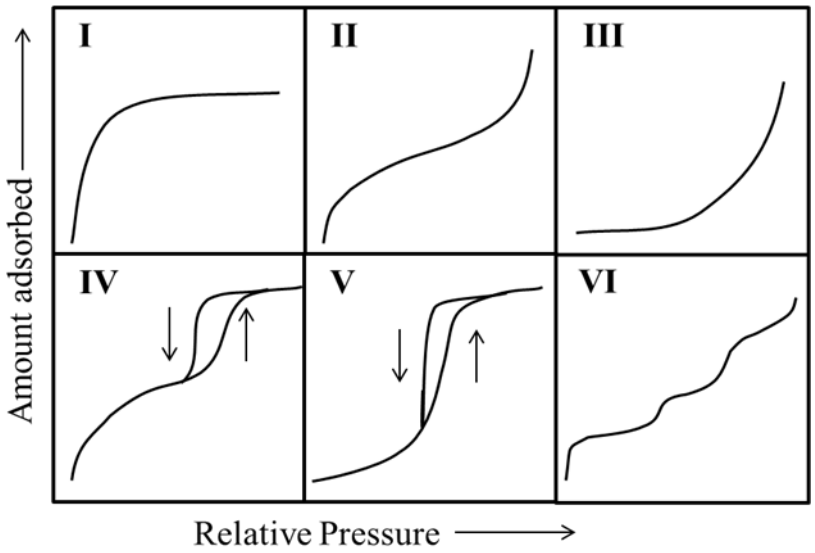

Figure 1-4: The different types of adsorption isotherm behaviours, as described by Sing *et al*.[31] More information is given in the text.

Type III and *Type V* isotherms are rarely seen, and indicate very weak interactions between the material and the adsorbant (the two types are for non-porous and porous materials, respectively). *Type IV* is based on Type II with monolayer-multilayer adsorption, but has a characteristic hysteresis loop which is associated with capillary condensation in mesopores. *Type VI* represents stepwise multilayer adsorption on a uniform, non-porous surface and the step heights are related to the monolayer capacity for each adsorbed layer.

1.4 *Spin Crossover*

Spin crossover has been known since 1931, when Cambi and Szegö reported certain iron(III) dithiocarbamate complexes which displayed temperature dependence of their magnetic susceptibility behaviour.[47] Since that time, there has been much research into materials that display this spin transition property,[10,48] not only out of simple academic curiosity, but also due to the potential applications of these materials as chemical sensors, optical displays and

as information storage media.[2,11] In order to understand spin crossover behaviour, it is necessary to understand the fundamentals of ligand field theory, and the determination of the *d*-orbital electronic configuration in transition metal complexes.

1.4.1 *Ligand Field Theory*

The *d*-orbital energies of transition metal complexes are split in a ligand field, due to electronic interactions between the orbitals and the ligands. In octahedral transition metal complexes, the orbitals are split into the t_{2g} and e_g subsets. The non-bonding t_{2g} set is comprised of the d_{xy}, d_{yz} and d_{xz} orbitals and is lower in energy than the anti-bonding e_g set, which consists of the $d_{x^2-y^2}$ and d_{z^2} orbitals.

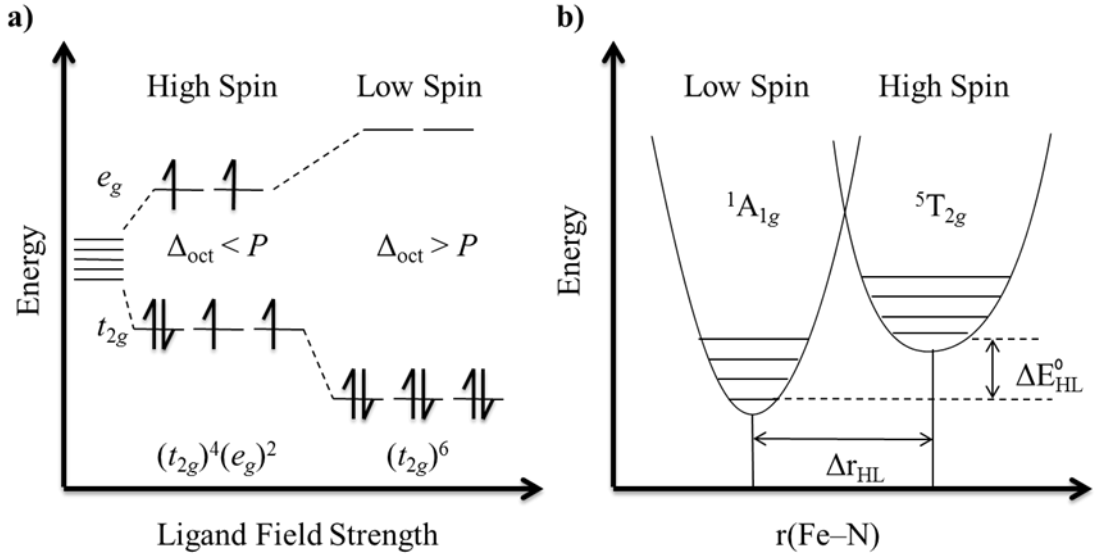

Figure 1-5: a) Electron configurations for octahedral d^6 Fe(II) in the high spin (HS) and low spin (LS) states; and **b)** adiabatic potential wells for the LS ($^1A_{1g}$) and HS ($^5T_{2g}$) states, with the metal–donor atomic distance r(Fe–N).

Octahedral transition metal complexes with a *d*-orbital occupancy of d^n ($4 \leq n \leq 7$) are able to assume at least two electronic configurations, the most common being either low spin (LS) or high spin (HS). Stabilisation of one configuration over another depends on the relative magnitudes of two parameters: *P*, the electron pairing energy, which results from the repulsion when two electrons are in the same orbital; and Δ_{oct}, the *d*-orbital splitting energy, which is the energy difference between the t_{2g} and e_g orbitals. If $P > \Delta_{oct}$, the favoured electronic configuration is HS, with maximum spin multiplicity and minimum electron

pairing. If $P < \Delta_{oct}$, LS is favoured, with electrons pairing in the t_{2g} orbitals preferentially to occupying the e_g orbitals. As an example, an Fe(II) d^6 system in a weak ligand field such that $P > \Delta_{oct}$ will have an electronic configuration with the maximum number of unpaired electrons, resulting in a paramagnetic HS complex ($t_{2g}^4 e_g^2$, $^5T_{2g}$, S = 2). Conversely, the same system in a strong ligand field, such that $P < \Delta_{oct}$, will completely fill the t_{2g} orbital and result in a diamagnetic LS complex ($t_{2g}^6 e_g^0$, $^1A_{1g}$, S = 0). A diagram of the energy configurations is shown in **Figure 1-5a**.

When the ligand field is of an intermediate strength, such that $P \approx \Delta_{oct}$, the energy difference between the zero points of the HS and LS states (ΔE_{HL}^0), see **Figure 1-5b**) is on the order of thermally accessible energy, $k_B T$ (where k_B = Boltzmann constant and T = temperature in Kelvin). This allows reversible spin transition between electronic configurations to occur upon an environmental perturbation, such as temperature, pressure, or light irradiation. This phenomenon is called *spin crossover* (SCO).

SCO is a result of the interplay between the enthalpic and entropic factors of the *d*-orbital electron occupancy. The LS state is stabilised by low temperatures as it has the lowest enthalpy, whereas higher temperatures allow thermal access to the HS state, which is entropically stabilised by the higher electronic degeneracy. The point at which spin transition occurs is when the enthalpic and entropic effects are balanced, and the *Gibbs free energy* of the system, $\Delta G = \Delta H - T \cdot \Delta S$, passes through zero. This occurs at the transition temperature, $T_{1/2}$, which is defined as the temperature at which the HS and LS fractions that are involved in the transition are equal, i.e., $\gamma_{HS} = \gamma_{LS} = 0.5$, where γ is the relative stoichiometric fraction. In the case of SCO systems that display a hysteretic behaviour, it is useful to define two transition temperatures, $T_{1/2}^{\downarrow}$ and $T_{1/2}^{\uparrow}$, to describe the relevant cooling and warming temperatures respectively.

1.4.2 *Cooperativity and Temperature-Dependence of Spin Crossover Behaviour*

There are many factors that influence the precise spin transition behaviour, but there are a few general classes into which the different behaviours can be categorised, as shown in **Figure 1-6**.[10,49]

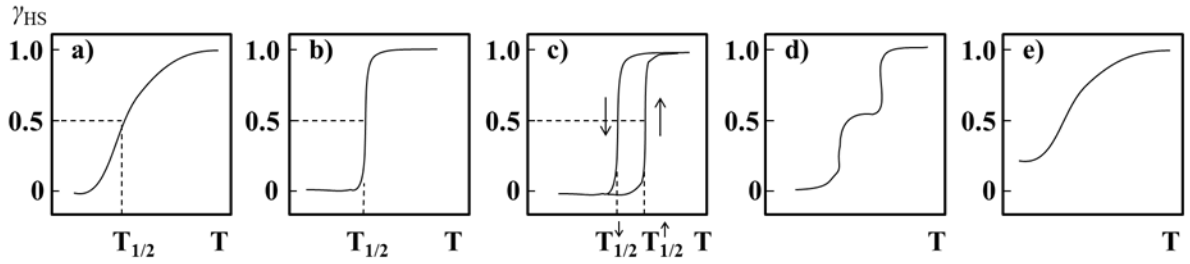

Figure 1-6: The major classes of spin transition displayed in SCO materials: **a)** gradual, **b)** abrupt, **c)** with hysteresis, **d)** with steps, and **e)** incomplete.

Where there is minimal communication between individual SCO centres, a gradual spin transition is observed, as shown in **Figure 1-6a**. This phenomenon has been well studied for complexes in the solution state, or dispersed in a polymer matrix, such that there are effectively no interactions between SCO-active sites.[50-53] A demonstrative example of gradual transition is found in the 1D coordination framework, $[Fe(btzp)_3](ClO_4)_2$ (btzp = 1,2-bis(tetrazol-1-yl)propane) (as shown in **Figure 1-7**).[54] This SCO material consists of 1D chains of Fe(II) centres connected by btzp linkers, and displays a typical gradual spin transition at low temperature. While the close proximity of the Fe(II) centres might be expected to lead to cooperativity and an abrupt transition, the flexibility of the 1,2-propane spacer between the tetrazole moieties acts as a 'shock absorber' against the elastic interactions between Fe(II) sites, decreasing communication of spin state and leading to a lack of cooperativity.

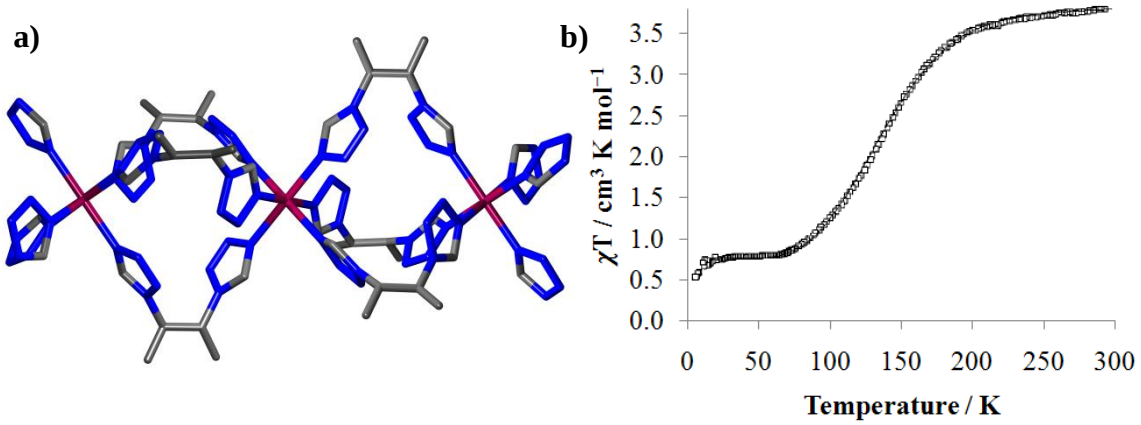

Figure 1-7: a) Single crystal structure of a single chain of $[Fe(btzp)_3](ClO_4)_2$ (counterion has been removed for clarity); and **b)** its SCO behaviour as characterised by variable temperature magnetic susceptibility.[54]

SCO materials can display a cooperative effect, depending on the strength of interactions between adjacent SCO sites.[49,55] This is due to *communication* of spin state information between SCO centres,[56] by inter- and intra-molecular interactions such as aromatic stacking interactions,[57] hydrogen bonding[58] and coordination bonding,[59] in which bridging ligands and host–guest interactions mediate the cooperativity. A system that has a high degree of communication between metal centres, such that the change of spin state at one site may induce spin transition at adjacent sites, will display cooperativity and give an abrupt transition (**Figure 1-6b** and **c**).

The change in bond length and electronic properties associated with spin transition at a discrete SCO site will affect interactions of its coordinated ligands. In a highly cooperative system, the different ligand–metal bond lengths resulting from the spin transition would create structural strain, as a crystal defect site has effectively been introduced and there would be sub-optimal coordination environments and/or crystal packing energetics at neighbouring SCO sites. In order to re-establish a structural energetic minimum in the crystal, spin transition is propagated to neighbouring SCO sites. In addition to this steric factor, there is also a generally weaker electronic effect in which the change in the electron density distribution at the metal site and coordinated ligands leads to communication of spin state between metal centres. The overall effect can be likened to a pressure wave,[12,60,61] in that the SCO initiated at one site will create a cascade effect on the neighbouring sites, leading to a cooperative transition. Metal dilution studies have been carried out on SCO materials, which support the idea that abrupt transitions are due to communication of spin state between active SCO sites.[12,62,63] It was found that increasing the dilution of non-SCO sites within a SCO material led to more gradual transitions which occurred at lower temperatures than their undoped parent materials. In this situation, the communication of spin state between SCO sites was interrupted, and the transition lost cooperativity.

A fine example of a discrete mononuclear SCO material which displays abrupt transition behaviour is $[Fe(L)_2](BF_4)_2$ (L = 2,6-di(4-chloro-pyrazol-1-yl)pyridine) (**Figure 1-8a**).[64] Through relatively strong parallel offset aromatic stacking interactions and edge-to-face C–Cl···π intermolecular interactions between the rigid ligands (**Figure 1-8b**), the identity of the local spin state is communicated between the SCO Fe(II) sites within the crystal, creating an abrupt transition with a small hysteresis (**Figure 1-8c**).

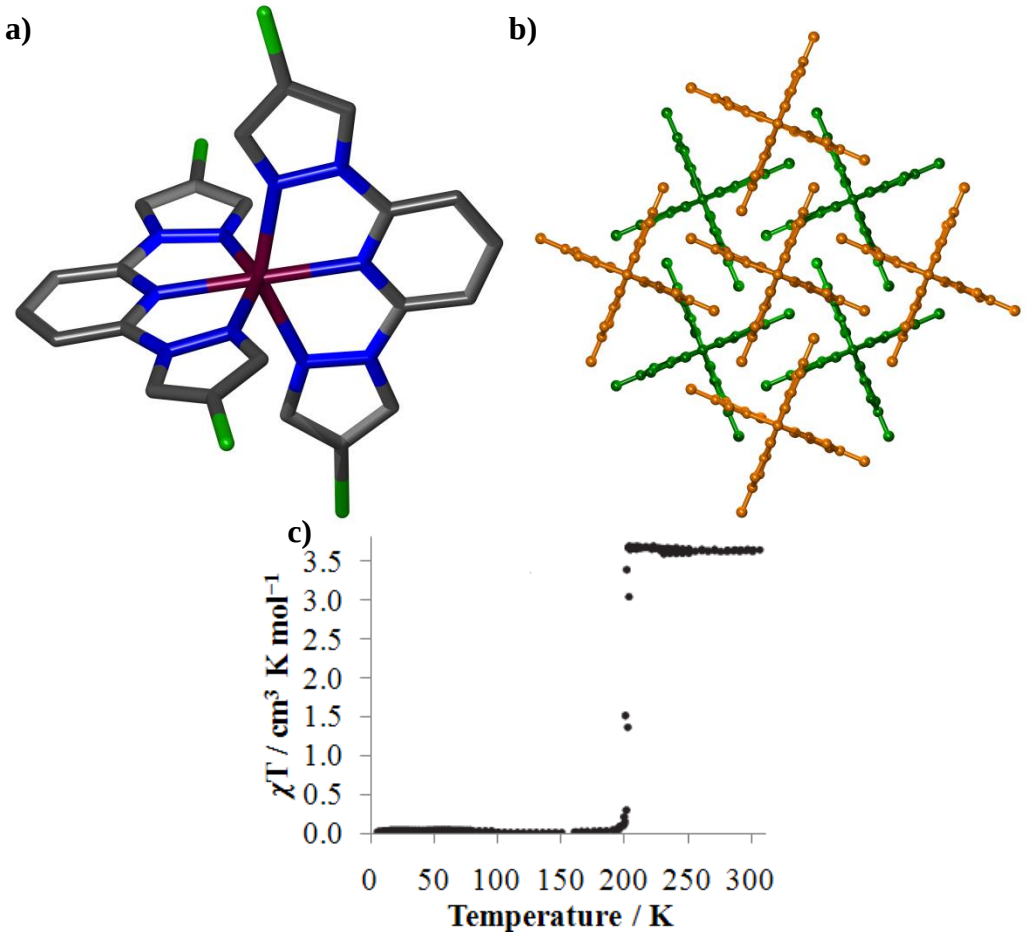

Figure 1-8: Crystal structure of aforementioned $[Fe(L)_2](BF_4)_2$ complex, showing **a)** a single complex molecule; **b)** the crystal packing (with counterion removed for clarity); and **c)** the SCO behaviour as demonstrated by variable temperature magnetic susceptibility.[64]

A material that displays cooperativity of sufficient strength could also generate thermal hysteresis (**Figure 1-6c**),[65] as spin transition of individual SCO sites would create a large amount of crystal strain, disfavouring the spin transition. There would then be a threshold energy at which a critical quantity of SCO sites would undergo spin transition, which cooperatively induces the entire crystallite to undergo transition. Hysteretic behaviour is then observed as a result of the SCO being suppressed in these systems.

As communication between SCO sites is facilitated through strong interactions within the material, the incorporation of SCO functionality into coordination frameworks is a promising tactic to create abrupt, cooperative spin transition behaviour.[66] An example of a SCO material that displays hysteretic behaviour is the 1D coordination polymer, $[Fe(Htrz)_{3-3x}(4\text{-}NH_2trz)_{3x}](ClO_4)_2{\cdot}nH_2O$ (trz = 1,2,4-1H-triazole, x = 0.05).[65,67] This material demonstrates

bistability at room temperature due to the very high degree of communication between adjacent Fe(II) sites within the polymer chains (**Figure 1-9**).

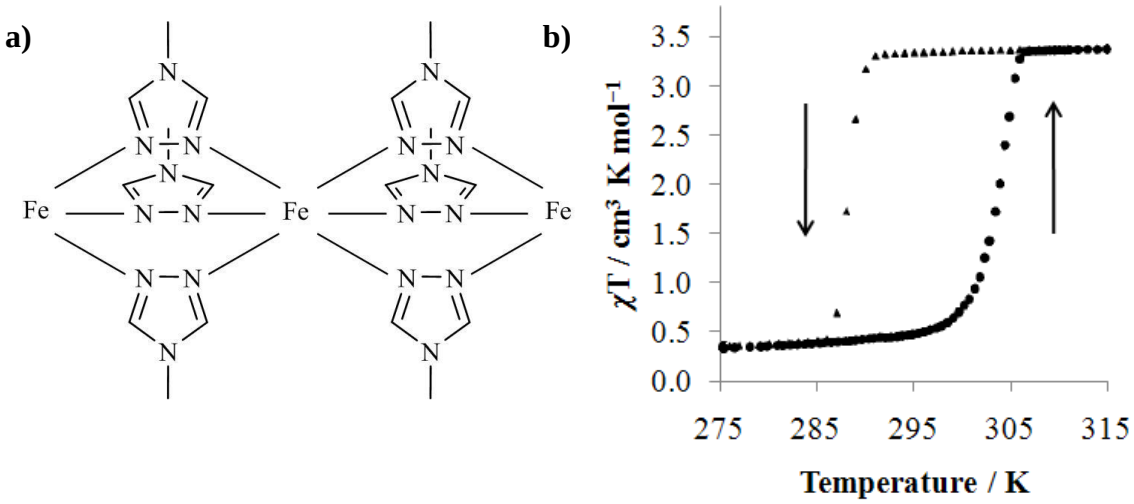

Figure 1-9: a) Illustration of the structure of the 1D coordination polymer of $[Fe(Htrz)_{3-3x}(4\text{-}NH_2trz)_{3x}](ClO_4)_2 \cdot nH_2O$ (x = 0.05); and **b)** the variable temperature magnetic susceptibility data for this material.[65]

As well as potentially displaying the previously described behaviour, SCO systems may also exhibit a multi-step transition due to the existence of, or conversion to multiple SCO environments (**Figure 1-6d**),[68-70] and may be incomplete (**Figure 1-6e**)[71], which primarily arises due to paramagnetic centres which do not have the ligand environment necessary for SCO. In SCO coordination frameworks, these could be due to lattice defect sites, or surface iron sites. Incomplete transitions may also occur due to an inability to access the necessary temperatures to induce SCO, or there may be structural constraints which preclude the material from undergoing complete SCO.

In addition to cooperativity due to mediated interactions between active SCO sites within the crystal structure, the spin transition behaviour is affected by other factors. The transition temperature is dependent on the ligand field strength, and so is affected by the precise ligand structure, including rigidity, aromaticity, hydrophilicity, steric effects and side groups, as well as the counter-anion.[72,73] Included guest molecules (unbound molecules within the structural voids) can play an important role in the outer coordination sphere of the complex, and through interactions with the ligand, anion and/or the metal centre, can alter the transition behaviour.[9,13]

The $[Fe_2(azpy)_4(NCS)_2]$ (azpy = *trans*-4,4′-azopyridine) coordination framework was the first material that demonstrated guest-dependent SCO behaviour with reversible uptake of guest species.[13] This framework, comprised of two interpenetrated rhombic grids (**Figure 1-10a**), is robust to guest removal and when solvated with different solvent guest species, shows markedly different spin transition properties. With methanol or ethanol guest, the framework displays a single transition step, while 1-propanol produces a two-step transition. The importance of the guest on the framework behaviour is made even more apparent by the behaviour of the desolvated sample, which does not undergo SCO at all (**Figure 1-10b**). By introducing a guest effect on the transition behaviour, such materials have the potential to act as molecular sensors, and the guest effect can be used as a probe to understand the subtle contributing effects that determine SCO behaviour.

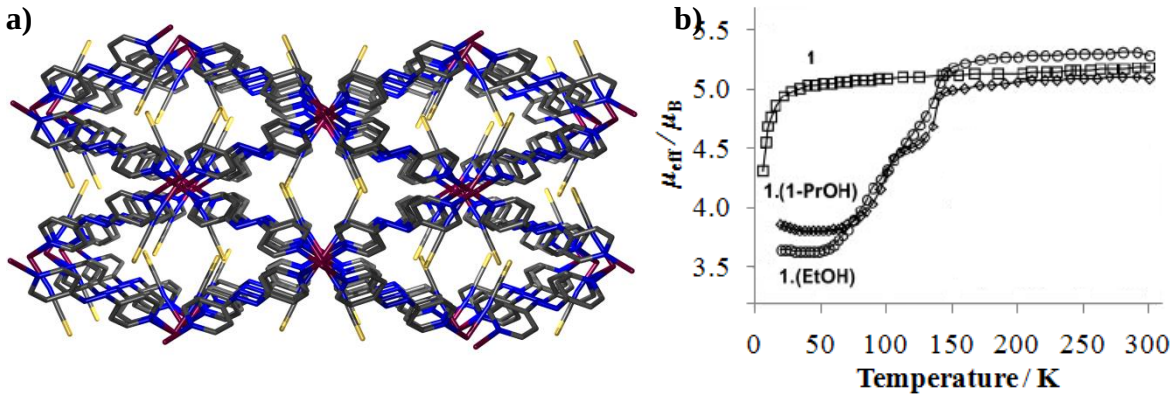

Figure 1-10: a) The crystal structure of guest-free $[Fe(azpy)_2(NCS)_2]$, showing the void spaces within the framework; and **b)** the variable temperature magnetic behaviour of the framework when solvated with different alcohol guests. Modified from Halder *et al*.[13]

1.4.3 *Pressure Effects*

In addition to temperature, another environmental factor that affects the behaviour of a SCO material is pressure.[74-78] Increasing the pressure favours the LS state, due to the shorter metal–ligand bonds, and the subsequently smaller volume this produces. Due to this LS stabilisation, a greater pressure will result in a higher transition temperature, and potentially increase the completeness of the spin transition.

Some materials are on the cusp of containing an appropriate environment for SCO, and are HS at atmospheric pressure, down to low temperature. By increasing the pressure, these materials can be induced to undergo spin transition. An example of such a material is the

discrete paramagnetic complex $[Fe(abpt)_2(NCS)_2]$ (abpt = 4-amino-3,5-bis(pyridine-2-yl)-1,2,4-triazole)[79] (**Figure 1-11a**). Increasing the ambient pressure on this material has been shown to make it SCO active, with greater pressures leading to higher spin transition temperatures (**Figure 1-11b**).

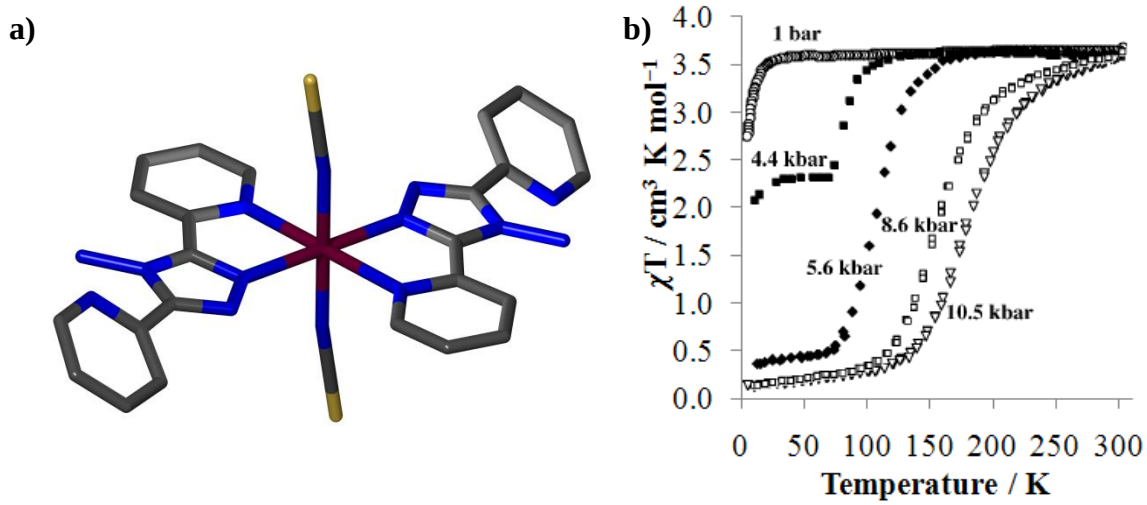

Figure 1-11: a) Single crystal structure of a single complex unit of $[Fe(abpt)_2(NCS)_2]$; and **b)** temperature-dependent magnetic behaviour of the material under different pressures. Modified from Gaspar *et al.*[79]

1.4.4 *Hofmann Frameworks*

Hofmann-type frameworks are characterised by a two-dimensional square grid of metal ions linked by cyanide units, with every second metal also coordinated by two axial ligands. The first known material of this type was discovered in 1897 by Hofmann, who formed a material consisting of square grids of nickel, with each of the metal centres connected to one another through four cyanide units, and every second metal centre also coordinated axially by two ammine ligands, with benzene guests filling the cavities, $[Ni(NH_3)_2Ni(CN)_4]\cdot C_6H_6$ (**Figure 1-12a**).[80-82] Hofmann-type clathrates have the form $[M(L)_2M'(CN)_4]$, and while they contain different metals, ligand and/or guest molecules, they nevertheless retain the same general structure as the original.[59,83-85]

The metal cyanide planes may be bridged by a linear *bis*-unidentate ligand, creating what is known as a *pillared Hofmann framework* (**Figure 1-12b**). These materials are three-dimensional and potentially robust porous frameworks.

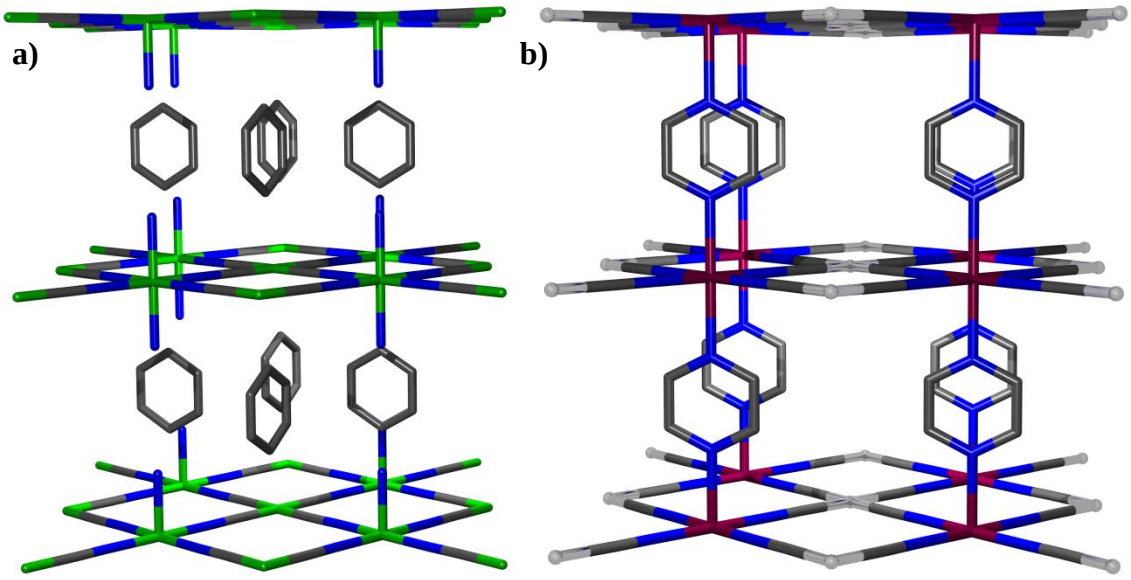

Figure 1-12: a) Crystal structure of the original Hofmann clathrate, $[Ni(NH_3)_2Ni(CN)_4]\cdot C_6H_6$;[80] and **b)** the crystal structure of [Fe(pyrazine)Pt(CN)$_4$], a pillared Hofmann-type framework which displays guest-dependent SCO behaviour.[8] Hydrogen atoms have been removed for clarity.

The Hofmann-type frameworks have a variety of desirable structural features for the study of SCO. The metal cyanide layer has a high degree of structural integrity, and with a suitably rigid choice of pillar ligand would produce a framework that is robust to desolvation and resolvation with minimal impact on the underlying structure. The $Fe(N)_6$ coordination sphere is appropriate to create SCO functionality for Fe(II), and the co-metal and pillar ligand provide a means to directly modify the ligand field strength. Choice of pillar ligand can also alter the shape and size of the framework pores, which combined with a guest-dependent effect, could give rise to new and interesting SCO behaviours.

Combining nanoporosity, such as is displayed by many Hofmann-type frameworks, with SCO behaviour creates a material that reversibly changes not only its magnetic behaviour, but also its void spaces when it undergoes SCO. This could in principle lead to controlled release/uptake of guest molecules. There is also often a strong host–guest interaction that affects the spin transition behaviour, leading to potential application of these porous SCO materials as molecular sensors.[86] The ease with which robust porous materials can undergo guest-exchange also allows for fundamental studies into structure–behaviour relationships of SCO materials. By analysis of the effects of adsorbed guests, the fine influences on spin transition behaviour can be systematically elucidated.

Certain Hofmann-type frameworks incorporating Fe(II) have already been shown to display SCO behaviour,[86-90] with the first such framework incorporating axially-bound pyridine coordinated to the Fe centres.[59] The first SCO pillared Hofmann framework, and the one on which there has been the most research, incorporated pyrazine as the pillar between adjacent Fe centres in the metal cyanide layers (**Figure 1-12b**).[8,91-95] This material has also been the major subject of research into the dynamic interplay between the SCO and host–guest function.[9,95]

1.4.5 *Effects and Characterisation of Spin Crossover Behaviour*

A number of physical properties of a SCO material change with the spin transition, due to the change in *d*-orbital occupancy between the LS and HS states. These can be analysed to give information on the SCO behaviour of the material.

The transfer of electrons between the t_{2g} and e_g orbitals alters the magnetic behaviour of the complex, and can be detected directly by measuring magnetic susceptibility as a function of temperature.[65] Due to the different electronic interactions between the ligands and the orbitals occupied in the HS and LS states, metal–ligand bond distances change.[96] For example, Fe(II) SCO materials usually have a coordination environment of six nitrogen donors around the iron, and typical Fe–N distances for the LS complex are 1.96–2.00 Å, and for the HS complex are 2.16–2.20 Å. This gives a typical transition bond length difference Δr_{LH} in the range 0.16–0.24 Å (see **Figure 1-5b**).[97] The change in bond length may also be accompanied by a change in the overall crystal structure, leading to a phase transition. These properties can be detected using variable temperature single crystal X-ray diffraction (SCXRD) and powder X-ray diffraction (PXRD). The change in *d*-orbital occupancy associated with a spin transition is accompanied by a thermochromic effect.[98] This visible colour change can be monitored using variable temperature UV/vis spectroscopy,[9] and often allows for preliminary identification of SCO behaviour, for example, by immersion of a potential SCO material in liquid nitrogen and visual identification of a colour change. Other methods for determining the spin transition behaviour by monitoring the relative proportion of the LS and HS states include ^{57}Fe Mössbauer spectroscopy,[66] and vibrational spectroscopy,[99-101] to analyse variation in the Fe–N bonds. Electron paramagnetic resonance,[66,102] nuclear magnetic resonance[102], X-ray absorption spectroscopy,[103] and calorimetry[104,105] can also be used.

Another property of the Fe(II) coordination sphere that can change over the spin transition is the octahedral angle distortion parameter (σ_{oct}). This is a measure of the variation in the observed coordination geometry away from a true octahedral geometry, and is the root mean square angle variation from 90°.[106] It is calculated using **Equation 1.1**, where θ_i are the 12 measured *cis* angles. Typical values for σ_{oct} are 1.8–4.1 for HS Fe(II), and 0–2.8 for LS Fe(II).[107]

$$\sigma_{oct}^2 = \frac{1}{12}\sum_{i=1}^{12}(\theta_i - 90°)^2 \qquad (1.1)$$

In calculating this quantity, the errors associated with the bond angle determination are highly correlated, so errors are not generally reported for this parameter.[108-111]

Variation in σ_{oct} commonly arises due to differences in the rigidity of coordination sphere between LS and HS Fe(II). In the HS state, the occupancy of the Fe(II) antibonding e_g orbitals produces a repulsive effect on the ligand orbitals which, in conjunction with the lower occupancy of electrons in the t_{2g} orbitals, favours the low energy distortion in the octahedral geometry. In the LS state, the e_g orbitals are empty and the t_{2g} orbitals have full occupancy. The repulsive interactions between the ligand orbitals and these metal orbitals, which lie between the ligand axes, lead to the complex favouring a more rigidly octahedral geometry, resulting in a lower octahedral angle distortion parameter.

Another relevant difference related to the ligand–metal bond over the spin transition is in the linearity of the Fe(II)–N≡C bond, which in turn is influenced by the strength of π backbonding behaviour through the metal–ligand bond. As shown in **Figure 1-13**, the Fe(II)–NC bond involves electron donation from the cyanide Highest Occupied Molecular Orbital (HOMO) to an empty orbital of the Fe(II) through a σ bond. Additionally, there is electron donation from a Fe(II) t_{2g} orbital to the Lowest Unoccupied Molecular Orbital (LUMO, π*) of the cyanide through π backbonding. In the LS state, the electron occupancy of the t_{2g} orbital increases, thus the π back-donation ability of the Fe(II) increases, leading to a stronger Fe(II)–NC bond and a shorter bond length. Furthermore, in order to maximise metal–ligand orbital overlap for the stronger, more geometrically demanding LS bond, a more linear Fe–N≡C conformation is favoured.

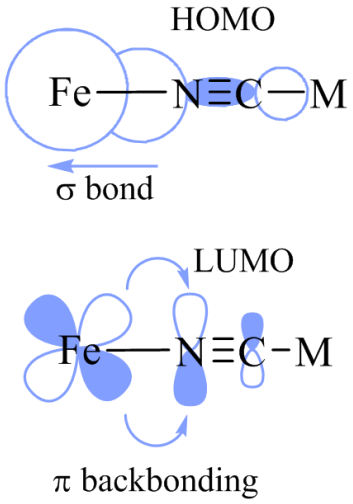

Figure 1-13: The Fe(II)–NC bond is stabilised by electron donation from the ligand HOMO to the metal through a σ bond, but also through π backbonding from a t_{2g} orbital of the Fe(II) to the LUMO (π*) orbital of the cyanide.

Unless otherwise stated, in this thesis the hysteresis width is calculated as the difference between the $T_{1/2}^{\uparrow}$ and $T_{1/2}^{\downarrow}$. A separate, and also useful, quantity is the *SCO range* parameter, which is a measure of the temperature interval over which the HS-to-LS or LS-to-HS transition occurs; here, this parameter is defined to be the temperature range over which the middle 90% of crossover sites undergo transition.

1.5 *Thermal Expansion*

As a material is heated, the added energy results in an increase in the population of higher vibrational modes in the inter-atomic bonds. As seen in **Figure 1-14**, the higher vibrational modes correspond to an increased average bond length, which in turn leads to macroscopic expansion in the material.

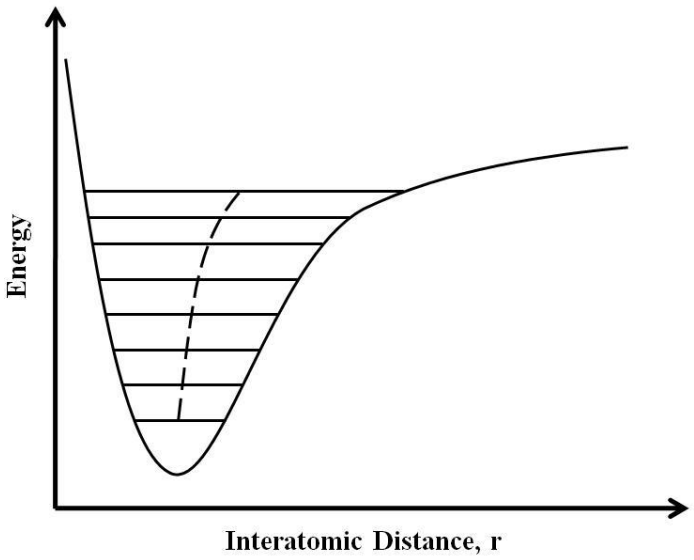

Figure 1-14: An anharmonic potential energy well, which is used here to describe the vibrational energies of an interatomic bond. Due to the anharmonicity, the slope of the lengthening side of the curve is lower than the shortening side, so as the higher vibrational states are occupied, the mean interatomic distance (dashed line) increases.

The rate at which a material expands is known as its *thermal expansion coefficient* (α), and is defined as the relative change in dimension with respect to temperature. As the different crystal axes can have different thermal expansion coefficients, it is useful to define both the volumetric (α_V) and linear (α_l) coefficients (**Equations 1.2** and **1.3**, respectively, where V_0 is the initial volume value, and l_0 is the initial unit cell parameter value):[112]

$$\alpha_V = \frac{\Delta V}{V_0 \Delta T} \tag{1.2}$$

$$\alpha_l = \frac{\Delta l}{l_0 \Delta T} \tag{1.3}$$

Furthermore, it can be shown that α is directly proportional to the change in the natural logarithm of the dimension with temperature. That is:

$$\frac{d}{dT}\ln(x) = \frac{1}{x} \cdot \frac{dx}{dT}$$

$$\therefore \alpha_x = \frac{d}{dT}\ln(x) \tag{1.4}$$

In isotropic solids, where the structure and thermal expansivity are equivalent along the three

crystallographic axes, **Equations 1.2** and **1.3** are related by $\alpha_V = 3\alpha_l$. However, the relationship between axial and volumetric thermal expansion coefficients in anisotropic materials is not so simple, as the thermal expansion behaviour may be different along each crystal axis. However, following from the result in **Equation 1.4**, it can be shown that in crystal systems with fixed angles (i.e., cubic, tetragonal, orthorhombic, hexagonal and rhombohedral crystal systems), the volume thermal expansion coefficient is equal to the sum of the coefficients of the unit cell parameters. That is:

$$\alpha_V = \alpha_a + \alpha_b + \alpha_c \tag{1.5}$$

Typical values for the thermal expansion coefficients of a material lie within the range $0 \times 10^{-6} < \alpha < 20 \times 10^{-6}$ K^{-1}.[113]

1.5.1 *Negative Thermal Expansion*

Due to the aforementioned principle that increased temperature leads to increased bond lengths, materials that contract upon warming are rarely observed, and their behaviour is generally due to supramolecular structural mechanisms. Several compounds have been shown to display negative thermal expansion (NTE), including certain metal oxides, zeolites and metal-organic frameworks.[112]

The mechanism by which NTE occurs depends greatly on the structural nature of the material. Oxide-based framework materials can be considered as a network of coordination polyhedra connected by single-atom linkages, either metal-oxygen-metal (M–O–M′, such as in ZrW_2O_8)[114] or oxygen–metal–oxygen (O–M–O′, such as in Cu_2O).[115] The NTE behaviour arises due to transverse vibrational displacement of the central linking atom away from the M···M′ or O···O′ axes, with the effect of bringing the outer atoms closer together (**Figure 1-15a**).[112] A similar effect is observed in cyanide-bridged materials, in which the cyanide linkers exhibit transverse vibrational modes of the metal–cyanide–metal (M–CN–M′) units, with the result that the metal anchors are drawn together along the M···M′ axis (**Figure 1-15b)**.[14,116-118]

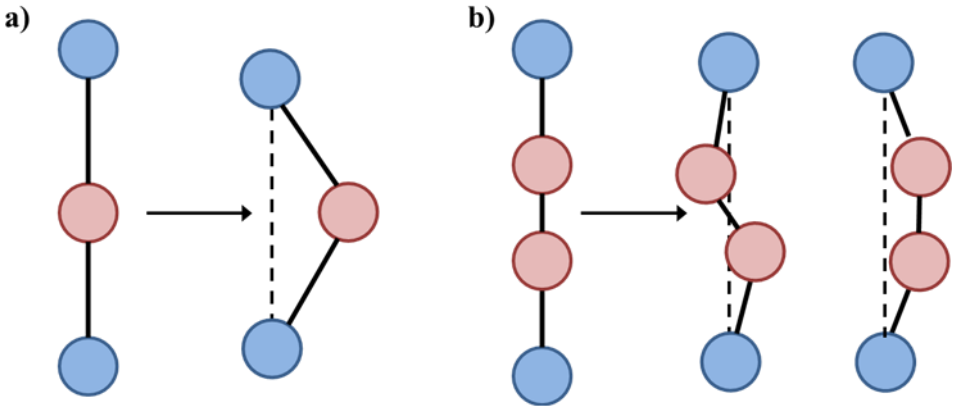

Figure 1-15: Transverse vibrational modes for **a)** an oxide-based framework material; and **b)** a cyanide-based framework material.

A major goal of thermal expansion research is to create materials that display anomalous thermal expansion properties of high magnitude. By studying such materials and the origin of their behaviour, greater understanding can be achieved of the underlying mechanisms involved, potentially leading to rational design of these properties in materials.

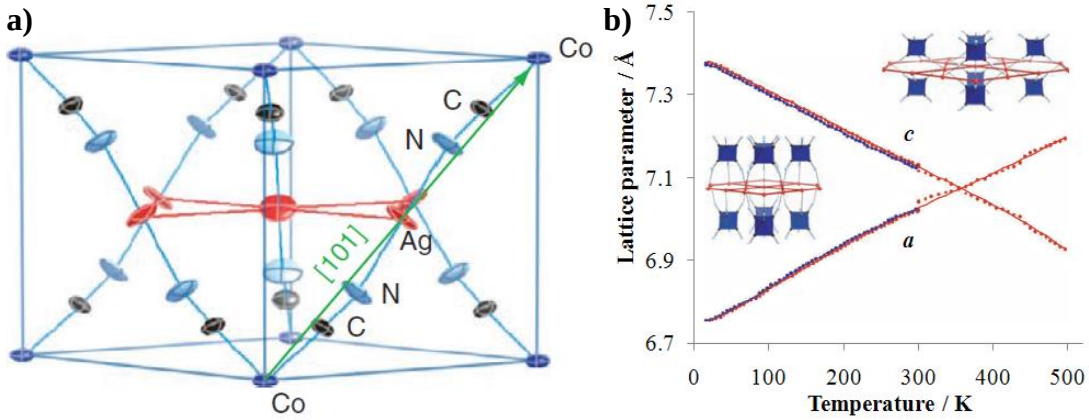

Figure 1-16: a) Crystal structure of the $Ag_3[Co(CN)_6]$ material, displaying argentophilic interactions between adjacent Ag atoms; and **b)** the temperature-dependence on the *a* and *c* unit cell parameters. It is clear that contraction in one dimension is coupled with expansion in the other. Reproduced from Goodwin *et al.*[119]

It was recently discovered that the framework material $Ag_3[Co(CN)_6]$ (**Figure 1-16)** displays anomalous uniaxial thermal expansion of a significantly greater magnitude than any previously reported, with $+130 \times 10^{-6} < \alpha_a < +150 \times 10^{-6}$ K^{-1} and $-120 \times 10^{-6} < \alpha_b < -130 \times 10^{-6}$ K^{-1}.[119] This result led to the definition of 'colossal' thermal expansion, to signify $|\alpha| \geq 100 \times 10^{-6}$ K^{-1}. This observed behaviour results from the combined effect of geometric

flexibility of the cyanide linkers with weak argentophilic interactions within the structure. The crystal acts in a similar way to garden lattice fencing: the linkage distances between structural nodes remain relatively constant, but the angles between the nodes have significant flexibility, such that compressing the lattice in one dimension leads to a corresponding expansion in the other, and *vice versa*.

A similar magnitude of uniaxial thermal expansion was observed in a single crystal of the organic molecule, (*S*,*S*)-octa-3,5-diyn-2,7-diol, with $+156 \times 10^{-6} < \alpha_a < +515 \times 10^{-6}$ K^{-1}, $-32 \times 10^{-6} < \alpha_b < -85 \times 10^{-6}$ K^{-1} and $-48 \times 10^{-6} < \alpha_c < -204 \times 10^{-6}$ K^{-1} (**Figure 1-17**).[120] Similar to the $Ag_3[Co(CN)_6]$ example, a large magnitude of positive thermal expansion in one dimension was coupled to negative thermal expansion in others, and arose due to the stacking energetics within the crystal. The molecules would arrange themselves to maintain shape complementarity, facilitating efficient packing and maximising interaction energies. As the atomic thermal displacement and bond lengths increased in keeping with normal thermal expansion behaviour, this led to a slight rearrangement of the stacking in order to optimise the intermolecular interaction energetics, and gave the resulting thermal expansion behaviour observed in the crystal.

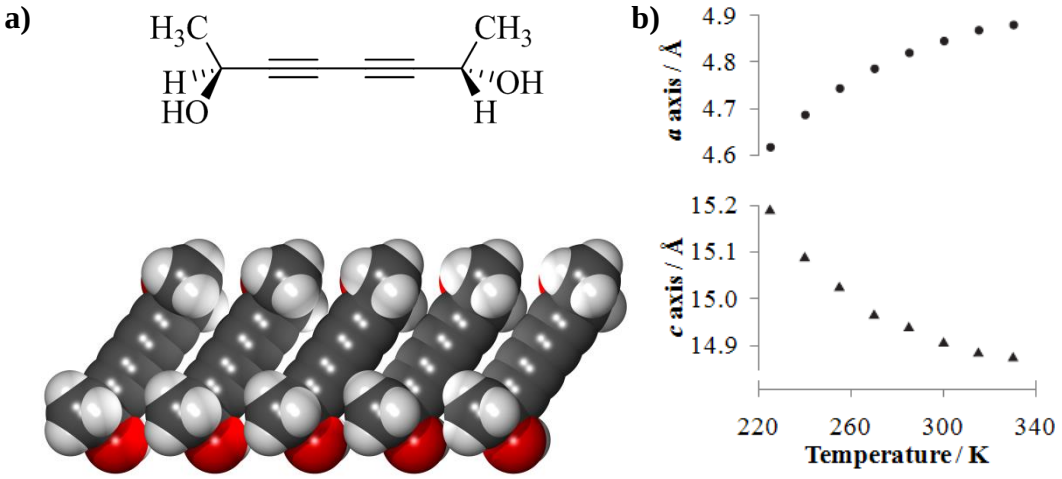

Figure 1-17: a) Molecular structure of (*S*,*S*)-octa-3,5-diyn-2,7-diol and crystal packing; and **b)** the temperature dependence of the *a* and *b* unit cell parameters. The inverse correlation between these parameters is clearly evident.[120]

As the thermal expansion coefficients are related to the *change* in the relevant unit cell parameter, it is often difficult to accurately establish this parameter at a given point when there are few or sparsely distributed data. It is therefore useful to fit a model equation to the

unit cell parameter values, and then use the derivative of this equation as the basis on which to calculate the thermal expansion coefficients at the temperatures studied.[121] The result is a smooth variation in the thermal expansion behaviour between each data point, with the exception of points of discontinuity, such as at phase transitions.

1.6 *Design of Nanoporous Fe(II) Spin Crossover Frameworks*

Nearly all known Fe(II) SCO materials contain an FeN_6 coordination sphere, in which the nitrogen donor atoms are usually aromatic and/or multiply-bonded to a carbon atom. Such coordination environments for SCO fall into three major categories:

1 All bound nitrogen-donor ligands are neutral, and the complex uses unbound counterions to balance the charge. $[Fe(3,3'\text{-dimethyl-}2,2'\text{-bipyridine})_3]^{2+}$ (**Figure 1-18a**) is a discrete example of such a system. The counterions often have a significant effect on the spin transition properties.[122]

2 Four nitrogen-donor ligands are aromatic and neutral with two negatively-charged cyanide derivatives coordinated to the Fe(II). The previously described $[Fe_2(4,4'\text{-azopyridine})_4(NCS)_4]$[13] material is an example of this environment within a coordination framework (**Figure 1-18b**).

3 Two aromatic nitrogen-donor ligands and four metal-bound cyanides coordinate to the Fe(II), assuming the structure of a *Hofmann-type* framework. The first such SCO material used pyridine at the axial sites of the Fe(II) and tetracyanidonickelate $[Ni(CN)_4]^{2-}$ to form the two-dimensional metal cyanide grid, $[Fe(pyridine)_2Ni(CN)_4]$ (**Figure 1-18c**).[59]

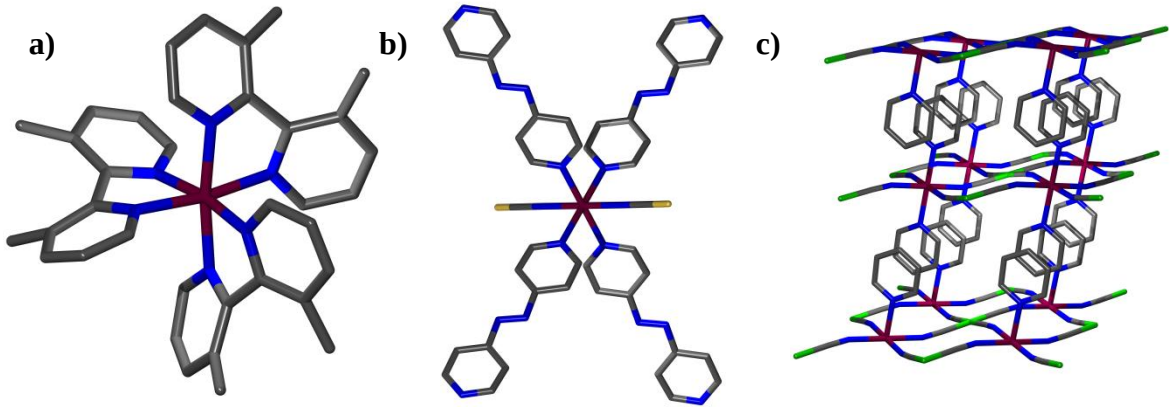

Figure 1-18: Examples of the different types of common Fe(II) SCO environments: **a)** $[Fe(3,3'\text{-dimethyl-}2,2'\text{-bipyridine})_3]^{2+}$;[122] **b)** a single complex unit of the coordination framework $[Fe(4,4'\text{-azopyridine})_2(NCS)_2]$;[13] and **c)** $[Fe(pyridine)_2Ni(CN)_4]$.[59] More information is given in the text.

The bis-unidentate pillar ligands pyrazine[8] and *trans*-4,4′-bispyridylethylene[123] (**Figure 1-19a**, **b**) have already been successfully incorporated into Hofmann-type SCO framework materials. The $[Fe(pyrazine)M(CN)_4]$ (M = Ni, Pd, Pt) frameworks have also been shown to demonstrate guest-dependent properties due to the robust porosity of lattice structure, which enabled significant variation in the spin transition behaviour. Through systematic study of these behaviours, theories as to some of the factors that contribute to the guest-dependent effect could be presented.[9,124]

Following the success of this framework family at producing such variable guest-dependent SCO behaviour, it was decided to incorporate the analogous bis-unidentate ligand, 1,2-bis(4′-pyridyl)acetylene (bpac) (**Figure 1-19c**) as a pillar ligand in Hofmann-type frameworks, and study the behaviour of the resulting frameworks. Bpac was chosen as it is a rigid, linear spacer terminated by pyridyl nitrogen donors, which have previously been incorporated into materials which display abrupt, cooperative spin transitions.[104,125-127] The length was anticipated to create significant porosity within the structure, enabling the potential for pronounced guest effects on the framework behaviour. Prior to this work, the bpac ligand had been incorporated in a limited number of coordination framework materials,[128,129] including in a pillared Hofmann-type framework.[130] Chapters 2 introduces these materials and their properties, and Chapter 3 focuses on guest-dependent studies on one of these materials.

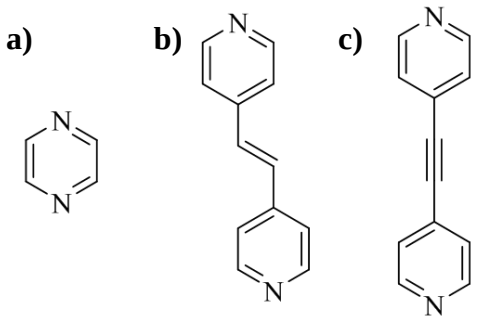

Figure 1-19: Pillar ligands incorporated into cyanide-bridged coordination frameworks: **a)** pyrazine, **b)** *trans*-1,2-bis(4′-pyridyl)ethylene, and **c)** 1,2-bis(4′-pyridyl)acetylene (bpac).

In addition to investigating the $[Fe(bpac)M(CN)_4]$ (M = Ni, Pd, Pt) materials, the linear cyanide linker, $[Au(CN)_2]^-$ was also incorporated into framework materials with bpac and Fe(II). The decreased connectivity of this unit was expected to increase the pore volume, further enhancing the guest effect in this framework. While the immediate ligand environment of the Fe(II) sites in the framework would be the same as for the $[M(CN)_4]^{2-}$ (M = Ni, Pd, Pt) based materials, the difference in the resulting structural topology would produce significantly different lattice behaviour and bulk properties of the framework. The linear linkers $[M(CN)_2]^-$ (M = Cu, Ag, Au) have already been incorporated in a limited number of SCO framework materials.[74,127,131] Chapter 4 introduces the properties of the framework $[Fe(bpac)(Au(CN)_2)_2]$, while Chapter 5 discusses its guest-dependent behaviour.

1.7 *References*

(1) Li, H.; Eddaoudi, M.; O'Keeffe, M.; Yaghi, O. M. *Nature* **1999**, *402*, 276.
(2) Kahn, O.; Martinez, C. J. *Science* **1998**, *279*, 44.
(3) Hollingsworth, M. D. *Science* **2002**, *295*, 2410.
(4) Lin, W. N., Helen L. *Chemistry of Nanostructured Materials* **2003**, 261.
(5) Hoskins, B. F.; Robson, R. *J. Am. Chem. Soc.* **1990**, *112*, 1546.
(6) Robson, R. *Dalton Trans* **2008**, 5113.
(7) Roland , A. F.; Christof, W. *Angew. Chem. Int. Ed.* **2008**, *47*, 8164.
(8) Niel, V.; Martinez-Agudo, J. M.; Muñoz, M. C.; Gaspar, A. B.; Real, J. A. *Inorg. Chem.* **2001**, *40*, 3838.
(9) Southon, P. D.; Liu, L.; Fellows, E. A.; Price, D. J.; Halder, G. J.; Chapman, K. W.; Moubaraki, B.; Murray, K. S.; Létard, J.-F.; Kepert, C. J. *J. Am. Chem. Soc.* **2009**, *131*, 10998.
(10) *Spin Crossover in Transition Metal Compounds*; Gütlich, P.; Goodwin, H. A., Eds., 2004; Vol. 1.
(11) Gütlich, P.; Garcia, Y.; Goodwin, H. A. *Chem. Soc. Rev.* **2000**, *29*, 419.
(12) Spiering, H.; Meissner, E.; Koppen, H.; Müller, E. W.; Gütlich, P. *Chem. Phys.* **1982**, *68*, 65.

(13) Halder, G. J.; Kepert, C. J.; Moubaraki, B.; Murray, K. S.; Cashion, J. D. *Science* **2002**, *298*, 1762.
(14) Goodwin, A. L.; Kepert, C. J. *Phys. Rev. B* **2005**, *71*, 1.
(15) Chapman, K. W.; Chupas, P. J.; Kepert, C. J. *J. Am. Chem. Soc.* **2006**, *128*, 7009.
(16) Desiraju, G. R. *Angew. Chem. Int. Ed.* **2007**, *46*, 8342.
(17) Kitagawa, S.; Kitaura, R.; Noro, S.-I. *Angew. Chem. Int. Ed.* **2004**, *43*, 2334.
(18) Kepert, C. J. *Chem. Commun.* **2006**, 695.
(19) Lehn, J.-M. *Angew. Chem.* **1988**, *100*, 91.
(20) Du, M.; Zhang, Z.-H.; Tang, L.-F.; Wang, X.-G.; Zhao, X.-J.; Batten, S. R. *Chem. Eur. J.* **2007**, *13*, 2578.
(21) Ockwig, N. W.; Delgado-Friedrichs, O.; O'Keeffe, M.; Yaghi, O. M. *Acc. Chem. Res.* **2005**, *38*, 176.
(22) Rowsell, J. L. C.; Yaghi, O. M. *Microporous Mesoporous Mater.* **2004**, *73*, 3.
(23) Ma, S.; Sun, D.; Forster, P. M.; Yuan, D.; Zhuang, W.; Chen, Y.-S.; Parise, J. B.; Zhou, H.-C. *Inorg. Chem.* **2009**, *48*, 4616.
(24) Cao, X.-Y.; Yao, Y.-G.; Batten, S. R.; Ma, E.; Qin, Y.-Y.; Zhang, J.; Zhang, R.-B.; Cheng, J.-K. *Cryst. Eng. Commun.* **2009**, *11*, 1030.
(25) Batten, S. R.; Robson, R. *Angew. Chem. Int. Ed.* **1998**, *37*, 1460.
(26) Batten, S. R.; Hoskins, B. F.; Robson, R. *New Journal of Chemistry* **1998**, *22*, 173.
(27) Long, J. R.; Yaghi, O. M. *Chem. Soc. Rev.* **2009**, *38*, 1213.
(28) Kuppler, R. J.; Timmons, D. J.; Fang, Q.-R.; Li, J.-R.; Makal, T. A.; Young, M. D.; Yuan, D.; Zhao, D.; Zhuang, W.; Zhou, H.-C. *Coord. Chem. Rev.* **2009**, 253.
(29) Czaja, A. U.; Trukhan, N.; Müller, U. *Chem. Soc. Rev.* **2009**, *38*, 1284.
(30) Zhao, D.; Timmons, D. J.; Yuan, D.; Zhou, H.-C. *Acc. Chem. Res.* **2011**, *44*, 123.
(31) Sing, K. S. W.; Everett, D. H. E.; Haul, R. A. W.; Moscou, L. M.; Pierotte, R. A. P.; Rouquerol, J.; Siemieniewska, T. *Pure & Appl. Chem.*, **1985**, *57*, 603.
(32) Noro, S.-i.; Kitagawa, S.; Kondo, M.; Seki, K. *Angew. Chem. Int. Ed.* **2000**, *39*, 2081.
(33) Corbin, D. R.; Abrams, L.; Jones, G. A.; Eddy, M. M.; Harrison, W. T. A.; Stucky, G. D.; Cox, D. E. *J. Am. Chem. Soc.* **1990**, *112*, 4821.
(34) Larsen, S. C. *J. Phys. Chem. C* **2007**, *111*, 18464.
(35) Kepert, C. J.; Rosseinsky, M. J. *Chem. Commun.* **1999**, *1999*, 375.
(36) Morris, R. E.; Wheatley, P. S. *Angew. Chem. Int. Ed.* **2008**, *47*, 4966.
(37) Kaye, S. S.; Dailly, A.; Yaghi, O. M.; Long, J. R. *J. Am. Chem. Soc.* **2007**, *129*, 14176.
(38) Eddaoudi, M.; Kim, J.; Rosi, N.; Vodak, D.; Wachter, J.; O'Keeffe, M.; Yaghi, O. M. *Science* **2002**, *295*, 469.
(39) Millward, A. R.; Yaghi, O. M. *J. Am. Chem. Soc.* **2005**, *127*, 17998.
(40) Culp, J. T.; Smith, M. R.; Bittner, E.; Bockrath, B. *J. Am. Chem. Soc* **2008**, *130*, 12427.
(41) Ma, S.; Zhou, H.-C. *Chem. Soc. Rev.* **2010**, *46*, 44.
(42) Kondo, M.; Shimamura, M.; Noro, S.-i.; Minakoshi, S.; Asami, A.; Seki, K.; Kitagawa, S. *Chem. Mater.* **2000**, *12*, 1288.
(43) Uemura, K.; Kitagawa, S.; Kondo, M.; Fukui, K.; Kitaura, R.; Chang, H.-C.; Mizutani, T. *Chem. Eur. J.* **2002**, *8*, 3586.

(44) Nouar, F.; Eckert, J.; Eubank, J. F.; Forster, P.; Eddaoudi, M. *J. Am. Chem. Soc.* **2009**, *131*, 10394.
(45) Murray, L. J.; Dinca, M.; Long, J. R. *Chem. Soc. Rev.* **2009**, *38*, 1213.
(46) Li, J.-R.; Kuppler, R. J.; Zhou, H.-C. *Chem. Soc. Rev.* **2009**, *38*, 1477.
(47) Cambi, L.; Szegö, L. *Ber. Dtsch. Chem. Ges.* **1931**, *64*, 2591.
(48) Halcrow, M. A., Ed. *Spin Crossover Materials: Properties and Applications*; Wiley & Sons, Ltd.: United Kingdom, 2013.
(49) Gütlich, P.; Hauser, A.; Spiering, H. *Angew. Chem. Int. Ed.* **1994**, *33*, 2024.
(50) Petty, R. H.; Dose, E. V.; Tweedle, M. F.; Wilson, L. J. *Inorg. Chem.* **1978**, *17*, 1064.
(51) Dose, E. V.; Hoselton, M. A.; Sutin, N.; Tweedle, M. F.; Wilson, L. J. *J. Am. Chem. Soc.* **1978**, *100*, 1141.
(52) Beattie, J. K. In *Advances in Inorganic Chemistry*; Sykes, A. G., Ed.; Academic Press: 1988; Vol. 32, p 1.
(53) König, E. *Structure & Bonding: Nature and dynamics of the spin-state interconversion in metal complexes*; Springer Berlin / Heidelberg, 1991; Vol. 76.
(54) van Koningsbruggen, P. J.; Garcia, Y.; Kahn, O.; Fournes, L.; Kooijman, H.; Spek, A. L.; Haasnoot, J. G.; Moscovici, J.; Provost, K.; Michalowicz, A.; Renz, F.; Gütlich, P. *Inorg. Chem.* **2000**, *39*, 1891.
(55) Real, J. A.; Gaspar, A. B.; Niel, V.; Muñoz, M. C. *Coord. Chem. Rev.* **2003**, *236*, 121.
(56) Murray, K. S.; Kepert, C. J. *Top. Curr. Chem.* **2004**, *233*, 195.
(57) Létard, J.-F.; Guionneau, P.; Codjovi, E.; Lavastre, O.; Bravic, G.; Chasseau, D.; Kahn, O. *J. Am. Chem. Soc.* **1997**, *119*, 10861.
(58) Hayami, S.; Gu, Z.-z.; Einaga, Y.; Kobayasi, Y.; Ishikawa, Y.; Yamada, Y.; Fujishima, A.; Sato, O. *Inorg. Chem.* **2001**, *40*, 3240.
(59) Kitazawa, T.; Gomi, Y.; Takahashi, M.; Takeda, M.; Enomoto, M.; Miyazaki, A.; Enoki, T. *J. Mater. Chem.* **1996**, *6*, 119.
(60) Spiering, H.; Willenbacher, N. *J. Phys.: Condens. Matter* **1989**, *1*, 10089.
(61) Willenbacher, N.; Spiering, H. *J. Phys. C: Solid State Physics* **1988**, *21*, 1423.
(62) Sorai, M.; Ensling, J.; Gütlich, P. *Chem. Phys.* **1976**, *18*, 199.
(63) Tayagaki, T.; Galet, A.; Molnár, G.; Muñoz, M. C.; Zwick, A.; Tanaka, K.; Real, J. A.; Bousseksou, A. *J. Phys. Chem. B* **2005**, *109*, 14859.
(64) Pritchard, R.; Kilner, C. A.; Halcrow, M. A. *Chem. Comm.* **2006**, 577.
(65) Kröber, J.; Codjovi, E.; Kahn, O.; Grolière, F.; Jay, C. *J. Am. Chem. Soc.* **1993**, *115*, 9810.
(66) Vreugdenhil, W.; Van Diemen, J. H.; De Graaff, R. A. G.; Haasnoot, J. G.; Reedijk, J.; Van Der Kraan, A. M.; Kahn, O.; Zarembowitch, J. *Polyhedron* **1990**, *9*, 2971.
(67) Michalowicz, A.; Moscovici, J.; Ducourant, B.; Cracco, D.; Kahn, O. *Chem. Mater.* **1995**, *7*, 1833.
(68) Garcia, Y.; Kahn, O.; Rabardel, L.; Chansou, B.; Salmon, L.; Tuchagues, J. P. *Inorg. Chem.* **1999**, *39*, 4663.
(69) Real, J. A.; Bolvin, H.; Bousseksou, A.; Dworkin, A.; Kahn, O.; Varret, F.; Zarembowitch, J. *J. Am. Chem. Soc.* **1992**, *114*, 4650.
(70) Amoore, J. J. M.; Kepert, C. J.; Cashion, J. D.; Moubaraki, B.; Neville, S. M.; Murray, K. S. *Chem. Eur. J.* **2006**, *12*, 8220.
(71) Kitchen, J. A.; Jameson, G. N. L.; Tallon, J. L.; Brooker, S. *Chem. Comm.*

2010, *46*, 3200.
(72) Murray, K. S. *Aust. J. Chem.* **2009**, *62*, 1081.
(73) Leita, B. A.; Neville, S. M.; Halder, G. J.; Moubaraki, B.; Kepert, C. J.; Létard, J. F.; Murray, K. S. *Inorg. Chem.* **2007**, *46*, 8784.
(74) Agustí, G.; Thompson, A. L.; Gaspar, A. B.; Muñoz, M. C.; Goeta, A. E.; Rodriguez-Velamazan, J. A.; Castro, M.; Burriel, R.; Real, J. A. *Dalton Trans.* **2008**, *5*, 642.
(75) Gütlich, P.; Ksenofontov, V.; Gaspar, A. B. *Coord. Chem. Rev.* **2005**, *249*, 1811.
(76) Real, J. A.; Gaspar, A. B.; Muñoz, M. C. *Dalton Trans.* **2005**, 2062.
(77) Garcia, Y.; van Koningsbruggen, P. J.; Lapouyade, R.; Fournes, L.; Rabardel, L.; Kahn, O.; Ksenofontov, V.; Levchenko, G.; Gütlich, P. *Chem. Mater.* **1998**, *10*, 2426.
(78) Breuning, E.; Ruben, M.; Lehn, J.-M.; Renz, F.; Garcia, Y.; Ksenofontov, V.; Gütlich, P.; Wegelius, E.; Rissanen, K. *Angew. Chem. Int. Ed.* **2000**, *39*, 2504.
(79) Gaspar, A. B.; Muñoz, M. C.; Moliner, N.; Ksenofontov, V.; Levchenko, G.; Gütlich, P.; Real, J. A. *Monatsh. Chem.* **2003**, *134*, 285.
(80) Buttner, H. G.; Kearley, G. J. *Acta Cryst. B* **1994**, *50*, 431.
(81) Iwamoto, T.; Kiyoki, M.; Ohtsu, Y.; Takeshige-Kato, Y. *Bull. Chem. Soc. Jap.* **1978**, *51*, 488.
(82) Hofmann, K. A. *Z. anorg. Ch.* **1897**, *14*, 262.
(83) Powell, H. M.; Rayner, J. H. *Nature* **1949**, *163*, 556.
(84) Rayner, J. H.; Powell, H. M. *J. Chem. Soc.* **1952**, 319.
(85) Rayner, J. H.; Powell, H. M. *J. Chem. Soc.* **1958**, 3412.
(86) Galet, A.; Gaspar, A. B.; Muñoz, M. C.; Bukin, G. V.; Levchenko, G.; Real, J. A. *Adv. Mater.* **2005**, *17*, 2949.
(87) Niel, V.; Galet, A.; Gaspar, A. B.; Muñoz, M. C.; Real, J. A. *Chem. Commun.* **2003**, 1248.
(88) Agustí, G.; Gaspar, A. B.; Muñoz, M. C.; Real, J. A. *Inorg. Chem.* **2007**, *46*, 9646.
(89) Nakao, K.; Hayami, S.; Akita, M.; Katsuya, I. *Chem. Lett.* **2008**, *37*, 292.
(90) Agustí, G.; Cobo, S.; Gaspar, A. B.; Molnár, G.; Moussa, N. O.; Szilágyi, P. Á.; Pálfi, V.; Vieu, C.; Muñoz, C. M.; Real, J. A.; Bousseksou, A. *Chem. Mater.* **2008**, *20*, 6721.
(91) Cobo, S.; Ostrovskii, D.; Bonhommeau, S.; Vendier, L.; Molnár, G.; Salmon, L.; Tanaka, K.; Bousseksou, A. *J. Am. Chem. Soc.* **2008**, *130*, 9019.
(92) Volatron, F.; Catala, L.; Riviere, E.; Gloter, A.; Stephan, O.; Mallah, T. *Inorg. Chem.* **2008**, 6584.
(93) Boldog, I.; Gaspar, A. B.; Martinez, V.; Pardo-Ibanez, P.; Ksenofontov, V.; Bhattacharjee, A.; Gütlich, P.; Real, J. A. *Angew. Chem. Int. Ed.* **2008**, *47*, 6433.
(94) Ohtani, R.; Yoneda, K.; Furukawa, S.; Horike, N.; Kitagawa, S.; Gaspar, A. B.; Muñoz, M. C.; Real, J. A.; Ohba, M. *J. Am. Chem. Soc.* **2011**, *133*, 8600.
(95) Muñoz Lara, F. J.; Gaspar, A. B.; Aravena, D.; Ruiz, E.; Muñoz, M. C.; Ohba, M.; Ohtani, R.; Kitagawa, S.; Real, J. A. *Chem. Comm.* **2012**, *48*, 4686.
(96) Konno, M. M.-K., M. *Bull. Chem. Soc. Jap.* **1991**, *64*, 339.
(97) Hauser, A.; Jeftic, J.; Romstedt, H.; Hinek, R.; Spiering, H. *Coord. Chem. Rev.* **1999**, *190-192*, 471.
(98) Lavrenova, L. G.; Yudina, N. G.; Ikorskii, V. N.; Varnek, V. A.; Oglezneva, I.

M.; Larionov, S. V. *Polyhedron* **1995**, *14*, 1333.
(99) Molnár, G.; Niel, V.; Gaspar, A. B.; Real, J. A.; Zwick, A.; Bousseksou, A.; McGarvey, J. J. *J. Phys. Chem. B* **2002**, *106*, 9701.
(100) Molnár, G.; Niel, V.; Real, J. A.; Dubrovinsky, L.; Bousseksou, A.; McGarvey, J. J. *J. Phys. Chem. B* **2003**, *107*, 3149.
(101) Molnár, G.; Bousseksou, A.; Zwick, A.; McGarvey, J. J. *Chem. Phys. Lett.* **2003**, *367*, 593.
(102) Ozarowski, A.; Shunzhong, Y.; McGarvey, B. R.; Mislankar, A.; Drake, J. E. *Inorg. Chem.* **1991**, *30*, 3167.
(103) Gopakumar, T. G.; Bernien, M.; Naggert, H.; Matino, F.; Hermanns, C. F.; Bannwarth, A.; Mühlenberend, S.; Krüger, A.; Krüger, D.; Nickel, F.; Walter, W.; Berndt, R.; Kuch, W.; Tuczek, F. *Chemistry – A European Journal* **2013**, *19*, 15702.
(104) Niel, V.; Gaspar, A. B.; Muñoz, M. C.; Abarca, B.; Ballesteros, R.; Real, J. A. *Inorg. Chem.* **2003**, *42*, 4782.
(105) Galet, A.; Muñoz, M. C.; Gaspar, A. B.; Real, J. A. *Inorg. Chem.* **2005**, *44*, 8749.
(106) Robinson, K.; Gibbs, G. V.; Ribbe, P. H. *Science* **1971**, *172*, 567.
(107) Halcrow, M. A. *Chemical Society Reviews* **2011**, *40*, 4119.
(108) Klingele, J.; Kaase, D.; Klingele, M. H.; b, J. L. *Dalton Trans.* **2012**, *41*, 1397.
(109) Falvello, L. R.; Forcen-Vazquez, E.; Mayoral, I.; Tomas, M.; Palacio, F. *Acta Crystallogr. C* **2011**, *67*, m359.
(110) Dudka, A.; Mill, B.; Pisarevsky, Y. *Crystallogr. Rep.* **2009**, *54*, 558.
(111) Moubaraki, B.; Leita, B. A.; Halder, G. J.; Batten, S. R.; Jensen, P.; Smith, J. P.; Cashion, J. D.; Kepert, C. J.; Létard, J.-F.; Murray, K. S. *Dalton Trans* **2007**, 4413.
(112) Miller, W.; Smith, C.; Mackenzie, D.; Evans, K. *J. Mater. Sci.* **2009**, *44*, 5441.
(113) Krishnan, R. S. S., R.; Devanarayanan, S. *Thermal Expansion of Crystals, Pergamon, Oxford, 1979*.
(114) Evans, J. S. O.; Mary, T. A.; Vogt, T.; Subramanian, M. A.; Sleight, A. W. *Chemistry of Materials* **1996**, *8*, 2809.
(115) Sanson, A.; Rocca, F.; Dalba, G.; Fornasini, P.; Grisenti, R.; Dapiaggi, M.; Artioli, G. *Phys. Rev. B* **2006**, *73*, 214305.
(116) Goodwin, A. L.; Chapman, K. W.; Kepert, C. J. *J. Am. Chem. Soc.* **2005**, *127*, 17980.
(117) Pretsch, T.; Chapman, K. W.; Halder, G. J.; Kepert, C. J. *Chem. Commun.* **2006**, 1857.
(118) Chapman, K. W.; Chupas, P. J.; Kepert, C. J. *J. Am. Chem. Soc.* **2005**, *127*, 15630.
(119) Goodwin, A. L.; Calleja, M.; Conterio, M. J.; Dove, M. T.; Evans, J. S. O.; Keen, D. A.; Peters, L.; Tucker, M. G. *Science* **2008**, *319*, 754.
(120) Das, D.; Jacobs, T.; Barbour, L. J. *Nat. Mater.* **2010**, *9*, 36.
(121) Phillips, A. E.; Halder, G. J.; Chapman, K. W.; Goodwin, A. L.; Kepert, C. J. *Journal of the American Chemical Society* **2009**, *132*, 10.
(122) Craig, D. C.; Goodwin, H. A.; Onggo, D. *Austr. J. Chem.* **1988**, *41*, 1157.
(123) Niel, V.; Muñoz, M. C.; Gaspar, A. B.; Galet, A.; Levchenko, G.; Real, J. A. *Chem. Eur. J.* **2002**, *8*, 2446.
(124) Fellows, E. A. PhD Thesis, University of Sydney, 2011.
(125) Niel, V.; Martinez-Agudo, J. M.; Muñoz, M. C.; Gaspar, A. B.; Real, J. A.

Inorg. Chem. **2001**, *40*, 3838.
(126) Muñoz, M. C.; Gaspar, A. B.; Galet, A.; Real, J. A. *Inorg. Chem.* **2007**, *46*, 8182.
(127) Agustí, G.; Muñoz, M. C.; Gaspar, A. B.; Real, J. A. *Inorg. Chem.* **2008**, *2008*, 2552.
(128) Dong, Y.-B.; Layland, R. C.; Smith, M. D.; Pschirer, N. G.; Bunz, U. H. F.; zur Loye, H.-C. *Inorg. Chem.* **1999**, *38*, 3056.
(129) Carlucci, L.; Ciani, G.; Proserpio, D. M. *Dalton* **1999**, 1799.
(130) Culp, J. T.; Natesakhawat, S.; Smith, M. R.; Bittner, E.; Matranga, C.; Bockrath, a. B. *J. Phys. Chem. C* **2008**, *112*, 7079.
(131) Niel, V.; Muñoz, C. M.; Gaspar, A. B.; Galet, A.; Levchenko, G.; Real, J. A. *Chem. Eur. J.* **2002**, *8*, 2446.

Chapter 2: Pillared Hofmann-Type Frameworks, $[Fe(bpac)M(CN)_4]\cdot 0.5(bpac)\{EtOH\}$ (M = Ni, Pd, Pt)

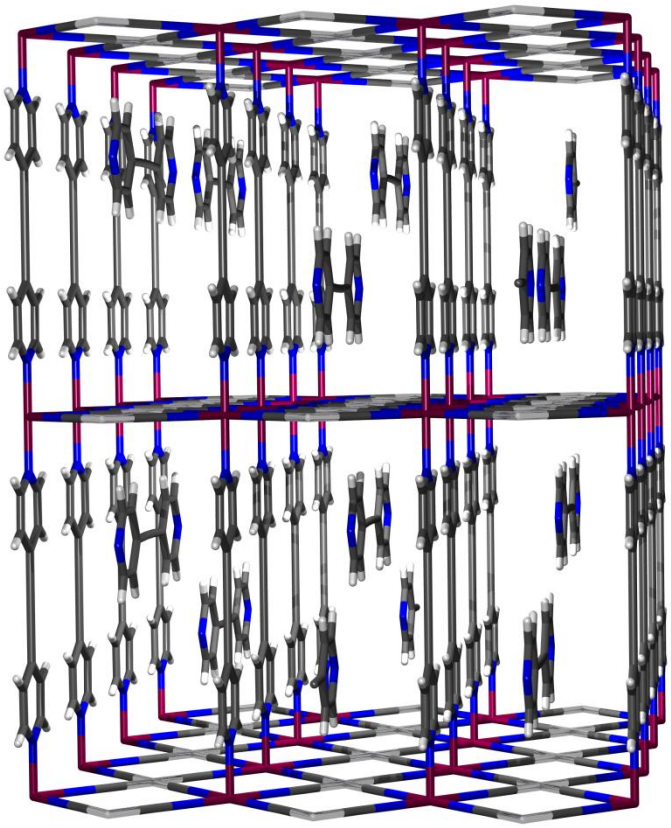

Structure of the $[Fe(bpac)M(CN)_4]\cdot 0.5(bpac)$ (M = Ni, Pd, Pt) frameworks

2.1 *Outline*

The synthesis and characterisation of the family of Hofmann-type SCO materials, $[Fe(bpac)M(CN)_4]\cdot 0.5(bpac)$ (bpac = 1,2-bis(4′-pyridyl)acetylene; M = Ni, Pd, Pt) is described. These frameworks display reversible SCO with hysteresis at close to room temperature and demonstrate a guest-dependent effect on the spin transition. This chapter will mainly focus on the structural properties of the framework, and the temperature-dependent behaviour of the ethanol-solvated material, and the following chapter will explore the guest-dependent effect on the behaviour of the framework.

It should be noted that these materials were first discovered and preliminary investigations into their properties took place during this candidate's Honours research, and are presented in the thesis for that degree (University of Sydney, 2009).[1] For completeness and ease of understanding, I have reproduced some of the data that were first published in my Honours thesis. Such data are acknowledged in the text.

It is of further note that while I was working on these materials, they were unreported and by all accounts, new. However, since I ceased research on these materials, Real and co-workers published data on them, including their structure and some of their properties.[2-4] While there is some overlap in results, mainly in the crystallography, the experiments published are quite different to those performed by me. However, they have cast into sharp relief the complexity of this system, and the great difficulty through which reproducible, fully explicable results would be obtained. In this thesis I make reference to the published results where they complement and help explain my results. Full acknowledgement of the published data is given where relevant.

2.2 *Preparation of the Frameworks*

The $[Fe(bpac)M(CN)_4]\cdot 0.5(bpac)$ (M = Ni, Pd, Pt, hereafter denoted as **Ni**, **Pd** and **Pt**, respectively) frameworks were prepared in bulk for analysis using the method described in **§7.3.1**.

It was discovered that bulk synthesis of these materials using different relative concentrations of bpac produced materials with significantly different spin transition properties. In order to ensure optimum ligand and guest occupancy of bpac, an excess of the ligand was used in the

synthesis.

2.3 *Single Crystal X-Ray Diffraction*

Single crystals were grown using the H-cell diffusion method described in **§7.3.2**, from a 1:1 solvent mixture of ethanol (EtOH) and water.

Preliminary structural solutions and refinements of **Pd** and **Pt** were first presented and described in my 2009 Honours thesis. It is important to note that in this thesis, curly brackets {} are placed after a framework material to indicate that the solvent guest molecule(s) written within the brackets are included within the framework pores. When presented without a preceding number, the precise quantity of guest within the framework is unknown. In a similar manner, '{Ø}' is used to indicate when sample analysis occurred under static vacuum.

Data were collected for full structural determination of **Pd**·{EtOH/H_2O} and **Pt**·{EtOH/H_2O} at 100 K, below the spin transition temperature. Data were unable to be collected above the spin transition temperature, as the crystal desolvated and the diffraction quality was poor. Structural data and refinement parameters are summarised in **Table 2-1** and full data tables are given in **Appendix A**.

The crystal structures determined for **Pd** and **Pt** are isostructural, and their topology is analogous to the Hofmann frameworks generated using pyrazine,[5] with the addition of unbound bpac molecules included within the pores of the structure. While diffraction-quality single crystals of **Ni** were not obtained, a Rietveld refinement using synchrotron X-ray powder diffraction data and a model based on **Pt** shows it to be isostructural with the other two frameworks (see **§2.4**).

The asymmetric units of **Pd**·{EtOH/H_2O} and **Pt**·{EtOH/H_2O} (**Figure 2-1**) include an Fe(II) centre coordinated to one quarter of a bpac molecule and a cyanide unit, which is also coordinated to a palladium/platinum atom. A quarter of a non-coordinated bpac guest molecule is also included in the asymmetric unit with half occupancy, as well as an additional guest water molecule with half occupancy in the **Pt** structure, which was modelled as an oxygen atom. It is expected that water would also be present in the **Pd** crystal, but it could not be resolved in the Fourier difference map for this structure, and it was subsequently not modelled.

Table 2-1: Summary of the single crystal X-ray collection and refinement for **Pd**·{EtOH/H_2O} in the *Pmmm* and *P*4/*mmm* space groups, and **Pt**·{EtOH/H_2O}. The *P*4/*mmm* solution is shaded grey as it is less chemically reasonable than the *Pmmm* model, as discussed in the text.

	Pd	**Pd**	**Pt**
Empirical formula	$C_{22}H_{12}FeN_7Pd$	$C_{28}H_{16}FeN_8Pd$	$C_{28}H_{18}FeN_8OPt$
Formula weight / g mol^{-1}	536.64	536.64	643.34
Temperature / K	100(2)	100(2)	100(2)
Wavelength / Å	0.71073	0.71073	0.71073
Crystal system	Orthorhombic	Tetragonal	Orthorhombic
Space group	*Pmmm*	*P*4/*mmm*	*Pmmm*
a / Å	7.1928(7)	7.1882(3)	7.1440(6)
b / Å	7.1870(6)	7.1882(3)	7.2021(6)
c / Å	13.6699(14)	13.6665(12)	13.6945(14)
V / Å^3	706.66(12)	706.15(7)	704.61(11)
Z	1	1	1
ρ_{calc} / Mg/m^3	1.261	1.262	1.516
μ / mm^{-1}	1.167	1.168	5.495
F(000)	265	265	307
Crystal size / mm^3	0.04 × 0.04 × 0.008	0.04 × 0.04 × 0.008	0.06 × 0.05 × 0.008
Theta range / °	4.01–28.27	4.01–30.15	4.02–34.30
Index ranges	$-9 \le h \le 9$	$-10 \le h \le 10$	$-11 \le h \le 11$
	$-9 \le k \le 9$	$-10 \le k \le 9$	$-11 \le k \le 10$
	$-10 \le l \le 18$	$-19 \le l \le 10$	$-13 \le l \le 21$
Reflections collected	5966	6659	10812
Independent reflections [R_{int}]	1051 [0.0468]	672 [0.0487]	1724 [0.0435]
Completeness to θ / %	98.3 (to 28.27°)	98.1 (to 30.15°)	99.6 (to 34.30°)
Data / restraints / parameters	1051 / 90 / 68	672 / 36 / 58	1724 / 36 / 70
Goodness-of-fit on F^2	1.060	1.241	1.132
R indices, I > 2σ(I), (R_1,[(a)] wR_2[(b)])	0.0601, 0.1581	0.0535, 0.1542	0.0255, 0.0672
R indices, all data, (R_1,[(a)] wR_2[(b)])	0.0780, 0.1743	0.0645, 0.1628	0.0257, 0.0672
Largest peak and hole / e.Å^{-3}	2.823 and −1.469	2.615 and −1.006	5.004 and −2.182

[(a)] $R_1 = \Sigma \, | \, |F_o| - |F_c| \, | \, / \, \Sigma \, |F_o|$, [(b)] $wR_2 = \{\Sigma \, [w(F_o^2 - F_c^2)^2] \, / \, \Sigma \, [w(F_o^2)^2]\}^{1/2}$

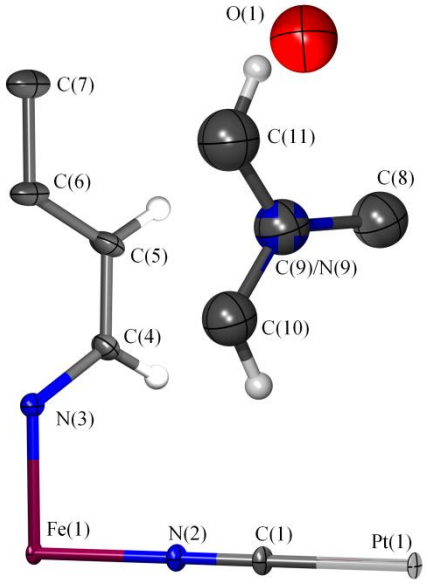

Figure 2-1: The crystallographic asymmetric unit of **Pt**·{EtOH/H_2O}. The asymmetric unit of **Pd**·{EtOH/H_2O} is identical, with the exception that the oxygen atom is not modelled (See **Figure B-1**).

Table 2-2: Fe(II)–N bond lengths and octahedral angle distortion parameter (σ_{oct}),[(1)] as obtained by SCXRD for **Pd**·{EtOH/H_2O} and **Pt**·{EtOH/H_2O} at 100 K.

	Pd	**Pt**
Fe–N_{CN} / Å	1.9424(1)	1.9333(1)
Fe–N_{bpac} / Å	1.9915(2)	1.9960(2)
Fe σ_{oct} / °	0.03	0.18

The Fe–N bond lengths for **Pd**·{EtOH/H_2O} and **Pt**·{EtOH/H_2O} can be seen in **Table 2-2**. All distances are indicative of a LS Fe(II) ligand field (see **§1.4.5**), and there is little difference in the Fe–N bond lengths between the two frameworks. Similarly, the σ_{oct} values are low, consistent with those expected for a LS Fe(II) coordination environment.[6]

The Fe(II) centre has an axially elongated octahedral environment with four nitrile-donating cyanido ligands in the equatorial plane and two axial pyridyl N-donors. The cyanido units are part of a square planar tetracyanidometallate(II) (metal = palladium/platinum) building unit, which combine with the Fe(II) to form a square grid of cyanido-bridged alternating Fe and

(1) The magnitude of this parameter is influenced to some degree by the crystal twinning properties, and would be zero for a 50:50 twin with unit cell parameters $a = b$, which is the case for the P4/mmm structure.

Pd/Pt atoms, following the standard Hofmann-type structure.[7-9] The X-ray crystal structures of the two frameworks were solved and refined successfully in the orthorhombic space group *Pmmm*. In these, the pyridyl rings lie parallel to each other locally, but have an overall disorder over the parallel and perpendicular positions relative to one another in the crystal. This was modelled using the twin law {010, 100, 00-1}, which refined to give a twin component parameter (BASF) of 0.513 for **Pd**·{EtOH/H_2O} and 0.169 for **Pt**·{EtOH/H_2O}. This number provides a quantitative measure of the relative portions of the framework that have the pyridyl rings placed over the two orientations.

Free bpac guest is present within the pores of both structures, centred approximately halfway between the centre of the pyridyl ring and the alkyne bond of the bound bpac. This bpac guest displays intermolecular interactions with the bound bpac ligand through off-centre parallel aromatic stacking interactions (there is a characteristic distance between bound and unbound bpac pyridyl rings of 3.5935(3) Å).[10] The bpac guest is disordered over two positions related by translation along the long axis of the molecule such that the pyridyl groups overlap their positions, leading to a shared half-occupancy of the pyridyl nitrogen and the opposite, alkyne-bonded carbon. The guest bpac rings in both frameworks lie parallel to the bound bpac rings (**Figure 2-2**).

It is worth noting that the most chemically reasonable crystallographic model of the unbound bpac has half occupancy of this molecule within the framework pores. There is not enough pore space for the bpac molecules to occupy positions with pyridyl rings directly above/below one another along the *c*-axis. This is demonstrated by the pyridyl C–H···H–C distances of 0.7120(1) Å in the **Pd**·{EtOH/H_2O} framework, and 0.9175(1) Å in the **Pt**·{EtOH/H_2O} framework, which are considerably shorter than the sum of their Van der Waals radii (~2.0 Å). Considering this physical restriction, the bpac guest molecules are expected to lie adjacent to one another in the *ab*-plane, and/or staggered over the two positions along the *c*-axis in the pores, with a maximum occupancy of 0.5 bpac guest per framework formula unit.

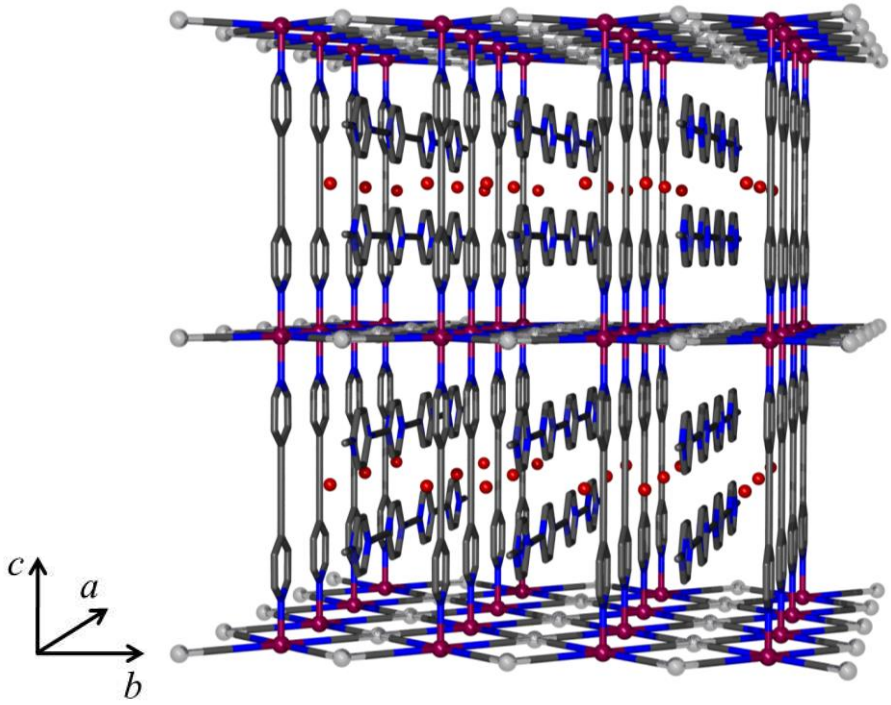

Figure 2-2: The structure of **Pt**·{EtOH/H_2O}, determined using single crystal X-ray diffraction. Hydrogen atoms are omitted for clarity. The **Pd**·{EtOH/H_2O} structure does not include the modelled lattice water molecule but is otherwise isostructural (**Figure B-4**).

The free, unbound bpac guest molecules introduce a potential degree of freedom linked to the occupancy of the molecule within the framework pores. It may be possible to generate different bpac guest concentrations in the lattice pores by limiting the amount of bpac ligand in the synthesis. This would create an increased solvent-accessible volume, and result in different guest internal pressure effects. This is an important feature, described in detail by Real,[3] and will be discussed further in the next chapter.

The **Pd**·{EtOH/H_2O} crystal structure also refined well in the tetragonal space group *P4/mmm* (shown in grey in **Table 2-1**). This results in a crystal structure with higher symmetry, in which the pyridyl rings of the bpac pillar ligands are 50:50 disordered fully within the framework, over positions parallel and perpendicular to one another. Chemically, it is believed that the pyridyl groups are aligned with each other locally, due to aromatic stacking interactions mediated by the guest bpac molecules. However, because the *a* and *b* unit cell parameters are so similar, this orientation may not be conveyed between layers, leading to disorder in the positions of the pyridyl groups across the lattice layers. There may also be discrete crystallite domains within lattice layers in which the pyridyl rings adopt parallel conformations locally, but have long-range disorder over the different domains. This

pseudo-merohedral twinning leads to an overall disorder of the pyridyl rings over the parallel and perpendicular positions, resulting in the apparent tetragonal symmetry. See **Appendix A** for further crystallographic information on this solution, and **Figure B-6** for pictures of the resulting crystal structure. Pseudo-merohedral twinning was similarly observed in the [Fe(pyrazine)Ni(CN)$_4$] framework, which was also refined in the orthorhombic *Pmmm* space group with a twin relation, but refined very well using the tetragonal *P*4/*mmm* space group.[5]

2.4 *Powder X-ray Diffraction*

Magnetic susceptibility measurements on the **Ni**·{EtOH}, **Pd**·{EtOH} and **Pt**·{EtOH} frameworks (**§2.6**) demonstrated that all three framework materials underwent spin transition. However, it was necessary to confirm that bulk synthesis of **Pd** and **Pt** produced the same material as was structurally characterised by single crystal X-ray diffraction. For this confirmation, powder X-ray diffraction (PXRD) studies were performed on the HS and LS states of the frameworks, and Le Bail fits to the powder patterns were used to confirm the structures. The fits successfully demonstrated that bulk synthesis produces a crystalline material with the expected unit cell parameters for the above frameworks, though guest bpac occupancy could not be determined using this refinement method. The relevant model fits can be seen in **Figure C-1** to **Figure C-5**.

These powder diffraction measurements were carried out at the Australian Synchrotron at 310 K (HS) and 250 K (LS). Synchrotron PXRD was also used to confirm that **Ni** is structurally analogous to **Pd** and **Pt**, and Rietveld methods were used to fit a model based on the **Pt** crystal structure to the data. The powder diffraction pattern demonstrated a greater degree of amorphous scattering for the **Ni** sample compared to the **Pd** and **Pt** samples. The resulting model gave the expected isostructural solution with R_{wP} = 0.061, and data are presented in **Appendix A**. The asymmetric unit can be seen in **Figure B-1** and the resulting framework lattice in **Figure B-5**, and fits to the powder diffractograms are given in **Figure C-6** and **Figure C-7**.

As seen in **Table 2-3**, there is some discrepancy between the unit cell parameters obtained by single crystal diffraction and powder diffraction of the LS **Pd**·{EtOH} and **Pt**·{EtOH}. Comparison of the *a*- and *b*-parameters for **Pt**·{EtOH} shows that the PXRD values differ from the SCXRD values by −0.033 Å and +0.028 Å respectively, becoming closer to a

tetragonal unit cell. The source of this apparent difference could be because the resolution of the powder diffractogram was not sufficiently high to detect the subtle change in magnitude of the *a*- and *b*-parameters even though the refinement was modelled on an orthorhombic cell, so it instead took an effective average of the two parameters.

Table 2-3: Unit cell parameters and linear Fe–M–Fe distance ($d_{Fe–M–Fe}$) for **Ni**·{EtOH}, **Pd**·{EtOH} and **Pt**·{EtOH} refined from Synchrotron PXRD at 310 and 250 K, and **Pd**·{EtOH/H_2O} and **Pt**·{EtOH/H_2O} refined from SCXRD at 100 K. Also shown are values for the orthorhombic *Pmmm* and tetragonal *P*4/*mmm* space group solutions of **Pd**·{EtOH}, and the SCXRD data for **Pt**·{H_2O}, published by Real and solved in the *P*4/*mmm* space group (shown at the bottom in grey).[2]

	Space Group	Unit Cell Parameter / Å			$d_{Fe–M–Fe}$ / Å
		a	*b*	*c*	
$Ni_{HS\ PXRD}$ 310 K	*Pmmm*	7.2697(4)	7.2719(6)	14.0212(7)	10.2825(7)
$Ni_{LS\ PXRD}$ 250 K	*Pmmm*	7.0171(5)	7.0210(8)	13.6464(8)	9.9264(9)
$Pd_{HS\ PXRD}$ 310 K	*Pmmm*	7.4461(6)	7.4534(6)	14.0374(2)	10.5355(8)
$Pd_{HS\ PXRD}$ 310 K	*P*4/*mmm*	7.4467(2)	7.4467(2)	14.0321(5)	10.5312(3)
$Pd_{LS\ PXRD}$ 250 K	*Pmmm*	7.2579(6)	7.1077(6)	13.63861(18)	10.1586(8)
$Pd_{LS\ PXRD}$ 250 K	*P*4/*mmm*	7.18139(9)	7.18139(9)	13.63886(19)	10.1560(1)
$Pd_{LS\ SCXRD}$ 100 K	*Pmmm*	7.1928(7)	7.1870(6)	13.6699(14)	10.1681(9)
$Pd_{LS\ SCXRD}$ 100 K	*P*4/*mmm*	7.1882(3)	7.1882(3)	13.6665(12)	10.165(1)
$Pt_{HS\ PXRD}$ 310 K	*Pmmm*	7.4342(3)	7.4395(3)	14.0151(1)	10.5173(4)
$Pt_{LS\ PXRD}$ 250 K	*Pmmm*	7.1777(3)	7.1741(2)	13.6375(1)	10.1483(4)
$Pt_{LS\ SCXRD}$ 100 K	*Pmmm*	7.1440(6)	7.2021(6)	13.6945(14)	10.1443(8)
$Pt_{LS\ SCXRD}$ 120 K	*P*4/*mmm*	7.1700(2)	7.1700(2)	13.6620(2)	10.1399(3)

However, this explanation cannot be applied to the 0.057 Å difference in the *c*-parameter, as the (00l) peaks are well defined and should refine to give an accurate value. A possible cause of this difference, and reason why the powder diffraction data were refined to the near-tetragonal unit cell, could be because the single crystal was solvated with EtOH and H_2O, while the powder was solvated with just EtOH. This difference in the included solvent may create different internal pressure effects, potentially leading to different framework bond lengths and distortion of the cyanide layers. Different occupancies of the bpac guest may also contribute to this difference, as they would also produce different internal pressure effects. It

is expected that there is a similar source for the discrepancy between the unit cell parameters published here for **Pt**, and those previously obtained by Real.[2]

As explained in **§1.4.5**, the spin transition can be followed by a change in the Fe–N bond distance. In these frameworks, this distance lies along the diagonal between the *a*- and *b*-parameters: $d_{\mathrm{Fe–M–Fe}} = \sqrt{a^2 + b^2}$, linearly intersecting the co-metal along the Fe–M–Fe dimension. As seen in **Table 2-3**, the $d_{\mathrm{Fe–M–Fe}}$ value in the HS **Pt**·{EtOH} is *ca*. 0.37 Å longer than that in the LS **Pt**·{EtOH} material, which is within the expected range of the HS-to-LS difference of two Fe–N bond lengths. The different $d_{\mathrm{Fe–M–Fe}}$ values between the **Ni**, **Pd** and **Pt** frameworks can be attributed to the different ionic radii of the co-metal in the framework (see **§2.7** for more detailed discussion on this).

When the powder diffractograms for **Pd**·{EtOH} were refined in an orthorhombic unit cell, the *a*- and *b*-parameters for the LS phase differed even more markedly from the single crystal model, by +0.065 Å and -0.079 Å respectively, with divergence of the unit cell parameters. The single crystal structure was solved equally well in a tetragonal unit cell, so to confirm that this observed change in the parameters was real, a tetragonal model was also fitted to the powder data. A comparison of these two fits is seen in **Figure C-2** and **Figure C-3**. As expected from their similar parameter values, both models appear to give nearly indistinguishable fits to the powder pattern, with the most notable difference being the (013) peak at *ca*. 2θ = 9.05°, which is better fitted using the orthorhombic unit cell. Conversely, the HS unit cell parameters are close to tetragonal, though the model was solved in an orthorhombic space group. This discrepancy between the PXRD and SCXRD data in the LS unit cell parameters may be attributed to similar solvent effects as were discussed above for **Pt**.

The similarities between the PXRD and SCXRD data for the calculated $d_{\mathrm{Fe–M–Fe}}$ values confirm that the differences between the unit cell parameters are predominantly due to apparent flexing of the cyanide layers, rather than major changes in the bond lengths. The $d_{\mathrm{Fe–M–Fe}}$ values differ by less than 0.01 Å for both **Pd** and **Pt**.

2.5 *Elemental Analysis*

As shown in the single crystal structures (**§2.3**), these frameworks contain guest bpac

molecules within the structural pores. In his work on these materials, Real has demonstrated the extreme importance of the proportion of free bpac molecules within the pores on the SCO properties.[3] In order to be able to compare this data with that of Real, it is necessary to determine the quantity of unbound bpac. The samples were desolvated by heating gently under vacuum, and sent to the elemental analysis facility at the University of Otago, New Zealand. Samples were analysed for Fe, C, N, H and the relevant co-metal, and where possible, two analyses were performed. The average quantities of these results are given in **Table 2-4**, and errors are shown where two analyses were performed which gave different results. Errors are estimated as the difference between the experimental results and the average.

Table 2-4: Experimental and calculated values (%) for the elemental composition of $[Fe(bpac)M(CN)_4]\cdot x(bpac)(H_2O)$, M = **Ni** ($x$ = 0.51), **Pd** (x = 0.55), and **Pt** (x = 0.55).

Ni	Exp.	Calc.	**Pd**	Exp.	Calc.	**Pt**	Exp.	Calc.
Fe	11	11.0		10	9.9		8.5(2)	8.6
M	11.5(5)	11.5		6.7	18.8		25.5(5)	29.9
C	52.54(11)	52.2		48.69(5)	48.16		41.52(9)	41.6
N	18.81(1)	19.3		17.45(2)	17.6		15.18(1)	15.24
H	2.74(7)	2.79		2.46(2)	2.57		2.25(5)	2.22
O	-	3.15		-	2.84		-	2.45

As seen in **Table 2-4**, the data match quite well to the calculated result for a formula containing ~0.5 equivalents guest bpac molecules, and one guest water molecule per formula unit. This result is in keeping with reported data of Real, which describe the **Pt** framework with half occupancy of bpac in the framework pores.[2] Given the high correlation of the other elements, the elemental proportions of Pd and Pt are assumed to be incorrect, possibly due to incomplete digestion of the sample for these metal analyses, or inaccuracies in the particular mass determination technique used for these components.

It is also interesting to note the necessity of including one molecule of water per formula unit in the calculations, even though the sample preparation was performed so that the sample would be solvent-free. This is not entirely unexpected – in their TGA results, Real noticed that a molecule of water per formula unit was lost at 390 K, and that the framework regained

the lost water molecule when left exposed to the air for 1 hour.[2] It was also reported that between 500 and 680 K, the $[Fe(bpac)Pd(CN)_4]\cdot 0.71\{bpac\}\cdot 1.3\{H_2O\}$ sample lost 31% of its mass, which is equivalent to *ca*. 1.0 bpac per formula unit. This lost bpac portion can be predominantly attributed to sublimation of guest bpac out of the pores, with some removal of lattice bpac ligand as well. The high temperatures required for guest bpac removal indicates its strong association within the framework pores.

2.6 *Magnetic Properties*

Spin transition behaviour is most effectively studied using variable temperature magnetic susceptibility. Features of the spin transition, such as abruptness, hysteresis, transition temperature, completeness and the existence of any sort of unusual behaviour are easily observed from a χT vs. T plot.

Magnetic susceptibility measurements were performed using the bulk synthesis product described in **§2.2**. An excess (*ca.* four molar equivalent compared to Fe(II)) of bpac ligand was used in the synthesis with the aim to provide sufficient ligand to pillar the cyanide layers as well as produce the optimum occupancy of bpac guest within the pores. The samples used for these measurements are the same as were characterised by elemental analysis in the section above. The frameworks thus prepared will be henceforth designated by **M·0.5(bpac)** (**M** = **Ni**, **Pd**, **Pt**). Powder X-ray diffraction was used to confirm that bulk synthesis produced the same material as was described above (see **§2.4**).

As shown in **Figure 2-3**, **Ni·0.5(bpac)**{EtOH}, **Pd·0.5(bpac)**{EtOH} and **Pt·0.5(bpac)**{EtOH} all display relatively abrupt spin transitions with hysteresis. It should be noted that wherever a magnetism plot displays bistability in this thesis, over the hysteresis the cooling data correspond to the curve with the higher magnetic susceptibility values, while the warming data have the lower values. The **Pd** and **Pt** analogues have similar behaviours, occurring with $T_{1/2}^{\downarrow}$ = 278 and 273 K respectively, and $T_{1/2}^{\uparrow}$ = 290 and 285 K respectively, thus giving a hysteresis width for both of 12 K. The **Ni** analogue occurs at lower temperature with $T_{1/2}^{\downarrow}$ = 253 K and $T_{1/2}^{\uparrow}$ = 257 K, giving a smaller hysteresis width of 4 K. All transitions go to reasonable completeness, with the residual HS fraction at low temperature attributable to non-SCO Fe(II) centres within the crystallites, such as on the surface and due to lattice defect sites.

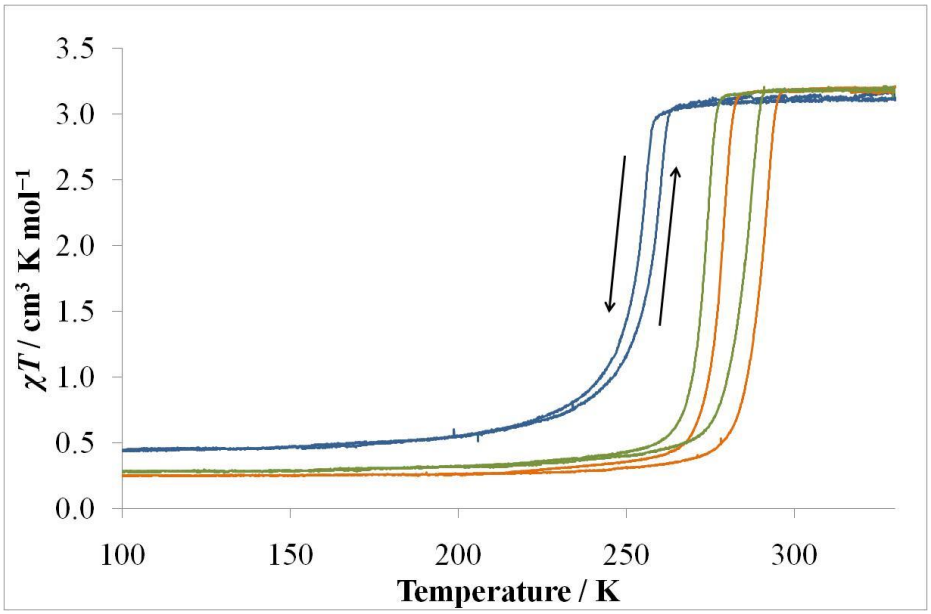

Figure 2-3: The magnetic susceptibility product χT vs. T for EtOH-solvated **Ni·0.5(bpac)**, **Pd·0.5(bpac)** and **Pt·0.5(bpac)**.

The reproducibility of the magnetic transition was studied using the **Pd·0.5(bpac)**{EtOH} sample. It was found that when the variable temperature magnetic measurement was cycled a second time, it produced a spin transition curve that was almost indistinguishable from the first, implying that the spin transition is fully reversible and reproducible.

2.7 *Discussion*

It is interesting to compare the magnetic behaviour of these frameworks with other properties of the materials. As shown in **Table 2-5**, there appears to be a correlation between the $T_{1/2}^{\downarrow}$ value observed in the magnetic data, the change in the $d_{\text{Fe–M–Fe}}$ value over the transition, and the ionic radius of the co-metal. For comparison, the ionic radius of Fe(II) is 0.78 Å in the HS state, and 0.61 Å in the LS state.

The first observation of interest is the value of the HS-to-LS $d_{\text{Fe–M–Fe}}$ difference. This quantity was chosen as it is a single quantity derived from the unit cell parameters, and as such it has a high degree of precision. The Fe–N bond lengths for each spin state can be expected to be very similar between the frameworks, as they are due to the ionic radius of the Fe(II), and the interactions between the metal and ligand orbitals. This is supported through comparison of the SCXRD-derived bond lengths shown in **Table 2-2**. The bond length of the co-metal to the

cyanide ligands would not change significantly over the spin transition, so the relative differences in $d_{Fe–M–Fe}$ must then arise from a change in the conformational distortion of the cyanide ligands.

Table 2-5: Comparison between certain properties of the **Ni**, **Pd** and **Pt** frameworks: SCO $T_{1/2}{}^{\downarrow}$, the difference between the HS and LS $d_{Fe–M–Fe}$ values, and the ionic radius of the co-metal (square planar, divalent oxidation state).[11]

	SCO $T_{1/2}{}^{\downarrow}$ / K	HS-to-LS $d_{Fe–M–Fe}$ difference / Å	Ionic radius of co-metal / Å
Ni·0.5(bpac){EtOH}	253	0.356(2)	0.49
Pd·0.5(bpac){EtOH}	278	0.375(2)	0.64
Pt·0.5(bpac){EtOH}	273	0.369(1)	0.60

As explained in **§1.5.1**, cyanide linkers have transverse vibrational modes which draw the connecting nodes together, and while the time- and space-averaged conformational position of the cyanide units may make the cyanide unit appear approximately straight, they are more likely to be distorted away from the Fe···M axis. Depending on the degree of dynamic distortion, the $d_{Fe–M–Fe}$ will change, with greater transverse vibrational displacement of the cyanide linker leading to a decrease in this value. Thus, it seems most probable that the relative differences in the $d_{Fe–M–Fe}$ values shown in **Table 2-5** arise due to different degrees of distortion associated with the displacement of the cyanide linkers away from a linear coordination between the metal nodes.

As explained in **§1.4.5**, the spin transition is accompanied by a change in the octahedral angle distortion parameter, which is reduced in the LS state. The closer the LS Fe(II) geometry is to octahedral, the greater the metal–ligand orbital overlap, which increases the strength of the metal–ligand bond, stabilising the LS state. This proposition is supported by comparison of the octahedral distortion parameters calculated for **Pd** and **Pt**, shown in **Table 2-2**: the LS Fe(II) coordination geometry in **Pd** exhibits less distortion, stabilising the LS state and contributing to its higher temperature transition. It should be also be noted that it is not clear whether the local distortion parameter in **Pd** would be significantly larger than that calculated for the bulk in the twinned dataset. The lower distortion parameter calculated for **Pd** arises due to the very close values for the *a* and *b* unit cell parameters in the crystal, and the concomitant greater twinning that is observed. The potential influence of crystal twinning on

the SCO properties is discussed further below.

In Hofmann-type frameworks, there are two major influences on the spin transition temperature that arise from the $M(CN)_4$ (M = Ni, Pd, Pt) units: the ligand field strength; and the ionic radius of the co-metal, which can affect the internal pressure resulting from guests in framework pores.[3,12] In discussing the behaviour observed for the **M·0.5(bpac)**{EtOH} (M = Ni, Pd, Pt) framework family, it is interesting to compare with the analogous [Fe(pyrazine)$M(CN)_4$]{EtOH} (M = Ni, Pd, Pt) frameworks. In the latter framework family, the dominant influence appears to be the ligand field effect of the metalloligands, as the frameworks follow the general transition temperature trend Ni > Pd > Pt (see **Figure 2-4**).[12] This is in contrast to the **M·0.5(bpac)**{EtOH} frameworks, which follow the trend Pd > Pt > Ni, implying that the dominant influence is the ionic radius of the co-metal. In order to understand the difference between the two framework families, it is useful to make a more detailed comparison.

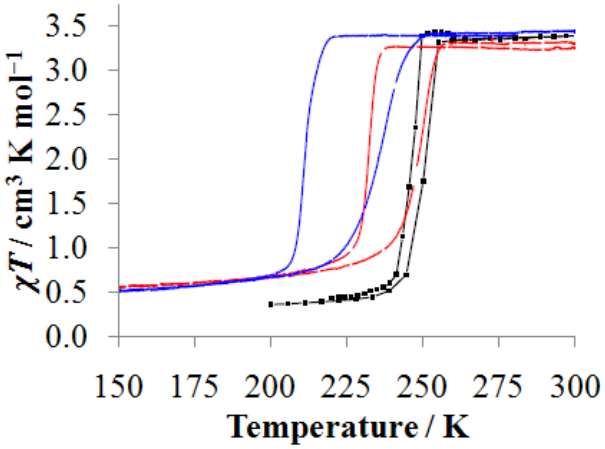

Figure 2-4: Temperature dependence on the magnetic behaviour of [Fe(pyrazine)$M(CN)_4$]{EtOH} (M = — Ni, — Pd, — Pt).[12]

As mentioned above, the major factor that determines the relative spin transition temperatures for the three **pz**-containing frameworks is the strength of the ligand field produced by the metalloligand, which depends on the electronegativity of the co-metal. Electronegativity was defined by Pauling as "the power of an atom when in a molecule to attract electrons to itself".[13,14] The more strongly electronegative the co-metal, the more electron density it will withdraw to itself from the cyanide ligands, and subsequently the less will be donated by these ligands to the Fe(II) atoms. This will result in a weaker ligand field around the Fe(II),

stabilising the HS state. The Pauling electronegativities of the co-metals are: Ni 1.91, Pd 2.20, and Pt 2.28.[15] The relative transition temperatures for **pz**-containing materials, in which Ni > Pd > Pt, correlate well with the expected strength of the Fe(II) ligand field that would be produced considering the different electronegativities of the co-metals.

The results of the **pz**-containing materials then lead to the question of why the **bpac**-containing frameworks do not follow the same electronegativity trend. While the bpac and pz ligands are different in size, structure and ligand strength, due to their coordinative position along the *c*-axis, they do not significantly influence the geometry of the metal cyanide layers. Therefore the major difference between the **bpac** and **pz**-containing framework families that could significantly affect the metal cyanide layer is the presence of unbound bpac molecules within the structural pores of the **bpac**-containing frameworks. The steric bulk of these guests would create an anisotropic internal pressure effect, stabilising the HS state. The smaller the framework, the more it would be affected by this, leading to lower transition temperatures. This would then account for the observed trend in the transition temperatures for the **bpac**-containing frameworks, and explain the change in the HS-to-LS $d_{\mathrm{Fe–M–Fe}}$ differences between the frameworks, which were limited due to the steric interaction between the lattice and guest bpac molecules.

In the **bpac**-containing frameworks, this steric effect of the bpac guest must have a greater effect on the relative transition temperatures than the electronegativity of the co-metal, in order to give rise to the observed behaviour. This steric interaction would also contribute to decreasing the flexibility of the cyanide ligands through the resulting increased lattice strain, leading to the greater octahedral distortion observed in the Fe(II) atoms of the $[Fe(bpac)Pt(CN)_4]\cdot 0.5(bpac)$ structure.

Another factor worthy of consideration is the incidence and effect of twinning in the framework lattice. If the *a*- and *b*-parameters of the unit cell are sufficiently similar, the resulting pseudo-merohedral twinning behaviour would produce strain on the framework lattice that forces these parameters to effectively average, such that an apparent tetragonal unit cell is observed. Due to the higher symmetry of this crystal system, a more regular, orthogonal coordination environment around the Fe(II) centres is produced, reducing the octahedral distortion parameter and stabilising the LS state due to more efficient ligand–metal orbital overlap. As noted in **§2.3**, the **Pd** framework single crystal had a high incidence of

pseudo-merohedral twinning, solving well in the *P*4/*mmm* space group and refining in the *Pmmm* space group with a twin component parameter of 0.514. As mentioned above, the octahedral distortion parameter of the Fe(II) centre was much lower than that of the **Pt** framework, which had a greater difference in the *a*- and *b*-parameters and a proportionally decreased incidence of twinning (the **Pt** model refined with a twin component parameter of 0.197). The twinning effect may also be a contributing factor in the relative spin transition temperatures of **Pd** and **Pt**.

2.8 *Conclusions*

These isostructural Hofmann-type framework materials display reversible spin transition with hysteresis. This is supported by variable temperature magnetic susceptibility measurements as well as powder X-ray diffraction. Elemental analysis of the bulk synthesis products demonstrated an approximate half occupancy of the framework pores with guest bpac molecules.

The different spin transition behaviours observed for the **Ni**, **Pd** and **Pt** analogues, including the transition temperatures and dimension changes over the transition, were explained based on the different framework dimensions that resulted from the different ionic radii of the co-metals, and the effect of this on the magnitude of steric interactions between guest bpac molecules and the lattice, as well as the incidence of pseudo-merohedral twinning in the framework. The inclusion of bpac guest molecules within the framework introduces a new potential variable in producing spin transition behaviour, which in conjunction with solvent guest effects, is explored in the next chapter.

2.9 *References*

(1) Mullaney, B. R. BSc(Hons) Thesis, University of Sydney, 2009.

(2) Bartual-Murgui, C.; Ortega-Villar, N. A.; Shepherd, H. J.; Muñoz, M. C.; Salmon, L.; Molnár, G.; Bousseksou, A.; Real, J. A. *J. Mater. Chem.* **2011**, *21*, 7217.

(3) Bartual-Murgui, C.; Salmon, L.; Akou, A.; Ortega-Villar, N. A.; Shepherd, H. J.; Muñoz, M. C.; Molnár, G.; Real, J. A.; Bousseksou, A. *Chem. Eur. J.* **2012**, *18*, 507.

(4) Muñoz Lara, F. J.; Gaspar, A. B.; Aravena, D.; Ruiz, E.; Muñoz, M. C.; Ohba, M.; Ohtani, R.; Kitagawa, S.; Real, J. A. *Chem. Comm.* **2012**, *48*, 4686.

(5) Southon, P. D.; Liu, L.; Fellows, E. A.; Price, D. J.; Halder, G. J.; Chapman, K. W.; Moubaraki, B.; Murray, K. S.; Létard, J.-F.; Kepert, C. J. *J. Am. Chem. Soc.* **2009**, *131*, 10998.

(6) Halcrow, M. A. *Chemical Society Reviews* **2011**, *40*, 4119.
(7) Niel, V.; Martinez-Agudo, J. M.; Muñoz, M. C.; Gaspar, A. B.; Real, J. A. *Inorg. Chem.* **2001**, *40*, 3838.
(8) Agustí, G.; Cobo, S.; Gaspar, A. B.; Molnár, G.; Moussa, N. O.; Szilágyi, P. Á.; Pálfi, V.; Vieu, C.; Muñoz, C. M.; Real, J. A.; Bousseksou, A. *Chem. Mater.* **2008**, *20*, 6721.
(9) Iwamoto, T.; Kiyoki, M.; Ohtsu, Y.; Takeshige-Kato, Y. *Bull. Chem. Soc. Jap.* **1978**, *51*, 488.
(10) Russel, V.; Scudder, M.; Dance, I. *J. Chem. Soc., Dalton Trans.* **2001**, 789.
(11) Dronkowski, R. *Computation Chemistry of Solid State Materials*; WILEY-VCH Verlag GmbH & Co. KGaA: Weinheim, Germany, 2005.
(12) Fellows, E. A. PhD Thesis, University of Sydney, 2011.
(13) Pauling, L. *J. Am. Chem. Soc.* **1932**, *54*, 3570.
(14) Pauling, L. *The Nature of the Chemical Bond*; Cornell University Press: Ithaca, New York, 1939.
(15) Allred, A. L. *J. Inorg. Nucl. Chem.* **1961**, *17*, 215.

Chapter 3: Guest-Dependent Behaviour in the Frameworks, $[Fe(bpac)M(CN)_4]\cdot x(bpac)\{guest\}$ (M = Ni, Pd, Pt)

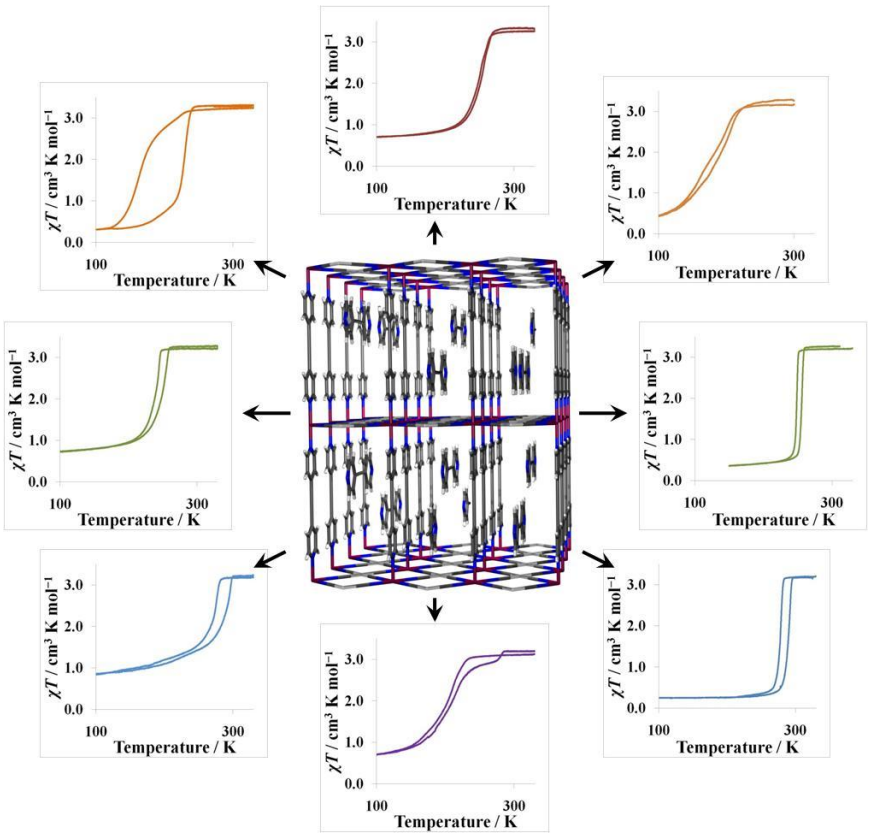

Through changing the occupancy of the $[Fe(bpac)Pd(CN)_4]\cdot x(bpac)$ framework pores with different quantities and types of guests, a variety of different spin transition behaviours are observed.

3.1 *Outline*

The porous nature of the [Fe(bpac)M(CN)$_4$]·*x*(bpac) (M = Ni, Pd, Pt) framework family has led to two degrees of freedom in the guest occupancy: unbound bpac molecules and solvent. This chapter describes the guest-dependent behaviour produced by two different bpac guest concentrations, and a variety of alcohol species.

The concentration of bpac guest within the framework pores has a profound effect on the resulting SCO behaviour. Synthesis of the material with less than the ideal quantity of bpac produces a sample with more framework defects, and desolvation followed by resolvation with ethanol increases the fraction of active SCO centres in the sample. Nitrogen gas and ethanol vapour adsorption isotherms confirm the robust porosity of this material and give an indication of potential non-bpac guest inclusion concentration.

The C1 to C5 *n*-alcohol series (i.e., methanol, ethanol, 1-propanol, 1-butanol and 1-pentanol) demonstrates a significant guest effect on the spin transition behaviour. The framework with a lower bpac guest concentration generally produced a larger SCO hysteresis than the framework with a higher bpac guest occupancy, and when solvated with 1-pentanol, it notably produces a spin transition with a maximum thermal hysteresis width of 67 K. As a representative example of a mixed solvent system, 1:1 methanol/ethanol was studied in the framework with partially-occupied bpac guest, which produces a spin transition at lower temperature than either of the independent guest species.

A Pressure-Temperature phase diagram was constructed using a series of ethanol adsorption isotherms and isobars for the **Pd** framework with partial bpac guest occupancy. A general trend was observed that higher vapour pressures produce a lower spin transition temperature with greater hysteresis, which is attributable to the guest effect.

3.2 *Ligand Concentration Dependence*

As described by Real,[1] the synthesis method has a significant impact on the amount of unbound bpac within the pores of the [Fe(bpac)M(CN)$_4$] (M = Ni, Pd, Pt) frameworks, and variation of this amount has an effect on the cooperativity and completeness of the spin transition. It was shown that higher bpac concentrations led to more complete transitions, and in the case of desolvated samples, also led to greater cooperativity, with a subsequent

increase in the thermal hysteresis widths.

Before the strong dependence on included bpac guest was discovered, the synthesis of the **Ni**, **Pd** and **Pt** frameworks was performed using one molar equivalent of bpac per Fe(II). The magnetic behaviour of the resulting material was studied, as well as preliminary investigations into the solvent-dependence of their properties (**§3.3**).

3.2.1 *Elemental Analysis*

Elemental analysis of C, H, N and Fe was performed twice on the **Pd** analogue of these frameworks, giving the average quantities shown in **Table 3-1**. Errors are estimated as the difference between the experimental results and the average. These results compare well with the calculated elemental proportions for a sample with the formula $[Fe(bpac)Pd(CN)_4]\cdot x(bpac)(H_2O)$ (x = 0.35 to 0.38). The quantity of bpac guest in this sample could therefore be best estimated as x = 0.37(2)

Table 3-1: Experimental and calculated values (%) for the elemental composition of $[Fe(bpac)Pd(CN)_4]\cdot 0.37(bpac)(H_2O)$.

	Exp.	Calc.
Fe	10.55(5)	10.51
Pd	-	20.0
C	46.29(1)	46.21
H	2.43(3)	2.46
N	17.64(1)	17.77
O	-	3.01

Even though one equivalent of bpac was used in the synthesis, the resulting material contained 1.37(2) equivalents of bpac per formula unit. This implies that the association of bpac guest within the framework pores is sufficiently strong and stable that bpac molecules preferentially lie within the framework pores, instead of coordinating to Fe(II) in a framework lattice. The inclusion of a molecule of water in the formula is consistent with the result of the **M·0.5(bpac)** frameworks (**§2.5**). As the **M·0.5(bpac)** frameworks all had very similar bpac guest concentrations, it is assumed that the frameworks synthesised with one equivalent of bpac would also have similar bpac guest concentrations. For simplicity, the

assumed bpac guest concentration will be approximated at 0.4 molecules per formula unit, and the frameworks will hereafter be referred to by **M·0.4(bpac)** (**M** = **Ni**, **Pd**, **Pt**).

As there are 0.37(2) bpac guest molecules per formula unit in the **Pd·0.4(bpac)** framework, this implies that *on average* the framework lattice contains this quantity of guest molecules. It is possible that the framework crystallites contain a range of bpac guest concentrations, which could produce different spin transition properties.

3.2.2 *Magnetic Properties*

It was observed that the **M·0.4(bpac)** frameworks displayed markedly different SCO behaviour to the **M·0.5(bpac)** materials, exemplified by the **Pd·*x*(bpac)**{EtOH} frameworks (**Figure 3-1**). The lower concentration of bpac in the **Pd·0.4(bpac)**{EtOH} framework results in a spin transition at a similar temperature to the **Pd·0.5(bpac)**{EtOH} material, though it has a larger hysteresis that is much more incomplete. There is also a second minor hysteretic spin transition at low temperature, which is not observed in the **Pd·0.5(bpac)**{EtOH} sample.

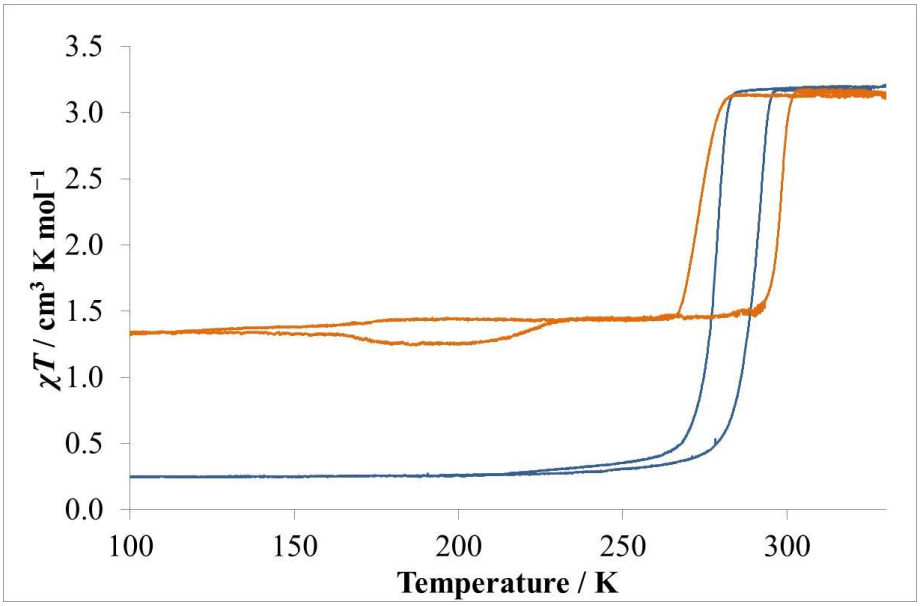

Figure 3-1: Comparison of the magnetic behaviour for EtOH-solvated samples of **Pd·0.5(bpac)**, and **Pd·0.4(bpac)**.

As shown in **Figure 3-2**, variable temperature magnetic susceptibility measurements of **Pd·0.4(bpac)**{EtOH} and **Pt·0.4(bpac)**{EtOH} show that the high temperature transitions of these frameworks occur with almost identical behaviours, in which $T_{1/2}^{\downarrow a} = 275$ K and

$T_{1/2}^{\uparrow a}$ = 295 K, giving hysteresis widths of *ca*. 20 K. However, in addition to this incomplete transition, both frameworks display another partial SCO that occurs more gradually, with $T_{1/2}^{\downarrow b}$ = 170 K and hysteresis widths of *ca*. 42 K. This hysteresis also has an unusual feature in that as the sample is warmed, it undergoes further HS-to-LS transition to what appears to be a stable state, before a LS-to-HS transition at $T_{1/2}^{\uparrow b}$ = 210 K. The large residual HS fraction can be predominantly attributed to inactive crystallites, which have too many framework defects to undergo SCO (this is discussed further in **§3.2.3**).

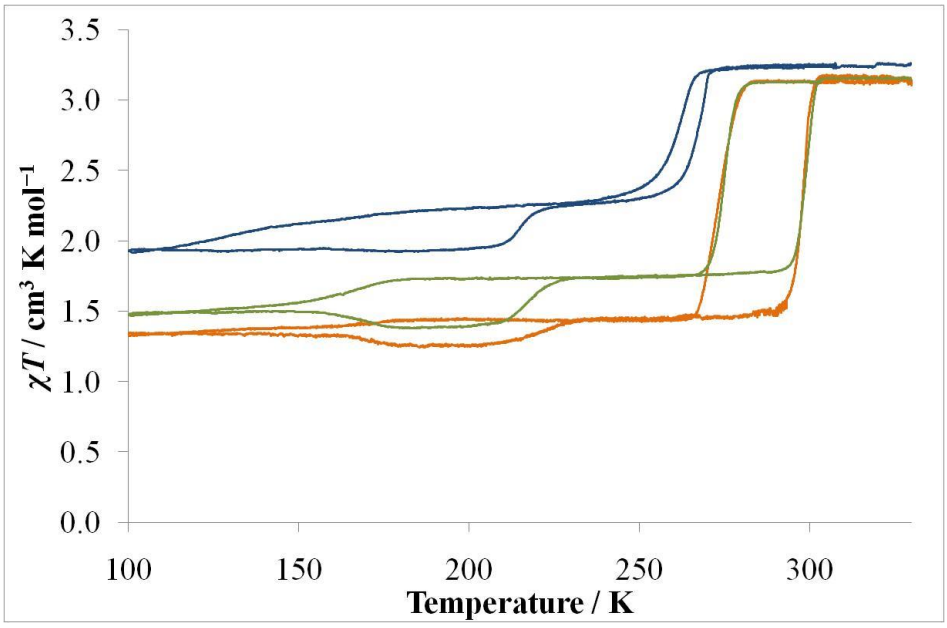

Figure 3-2: The magnetic susceptibility product χT vs. Temperature for **Ni·0.4(bpac)**{EtOH}, **Pd·0.4(bpac)**{EtOH}, and **Pt·0.4(bpac)**{EtOH}.

The transition behaviour of **Ni·0.4(bpac)**{EtOH} is similar to the other two frameworks, with two distinct stages to the spin transition. The high temperature transition occurs with $T_{1/2}^{\downarrow a}$ = 261 K and $T_{1/2}^{\uparrow a}$ = 267 K, giving a hysteresis of 6 K, while the low temperature transition is gradual, appearing to begin at *ca*. 220 K and continuing until the lowest temperature measured. After the sample is warmed from this point, the magnetic susceptibility remains constant at the lowest value attained, until it undergoes transition back to the intermediate state at $T_{1/2}^{\uparrow b}$ = 210 K.

This observed dependence on ligand concentration is remarkable (**Figure 3-1**), and not easily explained. In his paper, Real explains this dependence by saying '*In samples with a low proportion of included bpac molecules, the occurrence of different iron centers leads to*

incomplete and less-cooperative spin transitions. Conversely, when a large proportion of bpac molecules are included, the π–π stacking interaction between the bridging and included bpac molecules tends to homogenize the network and complete and cooperative spin transitions are observed.'[1] This explanation is presumably given to account for the reported behaviour of the desolvated samples, in which the only outer ligand field influence would be from the guest bpac molecules, and not other adsorbed solvent. However, this explanation is not sufficient to explain the observed behaviour here, in which a lower concentration of bpac molecules leads to a *greater* cooperativity, evidenced by the increased high temperature hysteresis width of **M·0.4(bpac)**{EtOH} compared to **M·0.5(bpac)**{EtOH}. These high temperature transitions can be compared well as they have similar $T_{1/2}{}^{\downarrow}$ temperatures. The PXRD data (**§3.2.3**) show that the frameworks are structurally congruent, so the difference in behaviour can only be attributed to the different guest occupancy in the framework pores.

An excess of bpac in the synthesis of the **M·0.5(bpac)** frameworks was employed to create an effective full occupancy of *coordinated* bpac molecules within the framework structure, and sufficient guest occupancy within the pores. Decreasing the available ligand in the synthesis to less than that required for full occupancy introduces absences in the bpac guest occupancy, and potentially also the framework lattice, which would increase the available pore space for guest solvent molecules. The concentration of non-bpac guest within the **M·0.4(bpac)** framework would be greater, increasing the number of host–guest interactions which may be rearranged with the SCO. As a result, the spin transition is disfavoured and a wider hysteresis is observed (compare **Figure 3-2** with **Figure 2-3**).

The second low temperature transition is puzzling, and without much further study we can only propose hypotheses as to its origin and nature. The first point of interest lies in the hysteresis shown, in conjunction with the relatively gradual transition. Of additional interest is the unusual behaviour shown in the **Pd·0.4(bpac)**{EtOH} and **Pt·0.4(bpac)**{EtOH} frameworks, in which the material undergoes further HS-to-LS transition upon warming. Lastly, and most perplexingly, is that the spin transition occurs in a completely different temperature range to the high temperature transition, with a different magnitude of completeness. Using this information, in conjunction with the variable temperature PXRD results (**§3.2.3**), we may infer that the two transitions involve separate crystallites. This result then raises the question of how and why these crystallites are different.

It is possible that there is a ‘critical point’ of ligand occupancy below which the crystallite will change from the higher to the lower spin transition. Among these crystallites, there would be a continuum of frameworks with differing bpac occupancies, leading to the gradual transitions. Similarly to the explanation given above, the larger hysteresis width is presumably created by the increased solvent accessible pore volume, and the subsequent increase in the quantity of host–guest interactions which must be rearranged over the spin transition.

Of further interest is the unusual transition behaviour upon warming (**Figure 3-2**), as the **Pd·0.4(bpac)**{EtOH} and **Pt·0.4(bpac)**{EtOH} frameworks undergo further SCO at the low temperature transition. This is unlikely to be attributed to whole crystallites because any that had not already undergone spin transition would have demonstrated their HS stability at those temperatures. Instead, this phenomenon probably occurs within crystallites that have partially undergone SCO, but as the EtOH in the surrounding medium froze (freezing point of EtOH = 159 K), they were trapped in an intermediate state by the immutability of the frozen solvent. Upon warming, as the EtOH melts, the structural influence of the LS Fe(II) sites in the framework encourages remaining HS sites to undergo SCO through the framework cooperativity, reaching a more energetically stable state.

The low-temperature behaviour of the **Ni·0.4(bpac)**{EtOH} material (**Figure 3-2**) shows significantly different behaviour to the **Pd·0.4(bpac)**{EtOH} and **Pt·0.4(bpac)**{EtOH} analogues, as the second HS-to-LS transition of the **Ni·0.4(bpac)**{EtOH} framework begins at a similar temperature to the others, but is very gradual and continues down to the lowest temperature studied. However, on warming the magnetic susceptibility of the material remains relatively constant at the lowest value until *ca*. 205 K, after which point there is a LS-to-HS transition at a similar temperature and abruptness to the other two frameworks, back to the intermediate state. This transition, similar to the **Pd·0.4(bpac)**{EtOH} and **Pt·0.4(bpac)**{EtOH} frameworks, is most likely to involve separate crystallites to those responsible for the high temperature transition. Furthermore, it appears that the Fe(II) sites within these crystallites undergo the low temperature HS-to-LS transition with little cooperativity, resulting in the gradual transition observed. In contrast, the LS-to-HS transition is fully cooperative. This is an unusual result that cannot be adequately explained without further investigation.

3.2.3 *Variable Temperature Powder X-Ray Diffraction*

While SCO can be effectively monitored using variable temperature magnetic susceptibility experiments, powder diffraction techniques give more information on the structural nature of SCO behaviour in a bulk sample, and thus functions as a complementary technique. Spin transition features, such as gradual, incomplete or hysteretic behaviour, can be corroborated and structurally explained using variable temperature diffraction. Similarly, phase transitions observed in diffraction data can be compared with the spin crossover behaviour shown in magnetic measurements to confirm or deny their connection to an electronic change.

Variable temperature powder X-ray diffraction was performed on **Pd·0.4(bpac)**{EtOH}, and the resulting diffractograms were treated with a Le Bail fit using a model in the orthorhombic *Pmmm* space group, in order to calculate unit cell parameters. The low temperature refinements were single-phase, though HS 'impurity' peaks were also present in the diffractograms. The powder diffractograms can be seen in **Figure C-8**, and a peak intensity plot is shown in **Figure 3-3a**.

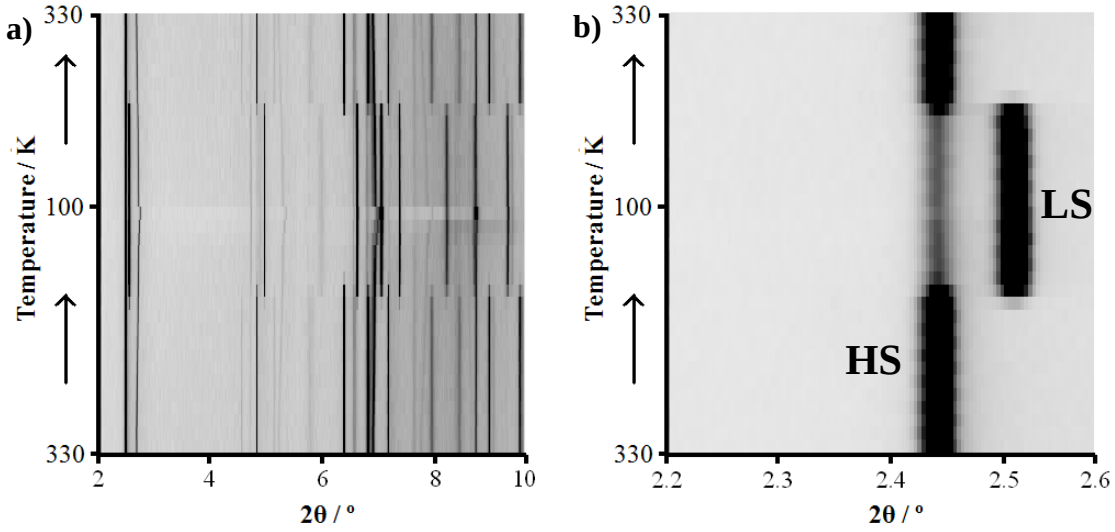

Figure 3-3: a) Intensity plot showing the powder diffraction peak evolution as the **Pd·0.4(bpac)**{EtOH} sample was cooled from 330 to 100 K, then warmed back up to 330 K; and **b)** a close-up of the (001) peak.

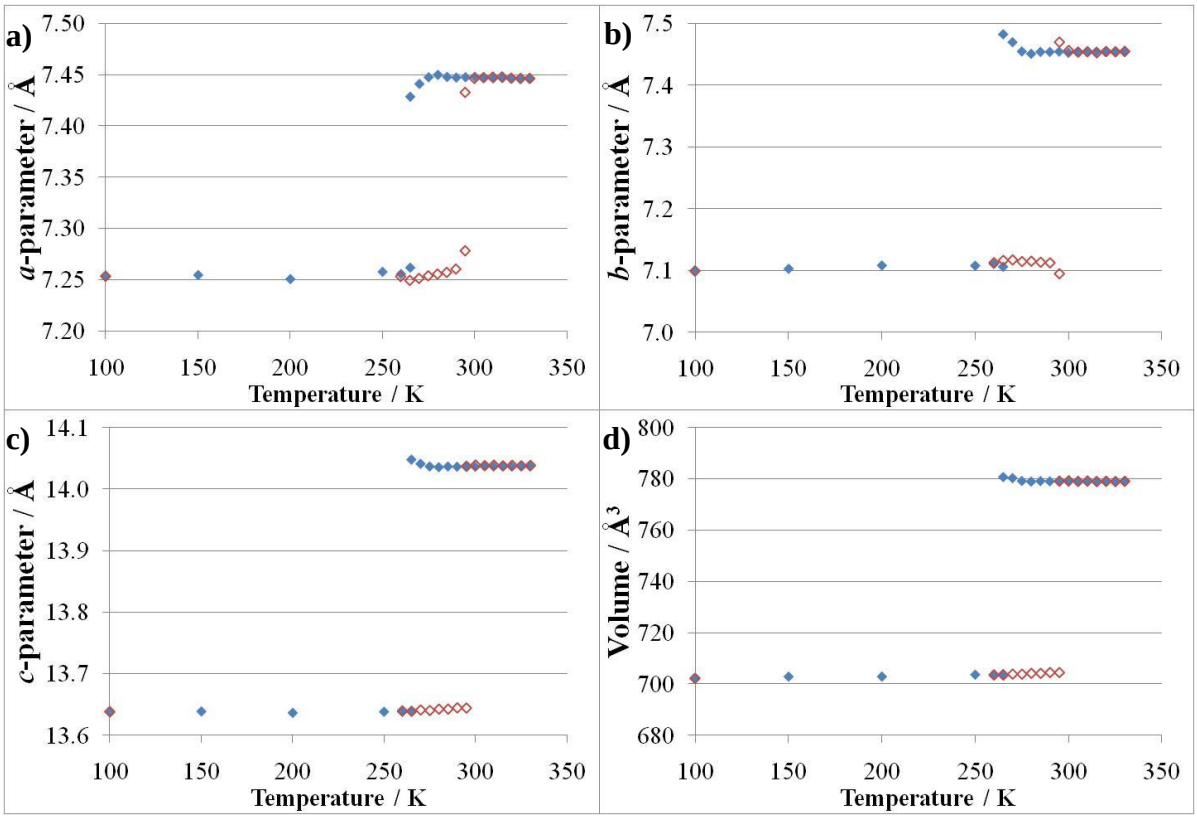

Figure 3-4: Variable temperature unit cell parameters for **Pd·0.4(bpac)**{EtOH} determined by Synchrotron PXRD: **a)** *a*-parameter; **b)** *b*-parameter; **c)** *c*-parameter; and **d)** unit cell volume, upon ◆ cooling and ◇ warming.

As shown in **Figure 3-4**, the unit cell parameters display a hysteretic phase transition, with $T_{1/2}^{\downarrow}$ = 265 and $T_{1/2}^{\uparrow}$ = 295 K, giving a hysteresis of *ca*. 30 K. The unit cell parameters do not change significantly below the spin transition, which supports the hypothesis that the lower temperature transition arises from different crystallites within the sample. If the low temperature spin transition had resulted from Fe(II) sites within the same crystallites as had previously undergone SCO, the average unit cell dimension would have changed and the peak positions would have shifted. Furthermore, there is a residual HS phase below the major spin transition, which is best demonstrated by the (001) peaks of the HS and LS phases (**Figure 3-3b**). At temperatures which correspond to the low temperature transition, the peak intensities of the HS and LS fractions change with decreasing temperature, getting smaller and larger respectively as the proportion of the LS phase increases (see **Figure C-9**). This further reinforces the proposition that the low temperature transition involves separate crystallites undergoing SCO.

In order to most clearly compare the powder diffraction and magnetism results, it is useful to convert both sets of data into the relative stoichiometric fraction of HS states using **Equation 7.1** (**§7.6**). For the powder diffraction data, a crude estimate to the HS proportion was obtained by comparing the intensity of the (001) peak.

The resulting comparison is shown in **Figure 3-5**. The structural phase transition correlates well with the SCO observed from the magnetic susceptibility data, with both occurring at approximately the same temperatures. It is suspected that the residual HS fraction at low temperature arises due to two major causes: defect sites on the surface and within the crystallites which do not undergo spin transition; and bulk sample inhomogeneity that results from varying bpac concentrations in the crystallites.

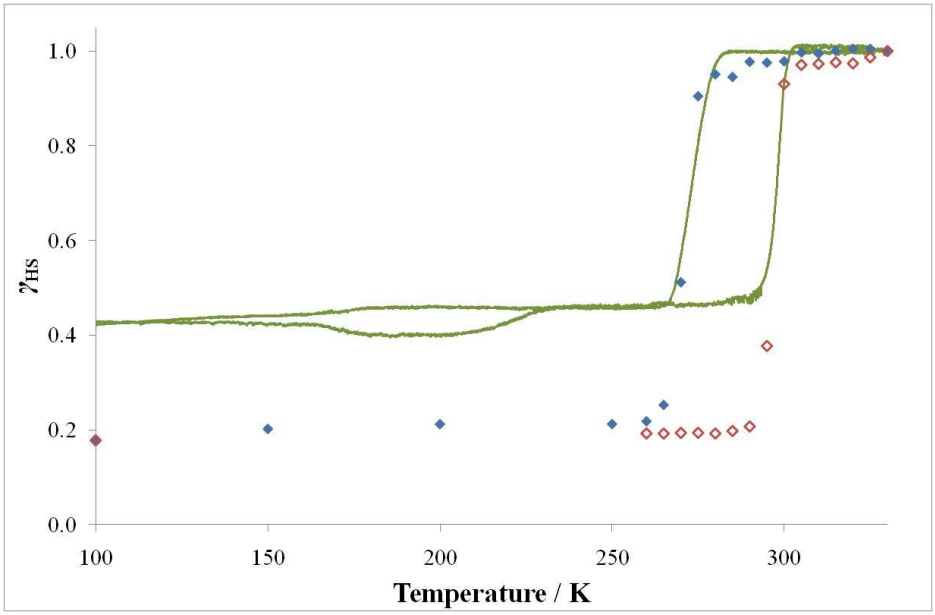

Figure 3-5: Comparison of the relative stoichiometric HS fraction of **Pd·0.4(bpac)**{EtOH} as determined by — the magnetic susceptibility; and powder diffraction upon ◆ cooling and ◇ warming.

In order for Fe(II) sites within a framework structure to undergo SCO, they need to be in the bulk phase.[2-3] As such, Fe(II) centres that are at, or close to the surface of a framework particle will not undergo SCO, as they do not have the appropriate ligand field strength. Similarly, defect sites within a cooperative SCO material will increase the proportion of SCO-inactive sites. Thus, even if a whole crystallite undergoes the phase transition to the LS phase, and appears to be fully LS in the diffraction experiment, there would still be HS sites within the crystallite, producing a higher residual HS fraction in the magnetic experiment.

The other suspected cause for the low temperature residual HS fraction lies in an inhomogeneous distribution of crystallites with different concentrations of coordinated and guest bpac molecules. As mentioned in **§3.2.1**, the quantity of bpac guest determined from the elemental analysis results of **Pd·0.4(bpac)** was the average amount over the whole sample, and it is possible that there is a range of bpac guest concentration within the different crystallites. Due to the high association strength of bpac guest within the framework, crystallites formed toward the beginning of the synthesis may include a quantity of bpac guest which was close to the most energetically favoured amount. This was shown in **§2.5** to be *ca*. 0.5 bpac guest molecules per formula unit, when the synthesis used an excess of ligand.

In order to achieve this favoured quantity of bpac molecules in the lattice and pores, the bpac used in the synthesis would be consumed at a higher rate than the other reactants. It therefore follows that if a framework crystallite is formed later in the synthesis, it would have a lower concentration of bpac available in the surrounding solvent medium compared to the other reactants, and the resulting concentration of bpac in the framework would be less. Furthermore, if bpac molecules are occupying the framework pores, it is possible that there may be absence defects in the bpac ligand within the framework lattice. This would result in a large number of lattice defects in which the Fe(II) may instead be axially coordinated by H_2O molecules (see **Figure 3-6**), losing SCO activity. If a framework particle has a sufficient number of these non-SCO Fe(II) centres, then the cooperativity of the framework will prevent the crystallite as a whole from undergoing SCO, resulting in a non-active framework crystallite, and the residual HS phase at low temperature. More information on the quantity of bound and unbound bpac in this sample is necessary to confirm or refute this hypothesis.

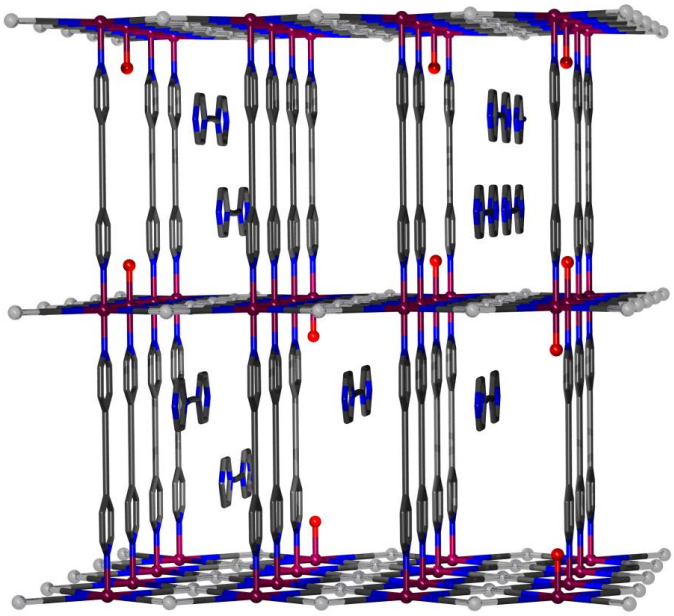

Figure 3-6: Example of a potential framework in which a significant number of lattice defects are introduced, such that some coordinated bpac molecules are replaced by H_2O ligands axially coordinating to the Fe(II). There is also partial occupancy of the framework pores by bpac molecules. Hydrogen atoms have been removed for clarity.

3.2.4 *Adsorption Properties*

In order to effectively economise on instrument time, and most fully explain the various influences that determine the properties of this framework family, it was decided to focus study on the guest dependent behaviour of the **Pd·0.4(bpac)** and **Pd·0.5(bpac)** frameworks.

3.2.4.1 Nitrogen Adsorption

These results were first published in my Honours Thesis (2009), but are reproduced here in order to give a more full understanding of the framework properties.

The gas adsorption properties of **Pd·0.4(bpac)** were analysed to quantitatively determine the effective porosity and robustness of the framework. This experiment was performed before the ligand dependence on framework properties was established, and unfortunately due to time constraints, a corresponding experiment on **Pd·0.5(bpac)** has not yet been performed.

The N_2 adsorption behaviour of the framework can be seen in **Figure 3-7**. The adsorption isotherm follows the typical Type I adsorption behaviour described in **§1.3.1**, indicating the presence of micropores. N_2 is rapidly adsorbed into the material until about 0.09 P/P_0, after which the linear curve indicates predominant adsorption onto the surface of the material. The

hysteresis shown would be expected from capillary condensation in mesoporous, rather than microporous materials, but nevertheless can be explained by the kinetics of adsorption. The very small pore size in the framework and presence of bpac guest molecules would lead to adsorbed N_2 taking a tortuous path through the material. This results in slow desorption kinetics, and the hysteresis observed.

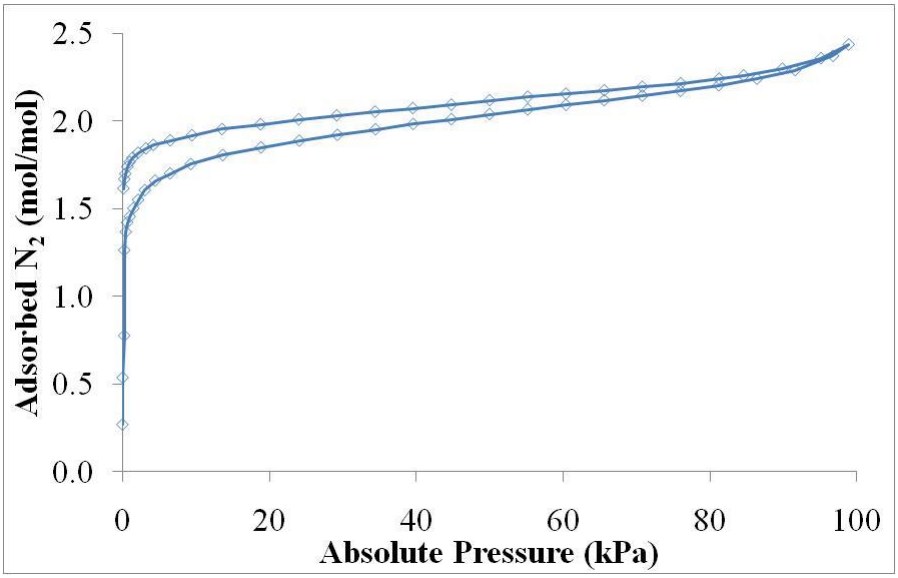

Figure 3-7: N_2 adsorption isotherm for **Pd·0.4(bpac)** obtained at 77 K, at which temperature the framework is in the LS state.

Computational analysis of the data reveals additional information about the properties of the framework pores. Using the BET and Langmuir models in the *ASAP 2020* software to analyse the data taken between 1.16×10^{-4} and 2.91×10^{-2} P/P_0, the surface area of **Pd·0.4(bpac)** was determined to be 299(3) and 299(4) $m^2\,g^{-1}$ respectively (both had correlation coefficients for the linear fit of 0.9996). Analysis of the point at 0.02914 P/P_0 yields a similar theoretical surface area of 296 $m^2\,g^{-1}$, and a pore volume of 0.122 $cm^3\,g^{-1}$ with an average pore width of 16 Å which classifies this material as microporous (see **§1.3.1**). Calculations of the pore volume from the crystal structure file using the *SOLV* routine in *PLATON*[4] is complicated by the crystallographic disorder and partial overlap of the pore bpac units; a hypothetical 100% bpac occupancy gives a theoretical solvent accessible volume of 8.7%, corresponding to a pore volume of 0.0714 $cm^3\,g^{-1}$, whereas 0% bpac occupancy gives an accessible volume of 53.8%, which is equivalent to 0.44 $cm^3\,g^{-1}$. The experiment value of 0.122 $cm^3\,g^{-1}$ is in keeping with these values and the significant overlap of symmetry-

equivalent bpac sites within the pores.

The number of moles of N_2 adsorbed into the framework pores can be approximated from the adsorbed quantity at P/P_0 = 0.8, which is 2.2 moles N_2 per formula unit of the framework. This N_2 adsorption isotherm demonstrates that the **Pd** framework material is robust to solvent removal, allowing the possibility to probe the guest-dependent behaviour of this framework, the details of which are discussed in **§3.3**.

Ethanol Adsorption

The EtOH adsorption behaviour of **Pd·0.4(bpac)** was studied as described in **§7.7.2**. The adsorption isotherm shown in **Figure 3-8** was obtained at 303.2 K, at which temperature EtOH starts condensing at 105 mbar. To avoid condensation, the isotherm was measured up to a pressure of 85 mbar (P/P_0 = 0.8). The framework is in the HS state at this point, and the quantity of adsorbed EtOH was determined to be 1.55 EtOH molecules per formula unit. This is comparable with the EtOH adsorption result obtained for the [Fe(pyrazine)Pd(CN)$_4$] framework of 1.5 molecules per formula unit.[5]

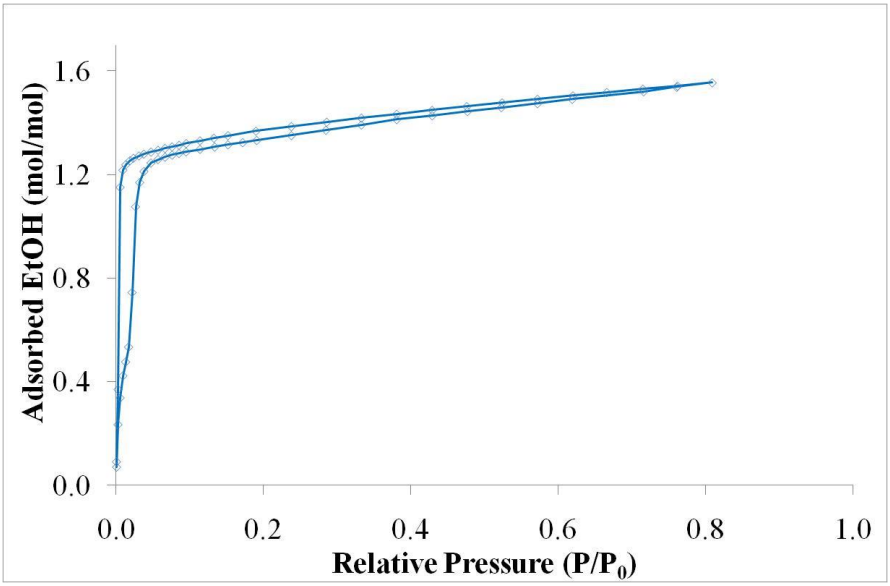

Figure 3-8: EtOH adsorption isotherm for **Pd·0.4(bpac)** obtained at 303.2 K, at which temperature the framework is in the HS state.

It is interesting to compare the guest adsorption results for N_2 and EtOH. Per formula unit, at 0.8 P/P_0 the LS framework is shown to adsorb 2.2 N_2 molecules, which is equivalent to 4.4 atoms. On the other hand, the HS framework adsorbs 1.55 guest EtOH molecules per formula

unit, which is equivalent to *ca*. 4.7 non-hydrogen atoms. It is reassuring that these two results correlate, with the ~7% difference potentially attributable to the ~10% volume change between the HS and LS states of the framework, as well as differences in packing efficiencies of the guests.

3.3 *Solvent Dependence of Pd·x(bpac)*

As mentioned previously, fewer data were obtained for **Pd·0.5(bpac)** compared to **Pd·0.4(bpac)**, as the former material was studied toward the end of the experimental period, and the significant effect of bpac concentration was discovered after many guest dependent studies had already been undertaken on **Pd·0.4(bpac)**. The results for both concentrations of bpac will be presented individually, and then compared and discussed together.

The straight-chain alcohols were chosen to study the guest-dependent behaviour of the materials, as the major difference between the alcohols is their size and it was hoped that this would minimise the complexity of deconvoluting the different solvent effects.

3.3.1 *Resolvation of Ethanol*

Before comparing the effect of different solvents on the spin transition properties, it is important to observe the effect on **Pd·0.4(bpac)** of desolvation under heat and vacuum, followed by resolvation with EtOH. As seen in **Figure 3-9**, the resulting material displays significantly different behaviour to the as-synthesised samples. The transition from HS-to-LS begins in a similar manner to the as-synthesised EtOH-solvated **Pd·0.4(bpac)** sample, but rapidly becomes more gradual after 274 K. Furthermore, the magnetism retains a hysteresis of ~15 K down to *ca*. 135 K, even though a gradual transition is observed. This hysteresis is marginally smaller than for the as-synthesised **Pd·0.4(bpac)** sample, and the transition goes to higher completion.

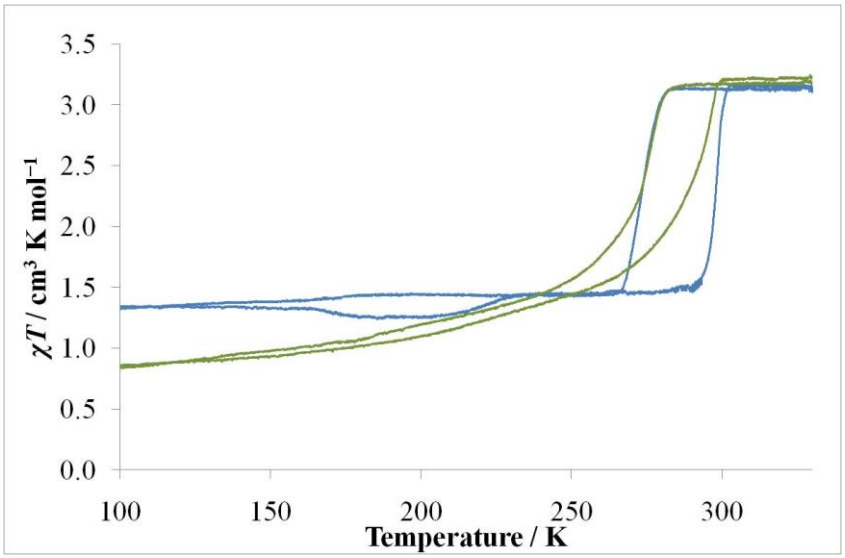

Figure 3-9: Comparison of the magnetic behaviour for **Pd·0.4(bpac)**{EtOH} — as-synthesised; and — after resolvation.

This change in the observed behaviour could only arise through a change in the constituent Fe(II) environments. A possible explanation for this difference may lie in bpac absence defects in the framework lattice. Following from the hypothesis proposed in **§3.2.3**, if a framework has insufficient bpac ligand in its synthesis, lattice defects may be introduced, in which some of the Fe(II) atoms could be axially coordinated by H_2O instead of bpac. When the framework is desolvated, water molecules coordinated to the Fe(II) centres may then be removed, introducing bare metal sites on the Fe(II). These bare metal sites are highly unstable, and would encourage coordination by any nearby unbound bpac molecules. This would decrease the amount of bpac guest, and more importantly, decrease the number of inactive Fe(II) centres, which increases the number of active framework particles, resulting in a spin transition of higher completion.

The concentration and proximity of bpac guest to ligand absence sites would determine how many of these molecules coordinate to bare metal sites of the Fe(II) centres when the material is under vacuum. The result of this redistribution of bpac would be a continuum of bound and unbound bpac concentrations in the framework particles. This continuum of frameworks would produce a correspondingly large distribution of different SCO temperatures.

The ~15 K hysteresis observed down to low temperature demonstrates that despite the variable number of lattice defects and guest bpac molecules, the SCO is still cooperative

within the frameworks, and the cooperativity is comparable across the crystallites. This is likely to be due to the solvent effect as explained in **§3.2.2**, which influences the enthalpic barrier to spin transition due to the rearrangement of host–guest interactions. Once again, in order to confirm or refute this hypothesis it is necessary to obtain quantitative information on the amount of bound and unbound bpac molecules in these samples.

3.3.2 *Solvent Dependence*

3.3.2.1 Preamble

Before these results are presented and discussed, it is important to understand the potential contributing factors that lead to the differences in the observed behaviours. There are a variety of proposed causes for SCO behavioural change due to adsorbed guests.[5-8] These can be broadly classified into the effect of the guest on a) the outer coordination sphere of the Fe(II), directly influencing the ligand field through distortion of electron density, resulting in a change in the relative magnitude of Δ_{oct} and P (**§1.4.1**); and b) the structural influences within the framework, through interactions between the guest and lattice molecules. Steric interactions of the guest can give rise to altered behaviour through internal pressure effects, changes in the entropy of the system through guest movement within and outside the framework pores, and potentially a change in the entropic factor associated with motion of the pyridyl units in the coordinated bpac molecules. A structural change in the framework would also affect the attractive and repulsive interactions between the framework host and adsorbed guest species, generating an enthalpy contribution to the energetic change of the system.

Guest-dependence on SCO behaviour was recently studied in an analogous family of framework materials. Elizabeth Fellows described in her PhD thesis (University of Sydney, 2011) the various guest influences that were determined to affect SCO behaviour in the isostructural framework series [Fe(pyrazine)M(CN)$_4$] (M = Ni, Pd, Pt).[5] She also described how the packing of guests within the pores, interactions between the guest and host, and limitations on the freedom of rearrangement combined to produce the behaviour observed.

When the alcohol guest series (methanol to 1-pentanol) were adsorbed into the [Fe(pyrazine)M(CN)$_4$] frameworks, it was shown that approximately the same number of atoms were adsorbed into the framework for each solvent. It was therefore concluded that the

main difference in the guest effects of these solvents was the number and type of host–guest interactions per molecule, rather than an internal pressure effect. The longer alcohols would have a greater incidence of favourable C–H···π interactions with the framework lattice, while the –OH moieties would hydrogen-bond to one another. When the lattice undergoes the structural transition associated with SCO, this would force a change in the geometry and distance of the C–H···π interactions. Thus, the more of these interactions there are to perturb, the higher the energy barrier to the transition, and the more the HS state is stabilised. C–H···π interactions have an average distance of 2.4–3.1 Å and an energy of 2–10 kJ mol^{-1}.[9-10] These host–guest interactions were proposed to explain the decreasing transition temperature with increasing alcohol length.

It was also found for the [Fe(pyrazine)$M(CN)_4$] frameworks that increasing the number of hydroxy units on a guest produced more gradual, low-temperature transitions than guests with fewer hydroxyl units but the same number of large (non-hydrogen) atoms. The reason given for this was that more hydroxy units leads to an increased quantity and strength of guest–guest interactions, which decreases the ease of guest rearrangement within the framework pores. These guests would then inhibit spin transition as the strong intermolecular hydrogen bonds of the guests would need to be rearranged as the framework lattice changes dimension with the transition (hydrogen bonds have an energy of 15–40 kJ mol^{-1}).[11] The behaviour of the frameworks would then also depend on the ease of mobility of the guests within the lattice pores.

3.3.2.2 *Influence of Guest Size*

The hypothesis that increased carbon chain length leads to a greater incidence of C–H···π interactions, thus enthalpically stabilising the HS state in the [Fe(pyrazine)$M(CN)_4$] frameworks, does appear to be consistent with the observed results. However, through critical analysis of this idea it is clear that the C–H···π interactions must be rearranged upon both the HS-to-LS and LS-to-HS transitions. If anything, it would result in an enthalpic stabilisation of both spin states in the framework, contributing to hysteretic behaviour. It is unlikely that an increased incidence of C–H···π interactions stabilises the HS state, leading to a lower spin transition.

In formulating an alternative hypothesis to explain the observed trend that longer alcohols produce SCO at lower temperature, it is necessary to consider the contributing energetics in

the framework. To simplify the system, focus will be placed on the two major factors at play: the SCO energetics of the framework, and host–guest repulsion. Cooperativity of the lattice favours abrupt spin state switching once the necessary threshold of the lattice SCO energetics ($\Delta G = 0$, **§1.4.1**) is reached. Countering this is the kinetic volume of the guest which is temperature-dependent: as temperature decreases, kinetic volume decreases. The pore volume of the lattice follows the kinetic volume of the guest, influencing the SCO behaviour as the favoured lattice dimension changes.

Another factor to consider is the compressibility of the guest. Smaller guests are able to be compressed more as there are fewer relatively incompressible covalent bonds, and a greater proportion of intermolecular interactions, which have more flexible interatomic distances and conformational geometries, and may be compressed more easily. As the guest size increases it becomes less compressible, producing a greater host–guest repulsion effect such that the comparative influence on temperature-dependent behaviour is more pronounced. It is important to note that this theory is consistent with the aforementioned result reported in Fellows' thesis, that roughly the same number of atoms of each alcohol guest species was adsorbed into the lattice pores.[5] The necessary observation to make in conjunction with this result is that while the number of atoms remains relatively constant, the number and nature of the interatomic bonds and intermolecular interactions changes between the different alcohols.

In these SCO systems, the guest can be treated as a partially compressible lattice component whose volume is temperature dependent, with the comparative effect of the guest kinetic volume influenced by the size of the guest. Conventionally in SCO coordination frameworks, abruptness of the spin transition is thought to be determined solely by the cooperativity of the framework. However, this model is insufficient to explain the significant effect on SCO from the adsorbed guest molecules in a framework material, while the lattice structure is not significantly affected. The rigidity of the [Fe(pyrazine)M(CN)$_4$][5] and [Fe(bpac)M(CN)$_4$]·*x*(bpac) (M = Ni, Pd, Pt) frameworks (*vide infra*) have been shown to retain an orthogonal lattice conformation with different adsorbed guest species. While structural data have not been obtained for all framework solvates of the [Fe(bpac)M(CN)$_4$]·*x*(bpac) series, it can be expected that they would also keep the same orthogonal structure described in **§2.3**, due to the rigidity of the lattice components and the presence of bpac guest, which would help to stabilise the pore space. Considering that the lattice cooperativity ought to be essentially the

same if the lattice structure is the same, the vastly different SCO behaviours must arise from the influence of the adsorbed guest molecules. It is therefore necessary to include the guest in an energetic treatment of the SCO behaviour in a framework lattice. Treating the guest as part of the lattice in a two-component system is a new concept.

Figure 3-10 provides a qualitative pictorial representation of the energetic contributions from cooperative SCO, and the lattice while incorporating a *small* guest. In the figure, the contributions to the Gibbs free energy (G) from the cooperative SCO[12] and the lattice are shown individually, as well as the total energy for both factors are combined. The lattice potential well depends on the repulsive host–guest effect on the framework, and in this case is modelled as very shallow due to the greater compressibility of small guest molecules, which are more flexible regarding potential conformations. At high temperature, the energetic minimum for both the SCO and lattice is for a fully HS state. As the temperature is decreased, the slope of the SCO free energy curve decreases in magnitude until it reaches a point of bistability, such that the fully HS and fully LS states are equally energetically favourable. The lattice contribution to the combined energy plot makes little difference to the spin transition energy barrier, and there may be some HS-to-LS conversion depending on the thermal energy of the system. As the temperature is decreased further, the fully LS state is favoured by the SCO energetics, and while an intermediate state is favoured by the lattice energetic contribution, the shallow nature of the lattice potential well means that it has minimal influence on the final spin state, and the fully LS framework is observed.

It should be noted that in **Figure 3-10** and **Figure 3-11**, the representation of the lattice potential well extends higher than $\gamma = 1$, representing the hypothetical scenario where the lattice dimension may be capable of expansion beyond the maximum value allowed in the fully-HS state. In the graphic, it is the lattice contribution to the SCO behaviour that is represented rather than the lattice dimension, and while it is physically unreasonable to have $\gamma > 1$, the potential well is shown beyond this value in order to allow a more complete understanding of the lattice effects.

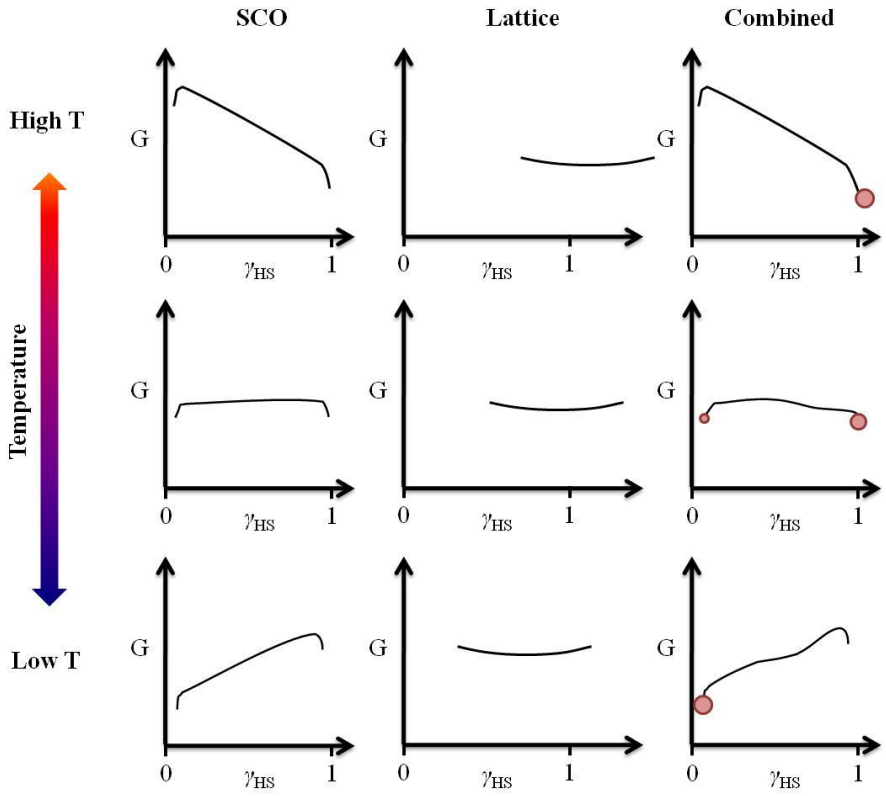

Figure 3-10: Graphic representation of the temperature-dependence on the Gibbs free energy (G) of spin transition in a cooperative system with a *small* guest species, considering both **SCO** and guest-dependent **lattice** contributions. Red circles represent the most energetically favourable spin state(s).

In contrast, very different behaviour occurs when a *large* guest is included in the cooperative framework (**Figure 3-11**). The repulsive host–guest interactions between a large guest species and the framework lattice create a much more pronounced limitation on the lattice energetics, which is represented by the greater slope in the potential well. Similar to the case for small guests, at high temperature the fully HS state is favoured by both the SCO and lattice energetic contributions. As the temperature is decreased, the fully LS state is favoured by the SCO energetics, but the fully HS state continues to be strongly favoured by the lattice energetics, with the result that overall the fully HS state is observed. As the temperature decreases further, thermal contraction of the guest reduces the internal pressure on the framework, so the lattice dimension may decrease and the favoured spin state for the lattice contribution becomes increasingly LS. Due to the strong influence of the lattice preferred state, this factor dominates in determination of the observed spin state. The major results from this model are that larger guests produce a lower and *more gradual* spin transition due

to the internal pressure effect from the kinetic volume and compressibility of the guests. It is necessary to undertake comprehensive temperature-dependent structural studies on SCO in framework materials in order to support this model, but it is proposed here as a potential explanation for the observed magnetic behaviour.

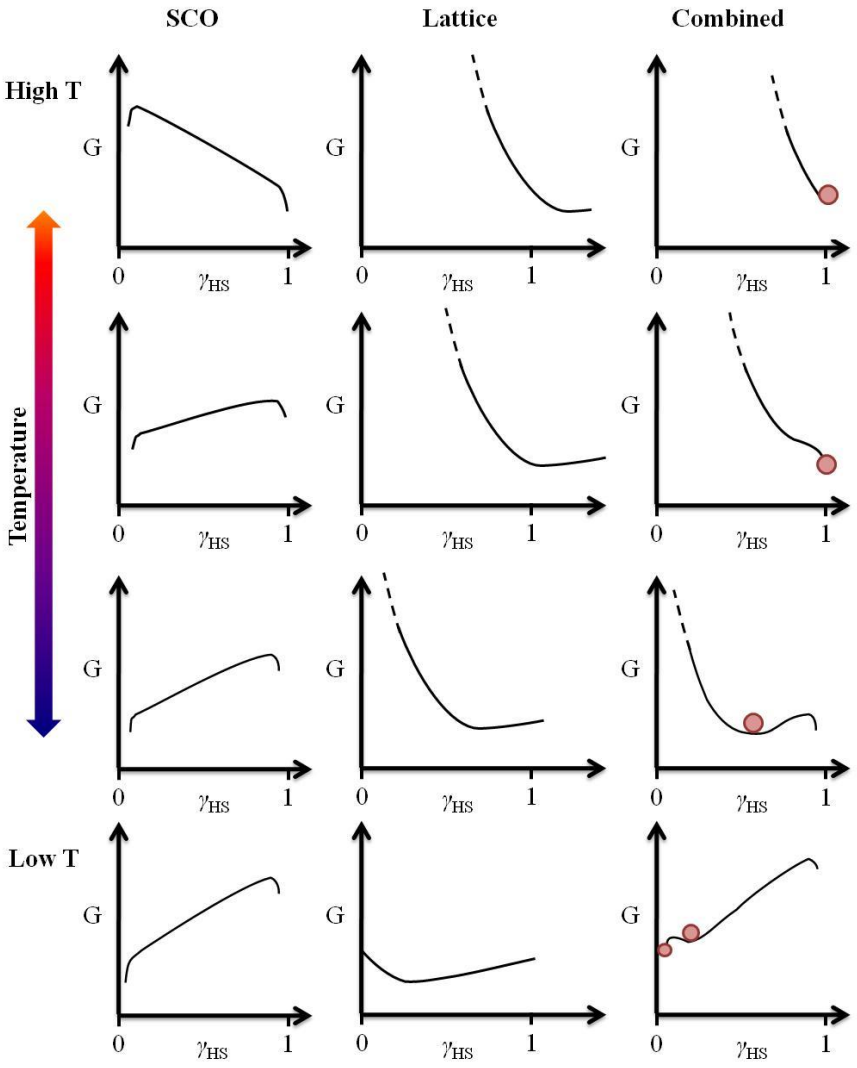

Figure 3-11: Graphic representation of the temperature-dependence on the Gibbs free energy (G) of spin transition in a cooperative system with a *large* guest species, considering both **SCO** and guest-dependent **lattice** contributions. Note that the lattice energy shown above $\gamma_{HS} = 1$ represents the hypothetical case where a larger pore dimension would be available. Red circles represent the most energetically favourable spin state(s).

Another factor that may produce gradual transitions is the number of potential guest conformations within the pores, and the degree of guest mobility. A smaller, more mobile guest would have fewer potential structural conformations, and may be able to rearrange in

order to adopt the preferred packing conformation in the pores of the HS and LS framework lattices. In contrast, a large, flexible guest molecule may adopt a large variety of different structural conformations within the lattice pores, and would be unable to rearrange as easily within the pores due to steric limitations. Due to the range of potential guest packing behaviours, larger, more flexible guests would produce a proportionally large range of local environments around Fe(II) centres in the framework, creating heterogeneous Fe(II) environments and a more gradual spin transition.

It has often been observed in published work[5] and this thesis that framework materials which exhibit uncooperative, gradual transitions also display hysteretic behaviour. This behaviour may arise due to the cooperative nature of the framework material, for although the transition occurs more gradually due to an internal pressure effect of the guest, the lattice cooperativity stabilises the spin state, creating bistability.

Adsorbed guest molecules may also be a contributing influence to the hysteresis that is often observed with gradual transitions. The change in pore dimension that accompanies spin transition may result in a rearrangement of the guest molecules between the HS and LS states, thus producing a reconfiguration of the host–guest and guest–guest intermolecular interactions. This rearrangement could be seen as a type of switch transition, whereby the guest 'switches' between different packing conformations in the HS and LS states. This would have a compound effect in conjunction with the lattice cooperativity, further stabilising the spin state and increasing the hysteresis width.

*3.3.2.3 Guest Effect on **Pd·0.5(bpac)***

As shown in **Figure 3-12**, the transition behaviour of **Pd·0.5(bpac)** changes significantly depending on the adsorbed alcohol guest. The spin transition behaviours are compared in **Table 3-2**. Of the systems measured, **Pd·0.5(bpac)**{EtOH} displays the highest spin transition temperature and largest hysteresis width, while **Pd·0.5(bpac)**{MeOH} (MeOH = methanol) produced a lower spin transition temperature, although it was still abrupt with a hysteresis of 8 K. **Pd·0.5(bpac)**{1-PnOH} (PnOH = pentanol) gave a markedly different behaviour, demonstrating a much more gradual transition with a SCO range of *ca*. 95 K, and a variable hysteresis width of 0–10 K.

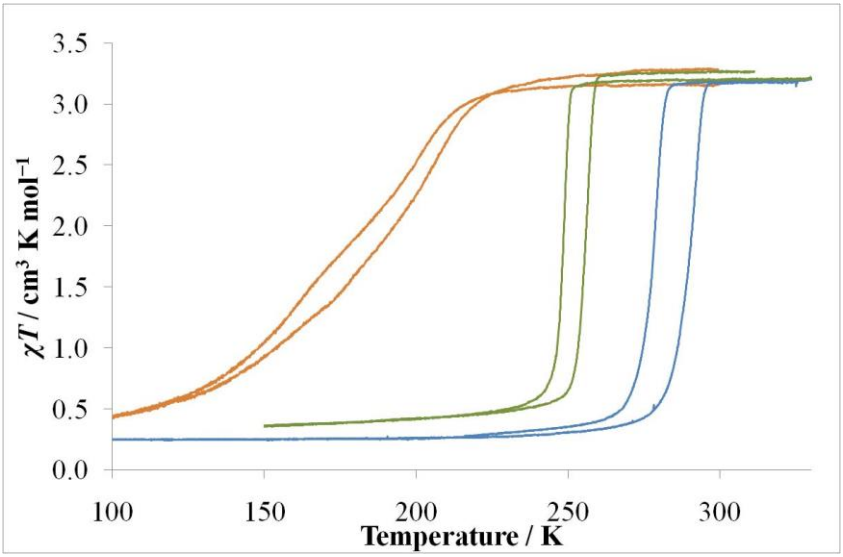

Figure 3-12: Temperature-dependent magnetic susceptibility data demonstrating the effect of different alcohol guests on the spin transition behaviour of **Pd·0.5(bpac)**: — MeOH, — EtOH, and — 1-PnOH.

Also of note is the minor difference in the abruptness and overall shape of the transition between the **Pd·0.5(bpac)**{MeOH} and **Pd·0.5(bpac)**{EtOH} samples, which reinforces the assumption that this framework has effectively fully occupied bpac ligand with minimal lattice defect sites, as well as sufficient bpac guest to occupy the pores. Desolvation and resolvation of the framework did not change the bulk properties in the same way as was observed for **Pd·0.4(bpac)** (**§3.3.1**).

Table 3-2: Comparison of the spin transition properties for **Pd·0.5(bpac)**{Alcohol}.

Alcohol	$T_{1/2}^{\downarrow}$ / K	$T_{1/2}^{\uparrow}$ / K	**SCO range / K**	**Hysteresis / K**
MeOH	248	256	11	8
EtOH	278	290	20	12
1-PnOH	176	185	95	0-10

*3.3.2.4 Guest Effect on **Pd·0.4(bpac)***

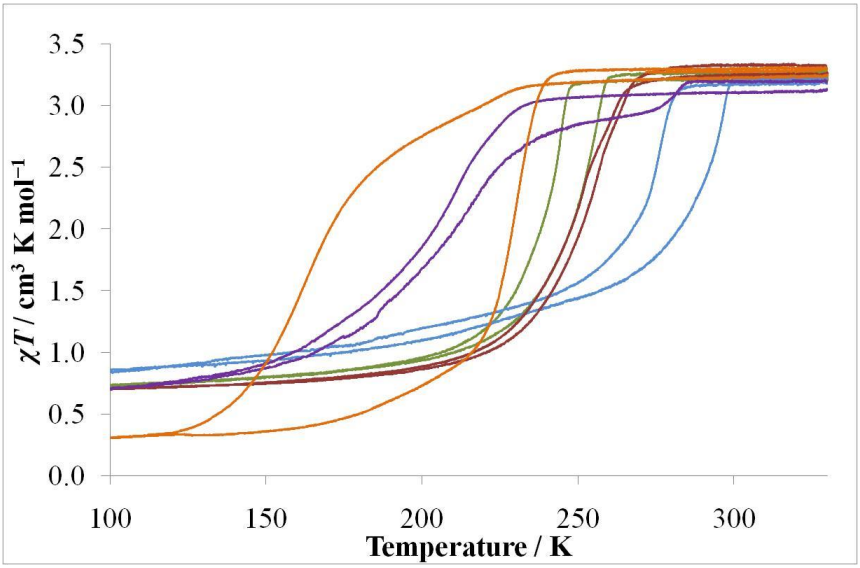

Figure 3-13: Variable temperature magnetic susceptibility data demonstrating the effect of different alcohol guests on the spin transition behaviour of **Pd·0.4(bpac)**: — MeOH, — EtOH, — 1-PrOH, — 1-BuOH, and — 1-PnOH.

The solvent-dependence on the SCO behaviour of **Pd·0.4(bpac)** is shown in **Figure 3-13**, and the spin transition properties are compared in **Table 3-3**. The **Pd·0.4(bpac)**{EtOH} sample still has the highest transition temperature, which is much more gradual than the **Pd·0.5(bpac)**{EtOH} analogue, though they both begin at very similar temperatures (see **Table 3-2**). The **Pd·0.4(bpac)**{MeOH} sample displays similar behaviour to the **Pd·0.5(bpac)**{MeOH} analogue as well (see **Figure 3-14** for a comparison graph), though it also displays a much more gradual transition, similar to the **Pd·0.4(bpac)**{EtOH} sample.

Table 3-3: Comparison of the spin transition properties for **Pd·0.4(bpac)**{Alcohol}.

Alcohol	$T_{1/2}^{\downarrow}$ / K	$T_{1/2}^{\uparrow}$ / K	SCO range / K	Hysteresis / K
MeOH	238	247	68	9
EtOH	267	282	138	15
1-PrOH	248	251	71	3
1-BuOH	201	208	90	7
1-PnOH	166	227	88	61

The **Pd·0.4(bpac)**{1-PrOH} (PrOH = propanol) sample displays a typical gradual spin

transition with a small hysteresis of 3 K, while **Pd·0.4(bpac)**{1-BuOH} (BuOH = butanol) produces an even more gradual transition over ~90 K with a hysteresis width of 7 K. The magnetic behaviour of **Pd·0.4(bpac)**{1-BuOH} also displays a secondary minor LS-to-HS transition at $T_{1/2}^{\uparrow}$ = 284 K. **Pd·0.4(bpac)**{1-PnOH} gives the most interesting result of all the alcohols studied, with a very gradual transition that seems to involve two stages, with an overall $T_{1/2}^{\downarrow}$ = 166 K and a maximum hysteresis width of 67 K. This is in sharp contrast to the **Pd·0.5(bpac)**{1-PnOH} sample, which displayed a much smaller hysteresis over a comparable temperature range.

3.3.2.5 *Comparison between **Pd·0.5(**bpac**)** and **Pd·0.4(bpac)** and General Observations*

Firstly, it is interesting to note that the $T_{1/2}^{\downarrow}$ transition temperature for the **Pd·0.5(bpac)**{alcohol} and **Pd·0.4(bpac)**{alcohol} samples were very similar, though the latter framework consistently underwent the HS-to-LS transition at a temperature *ca*. 10 K lower. This shift to lower temperature may be attributed to a change in the host–guest interactions. As the amount of bpac in the pores is decreased, a greater concentration of solvent guest molecules in the pores is possible. These results suggest that the higher concentration of adsorbed solvent guest leads to an increase in the guest repulsion effect on the framework lattice, which would result in the lower spin transition temperatures as described in **§3.3.2.1**. However, the relative effect on the lattice of bpac and solvent guest is as-yet unknown, and further studies are necessary to fully understand this behaviour.

The **Pd·0.5(bpac)**{MeOH} and **Pd·0.5(bpac)**{EtOH} samples produce abrupt spin transitions, but the **Pd·0.4(bpac)** analogues produce much more gradual transitions. As explained in **§3.3.1** the spin transitions of these **Pd·0.4(bpac)** samples are abrupt within the crystallites, but due to the distribution of bpac guest occupancies there is a continuum of crystallites that undergo spin transition over a range of different temperatures. It is expected that within the sample there is a small proportion of crystallites with a concentration of bpac guest that is close to the ideal half occupancy in the lattice pores, and that these crystallites display similar SCO behaviour to the **Pd·0.5(bpac)** material. As the bpac guest concentration in a crystallite decreases, the spin transition temperature of that crystallite decreases, creating the gradual transition 'tail' that is observed.

With the exception of EtOH in **Pd·0.4(bpac)**, increasing the alcohol chain length also results in a more *gradual* transition (shown in the SCO range values). As explained in **§3.3.2.2**, this

may arise due to the repulsive effect of guest molecules on the framework, which becomes more pronounced as the guest size increases, as well as the potential guest packing conformations, which would produce heterogeneous local environments around the Fe(II) centres.

There also seems to be a general trend, with the exception of MeOH, for longer alcohol chains to lead to a lower spin transition temperature. The temperature trend may be explained by a guest repulsion effect that depends on the compressibility of the guest species, and the temperature-dependence on the kinetic volume of the guest, as explained in **§3.3.2.2**. When solvated with MeOH, the pyrazine-based frameworks display a higher transition temperature than when solvated with EtOH, completing the trend.[5] It is therefore an unexpected result in the bpac-based frameworks that MeOH does not follow the trend.

3.3.2.6 Influence of Methanol

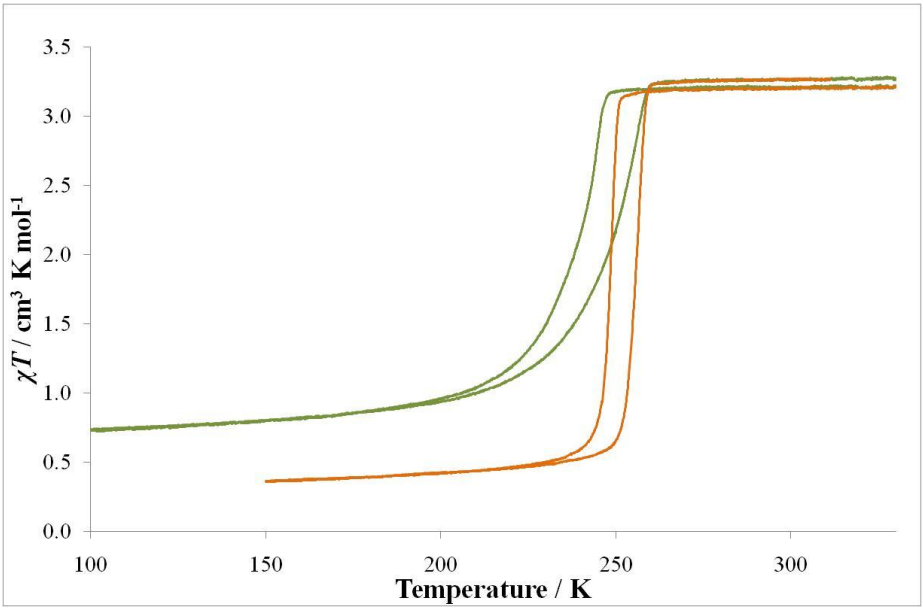

Figure 3-14: Comparison of the magnetic susceptibility data for MeOH-solvated **Pd·0.4(bpac)**; and **Pd·0.5(bpac)**.

In attempting an explanation for the transition behaviour of the MeOH-solvated samples (**Figure 3-14**), focus will be placed on the **Pd·0.5(bpac)** framework as its homogeneous structure is more fully understood and explained. The major structural differences between this framework and [Fe(pyrazine)Pd(CN)$_4$] are the length of the pillar, and the inclusion of bpac molecules within the framework pores (with an estimated half occupancy). The bpac

pillar ligand is ~3.5 times longer than pyrazine, leading to a corresponding increase in the *c*-axis dimension. However, it was shown that even with less than half occupancy of bpac guest in the pores, the frameworks adsorb a comparable amount of EtOH guest (see **§0**), implying that they have a similar amount of solvent accessible void space. It must then be the nature of the void space that determines this different behaviour.

An attempt has been made to rationalise the observed behaviour of **Pd·0.5(bpac)**{MeOH} based on the effect of the lattice pore space on potential solvent packing behaviour. In the liquid state, alcohols have been shown to adopt long hydrogen-bonding chains.[13-14] When in a restricted pore space, alcohols no longer have the conformational flexibility to produce these chains, and instead are more likely to adopt an alternating conformation in the pores, as described by Fellows for the [Fe(pyrazine)M(CN)$_4$] (M = Ni, Pd, Pt) frameworks.[5] This would also limit the extent of hydrogen-bonding guest–guest interactions, as any particular alcohol molecule in the pores would be sterically constrained to hydrogen-bond to only one or two other alcohol molecules. On the other hand, the **Pd·0.5(bpac)** material, while it has the same total solvent-accessible volume as the [Fe(pyrazine)M(CN)$_4$] frameworks, has wider pores which may enable hydrogen-bonding chains of MeOH (the smallest alcohol) to form, as the molecules are able to align along the same direction.

A very simplified illustration of this difference in guest packing is shown in **Figure 3-15**. While the small pore dimension in the [Fe(pyrazine)M(CN)$_4$] frameworks limits hydrogen-bonding chain formation of MeOH molecules, the longer pores in **M·0.5(bpac)** would allow hydrogen-bonding chains for MeOH, with the length of the chain determined by the number and position of guest bpac molecules. EtOH and the other larger alcohols are too big to adopt this chain conformation and still retain efficient packing in the pores, so hydrogen bonding clusters are much more limited in size.

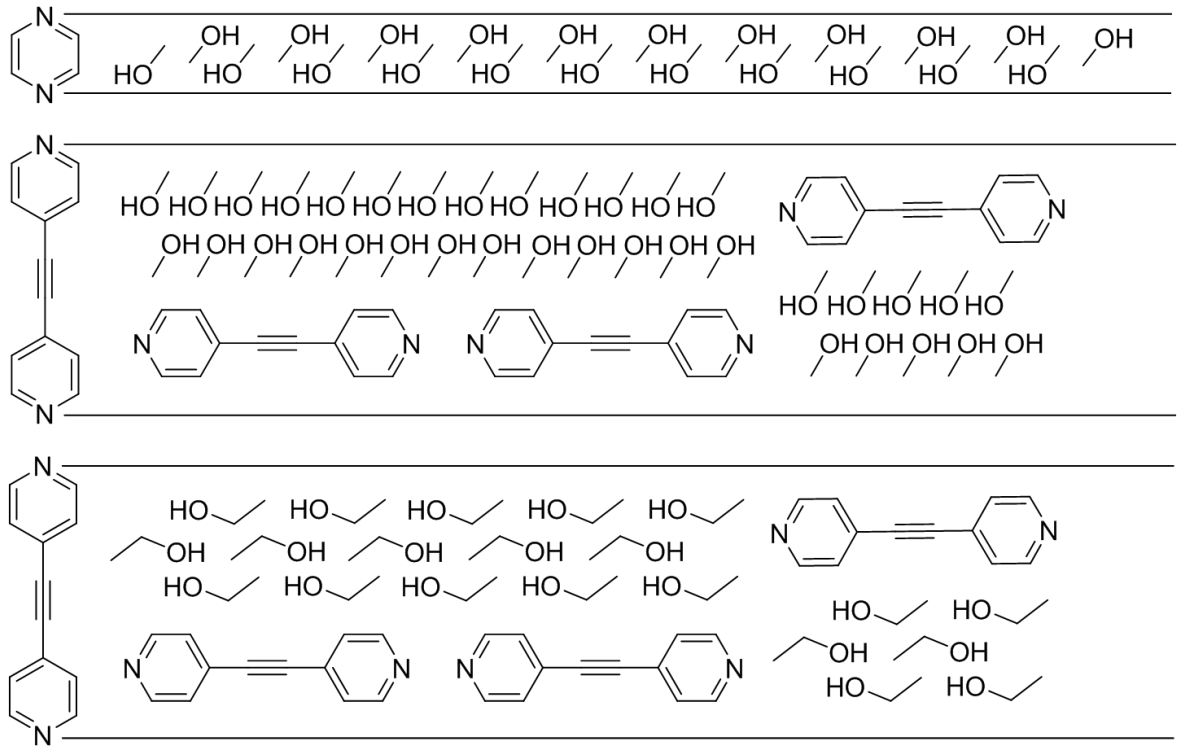

Figure 3-15: Simplified potential guest stacking modes for MeOH-solvated [Fe(pyrazine)M(CN)$_4$] (top) and **M·0.5(bpac)** (middle); and EtOH-solvated **M·0.5(bpac)** (bottom).

As MeOH is sterically allowed to adopt the hydrogen-bonding chain configuration in the **Pd·0.5(bpac)** framework, this leads to an increase in the extent of the strong hydrogen-bonding interactions between guests which may stabilise the HS state (as explained in **§3.3.2.1**), leading to the lower transition temperature for MeOH. The other alcohols are too large to adopt these hydrogen-bonding chains, and thus follow the regular transition temperature trend. Another potential effect could be the number of guest molecules that may be adsorbed within the framework pores. If MeOH is small enough that it may better access restricted pore spaces, then more MeOH molecules would be able to adsorb into the lattice pores, and the guest repulsion effect on the framework would be more pronounced, stabilising the HS state (as described in **§3.3.2.2**).

Following this hypothesis as to the origin of the unexpected spin transition behaviour with MeOH guest, EtOH must then be the guest that most successfully balances the concentration of guest–guest hydrogen-bonding interactions and quantity of adsorbed guest to produce spin transition at the highest temperature. In longer-chain alcohols, there would be an increase in the internal guest repulsion effect and the transition temperature subsequently decreases.

3.3.2.7 Influence of 1-Propanol and 1-Butanol

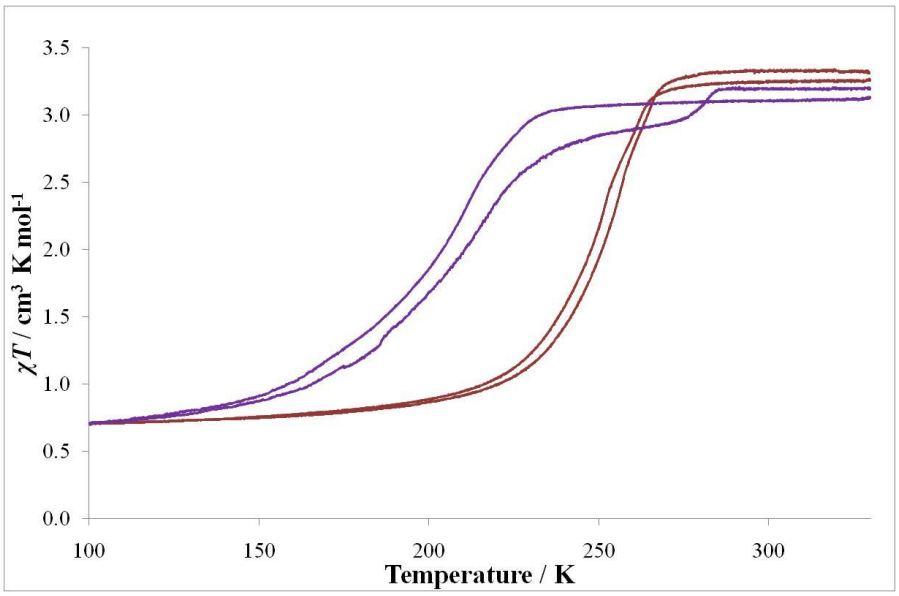

Figure 3-16: Magnetic susceptibility data for **Pd·0.4(bpac)** solvated with —1-PrOH, and —1-BuOH.

As seen in **Figure 3-16**, **Pd·0.4(bpac)**{1-PrOH} produces a gradual transition with a small hysteresis. The more gradual transition is most likely due to the combined effect of heterogeneous sample composition and the more pronounced guest internal pressure effect as described in **§3.3.2.2**. This effect has an even stronger influence in the **Pd·0.4(bpac)**{1-BuOH} material due to the larger 1-BuOH guest molecules, with the result that this sample displays a more gradual transition at lower temperature. The hysteresis width is greater than that observed in the **Pd·0.4(bpac)**{1-PrOH} sample, which may be due to the increased concentration of host–guest C–H···π interactions. These interactions would be rearranged as the material undergoes spin transition, thus enthalpically stabilising the spin state and increasing the bistability range.

3.3.2.8 Influence of 1-Pentanol

Pd·0.4(bpac){1-PnOH} produces the most interesting behaviour of all the alcohols studied. As shown in **Figure 3-17**, **Pd·0.5(bpac)**{1-PnOH} gives a gradual transition with small hysteresis that can be explained similarly to the behaviour of **Pd·0.4(bpac)**{1-BuOH}. On the other hand, **Pd·0.4(bpac)**{1-PnOH} displays a gradual transition with a very large hysteresis of up to 67 K. There also appear to be two different transition stages observed in the magnetic susceptibility data.

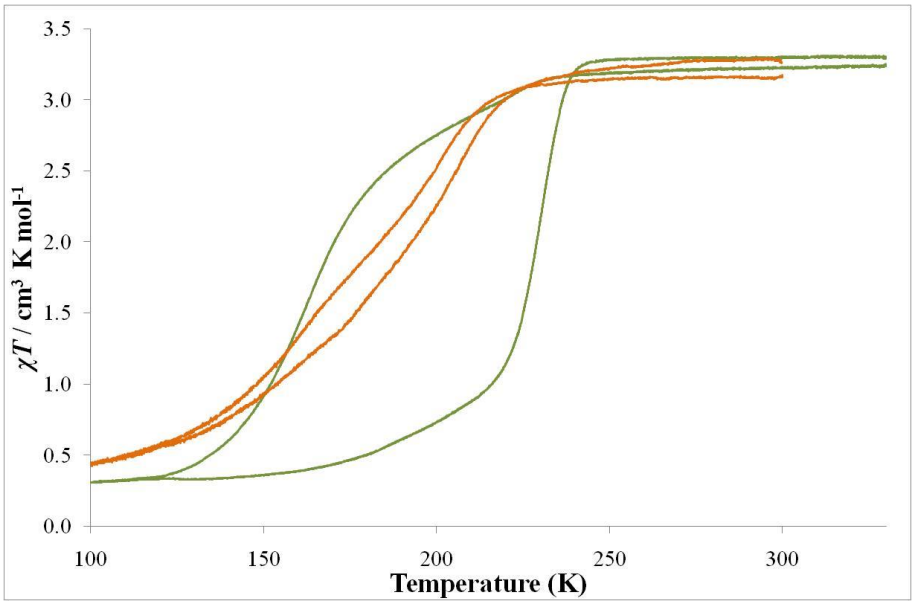

Figure 3-17: Comparison of the magnetic susceptibility data for 1-PnOH-solvated **Pd·0.4(bpac)**; and **Pd·0.5(bpac)**.

In order to explore this interesting behaviour further, a variable temperature PXRD experiment of **Pd·0.4(bpac)**{1-PnOH} was undertaken, and Le Bail fits performed to extract unit cell parameters. The expected *Pmmm* space group and unit cell were unsuccessful in fitting the data, and though many different unit cell and space group models were tried, the most successful fit was obtained using the minimal non-isomorphic supergroup, *Immm* with a doubling of each of the unit cell parameters. A comparison of these fits can be seen in **Figure C-11** and **Figure C-12**. An intensity plot of the powder diffractogram peaks is shown in **Figure 3-18**, the modelled unit cell parameters can be seen in **Figure 3-19**, a comparison between the magnetism and *a*-parameter behaviour can be seen in **Figure C-13**, and a portion of the original powder diffractograms is shown in **Figure C-14**.

According to the magnetic data, the HS-to-LS transition begins gradually at 231 K, until the gradient becomes steeper at *ca*. 192 K. This first stage of the spin transition accounts for ~20% of the observed SCO, while the second stage continues until 120 K and accounts for the remainder. The LS-to-HS transition follows a similar pattern, beginning with a gradual transition from 150 to 210 K, after which the transition rapidly becomes abrupt, finishing at *ca*. 240 K.

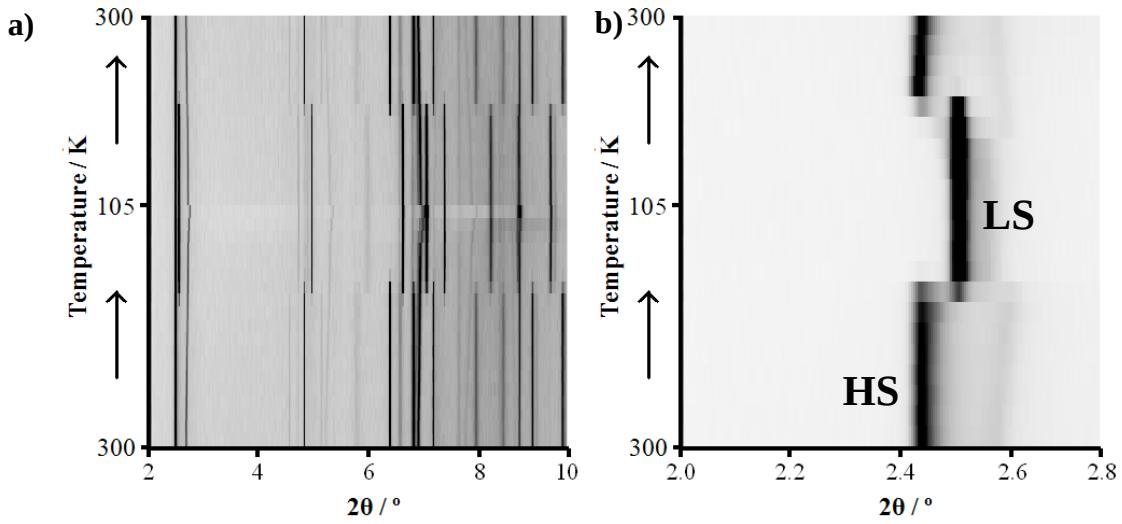

Figure 3-18: a) Intensity plot showing the powder diffraction peak evolution as the **Pd·0.4(bpac)**{1-PnOH} sample was cooled from 300 to 105 K, then warmed back to 300 K; and **b)** a close-up of the (002) peak.

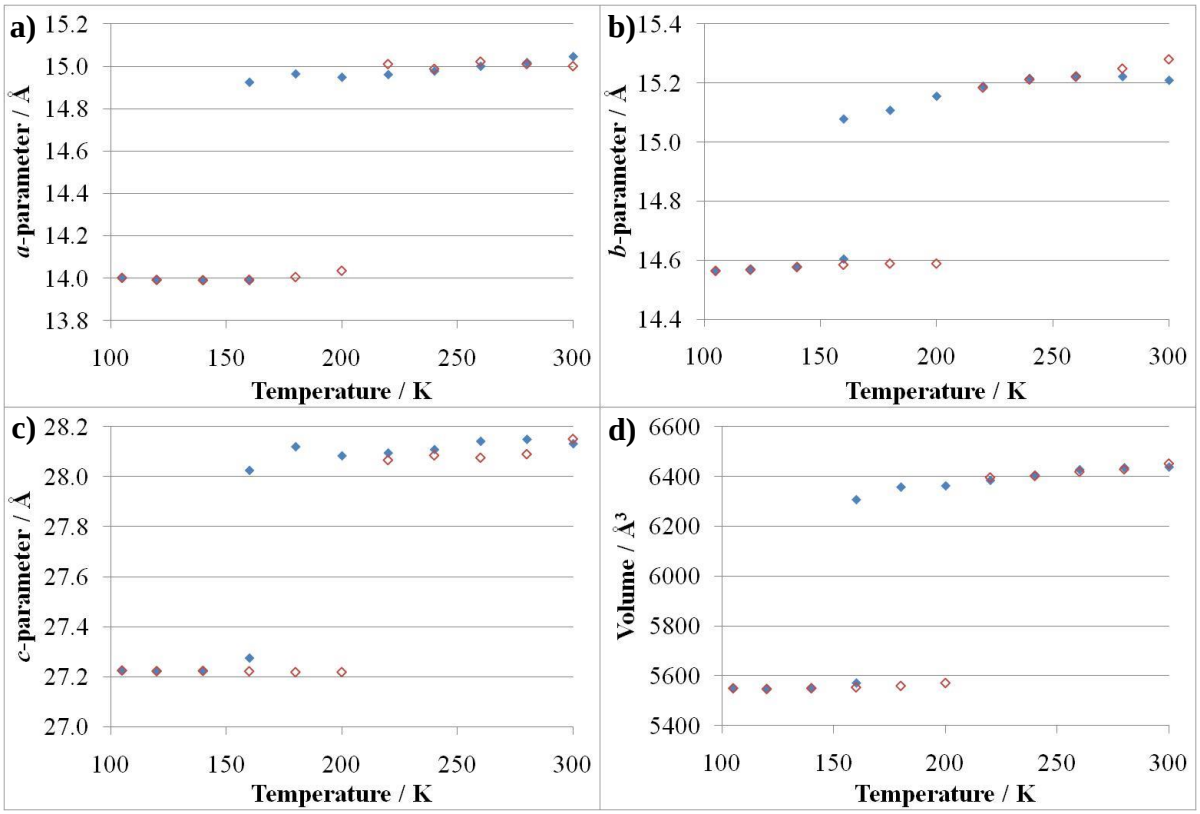

Figure 3-19: Variable temperature unit cell parameters for **Pd·0.4(bpac)**{1-PnOH}: **a)** *a*-parameter; **b)** *b*-parameter; **c)** *c*-parameter; and **d)** unit cell volume, upon ◆ cooling and ◇ warming.

In order to determine whether these two transitions are caused by different SCO phases within the bulk material, the magnetic and powder diffraction data must be carefully analysed and compared. The best way to do this is to convert the data into the relative stoichiometric fraction of the HS state, as described in **§7.6**. This comparison of the relative stoichiometric fraction (γ_{HS}) is shown in **Figure 3-20**.

The PXRD and magnetic data agree remarkably well, with both techniques demonstrating similar transition behaviour. It is noteworthy that upon cooling over the spin transition, the HS fraction shown in the PXRD results appears to be higher than that of the magnetic results. There are two major factors that may give rise to this observed difference: there is an inherent uncertainty in measuring the intensity of the peak, as it is not a quantitative measure of the phase stoichiometry; and peak broadening, which could arise from strain in the crystallites or a distribution of unit cell parameters, would also result in a lower peak intensity.

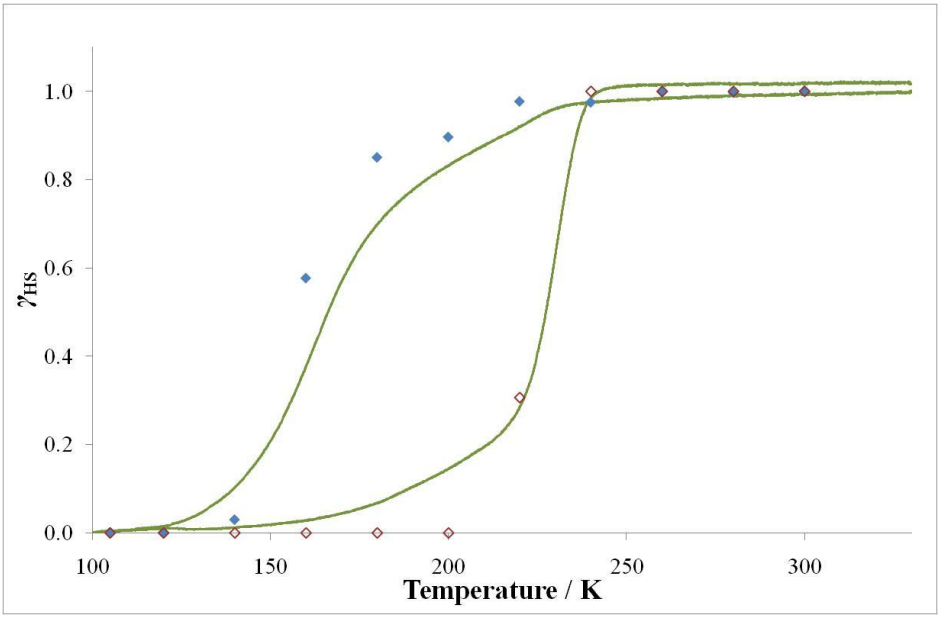

Figure 3-20: Comparison of the relative stoichiometric fraction of HS states (γ_{HS}) for **Pd·0.4(bpac)**{1-PnOH} — as determined through the magnetic susceptibility; and the relative intensity of the (002) peak of the HS phase, upon ◆ cooling and ◇ warming.

Over the transition, the PXRD results display two distinct HS and LS phases, demonstrated clearly by the (002) peak as shown in **Figure 3-18b**. The LS phase first appears in the diffractograms after cooling to 160 K, implying that the partial spin transition that occurs down to 180 K does not involve the transition of whole crystallites, but rather arises from the HS-to-LS transition of individual Fe(II) centres distributed within crystallites in the HS

phase. While no intermediate phase is observed, the modelled unit cell parameters (**Figure 3-19**) do decrease over the first stage of the HS-to-LS transition, though this behaviour may be principally attributed to thermal contraction, rather than partial transition to the LS state.

A similar explanation can be made for the behaviour at the beginning of the warming transition, in which the magnetism shows an increase in the HS sites, but the PXRD remains constant with all crystallites in the LS phase until *ca*. 220 K, at which temperature the HS phase is first observed. This implies that in the low temperature LS-to-HS transition stage, HS sites would be distributed within LS crystallites.

SCO materials which display gradual, non-cooperative transitions usually show a gradual change of the average unit cell dimension between the HS and LS states.[5] The behaviour seen here is then very unusual, as the transition is very gradual but there are two discrete HS and LS phases (as shown in **Figure 3-18b**). The large hysteresis also implies that there is a high energy barrier to spin transition which leads to the high cooperativity. This behaviour must arise through different structural mechanisms than are usually observed, which could potentially be explained through determining the cause of this disparity between the PXRD and magnetic data.

The first factor to consider in attempting to explain the observed behaviour is bulk heterogeneity. It is believed that this sample contains a distribution of framework phases with different occupancies of bpac ligand and guest (see **§3.2.3**). The sample can be treated as a continuum of framework states with different bpac occupancies in the lattice and pores, which would produce spin transition at different temperatures. This heterogeneity of the framework phases in the sample thus accounts for the observation that the gradual magnetic transition occurs with an abrupt phase transition within crystallites.

This observation may also help explain the two-stage behaviour observed in the magnetic data. If, as was proposed for the **Pd·0.4(bpac)**{EtOH} sample (**§3.3.1**), the bulk material of **Pd·0.4(bpac)**{1-PnOH} contains some crystallites with close to the ideal half-occupancy of bpac guest, then a portion of the sample will display the same behaviour as was observed in the **Pd·0.5(bpac)**{1-PnOH} material. The crystallites with a lower bpac concentration would then exhibit different behaviour. If the gradual magnetic behaviour of the **Pd·0.5(bpac)**{1-PnOH} sample is superimposed on a second, more abrupt spin transition

with a large hysteresis, then the two-stage spin transition behaviour of the **Pd·0.4(bpac)**{1-PnOH} sample may be observed (**Figure 3-21**). While the model represented in the figure is crude, this idea may partially account for the observed spin transition behaviour.

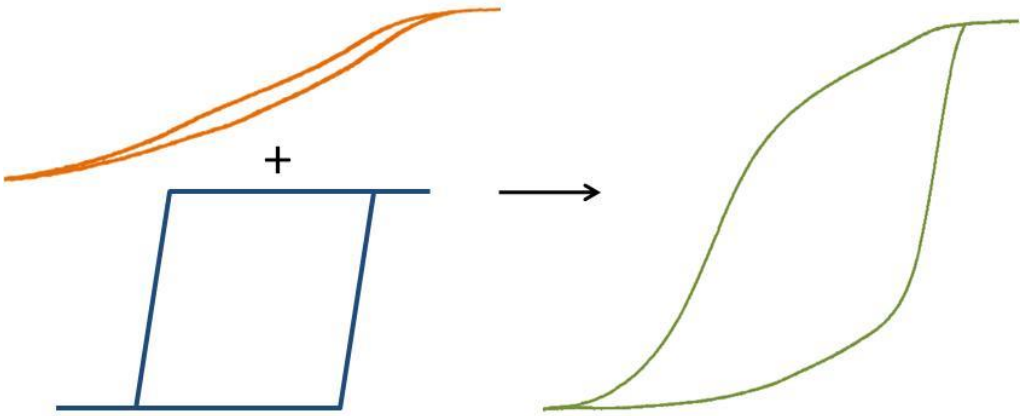

Figure 3-21: Cartoon representation of the way in which two spin transition behaviours, one gradual with small hysteresis and one abrupt with large hysteresis, may superimpose to produce the two-stage behaviour observed in **Pd·0.4(bpac)**{1-PnOH}.

The observations made thus far on the heterogeneous sample composition of **Pd·0.4(bpac)**{1-PnOH} help explain the gradual, two-stage magnetic transition while there are two distinct HS and LS phases, with no intermediate between them. However, the observations do not account for the disparity in the proportion of HS Fe(II) sites according to the magnetic and powder diffraction results. In particular, if each crystallite is expected to undergo an abrupt, cooperative spin transition, there would be evidence for a phase transition over the gradual magnetic transition stages, but instead there is scarce evidence for such a phase transition until the more abrupt magnetic transition stage.

In order to understand this result and attempt an explanation, it is useful to establish a few key observations and assumptions. Firstly, it is interesting to note that the spin transition behaviour of this sample goes to much higher completion than the other alcohols studied and there is no evidence of the HS phase at low temperature in the PXRD data, implying that the solvent guest has somehow activated previously inactive crystallites. The cooling data at 220–140 K, and the warming data at 160–200 K show that the crystallite phase as shown in the PXRD results remains wholly in the phase that dominates in the magnetism. This result, coupled to the fact that there is minimal evidence for intermediate phases in the PXRD data

implies that the minority spin states are dispersed in a matrix of the dominant spin state, and that the crystallite as a whole will retain the bulk crystallographic characteristics of the dominant state. This theory is also supported through study of the change in the HS unit cell volume in **Figure 3-19d**, which shows a decrease between 220 and 160 K that corresponds to ~11% of the difference between the HS and LS states. A distribution of LS centres in HS crystallites could account for the difference shown.

This bulk homogeneity argument is an alternative to the sample heterogeneity theory proposed above, and in the absence of additional structural information is proposed tentatively. In order to develop a working hypothesis of the mechanisms behind the gradual transition stages, attention will be focussed on the crystallographic conclusions that the *Immm* space group provides.

The *Immm* space group was used to model the unit cell parameters as the model peak positions best fit the data, while remaining crystallographically reasonable. As each unit cell parameter is doubled, the volume is multiplied by 8, and the asymmetric unit similarly increases in size. **Figure 3-22** compares the *Pmmm* asymmetric unit with a possible new asymmetric unit that produces the same full framework structure considering the symmetry operations associated with the *Immm* space group. Importantly, this new asymmetric unit contains 4 crystallographically distinct Fe atoms, and two half bpac ligands. The symmetry of the *Pmmm* space group has been somehow lost, potentially through asymmetric rotation of the bpac pyridyl rings, or through alignment of the guest 1-PnOH molecules in a regularly ordered manner within the framework.

With the four distinct Fe(II) sites in the lattice, it could be possible for one to undergo SCO without greatly affecting the bulk crystallographic properties, as the other three would maintain the unit cell parameters through their associated bond lengths. However, the bond lengths and positions associated with these three sites would change slightly to compensate for the bond length differences of the site which undergoes SCO, and overall would result in a slight decrease in the unit cell parameters, as seen in **Figure 3-19**. Following this logic, a maximum of 25% of the Fe(II) sites within the framework could undergo SCO without significantly affecting the bulk unit cell parameters. Once over this amount, however, the framework would be under sufficient strain for it to cooperatively undergo spin transition, structurally converting to the other phase. The effect on spin transition behaviour of multiple

crystallographically distinct Fe(II) sites which have the same ligand environment in a framework has been reported previously.[15-16]

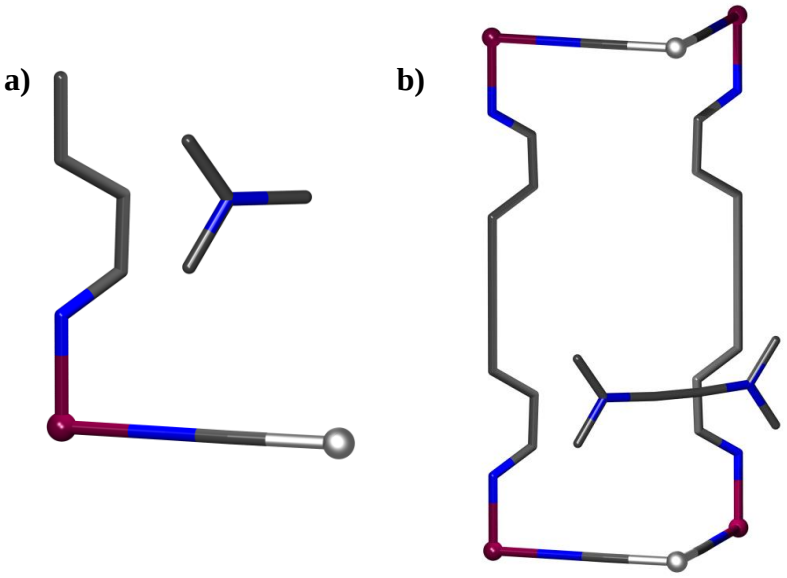

Figure 3-22: a) The asymmetric unit for **Pd·(bpac)** in the *Pmmm* space group; and **b)** a possible asymmetric unit for **Pd·(bpac)** in the *Immm* space group.

This explanation may account for the difference in the HS proportions as observed in the PXRD and magnetism data for the first gradual transition stage beginning the HS-to-LS transition, and the LS-to-HS transition. It could also account for the transition 'tail' at the end of the HS-to-LS transition, in which HS sites are dispersed in a matrix of the LS phase. This hypothesis regarding inequivalent Fe(II) environments in the crystallites provides a second potential explanation for the two-stage behaviour observed. It may be possible that this mechanism works in conjunction with the heterogeneous sample composition to produce a compound effect on the overall spin transition behaviour.

It is also interesting to compare the unit cell parameters for HS and LS **Pd·0.4(bpac)**{EtOH} and **Pd·0.4(bpac)**{1-PnOH}, shown in **Table 3-4**. Of particular note is the difference in the normalised volume: **Pd·0.4(bpac)**{1-PnOH} is 3% larger than **Pd·0.4(bpac)**{EtOH} in the HS state, and is 1% smaller in the LS state. While these values are not very sizable, the phenomenon of SCO is very sensitive to ligand field strength and outer ligand field effects, and the resulting behaviour is readily affected.

Table 3-4: Comparison of the unit cell parameters and linear Fe–Pd–Fe distance ($d_{Fe–Pd–Fe}$) for HS and LS **Pd·0.4(bpac)** solvated with EtOH and 1-PnOH. The **Pd·0.4(bpac)**{1-PnOH} parameters are halved, and the volume reduced by a factor of 8, to be fully comparable with the **Pd·0.4(bpac)**{EtOH} parameters.

Alcohol	***a*** **/ Å**	***b*** **/ Å**	***c*** **/ Å**	$d_{Fe–Pd–Fe}$ **/ Å**	**Volume / Å^3**
EtOH HS	7.4477(8)	7.4520(8)	14.0369(2)	10.5357(3)	779.0(1)
1-PnOH HS	7.5230(6)	7.6044(7)	14.0659(15)	10.697(2)	804.7(2)
EtOH LS	7.2534(4)	7.0994(3)	13.6377(2)	10.1495(2)	702.27(8)
1-PnOH LS	7.2820(3)	7.0001(11)	13.6124(8)	10.100(1)	693.9(1)

The increased HS unit cell created by 1-PnOH is probably due to the larger size of the guest creating a greater internal pressure effect due to a repulsive interaction between the guest and the framework. As explained in **§3.3.2.2**, this pressure effect would stabilise the HS state, and the increased bond lengths in the lattice would also decrease the ligand–metal interaction strength, further stabilising the HS state and decreasing cooperativity.

On the other hand, the decreased LS volume would lead to stabilisation of the LS state and greater cooperativity due to the greater ligand–metal bond strength due to increased orbital overlap (**§1.4.5**). As the framework undergoes SCO, the longer 1-PnOH guest molecules would also be required to rearrange within the lattice pores, disfavouring spin transition. The relatively large difference in the framework dimension between the HS and LS states also creates a potential energy barrier to transition, disfavouring the spin transition and contributing to the bistability.

The combination of these factors could then account for the large hysteresis observed with the gradual transition. However, the question still remains as to why the hysteresis is so much greater for **Pd·0.4(bpac)**{1-PnOH} than for **Pd·0.5(bpac)**{1-PnOH}. Without PXRD data for the latter these results cannot be fully compared, but it is known that the ultimate difference between these frameworks is the concentration of coordinated and guest bpac. Perhaps the larger hysteresis width of **Pd·0.4(bpac)**{1-PnOH} is due to a greater internal pressure effect and increased number of host–guest interactions due to the increased number of 1-PnOH guests in the available pore space. As explained in **§3.3.2.2**, these factors may lead to greater bistability of the framework spin state, and a wider hysteresis.

3.3.2.9 Influence of a 1:1 Methanol/Ethanol Solvent Mixture

A detailed study concerning the effect of mixed solvent guest incorporation into the [Fe(pyrazine)M(CN)$_4$] (M = Ni, Pd, Pt) frameworks has been previously performed by Elizabeth Fellows, with the results presented in her PhD thesis.[5] She demonstrated that depending on the specific guests mixed, and the relative proportions, the resulting behaviour may lie between the behaviours of the individual guest species, or it may result in a completely different, unexpected behaviour.

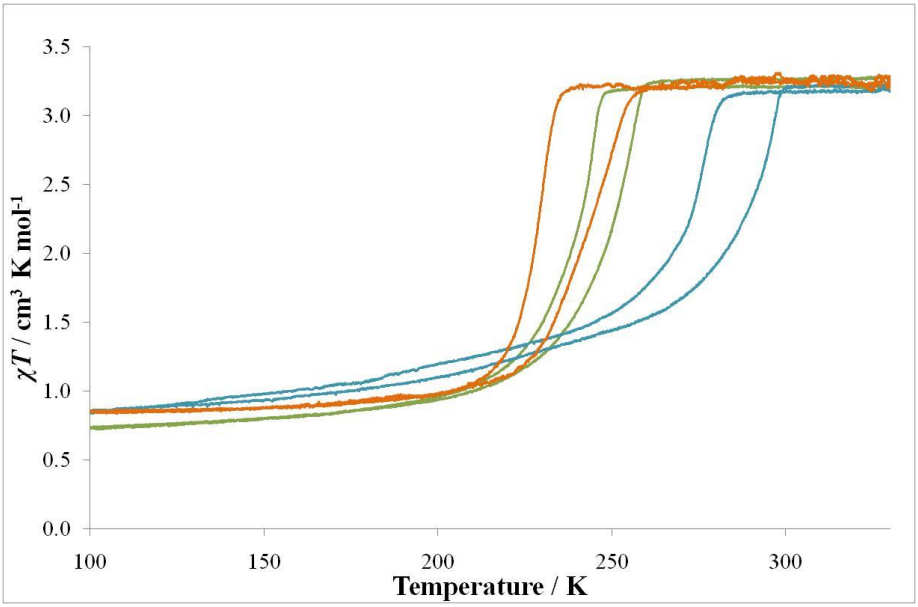

Figure 3-23: Variable temperature magnetic susceptibility data of **Pd·0.4(bpac)**, comparing the guest effect of — MeOH, — EtOH, and a — 1:1 MeOH/EtOH solvent mix.

As a representative study of the effect of introducing mixed solvent guest into the **Pd·0.4(bpac)** framework, a 1:1 (vol/vol) EtOH/MeOH solution was used. A volumetric equivalent mix, rather than a molar equivalent mix, was used as a best approximation in order for each solvent to occupy a roughly equal amount of the framework pore volume. In this way, it was anticipated that the overall number of host–guest interactions due to the component guest species would be roughly equal. However, as there would be more MeOH molecules in the pores than EtOH molecules, there would still be more guest–guest interactions involving MeOH molecules. Conversion of the 1:1 volumetric ratio to the equivalent molar ratio using the density and molar mass of the solvent molecules gives 1.44:1.00 MeOH/EtOH.

Considering the precedent from Fellows' work,[5] it is not unusual that a 1:1 volumetric mix of MeOH/EtOH produces a behaviour that does not lie between that of the independent solvents (see **Figure 3-23**). The cause of this discrepancy is likely to be a compound effect of both guests the framework pores. As described in **§3.3.2.6**, the MeOH guest is able to form hydrogen-bonding chains in the framework pores which stabilise the HS state, and which are likely to continue being formed with the inclusion of EtOH, though perhaps to a reduced degree. It was also proposed that MeOH molecules may be small enough to access restricted pore spaces in the framework, increasing the guest repulsion effect. In addition to the presence of these two potential effects, the larger EtOH guest molecule has a greater repulsion effect on the framework host than MeOH, which would further stabilise the HS state relative to **Pd·0.4(bpac)**{MeOH}. The lowered transition temperature is likely to be caused by the combined effect of these factors.

Of further interest is the abruptness of the transition. When converting from HS-to-LS, the transition for the solvent mix is more abrupt than for either of the independent solvents, yet the LS-to-HS transition is more gradual and occurs at a relatively constant rate, with a final hysteresis of the fully HS state which is close to that observed for pure EtOH. This could be potentially driven by the entropy associated with the movement of solvent molecules into and out of the framework. It would be entropically favourable to expel solvent molecules into the surrounding medium, as they would have significantly more degrees of freedom. This effect would be further increased in a mixed solvent system, leading to an abrupt transition due to the entropically favoured HS-to-LS transition. In contrast, it is entropically unfavourable to remove highly disordered molecules from the medium and constrain them within the framework, which could explain the gradual transition observed between the LS and HS states, which is accompanied by guest adsorption into the larger structural pores.

3.4 *Pressure-Temperature Phase Diagram for Pd·0.4(bpac){EtOH}*

As shown in **Figure 3-9**, the **Pd·0.4(bpac)**{EtOH} framework displays a spin transition with hysteresis at close to room temperature. This made it an interesting candidate for gravimetric analysis of solvent uptake at various temperatures and pressures, and for investigating the resulting effect on the spin transition. The dimension change associated with the spin transition results in a difference in the adsorption behaviour, which can be monitored using gravimetric analysis. These experiments can be run by keeping the temperature constant and

varying the pressure (isotherm), or by keeping the pressure constant and varying the temperature (isobar). An example of an isobar experiment can be seen in **Figure 3-24**. The hysteresis associated with the spin transition can be clearly seen.

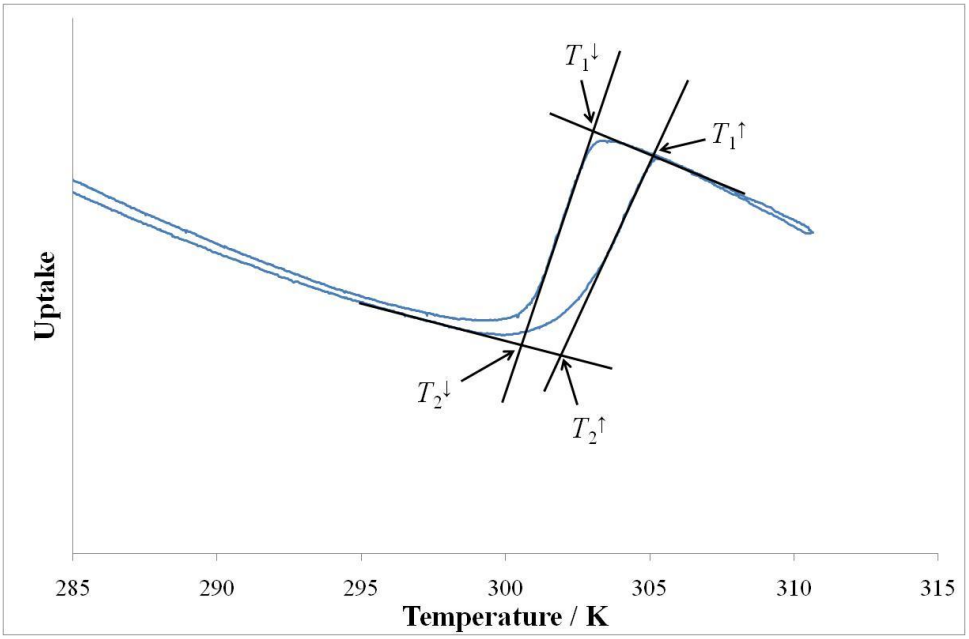

Figure 3-24: Method used to determine the spin transition parameters necessary to calculate the $T_{1/2}^{\downarrow}$, $T_{1/2}^{\uparrow}$ and SCO temperature range values using isobar experimental data. The fully HS and LS baselines are extrapolated, as are the most linear parts of the spin transition. The points at which they intersect give the necessary temperature values to calculate the desired spin transition quantities.

The $T_{1/2}^{\downarrow}$ and $T_{1/2}^{\uparrow}$ values, and the SCO temperature ranges, are approximated using values obtained by the method shown in **Figure 3-24**. It should be noted that these values are approximate because the magnetic behaviour of the spin crossover may not vary exactly linearly with the sorption properties. The SCO temperature ranges are bound by the T_1^x and T_2^x ($x = \downarrow, \uparrow$) values, and $T_{1/2}^x$ is the average of T_1^x and T_2^x, calculated using **Equation 3.2**. The spin transition temperatures determined from the isobar experiments are given in **Table 3-5**, and shown graphically in **Figure 3-25**.

$$T_{1/2}^x = (T_1^x + T_2^x)/2 \tag{3.2}$$

Table 3-5: Spin transition temperatures obtained from the EtOH adsorption isobar experiments on **Pd·0.4(bpac)**

Pressure / mbar	$T_{1/2}^{\downarrow}$ / K	$T_{1/2}^{\uparrow}$ / K	Hysteresis / K
7	302.3	304.1	1.8
14	301.7	303.4	1.7
30	298.6	302.0	3.4
45	293.3	299.8	6.5

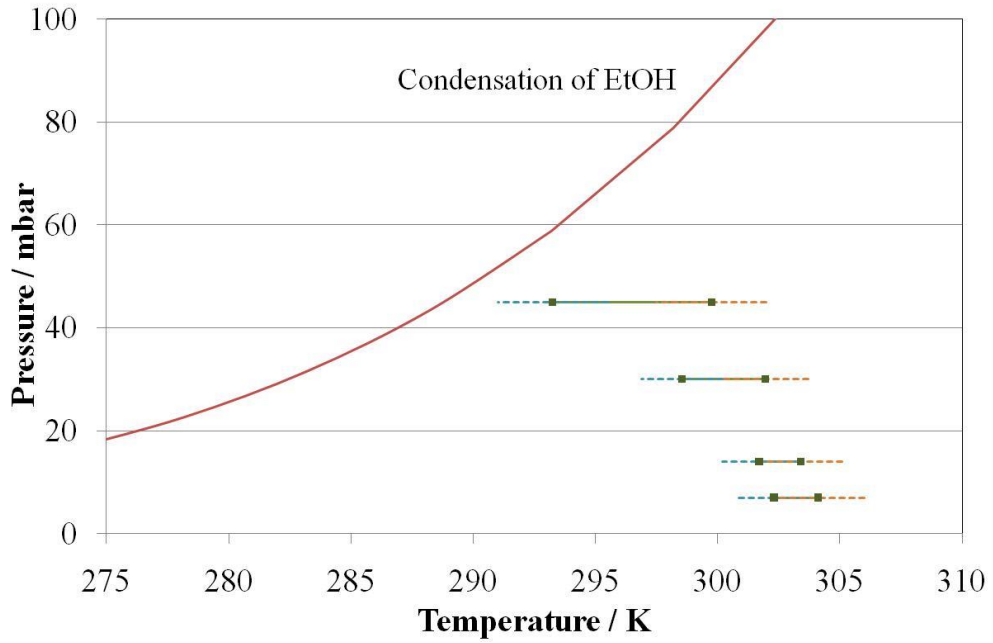

Figure 3-25: Plot of the spin transition behaviour observed in the EtOH adsorption isobars of **Pd·0.4(bpac)**. Shown in the graph are: — the temperature/pressure values at which EtOH condenses;[17] — the $T_{1/2}^{\downarrow}$ and $T_{1/2}^{\uparrow}$ values; and the SCO range upon - - - conversion to LS, and - - - conversion to HS.

The behaviour displayed in the isotherm experiments is more difficult to interpret. A plot of these isotherms can be seen in **Figure 3-26**. The 283.2 K isotherm shows no evidence of SCO behaviour at the data resolution obtained, implying that the sample was fully in the LS state above 0.5 mbar. However, starting at the 288.2 K isotherm, an unusual hysteresis is shown, resolving into a noticeable step at 298.2 K. As the temperature is increased, the hysteresis becomes larger and the step occurs at higher pressure.

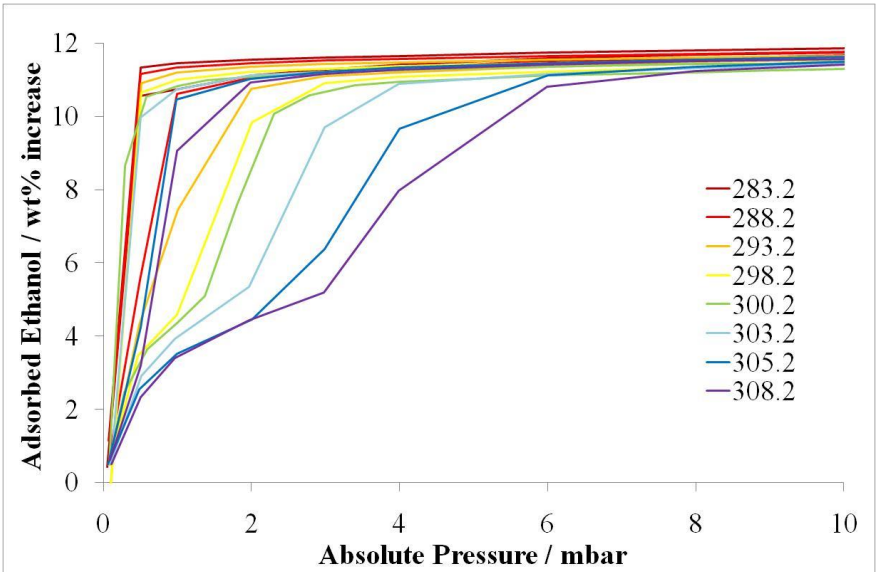

Figure 3-26: Part of the EtOH adsorption isotherms for **Pd·0.4(bpac)**. The legend at the right gives the temperatures (K) corresponding to the line colour.

As far as the experimental resolution allows, comparison of the low-pressure adsorption step between the different isotherms (**Figure 3-26**) shows that it occurs when the material has adsorbed *ca*. 5 wt% EtOH. Stepped adsorption behaviour in isotherms is often due to a distribution of pore sizes.[18] As discussed in **§3.2.3**, it is likely that there is a distribution of the bpac guest concentrations of this material within different crystallites, which would produce a range of pore dimensions. The random distribution of bpac guest molecules within an individual crystallite may also produce multiple different pore dimensions. It is therefore likely that the stepped adsorption behaviour in this material is due to multiple adsorption sites, rather than SCO.

The adsorption properties of the **Pd·0.4(bpac)** material are directly related to its structural properties. To complement the vapour sorption studies, and to better understand the low-pressure structural behaviour of this material, a variable temperature PXRD experiment was performed. Unfortunately, an appropriate space group and unit cell that sufficiently fit the powder diffraction data could not be determined, and so a full crystallographic understanding of the framework phase cannot be made. Nevertheless, useful information may be obtained by monitoring the (001) reflection, as this peak is in common with the solvated phases. It is a reliable indexing, as any peak splitting reflects HS/LS crystallites rather than possible symmetry lowering, which could cause the splitting of many other peaks. By analysing the

intensity of the (001) reflection of the HS phase, an approximation may be made of the relative stoichiometric fraction of the HS phase (see **Figure C-15** for a plot of the powder patterns). It should be noted that the calculation of the LS/HS fraction by peak intensity comparison is only approximate, with the relative intensity of the Bragg peaks being dependent on differences in framework structure and spin state as well as quantity of crystallites.

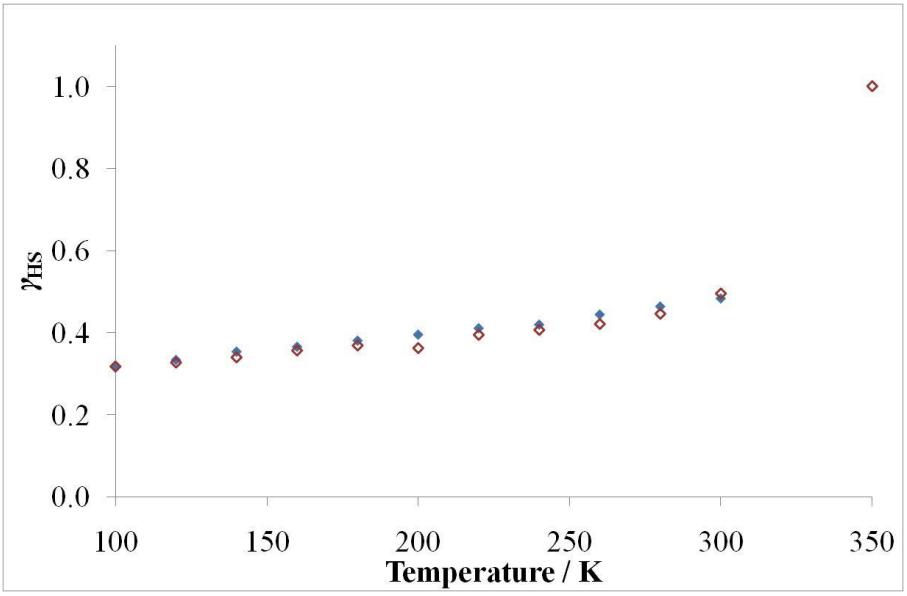

Figure 3-27: The relative stoichiometric fraction of HS states (γ_{HS}) for **Pd·0.4(bpac)**{Ø} as determined through the relative intensity of the (001) peak of the HS phase, upon ◆ cooling and ◇ warming.

As seen in **Figure 3-27**, at 300 K and below, the majority of the crystallites in the evacuated sample are in the LS state. The HS phase fraction gradually decreases as the temperature is decreased, leaving a large residual HS fraction at 100 K, which can be attributed to the sample inhomogeneity of the **Pd·0.4(bpac)** material as discussed in **§3.2.3**. As there is a distribution of crystallites with varying concentrations of bpac in the framework, individual crystallites would exhibit different spin transition behaviour. The LS-to-HS transition between 300 and 350 K of **Pd·0.4(bpac)**{Ø} is consistent with the desolvated results published by Real for **Pd·*x*(bpac)** with higher concentrations of bpac guest, as these samples underwent the LS-to-HS transition above 300 K.[1]

Considering these results, for the purposes of this discussion the sample can be treated as a two-phase mixture: one framework phase contains a higher concentration of bpac that is close

to the ideal occupancy, and which accounts for the SCO activity that occurs between 300 and 350 K; and the other has a lower concentration of bpac and accounts for the gradual spin transition stage, and the residual HS fraction at low temperature. It is possible that upon readsorption of guest molecules, the latter phase may become activated to undergo SCO, as discussed above (**§3.3**). All subsequent discussion on spin transition in this section is with reference to the framework phase that exhibits the more abrupt, high temperature SCO behaviour.

The observation that the material under vacuum is LS below 300 K is consistent with the adsorption isobar results shown in **Figure 3-25**: at 7 mbar, $T_{1/2}^{\downarrow}$ = 302.3 K. This implies that below 300 K and in the absence of unusual adsorption behaviour, the material can be assumed to be in the LS state over the entire experimental range of the isotherms.

As seen in **Figure 3-25**, there is a small range of temperatures over which an isotherm collection would result in the sample converting to the HS state upon increasing pressure. As such, an isotherm collection was obtained at 300.2 K to determine if this effect could be experimentally confirmed. At low pressure, the isotherm exhibits analogous behaviour to other lower temperature isotherms, but then at higher pressure there is a large second hysteresis observed (**Figure 3-28**). Upon increasing pressure, the sorption capacity of the material is increased, corresponding to a transition to the HS state. As the pressure is decreased, the sorption capacity shows a corresponding decrease, which is indicative of transition to the LS state. This is the behaviour expected from the results shown in **Figure 3-25**, in which the sample undergoes a LS-to-HS transition upon increasing pressure. Determination of the necessary SCO parameters of this transition stage was performed by taking the points at which the data diverged from the 'normal' behaviour of the majority of the isotherm (**Figure 3-28**).

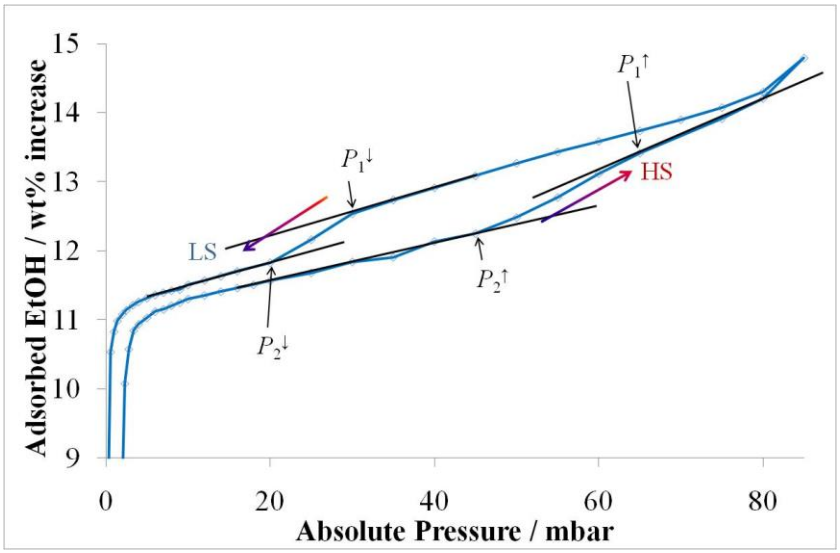

Figure 3-28: Method for determining spin transition pressure values for the high pressure SCO in the 300.2 K experimental isotherm data.

The isotherm behaviour at 300.2 K is in sharp contrast to that observed in the adsorption isotherm at 303.2 K (**Figure 3-29**). The latter isotherm does not display any major high pressure hysteretic transition, but instead only displays a minor hysteresis continuing from the first step until a point between 35 and 40 mbar. It is probable that this behaviour is due to bistability in this region, terminated by final conversion to the HS state. These results, in conjunction with the observed behaviour of the isobars, suggest that in the isotherms taken at higher temperatures the framework would not undergo spin transition, but would instead remain in the HS state over the entire experimental range of the isotherm.

A combined plot of the transition behaviour for those isotherm experiments which demonstrated SCO, and all isobar experiments, can be seen in **Figure 3-30**. The spin transition temperatures according to the magnetic susceptibility data are included for comparison.

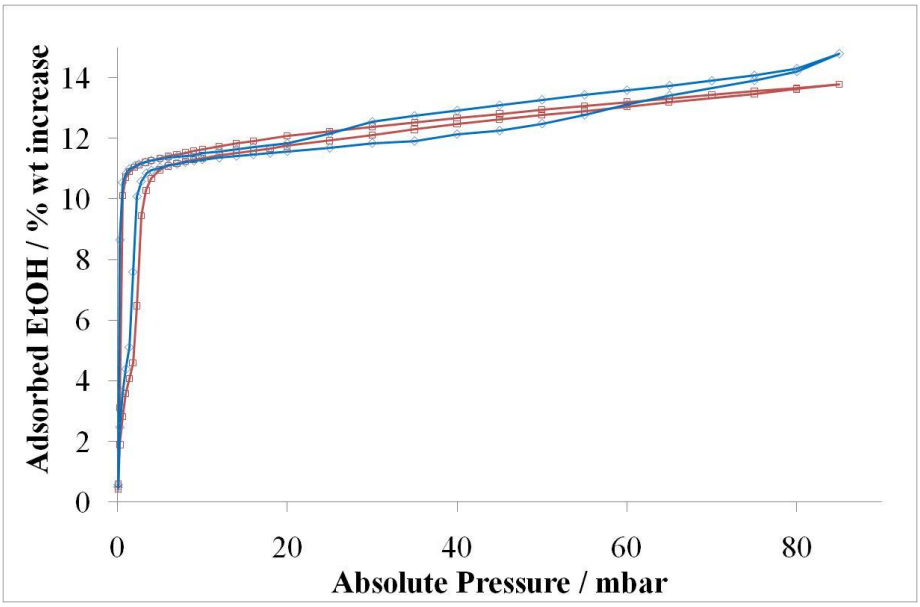

Figure 3-29: EtOH adsorption isotherm at 300.2 K and 303.2 K.

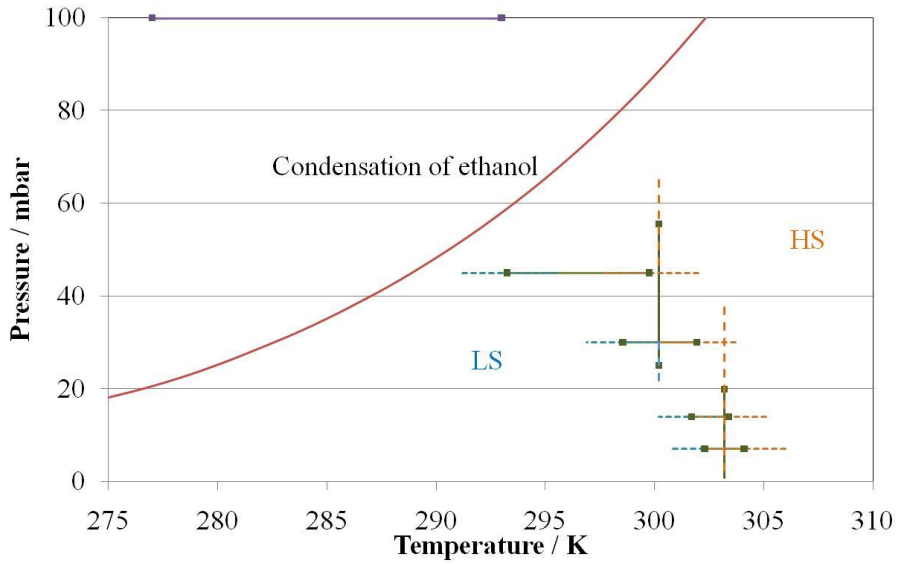

Figure 3-30: Combined graph of the EtOH isobars and isotherms for **Pd·0.4(bpac)**: the temperature/pressure values at which EtOH condenses;[17] the SCO hysteretic range according to magnetic susceptibility measurements; the T or $P_{1/2}^{\downarrow}$ and T or $P_{1/2}^{\uparrow}$ values where obtainable; and the SCO range upon conversion to the LS and HS states.

The observed spin state and transition points correlate well for the isobar and isotherm measurements. Using these results, a generalised phase diagram can be produced, as shown in **Figure 3-31**. It is clear that increasing the vapour pressure decreases the spin transition temperature, and increases the range of bistability. At first, the decreased transition

temperature seems to contradict previously documented pressure studies, in which increased pressure leads to an increased transition temperature, due to stabilisation of the more compressed LS state.[19-21] However, the published investigations were undertaken at very large pressures, predominantly in non-porous materials, and as such, the increased pressure only affected the compression of the crystallites, and did not involve a guest effect.

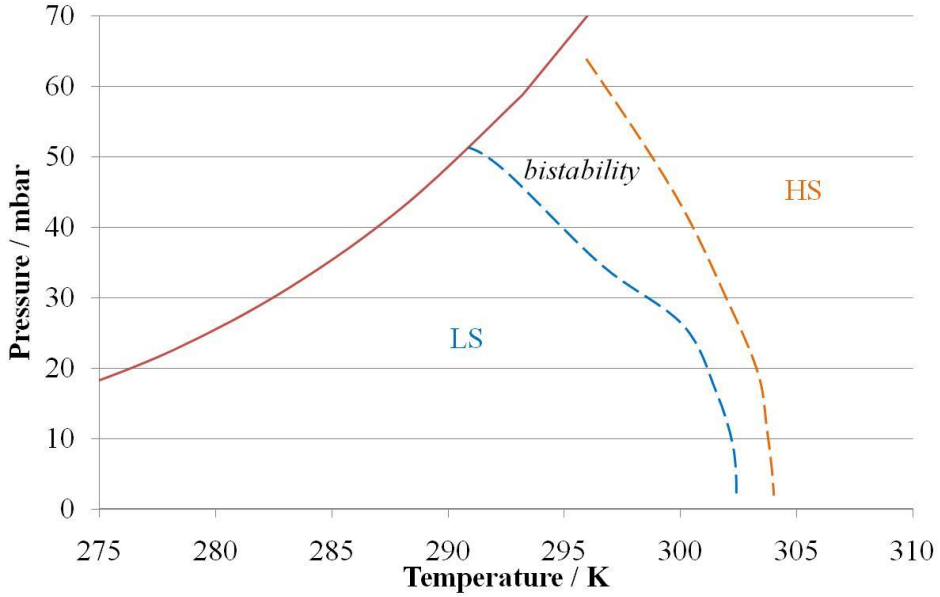

Figure 3-31: Generalised phase diagram for **Pd·0.4(bpac)**{EtOH}, showing the major spin state regions: - - - LS, - - - HS, and the region in which the sample displays *bistability*; and —— the points at which EtOH would condense.[17]

Due to the low pressures involved in this experiment with a porous framework, the guest effect dominates in determining the spin transition properties of the material. Increased pressures lead to a higher concentration of guest vapour, and a corresponding increased sorption of guest. This then leads to increased host–guest interactions and an increased internal pressure effect which, as explained in **§3.3.2.1**, lead to stabilisation of the HS state and the lower transition temperature observed.

In these systems, the major effect of increasing the pressure is to increase the quantity of adsorbed EtOH into the framework. As such, a SCO phase diagram for **Pd·0.4(bpac)**·*x*{EtOH} can be produced that relates the spin transition dependence on temperature and the relative quantity of EtOH (*x*) in the material. The relevant spin transition parameters for this phase diagram were taken from the quantity of adsorbed EtOH at the

appropriate T or $P_{1/2}$ values shown in **Figure 3-30**. The resulting Adsorbed EtOH *vs.* Temperature phase diagram is shown in **Figure 3-32**.

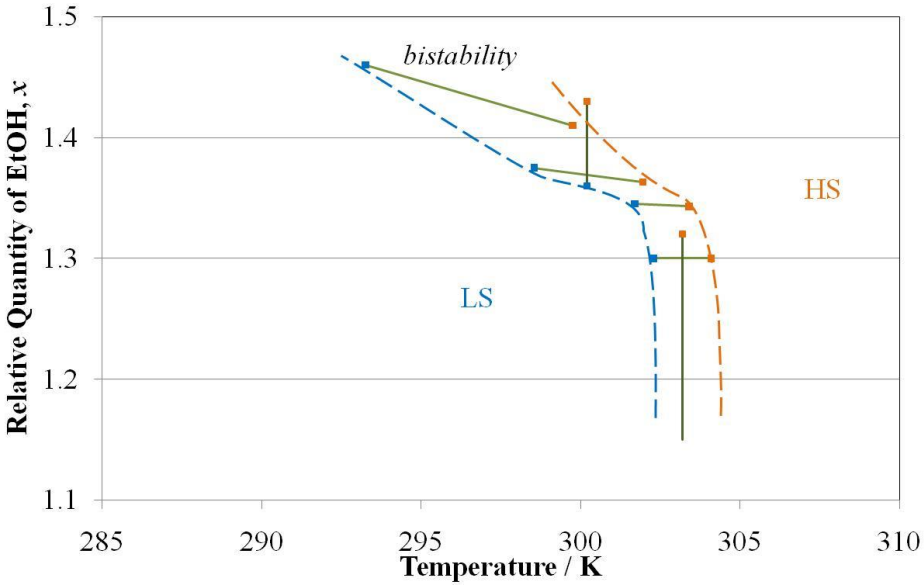

Figure 3-32: Phase diagram of SCO in **Pd·0.4(bpac)**·x{EtOH} depending on solvent loading and temperature. Data points represent the T or $P_{1/2}$ values upon conversion to ▪ LS or ▪ HS. Lines represent rough estimates of the major spin state regions: - - - LS, - - - HS, and the region in which the sample displays *bistability*.

This diagram is very interesting, as it clearly displays the strong influence of the quantity of adsorbed guest species on the spin transition. The coupling of SCO and host–guest energetics in this system produces an unprecedented phenomenon. There is a range of temperature and adsorbed EtOH in which the framework is in the LS state, but if the quantity of adsorbed EtOH is too high, or the temperature is too high, then the framework would be in the HS state. The high pressure LS-to-HS transition may be due to an internal pressure effect, such that the quantity of adsorbed EtOH exceeds a critical value and the kinetic volume of the guest forces the framework to expand, stabilising the HS state. In addition to this effect, decreasing temperature generally favours the LS state due to enthalpic stabilisation (**§1.4.1**), which accounts for the greater quantity of adsorbed EtOH necessary to undergo the LS-to-HS transition at lower temperature.

The behaviour demonstrated by this phase diagram leads to a further observation that relates to technological applicability. As the material undergoes the LS-to-HS transition, the quantity of adsorbed EtOH increases due to the larger pore size in the framework. The enthalpic

change of the system associated with this increased vapour sorption is negative, $\Delta H_{sorption} < 0$, as heat is released. Conversely, the enthalpic change associated with the LS-to-HS transition is endothermic, $\Delta H_{SCO} > 0$, and the entropy of the system increases (see **§1.4.1**). Combining these two factors leads to the result that $\Delta H_{total} < \Delta H_{sorption}$: less heat is produced by vapour adsorption as the energy is instead converted into increased entropy of the HS Fe(II) *d*-electrons. This entropic energy is recoverable through conversion back to the LS state, reducing the heat input necessary to liberate the adsorbed vapour. This result suggests the potential application of nanoporous SCO coordination frameworks for controlled uptake/release of vapour molecules using SCO as the control, while also reducing the change in the total energy of the system associated with vapour adsorption/desorption. The observation that there is a LS-to-HS transition with increasing pressure in the 300.2 K isotherm also suggests that such an application may occur with constant temperature, and/or at about room temperature.

There have been reports of high-pressure studies on spin transition properties, but following a search of the current literature,[19,22-24] it is believed that this is the first time a Pressure-Temperature phase diagram has been produced for a guest-dependent SCO framework that monitors spin transition behaviour upon addition of vapour guest.

3.5 *Conclusions and Final Remarks*

The [Fe(bpac)M(CN)$_4$]·*x*(bpac) (M = Ni, Pd, Pt, *x* = 0.4, 0.5) family of frameworks display a considerable guest-dependent effect on the SCO behaviour.

The bpac concentration dependence is difficult to study in a controlled manner, as there is evidence to suggest that synthesis with less bpac than is required for full ligand and guest occupancy produces a distribution of framework crystallites with varying concentrations of coordinated and guest bpac within the lattice. It may be possible to obtain a single phase with a homogeneous partial bpac guest concentration with full ligand bpac occupancy, but it would require careful study of various synthetic conditions, with subsequent study by elemental analysis, PXRD and magnetic measurements.

Nevertheless, it has been possible to determine some general observations on features and effects of bpac concentration. The as-synthesised **Pd·0.4(bpac)**{EtOH} sample contained three discrete SCO phases: those that produced the abrupt high temperature transition; those

that produced the more gradual low temperature transition; and those that were SCO inactive. Desolvation and resolvation with EtOH activated some of the previously inactive crystallites, producing a more complete transition. While the transition temperature for an individual crystallite varied depending on the bpac concentration, the transition hysteresis, and thus the cooperativity, remained relatively constant at ~15 K.

It was hypothesised that the increased SCO completeness is due to removal of water ligand from lattice defect sites in the framework crystallites, and subsequent coordination by nearby guest bpac molecules, increasing the number of active Fe(II) sites in the frameworks, and thus the number of active crystallites. The change in distribution of Fe(II) environments is not yet understood, but the relatively constant transition hysteresis could be due to host–guest interactions between the solvent and lattice, which can disfavour spin transition.

Compared to **Pd·0.5(bpac)**, the **Pd·0.4(bpac)** framework generally produced a larger hysteresis. This seems likely to be caused by an increased number of host–guest interactions due to increased sorption of non-bpac guest, which disfavours spin transition, leading to the increased hysteresis width.

The N_2 and EtOH adsorption isotherm experiments demonstrated the robust porosity of the framework. Calculations using the adsorbed quantity of guest produce a comparable number of non-hydrogen atoms per formula unit of 4.4 for N_2 in the LS **Pd·0.4(bpac)** framework phase and 4.7 for EtOH in the HS framework. The difference may be attributed to different guest packing behaviour, but is also consistent with the change in framework dimension associated with the spin transition.

A variety of alcohol guests were included within the framework pores, and the resulting behaviour analysed. With the exception of MeOH, increased chain length led to a more gradual spin transition at lower temperature. This result is consistent with the guest-dependent results of the [Fe(pyrazine)M(CN)$_4$] (M = Ni, Pd, Pt) frameworks, and can be predominantly attributed to the influence of the host–guest interactions: the kinetic volume and compressibility of the guest molecules determine the magnitude of the repulsive interaction between the guest molecules and the framework lattice. The temperature-dependence on the kinetic volume of the guest influences the favoured pore volume and thus the volume of the lattice, contributing to determination of the temperature and abruptness of

the spin transition. Longer alcohol chain lengths lead to an increase of this effect. The strength and extent of guest–guest interactions is another very important factor, and is the potential reason behind the relative transition temperature caused by MeOH compared to the other alcohols. The gradual transitions observed for the longer chain alcohols could also be due to decreased mobility of the guest, as there would be a larger number of potential guest packing arrangements, and a greater difficulty in rearranging the guest molecules upon spin transition, producing multiple local environments around the Fe(II) centres, with multiple associated spin transition temperatures.

The behaviour observed for **Pd·0.4(bpac)**{1-PnOH} was the most interesting, due to the two-stage SCO with very large hysteresis. The magnetic behaviour of this sample was partially explained as arising through the heterogeneous sample composition which included crystallites with different bpac guest concentrations, as the unusual two-stage behaviour could be treated as two different spin transition curves superimposed on one another. Another, possibly concurrent explanation was obtained through comparison of the magnetic with the crystallographic behaviour. The asymmetric unit of the framework in the *Immm* space group contained 4 distinct Fe(II) atoms, and it was proposed that one of these could undergo spin transition without significantly affecting the bulk crystallographic properties. This would explain the gradual first stage of the spin transition. The large hysteresis was then attributed to the comparatively large difference in the unit cell parameters from the HS-to-LS transition, and the subsequent effect this would have on ligand–metal bond strength and stabilisation of the spin state through a relatively high potential barrier for the structural transition which accompanies SCO.

The mixed solvent system, 1:1 MeOH/EtOH, produced spin transition at a lower temperature than either of the individual solvents did separately. This behaviour is most likely due to decreased mobility of the mixed solvent within the framework pores resulting from the combined effect of a large number of guest–guest and host–guest interactions.

By obtaining several EtOH adsorption isotherms and isobars, a Temperature-Pressure phase diagram of SCO in **Pd·0.4(bpac)**·*x*{EtOH} was produced, which gives regions of HS and LS phases. Higher pressure results in a lower spin transition temperature with increased hysteresis, which is due to the effect of increased host–guest interactions, and the bistability induced by EtOH adsorption. The isotherm at 300.2 K was interesting as it demonstrated that

with increasing pressure at this temperature, the sample apparently underwent a complete LS-to-HS transition. This result confirms the displayed shape of the phase diagram regions. These studies suggest that such nanoporous SCO materials may have potential application in controlled uptake/release of guest vapour molecules.

References

(1) Bartual-Murgui, C.; Salmon, L.; Akou, A.; Ortega-Villar, N. A.; Shepherd, H. J.; Muñoz, M. C.; Molnár, G.; Real, J. A.; Bousseksou, A. *Chem. Eur. J.* **2012**, *18*, 507.

(2) Boldog, I.; Gaspar, A. B.; Martinez, V.; Pardo-Ibanez, P.; Ksenofontov, V.; Bhattacharjee, A.; Gütlich, P.; Real, J. A. *Angew. Chem. Int. Ed.* **2008**, *47*, 6433.

(3) Volatron, F.; Catala, L.; Riviere, E.; Gloter, A.; Stephan, O.; Mallah, T. *Inorg. Chem.* **2008**, 6584.

(4) Spek, A. L.; Utrecht University: Utrecht, The Netherlands, 2007.

(5) Fellows, E. A. PhD Thesis, University of Sydney, 2011.

(6) Southon, P. D.; Liu, L.; Fellows, E. A.; Price, D. J.; Halder, G. J.; Chapman, K. W.; Moubaraki, B.; Murray, K. S.; Létard, J.-F.; Kepert, C. J. *J. Am. Chem. Soc.* **2009**, *131*, 10998.

(7) Muñoz Lara, F. J.; Gaspar, A. B.; Aravena, D.; Ruiz, E.; Muñoz, M. C.; Ohba, M.; Ohtani, R.; Kitagawa, S.; Real, J. A. *Chem. Comm.* **2012**, *48*, 4686.

(8) Halder, G. J.; Kepert, C. J.; Moubaraki, B.; Murray, K. S.; Cashion, J. D. *Science* **2002**, *298*, 1762.

(9) Takahashi, H.; Tsuboyama, S.; Umezawa, Y.; Honda, K.; Nishio, M. *Tetrahedron* **2000**, *56*, 6185.

(10) Nishio, M. *CrystEngComm* **2004**, *6*, 130.

(11) Roesky, H. W.; Andruh, M. *Coord. Chem. Rev.* **2003**, *236*, 91.

(12) Slichter, C. P.; Drickamer, H. G. *J. Chem. Phys.* **1972**, *56*, 2142.

(13) Narten, A. H.; Habenschuss, A. *J. Chem. Phys.* **1984**, *80*, 3387.

(14) Padro, J. A.; Saiz, L.; Guaria, E. *J. Molec. Struc.* **1997**, *416*, 243.

(15) Galet, A.; Muñoz, M. C.; Real, J. A. *Chem. Commun.* **2006**, *41*, 4321.

(16) Kitchen, J. A.; Jameson, G. N. L.; Tallon, J. L.; Brooker, S. *Chem. Comm.* **2010**, *46*, 3200.

(17) Lemmon, E. W.; McLinden, M. O.; Friend, D. G. In *NIST Chemistry WebBook, NIST Standard Reference Database Number 69*; Lindstrom, P. J., Mallard, W. G., Eds.; National Institute of Standards and Technology: Gaithersburg, MD, USA, http://webbook.nist.gov, (retrieved April 6, 2012), 2012.

(18) Dubbeldam, D.; Calero, S.; Vlugt, T. J. H.; Krishna, R.; Maesen, T. L. M.; Beerdsen, E.; Smit, B. *Physical Review Letters* **2004**, *93*, 088302.

(19) Gütlich, P.; Ksenofontov, V.; Gaspar, A. B. *Coord. Chem. Rev.* **2005**, *249*, 1811.

(20) Agustí, G.; Gaspar, A. B.; Muñoz, M. C.; Real, J. A. *Inorg. Chem.* **2007**, *46*, 9646.

(21) Agustí, G.; Thompson, A. L.; Gaspar, A. B.; Muñoz, M. C.; Goeta, A. E.; Rodriguez-Velamazan, J. A.; Castro, M.; Burriel, R.; Real, J. A. *Dalton Trans.* **2008**, *5*, 642.

(22) Shepherd, H. J.; Rosa, P.; Vendier, L.; Casati, N.; Létard, J.-F.; Bousseksou, A.; Guionneau, P.; Molnár, G. *Phys. Chem. Chem. Phys.* **2012**, *14*, 5265.
(23) Sugahara, A.; Moriya, K.; Enomoto, M.; Okazawa, A.; Kojima, N. *Polyhedron* **2011**, *30*, 3127.
(24) Shepherd, H. J.; Bonnet, S.; Guionneau, P.; Bedoui, S.; Garbarino, G.; Nicolazzi, W.; Bousseksou, A.; Molnár, G. *Phys. Rev. B* **2011**, *84*, 144107.

Chapter 4: An Interpenetrated Three-Dimensional Framework Material That Displays Spin Crossover And Anomalous Thermal Expansion Behaviour, $[Fe(bpac)(Au(CN)_2)_2]$

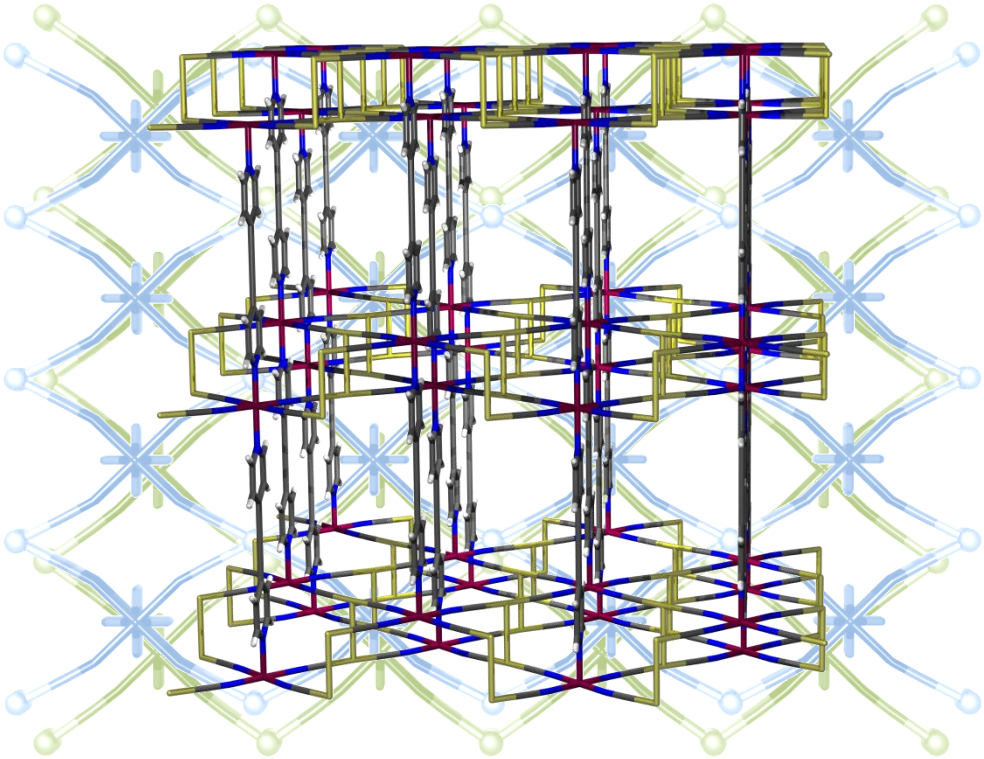

Structure of $[Fe(bpac)(Au(CN)_2)_2]$, a framework material which demonstrates colossal thermal expansion behaviour.

4.1 *Outline*

As described above, the Hofmann-type frameworks $[Fe(bpac)M(CN)_4]\cdot x(bpac)$ (M = Ni, Pd, Pt; x = 0.4, 0.5) exhibit SCO behaviour with a significant guest-dependent effect. Following from this success, the square planar cyanide-based metalloligand was replaced with a linear analogue, $[M(CN)_2]^-$ (M = Ag, Au), to determine the effect on the resulting framework properties. As shown in **Figure 4-1**, the dicyanidometallate linear linker was expected to produce a different overall framework topology, which would in turn result in different pore structures, bulk spin transition properties and guest effects.

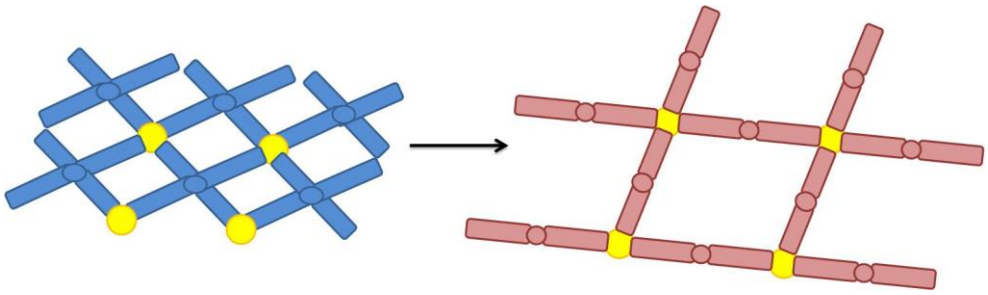

Figure 4-1: Replacing the square planar linker in the metal-cyanide layers with a linear one would produce different framework connectivity, leading to different bulk behaviours.

Toward this goal, the dicyanidoaurate $[Au(CN)_2]^-$ metalloligand was used in the synthesis of a coordination framework structure with Fe(II) and the bpac ligand. The resulting material has the formula $[Fe(bpac)(Au(CN)_2)_2]$ (**Au**), which was confirmed by elemental analysis. Structural analysis by single crystal X-ray diffraction determined that the structure consists of two interpenetrated α-Po nets, with the relative position of these nets determined by aurophilic interactions between adjacent dicyanidoaurate linkers.

The **Au**·{EtOH} material exhibits an abrupt spin transition with hysteresis, which is accompanied by an unusual change in the unit cell parameters that is due to scissor-type motion of the $\{Fe(Au(CN)_2)_2\}$ (4,4)-grids. As well as occurring over the spin transition, these grids show significant variation in the degree of thermal expansion behaviour over the temperature range studied.

Two crystal polymorphs were studied, which were solved in the *Cmma* and *Pbaa* space groups, with the latter structure exhibiting much greater lattice distortion but possessing the same connectivity and topology. Of the *Cmma* space group phase, two different crystals were

analysed, which were synthesised from either pure EtOH, or a 1:1 EtOH/MeOH solvent mixture. Each of these crystals was analysed at three temperatures: above and below the spin transition, and at 100 K. The resulting unit cell parameters demonstrated significant variation in the conformation of the $\{Fe(Au(CN)_2)_2\}$ (4,4)-grids between the different temperatures and the different solvents, and gave a preview of the guest effect on the structural properties.

A N_2 adsorption isotherm measurement demonstrated that this framework material has robust porosity, with a relatively high internal surface area and solvent accessible pore volume. As the framework is robust to guest removal, this allows detailed study into its guest-dependent properties.

4.2 *Single Crystal X-Ray Diffraction*

Single crystals of the $[Fe(bpac)(Au(CN)_2)_2]$ (**Au**) framework material suitable for single crystal X-ray diffraction were grown using the H-cell diffusion method described in **§7.3.2**.

4.2.1 *Crystal Structure of $[Fe(bpac)(Au(CN)_2)_2]\cdot\{EtOH\}$ in the Cmma Space Group*

The crystal on which these data were obtained was grown by Dr Laurence Goux from an EtOH-based diffusion. One of the crystals thus grown was analysed by single crystal X-ray diffraction at 100, 190 and 240 K. The latter two temperatures were chosen as they are below and above the spin transition respectively, as demonstrated by previously-obtained powder X-ray diffraction (**§4.4.1**) and magnetic (**§4.5**) data. The 100 K collection was used to assist in explaining unusual thermal expansion behaviour which had been shown by variable temperature PXRD experiments (**§4.4.1**). The transition from 240 to 190 K was observed to exhibit a thermochromic change in the crystal from yellow to deep red.

Full crystallographic details are provided in **Appendix A**. All structures of this crystal were solved in the orthorhombic *Cmma* space group.

All three crystallographic asymmetric units have the same structure, and include an Fe(II) centre coordinated to half a disordered bpac molecule and half a dicyanidoaurate ligand. The pyridyl rings of the bpac molecule are disordered over two positions orthogonal to one another, and the 100 and 190 K structures contain a partially-occupied, disordered EtOH molecule. The 190 K asymmetric unit is shown in **Figure 4-2**, and the asymmetric units for the 100 and 240 K structures are shown in **Figure B-2a** and **Figure B-2b** respectively.

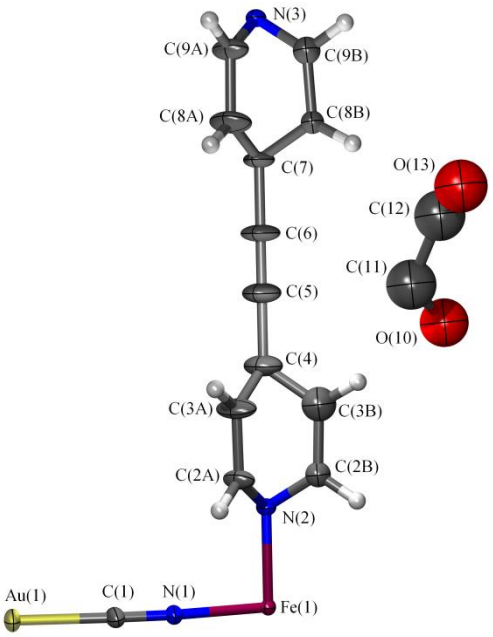

Figure 4-2: Crystallographic asymmetric unit of Au at 190 K.

The full lattice structure at 190K, viewed parallel to the *a*- and *c*-axes, is shown in **Figure 4-3**. A figure showing the aurophilic interactions and using standard atomic colouring is given in **Figure B-7**, and a comparison of the structure with solvent molecules included is shown in **Figure B-8**. Figures of the 100 and 240 K structures can be seen in **Figure B-9** and **Figure B-10**, and a summary of the crystal data and refinement details is given in **Table 4-1**.

Similarly to the **Pd** and **Pt** crystal structures described in Chapter 4, the Fe(II) centre has an axially elongated distorted octahedral environment with four nitrile-donating cyanide ligands coordinated equatorially, and two axial pyridyl donors. The bis-unidentate nature of the dicyanidoaurate ligands results in a square grid of alternating iron and gold atoms linked by cyanides. These grids are then bridged through the pyridyl units of bpac pillars, which are disordered over two orthogonal positions parallel to the *a*- and *b*-axes. The size of the structural voids within the network allows the formation of a second interpenetrated net within the first, and the dominating influences on the relative position of these two nets are internetwork aurophilic interactions between Au atoms in adjacent $[Au(CN)_2]^-$ units.

Table 4-1: Summary of the single crystal X-ray collection and refinement for **Au**·{EtOH} in the *Cmma* space group at 100, 190 and 240 K.

[Fe(bpac)(Au(CN)$_2$)$_2$].*x*EtOH at Temperature / K			
	100(2)	190(2)	240(2)
Empirical formula	$C_{18.8}H_{14.3}Au_2FeN_6O_{1.4}$	$C_{18.5}H_{14.2}Au_2FeN_6O_{1.25}$	$C_{16}H_8Au_2FeN_6$
X	1.4	1.3	–
Formula weight / g mol^{-1}	796.45	790.34	734.07
Wavelength / Å	0.71073	0.71073	0.71073
Crystal system	Orthorhombic	Orthorhombic	Orthorhombic
Space group	*Cmma*	*Cmma*	*Cmma*
a / Å	12.1331(11)	12.5570(6)	11.707(2)
b / Å	16.0387(14)	15.8316(9)	17.442(4)
c / Å	13.6761(12)	13.6771(8)	14.117(3)
V / Å^3	2661.4(4)	2719.0(3)	2882.6(11)
Z	4	4	4
ρ_{calc} / Mg/m^3	2.005	1.978	1.691
μ / mm^{-1}	11.556	11.313	10.657
F(000)	1474	1485	1320
Crystal size / mm^3	0.13 × 0.13 × 0.06	0.13 × 0.13 × 0.06	0.13 × 0.13 × 0.06
Theta range / °	3.36–36.31	3.24–28.28	3.48–26.36
Index ranges	−20 ≤ h ≤ 20	−16 ≤ h ≤ 13	−11 ≤ h ≤ 14
	−26 ≤ k ≤ 24	−21 ≤ k ≤ 17	−18 ≤ k ≤ 21
	−22 ≤ l ≤ 22	−10 ≤ l ≤ 18	−10 ≤ l ≤ 17
Reflections collected	31366	8111	5827
Independent reflections [R_{int}]	3423 [0.0501]	1821 [0.0350]	1553 [0.0610]
Completeness to θ / %	99.3 (to 36.31°)	99.2 (to 28.28°)	97.3 (to 25.00°)
Data/restraints/ parameters	3423 / 74 / 111	1821 / 15 / 100	1553 / 182 / 119
Goodness-of-fit on F^2	1.244	1.156	1.072
R indices, I > 2σ(I), (R_1,[(a)] wR_2[(b)])	0.0447, 0.0935	0.0291, 0.0706	0.0677, 0.1613
R indices, all data, (R_1,[(a)] wR_2[(b)])	0.0612, 0.1003	0.0375, 0.0761	0.1106, 0.1993
Largest peak and hole / e.Å^{-3}	5.140 and −4.065	2.801 and −1.400	5.464 and −1.938

[(a)] $R_1 = \Sigma \mid |F_o| - |F_c| \mid / \Sigma |F_o|$, [(b)] $wR_2 = \{\Sigma [w(F_o^2 - F_c^2)^2] / \Sigma [w(F_o^2)^2]\}^{1/2}$

The interpenetrated structural topology is analogous to previously reported 3-dimensional structures incorporating a first row transition metal and a $[M(CN)_2]^-$ (M = Ag, Au) anionic ligand.[1-3] The silver analogue, [Fe(bpac)(Ag(CN)$_2$)$_2$]·{EtOH}, was presented in this candidate's Honours Thesis (University of Sydney, 2009).[3] The network topology of [Fe(bpac)(Ag(CN)$_2$)$_2$]·{EtOH} is identical to that described here, but the framework does not

display inter-network argentophilic interactions and as a result the two nets are further separated. Real and co-workers also recently published a related material that displays SCO, $[Fe(bpac)_2(Ag(CN)_2)_2]$, in the structure of which the Ag atoms are additionally linked by bpac ligands. [2]

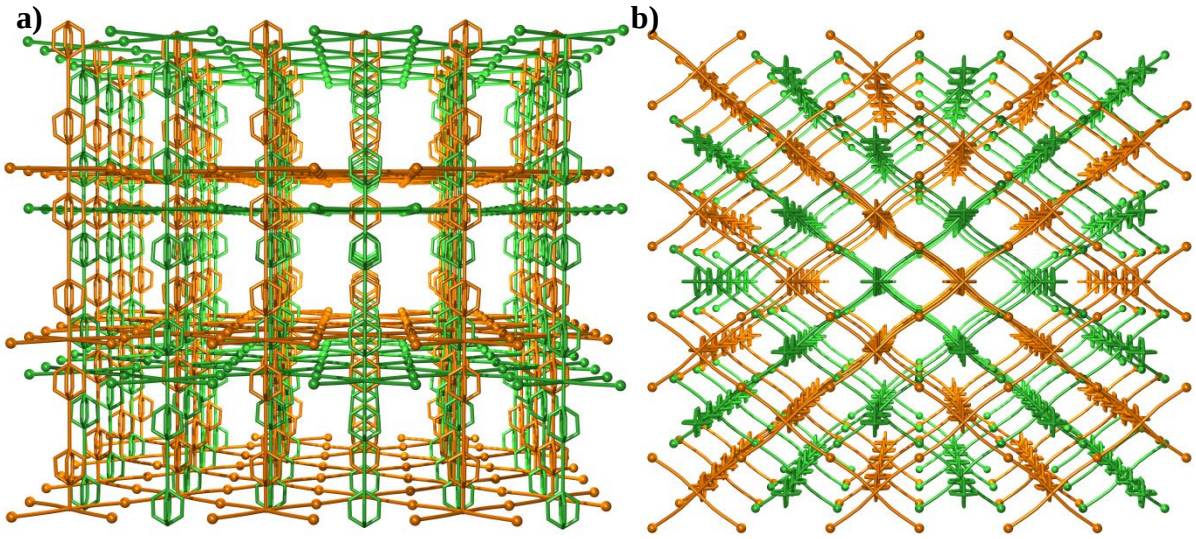

Figure 4-3: Perspective views of the single crystal structure of **Au**, viewed **a)** parallel to the *a*-axis; and **b)** parallel to the *c*-axis. Hydrogen atoms and solvent molecules are omitted for clarity. The colours are used to aid in differentiating between the two interpenetrated nets.

The quantity of guest solvent within the structural pores was calculated using the modelled guest solvent, and diffuse electron density that was determined using the SQUEEZE[4-5] routine in PLATON.[6] It was calculated that there are *ca*. 2.5 EtOH molecules per formula unit in the 100 and 190 K structures, and 2.2 for the 240 K structure.

The *c*-parameter is equivalent to the Fe···Fe distance across the bpac ligand, and the decrease in this quantity that accompanies the HS-to-LS transition is directly proportional to the decrease in the $Fe–N_{pyridyl}$ bond length. From 240 to 190 K the *c*-parameter contracts by 0.439(4) Å, which correlates well with the combined HS-to-LS contraction of the two $Fe–N_{pyridyl}$ bond lengths along this dimension, of 0.41(5) Å.

Similarly the *a*- and *b*-parameters, following the same simplification, would be expected to change by an amount dependent on the changes in the *a*- and *b*-axis components of the change in the $Fe–N_{CN}$ bond length, $\Delta d(Fe–N_{CN})$. There are four collinear $Fe–N_{CN}$ bonds which lie along the *a*- and *b*-axis dimensions, so that the change in the lattice parameters may

be roughly described by $\Delta a \approx 4 \cdot \Delta d_a(\text{Fe–N}_{\text{CN}})$ and $\Delta b \approx 4 \cdot \Delta d_b(\text{Fe–N}_{\text{CN}})$, where Δd_a and Δd_b are the differences in the components of said bonds along the *a* and *b*-axes respectively. Calculations using the single crystal structural data at 240 and 190 K thus give $\Delta d_a(\text{Fe–N}_{\text{CN}})$ = 0.14 Å, and $\Delta d_b(\text{Fe–N}_{\text{CN}})$ = 0.18 Å, and so the rough estimates for the expected HS-to-LS change in these unit cell parameters would be $\Delta a = -0.56$ and $\Delta b = -0.72$ Å. However, the observed changes in the *a* and *b*-axes are $\Delta a = +0.850(3)$ Å and $\Delta b = -1.610(5)$ Å, upon the transition from the HS (240 K) to LS (190 K) state, which is observed as a change in the scissor-type conformation of the (4,4)-nets in the framework lattice (**Figure 4-4**). It is clear that the Fe–N_{CN} bond length contraction simplification is not sufficient to explain the observed unit cell change over the spin transition, and that further parameters must be considered. Of particular note is that upon SCO the coordination geometry around the Fe(II) centres also changes, and upon the HS-to-LS transition, the coordination environment becomes closer to a regular octahedral geometry as the octahedral distortion parameter σ_{oct} decreases (**Table 4-3**, **§4.2.5**).

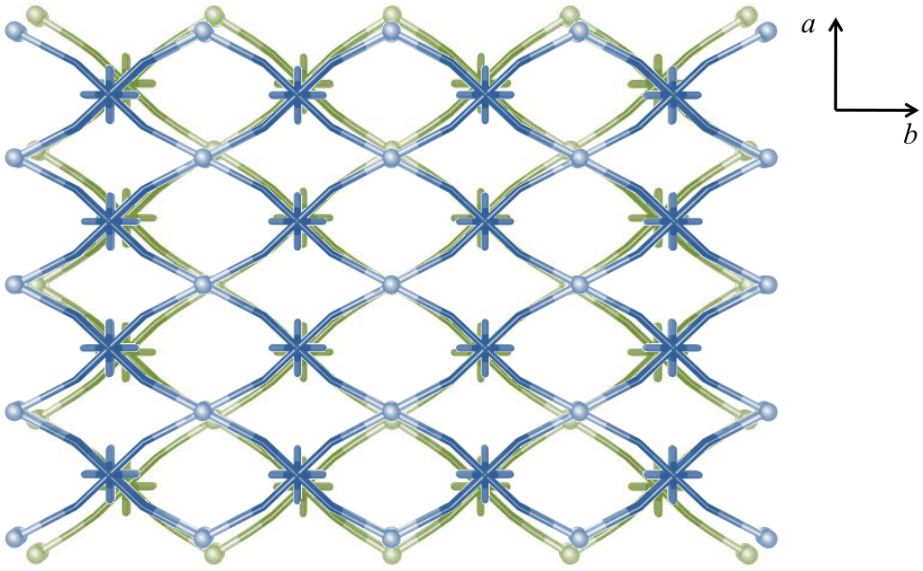

Figure 4-4: Comparison of the **Au**·{EtOH} cyanide nets in the HS 240 K (blue) and LS 190 K (green) *Cmma* structures. The HS structure is noticeably more compressed along the *a*-axis direction, with greater distortion of the cyanides.

To understand the mechanism for this unprecedented behaviour, we need to consider the various structural energetics involved. Firstly, it should be noted that there is expected to be very little energy penalty associated with scissor-type motion of the {Fe(Au(CN)$_2$)$_2$}

(4,4)-grids (**Figure 4-4**), with the framework topology highly underconstrained, allowing weak intermolecular bonds to affect the grid geometry. Factors that influence this include the weak inter-network ligand–ligand interactions, such as aromatic C–H···π interactions between pyridyl rings and adjacent cyanide and bpac molecules, and possible host–guest interactions. The inter-network interactions appear to favour distortion of the framework away from the regular orthogonal geometry, leading to bond characteristics such as non-linear Au–C≡N–Fe linkages and a distorted $Fe(N)_6$ octahedral coordination.

At temperatures above the spin transition, framework distortion is geometrically allowed by the HS Fe(II) centres, which may adopt a distorted octahedral geometry with non-linear coordination of the cyanide groups. At 240 K this distortion is observed in the Fe(II) octahedral distortion parameter, σ_{oct} = 1.98°, and the acute internal Au–Fe–Au angle, which provides a measure of the degree of the compression of the metal cyanide grid (explained in **§4.2.4**), and has a value in this structure of $\theta_{Au–Fe–Au}$ = 67.74(2)°. Conversely, LS Fe(II) is energetically driven to become more regularly octahedral as explained in **§1.4.5**, so that the $\{Fe(Au(CN)_2)_2\}$ (4,4)-grids assume a closer to orthogonal structure. At 190K the Fe(II) σ_{oct} = 1.17° and $\theta_{Au–Fe–Au}$ = 78.840(6)°. The scissor-type lattice flexing behaviour seems to be partially driven by the Fe(II) coordination geometry, as the more rigidly orthogonal LS environment induces a lattice conformation in the flexible framework such that $\theta_{Au–Fe–Au}$ is closer to 90°. In addition, LS Fe(II) influences the cyanide coordination to be more linear, due to the more efficient metal–ligand σ bond orbital overlap, which in turn strengthens the π backbonding behaviour (see **§1.4.5**). The more linear Fe–N≡C coordination reduces distortion of the dicyanidoaurate linkers, resulting a lattice geometry that is closer to an orthogonal conformation. These mechanisms are then responsible for the significant change in the *a*- and *b*-parameters over the SCO transition, as the transition to make the cyanide grid closer to orthogonal results in a corresponding expansion along the *a*-axis, and contraction along the *b*-axis.

4.2.2 *Crystal Structure of $[Fe(bpac)(Au(CN)_2)_2]\cdot\{MeOH/EtOH\}$ in the Cmma Space Group*

Diffraction-quality single crystals were grown by Laurence Goux from a liquid/liquid diffusion which used a 1:1 MeOH/EtOH solvent mix. A suitable crystal was selected and characterised by single crystal X-ray diffraction at 230, 200 and 100 K. The data were treated

in the same way as described in **§4.2.1**, with all crystal structures solved in the orthorhombic *Cmma* space group (**Table 4-2**).

Table 4-2: Summary of the single crystal X-ray collection and refinement for **Au**·{MeOH/EtOH} in the *Cmma* space group at 100, 200 and 230 K; and for **Au**·{EtOH} in the *Pbaa* space group at 230 K.

	[Fe(bpac)(Au(CN)$_2$)$_2$].*x*MeOH at Temperature / K			
	100(2)	200(2)	230(2)	230(2)
Empirical formula	$C_{17}H_{12}Au_2FeN_6O$	$C_{17}H_{12}Au_2FeN_6O$	$C_{16}H_8Au_2FeN_6$	$C_{16}H_8Au_2FeN_6$
x	1	1	–	–
Formula weight / g mol^{-1}	766.11	766.11	734.07	734.07
Wavelength / Å	0.71073	0.71073	0.71073	0.71073
Crystal system	Orthorhombic	Orthorhombic	Orthorhombic	Orthorhombic
Space group	*Cmma*	*Cmma*	*Cmma*	*Pbaa*
a / Å	12.6436(5)	12.7252(5)	11.7370(19)	10.1050(9)
b / Å	15.7398(6)	15.6808(6)	17.243(3)	17.7694(15)
c / Å	13.6087(6)	13.6184(6)	14.029(2)	14.0806(12)
V / Å^3	2708.24(19)	2717.43(19)	2839.2(8)	2528.3(4)
Z	4	4	4	4
ρ_{calc} / Mg/m^3	1.879	1.873	1.717	1.928
μ / mm^{-1}	11.350	11.311	10.820	12.150
F(000)	1392	1392	1320	1320
Crystal size / mm^3	0.048×0.032×0.016	0.048×0.032×0.016	0.048×0.032×0.016	0.079×0.016×0.008
Theta range / °	2.99–26.37	3.20–37.12	3.47–33.68	3.38–30.51
Index ranges	$-15 \le h \le 15$	$-21 \le h \le 21$	$-17 \le h \le 18$	$-14 \le h \le 7$
	$-19 \le k \le 19$	$-26 \le k \le 26$	$-25 \le k \le 26$	$-25 \le k \le 25$
	$-17 \le l \le 17$	$-23 \le l \le 23$	$-21 \le l \le 21$	$-15 \le l \le 20$
Reflections collected	22104	39852	30169	22119
Independent reflections [R_{int}]	1503 [0.0454]	3703 [0.0519]	3028 [0.0700]	3858 [0.0490]
Completeness to θ / %	99.6 (to 26.37°)	99.7 (to 37.12°)	99.6 (to 33.68°)	99.5 (to 30.51°)
Data/restraints/ parameters	1503 / 74 / 116	3703 / 12 / 90	3028 / 79 / 102	3858 / 0 / 117
Goodness-of-fit on F^2	1.213	1.198	1.038	1.090
R indices, I > 2σ(I), (R_1,[(a)] wR_2[(b)])	0.0372, 0.0979	0.0452, 0.1190	0.0444, 0.1179	0.0506, 0.1355
R indices, all data, (R_1,[(a)] wR_2[(b)])	0.0489, 0.1101	0.0668, 0.1519	0.0915, 0.1337	0.0809, 0.1559
Largest peak and hole / e.Å^{-3}	3.835 and −3.031	4.327 and −5.418	2.883 and −1.732	5.526 and −1.689

[(a)] $R_1 = \Sigma \, | |F_o| - |F_c| | \, / \, \Sigma \, |F_o|$, [(b)] $wR_2 = \{\Sigma \, [w(F_o^2 - F_c^2)^2] \, / \, \Sigma \, [w(F_o^2)^2]\}^{1/2}$

The lattice topology is identical to the **Au**·{EtOH} structure described above. Illustrations of

the asymmetric units are shown in **Figure B-3**, and the resulting frameworks are shown with and without included solvent molecules in **Figure B-11** to **Figure B-13**. The 200 and 100 K structures were also modelled with a disordered MeOH guest molecule in the asymmetric unit. Considering the crystallisation conditions, it is expected that the crystal also contained disordered MeOH and EtOH molecules which were not modelled in the crystal structures. As the **Au** framework exhibits a strong guest effect (see Chapter 5), this material is designated by **Au**·{MeOH/EtOH}, as both guest species are expected to be present in the framework pores even though only MeOH was modelled crystallographically.

4.2.3 *Crystal Structure of [Fe(bpac)(Au(CN)$_2$)$_2$]·{EtOH} in the Pbaa Space Group*

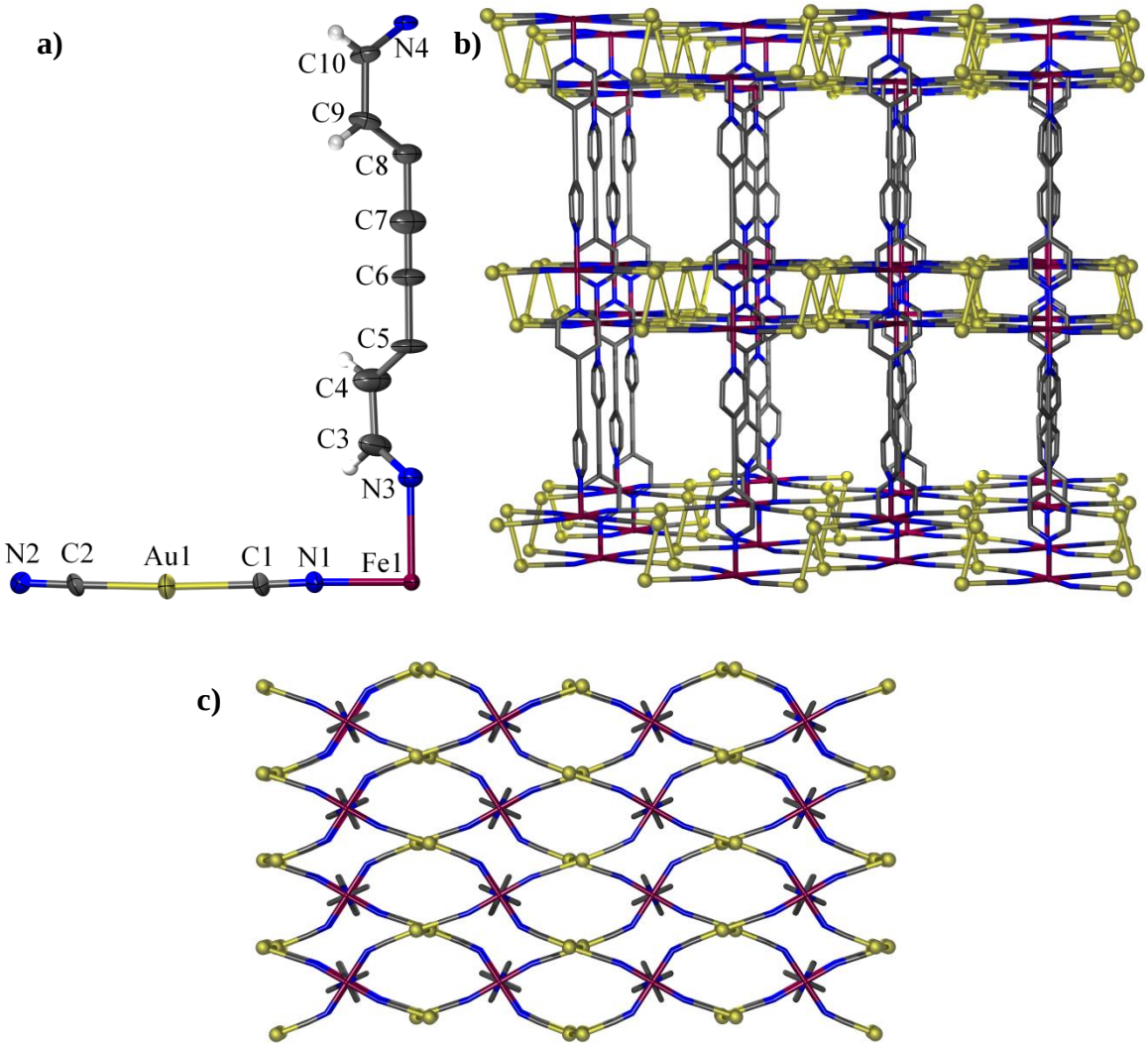

Figure 4-5: a) Crystallographic asymmetric unit of **Au** in the *Pbaa* space group; **b)** view of the framework structure through the pores; and **c)** view of the structure down the cyanide grid. Hydrogen atoms in the lattice structures have been removed for clarity.

Unexpectedly, the formation of a different crystal phase was observed and characterised after the crystals had been left for a few months in the EtOH mother liquor. The crystal structure of this phase at 230 K was solved in the orthorhombic space group *Pbaa* (**Table 4-2**) and while it displays the same overall topology of the *Cmma* phase, the atom connectivity is more distorted (**Figure 4-5**). There were no lattice solvent molecules modelled in this structure, though it is expected that the lattice pores contain disordered EtOH.

The driving force behind the formation of this phase is unknown, as it has not been observed in any powder X-ray diffraction experiments on **Au**·{EtOH}. At this stage, we can only speculate that occasionally and after an extended period of time, some crystals find a structural energetic minimum in the distorted *Pbaa* framework structure, converting to this phase rather than the more regular *Cmma* structure reported above. This crystal was also observed to display different SCO behaviour, as a rapid change in colour was not apparent on cooling below the expected spin transition temperature of **Au**·{EtOH}, but the crystal instead gradually changed colour from yellow to orange as the temperature was decreased below *ca*. 140 K. A full structural determination down to 100 K was not possible as the diffraction quality was too poor.

4.2.4 *Important Definitions for Discussion about this Framework*

As shown above, the **Au** framework may adopt a variety of different lattice conformations. Before further discussion on the lattice behaviour is undertaken, it is necessary to establish some key definitions, to aid in the clear understanding of the structural quantities used, and the descriptions of the lattice behaviour observed.

Compression is used in this and the following chapter to describe the process by which the *a*- and *b*-parameters in this lattice diverge; that is, the lattice becomes more closed, the pore width decreases, atoms along the *a*-axis move closer together, and atoms along the *b*-axis move further apart. *Decompression* is used to describe the opposite event, in which the *a*- and *b*-parameters partially converge, the lattice becomes more open, and the pore width increases (**Figure 4-6**). The term ‘expansion’ is not used to refer to this phenomenon, as this term has implications of an overall increase in area or volume, which is not necessarily the case.

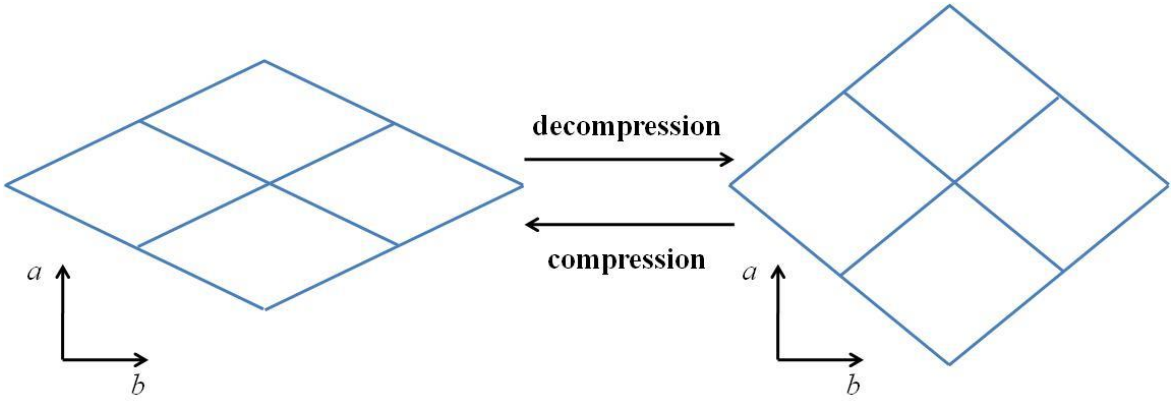

Figure 4-6: Cartoon illustrating the use of the terms *compression* and *decompression*.

The acute internal Au–Fe–Au angle, $\theta_{\text{Au–Fe–Au}}$, as shown in **Figure 4-7a**, is a direct measure of the degree of compression in the metal cyanide grids. This quantity is calculated using **Equation 4.1**, where *a* and *b* are the relevant axis parameters. Larger values for this quantity arise from a more decompressed framework lattice, and smaller values imply a greater degree of lattice compression.

$$\theta_{\text{Au–Fe–Au}} = 2\tan^{-1}\left(\frac{a}{b}\right) \tag{4.1}$$

As the *a*- and *b*-parameters can vary so widely depending on the compression state of the lattice, another useful quantity for comparison of the different structures is the linear Fe–M–Fe distance, $d_{\text{Fe–Au–Fe}}$ (**Figure 4-7a**). This quantity, introduced in **§2.4**, changes depending on the metal–ligand bond distances and the distortion of the cyanide linkers away from a linear geometry. In this framework lattice, it is calculated using **Equation 4.2**, where *a* and *b* refer to the unit cell parameters.

$$d_{\text{Fe–Au–Fe}} = \sqrt{a^2 + b^2}/2 \tag{4.2}$$

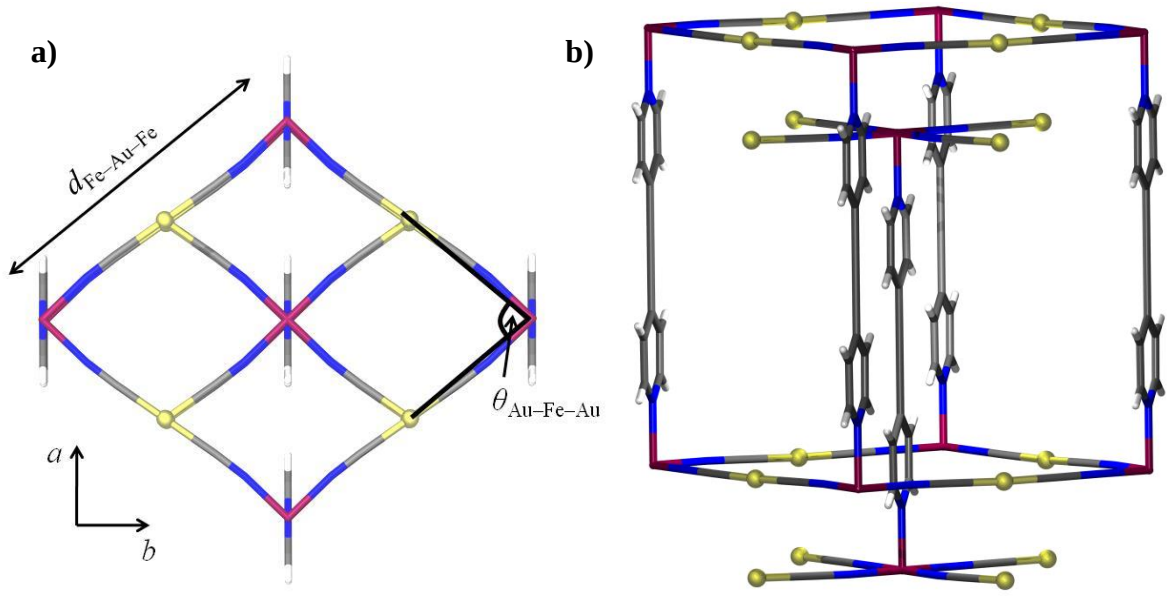

Figure 4-7: a) A small section of the **Au** framework, viewed in the *ab*-plane and showing the significance of the $d_{Fe–Au–Fe}$ and $\theta_{Au–Fe–Au}$ quantities; and **b)** for clarity, the same framework section viewed along the *a*-axis, showing portions of the two interpenetrated nets.

The metal cyanide unit shown in **Figure 4-7a** can be treated as a rhombus, as it is a quadrilateral with four non-orthogonal sides of equal length. It is important to point out that the area of a rhombus is given by **Equation 4.3**, so while the $d_{Fe–Au–Fe}$ value may remain constant with different compression states, the area of the cyanide grid, and subsequently the volume of the framework, will increase as the $\theta_{Au–Fe–Au}$ value increases with lattice decompression.

$$Area = d^2 \sin\theta \tag{4.3}$$

4.2.5 *Comparison of Single Crystal Structures*

The *Cmma* **Au**·{EtOH} and **Au**·{MeOH/EtOH} crystal structures are topologically identical, with very similar relative conformations of the component molecules and regular, orthogonal connectivities. In contrast, the *Pbaa* structure has a considerably different structural conformation of the lattice nets, adopting a more distorted geometry.

The major differences between the *Pbaa* and *Cmma* structures lie in the relative positions of adjacent Au atoms, and the pyridyl rings of the bpac ligand. In the *Pbaa* structure, the octahedral Fe(II) centres twist away from the normal axes, which leads to asymmetrisation of the dicyanidoaurate linkers, and non-orthogonal aurophilic interactions between adjacent Au

atoms in the interpenetrated nets. In the *Cmma* structures, the pyridyl rings of the bpac ligands were modelled as disordered over two perpendicular positions, while in the *Pbaa* structure, the pyridyl rings are modelled without disorder, but alternating between the two perpendicular conformations. In this latter space group solution, the two pyridyl groups within an individual bpac molecule are nearly perpendicular, with an acute torsion angle of 88.3°.

The regular, perpendicular conformation of the bpac pyridyl rings is due to packing constraints in the framework. As seen in **Figure 4-8**, the cyanide grid is so compressed that the plane of the bpac pyridyl ring which lies between cyanides of the adjacent net is sterically constrained to lie parallel to the cyanides. The steric bulk of the cyanides also prevents the other pyridyl ring from aligning parallel to the first, and it instead must adopt a perpendicular orientation in order to avoid a steric clash with these cyanide units. Rotation of this pyridyl ring is further limited by the position of other neighbouring pyridyl units.

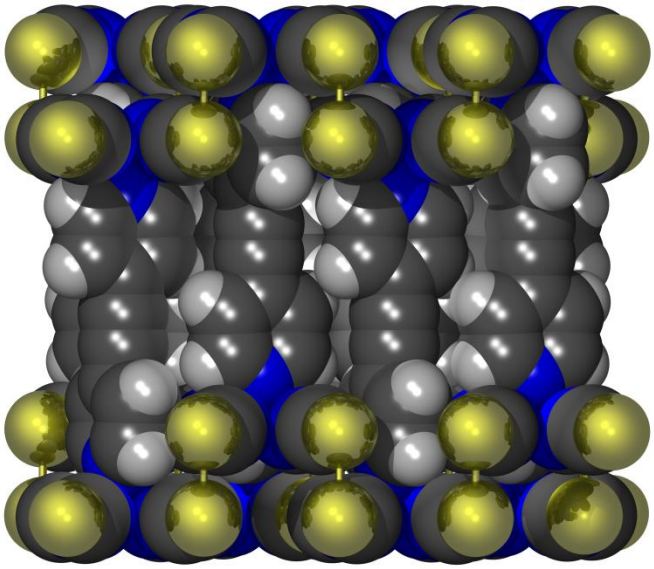

Figure 4-8: Space-filling representation of the *Pbaa* structure of **Au**, as viewed along the *b*-axis.

As mentioned in **§1.4.5**, the Fe–N bond length is a useful indicator for the spin state of the Fe(II) centres in a crystal. As shown in **Table 4-3**, the bond lengths for 100 and 190 K **Au**·{EtOH} and the 100 and 200 K **Au**·{MeOH/EtOH} structures are characteristic for Fe(II) in the LS state, and show very little variation between the different structures. In contrast, the 240 K **Au**·{EtOH} and 230 K **Au**·{MeOH/EtOH} *Cmma* structures, and the *Pbaa* structure

show bond lengths that are characteristic of the HS Fe(II) state.

Table 4-3: Comparison of the Fe–N bond distances and the octahedral angle distortion parameter σ_{oct}, of the Fe(II) atom in the six *Cmma* (*C*) structures, and the *Pbaa* (*P*) structure. The HS structures are indicated by a **bold** font.

	Fe–N_{CN} / Å	**Fe–$N_{bpac(1)}$ / Å**	**Fe–$N_{bpac(2)}$ / Å**	**Fe σ_{oct} / °**
C EtOH 100 K	1.919(3)	1.995(8)	2.001(7)	1.62
C EtOH 190 K	1.938(3)	1.996(7)	2.006(7)	1.17
***C* EtOH 240 K**	**2.16(1)**	**2.16(1)**	**2.25(2)**	**1.98**
C EtOH/MeOH 100 K	1.934(6)	1.98(1)	2.03(1)	1.22
C EtOH/MeOH 200 K	1.931(3)	1.99(1)	2.01(1)	1.03
***C* EtOH/MeOH 230 K**	**2.132(7)**	**2.21(1)**	**2.21(1)**	**1.26**
***P* EtOH 230 K**	**2.120(7)** **2.158(7)**	**2.22(1)**	**2.207(9)**	**2.23**

The octahedral angle distortion parameters provide additional information on the coordination environment of the Fe(II). The HS structures give higher distortion parameters, which is expected considering the predisposition of the HS Fe(II) state to allow a more distorted coordination geometry, as explained in **§1.4.5**. The 190 K **Au**·{EtOH} and 200 K **Au**·{MeOH/EtOH} structures display much smaller distortion parameters compared to their HS counterparts, which is congruent with the conversion of the Fe(II) centre to the LS state, with its more rigidly octahedral geometry. It is interesting that upon further cooling to 100 K, the Fe(II) coordination environments in the two *Cmma* crystals become more distorted, such that the overall distortion is higher than the average of the two higher-temperature structures for each solvated crystal. For an explanation of this behaviour, closer attention must be paid to the bulk crystallographic properties.

As shown in **Table 4-4**, the *c*-parameters for the HS structures are very similar, but with nevertheless notable differences. The lower value for the **Au**·{EtOH} *Pbaa* structure compared to the **Au**·{EtOH} *Cmma* structure is due to a slight reduction in the distance between the interpenetrated nets which results from buckling of the aurophilic interactions in the former structure (see **Figure 4-3**). The lower value for the **Au**·{MeOH/EtOH} *Cmma* structures compared to the **Au**·{EtOH} analogues is potentially due to different internal pressure effects resulting from the different solvents. However, there is a remarkable

difference in the *a*- and *b*-parameters between all seven structures, which can be attributed to flexing of the cyanide layer.

Table 4-4: Unit cell parameters, linear Fe–Au–Fe distance ($d_{Fe–Au–Fe}$) and acute Au–Fe–Au angle ($\theta_{Au–Fe–Au}$) for the six *Cmma* (*C*) structures, and the *Pbaa* (*P*) structure. The HS structures are indicated by a **bold** font.

	Unit Cell Parameter / Å			$d_{Fe–Au–Fe}$ / Å	$\theta_{Au–Fe–Au}$ / °
	a	*b*	*c*		
C EtOH 100 K	12.1331(11)	16.0387(14)	13.6767(12)	10.0555(9)	74.21(1)
C EtOH 190 K	12.5570(6)	15.8316(9)	13.6771(8)	10.103(2)	76.840(6)
***C* EtOH 240 K**	**11.707(2)**	**17.442(4)**	**14.117(3)**	**10.503(2)**	**67.74(2)**
C EtOH/MeOH 100 K	12.6436(5)	15.7398(5)	13.6087(6)	10.0946(4)	77.549(4)
C EtOH/MeOH 200 K	12.7252(5)	15.6808(6)	13.6184(6)	10.0972(4)	78.119(4)
***C* EtOH/MeOH 230 K**	**11.7370(19)**	**17.243(3)**	**14.029(2)**	**10.429(2)**	**68.484(18)**
***P* EtOH 230 K**	**10.1050(9)**	**17.7694(15)**	**14.0806(12)**	**10.221(3)**	**59.251(9)**

As mentioned in **§4.2.1**, the interpenetrated nets of these structures are bonded together through weak aurophilic interactions between adjacent Au centres. These bonds have significant flexibility, and adjacent linear $[Au(CN)_2]^-$ units have a great degree of conformational freedom relative to one another. This factor coupled with potential flexibility within the dicyanidoaurate metalloligand leads to a large range of possible lattice conformations. The precise grid geometry would then depend on other features of the framework structure, including the Fe(II) spin state, and properties of adsorbed guest species.

The decreased $d_{Fe–Au–Fe}$ value of the HS **Au**·{EtOH} *Pbaa* structure compared to the HS **Au**·{EtOH} and **Au**·{MeOH/EtOH} *Cmma* structures is indicative of much greater distortion of the cyanide linkers, as the HS Fe–N distances are very similar (as shown in **Table 4-3**). There is also a significantly higher degree of lattice compression in this structure compared to the others, as indicated by the $\theta_{Au–Fe–Au}$ value. The increased distortion in this framework could account for the gradual SCO behaviour that was visually observed as the crystal was cooled, as the distorted cyanide linkers would contribute much less to spin state communication due to decreased structural rigidity.

The difference in $d_{Fe–Au–Fe}$ between the 240 and 190 K **Au**·{EtOH} *Cmma* structures is

0.400(4) Å. The difference in the Fe–N_{CN} bond length according to **Table 4-3** is 0.22(1) Å, so with the two such bonds along the length, this would contribute a 0.44(2) Å difference. The observed $d_{Fe–Au–Fe}$ difference is less than expected, and must be due to a decrease in distortion of the dicyanidoaurate metalloligand upon transition to the LS state, leading to an elongation of $d_{Fe–Au–Fe}$ and the lower observed distance difference. Transition to the LS state also leads to decompression of the cyanide grid, evidenced by the increase in $\theta_{Au–Fe–Au}$. A comparison of the cyanide nets of these two structures is given in **Figure 4-4**, which clearly demonstrates a change in the degree of lattice compression and cyanide distortion over the spin transition.

There is a slight decrease in $d_{Fe–Au–Fe}$ for the HS **Au**·{MeOH/EtOH} *Cmma* structure compared to the HS **Au**·{EtOH} *Cmma* structure, implying a greater degree of cyanide distortion in the former structure. The $d_{Fe–Au–Fe}$ difference between the 230 and 200 K **Au**·{MeOH/EtOH} crystal structures is 0.332(2) Å, while the combined difference in the Fe–N_{CN} bond length is 0.404(18) Å. Again, this greatly reduced observed difference is due to a decrease in the cyanide distortion of the LS state, which lengthens $d_{Fe–Au–Fe}$, resulting in a decreased HS-to-LS difference. The *a*- and *b*-parameters over the transition also display decompression after transition to the LS state, to a greater degree than the **Au**·{EtOH} *Cmma* structure. This behaviour is shown most clearly through comparison of the cyanide grids (**Figure 4-9**).

There is a small decrease in $d_{Fe–Au–Fe}$ for both *Cmma* crystals between the 190/200 K and 100 K structures, indicating an increase in the cyanide distortion. This is accompanied by a greater compression of the lattice as indicated by the lower $\theta_{Au–Fe–Au}$ value. A possible origin of this behaviour could be an internal pressure effect of included solvent molecules: as the temperature decreases, the included solvent molecules undergo thermal contraction. The highly flexible cyanide grid could then compress to minimise free space, leading to a more distorted lattice geometry.

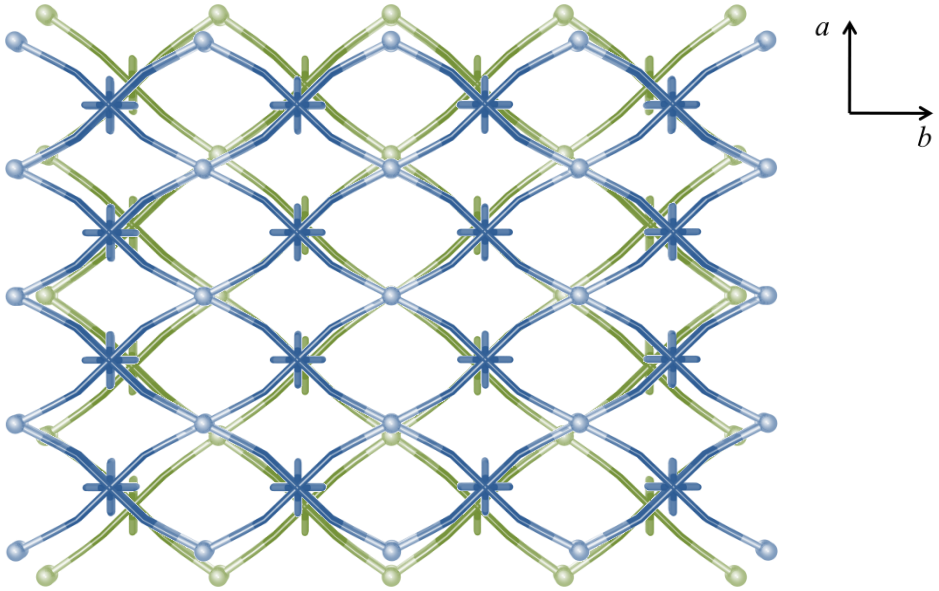

Figure 4-9: Comparison of the **Au**·{EtOH/MeOH} cyanide nets in the HS 230 K (blue) and LS 200 K (green) structures. Similarly to the **Au**·{EtOH} *Cmma* crystal, transition to the LS state results in a decrease of the lattice compression.

It has been demonstrated that the **Au** framework material exhibits significant variation in the structural conformation of the lattice, while retaining the same interpenetrated topology. The temperature-dependence of the structural parameters was investigated using variable temperature powder X-ray diffraction (**§4.4.1**). The results shown by the **Au**·{EtOH} and **Au**·{EtOH/MeOH} crystals give a brief preview of the significant guest-dependence on the structural behaviour of this framework, which will be explored in detail in the next chapter.

4.3 *Elemental Analysis*

Table 4-5: Comparison of the calculated ($C_{16}H_8N_6FeAu_2$) and experimental elemental analysis values for the bulk **Au** sample.

	Exp. (%)	Calc. (%)
Fe	7.6	7.61
Au	53.9	53.66
C	25.8	26.18
H	1.2	1.10
N	11.1	11.45

In order to determine the bulk sample purity of **Au**, elemental analysis was performed. The samples were prepared by heating gently under vacuum, and sent to the elemental analysis

facility at the University of Otago to be analysed for Fe, Au, C, H and N. The results, shown in **Table 4-5**, show a clear agreement between the calculated and experimental proportions for the elemental composition.

4.4 *Powder X-ray Diffraction*

To confirm that bulk synthesis of **Au** produced the same material as was structurally characterised by single crystal X-ray diffraction, powder X-ray diffraction (PXRD) studies were performed on the HS and LS states of the **Au**·{EtOH} framework, and Le Bail fits to the powder patterns were used to confirm the structures. The fits successfully demonstrated that bulk synthesis produces the expected framework in the *Cmma* spacgroup, and can be seen in **Figure C-16** and **Figure C-17**.

A comparison of the unit cell parameters and $d_{Fe–Au–Fe}$ obtained by SCXRD and PXRD is shown in **Table 4-6**. At each temperature, the single crystal displayed a greater degree of lattice compression than the powder sample, as indicated by the $\theta_{Au–Fe–Au}$ values (**Table 4-6**). The *c*-parameter was also greater in the single crystal measurements.

Table 4-6: Comparison of the unit cell parameters, $d_{Fe–Au–Fe}$ and $\theta_{Au–Fe–Au}$ for **Au**·{EtOH} as obtained by SCXRD and PXRD at 100, 190 and 240 K.

	Unit Cell Parameter			$d_{Fe–Au–Fe}$ / Å	$\theta_{Au–Fe–Au}$ / °
	a	*b*	*c*		
100 K SCXRD	12.1331(11)	16.0387(14)	13.6767(12)	10.0555(9)	74.21(1)
100 K PXRD	13.1545(10)	15.3026(13)	13.6200(11)	10.0878(11)	81.366(9)
190 K SCXRD	12.5570(6)	15.8316(9)	13.6771(8)	10.103(2)	76.840(6)
190 K PXRD	12.9112(5)	15.5307(5)	13.6333(5)	10.0983(3)	79.476(4)
240 K SCXRD	11.707(2)	17.442(4)	14.117(3)	10.503(2)	67.739(2)
240 K PXRD	12.2979(4)	16.8919(6)	14.0164(4)	10.4472(4)	79.112(4)

It is interesting to compare the $d_{Fe–Au–Fe}$ values between the powder and single crystal results over the different temperatures: at 240 K this distance is greater in the single crystal, at 190 K it is almost the same, and at 100 K the distance is less than the powder diffraction results. This implies that at higher temperatures the powder sample has a greater degree of dicyanidoaurate linker distortion, and as the temperature decreases, this distortion in the

powder decreases at a greater rate than in the single crystal, until the powder sample has the lesser degree of cyanide distortion at low temperatures.

While the single crystal samples of both **Au**·{EtOH} and **Au**·{MeOH/EtOH} displayed an increase in the degree of lattice compression upon cooling to 100 K, the powder sample instead showed further decompression. The difference in the lattice structures is exemplified by comparison of the $\theta_{\text{Au–Fe–Au}}$ values.

The differences in the structural behaviour of the single crystal and powder samples may be attributed to a solvation effect that is dependent on the sample environment: the PXRD measurement took place under solvent in a capillary while the crystal in the SCXRD experiment was coated in Paratone® oil and left open to the atmosphere. These different environments would produce different solvent effects and internal/external pressures on the sample, in turn giving different degrees of lattice compression and linker distortion.

The increase in the single crystal **Au**·{EtOH} lattice compression between 190 and 100 K was attributed to a decrease in the internal pressure of solvent molecules as they underwent thermal contraction, which created an increase in the lattice distortion to minimise free space (see **§4.2.5**). In the powder sample the crystallites are surrounded by EtOH solvent, which may enter into the framework pores as free space becomes available. Other influences are thus able to dominate determination of the lattice behaviour, and it becomes more decompressed.

It has been demonstrated that this framework exhibits anomalous flexibility and extreme sensitivity to environmental conditions. There may be a structural influence that makes decompression of the framework energetically favourable at lower temperatures, but in order to undergo this lattice expansion, the resulting additional pore volume must be filled. If this potential pore volume cannot be filled, as is the case in the single crystal experiment, then the compressive influence in the framework dominates the structural behaviour.

4.4.1 *Variable Temperature Powder X-ray Diffraction*

The anomalous thermal expansion properties of this material were studied in more detail using variable temperature PXRD. Le Bail refinements were performed on the powder diffractograms, using a model based on the relevant HS or LS *Cmma* crystal structures. The

resulting unit cell parameters, and the corresponding thermal expansion coefficients, can be seen in **Figure 4-10**, and the raw diffractograms are shown in **Figure C-18**. Thermal expansion coefficients were calculated using a least-squares refinement on the model shown in **Equation 4.4**.

$$x = \left[\frac{A - B}{1 + exp\left(\frac{T - C}{T_{SCO}}\right)} + B\right] + DT + ET^2 + FT^3 \qquad (4.4)$$

This equation was developed by Kepert to model the behaviour of the unit cell parameters *x* as a function of temperature *T*. The first part of the equation is a sigmoid function to fit the SCO region, where applicable. The *A* and *B* parameters model the upper and lower bounds of the transition, *C* is a term that models the abruptness of the transition, and T_{SCO} is the transition temperature (as defined in **§1.4.1**). The polynomial portion of the equation is used to model the unit cell parameter behaviour outside the spin transition temperature range, and uses the constants *D*, *E* and *F*.

A good indication of the reliability of the unit cell parameter model is obtained by comparing the model result for the volume thermal expansion behaviour, with the values calculated using **Equation 1.5**, which is the sum of the thermal expansion coefficients of the unit cell parameters. A comparison is shown in **Figure C-19**, which shows a very high correlation between the modelled and calculated values above the spin transition, and a moderately high correlation for the cooling values below the spin transition. There is less agreement for the warming data below the spin transition, which can be potentially attributed to the lack of data points above the low temperature phase transition, which could lead to comparatively poor fitting of the unit cell parameter data in this region. Overall, the model and calculated values are consistent, implying that the model gives a fairly accurate determination of the thermal expansion properties.

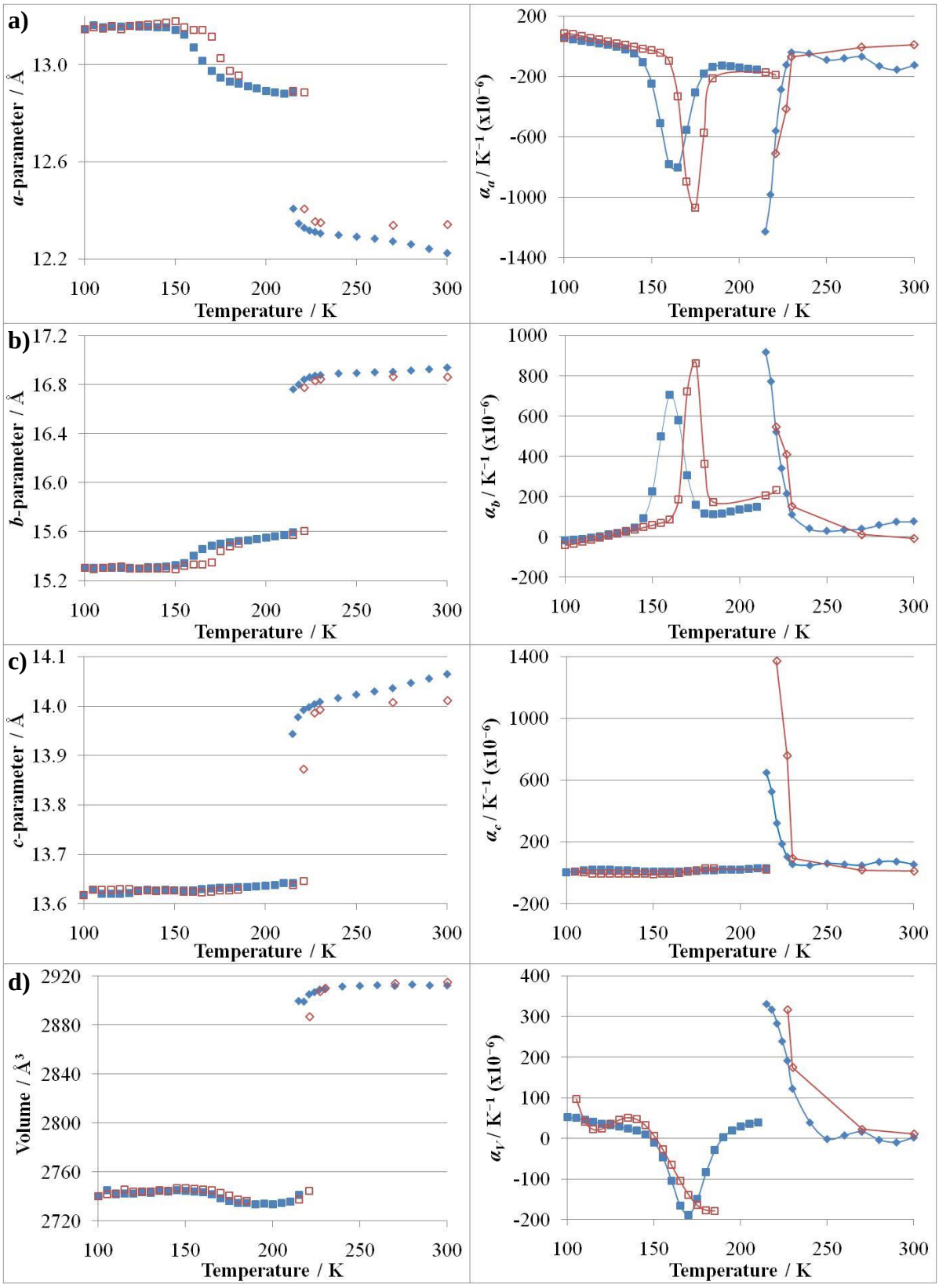

Figure 4-10: Temperature-dependence on the unit cell parameters (left) and related thermal expansion coefficients (right) of **Au**·{EtOH}: **a)** *a*-parameter; **b)** *b*-parameter; **c)** *c*-parameter; and **d)** volume, upon ◆ cooling and ◇ warming. Shapes represent ◆ HS, and ■ LS phases.

The first and most expected feature of the variable temperature unit cell parameter graphs is the discontinuity associated with the spin transition at *ca*. 215 and 221 K for the cooling and warming curves, respectively. The *b*- and *c*-parameters and the unit cell volume all decrease in size upon transition to the LS state at low temperature while the *a*-parameter undergoes a significant increase in magnitude, which is congruent with lattice decompression behaviour observed in the single crystal experiments (see **§4.2**). A lesser degree of lattice flexing was also observed above and below the spin transition as well as in a second, non-SCO gradual hysteretic phase transition at *ca*. 165 K (see **§4.5** for comparison with magnetic data).

The thermal expansion coefficients shown in the figure give a clear indication of the flexibility of this framework lattice which results in the colossal magnitude of thermal expansion. While most materials have thermal expansion coefficients of $0 \times 10^{-6} < \alpha < 20 \times 10^{-6}$ K^{-1},[7] below the spin transition this framework has thermal expansion coefficients for the *a*- and *b*-parameters of $-1070 \times 10^{-6} < \alpha_a < 85 \times 10^{-6}$ K^{-1} and $-39 \times 10^{-6} < \alpha_b < 862 \times 10^{-6}$ K^{-1} respectively. This anomalous behaviour is not observed in the *c*-parameter, which shows no unusual variation in the unit cell parameters above and below the transition.

As explained for the single crystal results (**§4.2.1**), the *c*-parameter is directly correlated to the Fe–$N_{pyridyl}$ bond, which lies parallel to the *c*-axis. From 224 to 210 K this parameter contracts by 0.356(1) Å, which is in the expected range for the contraction of two metal–ligand bonds when the Fe(II) undergoes a HS-to-LS transition. However, the variation in the *a*- and *b*-parameters is predominantly due to scissor-type flexing behaviour in the metal cyanide grid. Due to this behaviour, it is useful to calculate and study the linear Fe–Au–Fe distance ($d_{Fe–Au–Fe}$) from the *a*- and *b*-parameters (as explained in **§4.2.4**), as $d_{Fe–Au–Fe}$ does not depend on the degree of lattice compression.

Upon transition to the LS state, there is a decrease in the $d_{Fe–Au–Fe}$ value (shown in **Figure 4-11a)** of 0.34 Å, which is comparable to that observed for the *c*-parameter, and corresponds to the expected contraction of two Fe–N bonds. As was observed in the single crystal data, this decrease in the bond length is probably also coupled to a reduction in the cyanide distortion, which would slightly reduce the magnitude of the difference in $d_{Fe–Au–Fe}$. It is also interesting to note that this quantity shows little variation above and below the spin transition, implying that the degree of cyanide distortion in these temperature ranges remains relatively constant, while the cyanide grids undergo significant flexing.

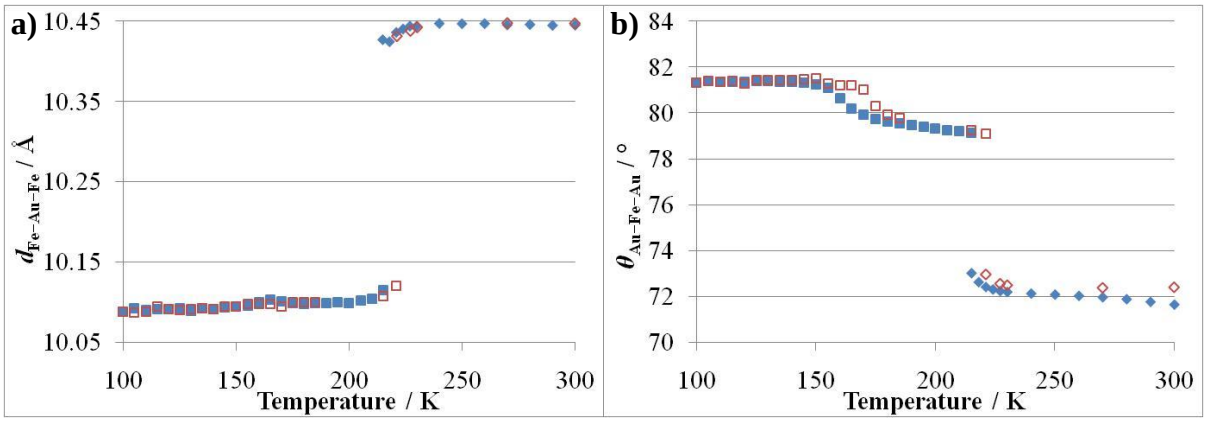

Figure 4-11: Temperature-dependence on the **a)** linear Fe–Au–Fe distance ($d_{Fe–Au–Fe}$), and **b)** acute Au–Fe–Au angle ($\theta_{Au–Fe–Au}$) of the **Au**·{EtOH} framework as calculated from the variable temperature unit cell parameters shown in **Figure 4-10**, upon ◆ cooling and ◇ warming.

As explained in **§4.2.1**, the spin transition in the **Au**·{EtOH} material produces a significant change in the lattice compression. The variation in $\theta_{Au–Fe–Au}$ (**Figure 4-11b**) confirms that the lattice compression state is the cause of the anomalous structural behaviour displayed by the *a*- and *b*-parameters.

Once the material has undergone transition to the LS state, the dynamic balance between the aforementioned weak intermolecular forces continues, resulting in further lattice decompression. A possible contributing factor in this continuing change is that decreasing temperature gradually causes a decrease in the ligand–metal bond length through thermal contraction, which would reinforce the LS Fe(II) to become closer to an octahedral geometry. Eventually the energetics reach a critical point, where the distortive force is too weak to counteract the decompressive influence, and the material undergoes the second structural transition at 170 K.

The small lower-temperature phase transition appears to be limited by the freezing point of EtOH, which occurs at 159 K.[8] Below *ca*. 150 K the behaviour becomes more conventional, with the parameters showing little variation down to 100 K. At these temperatures, the framework crystallites are presumably trapped by the immutable solvent medium, disfavouring any significant change in the lattice parameters.

Even though the $d_{Fe–Au–Fe}$ (**Figure 4-11a)** shows little change below the spin transition, the

unit cell volume (**Figure 4-10d**) shows significant variation, leading to thermal expansion coefficients of $-188 \times 10^{-6} < \alpha_a < 53 \times 10^{-6}$ K^{-1}, excluding points of discontinuity. This volume thermal expansion behaviour is also interesting because it does not follow the same pattern as any of the other quantities discussed. The major region of unusual behaviour occurs over the low temperature phase transition, in which the volume undergoes a significant degree of negative thermal expansion. This behaviour results from the lattice decompression of the rhomboid metal cyanide grids, which increases the unit cell volume as explained in **§4.2.4**.

As mentioned above, the low-temperature phase transition is likely to occur as the distortive inter-network ligand–ligand interactions become so weak that they cannot counteract the decompressive influence. The change in these ligand–ligand interactions would then result in a change in the preferred ligand conformation, which could also contribute to a change in the unit cell dimensions. **Figure 4-12** shows the single crystal structure of **Au**·{MeOH/EtOH} at 200 K, in which the cyanide grid is the least compressed of all the single crystal structures obtained, and the disorder of the pyridyl rings has been removed with the rings aligning along the *a*-axis. This observation suggests that with a sufficiently decompressed structure, the bpac pyridyl rings will align, presumably due to favourable inter-network interactions. While this orientation maximises these favourable interactions, it also creates a minor repulsive force between the adjacent bpac molecules along the *a*-axis (**Figure 4-13**), resulting in the additional lattice decompression observed at the low temperature structural transition.

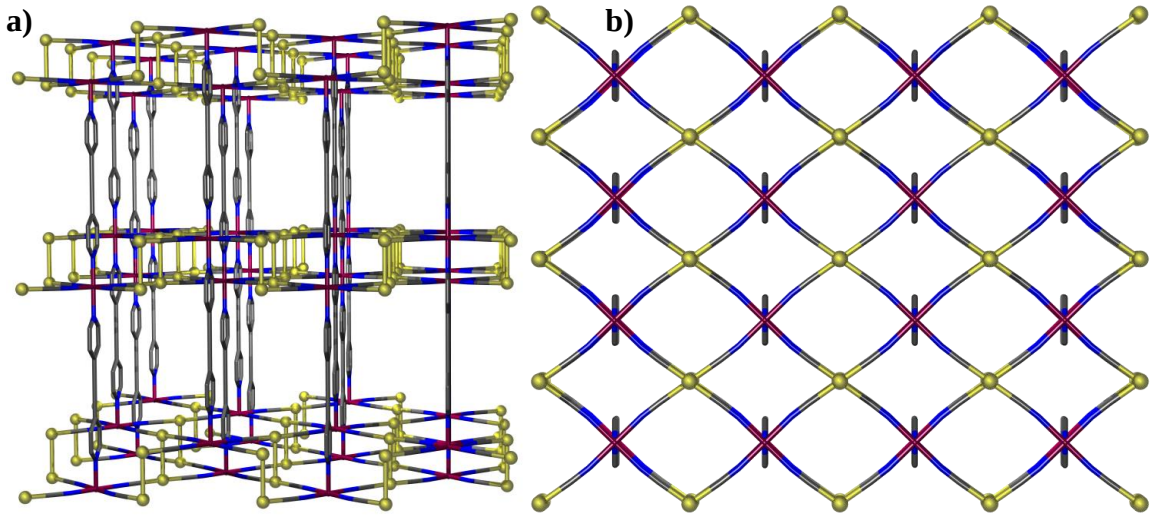

Figure 4-12: Single crystal structure of **Au**·{MeOH/EtOH} at 200 K, as viewed **a)** parallel to the *b*-axis; and **b)** parallel to the *c*-axis. Note that both independent interpenetrated nets are shown in the figures. Solvent molecules and hydrogen atoms have been removed for clarity.

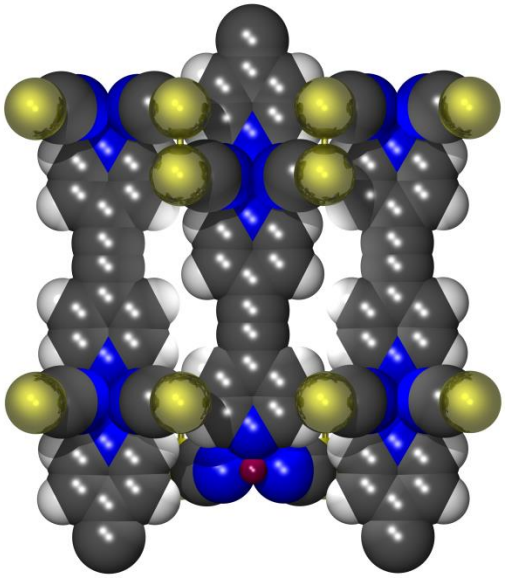

Figure 4-13: Space-filling representation of **Au**·{MeOH/EtOH} as viewed down the *b*-axis. Solvent molecules have been removed for clarity.

The coupling of SCO with such a large degree of lattice flexibility is unprecedented, though similar 'lattice fence'-type behaviour has been observed in other materials, which also exhibit colossal uniaxial thermal expansion behaviour.[7,9] Further investigations into modifying the spin transition behaviour to be more gradual using metal dilution were undertaken by Dr Laurence Goux. The resulting frameworks, $[Fe_xNi_{1-x}(bpac)(Au(CN)_2)_2]$, displayed a dilution

concentration dependence on the abruptness of the spin transition, and thus the temperature range over which the colossal magnitude of thermal expansion occurred. The maximum level of negative thermal expansion was obtained from the x = 0.84 framework, with a value of $\alpha_a = -3087 \times 10^{-6}\,K^{-1}$. This negative thermal expansion is an order of magnitude greater than any yet reported, and these results are soon to be published.

4.5 *Magnetic Properties*

The bulk spin transition behaviour of **Au**·{EtOH} was studied using variable temperature magnetic susceptibility. As shown in **Figure 4-14**, **Au**·{EtOH} displays an abrupt spin transition with hysteresis. The transition occurs with $T_{1/2}{}^{\downarrow}$ = 218 K and $T_{1/2}{}^{\uparrow}$ = 224 K, giving a hysteresis of 6 K. It also goes to relatively high completeness, with the residual HS fraction attributed to non-SCO Fe(II) centres at the surface of the framework crystallites and at lattice defect sites.

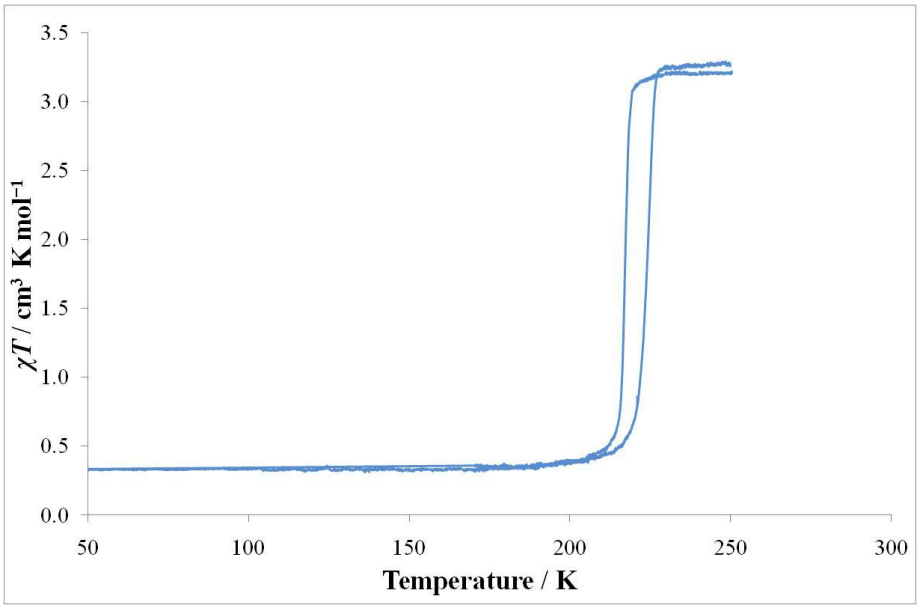

Figure 4-14: Temperature-dependence on the magnetic susceptibility for **Au**·{EtOH}.

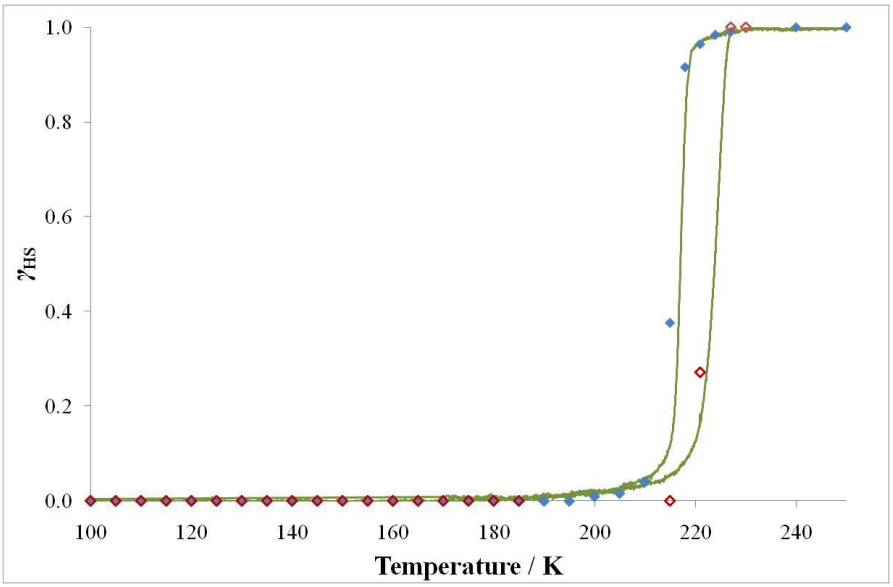

Figure 4-15: Comparison of the relative stoichiometric fraction of HS states (γ_{HS}) as determined through — the magnetic susceptibility; and the relative intensity of the (001) peak of the HS phase, upon ◆ cooling and ◇ warming. It should be noted that over time the sample suffered radiation damage, decreasing the intensity of the HS peak for the warming data. The HS proportion at these temperatures is adjusted to compensate for this.

To confirm that the behaviour observed by magnetic susceptibility and variable temperature powder X-ray diffraction studies correlate, the relative stoichiometric fraction of HS states (γ_{HS}) was used. **Figure 4-15** compares this fraction calculated from the magnetic data and the relative intensity of the (001) peak in the HS phase. The data agree remarkably well. This also confirms that only the abrupt phase transition observed in the variable temperature PXRD measurements was due to the spin transition; all other lattice flexing behaviour was independent of the spin transition.

4.6 *Adsorption Properties*

The N_2 adsorption properties of **Au** were analysed at 77 K to quantitatively determine the effective porosity and robustness of the framework. The resulting isotherm can be seen in **Figure 4-16**.

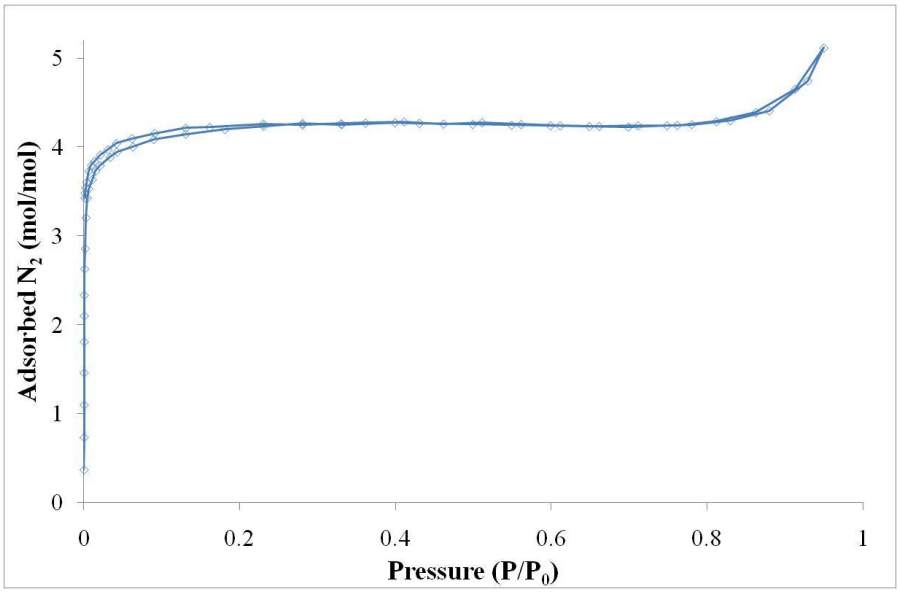

Figure 4-16: Nitrogen adsorption isotherm for **Au** obtained at 77 K, at which temperature the framework is in the LS state.

The adsorption isotherm follows a typical Type I adsorption curve as described in **§1.3.1**, which is indicative of a microporous (or nanoporous) material. N_2 is rapidly adsorbed into the sample until *ca*. 4.08×10^{-3} P/P_0, after which the curve slowly becomes more level. There is a slight decrease in the adsorption between *ca*. 0.399 and 0.699 P/P_0, which is unusual as increasing pressure normally leads to increased deposition of surface multilayers. This behaviour is most likely due to lattice compression of the framework upon increasing pressure, which decreases the guest accessible volume, in turn reducing the quantity of adsorbed guest. The increasing slope above 0.830 P/P_0 can be attributed to the N_2 reaching a pressure at which it starts to condense. There is a minor hysteresis shown at low pressure, which is expected from capillary condensation in mesoporous materials.

Computational analysis of the data reveals additional information about the properties of the framework pores. Using the BET model in the *ASAP 2020* software to analyse the data taken between 0.042 and 0.23 P/P_0, the surface area of **Au** was determined to be 441(12) $m^2\ g^{-1}$ (with a correlation coefficient for the linear fit of 0.9985). Analysis of the point at 0.2304 P/P_0 yields a theoretical surface area of 448 $m^2\ g^{-1}$, and a pore volume of 0.250 $cm^3\ g^{-1}$, which is equivalent to 44.5% of the total volume of the material. The average pore width was calculated to be 23 Å, which technically classifies this material as mesoporous (see **§1.3.1**). Observation of the adsorbed quantity at $P/P_0 = 0.83$ gives a value of

4.4 moles of guest N_2 per mole of the framework.

Calculations were performed using the *SOLV* routine in *PLATON*[6] on the single crystal structure of **Au**. The 200 K **Au**·{MeOH/EtOH} crystal structure was chosen, as this was believed to best represent the framework structure at the experimental temperature. Solvent molecules were removed from the crystal model in order to obtain an accurate calculation of the pore properties. The theoretical solvent accessible volume was determined to be 46.3%, corresponding to a pore volume of 0.260 $cm^3\ g^{-1}$. This is very close to the experimental value, and the difference is most likely attributed to a change in the accessible pore space depending on the degree of compression in the cyanide grids.

This N_2 isotherm demonstrates that the **Au** framework is robust to solvent removal, and that it has a significant quantity of guest accessible pore volume and a large internal surface area. These factors make this framework of interest for studying the guest effect on the framework behaviour, which is discussed in detail in the following chapter.

4.7 *Discussion*

The **Au** framework displays a remarkably flexible structure, producing an unprecedented dimension change between 300 and 100 K with a magnitude of thermal expansion that is greater than any yet reported. This flexibility arises from the very small energy penalty associated with scissor-type motion of the {$Fe(Au(CN)_2)_2$} (4,4)-grids, coupled with the highly underconstrained framework topology. Weak inter-network interactions are then able to govern the precise grid geometry.

There is a dynamic balance between temperature-dependent compressive and decompressive influences. Those factors that favour compression include C–H···π interactions between pyridyl rings and adjacent cyanide and bpac molecules, and possible host–guest interactions. Decompression is favoured by a non-distorted octahedral environment around the Fe(II), as well as interactions between parallel bpac pyridyl rings which align along the *a*-axis.

The magnetic behaviour of **Au**·{EtOH} displays an abrupt, hysteretic spin transition at $T_{1/2}^{\downarrow}$ = 218 K. This transition was also observed in the powder diffraction data, and was shown to create a major change in the lattice conformation. Upon transition to the LS state, the lattice undergoes a large degree of decompression, due to the geometric influence of the

more rigidly orthogonal LS octahedral Fe(II) centres. There is also a decrease in the cyanide linker distortion, which contributes to expansion of the unit cell parameters.

The **Au**·{EtOH} and **Au**·{MeOH/EtOH} *Cmma* single crystal structures demonstrated the guest-dependent effect on the framework compression, which gave significantly different unit cell parameters. The 200 K **Au**·{MeOH/EtOH} structure was the least compressed of all those studied, and resulted in bpac pyridyl rings that were aligned parallel along the *a*-axis, due to favourable interactions between adjacent pyridyl units. This result gives a potential explanation for the low temperature phase transition observed in the powder diffraction data: as the framework becomes more decompressed with decreasing temperature, the inter-network interactions that favour the compressed state become so weak that they lose their influence over the framework geometry. Once the lattice is in a sufficiently decompressed state, the decompressive interactions dominate, and the framework undergoes the low temperature structural transition.

A single crystal polymorph of the **Au**·{EtOH} material was discovered, and solved in the *Pbaa* space group. This structure was found to have a much more distorted conformation than the *Cmma* structures, and the lattice was so compressed that the bpac pyridyl rings were forced to adopt perpendicular conformations. It was also observed that this crystal underwent a gradual thermochromic transition below *ca*. 140 K, but a structural solution was unable to be obtained below this temperature due to poor diffraction quality of the crystal.

The N_2 adsorption isotherm proved that this framework is robustly porous, with high internal surface area and solvent accessible pore volume. The fact that this framework is robust to guest removal makes it an ideal candidate to investigate the guest-dependent effect on its properties, which was briefly previewed in the mixed-solvent single crystal structure results. This guest effect is discussed in detail in the following chapter.

References

(1) Niel, V.; Muñoz, M. C.; Gaspar, A. B.; Galet, A.; Levchenko, G.; Real, J. A. *Chem. Eur. J.* **2002**, *8*, 2446.
(2) Shepherd, H. J.; Bartual-Murgui, C.; Molnár, G.; Real, J. A.; Muñoz, C. M.; Salmona, L.; Bousseksou, A. *New J. Chem.* **2011**, *35*, 1205.
(3) Mullaney, B. R. BSc(Hons) Thesis, University of Sydney, 2009.
(4) van der Sluis, P.; Spek, A. L. *Acta Cryst.* **1990**, *A46*, 194.
(5) Spek, A. L. *J. Appl. Cryst.* **2003**, *36*, 7.

(6) Spek, A. L.; Utrecht University: Utrecht, The Netherlands, 2007.
(7) Goodwin, A. L.; Calleja, M.; Conterio, M. J.; Dove, M. T.; Evans, J. S. O.; Keen, D. A.; Peters, L.; Tucker, M. G. *Science* **2008**, *319*, 754.
(8) Lemmon, E. W.; McLinden, M. O.; Friend, D. G. In *NIST Chemistry WebBook, NIST Standard Reference Database Number 69*; Lindstrom, P. J., Mallard, W. G., Eds.; National Institute of Standards and Technology: Gaithersburg, MD, USA, http://webbook.nist.gov, (retrieved April 6, 2012), 2012.
(9) Das, D.; Jacobs, T.; Barbour, L. J. *Nat. Mater.* **2010**, *9*, 36.

Chapter 5: Guest-Dependent Behaviour in the Framework, $[Fe(bpac)(Au(CN)_2)_2]$

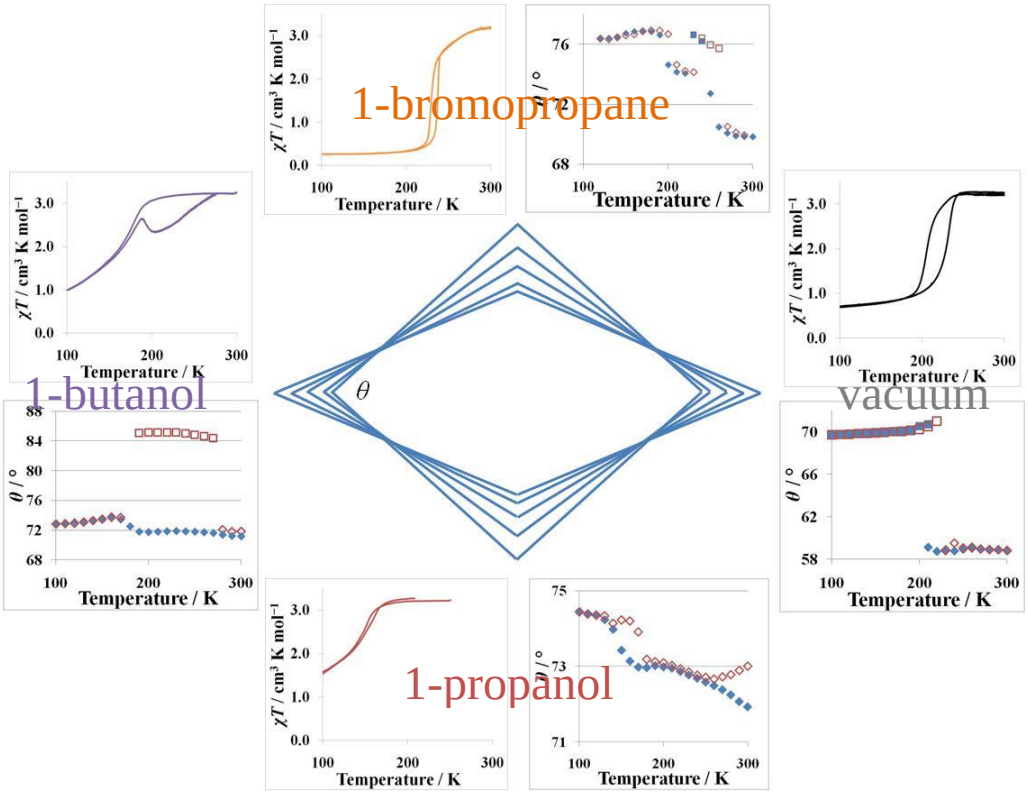

The $[Fe(bpac)(Au(CN)_2)_2]$ framework exhibits a strong synergistic relationship between the spin transition, structural properties and adsorbed guest species.

5.1 *Outline*

As described in the previous chapter, the [Fe(bpac)($Au(CN)_2)_2$] (**Au**) framework displays SCO, colossal uniaxial positive and negative thermal expansion, and nanoporosity. As the framework is robust to guest removal, this allows detailed, systematic study of the effect of different adsorbed guest species on the framework properties.

The results in this chapter begin by presenting the properties of guest-free **Au** under static vacuum, and under N_2 at atmospheric pressure. There are then two major solvent families that were investigated: alcohols and halogenated alkanes. Finally, a few other miscellaneous guest species were studied. The results for these are initially discussed and compared within the individual families, then compared between each other. Where possible, conclusions are drawn regarding the various factors that determine the solvent effect on this framework behaviour.

The **Au** framework demonstrates significant conformational flexibility, which depends on the properties of host–guest interactions, solvent guest packing behaviour and the conformational freedom of the framework crystallites. There is a synergistic effect between the framework lattice conformation and the spin transition behaviour, with each property affecting the other. With the exception of **Au**·{MeCN}, transition to the LS state results in conversion of the framework lattice to a more decompressed conformation and the dicyanidoaurate ligands adopt a more linear coordination geometry between Fe(II) centres. The framework displays more gradual spin transition behaviour when the conformational freedom of the framework lattice is decreased, and/or when the framework lattice displays a non-orthogonal coordination of the bpac pillar ligand, resulting in a decrease in the ease of communication of spin state.

It should be noted that due to the nature of the sample containment with solvent, it was very difficult to accurately determine the guest-free mass of the framework sample for determination of the magnetic susceptibility. As a result, all of the magnetic data in this chapter are scaled such that the HS value is the same as was determined for the **Au**·{EtOH} sample, of *ca*. 3.20 cm^3 K mol^{-1}.

5.2 *Vacuum*

The preparation of this sample for the magnetism measurement was slightly different to that of the solvated samples. An air-dried sample was loaded into the sample tube and packed down with cotton wool as described in **§7.6**, then placed under dynamic vacuum for 6 hr with gentle heating in a water bath. Instead of using a second plug, the top of the sample tube was heat-sealed closed slightly above the cotton wool while under dynamic vacuum such that the vacuum assisted in drawing the sample tube walls together while the heat melted the tube sufficiently to seal it. The rest of the sample preparation was identical to the solvated samples.

Preparation of the sample in a capillary for the PXRD experiment was performed similarly, with removal of guest performed under dynamic vacuum with the sample in a capillary, then heat-sealing the capillary while still under vacuum.

Au·{Ø} displays a relatively gradual magnetic spin transition with hysteresis (**Figure 5-1**). The transition occurs with $T_{1/2}^{\downarrow}$ = 207 K and $T_{1/2}^{\uparrow}$ = 230 K, giving a hysteresis of 17 K. It has a higher residual HS fraction than the **Au**·{EtOH} sample, and displays a very gradual linear decrease in the magnetic susceptibility down to low temperature.

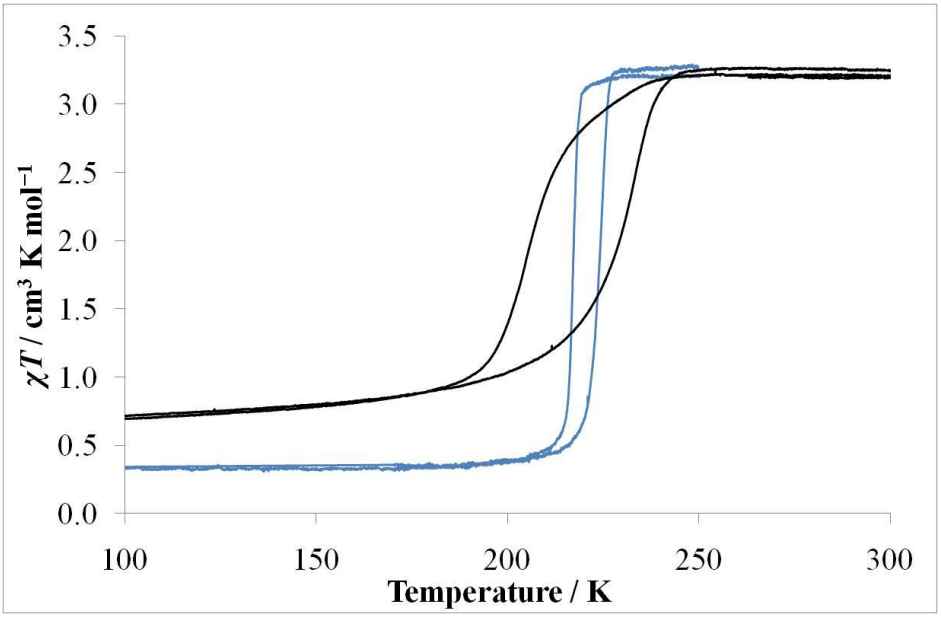

Figure 5-1: Temperature-dependence on the magnetic susceptibility for — **Au**·{Ø}, compared with — **Au**·{EtOH}.

The shape of this magnetic behaviour is reminiscent of the spin transition displayed by the **Pd·0.4(bpac)**{1-PnOH} sample described in **§3.3.2.8**. There appear to be two distinct stages to the spin transition, in which the material begins with a gradual transition and after a critical point becomes more abrupt, with a larger hysteresis than might be expected for a relatively gradual transition. More information on the nature of this transition can be determined by comparison with the powder diffraction data.

Most of the peaks in the powder X-ray diffractograms (shown in **Figure C-20**) are very broad, which is likely due to a range of framework lattice parameters in the crystallites. As a result, it was difficult to determine a unit cell and space group that appropriately fit the peaks. In the **Au**·{EtOH} framework, the major peak immediately after the large (001) peak corresponds to the (020) reflection. It was therefore assumed that the same was true for the vacuum sample, which, when the (020) reflection of the HS phase is converted to the equivalent *d*-spacing, gives a value for the *b*-parameter of *ca*. 17.7 Å. This value is closest to the *b*-parameter determined for the single crystal structure of the *Pbaa* phase, described in **§4.2.3**. Considering this, and the success by which the powder diffractogram reflection peaks were fit by the space group, a model based on this crystal system was used to refine the unit cell parameters of the vacuum sample, using the *Pbaa* space group. The *Cmma* space group was not used for the HS phase as it did not fit as many peaks as the equivalent cell in *Pbaa*. It is possible that this sample has a different space group from the one used, but the quality of the data was not sufficient to determine an alternative space group. The *Pbaa* space group was successful in determining unit cell parameters that made physical sense considering the structural behaviour of this material as described in Chapter 4. Upon transition to the more decompressed LS phase, the peaks were best fit using a model in the *Cmma* space group. This is consistent with the HS **Au**·{EtOH} sample, which displayed a similar degree of compression, with $\theta_{\text{Au–Fe–Au}} \approx 70°$ (*vide infra*).

As shown in **Figure C-20**, the *Pbaa* fit is considerably poorer than the corresponding fits for the *Cmma* **Au**·{EtOH} sample, which is due to the lower intensity and broader nature of the peaks for the sample under vacuum. The broad peak profiles are in turn probably caused by a distribution of crystallite lattice parameters which result from the extreme framework flexibility.

As shown in **Figure 5-2c**, the *c*-parameter of **Au**·{Ø} displays the expected change in

magnitude as it follows the spin transition, with a decrease of 0.39 Å upon transition to the LS state. However, the *a*- and *b*-parameters show interesting temperature-dependent behaviours which are in stark contrast to that observed for **Au**·{EtOH}. Above and below the spin transition in **Au**·{Ø} these parameters show little variation, implying that the significant lattice flexing observed in **Au**·{EtOH} must result from guest effects. The *a*- and *b*-parameters are also much more compressed in **Au**·{Ø}, which might be expected considering the vacuum environment of the sample, and the energetic drive to minimise free space in the flexible framework lattice and maximise inter-network interactions. The *Pbaa* space group is consistent with this compression state, as the crystal structure described in **§4.2.3** demonstrates ligand conformations that are determined by steric interactions that result from this high degree of lattice compression.

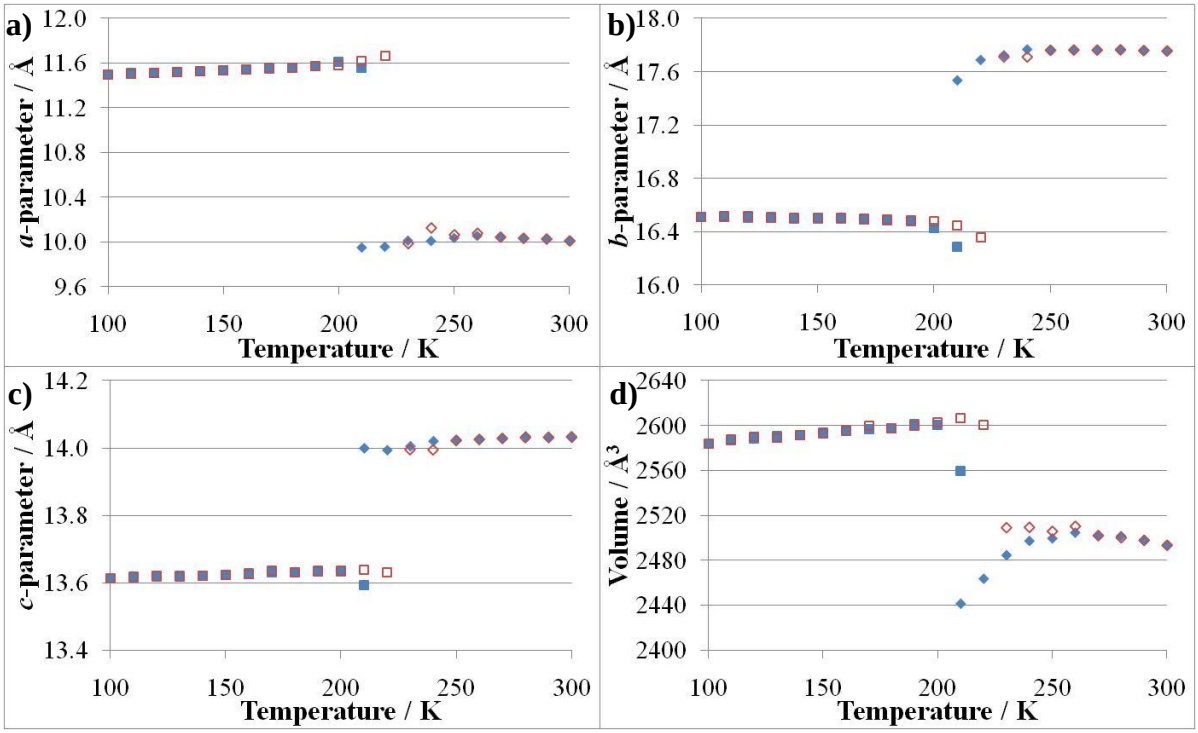

Figure 5-2: Temperature-dependence on the unit cell parameters of **Au**·{Ø}: **a)** *a*-parameter; **b)** *b*-parameter; **c)** *c*-parameter; and **d)** volume, upon ◆ cooling and ◇ warming. Shapes represent ◆ HS (*Pbaa*), and ■ LS (*Cmma*) phases. Note that while both HS and LS phases were present in the 220 and 230 K warming data, the data were too poor to accurately determine unit cell parameters for the minority phase.

Lattice decompression is observed over the spin transition, which is driven by the LS Fe(II) centres adopting a more rigidly octahedral coordination geometry. This decompression

results in a transition to the *Cmma* phase, implying that the LS framework conformation is similar to that observed in the *Cmma* **Au**·{EtOH} sample (**§4.4.1**). Before full transition to the LS state, the HS phase volume also decreases, presumably due to individual Fe(II) sites undergoing spin transition within the HS *Pbaa* crystallites, which results in a decrease in the average Fe–N bond lengths. It is only after the full crystallite converts to the LS phase that the lattice undergoes decompression.

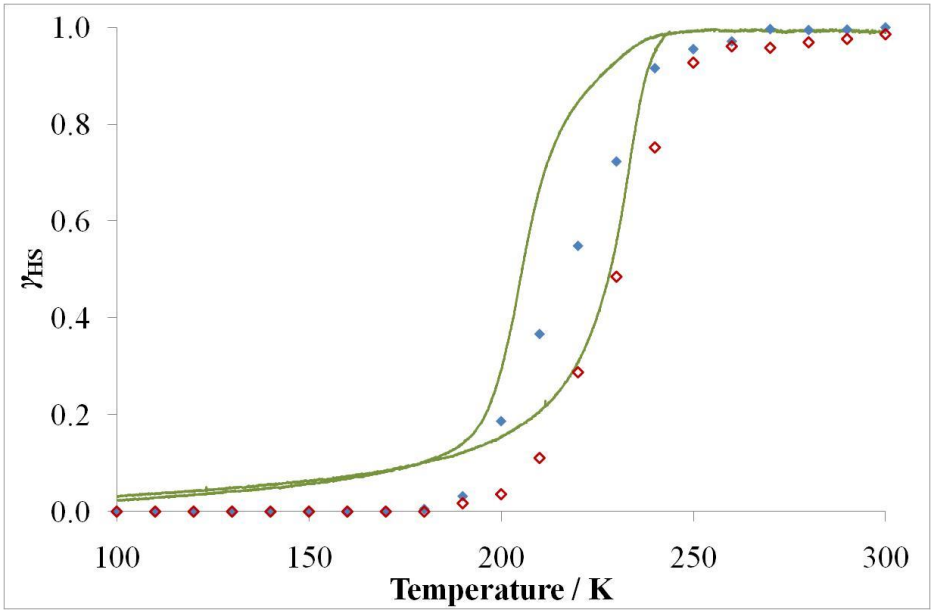

Figure 5-3: Comparison of the relative stoichiometric fraction of HS states (γ_{HS}) for **Au**·{Ø} as determined through — the magnetic susceptibility; and the relative intensity of the (001) reflection of the HS phase, upon ◆ cooling and ◇ warming.

In determining the mechanism for the behaviour over the spin transition, it is useful to compare the relative stoichiometric fraction for the HS state of **Au**·{Ø} as obtained by PXRD and magnetic susceptibility (**Figure 5-3**). The data correlate well, demonstrating similar transition temperatures. The low temperature linear decrease in the magnetic data is due to residual SCO-active HS Fe(II) sites within LS crystallites. As shown in **Figure C-22**, there are two distinct HS and LS states that coexist over the transition, which indicates an abrupt, cooperative transition within crystallites, but that there is a range of temperatures over which all of the crystallites undergo spin transition. There is also a slight movement of the (001) peaks as the bulk material undergoes SCO which, as shown in the modelled unit cell parameters (**Figure 5-2**), is due to some of the Fe(II) sites within the crystallites undergoing a non-cooperative transition as well. Using this information, coupled with the crystallite phase

behaviour shown in **Figure 5-3**, it can be concluded that the transition of **Au**·{Ø} is mainly cooperative with individual crystallites undergoing spin transition over a temperature range of *ca*. 50 K. However, there are also Fe(II) sites within the crystallites that do not contribute to this cooperative transition, and instead undergo spin transition independently of the rest of the crystallite. This accounts for the observation of characteristics of both abrupt and gradual transition behaviours in the magnetic data.

The linear Fe–Au–Fe distance ($d_{Fe–Au–Fe}$), shown in **Figure 5-4a**, gives more information about the nature of the spin transition, and displays notably different temperature-dependent behaviour to the unit cell volume. The transition from HS-to-LS occurs with a decrease of *ca*. 0.15 Å along this dimension, which is much less than the expected change for two Fe–N_{CN} bond lengths of *ca*. 0.40 Å (**§4.2.5**). As is the case for **Au**·{EtOH}, the discrepancy in the observed and expected value of this quantity can be attributed to a decrease in the dicyanidoaurate distortion (**§4.2.4**), which leads to a relative expansion in $d_{Fe–Au–Fe}$, counteracting the length contraction due to the decreased Fe–N_{CN} bond length, giving an overall reduction in the distance difference. The HS-to-LS transition also occurs with a gradual decrease in $d_{Fe–Au–Fe}$ in the HS phase to a value comparable to the fully LS quantity. At 210 K, where both phases are present and modelled, the LS phase has a greatly reduced $d_{Fe–Au–Fe}$, which possibly occurs as an artefact of the more distorted cyanide linker of the HS phase. The $d_{Fe–Au–Fe}$ value then rapidly increases as the temperature decreases, until the cyanide distortion reaches the low temperature equilibrium value.

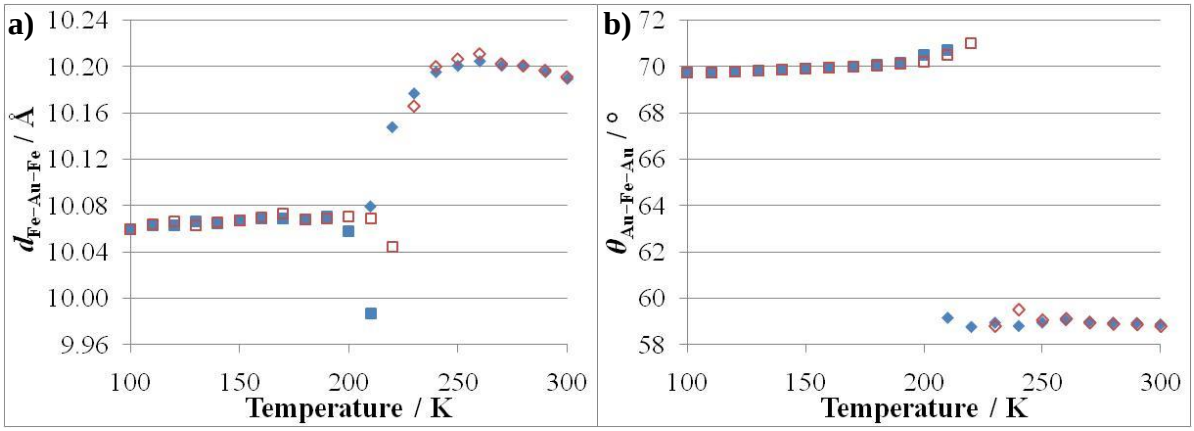

Figure 5-4: Temperature-dependence on the **a)** linear Fe–Au–Fe distance ($d_{Fe–Au–Fe}$); and **b)** acute Au–Fe–Au angle ($\theta_{Au–Fe–Au}$) of the **Au**·{Ø} framework as calculated from the variable temperature unit cell parameters shown in **Figure 6-2**, , upon ◆ cooling and ◇ warming.

The HS-to-LS volumetric expansion (**Figure 5-2c**) is due to the large magnitude of decompression observed in the framework lattice. As explained in **§4.2.4**, the degree of compression affects the area of the cyanide grid, and thus the volume of the framework. Consequently, even though there is a decrease in the *c*-parameter and $d_{Fe–Au–Fe}$ value over the spin transition, the large degree of lattice decompression gives a net increase in the unit cell volume.

The change in the Au–Fe–Au angle ($\theta_{Au–Fe–Au}$, **Figure 5-4b**) confirms that there is very little variation in the degree of compression of the framework, except over the spin transition. The HS value of $\theta_{Au–Fe–Au} \approx 59°$ indicates the high degree of lattice compression in the framework. This value compares well with the HS value for the *Pbaa* single crystal of **Au**·{EtOH}, which had $\theta_{Au–Fe–Au} = 59.251(9)°$, further confirming the validity of the solution with this space group and the associated structural conformation.

5.3 *Nitrogen*

Au·{N_2} was studied as a representative investigation into the effect on the **Au** framework of incorporating a gaseous guest in the sample, and to determine the transition behaviour of the framework without solvent guest, yet under normal atmospheric pressure. As a gas, N_2 would have a weak interaction with the framework producing a correspondingly weak guest effect, but the sample would not be under a vacuum environment, and would thus be more freely able to adopt the most energetically favourable conformational geometry. This sample was prepared for the experiments in a similar manner as the **Au**·{Ø} sample, except that the sample containers were filled with nitrogen gas before sealing.

The variable temperature magnetic behaviour of **Au**·{N_2} (**Figure 5-5**) demonstrates that spin transition occurs with $T_{1/2}^{\downarrow} = 223$ K with a SCO range of 39 K, and $T_{1/2}^{\uparrow} = 243$ K with a SCO range of 25 K, giving a hysteresis width for the spin transition of 10 to 20 K.

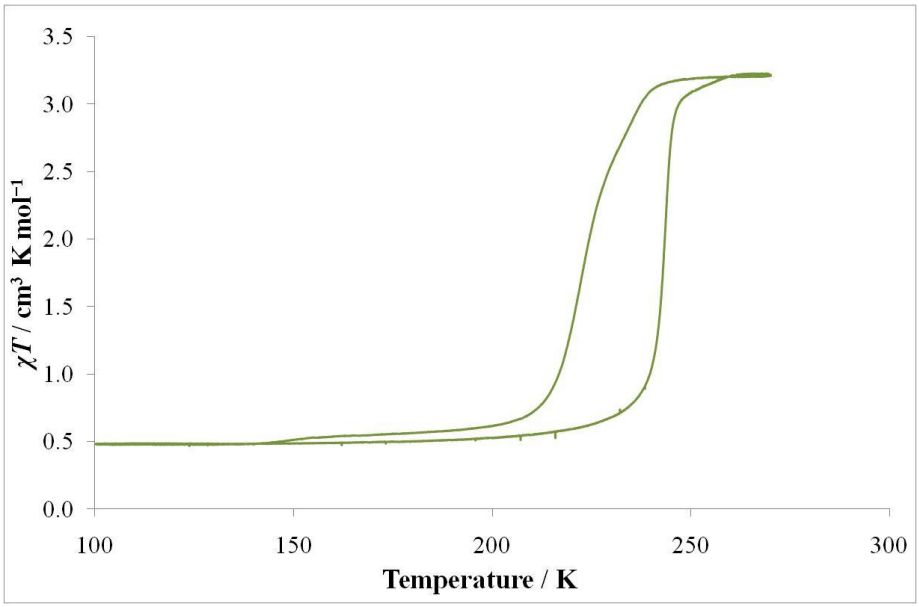

Figure 5-5: Temperature-dependence on the magnetic susceptibility for **Au**·{N_2}.

Variable temperature powder diffraction experiments provided structural information regarding the nature of the spin transition in the framework sample. A model that was fit to the powder diffractograms using Le Bail methods produced the unit cell parameters shown in **Figure 5-6**. At high temperature, the data were best fit using a model in the *Pbaa* space group. This is consistent with the results of the **Au**·{Ø} sample, which was observed to display a similarly high degree of lattice compression, and was modelled in the same space group. Upon cooling, the material undergoes spin transition and, similarly to the **Au**·{Ø} sample, the LS phase in the powder diffractograms display a peak distribution that is best fit using a model in the *Cmma* space group. Over the transition there is a mix of HS and LS phases, with individual crystallites undergoing spin transition abruptly, but with different crystallites undergoing transition over a range of temperatures. This behaviour is best observed through the *c*-parameter (**Figure 5-6c**), which is a generally reliable measure of the spin state in the **Au** material; the spin transition is also accompanied by significant decompression of the framework, as observed in the $\theta_{Au–Fe–Au}$ value (**Figure 5-7b**).

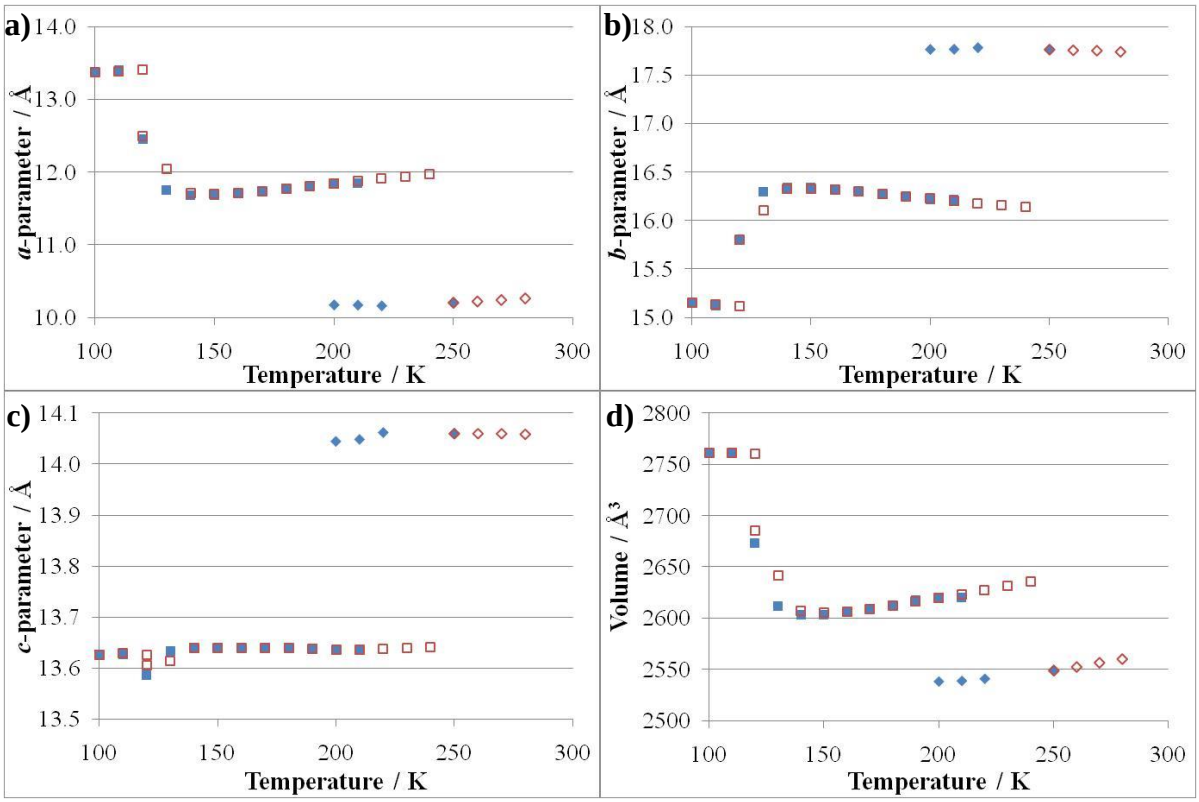

Figure 5-6: Temperature-dependence on the unit cell parameters of **Au**·{N_2}: **a)** *a*-parameter; **b)** *b*-parameter; **c)** *c*-parameter; and **d)** volume, upon ◆ cooling and ◇ warming. Shapes represent ◆ HS (*Pbaa*), and ■ LS (*Cmma*) phases.

As the temperature is decreased, the LS phase displays gradual compression behaviour as the $\theta_{Au–Fe–Au}$ value slowly decreases. At *ca*. 130 K there is another phase transition, in which the lattice undergoes further decompression. The structural behaviour upon warming is similar to the cooling behaviour, with the exception that there is a hysteresis observed in both phase transitions, and the spin transition appears to occur much more abruptly, with little evidence for a mixed phase at the transition temperature.

Analysis of the $d_{Fe–Au–Fe}$ value (**Figure 5-7a**) in **Au**·{N_2} shows a similar value in the HS state (*ca*. 10.25 Å) as was observed in the HS **Au**·{Ø} (*ca*. 10.20 Å, **§5.2**) and the *Pbaa* **Au**·{EtOH} single crystal (10.221(3) Å, **§4.2.5**) samples, and is indicative of a high degree of distortion in the dicyanidoaurate linker, which seems to be characteristic of the framework in this lattice conformation. When the **Au**·{N_2} sample undergoes transition to the LS state, the $d_{Fe–Au–Fe}$ value decreases to *ca*. 10.04 Å, which is a change of 0.21 Å along this dimension. This distance difference is much less than the expected value from the change in two Fe–N

bonds of *ca*. 0.40 Å (see **§4.2.5**), with the discrepancy attributable to a large decrease in the distortion of the dicyanidoaurate linkers, similarly to the explanation for the analogous behaviour observed in the **Au**·{Ø} sample (**§5.2**). The greater linearity of the metalloligands effectively lengthens the linker along the Fe–Au–Fe dimension, counteracting the effect of the Fe–N bond contraction and decreasing the HS-to-LS difference in $d_{Fe–Au–Fe}$.

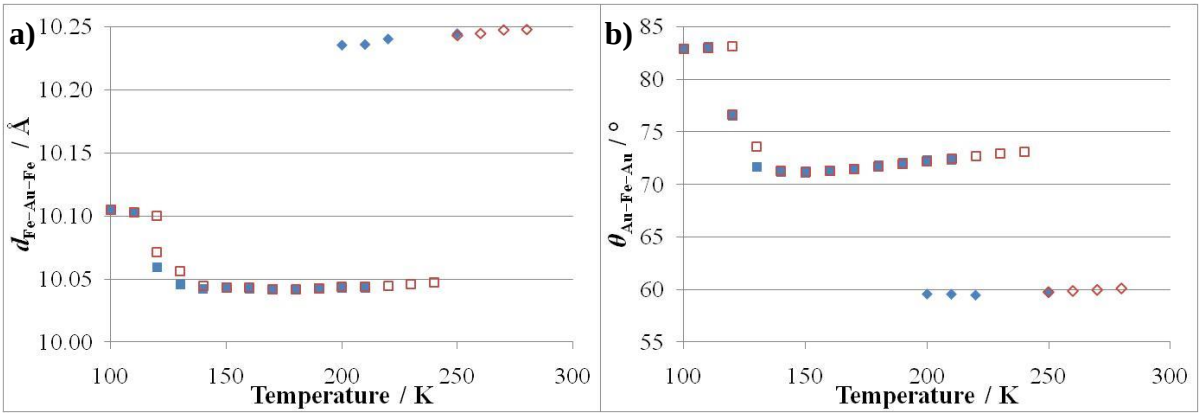

Figure 5-7: Temperature-dependence on the **a)** linear Fe–Au–Fe distance ($d_{Fe–Au–Fe}$), and **b)** acute Au–Fe–Au angle ($\theta_{Au–Fe–Au}$) of the **Au**·{N_2} framework as calculated from the variable temperature unit cell parameters shown in **Figure 5-6**, upon ◆ cooling and ◇ warming.

The spin transition is also accompanied by lattice decompression, as shown by the large increase in the magnitude of $\theta_{Au–Fe–Au}$ (**Figure 5-7b**). Similar to the **Au**·{Ø} sample, transition to the LS state also results in a net increase in the volume of the framework, even though there is contraction in both the *c*-parameter and $d_{Fe–Au–Fe}$. This volumetric expansion, as explained in **§4.2.4,** is due to the angle-dependence on the area of a rhombus. As the internal angles of the rhombus tend closer to 90°, the area of the quadrilateral, and subsequently the volume, increases. Over the spin transition, the $\theta_{Au–Fe–Au}$ value of the rhomboid metal-cyanide grid increases significantly, leading to a corresponding increase in the effective area of the cyanide plane, thus increasing the volume. The effect of this factor on the framework volume is greater than the negative contribution to the volume that arises from the Fe–N bond contraction, with the result that the volume increases over the spin transition.

At the low temperature phase transition, $d_{Fe–Au–Fe}$ increases to *ca*. 10.10 Å, which is similar to the LS value for this quantity that was observed in the **Au**·{EtOH} sample (*ca*. 10.10 Å,

§4.4.1). In addition, this expansion effect is accompanied by further decompression of the framework lattice, which, as explained above, also contributes to volumetric expansion in the framework. As a result of this combined effect, the lattice volume is greater below the low temperature phase transition.

Comparison of the relative stoichiometric fraction of the HS state as determined by magnetism and powder diffraction (**Figure 5-8**) shows relatively good agreement regarding the abruptness of the spin transition, but poorer agreement regarding the temperature at which the transition occurs. Upon cooling, the spin transition occurs over *ca*. 39 K, which the powder diffraction results confirm as occurring predominantly due to individual crystallites undergoing abrupt SCO, over a range of temperatures. However, the transition temperatures as determined through the powder diffraction experiment occur *ca*. 14 K lower than those displayed by the magnetic experiment. This discrepancy may be due to the different sample environments used for the two experiments, which could affect the subtle interactions that determine the precise spin transition behaviour. In this case, the extent of N_2 adsorption into the framework will depend greatly on the sealed volume and the sample mass: in the diffraction experiment, the long sealed capillary with a small amount of sample has a higher proportion of contained N_2 than the magnetism sample, which would lead to a greater amount of adsorbed N_2 upon sample cooling. A similar difference can be seen in the **Au**·{MeOH} (**§5.4.2**) and **Au**·{1-PrOH} (**§5.4.4**) samples. This sample environment-dependence on the spin transition temperature does not seem to significantly affect the LS-to-HS transition, as the relative stoichiometric fraction of HS states determined by both magnetic and diffraction analysis techniques agree well.

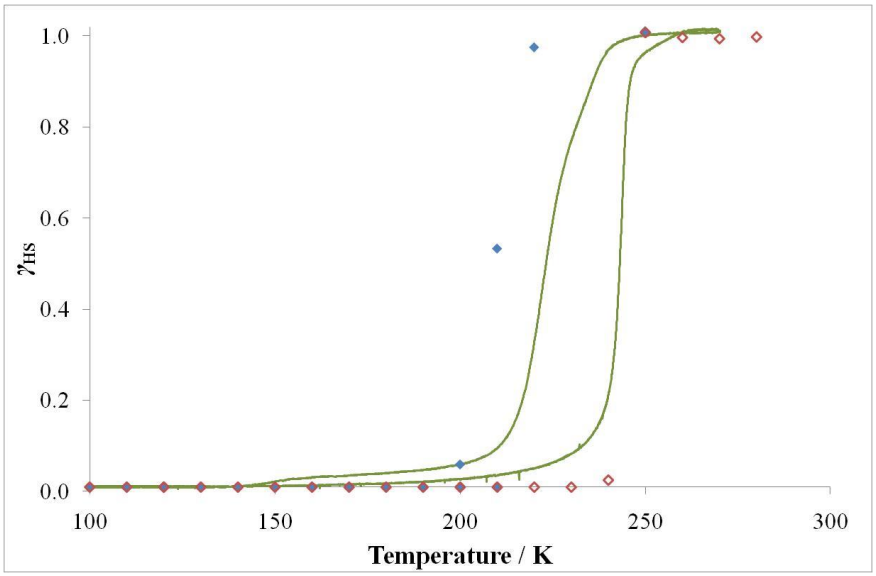

Figure 5-8: Comparison of the relative stoichiometric fraction of HS states (γ_{HS}) for **Au**·{N_2} as determined through — the magnetic susceptibility; and the relative intensity of the (001) peak of the HS phase, upon ◆ cooling and ◇ warming.

It is interesting to more fully compare the behaviour observed in **Au**·{N_2} with the behaviour of the **Au**·{Ø} material. In the HS state, both samples were modelled in the *Pbaa* space group with very high compression states ($\theta_{Au–Fe–Au} \approx 59°$). Upon transition to the LS state, both samples were modelled in the *Cmma* space group and were shown to undergo significant decompression with LS $\theta_{Au–Fe–Au} \approx 71°$, resulting in a net increase in the volume. Upon further cooling below the transition, the framework lattice of both samples becomes more compressed, leading to a decrease in the volume. This effect may arise due to thermal contraction of the ligand units in the framework: as discussed in **§4.4.1**, there are inter-network interactions between adjacent ligand molecules, which would undergo normal thermal contraction as the temperature is decreased. As the thermal radii of the atoms get smaller, in order to maintain the optimum conformation that maximises the inter-network interactions within the framework, the distance between adjacent interacting molecules would decrease, and the flexible framework undergoes compression. The continuous compressive behaviour observed below the spin transition in these framework samples, which would have little to no guest adsorption at the temperatures studied, implies that the *decompressive* behaviour below the spin transition of **Au**·{EtOH} must be due to a guest effect.

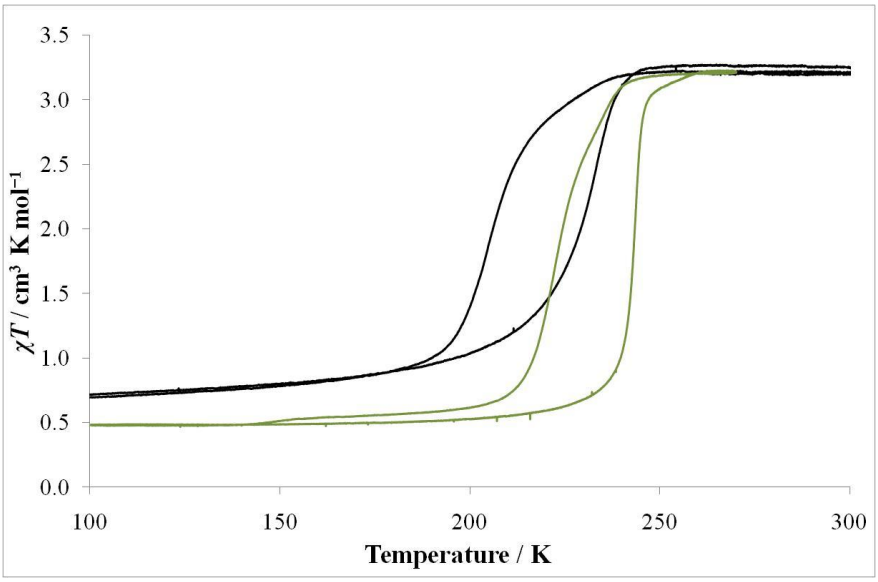

Figure 5-9: Comparison of the variable temperature magnetic behaviour for — **Au**·{N_2} and — **Au**·{Ø}.

Despite the similarities between the **Au**·{N_2} and **Au**·{Ø} samples, there are also some significant differences. As shown in **Figure 5-9**, the spin transition of **Au**·{N_2} occurs more cooperatively and at a temperature *ca*. 19 K higher than for **Au**·{Ø}. This difference is likely to be due to a minor guest effect of adsorbed N_2 in the **Au**·{N_2} sample. While the amount of adsorbed gas would be very low at *ca*. 200–250 K, there would nevertheless be an effect on the spin transition properties, and as the temperature decreases and the amount of adsorbed guest increases, this effect would become more pronounced. As shown in **Figure 5-6**, the HS-to-LS transition results in a volumetric expansion, so it can be inferred that adsorbed guest, which would increase the internal pressure on the framework, would then also stabilise the LS state and increase the spin transition temperature.

The **Au**·{N_2} sample also displays a second phase transition at *ca*. 130 K in which the dicyanidoaurate linkers become less distorted, and the framework lattice undergoes further decompression. This behaviour is not observed in the **Au**·{Ø} sample, implying that the contributing factor toward this structural feature is the presence of guest molecules in the **Au**·{N_2} framework. As the temperature decreases, the amount of adsorbed N_2 in the framework would increase. It seems that below 130 K, the internal pressure on the sample reaches a critical point such that the conformational energetics of the **Au**·{N_2} framework favour the more decompressed phase due to its increased volume, which can accommodate

additional guest molecules.

5.4 *Alcohols*

5.4.1 *Overview and General Observations*

The first family of solvent guests that was analysed for its effect on the behaviour of **Au** was the C1-C5 alcohols. **Figure 5-10** shows the temperature-dependent magnetic behaviour of the framework when solvated with the straight-chain alcohols, and demonstrates the wide variety of behaviours obtained by simply extending the hydrocarbon chain. **Table 5-1** summarises and compares the spin transition parameters for these samples. Where the sample shows an incomplete transition due to insufficient low temperature data, the parameters are calculated using the known values without extrapolation.

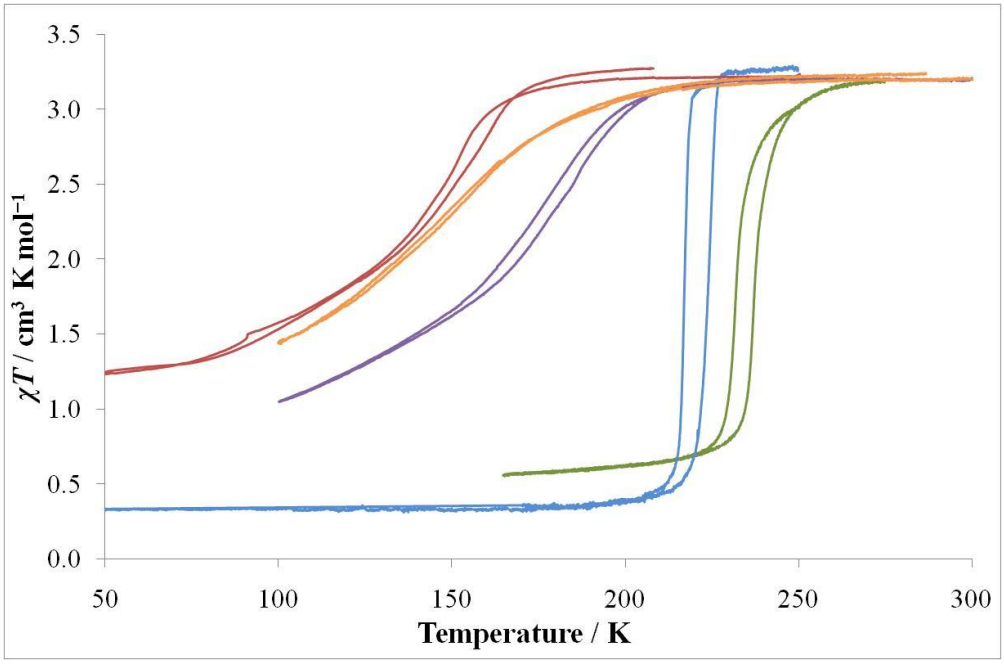

Figure 5-10: Variable temperature magnetic susceptibility data comparing the effect of different alcohol guests on the spin transition behaviour of **Au**: MeOH, EtOH, 1-PrOH, 1-BuOH, and 1-PnOH.

Table 5-1: Comparison of the spin transition properties for **Au**·{1-Alcohol}.

Alcohol	$T_{1/2}^{\downarrow}$ / K	$T_{1/2}^{\uparrow}$ / K	SCO range / K	Hysteresis / K
MeOH	232	237	30	5
EtOH	217	224	7	7
1-PrOH	148 95	151 99	93	3 4
1-BuOH*	169	173	92	4
1-PnOH*	149	152	101	3

* Low-temperature data are incomplete to show full spin transition.

From the magnetism data, there is a general observed trend that longer alcohols produce more gradual transitions at lower temperature, which is consistent with the result for the [Fe(bpac)M(CN)$_4$]·*x*(bpac){Alcohol} (M = Ni, Pd, Pt) frameworks described in Chapter 3, and the analogous [Fe(pyrazine)M(CN)$_4$]·{Alcohol} frameworks. The exception to the temperature trend is 1-PrOH, which produces a spin transition at lower temperature than all of the other alcohols studied, and also displayed a very gradual two-step spin transition. MeOH also displays an unusual transition, in that it starts at high temperature with a gradual stage, before completing the transition abruptly. All samples also achieve different degrees of completeness, which seems to be correlated to the total abruptness of the transition.

As for the alcohol-solvated **Pd** framework described in **§3.3.2**, the overall trend of a longer alcohol chain leading to gradual spin transition behaviour at lower temperatures can be attributed to a repulsive interaction between the guest and the host lattice, which is due to the kinetic volume and compressibility of the guest. This internal pressure effect increases in magnitude as the guest size increases. Decreasing the temperature of the sample results in a corresponding decrease in the kinetic volume of the guest, thus reducing the pore volume necessary to accommodate the guest and enabling the framework to undergo the HS-to-LS transition. The potential compressibility of the guest influences the abruptness of the transition and, as larger guests are less compressible, the resulting spin transitions occur more gradually (see **§3.3.2.2** for a more detailed discussion). The unexpected behaviours of the MeOH and 1-PrOH analogues are very interesting, and are discussed further below.

5.4.2 *Influence of Methanol*

In contrast to the behaviour observed in the **Pd** framework, the **Au**·{MeOH} sample displays a higher spin transition temperature than the **Au**·{EtOH} sample, following the alcohol trend established by the [Fe(pyrazine)M(CN)$_4$] (M = Ni, Pd, Pt) framework series.[1] In **Au**·{MeOH}, there is a slightly smaller hysteresis than in **Au**·{EtOH}, and the transition begins with an unusual gradual SCO, before completing the transition with an abrupt conversion to the LS state (**Figure 5-10**).

Powder X-ray diffraction provides valuable information about the nature of this spin transition. The powder diffractograms (shown in **Figure C-26**) were fit using a model with a unit cell in the *Cmma* space group, producing the parameters shown in **Figure 5-11**. There is a hysteretic phase transition centred at *ca*. 290 K that is unrelated to the spin transition observed in the magnetic susceptibility data. Above this transition, the model uses the expected unit cell parameters modelled in the *Cmma* space group as were determined from other powder diffraction experiments, with very similar values as were obtained for **Au**·{EtOH} at these temperatures (**§4.4.1**). However, below this phase transition, for both the HS and LS phases, the model best fits the data using a unit cell with a doubled *c*-parameter, while retaining the *Cmma* space group setting (see **Figure C-24** and **Figure C-25**, which compare the fits using both the normal and doubled values for the *c*-axes). This space group and unit cell setting ($c' = 2c$) is a maximal isomorphic subgroup of lowest index for *Cmma*.

Between *ca*. 200–240 K, there is a clear gradual HS-to-LS transition observed in the unit cell parameters, which is also accompanied by a slight amount of cyanide grid decompression, as shown by an increase in $\theta_{\text{Au–Fe–Au}}$ (**Figure 5-12b**). Below 200 K, once the spin transition is complete, the cyanide grid then undergoes a slight amount of compression. This is in contrast to the behaviour observed in the **Au**·{EtOH} sample, which displays lattice decompression below the spin transition.

It is noteworthy that $d_{\text{Fe–Au–Fe}}$ (**Figure 5-12a**) decreases by 0.34 Å over the spin transition, which is the same value as was observed in **Au**·{EtOH} (**§4.4.1**). Compared to **Au**·{EtOH}, the values for this distance are also 0.04 Å lower in **Au**·{MeOH} in both the HS and LS phases, implying a slightly greater degree of cyanide distortion.

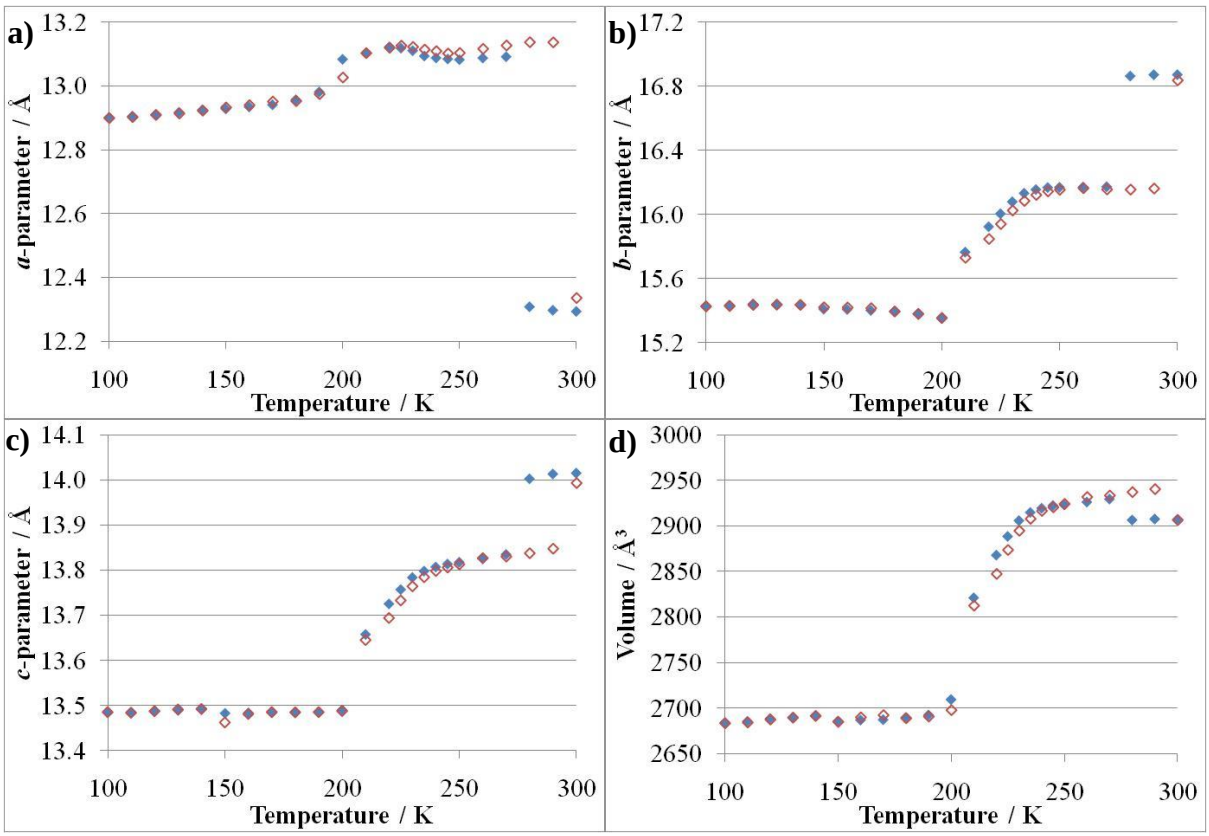

Figure 5-11: Temperature-dependence on the unit cell parameters of **Au**·{MeOH}: **a)** *a*-parameter; **b)** *b*-parameter; **c)** *c*-parameter; and **d)** volume, upon ◆ cooling and ◇ warming. Note that all *c*-parameter and volume values below the high temperature phase transition are halved, for ease of comparison with all other such data presented for this framework.

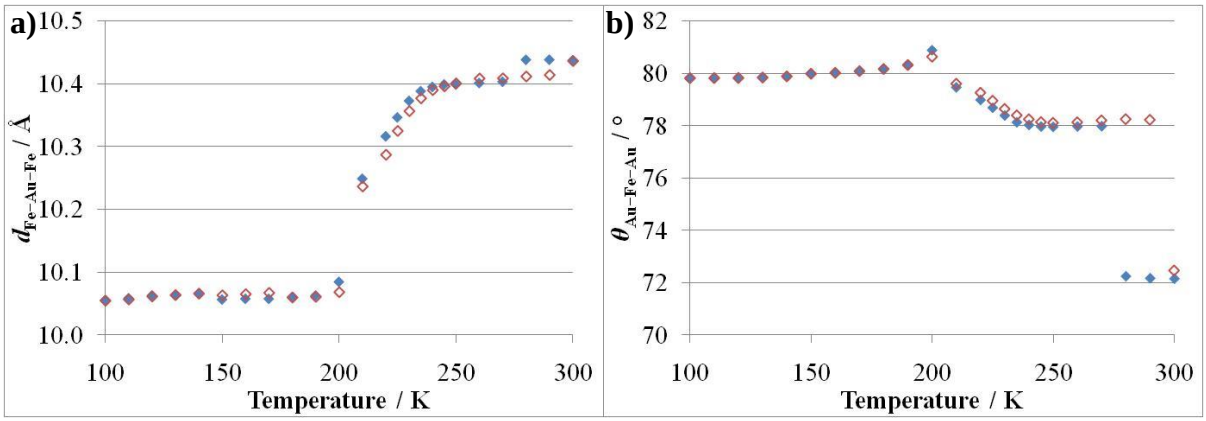

Figure 5-12: Temperature-dependence on the **a)** linear Fe–Au–Fe distance ($d_{Fe–Au–Fe}$), and **b)** acute Au–Fe–Au angle ($\theta_{Au–Fe–Au}$) of the **Au**·{MeOH} framework as calculated from the variable temperature unit cell parameters shown in **Figure 5-11**, upon ◆ cooling and ◇ warming.

Further inspection of **Figure 5-12b** reveals that there is a major lattice decompression of the cyanide layers below the high temperature phase transition, and the normalised *c*-parameter (**Figure 5-11c**) decreases in value, even though there is no spin transition at these temperatures. The most likely cause of the doubling along this dimension and the decrease in its normalised magnitude are due to an asymmetric buckling along this axis, creating a slight accordion-like conformation of the bpac ligands along the *c*-axis (**Figure 5-13**). However, even with this decrease along the *c*-axis, the volume undergoes an overall increase. Similar to the behaviour observed in the **Au**·{Ø} and **Au**·{N_2} samples, this volumetric increase is due to lattice decompression, as a greater area is produced by the rhomboid metal cyanide grid as it becomes closer to an orthogonal geometry, thus producing a greater volume in the framework lattice (see **§4.2.4**).

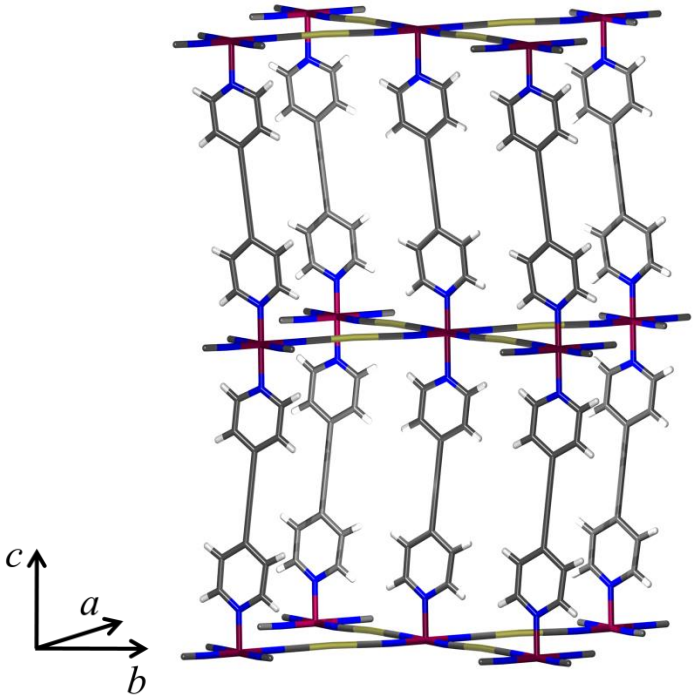

Figure 5-13: Representation of the proposed 'accordion-like' buckling of bpac pillar ligands along the *c*-axis. For clarity, only one net is shown.

Assuming that the Fe···Fe distance through individual bpac ligands is approximately the same above and below the high temperature phase transition, trigonometric calculations using the doubled *c*-parameter value at 270 K give an effective obtuse angle between the cyanide layer and the bpac ligand coordination of *ca*. 99°.

As shown in **Figure 5-14**, the *c*-parameter shifts gradually between 240 and 210 K, covering

ca. 43% of the HS-to-LS change in the parameter, and implying a non-cooperative SCO. Between 210 and 200 K, this parameter drops the remaining 57% to the fully LS value in an abrupt, cooperative transition. The general behaviour shown by the magnetic and diffraction data are comparable, with a gradual transition over *ca*. 30 K followed by an abrupt transition over less than 10 K. However, there is a difference in the relative proportions of the two stages and the temperatures at which they occur: the magnetic transition is effectively complete at 225 K with *ca*. 36% of the transition taking place over the gradual stage, compared to 200 K and 43% for the diffraction transition. For a non-abrupt transition, the position of the *c*-parameter is expected to be directly correlated to the proportion of HS Fe(II) sites in the framework crystallites, so the data should fully represent the HS fraction. The observed difference is then most likely due to the different sample environments, which would produce slightly different pressure and solvation effects, as well as potentially different crystallite sizes. This framework is highly sensitive to subtle changes in the sample medium, and any minor change is likely to affect the transition behaviour (see **§5.4.5** for a more detailed study of this effect).

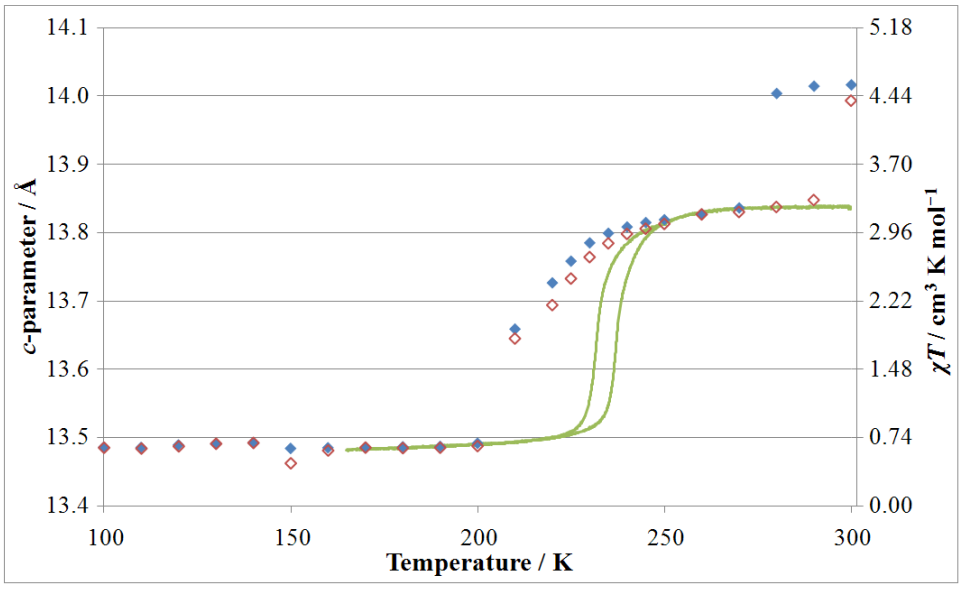

Figure 5-14: Comparison of the temperature-dependence of — the magnetic susceptibility; and the normalised *c*-parameter upon ◆ cooling and ◇ warming for **Au**·{MeOH}.

The distortion along the *c*-axis may result from a combination of guest–guest and host–guest interactions such that the optimum minimised lattice energy at these temperatures is obtained with distortion of the bpac linker. The gradual transition stage would be a result of distortion

in the cyanide and bpac ligands of the framework. As the ligands adopt orientations that deviate from an orthogonal geometry, there is a decreased ligand–metal orbital overlap and a decrease in the lattice rigidity. The communication of spin state between Fe(II) centres thus also decreases, resulting in a framework with less cooperativity. However, it appears that after a threshold quantity of Fe(II) centres undergo transition to the LS state, this places sufficient geometric pressure on the framework to cooperatively complete the SCO, producing the abrupt transition stage.

5.4.3 *Influence of 1:1 Methanol/Ethanol*

Solvation of **Au** with a 1:1 vol/vol MeOH/EtOH solvent mixture produces behaviour that is remarkably different to that produced by either of the component solvents individually. As with the **Pd** framework, the resulting transition temperature occurs below that produced by both of the pure solvents, and it occurs gradually with a small hysteresis, and with two distinct stages (shown in **Figure 5-15**). The first transition stage is unusual in that it begins at 237 K with the normal shape for a gradual transition curve, but then decreases almost linearly with a relatively constant slope from 224 to 195 K. The second transition stage has a more conventional shape, tailing off down to *ca*. 166 K. The warming curve produces a hysteresis such that the two stages are roughly equidistant with the cooling transition curve, giving a hysteresis width of *ca*. 4 K.

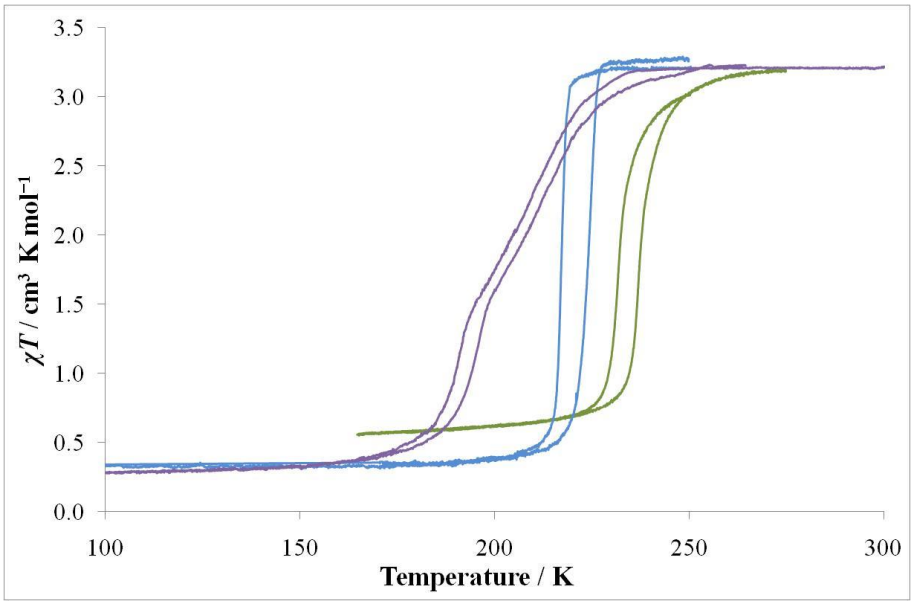

Figure 5-15: Comparison of the magnetic behaviour for: —MeOH, —EtOH, and —1:1 MeOH/EtOH.

Without powder diffraction data on this sample, a full structural explanation of the behaviour cannot be made. However, the single crystal data (**§4.2.2**) may be able to provide some information on the conformational behaviour of the framework. Firstly, it should be noted that the single crystal data for **Au**·{EtOH} gave a more compressed lattice structure than was shown in the powder diffraction experiment for this sample at all temperatures studied, and it is possible that the same will be true in this case also. A comparison of the unit cell parameters for the three solvent systems is given in **Table 5-2**.

Table 5-2: Comparison of unit cell parameters, $d_{Fe–Au–Fe}$ and $\theta_{Au–Fe–Au}$ at 100, 200 and 230 K for **Au** solvated with MeOH, 1:1 MeOH/EtOH, and EtOH. The mixed solvent data are taken from the single crystal results in **§4.2.2**.

	Unit Cell Parameter / Å			$d_{Fe–Au–Fe}$ / Å	$\theta_{Au–Fe–Au}$ / °
	a	*b*	*c*		
MeOH 100 K	12.9001(5)	15.4275(7)	13.4853(6)	10.0551(4)	79.803(5)
EtOH/MeOH 100 K	**12.6436(5)**	**15.7398(5)**	**13.6087(6)**	**10.0946(4)**	**77.549(4)**
EtOH 100 K	13.1467(13)	15.3043(18)	13.6175(15)	10.0878(11)	81.326(12)
MeOH 200 K	13.0830(18)	15.3499(27)	13.4912(15)	10.0844(16)	80.883(18)
EtOH/MeOH 200 K	**12.7252(5)**	**15.6808(6)**	**13.6184(6)**	**10.0972(4)**	**78.119(4)**
EtOH 200 K	12.8929(5)	15.5486(5)	13.6358(5)	10.0993(3)	79.331(4)
MeOH 230 K	13.1102(8)	16.0776(12)	13.7845(6)	10.3726(7)	78.389(8)
EtOH/MeOH 230 K	**11.7370(19)**	**17.243(3)**	**14.029(2)**	**10.429(2)**	**68.484(18)**
EtOH 230 K	12.3045(4)	16.8791(6)	14.0088(4)	10.4440(4)	72.182(4)

As expected from the aforementioned **Au**·{EtOH} results, at each temperature studied the **Au**·{1:1 MeOH/EtOH} single crystal shows greater compression of the cyanide grid (as shown by $\theta_{Au–Fe–Au}$ in **Table 5-2**) than was observed in the powder diffraction data for both independent solvents. The single crystal was solved in the *Cmma* space group without doubling of the *c*-axis or distortion in the bpac linkers, and the *c*-parameters of **Au**·{1:1 MeOH/EtOH} are most similar to the **Au**·{EtOH} results. The $d_{Fe–Au–Fe}$ values of **Au**·{1:1 MeOH/EtOH} are also most similar to the **Au**·{EtOH} values, so the cyanide distortion can be expected to be similar. The closeness of the **Au**·{1:1 MeOH/EtOH} values to the **Au**·{EtOH} values implies that, in general, the structural contributions to the framework behaviour would be most comparable to the EtOH sample, and the lattice

contribution to framework cooperativity can be expected to be similar.

Unfortunately the behaviour of a single crystal of the material is not indicative of bulk behaviour, and individual crystallites may exhibit different spin transition properties depending on the relative degree of solvation of the constituent solvent species. It is therefore possible that the two transition stages occur as a result of differently-solvated crystallites.

The more gradual, lower-temperature transition of the **Au**·{1:1 MeOH/EtOH} sample compared to the **Au**·{MeOH} and **Au**·{EtOH} samples may have a similar origin as was provided to explain the behaviour of **Pd·0.4(bpac)**{1:1 MeOH/EtOH} (see **§3.3.2.9**). MeOH produces more hydrogen-bonding guest–guest interactions, which need to be rearranged with the spin transition, and EtOH is larger and less compressible, increasing the effective internal pressure from the guest on the framework lattice. The combination of these effects stabilises the HS state and disfavours abrupt transition, resulting in a more gradual spin transition at lower temperature.

5.4.4 *Influence of 1-Propanol*

While the other 1-alcohols studied followed the established trend that a longer carbon chain results in a lower transition temperature, 1-PrOH defies this trend and results in a transition temperature lower than all other alcohols studied. The **Au**·{1-PrOH} sample also shows very gradual two-step behaviour, with two distinct hysteresis loops accounting for *ca*. 2/3 and 1/3 of the total spin transition for the high and low temperature transitions, respectively (**Figure 5-10**).

Powder X-ray diffraction data (shown in **Figure C-27**) were analysed to provide more structural information on this transition, though data were only able to be obtained down to 100 K due to the instrumental limitations of the cryostream used. As the low temperature hysteresis loop occurred below 100 K, it was unable to be monitored.

The powder diffractograms were fit using a model in the *Cmma* space group with unit cell parameters similar to those obtained for **Au**·{EtOH}. The resulting parameters, shown in **Figure 5-16**, display a smooth variation over the temperature range studied, with no points of discontinuity. The *c*-parameter and the volume clearly display the gradual spin transition as a reduction in the dimensions, and the *a*- and *b*-parameters demonstrate significant lattice

flexing above and over the transition.

At 100 K, the *c*-parameter (**Figure 5-16c**) is at a much higher value than any of the values presented previously for the fully LS framework, which is consistent with the magnetism results, confirming that the sample crystallites had not fully undergone spin transition at this temperature. This is corroborated by $d_{Fe–Au–Fe}$ (**Figure 5-17a**), which has a HS value at 200 K of 10.4673(10) Å, which is similar to other such HS values, but a value at 100 K of 10.2916(17) Å, which corresponds to *ca*. 50% of the expected change (assuming a fully LS value of *ca*. 10.10 Å, as was observed in **Au**·{EtOH}, **§4.4.1**). This result indicates that the second, low-temperature hysteretic transition occurs within the same crystallites as the first transition. It is possible that the transition behaviour converts to the low temperature stage due to freezing of the surrounding solvent: the low temperature stage begins at *ca*. 140 K, and 1-PrOH freezes at 149 K. The frozen solvent medium would exert restrictions on the framework flexibility, altering the spin transition properties accordingly.

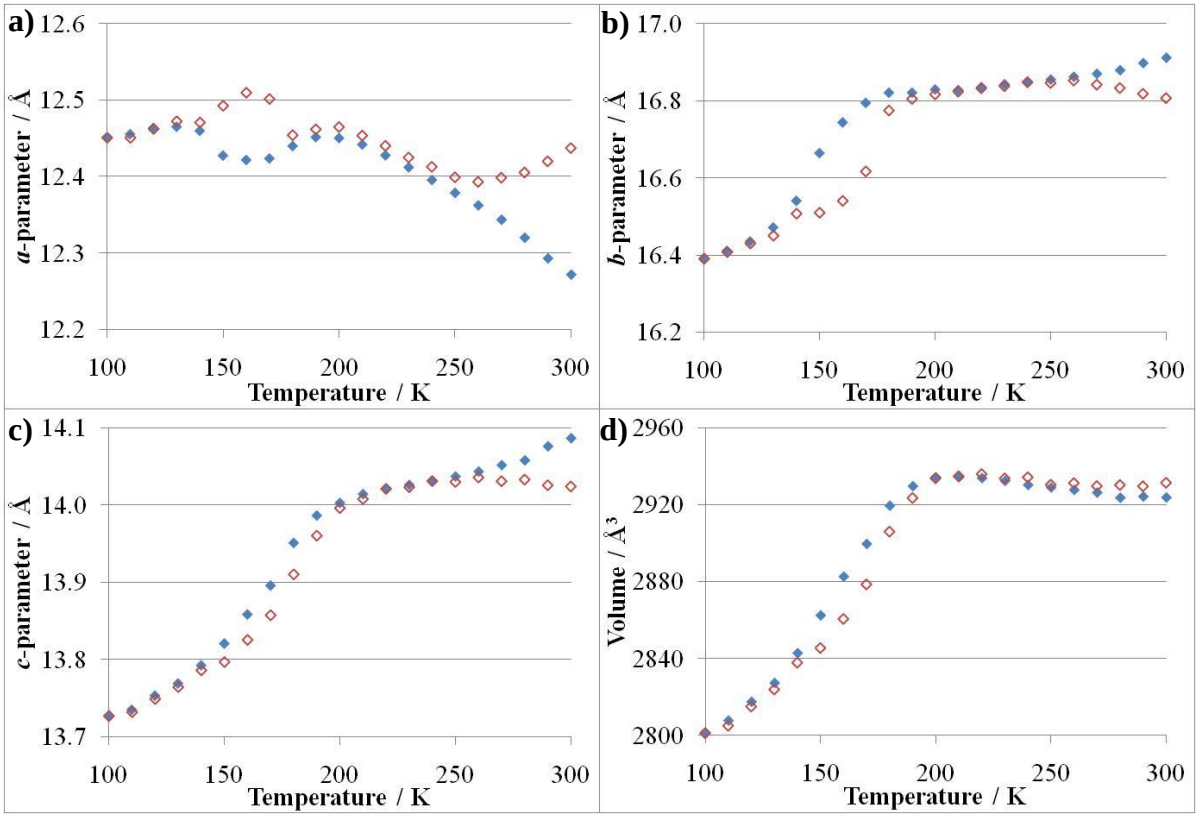

Figure 5-16: Temperature-dependence on the unit cell parameters of **Au**·{1-PrOH}: **a)** *a*-parameter; **b)** *b*-parameter; **c)** *c*-parameter; and **d)** volume, upon ◆ cooling and ◇ warming.

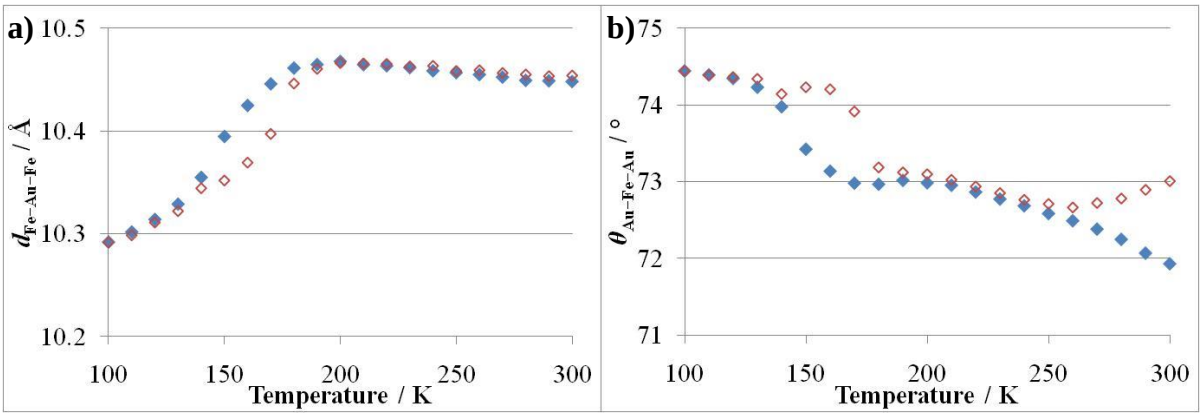

Figure 5-17: Temperature-dependence on the **a)** linear Fe–Au–Fe distance ($d_{Fe–Au–Fe}$), and **b)** acute Au–Fe–Au angle ($\theta_{Au–Fe–Au}$) of the **Au**·{1-PrOH} framework as calculated from the variable temperature unit cell parameters shown in **Figure 5-16**, upon ◆ cooling and ◇ warming.

The gradual spin transition is accompanied by a gradual decompression of the lattice, shown by $\theta_{Au–Fe–Au}$ (**Figure 5-17b**). This decompression appears to be suppressed below *ca*. 140 K, which corresponds to freezing of 1-PrOH in the solvent medium, effectively trapping the lattice conformation. Upon warming, once the solvent melts the framework is once again freely able to adopt the favoured conformation depending on its spin state. The spin transition exhibits thermal hysteresis in the diffraction experiments, which is especially pronounced in the *a*- and *b*-parameters, and the $\theta_{Au–Fe–Au}$ values, and is due to significant lattice 'scissor-type' motion. The hysteretic behaviour observed in these parameters is greater than that observed in the *c*-parameter, volume and magnetic data, implying that the 'scissor-type' motion of the lattice lags somewhat behind the spin transition, creating the wider hysteresis.

Above the spin transition, there are very interesting behaviours observed for the *a*- and *b*-parameters, which fluctuate depending on the degree of lattice compression. When cooling above the spin transition, there is an extended temperature range with lattice decompression, resulting in thermal expansion parameters of $-212 \times 10^{-6} < \alpha_a < -34 \times 10^{-6}$ K^{-1} and $17 \times 10^{-6} < \alpha_b < 87 \times 10^{-6}$ K^{-1} between 290 and 200 K. Over these temperatures there is also an unusually high degree of positive thermal expansion observed for the *c*-parameter of $13 \times 10^{-6} < \alpha_c < 139 \times 10^{-6}$ K^{-1}. This is potentially due to a change in the internal pressure from solvent as the lattice undergoes decompression, as this increases the solvent accessible volume, subsequently decreasing the solvent pressure on the framework lattice.

As shown in **Figure 5-18**, the spin transition shows notably different behaviour in the diffraction and magnetism results. It is expected that the *c*-parameter would provide an accurate measure of the relative proportion of spin states along this gradual transition. However, the diffraction experiment displays spin transition at a temperature *ca*. 25 K higher than the magnetism experiment, and it occurs more gradually. It is interesting to compare this result with the analogous experiments performed on **Au**·{MeOH} (**§5.4.2**), which also displayed gradual transition properties. Both diffraction experiments demonstrate a more gradual transition than the analogous magnetism result, but while the diffraction transition for **Au**·{1-PrOH} occurred at a higher temperature, the diffraction transition for **Au**·{MeOH} occurred at a lower temperature. Conversely, the magnetism and diffraction experiments of the **Au**·{EtOH} material agree very well. These observations suggest that there is a strong environment-dependent effect on spin transition behaviour in this framework, though more information is needed before the precise source of the effect can be determined.

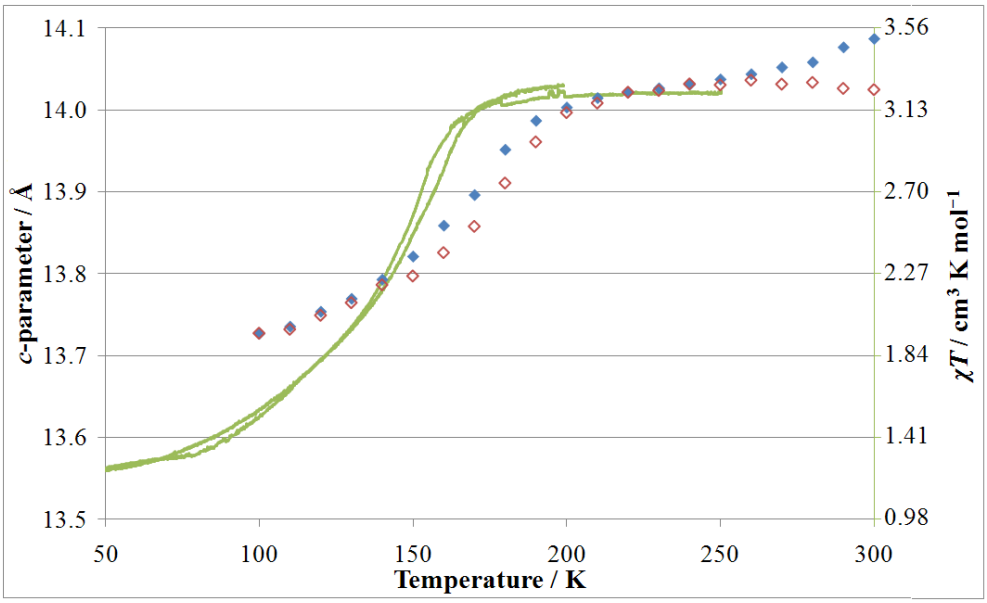

Figure 5-18: Comparison of the temperature-dependence of — the magnetic susceptibility; and the *c*-parameter upon ◆ cooling and ◇ warming for **Au**·{1-PrOH}. The plots are scaled for ease of qualitatively comparing the relative proportion of HS states over the spin transition.

Although explanations have been presented for most of the structural behaviour observed above, the reason that the behaviour of **Au**·{1-PrOH} occurs at a lower temperature than all other alcohols is still unknown. One potential explanation is that the packing of 1-PrOH within the lattice pores may produce a high barrier to spin transition due to optimal

arrangement of guest–guest and host–guest interactions, similar to the explanation posited for the unexpected transition behaviour of **Pd**·{MeOH} (**§3.3.2.6**).

5.4.5 *Influence of 1-Butanol*

The extreme sensitivity of this framework behaviour to sample environment and solvation is most clearly demonstrated when solvated with 1-BuOH. It was the highly variable behaviour of this sample that prompted the development and use of a consistent, sealed sample tube setup for magnetic measurements. The traditional sample setup was only sealed with Teflon® tape and Vaseline® grease (shown in **Figure 7-2a**), and was prone to partial desolvation. The magnetic data displayed in **Figure 5-10** above was obtained using the new sample preparation method, which was developed to avoid desolvation (**Figure 7-2b**).

As a demonstrative example of the variability of this solvation behaviour and effect of the precise sample environment, the different magnetic experiments performed on **Au**·{1-BuOH} are shown in **Figure 5-19** for the traditional sample tube, and **Figure 5-20** for the developed sample tube.

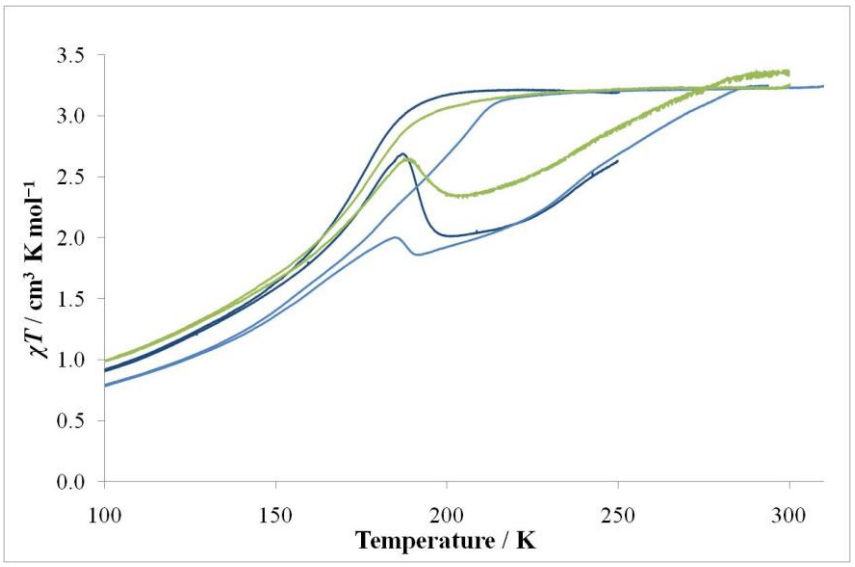

Figure 5-19: Variable temperature magnetic susceptibility data comparing the effect of different sample environments on the spin transition behaviour of **Au**·{1-BuOH} enclosed in the traditional sample tube: —sealed with Teflon® and Vaseline®, —heat-sealed closed, and — the same sample after 1 week.

When placed in the traditional sample containment (—), the cooling transition demonstrates gradual SCO behaviour. On heating, the sample follows the cooling curve with a small

hysteresis until *ca*. 185 K, at which point 1-BuOH melts. After this point, the magnetism drops, presumably as a result of the increased conformational freedom of the crystallites in the liquid medium. Once the crystallites are able to adopt their preferred conformations, the internal structural pressure from LS sites in the cooperative crystallites encourages transition of these crystallites to the LS phase, which also increases the number of LS Fe(II) sites, decreasing the HS fraction accordingly. After this unusual transition, the magnetism shows a very gradual increase back to the fully HS state. Once this experiment was complete, it was observed visually that the sample was no longer under a layer of solvent, suggesting that it had undergone partial desolvation in the magnetometer.

In a first attempt to control desolvation, a sample was loaded in the traditional sample containment tube, which was then the subject of an attempt to heat-seal it shut with a soldering iron. The resulting magnetism (—) displayed a very similar result to the first, though the warming HS-to-LS transition occurred with a greater magnitude, and the temperature range was incomplete in order to fully observe the transition behaviour. It was clear that the seal in this sample tube was ineffective, as the sample still came out of the magnetometer dry. Another experiment was performed on the same sample a week later (—), giving a transition that starts at higher temperature, though still displaying a small HS-to-LS transition step in the warming curve. The increased transition temperature is expected after partial desolvation of the sample, as there would be fewer guest molecules within the pores, resulting in fewer host–guest interactions and a decreased internal pressure effect, stabilising the LS state.

The sample behaviour in the developed sample tube environment (—) has a very similar cooling curve to that produced in the traditional sample tube (**Figure 5-20**). However, on warming, the curve follows the gradual cooling curve with a small hysteresis, and does not display any conversion back to the LS state. To test if this was due to a pressure effect caused by the insertion of the second PMMA plug, a sample was prepared with the same setup, except that the tube was sealed by clamping and heating, rather than using a plug (—). This sample was cycled twice in order to test the seal. The first cycle closely followed the behaviour of the plugged sample, while the second cycle occurred at much higher temperature, undoubtedly due to desolvation of the sample as the sample environment was not fully sealed. This leads to another interesting observation: that the warming HS-to-LS

behaviour observed in the traditional sample tube was not simply due to desolvation.

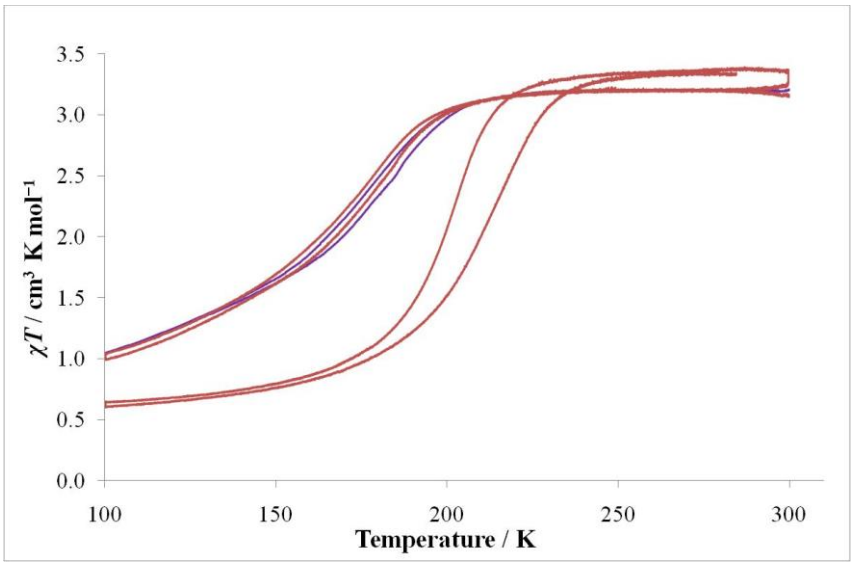

Figure 5-20: Magnetic behaviour of **Au**·{1-BuOH} when contained in the developed sample tube environment: — with PMMA plug, and — without plug and sealed by heating and clamping instead. The latter sample was cycled twice.

The significant variability in these results demonstrates the extreme sensitivity of the **Au** framework to the degree of solvation, and the precise sample environment. Even seemingly trivial changes can give rise to different behaviours. Considering the potential complicating factor of the degree of solvation, to provide confidence in the comparability of the experiments, particular care was given to the experiments performed on this material to ensure that the sample environment was consistent, and the material was fully immersed in solvent for all relevant experiments.

Variable temperature PXRD was used to study this material further, using the in-house powder diffractometer. Crude information on the spin transition can be gained by monitoring the peak reflection movement and phase changes. The raw powder diffractograms can be seen in **Figure C-28**, and an intensity plot is shown in **Figure 5-21a**.

When the sample is cooled, at 180 K the powder diffractograms display a new phase with small intensity, indicated by the presence of a few new peaks. This transition corresponds well to the freezing point of 1-BuOH (185 K), and it is possible that conversion to this minority phase is favourable, but solidification of the solvent medium traps the majority of crystallites in the initial phase. Close inspection of the (001) reflection in **Figure 5-21b**

shows the appearance of a peak at higher angle, which is evidence for a LS phase. At 170 K and below, peaks are also observed due to crystalline frozen 1-BuOH, with the most intense occurring at *ca*. $2\theta \approx 24°$. With decreasing temperature between 180 and 100 K, the framework peaks shift to higher angle, which corresponds to a decrease in the unit cell parameters, and is consistent with a gradual transition of the Fe(II) sites to the LS state.

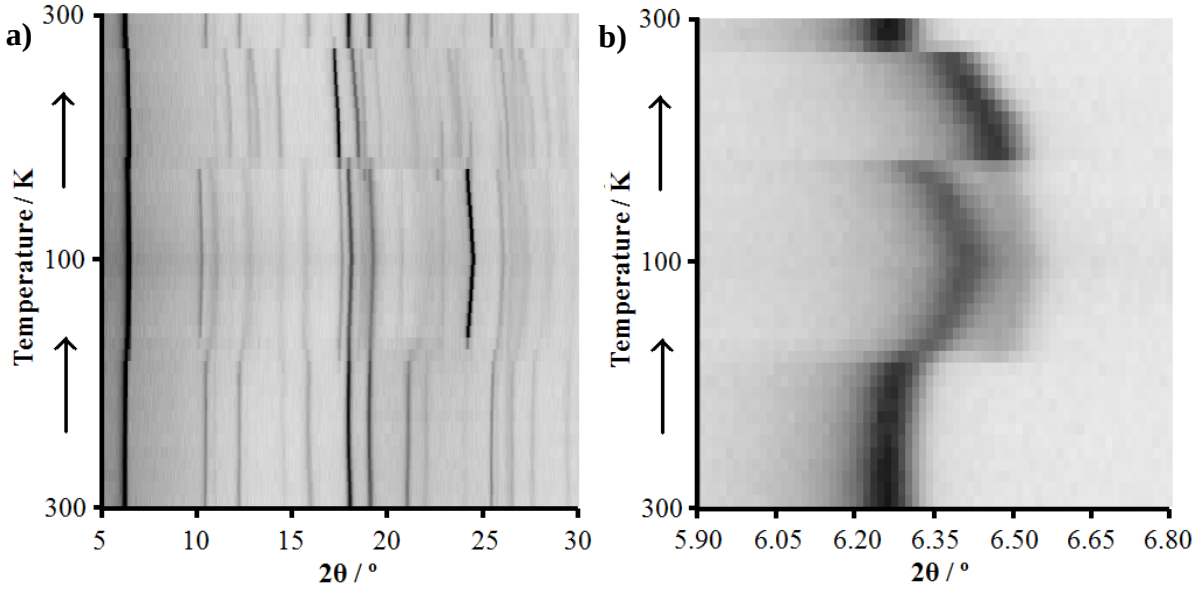

Figure 5-21: a) Intensity plot showing the powder diffraction peak evolution as the **Au**·{1-BuOH} sample was cooled from 300 to 100 K, then warmed back to 300 K; and **b)** a close-up of the (001) peak.

Upon warming to 170 K the peaks display the expected movement contrary to the cooling data, then a full phase transition occurs at 180 K to the previously observed minority phase, which correlates well with the unusual warming HS-to-LS transition observed in the magnetic data. In this new phase, the 2θ region between 10° and 17° is particularly interesting, as the peaks that previously corresponded to the (020) and (021) reflections move to much higher angle (implying a decrease in the *b*-parameter), while the (200) and (201) peaks move to lower angle (implying an increase in the *a*-parameter). The convergence of these peaks is due to a significant decompression effect. This phase persists until 280 K, at which point the material undergoes transition to the HS phase, which is in accordance with the magnetic measurements obtained for the sample contained in the traditional sample environment (**Figure 5-19**).

Le Bail methods were used to determine the unit cell parameters from the powder diffraction

data, producing the results shown in **Figure 5-22**. Below the full phase transition to the decompressed phase upon warming, a model with a unit cell similar to that determined for the **Au**·{EtOH} sample in the *Cmma* space group refined well. However, the decompressed diffractograms proved difficult to fit successfully using the normal cell, so alternative unit cells and space groups were investigated (see **Figure C-29** and **Figure C-30**). The best crystallographically reasonable fit was obtained using the monoclinic *C*2/*m* space group with an angle of *ca*. $\alpha = 92°$. This space group is a maximal non-isomorphic subgroup of *Cmma*.

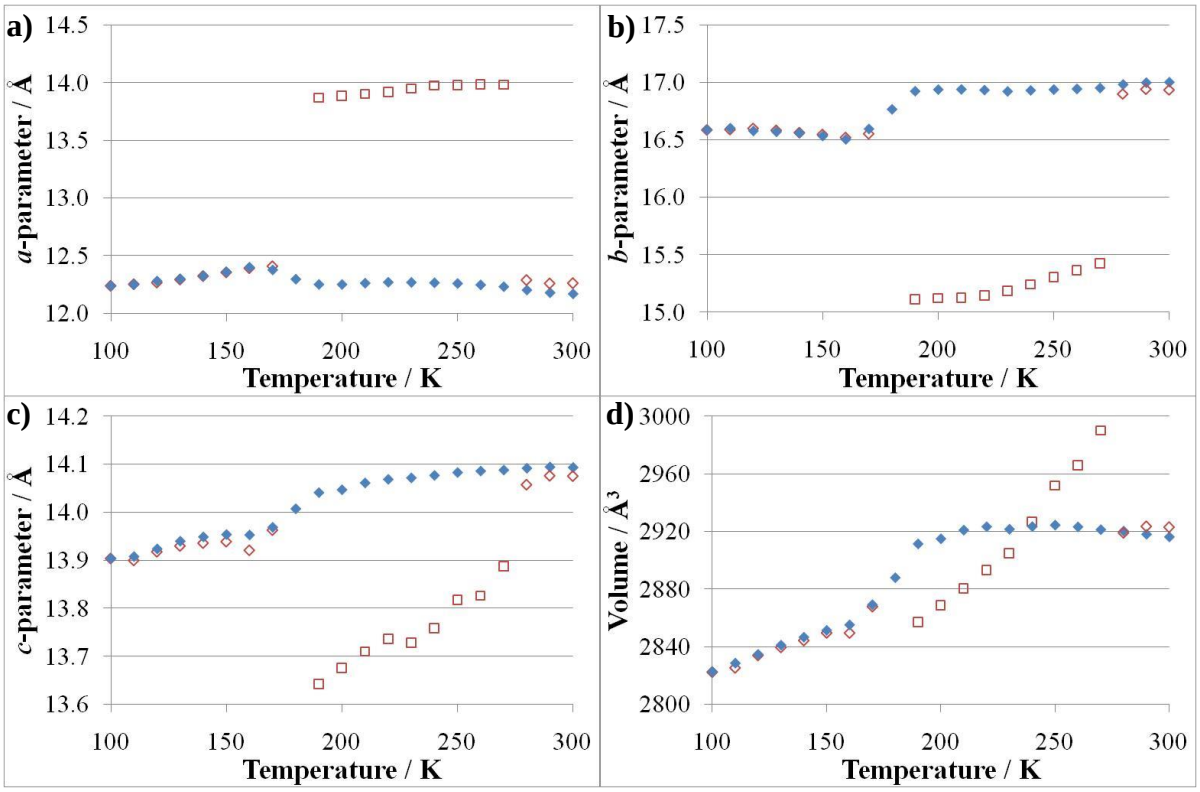

Figure 5-22: Temperature-dependence on the unit cell parameters of **Au**·{1-BuOH}: **a)** *a*-parameter; **b)** *b*-parameter; **c)** *c*-parameter; and **d)** volume, upon ◆ cooling and ◇ warming. Shapes represent ◆ *Cmma*, and ■ *C*2/*m* phases. The warming data at 180 K were not of sufficiently high resolution to accurately perform a two-phase refinement.

The transformation of the crystallites to the *C*2/*m* space group results in distortion of the unit cell between the *b*- and *c*-axes, creating a non-90° α-angle (**Figure 5-23**). This distortion is likely to be due to loss of linearity along the bpac pillars, in a similar manner as was postulated to explain the *c*-parameter compression in the **Au**·{MeOH} sample (see **§5.4.2**). However, in the **Au**·{1-BuOH} sample the *c*-parameter is not doubled, and distortion occurs in the same direction between framework layers. It is also possible that twinning occurs

within the crystallites, such that the *c*-parameter distortion is uniform in crystallite domains, but disordered over the whole crystallite. Nevertheless, the behaviour is distinctly different from the accordion-like alternation of bpac distortion observed in the *Cmma* **Au**·{MeOH} sample.

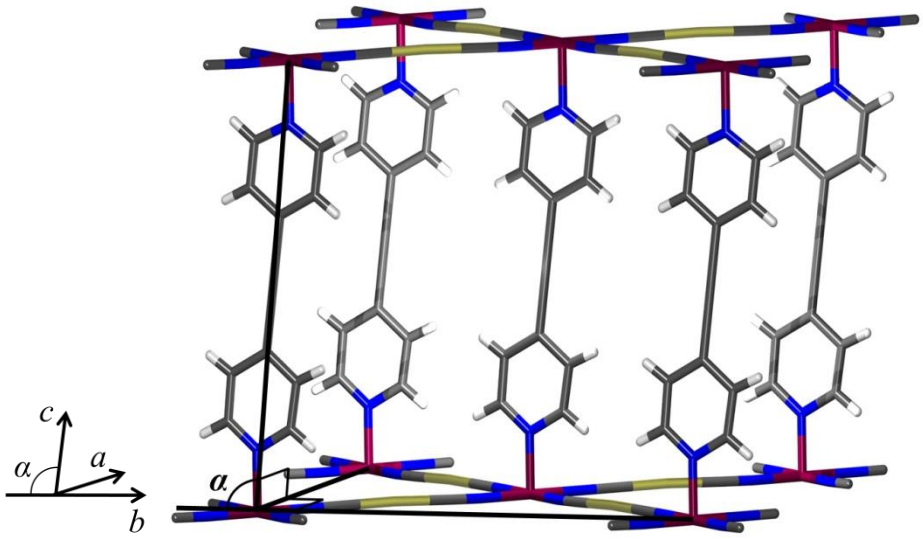

Figure 5-23: Representation of the *C*2/*m* phase of the **Au**·{1-BuOH} framework, which is distorted between the *b*- and *c*-axes, producing a non-90° α-angle. For clarity, only one net is shown.

Due to the unusual temperature-dependent behaviour of the unit cell parameters, the best measure of the spin transition as determined through the structural variation is observed in $d_{\text{Fe–Au–Fe}}$. As shown in **Figure 5-24a**, the HS $d_{\text{Fe–Au–Fe}}$ value is *ca*. 10.45 Å, which is very close to previously observed values produced by solvation with other guests. On cooling, there is a relatively abrupt decrease between 190 and 160 K, after which there is a slight decrease down to 100 K. Upon warming, the curve closely follows the cooling behaviour until 180 K, at which point $d_{\text{Fe–Au–Fe}}$ drops to the lowest value of 10.25 Å, corresponding to the transition to the *C*2/*m* phase. After this point the distance gradually increases back to the fully HS value at 290 K. It is noteworthy that the lowest value for $d_{\text{Fe–Au–Fe}}$ is significantly higher than that expected for the fully LS state, of *ca*. 10.10 Å.

The compression behaviour of the lattice is clearly shown by $\theta_{\text{Au–Fe–Au}}$ in **Figure 5-24b**. On cooling, the compression state is relatively constant until 190 K, at which temperature the lattice begins the decompressive behaviour which accompanies the spin transition. This decompression ceases at 170 K, which also corresponds to the appearance of crystalline

frozen 1-BuOH. As is observed in other solvated **Au** samples, the solid solvent medium suppresses lattice flexing by immobilising the framework crystallites in a relatively immutable environment. Upon warming, after the 1-BuOH melts the sample undergoes a high degree of lattice decompression to the *C*2/*m* phase, which persists until 280 K, at which point the sample converts back to the original compressed phase.

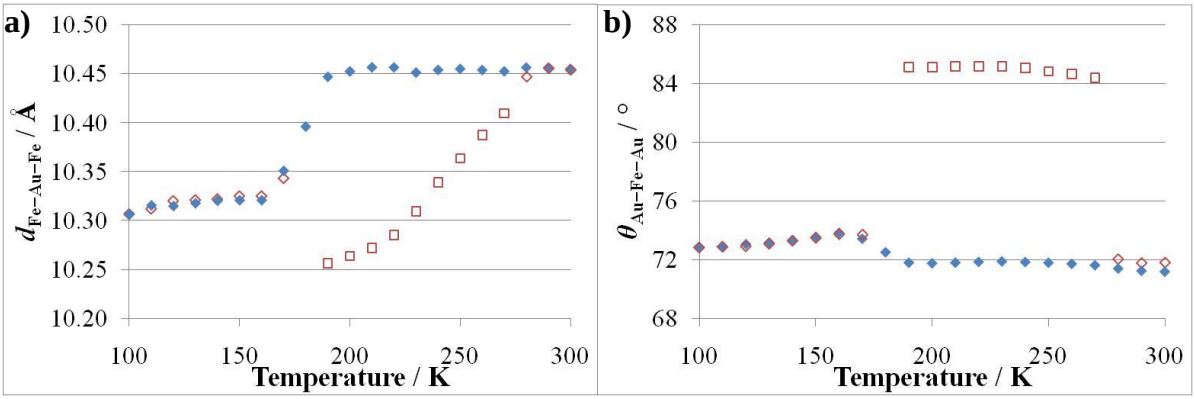

Figure 5-24: Temperature-dependence on the **a)** linear Fe–Au–Fe distance ($d_{Fe–Au–Fe}$), and **b)** acute Au–Fe–Au angle ($\theta_{Au–Fe–Au}$) of the **Au**·{1-BuOH} framework as calculated from the variable temperature unit cell parameters shown in **Figure 5-22**, upon ◆ cooling and ◇ warming.

By comparing the data obtained by magnetic and diffraction experiments, the anomalous spin transition behaviour can be more fully understood. **Figure 5-25** compares the relative stoichiometric fraction of HS states according to the magnetic and diffraction data, with the latter calculated from $d_{Fe–Au–Fe}$, assuming a fully LS value of 10.10 Å. The diffraction result confirms the unusual magnetic behaviour observed when the sample is contained within the traditional magnetic susceptibility sample environment. On cooling, the gradual magnetic transition is matched by the diffraction experiment until it plateaus at 160 K. It is likely that the frozen solvent medium disfavours any further lattice contraction, and while the magnetic transition continues down to 100 K, the structure minimises contraction by modifying the conformational position of dicyanidoaurate ligands, potentially by decreasing distortion. As the bpac ligand does not have the flexibility of the cyanide grid, the *c*-axis does undergo contraction with the spin transition (**Figure 5-22c**), leading to a subsequent decrease in the overall volume (**Figure 5-22d**).

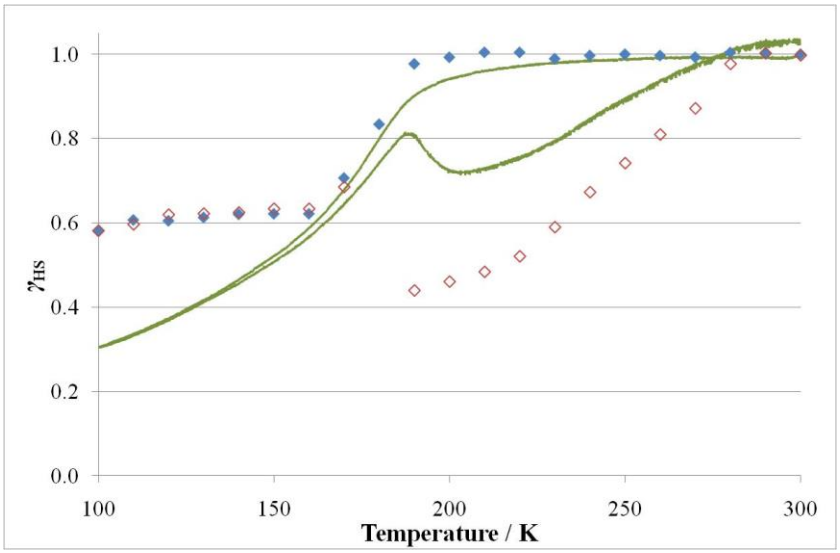

Figure 5-25: Comparison of the temperature-dependence on the relative stoichiometric fraction of HS states (γ_{HS}) in **Au**·{1-BuOH} as determined by — the magnetic susceptibility; and $d_{Fe–Au–Fe}$ upon ◆ cooling and ◇ warming.

Upon heating, the magnetic transition at ca. 185 K is accompanied by the full phase transition in the sample to the *C*2/*m* phase. This unusual structural and magnetic change may be attributed to the interplay between the cooperativity of the framework lattice, and the behaviour of the guest solvent molecules. In this framework sample, the temperature at which pore solvent changes from static to dynamic behaviour occurs within the hysteresis loop. On cooling, the cooperativity of the lattice ensures that the solvent 'freezes' in the pores in a particular orientation that relatively favours the HS states. Upon further cooling, the spin crossover energetics induce the framework to undergo a gradual spin transition to a partial LS state. Thus, when the sample is subsequently warmed to the temperature at which pore solvent may change from static to dynamic, the HS cooperativity has been removed and the solvent guest molecules are able to adopt a configuration within the pores that more favours the LS state. This in turn leads to more Fe(II) sites undergoing the HS-to-LS transition, decreasing the magnetic and further decreasing $d_{Fe–Au–Fe}$.

With increasing temperature, the proportion of LS Fe(II) sites decreases, leading to the expected increase in $d_{Fe–Au–Fe}$. Due to the more distorted nature of this phase, communication between Fe(II) sites decreases, and the magnetic transition occurs more gradually than the cooling transition. It is interesting to note that between 270 and 280 K the abrupt phase transition to the original *Cmma* phase occurs only when practically all of the Fe(II) sites

within the crystallites are in the HS state. This tendency is corroborated by the cooling behaviour, which showed partial conversion to the decompressed phase even though the magnetic susceptibility showed very little transition of the Fe(II) sites to the LS state. These results suggest that when the lattice is not in a structurally restrictive environment, it is most energetically favourable to adopt the distorted conformation when a very minor proportion of Fe(II) sites are in the LS state.

It is clear from the significant variation in the variable temperature magnetic behaviour that the spin transition has a strong dependence on the precise sample environment, including the surrounding solvent medium. The frozen 1-BuOH outside and within the framework prevents full conversion of the crystallites to the favoured distorted phase, but when the solvent melts the crystallites are freely able to adopt this phase, resulting in further transition of Fe(II) sites to the LS state.

The freezing point of 1-BuOH may potentially be used to explain the different behaviour with different sample environments. If a sample environment encourages an increase in the solvent melting point through pressure effects or a difference in the sample packing, then on warming the proportion of LS Fe(II) sites could decrease below a critical level before the solvent melts, so the sample would not undergo transition to the decompressed phase. It is also interesting to note that partial desolvation, such that the sample is no longer under a layer of solvent, also produces similar warming transition behaviour (as shown in **Figure 5-19**). This supports the idea that there is an influence from the 'freezing' of adsorbed solvent within the framework pores.[2]

5.4.6 *Influence of 2-Butanol*

All alcohol species discussed so far have been the terminal alcohol isomer. As a representative experiment to investigate the effect of alcohol guest shape as opposed to size, the effect of 2-BuOH on the behaviour of **Au** was studied.

As shown in **Figure 5-26**, **Au**·{2-BuOH} produces spin transition at a similar temperature and abruptness to **Au**·{1-BuOH}, though with notable differences. **Au**·{2-BuOH} begins undergoing spin transition upon cooling at 217 K, which is *ca*. 10 K higher than for **Au**·{1-BuOH}, and **Au**·{2-BuOH} displays two transition stages with different transition slopes: the high temperature stage continues down to *ca*. 163 K, with a hysteresis of *ca*. 3 K,

while the low temperature stage occurs more gradually, with a near-linear slope that continues down to *ca*. 80 K without hysteresis. Overall, the sample undergoes spin transition with a SCO range of 127 K. The temperature at which the sample begins the low temperature stage is likely to be related to the freezing point of 2-BuOH (158 K),[3] as the solid solvent medium would restrict the conformational freedom of the sample, affecting the spin transition behaviour. Overall, the spin transition of **Au**·{2-BuOH} occurs with $T_{1/2}$ = 171 K, which is close to the approximated value for **Au**·{1-BuOH} of $T_{1/2}$ = 173 K.

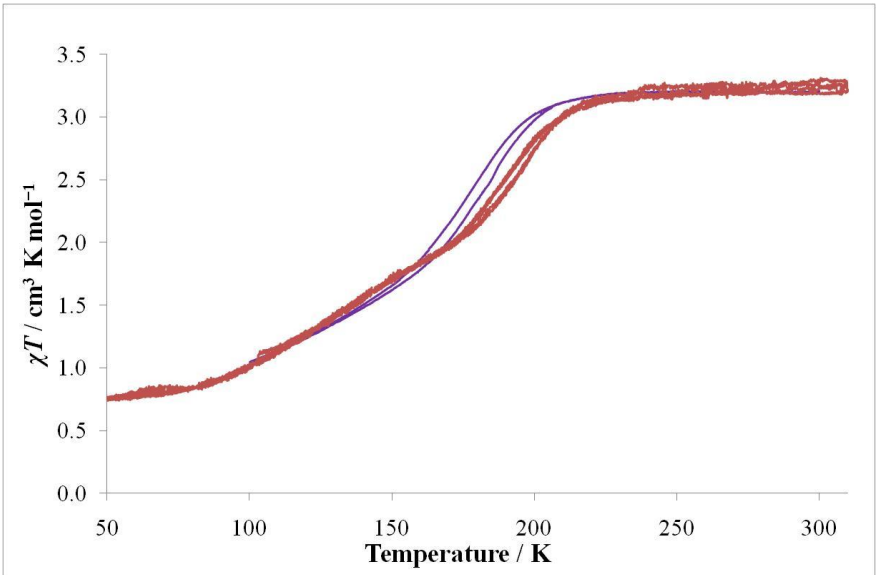

Figure 5-26: Comparison of the magnetic behaviour of **Au**·{2-BuOH} and **Au**·{1-BuOH}.

Although 1-BuOH and 2-BuOH have approximately the same size, they will pack differently within the framework pores due to their different shapes, leading to slightly different guest–guest and host–guest interaction energetics. Due to its more sterically constrained structure and the racemic mixture of the (*R*)- and (*S*)-enantiomers, 2-BuOH is likely to pack less efficiently in the pores than 1-BuOH, leading to fewer adsorbed molecules. As discussed in **§3.3.2.2**, this would reduce the magnitude of the host–guest repulsion effect, stabilising the LS state and increasing the spin transition temperature of **Au**·{2-BuOH} relative to the **Au**·{1-BuOH} sample.

In order to understand the structural behaviour, variable temperature powder X-ray diffraction experiments were performed on the **Au**·{2-BuOH} sample. As shown in the intensity plot (**Figure 5-27**), the high temperature behaviour displays divergence of peaks

with decreasing temperature between 4° and 6°, corresponding to lattice compression. There is a phase transition at 220 K, which is accompanied by convergence of the aforementioned peaks, indicating lattice decompression. This phase transition occurs before the spin transition begins. Between 220 and 100 K the peaks all move to higher angle which corresponds to a decrease in the unit cell parameters, congruent with gradual spin transition. Upon heating from 100 to 300 K, the sample displays the same behaviour in reverse, with the transition back to the high temperature phase occurring at 240 K.

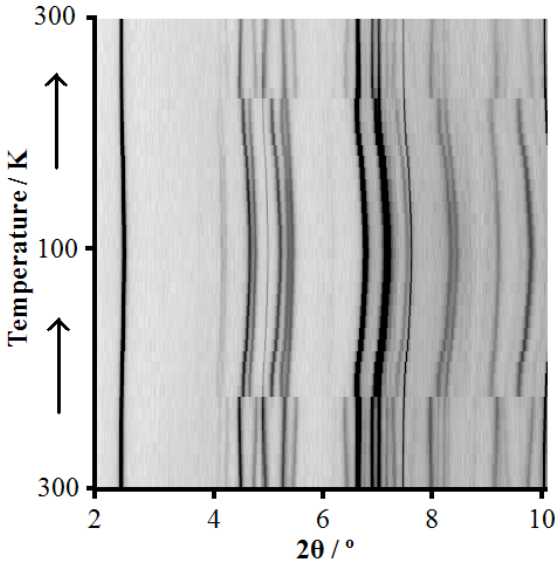

Figure 5-27: Intensity plot showing the powder diffraction peak evolution as the **Au**·{2-BuOH} sample was cooled from 300 to 100 K, then warmed back up to 300 K.

The powder diffractograms (**Figure C-31**) were difficult to interpret, as they displayed many more reflection peaks than had previously been observed for this framework. There were certain notable peaks that showed splitting (including those corresponding to the (111) and (221) reflections), with each split peak of roughly equal intensity, implying transition to a crystal system with lower symmetry than the normal orthorhombic system. A monoclinic unit cell based on the *C*2/*m* unit cell observed in the **Au**·{1-BuOH} sample (**§5.4.6**) did not fit all the observed reflections. Upon further analysis, all peaks were fit best by using a triclinic cell, with variable α- and β-angles, though still retaining a γ-angle of effectively 90°.

The common axis that is bound by the α- and β-angles is the *c*-axis, implying that there has been an angle distortion along this length, presumably due to a non-orthogonal coordination

of the bpac linker ligand. While the monoclinic cell produced by **Au**·{1-BuOH} had a non-90° α-angle, implying that the bpac was distorted specifically along the *b*-axis, the existence of non-orthogonal α- and β-angles in **Au**·{2-BuOH} implies that the bpac distortion lies *between* the *a*- and *b*-axes. The degree of distortion along these two axes determines the relative magnitude of the resulting α- and β-angles.

Even though the third angle does not significantly deviate from 90°, the presence of two non-90° angles in the unit cell means that the crystal system of this phase is triclinic. However, while there should theoretically be no systematic absences in a triclinic cell, there are many theoretical reflections produced by the *P*1 space group which are not observed (**Figure C-32**). Introducing the systematic absences of the base-centred monoclinic *C*2/*m* space group (**Figure C-33**) removes most of these unobserved reflections, while still fitting all of the observed peaks. There is no base-centred triclinic space group, but it is likely that there is a base-centred pseudosymmetry in the framework which results in many reflections which have very low intensity such that they are not observed within the experimental resolution. This pseudosymmetry cannot be properly modelled using a Le Bail model in a triclinic crystal system.

In order to best model the unit cell parameters from the data, two different strategies were used. In the high temperature phase, the relatively large β-angle prompted the use of the *P*1 space group, which most fully fit the observed peaks. Below the phase transition, the β-angle significantly decreases, as evidenced by convergence of the split peaks, so it was decided to approximate this angle to 90° and use a monoclinic *C*2/*m* space group model, which represented the observed reflection peaks much more accurately than the triclinic *P*1 space group. The resulting unit cell parameters can be seen in **Figure 5-28**.

As for the other **Au** samples, $d_{\mathrm{Fe–Au–Fe}}$ provides a relatively accurate indication of the spin state of this material. As shown in **Figure 5-29a**, this distance remains fairly stable above 220 K, other than a minor feature in the warming curve which may be attributed to a slight change in the cyanide grid distortion. Below 220 K the distance gradually decreases, with two noticeable transition stages of differing slope. The higher temperature stage displays a small hysteresis, while warming data of the lower temperature stage closely match the cooling data.

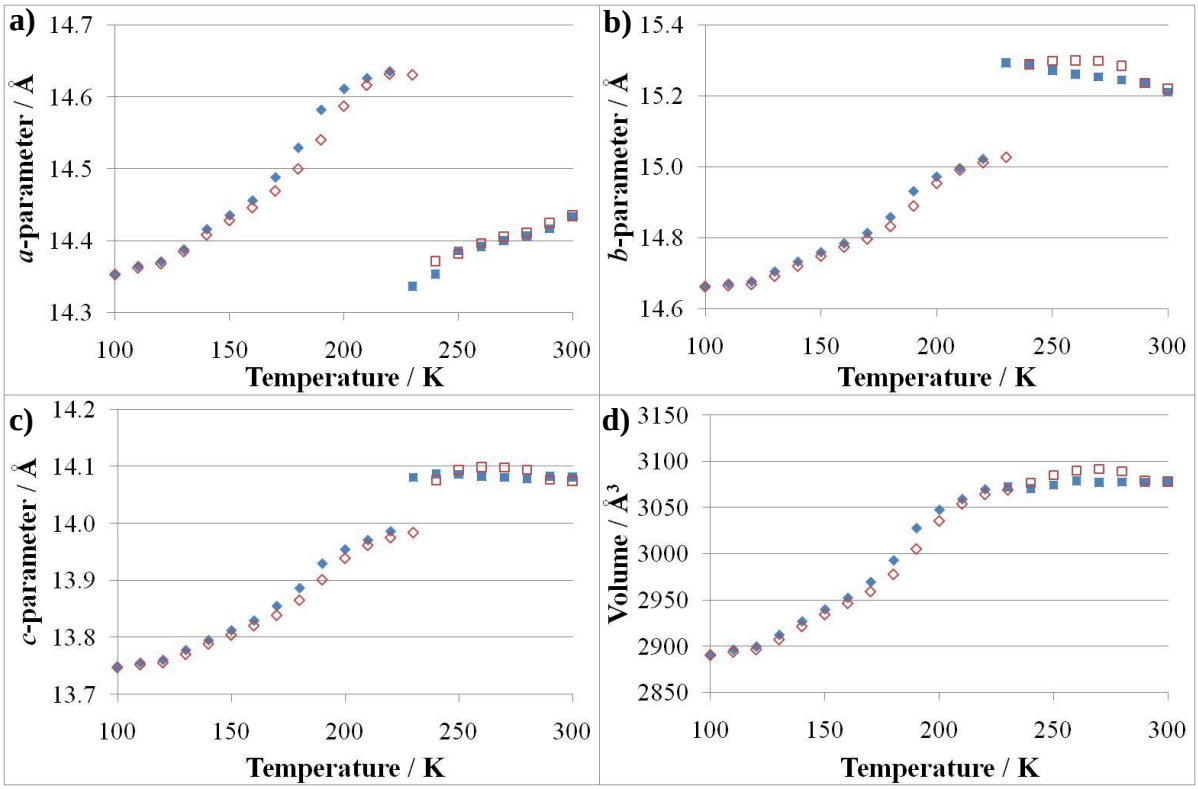

Figure 5-28: Temperature-dependence on the unit cell parameters of **Au**·{2-BuOH}: **a)** *a*-parameter; **b)** *b*-parameter; **c)** *c*-parameter; and **d)** volume, upon ◆ cooling and ◇ warming. Shapes represent ■*P*1, and ◆ *C*2/*m*-modelled phases.

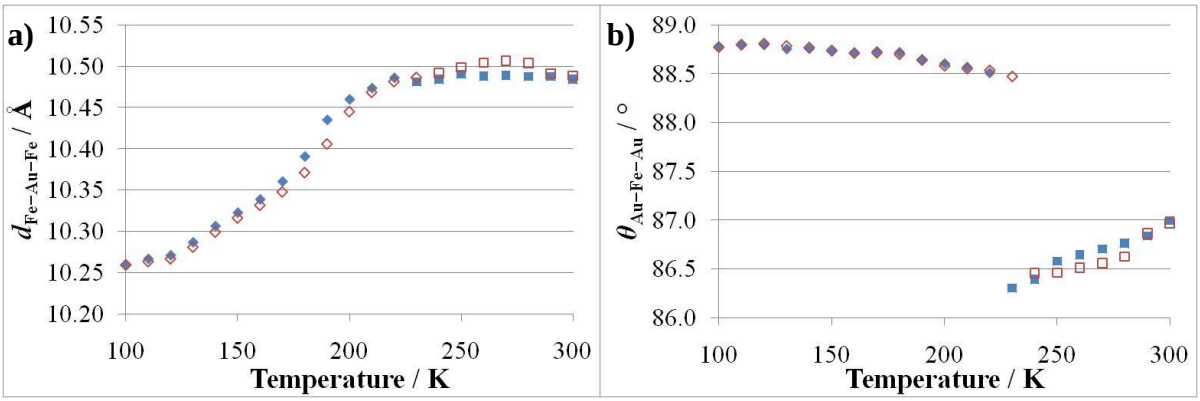

Figure 5-29: Temperature-dependence on the **a)** linear Fe–Au–Fe distance ($d_{Fe–Au–Fe}$), and **b)** acute Au–Fe–Au angle ($\theta_{Au–Fe–Au}$) of **Au**·{2-BuOH} upon ◆ cooling and ◇ warming. Shapes represent ■ *P*1, and ◆ *C*2/*m*-modelled phases, and values are calculated from the variable temperature unit cell parameters shown in **Figure 5-28**.

The $\theta_{Au–Fe–Au}$ values (**Figure 5-29b**) for both phases of **Au**·{2-BuOH} are the highest values observed for any of the alcohol-solvated systems, indicating that the framework lattice of this sample has the greatest degree of decompression. Above the phase transition, lattice

compression was observed as the angle decreased with decreasing temperature. However, below the phase transition the framework demonstrated decompressive behaviour, which results from the spin transition and is consistent with the behaviour observed in other alcohol-solvated samples (see **Table 5-3** below). The magnitude of this decompression is very small, and is likely to be limited by the near-orthogonal nature of the metal cyanide grids, which is not observed to such an extent in any other solvated sample.

The α-angle (**Figure 5-30**) of the unit cell provides information regarding the distorted conformation of the bpac ligand along the *c*-axis. The high temperature *P*1-modelled phase has a high degree of distortion along this dimension, which decreases significantly below the transition to the *C*2/*m* phase. The more orthogonal nature of the decompressed metal cyanide grid of this phase is thus accompanied by a more orthogonal conformation of the *c*-axis. As the sample undergoes spin transition, the α-angle further decreases in magnitude, which is expected considering the preference for LS Fe(II) to adopt a more rigidly orthogonal octahedral geometry (see **§1.4.5**).

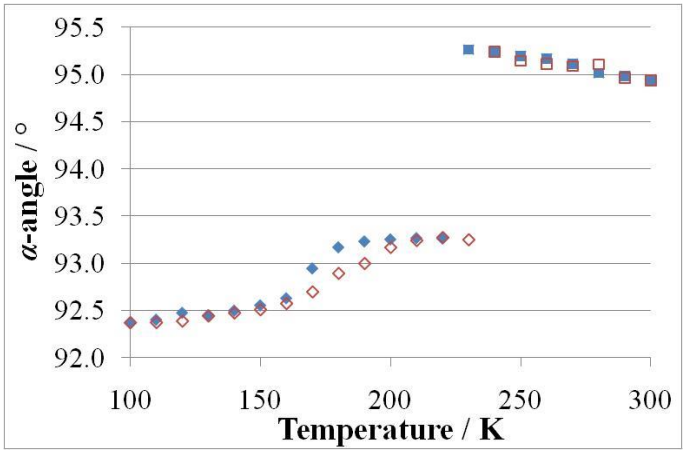

Figure 5-30: Temperature-dependence on the α-angle of the **Au**·{2-BuOH} framework upon ◆ cooling and ◇ warming. Shapes represent ■ *P*1, and ◆ *C*2/*m*-modelled phases.

To compare the spin transition behaviour as determined by the magnetism and diffraction results, the relative stoichiometric fraction of HS states was used. For the diffraction data, $d_{\text{Fe–Au–Fe}}$ was used to approximate this quantity, with the fully LS value assumed to be 10.10 Å, in accordance with previously-obtained data (eg: **Au**·{EtOH}, **§4.4.1**). As shown in **Figure 5-31**, there is close agreement in the spin transition behaviour observed by both techniques down to low temperature. The two transition stages are shown, with the

conversion from one stage to the other occurring close to the freezing point of 2-BuOH (158 K).[3] While crystalline solvent was observed in the powder diffractograms of **Au**·{1-BuOH}, it was not observed below the solvent freezing point in the powder diffractograms of **Au**·{2-BuOH}, implying that the frozen solvent is amorphous.

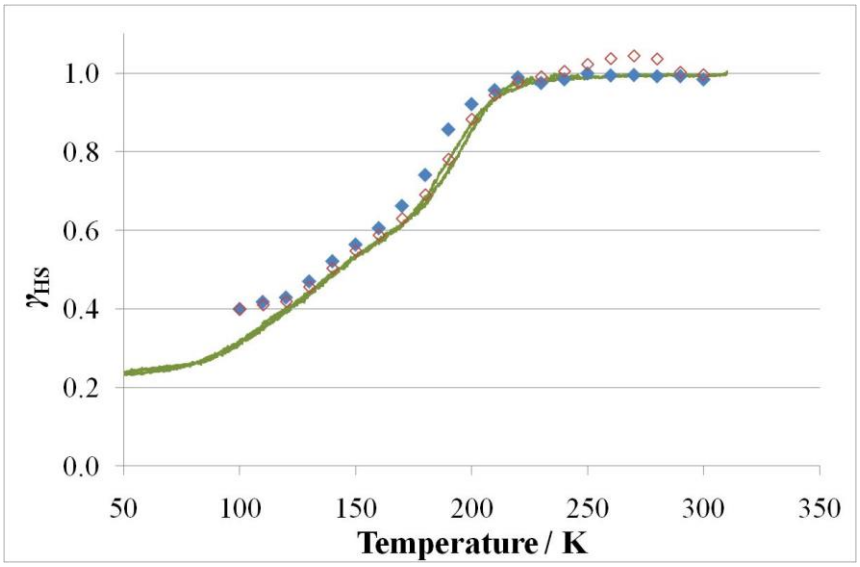

Figure 5-31: Comparison of the temperature-dependence on the relative stoichiometric fraction of HS states (γ_{HS}) in **Au**·{2-BuOH} as determined by — the magnetic susceptibility; and $d_{Fe–Au–Fe}$ upon ◆ cooling and ◇ warming.

The spin transition upon cooling appears to begin slightly below the structural transition to the decompressed phase at 220 K. It is possible that the phase transition is completely unrelated to the SCO, but the temperature at which it occurs is very similar to the temperature at which the SCO begins (~217 K), implying that there may be a causal relationship. Without further studies on the system, any proposed relationship would be pure speculation. Once the material undergoes the structural transition to the decompressed phase, it remains in this phase throughout the temperature range of the spin transition.

In summary, in the fully HS state, the **Au**·{2-BuOH} sample adopts a distorted lattice geometry in which the bpac pillar ligands are no longer linearly bridging the cyanide grids, instead 'leaning' between the *a*- and *b*-axes, creating non-orthogonal *α*- and *β*-angles. There is limited spin state cooperativity due to reduced communication between Fe(II) sites, evidenced by the very gradual spin transition. Upon cooling, the sample undergoes structural transition to a more decompressed phase, which is closely followed by the gradual spin transition. In the decompressed phase, the bpac ligand distortion decreases significantly and

occurs almost entirely over the *b*-parameter as the *β*-angle becomes close to 90°. The high level of bpac distortion in the framework reduces the cooperativity of the spin transition, producing the gradual SCO behaviour.

5.4.7 *Influence of 1-Pentanol*

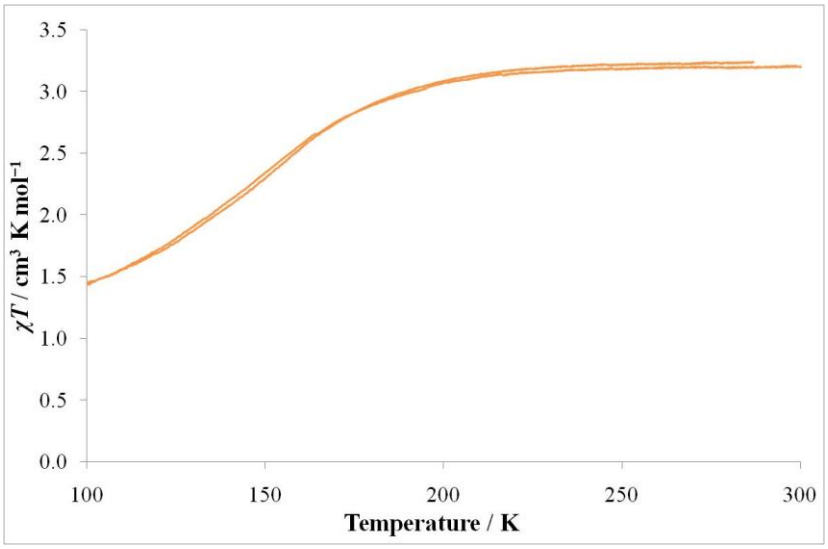

Figure 5-32: Temperature-dependence on the magnetic susceptibility of **Au**·{1-PnOH}.

The **Au**·{1-PnOH} framework undergoes spin transition more gradually than any of the other alcohol-solvated samples studied, and with the anomalous exception of 1-PrOH, occurs at the lowest temperature. This result is similar to the behaviour observed in **§3.3.2.8** for **Pd·0.5(bpac)**{1-PnOH}, and is related to the host–guest properties of the solvent: as the length of the carbon chain in the guest alcohol increases, its kinetic volume increases and its compressibility and mobility decrease. The subsequent internal pressure effect on the host lattice results in a more gradual spin transition at lower temperature, while the multiple guest packing conformations create different local environments around the Fe(II) centres, further influencing the transition to be gradual (see **§3.3.2.2**).

5.4.8 *Comparison of Alcohol Guests*

The guest-dependent behaviour of **Au** when solvated with different alcohols has not only provided a systematic study of a family of solvents, but it has also demonstrated the extreme variety of magnetic and structural behaviour of which this framework is capable.

Table 5-3 shows a comparison of many of the structural properties of the different HS and

LS alcohol-solvated samples that were characterised by variable temperature powder X-ray diffraction. The temperature values were chosen to be immediately above and below the spin transition, or in the case of incomplete transition, the lowest temperature obtained. This was because there was often significant variation of the structural properties independent of the spin transition, due to the flexibility of the framework lattice. It was determined that standardising the chosen parameters in this way would provide the most valid comparison of the HS and LS structures above and below the spin transition, respectively. The $d_{Fe–Au–Fe}$ and $\theta_{Au–Fe–Au}$ values are given instead of the *a*- and *b*-parameters as the former quantities provide more useful information regarding the conformation of the framework lattice.

Table 5-3: Comparison of the space groups, *c*-parameter, volume, $d_{Fe–Au–Fe}$ and $\theta_{Au–Fe–Au}$ for the HS and LS **Au**·{solvent} framework materials when solvated with the alcohols studied.

Solvent	**Temp / K**	**Space Group**	***c*-parameter / Å**	**Volume / Å^3**	**$d_{Fe–Au–Fe}$ / Å**	**$\theta_{Au–Fe–Au}$ / °**
High Spin						
MeOH	250	*Cmma*	13.8185(6)*	2922.7(5)*	10.3988(7)	77.955(7)
EtOH	227	*Cmma*	14.0041(4)	2909.2(3)	10.4439(3)	72.224(3)
1-PrOH	200	*Cmma*	14.0033(6)	2934.2(7)	10.4673(10)	71.930(5)
1-BuOH	200	*Cmma*	14.0471(25)	2915.0(8)	10.4526(5)	71.744(5)
2-BuOH	230	*P*1	14.0804(13)	3072.3(5)	10.4809(7)	86.302(7)
Low Spin						
MeOH	190	*Cmma*	13.4865(7)*	2692.4(3)*	10.0627(4)	80.330(4)
EtOH	210	*Cmma*	13.6420(6)	2735.9(4)	10.10384(5)	79.190(5)
1-PrOH	100†	*Cmma*	13.7267(11)	2801.3(11)	10.2916(17)	74.444(17)
1-BuOH	190†‡	*C*2/*m*	13.642(12)	2857.1(3)	10.2563(15)	85.090(16)
2-BuOH	100†	*C*2/*m*	13.7473(11)	2890.7(6)	10.2592(13)	88.773(15)

* The *c*-parameter and volume values shown for the MeOH structures have been normalised to half the actual value obtained, so as to be comparable with the other values shown.
† Incomplete spin transition
‡ The warming 190 K (decompressed) structure is used for LS 1-BuOH, as this is the energetically favoured phase. Below this temperature, the framework is trapped by frozen solvent in the original compressed phase.

The LS values of **Au**·{1-PrOH}, **Au**·{1-BuOH} and **Au**·{2-BuOH} are not representative of

the fully LS framework, so the ability to draw accurate comparisons with these parameters is severely limited. On the other hand, the HS values for all solvated **Au** structures ought to be fully comparable. However, even though these results are the most comparable, due to the high sensitivity of the framework lattice conformation to many contributing influences, deconvolution of these factors is challenging. Nevertheless, using the conclusions drawn in the previous sections, it is possible to explain many of the observed trends in the relative values of the lattice parameters.

As mentioned in **§5.4.2**, the normalised *c*-parameter for HS **Au**·{MeOH} is lower than expected due to an accordion-like compression effect of the bpac linkers bridging the cyanide layers, such that they distort away from an orthogonal geometry with a slight zig-zag conformation, resulting in a doubling of the *c*-parameter, and decreasing the distance between the cyanide layers. The $d_{\text{Fe–Au–Fe}}$ value is the smallest for this sample, implying that is has the greatest degree of distortion in the dicyanidoaurate linkers. Even with the decreased values for these parameters, **Au**·{MeOH} has a greater normalised volume compared to **Au**·{EtOH}, which is due to the more decompressed nature of the cyanide layer, as demonstrated by $\theta_{\text{Au–Fe–Au}}$. As explained in **§4.2.4**, this decompressed framework geometry produces a greater area in the rhomboid metal-cyanide grid, and hence a greater lattice volume.

The *c*-axis distortion of the **Au**·{MeOH} sample may arise from guest packing effects. Due to the smaller size of the MeOH molecule, in order to achieve maximum packing efficiency with host–guest and guest–guest interactions, the framework lattice distorts to decrease the distance between the cyanide layers of the lattice nets. However, above a certain temperature (see **§5.4.2**) this distortion disappears as the lattice forms the fully orthogonal framework conformation, potentially due to the increase in the effective kinetic diameter of the guests as they undergo thermal expansion. Thermal expansion of the guests would increase the internal guest pressure until the energetics of the system favour the non-distorted lattice geometry.

The degree of compression is similar for HS **Au**·{EtOH), **Au**·{1-PrOH} and **Au**·{1-BuOH}, with a slight tendency toward greater compression with longer alcohols. The volume follows the trend EtOH < 1-BuOH < 1-PrOH, which is due to distortion of the dicyanidoaurate linkers: as the dicyanidoaurate metalloligands become more linear (less distorted), there is an increase in the $d_{\text{Fe–Au–Fe}}$ value, and the volume increases proportionally. In contrast, the

relative values of the *c*-parameters are EtOH ≈ 1-PrOH < 1-BuOH. The major cause of the difference in the $d_{Fe–Au–Fe}$ and *c*-parameter values is the internal guest pressure on the framework lattice, with larger solvents generally producing a greater effect due to steric interactions associated with the size of the guest. From these results, it appears that this internal pressure effect along the *c*-axis is very similar for EtOH and 1-PrOH, presumably due to similar solvent packing behaviour along this dimension, while the pressure effect is greater for 1-BuOH, due to its larger size. However, in the *ab*-plane the increased $d_{Fe–Au–Fe}$ and volume from 1-PrOH implies that within this plane the internal pressure from 1-PrOH is greater than for 1-BuOH, potentially due to better packing efficiency of the former solvent in the *ab*-plane of the framework pores, which increases the amount of solvent, and thus the internal pressure. The greater $d_{Fe–Au–Fe}$ value in the 1-BuOH sample compared to EtOH is expected due to its larger size.

The packing efficiency of 1-PrOH in the framework pores could also explain the anomalous spin transition behaviour of this sample observed in the magnetic experiment, as it occurs at lower temperature than any of the other alcohols studied. If the size and shape of the 1-PrOH molecule allows more efficient packing than other alcohol guests within the framework, then more guests could adsorb into the framework, increasing the number of guest–guest and host–guest interactions, and internal pressure in the framework proportionally. As explained in **§3.3.2.2**, these factors stabilise the HS state, producing more gradual spin transition at lower temperature.

The HS **Au**·{2-BuOH) sample has a significantly more decompressed structure than the other HS alcohol-solvated samples, as well as the greatest values for the *c*-parameter, volume, and $d_{Fe–Au–Fe}$. This result arises from the large, sterically rigid shape of the 2-BuOH guest, which forces the framework lattice to adopt a more open, expanded conformation to accommodate the guest molecules, and the resulting guest packing arrangement in the pores. In order to achieve effective packing of the bulky guest in the framework, and to optimise host–guest interactions, the lattice would be forced to adopt a distorted geometry, such that the bpac pillar ligands are bent away from the orthogonal axes.

Upon transition to the LS state, all the alcohol-solvated samples studied demonstrate conversion of the framework lattice to a more decompressed conformation. This is due to the influence of the coordination environment of LS Fe(II), which favours a more rigidly

octahedral environment, while the HS state allows a distorted environment (as explained in **§1.4.5**). The greatest degree of such transition-driven decompression is demonstrated by **Au**·{1-BuOH}, in which conversion to the energetically favoured LS phase increases the value of $\theta_{Au–Fe–Au}$ from 71.744(5)° to 85.090(16)°. This decompression is accompanied by a phase transition to the distorted *C*2/*m* space group.

A similar highly decompressed, distorted unit cell phase was observed in the structure of the **Au**·{2-BuOH} sample. From these, and the **Au**·{1-BuOH} results, it would appear that the unit cell distortion and high degree of decompression are correlated, such that the energetics of the lattice favour both conformational behaviours occurring together. However, further examples of this behaviour are necessary before a confident confirmation of this correlation can be made.

5.5 *Halogenated Alkanes*

5.5.1 *Overview and General Observations*

The purpose of including a series of halogenated solvents in the **Au** framework was to study the effect from the size and shape of guests on the framework properties, while attempting to minimise the strong guest–guest interactions that occurred in the hydrogen-bonding alcohols (**§5.4**). It was anticipated that minimising the potential preference for guest–guest interactions to form ordered structures within the pores would aid in the deconvolution of the contributing guest influences on framework behaviour.

Toward this aim, a selection of available solvents were used, based on a methane, ethane or propane carbon backbone, with chloro, bromo and/or iodo substituents. Where a particular solvent in a series is not included, this is due either to the unavailability of the solvent, or because introduction of the solvent caused degradation of the framework such that SCO functionality was severely impaired, and meaningful data were not obtained.

In the following discussion it is important to note the van der Waals volumes of the relevant functional groups, shown in **Table 5-4**. As the functional groups of the guest molecule change there is a corresponding change in the size of the molecule, and thus the incidence and nature of intermolecular interactions, leading to a change in the macroscopic properties of the solvent.

Table 5-4: Comparison of van der Waals volumes for relevant functional groups.[4]

Group	VDW Volume / Å^3
CH_3 (sp^3)	19.64
Cl	18.20
Br	23.17
I	30.46

In order to efficiently compare between different framework solvates, the spin transition parameters for the haloalkane guests are presented together in **Table 5-5**. A selection of the guest properties is given in **Appendix C**.

Table 5-5: Comparison of the spin transition properties of **Au** solvated with the haloalkanes studied.

	Spin Transition Properties			
Guest	$T_{1/2}^{\downarrow}$ / K	$T_{1/2}^{\uparrow}$ / K	SCO range / K	Hysteresis / K
Dichloromethane (**$MeCl_2$**)	183	187	102	4
Bromochloromethane (**MeBrCl**)	219	227	14	8
1:1 $MeCl_2$/MeBrCl	221	229	6	8
Bromoethane (**EtBr**)	211	227	13	16
Iodoethane (**EtI**)	185	191	99	0–8
1,2-dichloroethane (**1,2-$EtCl_2$**)	207	-	91↓/118↑	0–27
1,2-dibromoethane (**1,2-$EtBr_2$**)	227	235	67	10, 6
1-chloropropane (**1-PrCl**)	212	225	31	13
1-bromopropane (**1-PrBr**)	231	238	58	7
1-iodopropane (**1-PrI**)	214	221	69	7
1:1 PrBr/PrI	229	234	47	5
1:1 PrCl/ EtBr	215	229	27	7–21

5.5.2 *Halomethane Guests*

As shown in **Figure 5-33**, the **Au**·{$MeCl_2$} sample displays an unusual gradual transition over ~82 K, which has an almost linear slope and a relatively constant hysteresis width of 4 K. Furthermore, the solvent freezing point occurs well below the start of the transition but does not seem to affect the transition behaviour, evidenced by little variation in the transition behaviour within the SCO range. The **Au**·{MeBrCl} displays spin transition that begins at about the same temperature as the $MeCl_2$ analogue, but with much more abrupt behaviour, and a larger hysteresis of 8 K.

In the absence of crystallographic data, any proposal for the structural effects on the transition behaviour for these materials would be based on conjecture. However, as seen in **§5.4** for the alcohol guest series, most of the features displayed in the spin transition behaviour of the **Au** framework can be attributed to structural effects, especially those due to distortion of the lattice. Through the results obtained from the alcohol-solvated samples, it is possible to make educated deductions regarding the potential framework structural behaviour.

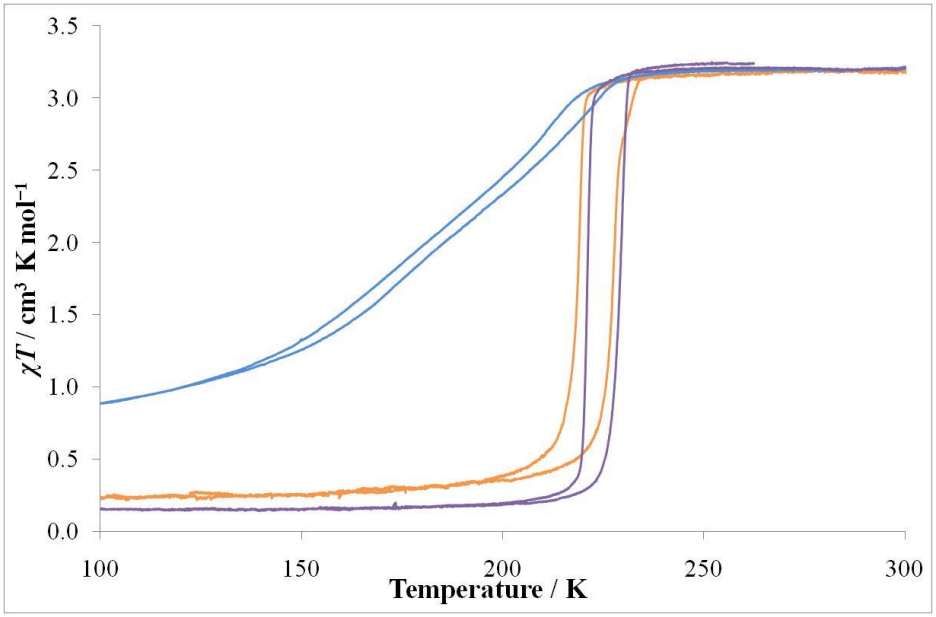

Figure 5-33: Variable temperature magnetic susceptibility data comparing the effect of different halomethane guests on the spin transition behaviour of **Au**: —$MeCl_2$, —MeBrCl, and —1:1 $MeCl_2$/MeBrCl.

$MeCl_2$ may be small enough and pack in the framework such that the lattice distorts to best accommodate the guest molecules. This would lead to more gradual spin transition behaviour

as a result of decreased communication of spin state in the distorted framework. When the framework is solvated with MeBrCl, the guest appears to be of a suitable size and shape to pack in such a manner to produce a more regularly orthogonal lattice conformation, similar to **Au**·{EtOH} (**§4.4**). The higher symmetry structure would then allow more effective communication of spin state between Fe(II) sites through long-rage elastic interactions in the more rigid structure, resulting in the abrupt spin transition observed.

When solvated with a 1:1 vol/vol $MeCl_2$/MeBrCl solvent mix, the **Au** framework produces transition behaviour that is very similar to that observed for **Au**·{MeBrCl}, implying that the lattice structural properties of these two samples are very similar. Compared to **Au**·{MeBrCl}, the **Au**·{1:1 $MeCl_2$/MeBrCl} spin transition occurs at slightly higher temperature and more abruptly, though with the same hysteresis width. The more abrupt, higher-temperature transition may be attributed to the presence of the smaller $MeCl_2$ guest molecule, which would create a less pronounced internal pressure effect, stabilising the LS state and increasing cooperativity as explained in **§3.3.2.2**. It should be noted that calculation of the molecular ratio of the two solvents gives 1.04:1.00 $MeCl_2$:MeBrCl, so the proportion of $MeCl_2$ and MeBrCl can be approximated to be equivalent by volume and number of molecules. This approximation also assumes that the framework does not display any selectivity of adsorbing one guest over the other, but considering how similar the two guest species are, this is a reasonable assumption. The similar behaviours of the spin transitions of **Au**·{1:1 $MeCl_2$/MeBrCl} and **Au**·{MeBrCl}, coupled with the fact that $MeCl_2$ and MeBrCl are the same rigid shape and very close in size, mean that it is probable that the 1:1 $MeCl_2$/MeBrCl and pure MeBrCl solvent systems would display similar guest packing behaviour in the framework pores.

In order to better understand the underlying mechanisms involved in determining the spin transition properties of these solvated systems, it is necessary to undertake crystallographic studies to elucidate the structural behaviour of the samples. It would also be useful to vary the relative concentration of $MeCl_2$ and MeBrCl in mixed solvent systems, and see what effect this has on the internal pressure in the framework. There may be a critical concentration at which the framework behaviour will convert from being similar to pure MeBrCl, to being closer to that observed for pure $MeCl_2$. For a more comprehensive study on the effect of different concentrations of mixed guest inclusion in SCO frameworks, see Fellows' thesis

(University of Sydney, 2011).[1]

5.5.3 *Haloethane Guests*

As light causes the decomposition of EtI to I_2 and butane, it was necessary to purify this solvent before introducing it into the **Au** framework for analysis. For this purification, EtI (10 ml) was washed with aqueous sodium thiosulphate (1 M, 3 × 5 ml) to remove the iodine and decolourise the solvent, then water (2 × 5 ml), and finally dried over anhydrous $CaCl_2$. The purified solvent was then used immediately, and care was taken to avoid exposing the sample to light.

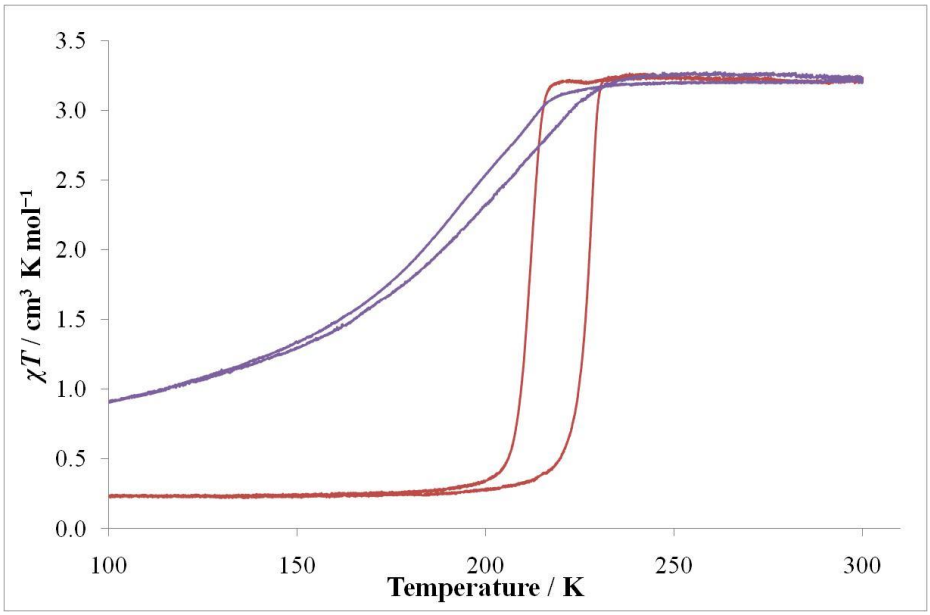

Figure 5-34: Variable temperature magnetic susceptibility data comparing the effect of different haloethane guests on the spin transition behaviour of **Au**: — EtBr, and — EtI.

As shown in **Figure 5-34**, the **Au**·{EtBr} framework produces an abrupt spin transition with a hysteresis width of 16 K. In contrast, the **Au**·{EtI} analogue displays a very gradual transition over 99 K, with a hysteresis width of up to 8 K. This result, in which the larger halogen leads to the gradual transition, is the opposite behaviour to that observed for the halomethane-solvated samples. In explaining this behaviour, it is useful to compare the transition behaviours produced by the haloethane-solvated framework, with that observed when the framework is solvated with the halomethane guests studied, as all these guest species have the general formula MeXY (X,Y = CH_3, Br, Cl and/or I).

It is clear from **Figure 5-35** that there are two distinct categories of spin transition observed for the halomethane/haloethane-solvated **Au** framework: the very gradual transition with small hysteresis width, and the abrupt transition with larger hysteresis. The origin of these two transition regimes most likely arises due to different structural properties of the framework samples, which in turn is due to the effect of solvent within the lattice pores.

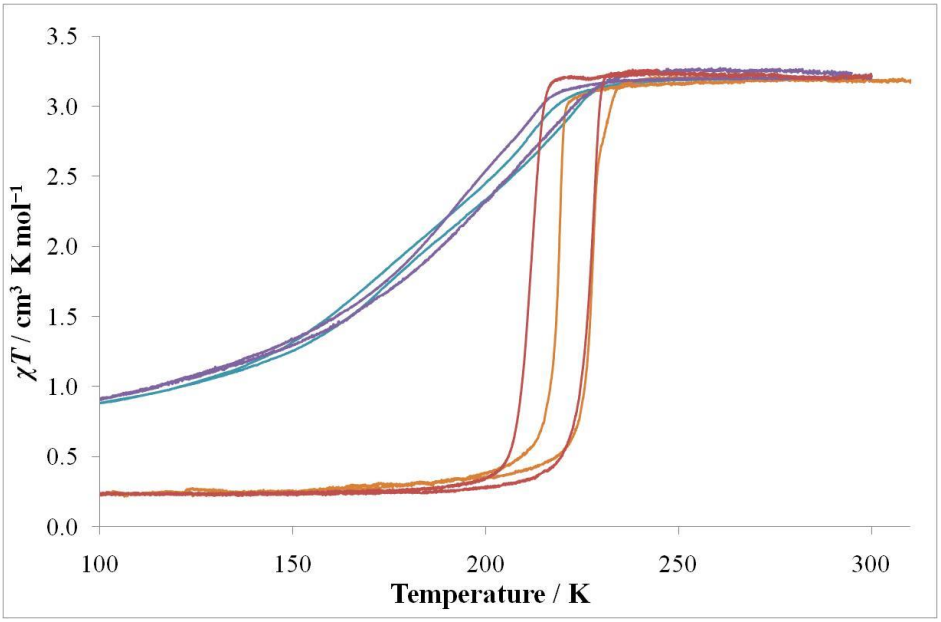

Figure 5-35: Comparison of the spin transition behaviour of **Au** solvated with: —$MeCl_2$, —MeBrCl, —EtBr, and —EtI.

EtBr is very close in size and shape to MeBrCl, with the sole difference in their structures being the replacement of a chloro substituent for a methyl group, which have similar van der Waals volumes (**Table 5-4**). It is then not surprising that the transition behaviours observed for the two solvents are very similar, as the guests can be expected to pack in a similar manner within the framework pores, producing a similar framework structure. The increased hysteresis width of EtBr may be loosely attributed to the greater number C–H···π interactions between the additional methyl group and the framework lattice molecules, which must be rearranged with the spin transition, creating an increased energetic barrier to SCO, disfavouring transition and widening the hysteresis. The slightly larger size of the methyl group compared to the chloro group would also create a greater internal pressure effect, stabilising the HS state and resulting in the decreased HS-to-LS transition temperature.

On the other hand, $MeCl_2$ and EtI are not as similar in their size and shape, yet they produce

very similar gradual transition behaviour at similar temperatures. This implies that they both influence the framework in such a way that it is forced to assume a particular lattice conformation, with a presumably distorted geometry. Further studies are necessary to determine the reason that these two molecules display such similar behaviour, even though their size and shape are dissimilar. Similar to the case for EtBr, the larger hysteresis observed for EtI compared to $MeCl_2$ may be attributed to the increased incidence of host–guest C–H···π interactions from the additional CH_3 group in EtI.

The effect of incorporating the symmetrical 1,2-EtX_2 (X = Cl, Br) guests into the **Au** framework was studied as part of the systematic investigation into haloalkane guest behaviour. The dihaloethane species are longer versions of the dihalomethane analogues, and are isostructural to the halopropane guests described in **§5.5.4**. As seen in **Figure 5-36**, the **Au**·{$EtCl_2$} and **Au**·{$EtBr_2$} samples displayed unusual, multi-step behaviour with features that were not seen for any other **Au** sample. Once again, the absence of structural information on the transition behaviour means that any potential explanation for the origin of the unusual behaviour would be conjecture, but certain observations can nevertheless be made.

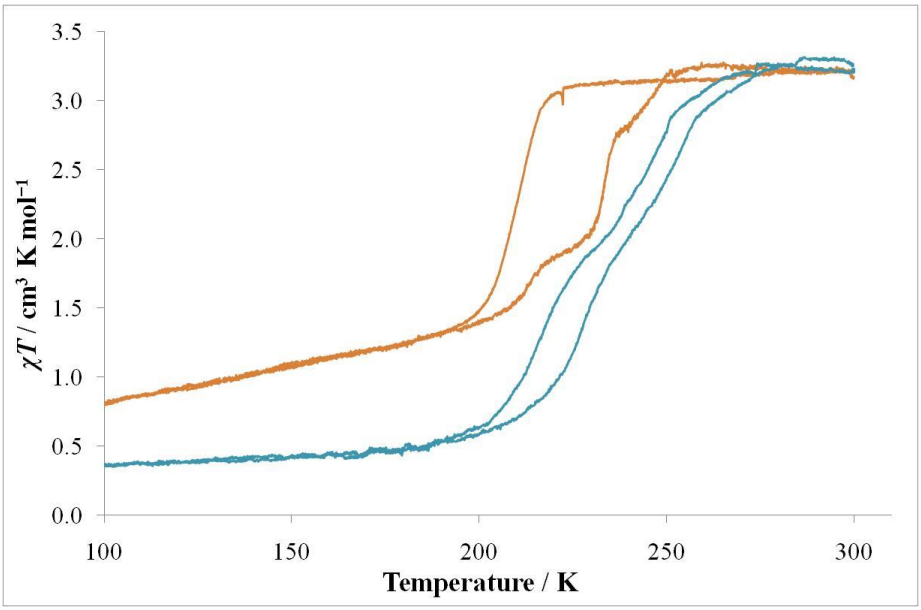

Figure 5-36: Variable temperature magnetic susceptibility data comparing the effect of different dihaloethane guests on the spin transition behaviour of **Au**: — 1,2-$EtCl_2$, and — 1,2-$EtBr_2$.

Upon cooling, the **Au**·{$EtCl_2$} framework commences spin crossover at a temperature below the melting point of the solvent (**Table 5-5**). The transition occurs in two stages: the first is

relatively abrupt, occurring over *ca*. 18 K from 222 to 204 K, and accounts for approximately half of the expected number of SCO sites in this framework. The second stage occurs from 204 K, decreases linearly and is incomplete down to 100 K, at which temperature the sample had not yet reached a low temperature plateau, implying that there would most likely be further spin transition below the temperature range studied.

Upon warming, at low temperature the transition behaviour of the **Au**·{$EtCl_2$} framework closely follows the cooling behaviour, and continues increasing linearly until *ca*. 209 K, at which point approximately half of the Fe(II) sites in the framework are HS, producing a thermal hysteresis. Above this point there are three steps in the LS-to-HS transition, with the number of SCO sites involved in the transition steps roughly occurring in the ratio 1:2:1. The top of the second transition step occurs at *ca*. 236 K, coinciding with the melting point of $EtCl_2$.

The behaviour observed for **Au**·{$EtBr_2$} is similar to that displayed by **Au**·{1:1 MeOH/EtOH} (**§5.4.3**), in which two gradual reversible stages are observed with hysteresis. The whole spin transition occurs below the melting point of $EtBr_2$ (283 K).

It is important to note that the four straight-chain non-hydrogen atoms in these guest molecules may adopt either the *trans* or *gauche* conformers (see **Figure 5-37**). The relative proportion of molecules in these two states depends on the magnitude of steric interactions between the halogen atoms. Due to these different conformers, there may be multiple solvent packing energetic minima such that different framework regions or crystallites may have different occluded solvent packing behaviour. This would then produce different spin transition behaviour, and the multiple transition steps observed. As the bromo substituents are larger than their chloro analogues, the stronger electrostatic repulsion from the bromo groups in the *gauche* conformer of $EtBr_2$ would lead a stronger preference for the *trans* conformer, and impose a greater limitation on the variety of solvent packing behaviours.[5] As a result, there are only two major spin transition stages observed in the **Au**·{$EtBr_2$} framework, rather than the four stages observed in the warming behaviour of the **Au**·{$EtCl_2$} sample.

Another possible origin of the multi-step spin transition behaviour in **Au**·{$EtCl_2$} and **Au**·{$EtBr_2$} could be phase changes in the framework lattice. Depending on the framework structural conformation, there may also be multiple crystallographically distinct Fe(II) sites,

which could undergo spin transition differently, leading to the multi-step behaviour. Such behaviour could arise from packing influences of the guest solvent. However, it is essential to obtain further temperature-dependent structural information on the framework before a suitable explanation can be made for the origin of this spin transition behaviour.

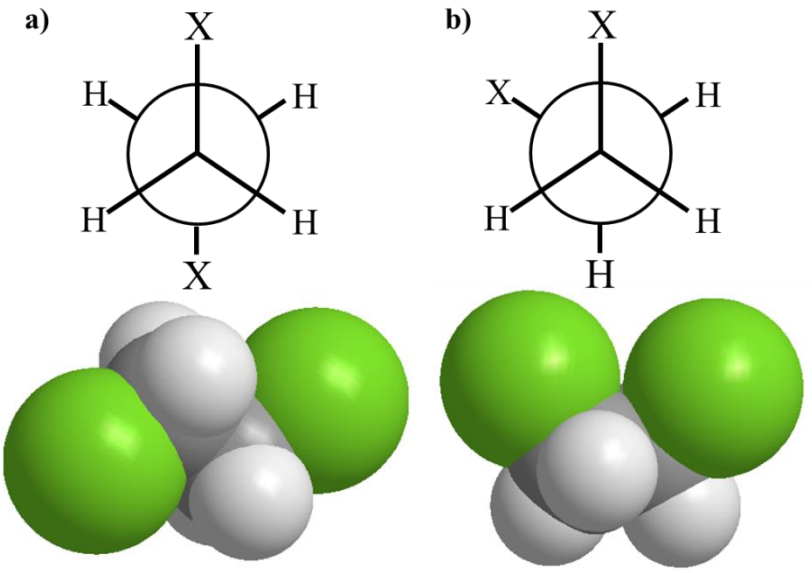

Figure 5-37: Newman projections and 3D space-filling representations for the **a)** *trans*; and **b)** *gauche* conformations of a 1,2-dihaloethane molecule. There are two *gauche* isomers, related by a mirror plane drawn vertically through the Newman projection.

5.5.4 *Halopropane Guests*

Similar to the EtX_2 (X = Cl, Br) guest solvent species, the 1-PrX (X = Cl, Br, I) guests are flexible, and may adopt either the *trans* and *gauche* conformers. The relative proportion of these isomers depends on the steric bulk of the attached halogen, with the larger halogens producing greater electrostatic repulsion in the *gauche* conformer, leading to a stronger preference for the *trans* conformer.

As shown in **Figure 5-38**, the **Au**·{1-PrCl} framework displays similar spin transition behaviour to the **Au**·{MeBrCl} and **Au**·{EtBr} samples, of a relatively abrupt transition with hysteresis at similar temperature. Although conclusive structural information on this sample has not been obtained, it is likely that the framework conformation of the **Au**·{1-PrCl} sample is similar to these samples, leading to such similar behaviour.

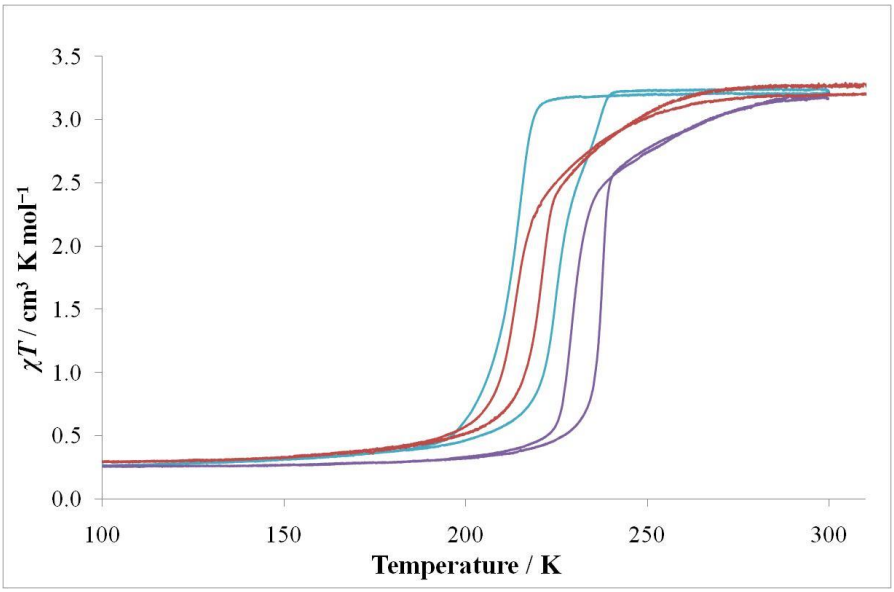

Figure 5-38: Variable temperature magnetic susceptibility data comparing the effect of different 1-halopropane guests on the spin transition behaviour of **Au**: —1-PrCl, —1-PrBr, and —1-PrI.

In contrast, the **Au**·{1-PrBr} and **Au**·{1-PrI} samples produce spin transition behaviour that is completely different to the **Au**·{1-PrCl} framework, and much more similar to the behaviour of the **Au**·{MeOH} sample. Upon cooling, the transitions of **Au**·{1-PrBr} and **Au**·{1-PrI} begin gradually, then after a threshold proportion (*ca*. 1/3) of the Fe(II) sites have undergone spin transition, the rest of the frameworks cooperatively undergo an abrupt transition to full completion. Upon warming, there is a small hysteresis produced for the abrupt transition stage of the two samples, and then the gradual transition stage closely follows the cooling behaviour with no significant hysteresis.

The similar transition behaviour for **Au**·{1-PrBr} and **Au**·{1-PrI} implies that the samples have similar lattice conformational geometries, which would be produced by very similar, if not identical guest packing arrangements within the framework pores. However, compared to the bromo group, the larger size of the iodo substituent creates a greater internal pressure effect, which would stabilise the HS state and decreasing the spin transition temperature of **Au**·{1-PrI}, as explained in **§3.3.2.2**.

In order to more fully understand the transition behaviour of the **Au**·{1-PrBr} framework sample, powder X-ray diffraction was used to provide structural information on the nature of the transition. As shown in the intensity plot in **Figure 5-39**, there are three noticeable phase

transitions in the diffractograms upon both cooling and warming. There is also the appearance of a new phase below 160 K, due to frozen 1-PrBr solvent.

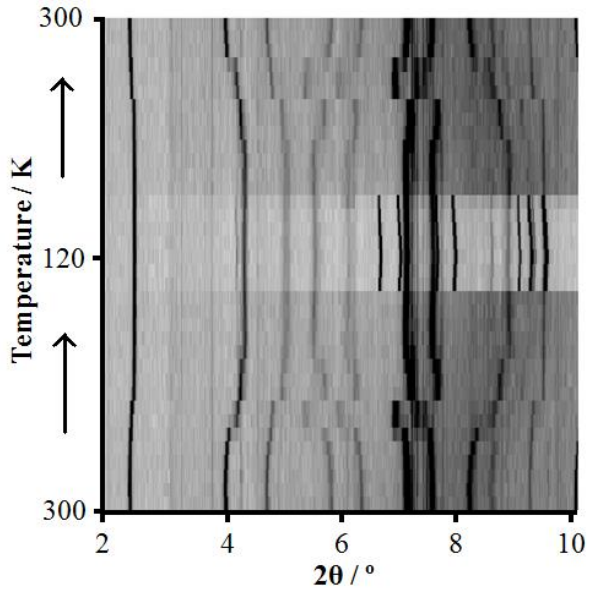

Figure 5-39: Variable temperature intensity plot showing the powder diffraction peak change as the **Au**·{1-PrBr} sample was cooled from 300 to 120 K, then warmed back up to 300 K.

Fitting a unit cell model using Le Bail methods yields the unit cell parameters shown in **Figure 5-40**. While the orthorhombic *Cmma* space group appropriately fit most of the diffraction patterns, the phase between *ca*. 230 and 260 K required the monoclinic *C*2/*m* space group to appropriately fit all of the reflection peaks.

As seen in the variable temperature peak intensity profile (**Figure 5-39**) and the refined unit cell parameters (**Figure 5-40**), there are significant changes in the magnitudes of the lattice parameters, and the degree of compression of the framework lattice. In order to provide a clearer understanding of the framework behaviour, it is important to consider the $d_{\text{Fe–Au–Fe}}$ (**Figure 5-41a**) and $\theta_{\text{Au–Fe–Au}}$ (**Figure 5-41b**) values, both of which are directly calculated from the unit cell parameters. Comparison of these quantities clearly shows that the major variations in the *a*- and *b*-parameters are primarily due to lattice compression/decompression behaviour, though the phase transition at *ca*. 230 K is due to conversion to the fully LS phase.

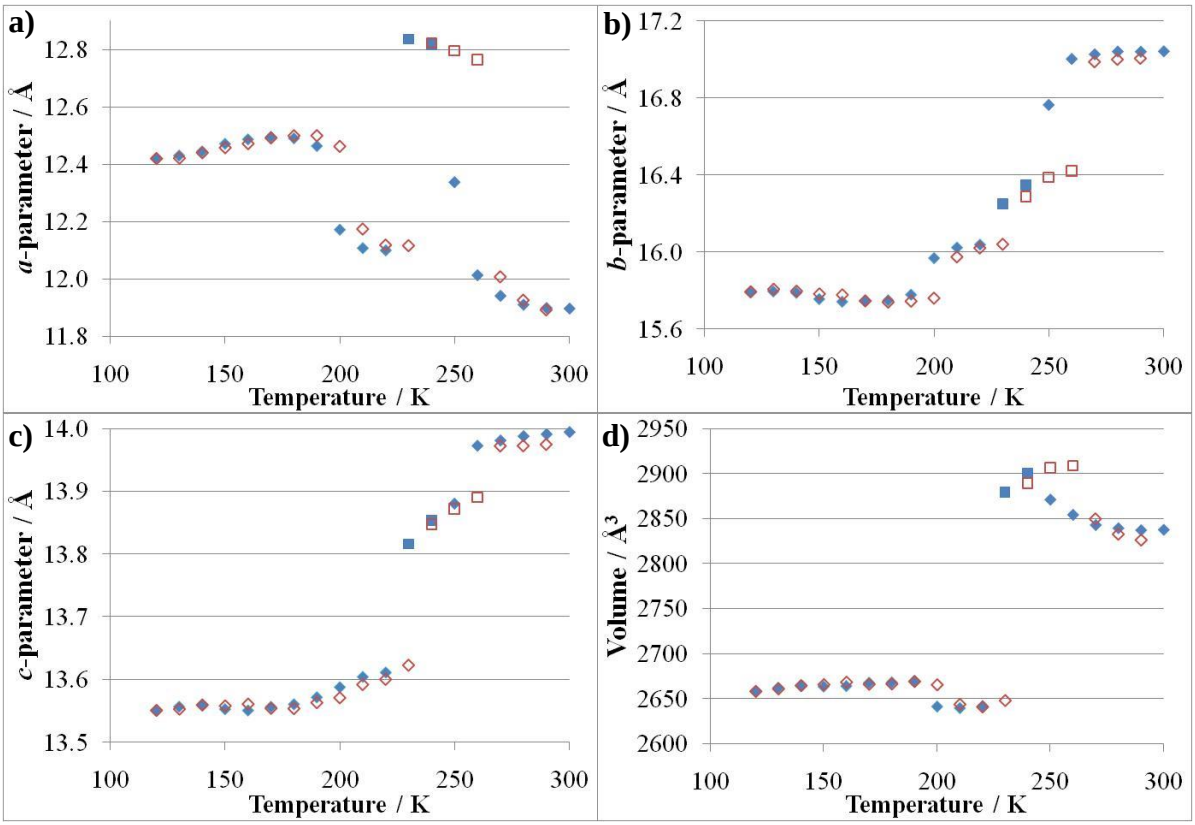

Figure 5-40: Temperature-dependence on the unit cell parameters of **Au**·{1-PrBr}: **a)** *a*-parameter; **b)** *b*-parameter; **c)** *c*-parameter; and **d)** volume, upon ◆ cooling and ◇ warming. Shapes represent ◆ *Cmma*, and ■ *C*2/*m* modelled phases.

Upon cooling, the $d_{\text{Fe–Au–Fe}}$ value (**Figure 5-41a**) remains relatively constant until 250 K, implying that the framework crystallites are fully in the HS state. From *ca*. 250 to 230 K this quantity displays a slight decrease, attributable to a gradual, non-cooperative transition in the crystallites. Below 230 K the crystallites are fully in the LS phase after an abrupt, cooperative transition. Upon warming, this quantity closely follows the cooling behaviour, with a small hysteresis in the transition.

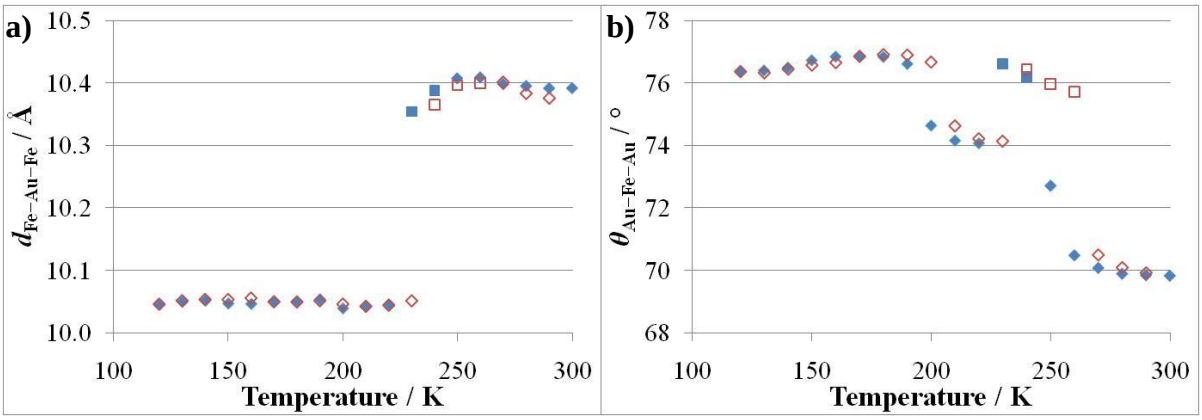

Figure 5-41: Temperature-dependence on the **a)** $d_{Fe–Au–Fe}$, and **b)** $\theta_{Au–Fe–Au}$ of the **Au**·{1-PrBr} framework upon ◆ cooling and ◇ warming. Shapes represent ◆ *Cmma*, and ■ *C*2/*m* modelled phases, and values are calculated from the variable temperature unit cell parameters shown in **Figure 5-40**, upon ◆ cooling and ◇ warming.

It is interesting to compare the behaviour of $d_{Fe–Au–Fe}$ with that displayed by $\theta_{Au–Fe–Au}$ (**Figure 5-41b**). As the framework is cooled from 300 to 250 K the angle increases, indicating lattice decompression. Between 250 and 230 K this framework was modelled in the monoclinic *C*2/*m* phase, which was also observed in the **Au**·{1-BuOH} framework (**§5.4.5**). This space group was associated with a gradual transition due to distortion in the framework geometry, leading to decreased communication through the less rigid framework lattice. The **Au**·{MeOH} sample (**§5.4.2**), which produced similar transition behaviour to this **Au**·{1-PrBr} framework, also displayed a distorted lattice geometry with a similar degree of compression. This phase also corresponds to the gradual spin transition stage observed in the $d_{Fe–Au–Fe}$ value of **Au**·{1-PrBr}.

Below 230 K the crystallites convert back to the original *Cmma* space group and $\theta_{Au–Fe–Au}$ abruptly decreases as the lattice converts to a more compressed conformation. At *ca*. 200 K there is another phase transition that is independent of the spin transition, in which the lattice undergoes decompression, evidenced by the increase in $\theta_{Au–Fe–Au}$. This phase change shows similar behaviour to that observed at low temperature in the **Au**·{EtOH} (**§4.4.1**) and **Au**·{N_2} (**§5.3**) frameworks, and may similarly be due to intermolecular host-host interactions of the bpac pyridyl units in the framework adopting a favoured geometrical configuration. It is anticipated that the bpac pyridyl rings of the host framework align to maximise favourable interactions, but to minimise the steric repulsion inherent in this conformation, the framework undergoes decompression. This effect also produces a larger

volume, as shown in **Figure 5-40d**. Upon warming, the degree of compression closely follows the cooling behaviour, though each phase change displays thermal hysteretic behaviour.

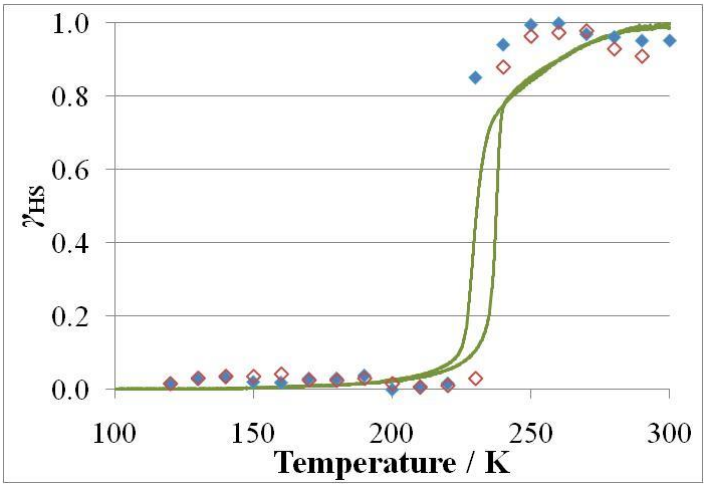

Figure 5-42: Comparison of the temperature-dependence on the relative stoichiometric fraction of HS states (γ_{HS}) in **Au**·{1-PrBr} as determined by — the magnetic susceptibility; and $d_{Fe–Au–Fe}$ upon ◆ cooling and ◇ warming.

To compare the spin transition behaviour as observed by magnetic and diffraction studies, the temperature-dependence on the relative stoichiometric fraction of HS states was calculated (**Figure 5-42**). For the diffraction results, this quantity was calculated from $d_{Fe–Au–Fe}$, scaling the values such that the largest distance observed was equivalent to the HS fraction of 1.0, and the smallest distance was equivalent to a HS fraction of 0. The temperatures for the abrupt transition stage correlate well, though much of the gradual stage of the magnetic spin transition is not observed in $d_{Fe–Au–Fe}$. This may be due to a decrease in the distortion of the linear dicyanidoaurate linkers, which lie along this dimension: As the material undergoes gradual spin transition, the decrease in the average Fe–N_{CN} bond length may be accompanied by a decrease in the distortion of the dicyanidoaurate units, which would effectively lengthen $d_{Fe–Au–Fe}$ as these linkers become more linear. The net effect is that the Fe–N_{CN} bond length contraction and the lengthening of the dicyanidoaurate linker effectively negate each other, and there is little difference observed in $d_{Fe–Au–Fe}$. While the high temperature part of the gradual transition stage is not observed in $d_{Fe–Au–Fe}$, there is expected to be a change in the degree of compression as the framework undergoes gradual spin transition, as was observed in the **Au**·{MeOH} (**§5.4.2**) and **Au**·{1-PrOH} (**§5.4.4**) samples. This expectation is

confirmed by the change in the $\theta_{Au–Fe–Au}$ value of **Au**·{1-PrBr} (**Figure 5-41b**), which does increase on cooling between *ca*. 260 and 230 K, corresponding to the expected decompression that accompanies the HS-to-LS transition in the **Au** framework.

As **Au**·{1-PrBr} and **Au**·{1-PrI} produced very similar spin transition behaviours, a 1:1 (vol/vol) 1-PrBr/1-PrI mixed solvent system was incorporated into the **Au** framework, to determine the effect on the spin transition of combining the two individual guest species within the lattice pores. The resulting magnetic behaviour is shown in **Figure 5-43**. The gradual stage of the HS-to-LS transition of **Au**·{1:1 1-PrBr/1-PrI} begins at a temperature approximately halfway between the two individual solvent systems. This gradual stage also occurs more abruptly than the **Au**·{1-PrBr} and **Au**·{1-PrI} samples, with a decreased SCO range (**Table 5-5**). As mentioned above, the two independent solvent samples begin the abrupt transition stage once a threshold quantity of Fe(II) sites had undergone gradual spin transition to the LS state. As the gradual spin transition stage produced by the **Au**·{1:1 1-PrBr/1-PrI} sample occurs more cooperatively than the independent pure-solvated samples, this threshold quantity of LS Fe(II) sites is reached within a smaller temperature range. The abrupt spin transition stage is then observed at a similar temperature as was displayed by the **Au**·{1-PrBr} sample, with a decreased thermal hysteresis width compared to the behaviour produced by both solvents independently.

Due to the different densities and molar masses of 1-PrBr and 1-PrI, the 1:1 volumetric ratio of the two solvents would be equivalent to a 1.07:1.00 molar ratio of the components. Assuming negligible selectivity of the framework for one guest over the other, the relative proportion of each adsorbed guest in the framework can be treated as effectively equal. The observation that the gradual transition of **Au**·{1:1 1-PrBr/1-PrI} begins between **Au**·{1-PrBr} and **Au**·{1-PrI} implies that the mixed solvent system produces an internal pressure that is intermediate between the individual solvents. This is expected considering that the mixed system will have an effective molecular volume for the guest that is the average of the two individual components, and because both guests are likely to pack together in a similar manner within the framework pores.

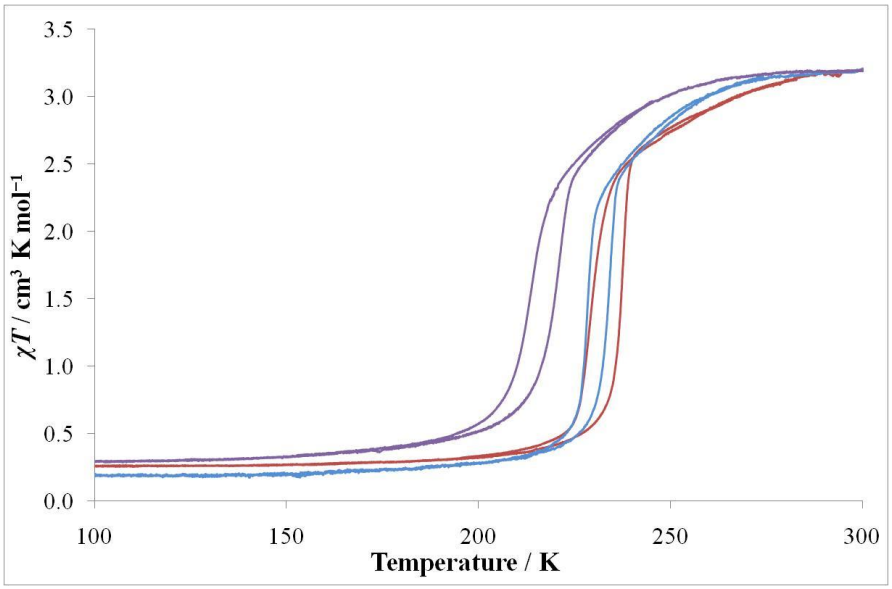

Figure 5-43: Variable temperature magnetic susceptibility data comparing the effect of combining two halopropane guests which produce similar transition behaviours at different termperatures when incorporated in **Au**: —1-PrBr, —1-PrI, and —1:1 1-PrBr/1-PrI.

Without further information, the more abrupt spin transition observed in the mixed solvent system cannot be definitively explained, though it may be potentially attributed to a more homogeneous sample composition. Sample heterogeneity can lead to broadening of the spin transition range due to slightly different SCO environments, and if such a sample were to somehow become more homogeneous, this could lead to a more abrupt spin transition. At this stage, the manner in which the **Au**·{1:1 1-PrBr/1-PrI} sample would be more homogeneous than the pure solvent analogues is unknown. The observation that a mixed solvent system can produce a more abrupt spin transition than the component solvents individually was also observed in the **Au**·{1:1 $MeCl_2$/MeBrCl} sample.

The **Au**·{MeBrCl}, **Au**·{EtBr} and **Au**·{1-PrCl} samples all displayed relatively abrupt spin transition with hysteresis, at approximately the same temperature. As it is likely that these three frameworks all possess analogous framework conformations, it was decided to investigate the effect of incorporating into the **Au** framework a mixture of two of these guest species. As seen in **Figure 5-44**, **Au**·{1:1 EtBr/1-PrCl} displays spin transition in roughly the same temperature range as the individual solvent guests, but with an unexpected two-step behaviour with a variable thermal hysteresis width of 7–21 K.

Upon cooling, the first transition stage occurs abruptly between 223 and 214 K, and accounts

for ~70% of the total SCO. The second cooling transition stage occurs between 214 and 190 K, as the remainder of the active SCO Fe(II) sites undergo transition to the LS state. Upon warming, the low temperature stage occurs between 215 and 222 K, more abruptly than the equivalent cooling stage, and corresponds to ~33% of the total LS-to-HS transition of active SCO Fe(II) sites. The high temperature warming transition stage then begins gradually from 222 K, and rapidly increases in abruptness, completing the transition at 237 K.

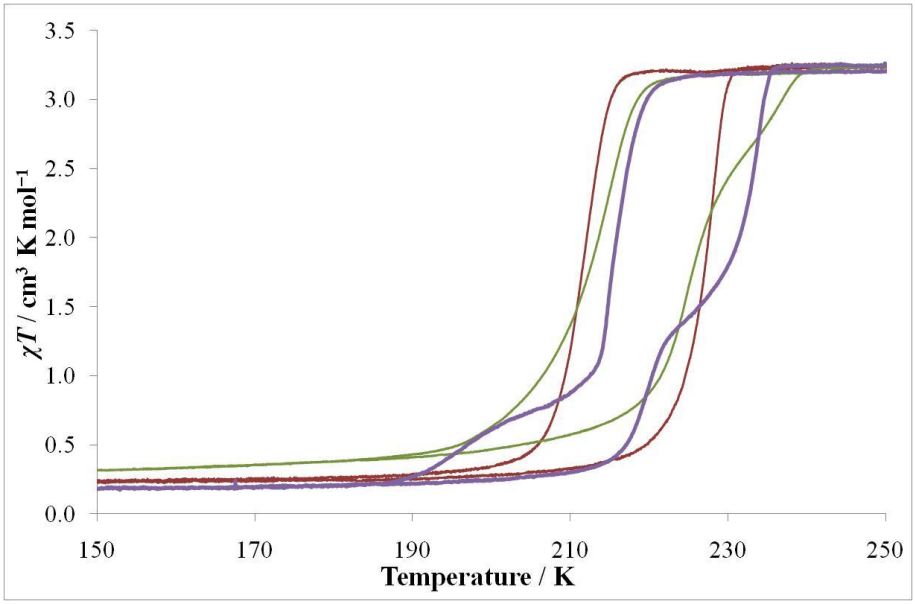

Figure 5-44: Variable temperature magnetic susceptibility data comparing the effect of combining two haloalkane guests which produce similar transition behaviours at similar temperatures when incorporated in **Au**: —EtBr, —1-PrCl, and —1:1 EtBr/1-PrCl.

It is important at this point to make some relevant observations. The 1:1 volumetric ratio of EtBr/1-PrCl is equivalent to a 1.18:1.00 molar ratio, so assuming that there is no significant preference for the framework to adsorb one guest species over the other, there would be marginally more molecules of EtBr than 1-PrCl in the sample. Additionally, unlike in the **Au**·{1:1 1-PrBr/1-PrI} sample, the two component guest species in **Au**·{1:1 EtBr/1-PrCl} have different shapes, which would lead to different packing conformations than were observed for the independent solvent systems. 1-PrCl can also adopt the *gauche* and *trans* conformations as illustrated in **Figure 5-37**, which may affect the spin transition behaviour depending on the relative proportion of molecules which adopt these two conformations.

Considering these factors, the two-stage spin transition may potentially be attributed to the guest packing behaviour within the framework pores. The single-step behaviour observed for

Au·{1-PrCl} may be due to regular guest packing within the lattice pores, possibly through effectively all guest molecules adopting the same conformation. When EtBr is introduced, this inhibits regular ordering of the 1-PrCl molecules, and there may be a greater incidence of both the *gauche* and *trans* conformational isomers. There are two *gauche* isomers and one *trans* isomer (**Figure 5-37**), so assuming an equal preference under these circumstances for the molecule to adopt each isomer, this gives a ratio for the number of molecules in the *gauche*/*trans* conformers of 2:1. This is roughly equivalent to the relative proportion of SCO-active Fe(II) sites which undergo each spin transition stage. This correlation supports the hypothesis that the precise transition behaviour of a particular Fe(II) site depends on the conformation of the guest molecules in its surrounding environment, as the shape of the guest and the resulting packing behaviour will exert different local pressure effects on the framework lattice.

5.5.5 *Comparison of Haloalkane Guests*

The systematic study of incorporating different haloalkane guest species into the **Au** framework has demonstrated the extreme sensitivity of this framework to the precise guest size and shape, and the resulting packing arrangement of the guest within the framework pores.

The **Au**·{$MeCl_2$} and **Au**·{EtI} samples demonstrated similar gradual transition behaviour, which, in the absence of structural data, is assumed to be caused by a distorted framework conformation that leads to reduced cooperativity between Fe(II) centres. In contrast, the **Au**·{MeBrCl}, **Au**·{1:1 $MeCl_2$/MeBrCl}, **Au**·{EtBr} and **Au**·{1-PrCl} samples all displayed an abrupt transition with hysteresis at very similar temperatures (shown in **Figure 5-45**). Furthermore, the transition behaviour of **Au**·{EtOH} also occurred with similar behaviour to these samples.

The observation that so many solvents produce abrupt, hysteretic transitions at such similar temperatures is an interesting result, and should not be ignored. Considering the transition behaviour observed for other solvent systems and the strong relationship with framework structure and lattice distortion, it is very likely that the abrupt transitions observed in all these frameworks result from the normal orthorhombic *Cmma* space group. It is possible that there is a certain guest packing arrangement that produces sufficient internal pressure on the

framework lattice to adopt this orthogonal lattice conformation, and produce the spin transition within this temperature range. Variations in the guest solvent properties and the nature and strength of host–guest and guest–guest intermolecular interactions would then affect the precise transition temperature, abruptness and thermal hysteresis width.

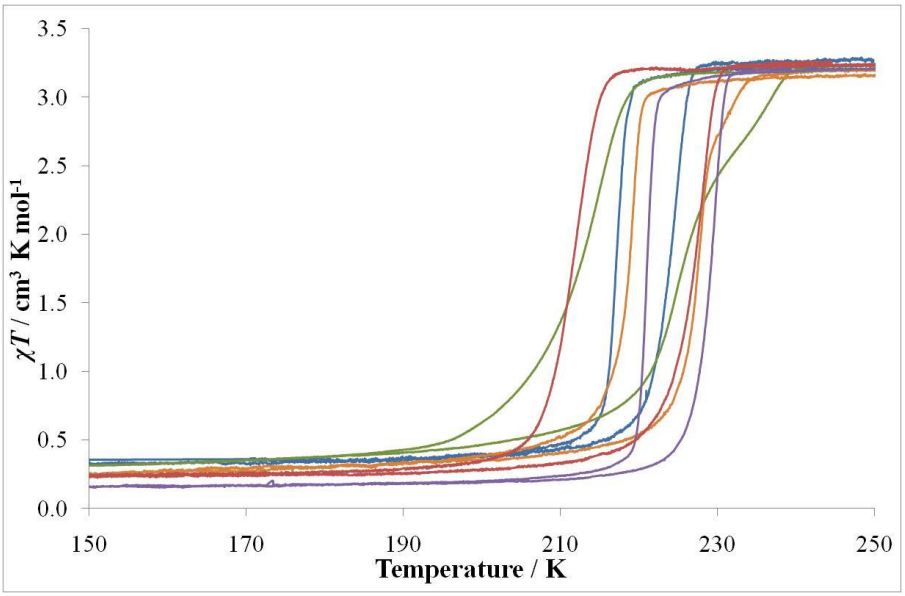

Figure 5-45: Comparison of the variable temperature magnetic susceptibility data for **Au** solvated with: MeBrCl, 1:1 $MeCl_2$/MeBrCl, EtBr, 1-PrCl and EtOH.

Au·{1:1 EtBr/1-PrCl} displays an unusual two-step transition with hysteresis, which was attributed to the co-existence of both the *gauche* and *trans* conformers of 1-PrCl. Considering that **Au**·{1-PrCl} did not show such prominent two-step behaviour, it was determined that EtBr inhibits regular packing of a single conformer of 1-PrCl within the framework pores, such that both 1-PrCl conformers are then present in the mixed solvent system. This then produces different SCO environments due to the varying local internal pressures exerted by the guest on the framework lattice.

Au·{1-PrBr}, **Au**·{1-PrI} and **Au**·{1:1 1-PrBr/1-PrI} all produce similar transition behaviour, with the HS-to-LS transition occurring with a gradual transition stage followed by an abrupt transition once a threshold quantity of Fe(II) sites convert to the LS state. Structural studies on **Au**·{1-PrBr} showed that the fully HS framework is in the orthorhombic *Cmma* space group, but the gradual transition occurs while the framework is in the distorted monoclinic *C*2/*m* space group, before converting back to a *Cmma* phase once the framework undergoes the abrupt transition stage and is fully LS. Due to the similar spin transition behaviours

observed in **Au**·{1-PrBr}, **Au**·{1-PrI} and **Au**·{1:1 1-PrBr/1-PrI}, it is expected that they also display similar structural properties brought about by similar solvent packing behaviour. The lower transition temperature observed for **Au**·{1-PrI} was explained due to an increased internal pressure effect from the larger guest, which stabilises the HS state.

Au·{$EtCl_2$} and **Au**·{$EtBr_2$} produce unusual multi-step spin transition behaviour that was attributed to the relative proportion of guest molecules in the *gauche* and *trans* conformational isomers, which would give different local pressure effects in the crystallites, and thus produce Fe(II) sites with different spin transition properties. One of the steps in the transition of **Au**·{$EtCl_2$} was attributed to solvent melting, which would allow the framework lattice to adopt a more energetically favoured conformational geometry, changing the spin transition properties.

5.6 *Miscellaneous Solvents*

In addition to the systematic study of straight-chain alcohol and haloalkane species, the effects of water (H_2O), acetonitrile (MeCN) and carbon disulfide (CS_2) guest species on the spin transition behaviour of **Au** were also studied. The resulting magnetic behaviours are shown in **Figure 5-46**.

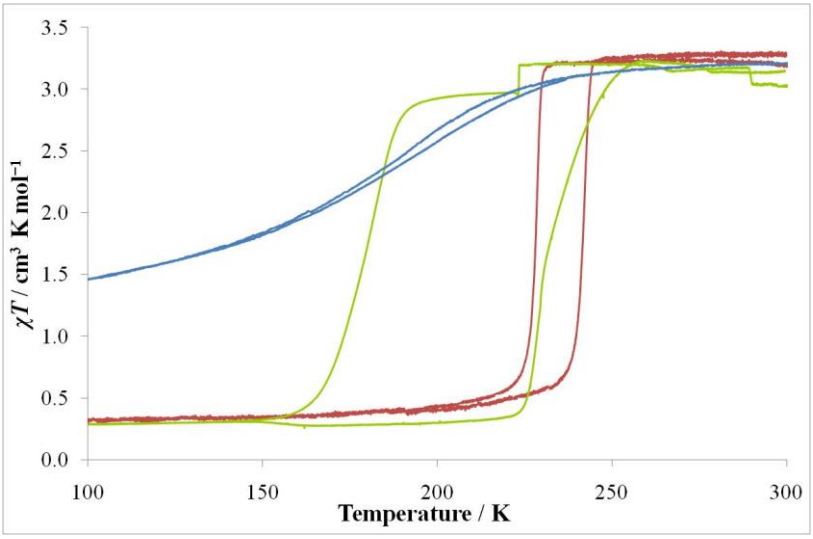

Figure 5-46: Variable temperature magnetic susceptibility data comparing the effect of different non-alkane-derived guests on the spin transition behaviour of **Au**: MeCN, CS_2, and H_2O.

5.6.1 *Water*

Water is a small, highly polar molecule that is able to form many strong hydrogen bonds within a small volume. It has a relatively high melting point, and considering the mass of its component atoms, a relatively high density.[6]

The magnetic behaviour of **Au**·{H_2O} (**Figure 5-46**) displays a gradual spin transition with hysteresis. The transition is incomplete in the temperature range studied, but analysis of just the observed behaviour gives $T_{1/2}$ = 181 K, a hysteresis width of 0–6 K (between 172 and 233 K) and a SCO range of 127 K. To determine the structural behaviour associated with this spin transition, **Au**·{H_2O} was also studied by variable temperature powder diffraction using the in-house powder diffractometer at the University of Sydney.

The variable temperature intensity plot obtained for the **Au**·{H_2O} sample is shown in **Figure 5-47**. Where possible, unit cell parameters were modelled using a Le Bail fit to the powder diffraction data, and the resulting parameters are shown in **Figure 5-48**. Significant peaks were observed below 280 K due to frozen water, and to determine unit cell parameters for the framework sample at these temperatures it was necessary to exclude the 2θ region between 22 and 26°. It is important to note that the (221) reflection at *ca*. 2θ = 20° is split, indicating a similar distorted lattice structural conformation as was observed in the **Au**·{2-BuOH} sample (**§5.4.6**). This is more clearly seen by comparing the raw powder diffractograms for **Au**·{H_2O} (**Figure C-36**) and **Au**·{2-BuOH} (**Figure C-31**), both of which demonstrate a partial convergence of the (221) peak upon a cooling structural transition (note that the radiation wavelengths used for the two experiments were different, so the angles of the reflection peaks are different). As with the **Au**·{2-BuOH} sample, the distortion of the **Au**·{H_2O} sample would be due to a non-orthogonal bpac coordination between adjacent Fe(II) centres, as the bpac ligand 'leans' between the *a*- and *b*-axes. Unfortunately, due to the poor resolution and limited range of the **Au**·{H_2O} powder diffractograms this distorted phase could not be accurately modelled, and the *Cmma* space group and standard unit cells for the **Au** framework were used to fit the powder diffractograms instead.

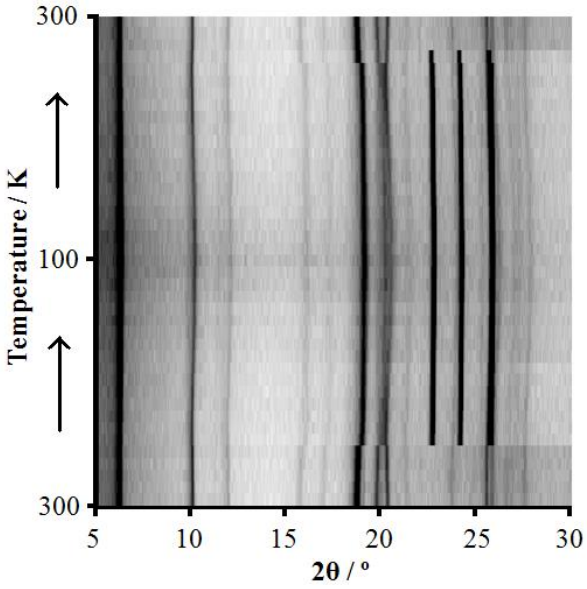

Figure 5-47: Variable temperature intensity plot showing the powder diffraction peak change as the **Au**·{H_2O} sample was cooled from 300 to 100 K, then warmed back up to 300 K.

The strongest diffraction peaks that were fit in the Le Bail model corresponded to the (020) and (220) reflections, and so the data for the *a*- and *b*-parameters are fairly reliable. Unfortunately the *c*-parameter is less reliable, as the model solution used was of orthorhombic, rather than the more crystallographically accurate triclinic symmetry which was indicated by the split (221) reflection. As explained above, the unit cell would be expected to have non-90° α and β angles, and a γ angle of effectively 90°. As the α and β angles both affect the *c*-axis, the (h k l) peak reflections would be fit poorly and the *c*-parameter would be inaccurate. Nevertheless, the $d_{Fe–Au–Fe}$ and $\theta_{Au–Fe–Au}$ values, which are directly calculated from the *a*- and *b*-parameter values, can provide interesting information about the spin state of the framework and the degree of lattice compression, respectively.

Where frozen water first appears in the powder diffractograms, there is a minor phase change observed in the framework lattice, most obviously shown as a decrease in the *a*-parameter (**Figure 5-48a**), and subsequently in the volume (**Figure 5-48d**).

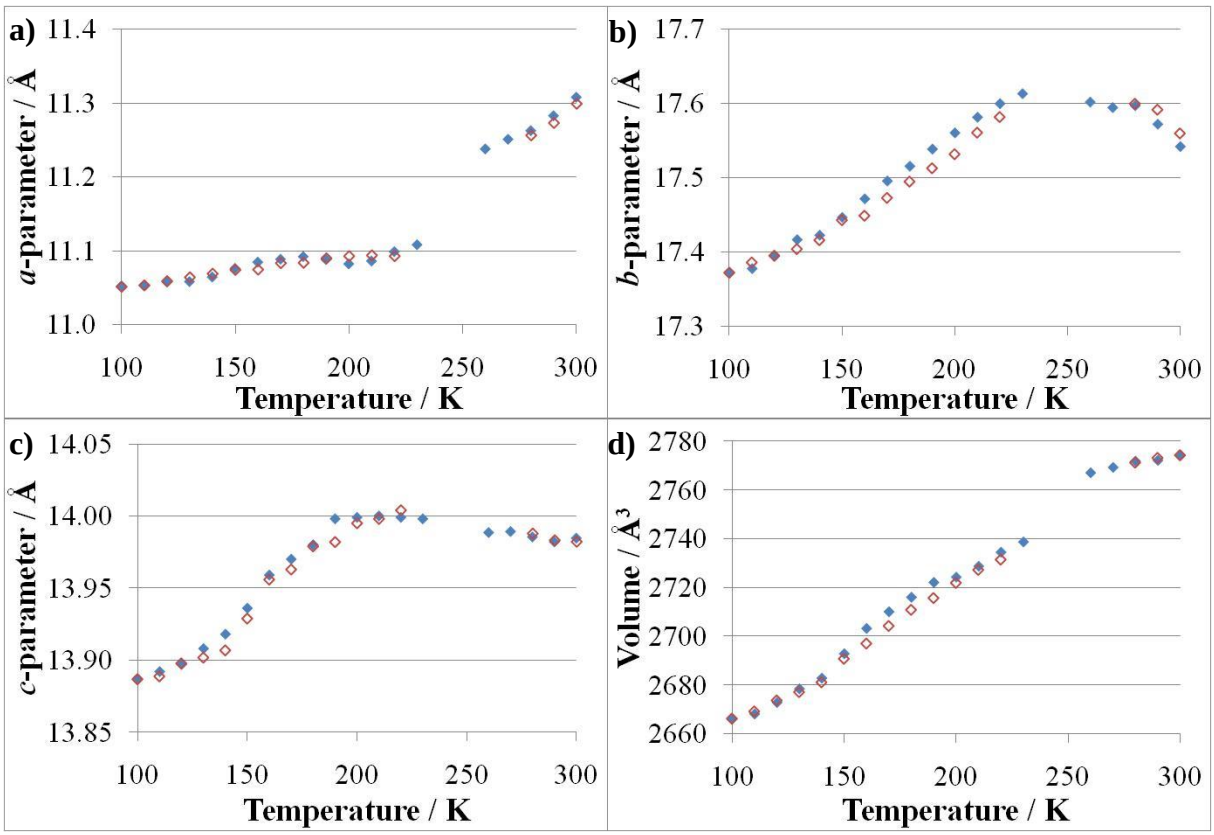

Figure 5-48: Temperature-dependence on the unit cell parameters of **Au**·{H_2O}: **a)** *a*-parameter; **b)** *b*-parameter; **c)** *c*-parameter; and **d)** volume, upon ◆ cooling and ◇ warming. Meaningful structural information was unable to be obtained from powder diffractograms between 230 and 270 K due to poor peak resolution.

As shown in **Figure 5-49a**, upon cooling the $d_{Fe–Au–Fe}$ value remains relatively constant from 300 to 260 K, below which it gradually decreases in magnitude to 100 K. On warming, the behaviour closely follows the cooling behaviour, though with a small hysteresis. Upon cooling at high temperature, the $\theta_{Au–Fe–Au}$ quantity (**Figure 5-49b**) decreases in magnitude, corresponding to lattice compression. After the appearance of crystalline frozen water at 250 K, the framework undergoes a phase change to a more compressed lattice conformation, and the angle gradually increases in magnitude as the lattice undergoes decompression. As with other samples of the **Au** framework, the decompression accompanies spin transition.

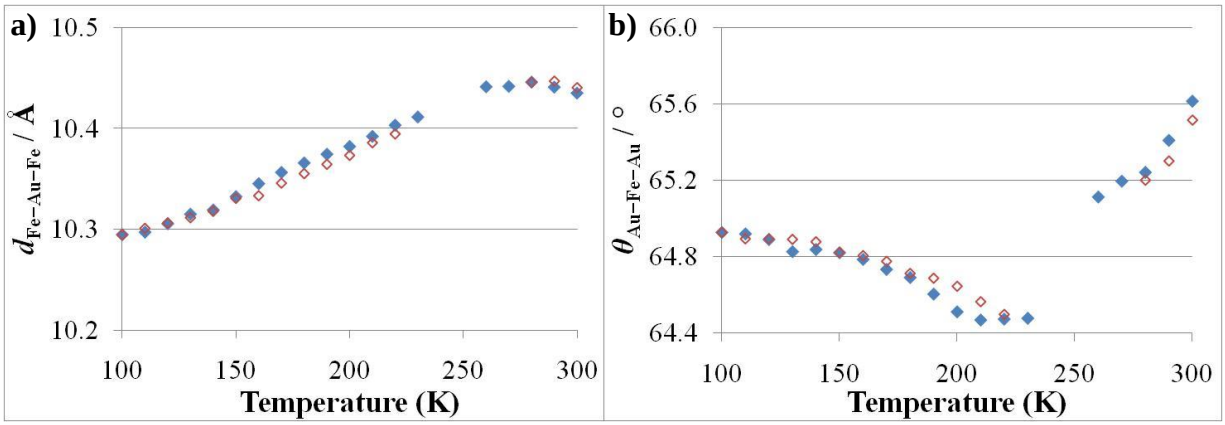

Figure 5-49: Temperature-dependence on: **a)** $d_{Fe–Au–Fe}$, and **b)** $\theta_{Au–Fe–Au}$ in the **Au**·{H_2O} framework upon ◆ cooling and ◇ warming. Values are calculated from the variable temperature unit cell parameters shown in **Figure 5-48**.

Figure 5-50 displays a comparison of the relative stoichiometric fraction of HS states as observed through magnetic susceptibility and powder diffraction, with the latter experiment demonstrated through the change in $d_{Fe–Au–Fe}$. In scaling this distance, the highest value observed in the **Au**·{H_2O} sample was used for the fully HS value (1.0), and the fully LS value observed in the **Au**·{EtOH} sample was used, of 10.10 Å (corresponding to a relative stoichiometric HS fraction of 0.0).

The two analysis techniques display spin transition with similar temperatures and behaviours. However, the calculated quantity from the $d_{Fe–Au–Fe}$ value over most of the spin transition corresponds to a much higher proportion of HS states than is shown by the magnetic measurements. This result is similar to that observed in **Au**·{1-BuOH} (**§5.4.5**), in which frozen solvent severely limits the ability of the framework to adopt the energetically favoured lattice conformation, and the decrease in the $d_{Fe–Au–Fe}$ value is reduced in magnitude. This is observed because the dicyanidoaurate linkers become less distorted, to partially ameliorate the decrease in the average Fe–N_{CN} bond length in the framework.

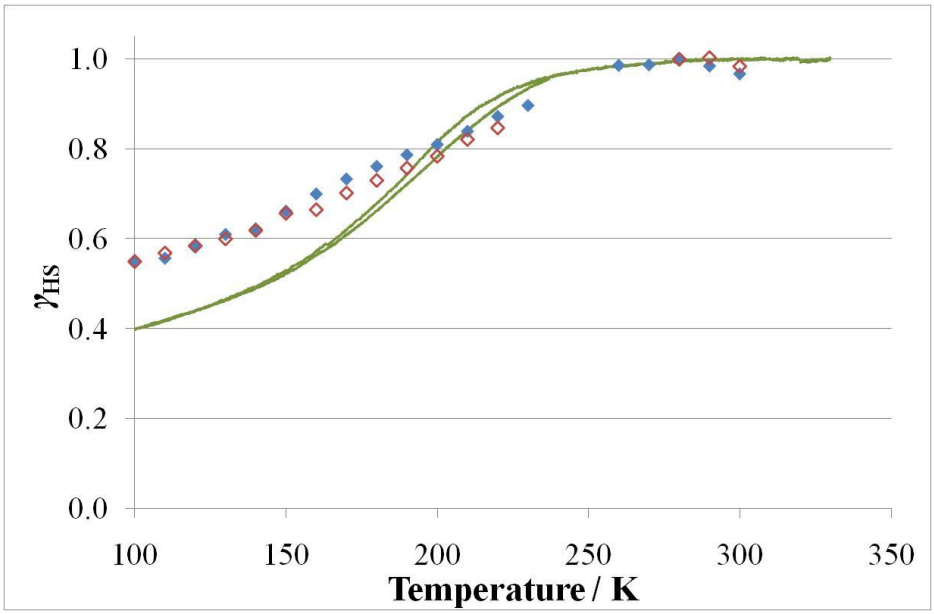

Figure 5-50: Comparison of the temperature-dependence on the relative stoichiometric fraction of HS states (γ_{HS}) in **Au**·{H_2O} as determined by — the magnetic susceptibility; and $d_{Fe–Au–Fe}$ upon ◆ cooling and ◇ warming.

The gradual nature of the transition of **Au**·{H_2O} would be partially due to the conformational limitations imposed on the framework crystallites by the frozen solvent medium. As the H_2O guest and surrounding solvent is frozen over the entire spin transition, there is no temperature at which the flexible framework lattice may adopt a favourable geometry to stabilise the LS state, and an abrupt spin transition is disallowed. Another cause of the gradual transition would be the distorted conformation of the framework lattice, as the decreased rigidity results in a decrease in the ease of communication of spin state through elastic interactions in the framework.

5.6.2 *Acetonitrile*

Acetonitrile (MeCN) is the first solvent species investigated in this thesis which incorporates a non-single bond. The linear geometry of the guest molecule would be expected to produce efficient packing arrangements within the framework pores and lead to interesting spin transition behaviour. Similarly to the **Au**·{1-BuOH} sample (**§5.4.5**), **Au**·{MeCN} displayed behaviour that was dependent on the precise sample environment (see **§7.6** for a thorough description of these sample containers).

As shown in **Figure 5-51**, when contained in the traditional sample tube, the material

displays very unusual spin transition behaviour. Upon cooling, the material undergoes an abrupt partial transition at 261 K, corresponding to the HS-to-LS transition of *ca*. 39% of active SCO Fe(II) sites. From 260 to 237 K the magnetic susceptibility is relatively constant, then between 237 and 144 K it very gradually decreases as *ca*. 24% more Fe(II) sites undergo spin transition. Between 144 and 127 K the material undergoes another relatively abrupt transition, involving the remaining 37% of active Fe(II) sites in the sample. Upon warming, this material shows little variation from the fully LS value until 266 K, at which point the material undergoes a single abrupt LS-to-HS transition. Unfortunately the experiment was terminated before the material could reach the fully HS state, and a second attempt to measure the SCO behaviour of **Au**·{MeCN} gave completely different results. Due to the vastly different transition behaviour observed when cooling and warming the material, there is a very large maximum hysteresis width of 138 K.

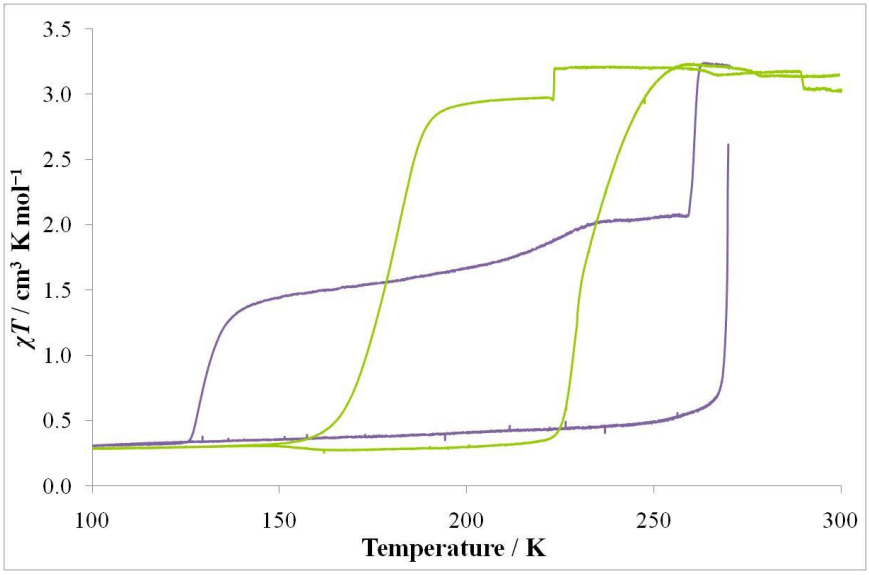

Figure 5-51: Comparison of the variable temperature magnetic behaviour of **Au**·{MeCN} when contained in: — the traditional sample tube, sealed with Teflon® and Vaseline®; and — the developed sample tube (explained in **§7.6**).

When **Au**·{MeCN} is contained within the developed sample tube, the spin transition behaviour is significantly different. Upon cooling from 300 K, there is a small sharp increase in the magnetic susceptibility at 290 K, and other than a minor transition feature at 269 K it stays relatively stable until 224 K, at which temperature the magnetic susceptibility drops abruptly by 0.2 cm^3 K mol^{-1}. It should be noted that this temperature is close to the melting point of MeCN (229 K),[6] and it is likely that this has something to do with the abrupt change

observed. The magnetic susceptibility then remains relatively constant until *ca*. 195 K, at which temperature the material begins full spin transition to the LS state, with $T_{1/2}^{\downarrow}$ = 179 K and a SCO range of 23 K. The warming magnetic data do not show notably unusual behaviour, but simply displays a spin transition with $T_{1/2}^{\uparrow}$ = 232 K and a SCO range of 21 K, producing a large thermal hysteresis width of *ca*. 52 K. In order to confirm that this behaviour was reproducible, the magnetic experiment was cycled twice, and the same magnetic susceptibility curve was obtained.

As with the **Au**·{1-BuOH} results (**§5.4.5**), the likely reason that there were two different behaviours observed for the different sample environments is in the degree of solvation, and quantity of external solvent for the two samples. The traditional sample container was prone to desolvation, and under the experimental conditions of the magnetometer, the framework would lose solvent. The precise solvation characteristics of SCO frameworks have been shown to greatly affect the resulting spin transition behaviour (see **§3.4** for a study on this), and the degree of solvation is thus the most likely candidate to account for the different observed behaviour.

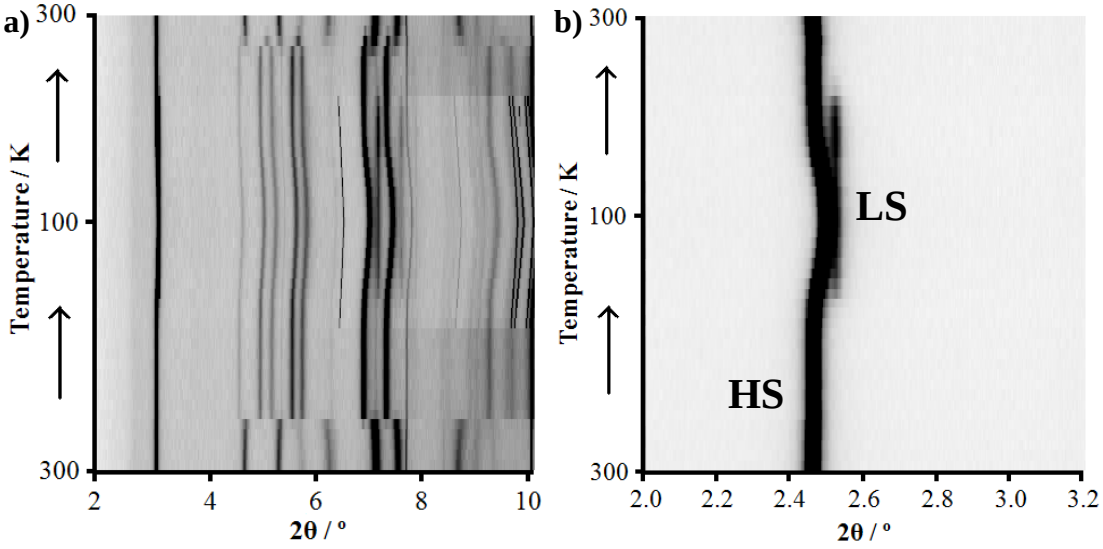

Figure 5-52: Intensity plot showing **a)** the powder diffraction peak evolution within the 2θ range of 2–10°, and **b)** just the (001) peak, as the **Au**·{MeCN} sample was cooled from 300 to 100 K, then warmed back up to 300 K.

A variable temperature powder diffraction experiment at the Australian Synchrotron was used to determine whether features of either magnetic behaviour observed for the

Au·{MeCN} sample might be explained considering the framework lattice behaviour (**Figure C-37**). As shown in the variable temperature intensity plot of the powder diffractograms (**Figure 5-52a**), the cooling structural behaviour of this sample is reflected in the warming behaviour, and there is a phase transition at *ca*. 270 K. Frozen MeCN solvent is observed below *ca*. 210 K. There is the formation of another minority phase below 170 K, which is most clearly seen by close inspection of the (001) peak (**Figure 5-52b**). This new phase is due to the transition of some of the framework crystallites to a more contracted lattice phase, and does not appear to change over the temperature range in which it is present, persisting in the warming data until *ca*. 240 K. The (001) peak of this new phase occurs at 2.52°, which corresponds to a *c*-parameter of *ca*. 13.75 Å, and the new (220) peak occurs at 6.85°, corresponding to a $d_{\text{Fe–Au–Fe}}$ value of *ca*. 10.1 Å. Comparison of these values with previously obtained data (eg: **Au**·{MeOH}, **§5.4.2**) show that this phase displays features that are characteristic of the **Au** framework being almost fully in the LS state.

While the resolution of the minority phase peaks was not sufficient to accurately model a unit cell, a Le Bail model was used to fit the diffraction peaks corresponding to the major **Au** phase, yielding the unit cell parameters shown in **Figure 5-53**. Inspection of the phase change at *ca*. 260 K shows that it occurs only in the *ab*-plane with no significant change in the *c*-parameter, and is due to an abrupt decompression of the metal cyanide grids. Below this temperature, the phase remains stable until 190 K, below which the material undergoes a gradual spin transition, evidenced most clearly in the *c*-parameter (**Figure 5-53c**). The transition is incomplete at 100 K, as the expected *c*-parameter for a fully LS **Au** framework is ~13.66 Å, so the decrease from 14.02 to 13.83 Å in this phase corresponds to a transition of *ca*. 50% of the Fe(II) sites. The warming behaviour closely follows the cooling behaviour, though with a small hysteresis in the spin transition, and a *ca*. 20 K hysteresis in the high temperature phase transition.

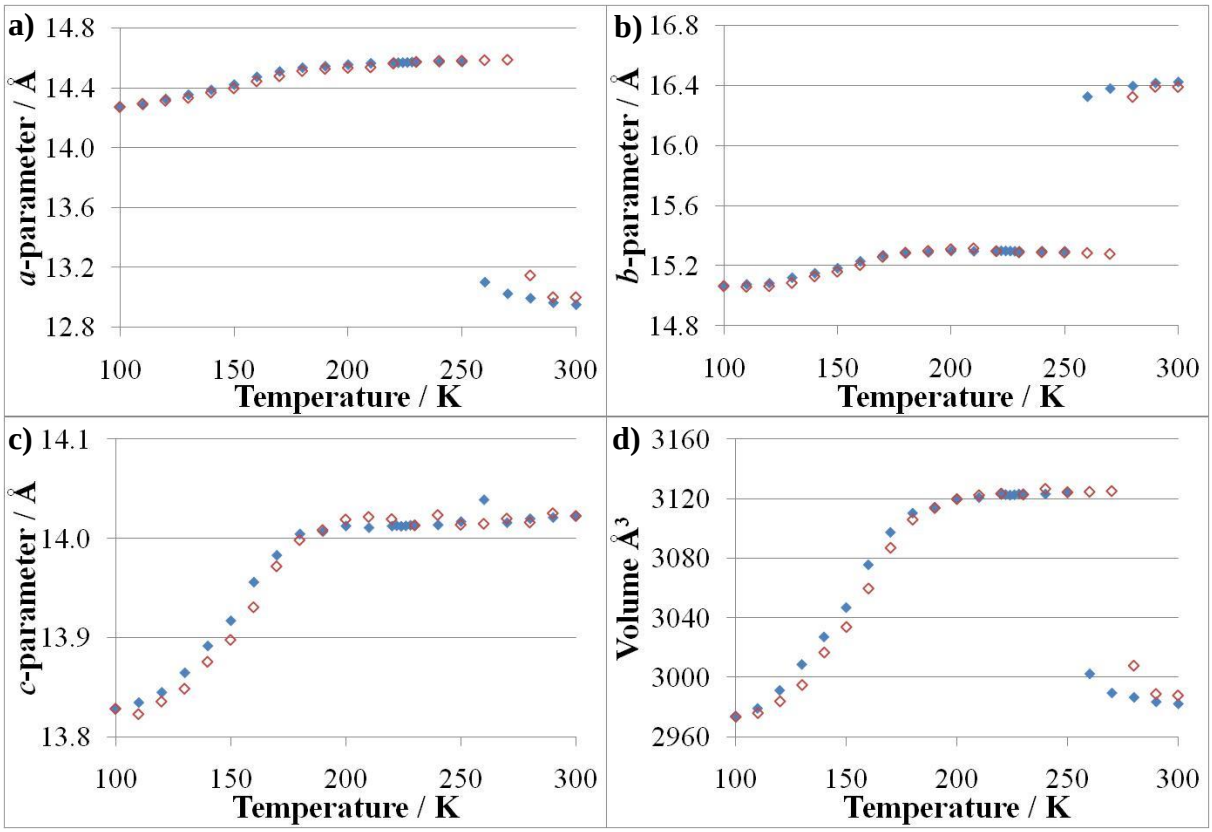

Figure 5-53: Temperature-dependence on the unit cell parameters of **Au**·{MeCN}: **a)** *a*-parameter; **b)** *b*-parameter; **c)** *c*-parameter; and **d)** volume, upon ◆ cooling and ◇ warming. The warming diffractogram at 280 K displayed peaks corresponding to both high and low temperature phases, but the low temperature phase peaks were not of sufficient resolution to accurately model.

As with the other **Au** framework samples, calculation of the $d_{Fe–Au–Fe}$ and $\theta_{Au–Fe–Au}$ values provides useful information regarding the framework lattice conformation. As shown in **Figure 5-54a**, at high temperatures $d_{Fe–Au–Fe} \approx 10.46$ Å, which is similar to that observed for other samples of the **Au** framework in the HS state (eg: **Au**·{EtOH} has a value for this quantity of 10.45 Å, **§4.4.1**). However, below the high temperature phase transition, $d_{Fe–Au–Fe}$ increases significantly to ~10.56 Å, which is higher than any other sample studied. This distance increase would arise from a lengthening of the dicyanidoaurate linkers as they adopt a more rigidly linear geometry and distortion along the linker decreases. Below this phase transition, $d_{Fe–Au–Fe}$ remains relatively constant until *ca*. 190 K, below which this quantity gradually decreases as the framework phase undergoes a gradual spin transition.

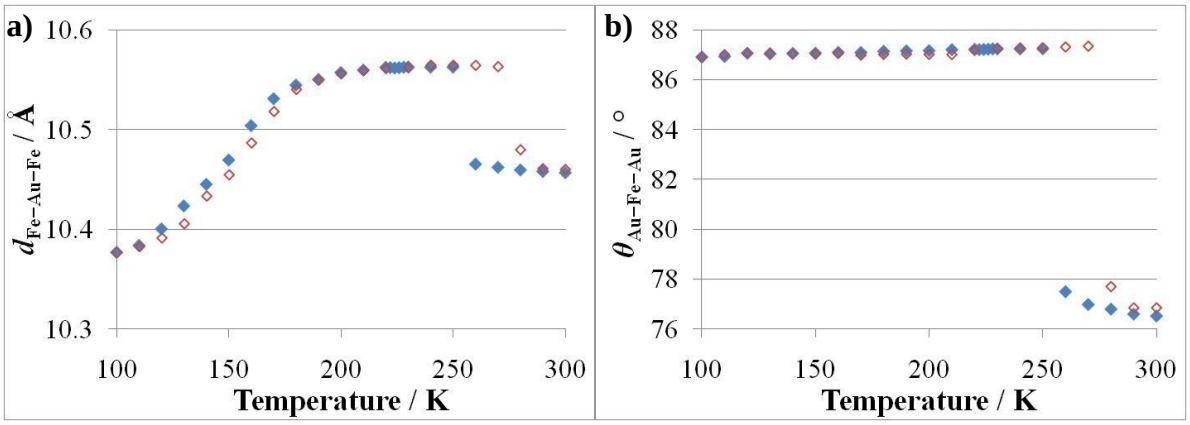

Figure 5-54: Temperature-dependence on **a)** $d_{Fe–Au–Fe}$, and **b)** $\theta_{Au–Fe–Au}$ in the **Au**·{MeCN} framework upon ◆ cooling and ◇ warming. Values are calculated from the variable temperature unit cell parameters shown in **Figure 5-53**.

As well as significantly lengthening the dicyanidoaurate linker below the high temperature phase transition, the **Au**·{MeCN} framework also undergoes a high degree of decompression, evidenced by the large increase in $\theta_{Au–Fe–Au}$ (**Figure 5-54b**). With an acute lattice angle of 87.3°, this sample is one of the most decompressed of all the **Au** samples studied, and is second only to **Au**·{2-BuOH}, which displays a maximum lattice angle of 88.8° (**§5.4.6**). The highly decompressed conformation of the **Au**·{MeCN} framework phase, coupled with the large value of $d_{Fe–Au–Fe}$, produce an increase in the volume of the framework lattice (**Figure 5-53d**) to 3125 Å^3, which is the largest yet observed for the **Au** framework. Below the phase transition, $\theta_{Au–Fe–Au}$ in the **Au**·{MeCN} framework remains constant as the framework undergoes spin transition. This is in contrast to the behaviour observed in other samples of the **Au** framework, which display an increase in this angle quantity as the material undergoes gradual spin transition.

The behaviour observed in the powder diffraction experiment of **Au**·{MeCN} was expected to follow the behaviour observed in one of the magnetic susceptibility experiments. As the behaviour is completely different to that observed in both magnetic experiments, the diffraction experiment was repeated using the in-house powder diffractometer using a fresh sample, to confirm that the original sample was in fact the correct one. The repeat experiment showed the same behaviour as was observed in the experiment undertaken at the Australian Synchrotron.

The observation that the **Au**·{MeCN} material can produce completely different spin

transition behaviours in different sample environments is perplexing, and further investigation is necessary in order to sufficiently explain this variation in the framework properties. However, some clues may be obtained through the minority **Au** phase that was present in the powder diffraction data. This phase is present in the cooling data from *ca*. 170 K, and disappears in the warming data at *ca*. 240 K. This behaviour was similarly observed in the major magnetic spin transition of the **Au**·{MeCN} material contained in the developed sample tube, which displayed transition temperatures of $T_{1/2}^{\downarrow}$ = 179 K and $T_{1/2}^{\uparrow}$ = 232 K. This minority phase also displayed no observable change over the temperature range studied, consistent with the magnetic behaviour, which showed the spin state to remain stable outside of the major transition stages. This comparison leads to the preliminary conclusion that the minority phase observed at low temperature in the powder diffraction experiment is the same phase as was observed in the magnetic results for the sample contained in the developed sample tube.

However, this result does not explain the observation that only a small portion of crystallites in the powder diffraction sample converted to this phase, with the remainder appearing to be trapped in the phase that produces the gradual transition behaviour. This behaviour appears to be dependent on the sample environment, and while the specific effects that produce the observed SCO behaviour are as-yet unknown, certain observations may be made to aid in understanding the origin of the gradual transition observed in the powder diffraction data. As mentioned above, the unit cell volume of this phase when fully HS is 3125 Å^3, which is greater than any other **Au** sample studied. Rough calculations based on the position of the (001) and (220) reflections give *c*-parameter (13.75 Å) and $d_{\text{Fe–Au–Fe}}$ (10.1 Å) values that are similar to those observed in other fully LS framework samples, so the unit cell volume of this phase can be expected to be similar as well (eg: **Au**·{EtOH} has a LS volume of 2740 Å^3 at 100 K). In order to make this phase change, the unit cell volume of **Au**·{MeCN} would need to contract by *ca*. 10%, so it is unsurprising that this phase transition is suppressed when the sample is surrounded by rigid frozen solvent within a highly confined, unyielding sample tube. However, the differences in the sample environment of the powder diffraction and magnetic susceptibility containers are unknown, and further studies are necessary to understand the precise influences from the sample container that produce the different transition behaviours.

The large change in the framework conformation of this phase between the HS and LS states may also be the factor that created the large thermal hysteresis observed in the magnetic data for this sample. Having such different lattice conformations and volumes in the different phases would create a large potential barrier to transition between them, and produce a wide thermal hysteresis for the spin transition.

5.6.3 *Carbon Disulfide*

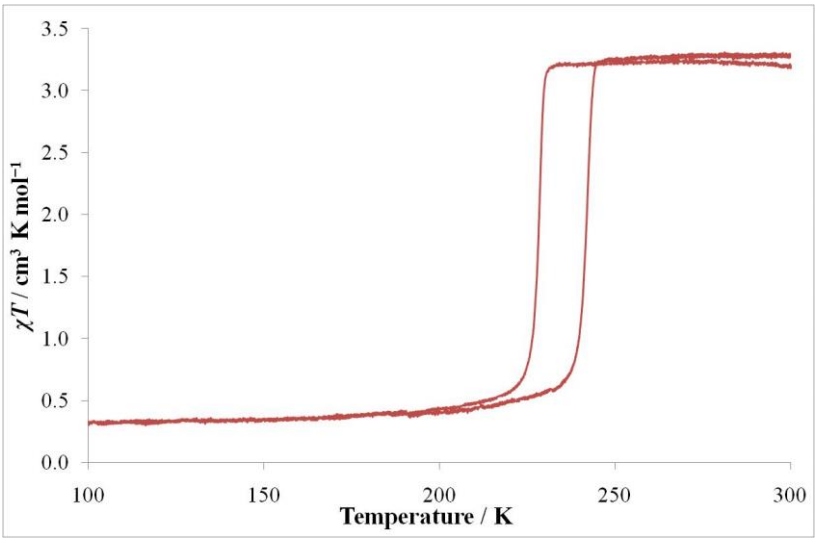

Figure 5-55: Variable temperature magnetic susceptibility data for **Au**·{CS_2}.

A magnetic susceptibility experiment on the **Au**·{CS_2} sample (**Figure 5-55**) displays a typically abrupt spin transition with $T_{1/2}^{\downarrow}$ = 228 K and $T_{1/2}^{\uparrow}$ = 242 K, with a SCO range of 6 K and a thermal hysteresis width of 14 K. This is the highest temperature for a single-step abrupt spin transition observed for the **Au** framework. The spin transition occurs entirely above the melting point of CS_2 (**Appendix D**).

The stabilisation of the LS state in **Au** by CS_2 may be potentially attributed to an increased ligand field strength produced by the guest. There may be interactions between the sulfur atoms of CS_2 guest and the gold(I) atoms in the dicyanidoaurate linkers. These interactions may result in donation of electron density from the CS_2 molecules to the metalloligands, which would in turn increase the electron donation strength of the ligand to the Fe(II) sites, resulting in stronger Fe–N bonds, a stronger ligand field, and stabilisation of the LS state. Due to the sensitivity of SCO to subtle changes in the ligand field strength, even a very slight electron-donation effect from the host–guest interaction would produce an observable

difference in the spin transition behaviour.

Au·{CS_2} also displays highly cooperative behaviour, evidenced by the abrupt transition with relatively large thermal hysteresis width. As shown in **Appendix D**, CS_2 has a low viscosity, which implies that rearrangement of guest within the pores would be facile, allowing an abrupt, cooperative transition.

5.7 *Comparison of Specific Solvent Behaviours*

As shown above, there are many different magnetic and structural behaviours displayed by the **Au** framework when it is solvated with different guest species. There are several broad categories into which the different transition behaviours may be placed, which facilitates comparison and discussion of the potential factors that determine the observed behaviour.

The *abrupt* spin transition category (**Figure 5-56**) includes samples which produce a single-step SCO with SCO range < 10 K. The spin transition parameters occur in the ranges $211 < T_{1/2}{}^{\downarrow} < 228$ K and $218 < T_{1/2}{}^{\uparrow} < 242$ K, with hysteresis widths of 6–16 K. Of these samples, the structural behaviour of only the **Au**·{EtOH} sample was determined, which demonstrates that the framework crystallites undergo a fully abrupt structural transition which accompanies the spin transition, and both HS and LS phases were modelled in the *Cmma* space group. Considering the similar transition behaviour of these samples, it can be assumed that they would also display similar structural behaviour. The differences in their specific spin transition properties must then be primarily due to host–guest effects within frameworks with non-distorted structural topologies.

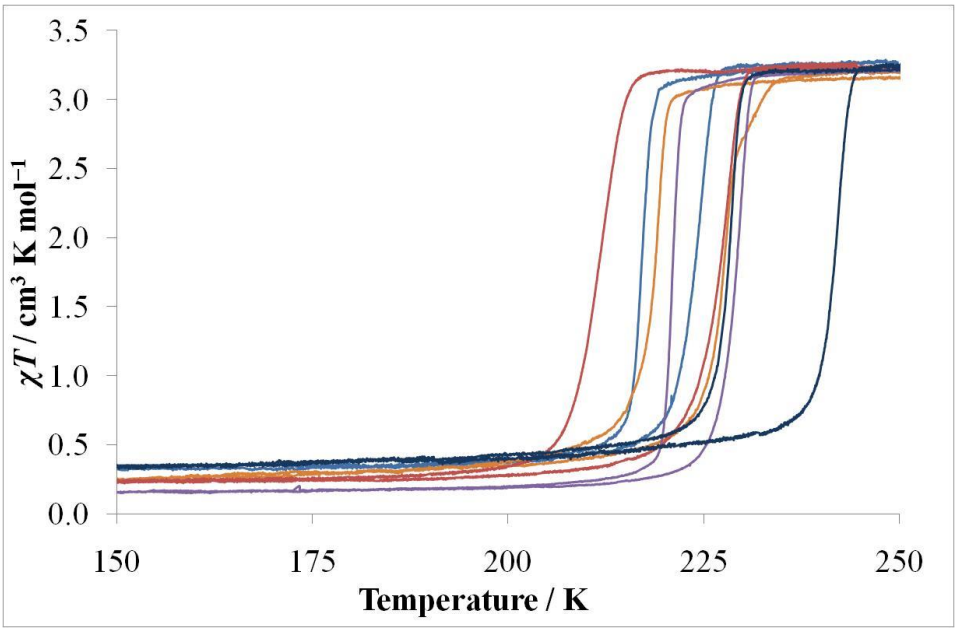

Figure 5-56: The '*abrupt*' spin transition category of **Au**, produced when solvated by the guests: EtOH, MeBrCl, 1:1 $MeCl_2$/MeBrCl, EtBr, and CS_2.

The *gradual* category (**Figure 5-57**) is characterised by single-step transitions that occur with SCO range > 80 K. These samples undergo transition with 149 < $T_{1/2}^{\downarrow}$ < 185 K, hysteresis widths in the range 0–8 K, and SCO ranges between 92 and 127 K. Of these samples, the **Au**·{H_2O} and **Au**·{1-PnOH} samples begin spin transition below the melting point of the included solvent, and all other samples begin spin transition above the solvent melting point. The **Au**·{H_2O} and **Au**·{2-BuOH} samples display distortion of the framework lattice at all temperatures, with a non-orthogonal linkage of the bpac ligand between adjacent Fe centres, but due to resolution limitations the **Au**·{H_2O} sample was modelled using a unit cell with orthorhombic *Cmma* space group symmetry. The **Au**·{1-BuOH} sample displays an orthogonal unit cell in the HS phase that was trapped at low temperature by the frozen solvent medium, but when the solvent melts upon warming the framework undergoes a structural transition to a more distorted cell, similar to that shown by the **Au**·{H_2O} and **Au**·{2-BuOH} samples. All these samples demonstrate a gradual structural transition to the LS phase, with a continuous change in the unit cell parameters over the transition temperature range.

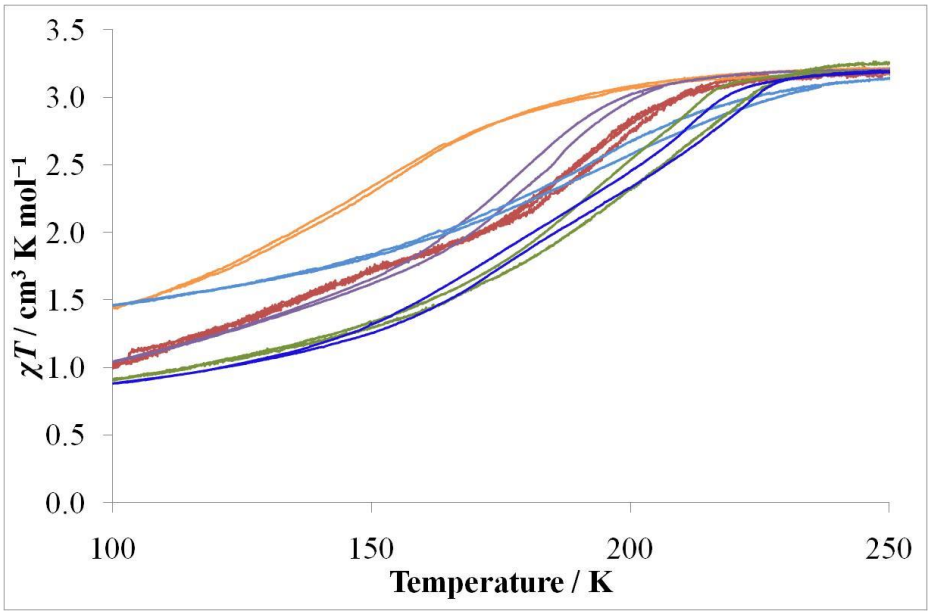

Figure 5-57: The '*gradual*' spin transition category of **Au**, produced when solvated by the guests: H_2O, $MeCl_2$, EtI, 1-BuOH, 2-BuOH, 1-PnOH.

The *gradual-to-abrupt* category (**Figure 5-58**) is characterised by a transition that occurs at high temperature with a relatively gradual slope without hysteresis, then once a threshold quantity of iron sites have undergone HS-to-LS transition, the rest of the active SCO centres in the sample undergo abrupt transition to the LS state. The **Au**·{MeOH} sample displays a distorted bpac linker coordination in both HS and LS states, which was determined from a doubling of the unit cell and effective decrease in the *c*-axis dimension as the lattice adopts a slight 'accordion-like' buckling conformation of the bpac ligands. In contrast, the **Au**·{1-PrBr} sample retains an orthorhombic unit cell above and below the spin transition, but over the gradual stage of the spin transition the powder diffraction patterns were best fit using a monoclinic *C*2/*m* unit cell, in which the bpac coordination was distorted away from the normal orthogonal geometry.

The structural behaviour of the **Au**·{MeOH} and **Au**·{1-PrBr} samples demonstrate that the gradual transition stage of this spin transition category occurs with a distorted framework lattice conformation. This result is consistent with the elastic theory of cooperativity in SCO materials, such that a decrease in the rigidity of linkages between SCO centres leads to a reduction in the communication of spin state between them, and thus decreased cooperativity.[7] The distorted bpac coordination in these framework samples decreases the coordination rigidity, producing this effect. However, the major difference between these two

samples is that the **Au**·{MeOH} material retains the distorted coordination in the HS and LS states and over the spin transition, whereas the **Au**·{1-PrBr} material only has this distortion over the gradual spin transition stage. These two different structural mechanisms are likely to be due to different solvent packing and internal pressure effects in the two materials.

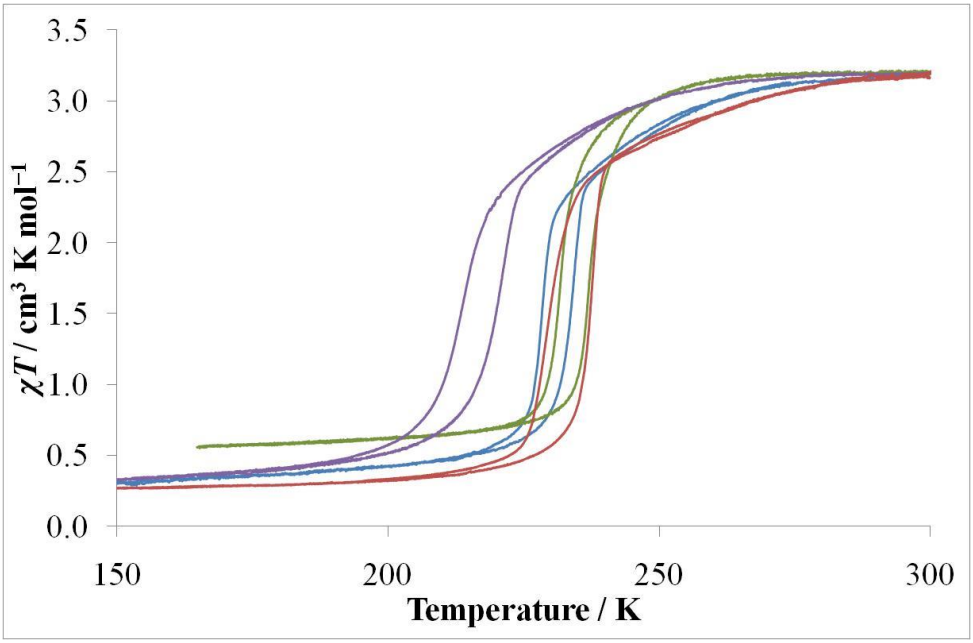

Figure 5-58: The '*gradual-to-abrupt'* spin transition category of **Au**, produced when solvated by the guests: MeOH, 1-PrBr, 1-PrI, 1:1 1-PrBr/1-PrI.

The *multistage* category (**Figure 5-59**) contains samples which demonstrate spin transition with more than one distinct transition stage, which do not display the *gradual-to-abrupt* behaviour displayed in **Figure 5-58**. The **Au**·{1-PrOH} behaviour is unusual, as the spin transition occurs below all other alcohols studied, and is gradual even though the powder diffractograms were modelled in the orthorhombic *Cmma* space group, implying that there is no distortion of the bpac ligand coordination in this sample. It is possible that the two-stage behaviour is due to freezing of the 1-PrOH solvent, but another contributing factor could be different energetic minima in the solvent packing behaviour that result from the *trans* and *gauche* conformers which the guest molecule can adopt. Without much further study into these samples, it is believed that this is the major source of the multiple stages in the transition behaviour of all those samples shown in **Figure 5-59**: that there are multiple potential solvent packing conformations which may occur locally within the framework crystallites, leading to different spin transition properties of the nearby Fe(II) centres.

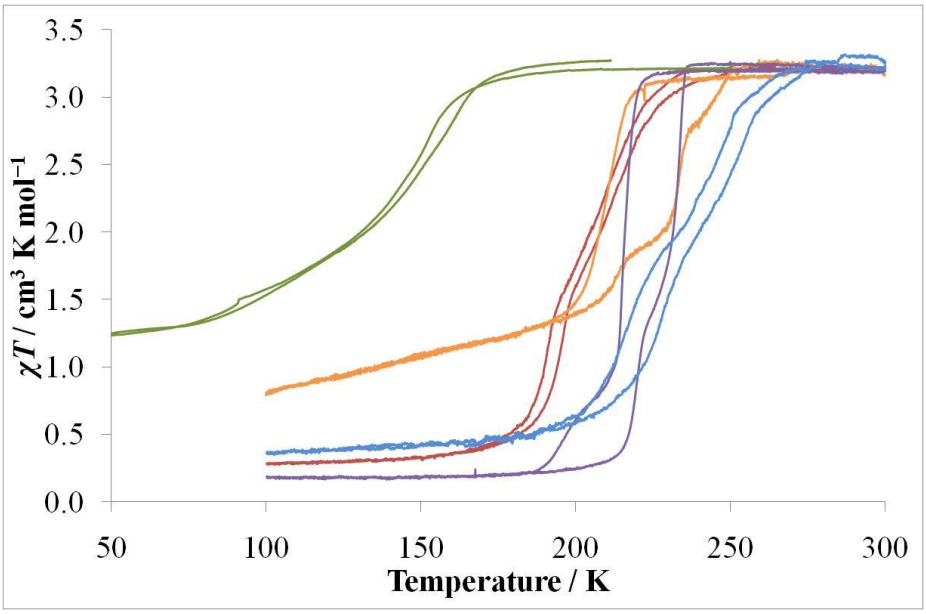

Figure 5-59: The '*multistage*' spin transition category of **Au**, produced when solvated by the guests: — 1,2-$EtCl_2$, — 1,2-$EtBr_2$, — 1-PrOH, — 1:1 EtBr/1-PrCl, and — 1:1 MeOH/EtOH.

The *solvent-free* category (**Figure 5-60a**) includes those samples which do not contain solvent guest, such that host–guest interactions do not play a significant role in determining the framework behaviour. The spin transition properties then result from the framework alone, and the major difference between the **Au**·{Ø} and **Au**·{N_2} materials was the external pressure on the samples. Both these samples have highly compressed lattice conformations in the HS phase, and were modelled in the *Pbaa* space group. Transition to the LS phase results in significant decompression in both, producing a net increase in the volume, and a structure with *Cmma* space group symmetry. The higher temperature spin transition of **Au**·{N_2} may be attributed to the increased pressure under which the sample was measured, which stabilises the LS state.

The **Au**·{MeCN} and **Au**·{1-PrCl} were placed in the *miscellaneous* category (**Figure 5-60b**) as they did not properly fit into any of the other categories. **Au**·{1-PrCl} displays a transition that is less abrupt than those displayed in **Figure 5-56**, with a SCO range of 31 K, but it also displays a relatively large hysteresis width of 13 K. It is possible that the less abrupt nature of the transition is due to the larger size of the 1-PrCl guest, which would produce a greater internal pressure effect as discussed in **§3.3.2.2**. Another potential source of the more gradual transition could be a range of different solvent packing behaviour within the

framework pores: depending on the relative proportion of *trans* and *gauche* conformers of the 1-PrCl molecules, there may be regions within crystallites, or even whole crystallites, which have different internal pressure effects from the guest molecules, leading to different spin transition behaviours.

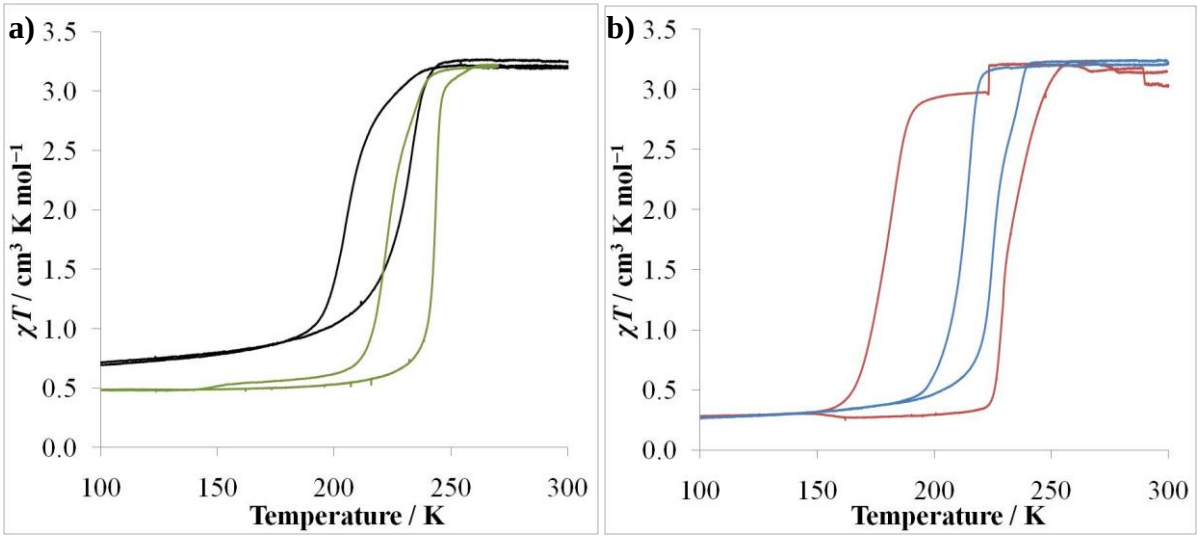

Figure 5-60: a) The '*solvent-free*' spin transition category, produced by: — **Au**·{Ø}, and — **Au**·{N_2}; and **b)** The '*miscellaneous*' spin transition category, for samples which do not properly fit into any other category: — **Au**·{MeCN}, and — **Au**·{1-PrCl}.

The **Au**·{MeCN} sample also displays a less abrupt transition with a SCO range of 28 K, but with a very large hysteresis width of *ca*. 52 K. The powder diffraction data was confusing as the majority of the sample demonstrates structural behaviour that did not at all correlate with the magnetic data, with only a minor phase providing evidence for behaviour which corresponded to that which was observed in the magnetism. The large hysteresis observed in this sample is likely to arise from the large difference in the HS and LS lattice conformations (see **§5.6.2** for a full discussion). This would create a high potential barrier to transition between the two states, generating the wide thermal hysteresis observed.

5.8 *Discussion*

There is a strong synergistic effect between the SCO, the structural behaviour and the guest effect of the **Au** framework. The flexible framework lattice may adopt a range of conformations which affect and are affected by the spin transition, and the host–guest interactions with adsorbed guest species.

Structurally, the **Au** lattice demonstrates a wide variety of compression states in the cyanide grid, as well as variable degrees of distortion in the dicyanidoaurate linkers away from a linear coordination. In some cases, the framework also demonstrates distortion of the bpac linker away from an orthogonal coordination between adjacent Fe(II) centres. The precise framework conformation appears to have a strong dependence on the solvent packing behaviour, and the subsequent internal pressure effect on the framework lattice. It was also observed that the LS framework phase has a strong energetic preference toward a decompressed lattice, due to the influence of the more rigidly octahedral coordination environment of the LS Fe(II) centres, and the more linear conformation of the dicyanidoaurate linkers between these centres.

In the absence of solvent guest molecules to fill the pores, the framework adopts a highly distorted lattice conformation in the HS state, as the **Au**·{Ø} (**§5.2**) and **Au**·{N_2} (**§5.3**) samples demonstrate. In order to maximise packing efficiency in this conformation, the pyridyl rings of the bpac ligands lie perpendicular to one another and the aurophilic interactions between the adjacent nets are distorted, producing a unit cell with *Pbaa* space group symmetry. This conformation is energetically favoured due to the resulting internetwork interactions between the ligands in the two nets, as shown in **§4.2.3**. Upon transition to the LS state, the framework lattice undergoes significant decompression due to the more rigidly octahedral LS Fe(II) centres, and the dicyanidoaurate linkers adopt a conformation that is closer to a linear geometry, as explained in **§1.4.5**. These two factors produce a net increase in the lattice volume and the framework undergoes the HS-to-LS transition.

The strong guest dependence and flexibility of the **Au** framework were effectively demonstrated by the **Au**·{alcohol} series. The properties and solvent packing of the MeOH guest led to an effective compression along the *c*-axis, while retaining the orthorhombic *C*-centred symmetry of the **Au**·{EtOH} framework. It was determined that this effect in the **Au**·{MeOH} sample arose due to an accordion-like distortion of the bpac linkers away from an orthogonal pillar coordination. The **Au**·{EtOH} and **Au**·{1-PrOH} samples were both modelled with orthorhombic *Cmma* symmetry at all temperatures studied, but while the **Au**·{EtOH} sample displays an abrupt, cooperative spin transition, the **Au**·{1-PrOH} sample displays a gradual, uncooperative transition at low temperature. The HS phase of

Au·{1-BuOH} was also modelled with an orthogonal lattice modelled in the *Cmma* space group, but the energetically favoured LS phase lost the orthorhombic symmetry, and was instead modelled with the monoclinic *C*2/*m* space group, indicating a non-orthogonal coordination of the bpac pillar. The **Au**·{2-BuOH} sample was modelled in a triclinic unit cell with base-centred pseudosymmetry, in which the *c*-axis was distorted between the *a*- and *b*-axes, giving non-90° α- and β-angles. The distorted phases of both **Au**·{1-BuOH} and **Au**·{2-BuOH} were observed to be highly decompressed, with $\theta_{\text{Au–Fe–Au}}$ values that were close to 90°. From these results, it appeared that there is an optimum guest size and shape that would result in a framework with the orthogonal *Cmma* symmetry, which is satisfied by the EtOH and 1-PrOH guest species. The MeOH guest is too small and causes a symmetrical distortion of the lattice, while the 1-BuOH and 2-BuOH guests are too big, and result in an asymmetric distortion of the lattice.

The **Au**·{H_2O} sample also demonstrates distortion of the bpac ligand coordination, though the data resolution was not sufficient to accurately model this distortion, so it was instead modelled using the *Cmma* space group. Interestingly, the $\theta_{\text{Au–Fe–Au}}$ value of this sample lay in the range 64–66°, unlike the near-90° values of the **Au**·{1-BuOH} and **Au**·{2-BuOH} samples, so the degree of lattice compression and framework distortion are not simply correlated. The H_2O guest would be expected to produce a high density of strong hydrogen bonds, with potential weak coordination of guest molecules to the Au atoms in the dicyanidoaurate units. It is possible that the framework lattice of this sample was distorted to best accommodate the strong guest–guest interactions and solvent packing within the framework pores.

It was observed that distortion in the bpac coordination produces gradual spin transitions in this framework. This was also displayed by the **Au**·{1-PrBr} sample, which was modelled in the distorted monoclinic *C*2/*m* space group over the gradual spin transition stage. In general, larger or more bulky guests produce a more decompressed lattice conformation with a larger volume, and partially stabilised the HS state due to increased internal pressure from the guest molecules.

The strong dependence on the precise sample environment and degree of solvation was best observed in the **Au**·{1-BuOH} sample, which displays many different spin transition behaviours. **Au**·{MeCN} also demonstrates this effect, and there is only marginal powder

diffraction evidence to support the behaviour observed in the magnetic experiment. The very large hysteresis shown in the magnetic susceptibility data is likely to be due to the significant difference in the lattice conformations of the HS and LS states, which would produce a large potential energy barrier to transition between the two phases.

Guests which may adopt multiple conformations produce multiple spin transition stages when included in the **Au** framework. Importantly, the 1,2-EtX_2 (X = Cl, Br) and 1:1 EtBr/1-PrCl guest species display multi-step behaviour, which could be attributed to multiple guest packing behaviours within crystallites, which produce different local pressure effects on the framework, and thus change the spin transition behaviour of nearby Fe(II) sites.

The sheer variety of structural and magnetic behaviour in the **Au** framework and the strong dependence on adsorbed guest species make this framework of intense interest for studying the dynamic interplay between these properties. The magnitude of the lattice conformation changes is unprecedented, and the potential to vary this extraordinary material behaviour depending on adsorbed guest and the related spin transition provides a tool to probe the subtle contributing influences on the behaviour. Through such detailed investigations into the framework properties and determination of the specific structural and environmental factors, it may be possible in the future to use rational design to tune the properties of this framework and related materials.

References

(1) Fellows, E. A. PhD Thesis, University of Sydney, 2011.
(2) Lev, D. G.; Gubbins, K. E.; Radhakrishnan, R.; Sliwinska-Bartkowiak, M. *Reports on Progress in Physics* **1999**, *62*, 1573.
(3) 2-butanol, http://webbook.nist.gov, **2012**, (accessed on July 30, 2012)
(4) Ben-Amotz, D.; Willis, K. G. *The Journal of Physical Chemistry* **1993**, *97*, 7736.
(5) Lee, I. C.; Hamaguchi, H.-O.; Shigeto, S. *Chemical Physics Letters* **2008**, *466*, 144.
(6) Lide, D. R. *CRC Handbook of Chemistry and Physics*; 84 ed.; CRC Press: Boca Raton, FL, USA, 2003-2004.
(7) Hauser, A.; Jeftic, J.; Romstedt, H.; Hinek, R.; Spiering, H. *Coord. Chem. Rev.* **1999**, *190-192*, 471.

Chapter 6: Concluding Remarks and Future Work

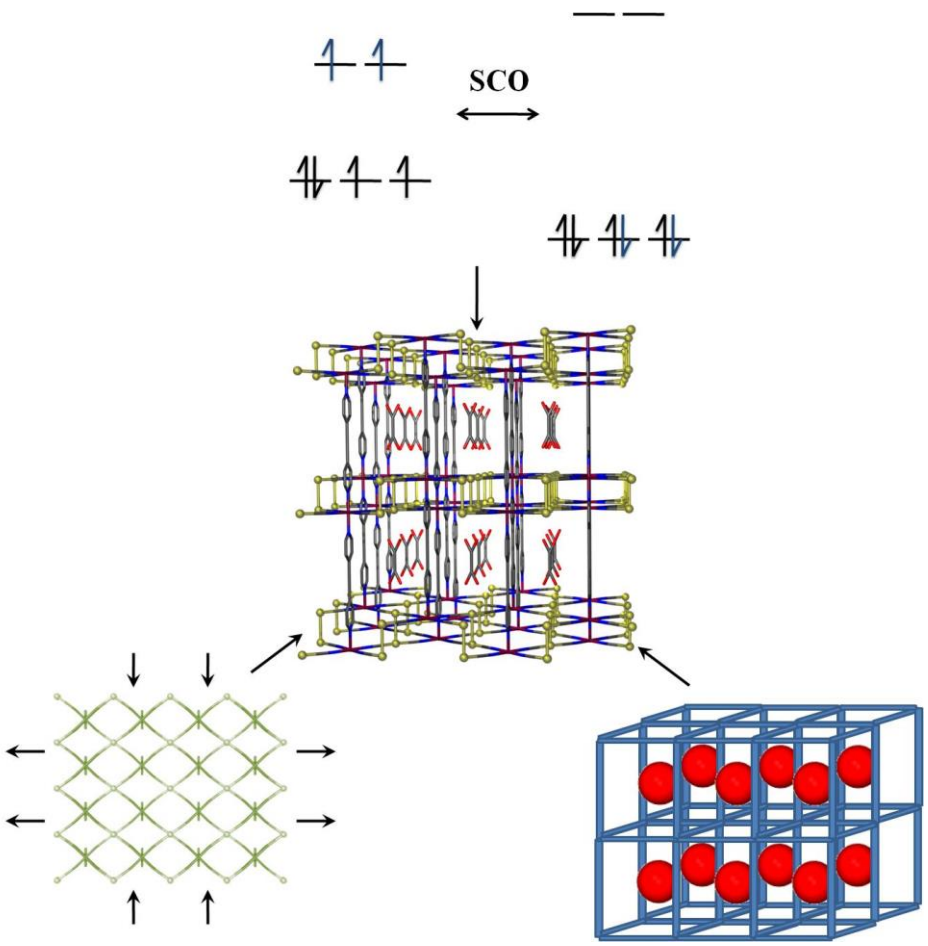

Multifunctional materials are a major goal in chemistry, and the [Fe(bpac)($Au(CN)_2$)] framework exhibits the properties of spin crossover, anomalous thermal expansion, and guest-dependence through its robust porosity.

6.1 *Hofmann Series*

The [Fe(bpac)M(CN)$_4$]·*x*(bpac){solvent} (M = **Ni**, **Pd**, **Pt**; *x* = 0.4, 0.5) framework series has been shown to exhibit significant guest-dependent variation in the spin transition properties of the materials. These frameworks incorporated degrees of freedom in both the quantity of occluded bpac guest, and the type and quantity of adsorbed solvent guest, which both affected the spin transition.

Through analysis of the crystal structure of **Pd** and **Pt**, it was determined that the maximum physically reasonable quantity of bpac guest that could reside within the framework pores would be 0.5 molecules per formula unit of the framework. This was due to the relative proximity of the two disordered bpac guest molecule positions along the *c*-axis direction, which were too close for both positions to be occupied simultaneously.

The relative spin transitions of the **M·0.5(bpac)**{EtOH} (**M** = **Ni**, **Pd**, **Pt**) series were determined to arise primarily through steric effects from the occluded bpac guest molecules and the atomic radii of the framework co-metal. It was also observed that in the **Pd** single crystal, in which the *a*- and *b*-parameters were very similar, the crystal exhibited a significant degree of merohedral twinning. The near-tetragonal symmetry of the lattice influences the octahedral coordination environment of Fe(II) to become closer to an orthogonal geometry, thus stabilising the LS state through more efficient ligand–metal orbital overlap.

The **Pd·*x*(bpac)**{1-alcohol} (*x* = 0.4, 0.5) solvated framework series demonstrated similar trends as was observed for the [Fe(pyrazine)M(CN)$_4$]{1-alcohol} (M = Ni, Pd, Pt) series: that a longer alcohol chain produced spin transition at a lower temperature.[1] This trend was explained as arising from a more pronounced internal pressure effect between the longer alcohol guests and the host framework, which produce an enthalpic barrier to spin transition, stabilising the HS state. The kinetic volume and relative compressibility of the guest were also used to explain the more gradual spin transitions produced by longer alcohol guests. Another potential source of the gradual transition of longer alcohol guests could be from a greater number of potential guest conformations in the pores, which may create heterogeneous local environments around the Fe(II) centres, in turn producing a range of spin transition temperatures and an overall gradual SCO behaviour. The exception to this trend was observed in the **Pd·*x*(bpac)**{MeOH} samples, which produced spin transitions at a lower

temperature than the **Pd·*x*(bpac)**{EtOH} samples. This behaviour was attributed to solvent packing behaviour, which was believed to be more efficient in the **Pd·*x*(bpac)**{MeOH} sample, as the small MeOH guest may adopt a packing conformation that maximises guest–guest hydrogen-bonding and increased quantity of adsorbed guest, leading to a greater internal host–guest repulsion effect, which would stabilise the HS state and decrease the cooperativity of the transition.

The **Pd·0.4(bpac)**{1-PnOH} sample demonstrated a very large hysteresis width, with a relatively gradual, two-stage transition. The two-stage behaviour of the transition was partially attributed to the heterogeneity of the sample composition, which would give rise to multiple SCO behaviours. The unit cell model determined for this sample included axis parameters that were doubled compared to the **Pd·0.4(bpac)**{EtOH} sample, and used the *Immm* space group. In this unit cell model, the asymmetric unit increased by a factor of four and thus contained four crystallographically independent Fe(II) sites. A secondary explanation for the unusual two-stage spin transition behaviour observed in the magnetic experiment was given as arising due to the multiple distinct Fe(II) sites in the framework. The large hysteresis was attributed to host–guest interactions, guest mobility and the significant difference in the lattice dimension of the HS and LS states, which would introduce a larger energetic barrier to spin transition.

By obtaining a variety of EtOH adsorption isotherms and isobars, a Temperature-Pressure phase diagram of SCO was obtained for the **Pd·0.4(bpac)** material, depending on solvation of the framework with EtOH. It was shown that at higher pressures, the bistability range increased and the transition temperature decreased. A plot of the spin transition dependence on the quantity of adsorbed EtOH demonstrated that increasing the quantity of EtOH guest in this framework leads to increased bistability and decreased transition temperature, presumably due to the subsequent increase in host–guest interactions.

Due to the great versatility of this framework family to modification, there is a proportionally large variety of potential future studies which may be performed on it. Directly following the results reported here, further systematic solvent studies would provide more information about the guest effect on the spin transition and structural properties of the framework. Completing the **Pd·0.5(bpac)**{1-alcohol} series and comparing the results with the **Pd·0.4(bpac)**{1-alcohol} data would assist in explaining the origin of the framework

behavioural dependence on bpac guest concentration. Systematically investigating other solvent families, such as the halogenated alkanes, would provide additional information on the guest effect in this framework, such as the role of guest size and shape, and solvent packing behaviour. Repeating the EtOH adsorption isotherm/isobar experiments using the **Pd·0.5(bpac)** material would give much cleaner, reproducible results due to the homogeneous sample composition.

Real has already undertaken studies of the SCO dependence on the bpac guest concentration,[2] but a more comprehensive study on the solvent guest-dependent behaviour of the framework in conjunction with different bpac guest concentrations would be expected to produce interesting properties, and provide useful information about the nature of SCO in porous coordination framework materials, such as the influence of pore size. Real has performed preliminary investigations into the effect of incorporating different aromatic guests within the pores of $[Fe(dpe)Pt(CN)_4]\cdot 0.5(dpe)$ (dpe = *trans*-1,2-di(4′-pyridyl)ethylene), replacing the guest dpe.[3] A systematic study on the cooperative effect of occluded aromatic molecules and solvent guests in the $[Fe(bpac)M(CN)_4]\cdot x(bpac)$ (M = Ni, Pd, Pt) frameworks would yield interesting behaviours, and provide more information on the guest-dependent nature of the spin transition in these materials. It was recently reported in the $[Fe(pyrazine)M(CN)_4]$ (M = Pd, Pt) frameworks that thiourea guest produces hysteresis widths of up to 64 K near room temperature.[4] It would be interesting to see the effect of this guest on the transition properties of the $[Fe(bpac)M(CN)_4]\cdot x(bpac)$ (M = Ni, Pd, Pt) framework family.

An experiment that investigates the effect of mixing the co-metal (eg: synthesis with a 1:1 mix of $[Ni(CN)_4]^{2+}/[Pd(CN)_4]^{2+}$) could provide information about the SCO dependence on the framework dimension and the importance of absolute structural homogeneity of the lattice.

There are many potential pillar ligands which could produce interesting spin transition behaviour when incorporated in a Hofmann-type framework. Based on the results presented in this thesis, the most promising ligand as a pillar in such frameworks would be 1,4-bis(4′-pyridyl)butadiyne (bpbd, **Figure 6-1**). This ligand is wholly analogous to the bpac ligand used in this thesis, but with a greater length provided by the additional acetylene unit between the pyridyl rings. While the bpac pillar was not of sufficient length to allow full occupancy of the bpac guest within the **M·*x*(bpac)** (**M** = **Ni**, **Pd**, **Pt**) framework pores, the length of the

bpbd pillar would be sufficient to allow an aromatic guest to occupy both potential pore positions along the *c*-axis parallel to the pyridyl rings of the bpbd ligands. This increased potential for aromatic guest occupancy could increase the influence of long-range elastic interactions within the framework mediated by aromatic stacking interactions between the guest and bpbd linkers, which could increase the framework cooperativity, and potentially produce a greater bistability. Depending on the concentration of aromatic guest molecules, the longer pillar may also enable increased adsorption of solvent guest, producing a more pronounced guest-dependent effect.

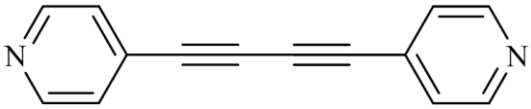

Figure 6-1: Potential ligand for incorporation into SCO pillared Hofmann-type frameworks, 1,4-bis(4′-pyridyl)butadiyne (bpbd).

It appears that once a bidentate pillar ligand in a Hofmann-type framework exceeds a particular length, the resulting pore dimension allows incorporation of the pillar molecule as a guest within the framework. This guest is stabilised due to energetically favourable parallel aromatic stacking interactions. Unfortunately, this unbound aromatic guest has also been shown to produce an internal pressure effect on the framework, stabilising the HS state. If a method could be developed that can remove this guest from the framework pores without compromising the structural integrity of the framework lattice, it is expected that the HS state would not be stabilised to such an extent, and spin transitions at higher temperature may be possible, at least in the desolvated framework.

A potential method for producing the solvent-free framework could involve a similar procedure as was used by Real to form single crystals of the $[Fe(dpe)Pt(CN)_4]\cdot n$G (G = phenazine, anthracene, naphthalene) species:[3] If the synthesis solvent contains a large molar excess of benzene (or another small, non-coordinating aromatic molecule with a high vapour pressure), this molecule would be expected to occupy the framework pores instead of bpac molecules. One molar equivalent of bpac and a large excess of benzene would be necessary and the synthesis should be left to react for a while, potentially with mild heating, so that the desired thermodynamic product may be produced with full occupancy of the bpac pillar ligand and benzene molecules lying within the pores. The benzene guest may then be

removed using relatively mild heating and vacuum conditions, leaving the guest-free framework. Once the guest-free framework is obtained, the degree of bpac or other aromatic guest occupancy may be carefully controlled by exposing the framework to the desired molar equivalent of the aromatic guest dissolved in an appropriate solvent.

6.2 *Interpenetrated Framework*

The **Au** framework demonstrated unprecedented multifunctional behaviour, and displayed a synergistic interplay between the SCO, lattice structure and host–guest properties. The flexibility of the framework lattice arises from the facile scissor-type motion of the $\{Fe(Au(CN)_2)_2\}$ (4,4)-grids, and the precise grid geometry is determined by weak inter-network and host–guest interactions. Importantly, as the framework undergoes transition to the LS state, the coordination environment of the Fe(II) sites becomes more rigidly octahedral, and distortion in the coordination geometry of the dicyanidoaurate units decreases as the linker becomes more linear. These effects result in decompression of the framework lattice.

Compressive/decompressive behaviour may also occur independently of spin transition, and appears to be caused by a dynamic balance between inter-network and host–guest interactions. This balance is affected by thermal vibrations of the framework and guest molecules, and there is thus a temperature dependence on the framework lattice geometry. Furthermore, the compression state of the lattice affects the amount of guest that may adsorb into the framework pores due to the resulting change in solvent accessible volume. This difference in the amount of adsorbed solvent may then affect the spin transition and structural properties of the material due to the subsequent change in the host–guest interactions and the internal pressure effect on the framework lattice.

The extreme magnitude of the framework flexing behaviour was clearly observed in the **Au**·{EtOH} sample. As this material underwent the HS-to-LS transition, the *a*- and *b*-parameters changed by *ca.* 0.8 and −1.4 Å respectively, and below the spin transition the *a*-parameter demonstrated a maximum thermal expansion coefficient of -1070×10^{-6} K^{-1}. This value is an order of magnitude greater than any yet reported for this quantity.

Guest-dependent studies on the **Au** framework have demonstrated the strong effect of guest properties on the lattice compression state, distortion of the dicyanidoaurate linkers, as well

as distortion of the bpac linker away from an orthogonal coordination between the adjacent Fe(II) centres. The precise framework conformation appears to depend on the solvent packing behaviour, and the subsequent internal pressure effect on the framework lattice.

In the desolvated state, the HS **Au** lattice adopts a highly compressed, distorted conformation with a unit cell in the *Pbaa* space group, while the more decompressed LS lattice of the desolvated framework was solved in the *Cmma* space group. Interestingly, the change in lattice conformation results in a net increase in the lattice volume over the HS-to-LS transition.

In addition to flexibility in the metal-cyanide grid conformation, the **Au** framework has also demonstrated flexibility in the bpac coordination between adjacent Fe(II) centres. The **Au**·{alcohol} series displayed bpac coordination geometries that included a fully orthogonal coordination (**Au**·{EtOH}, **Au**·{1-PrOH}), an accordion-like symmetric distortion along the *c*-axis (**Au**·{MeOH}), unidirectional distortion which lay solely along the *b*-axis (**Au**·{1-BuOH}), and distortion that occurred between the *a*- and *b*-axes (**Au**·{2-BuOH}). It is likely that the level of bpac distortion is due to the solvent packing behaviour within the framework pores, as the flexible framework adopts the conformation which maximises favourable host–guest and guest–guest interactions.

The **Au**·{1-BuOH} sample demonstrated an interesting interplay between the SCO and host–guest energetics, leading to a partial HS-to-LS transition upon sample warming. This could in principle lead to enhanced SCO hysteresis as well as the unusual SCO behaviour seen in this sample.

Distortion in the bpac coordination appears to be correlated with gradual spin transitions in this framework. This is presumably due to a decrease in the rigidity of the framework as it distorts away from an orthogonal coordination, which decreases the strength of the long-range elastic interactions that produce cooperativity in the spin transition.

The extreme flexibility of the framework and the synergistic relationship of its properties lead to a significant dependence of the framework behaviour on the precise sample environment and degree of solvation (eg: **Au**·{1-BuOH} and **Au**·{MeCN}). It was also shown that flexible guests, which may adopt multiple conformations, produced multiple spin transition stages when included in the **Au** framework. The multi-step behaviour observed in the

Au·{1,2-EtX_2} (X = Cl, Br) and **Au**·{1:1 EtBr/1-PrCl} samples could be attributed to multiple potential guest packing behaviours within crystallites, which would produce different local pressure effects on the framework, in turn changing the spin transition behaviour of nearby Fe(II) sites.

To say that this framework has demonstrated unprecedented properties does not sufficiently convey the complexity and versatility of its behaviour. The **Au** lattice has extreme flexibility, and its multifunctional nature allows significant variation of its structural and magnetic properties depending on quantity and type of adsorbed guest species, temperature, pressure and presumably a plethora of other, as-yet unknown influences. It is important that although the framework has significant flexibility, it is also robust to solvent removal and is stable to the introduction of many different solvent guest molecules. The research presented in this thesis has only scratched the surface of potential study into the properties of the **Au** framework, and there is much future work which may be performed on this, and related materials.

Following the research already completed on the **Au** framework, structural studies on the effect of haloalkane guests would provide more information on the framework conformation of these samples, and the structure–behaviour relationship of the material. While discussion of the effect of mixed haloalkane guests assumed an approximately equal affinity of the different guests with the framework, it is conceivable that the framework might preferentially absorb one guest over another; it may be possible to devise an experiment to test the relative proportion of guests that are absorbed into the material, perhaps by exposing a sample to the solvent mix, then analysing the mother liquor using a quantitative technique such as NMR, HPLC, gas chromatography, etc.

More thorough investigations on the effect from the degree of solvation may give information on the internal and external effect of solvent, and the study of different guest families, such as gaseous or aromatic guests, may help probe the subtle effects that determine the bulk material properties. The data presented in this thesis were somewhat convoluted by the different melting points of the studied solvents, and it may be possible to mix the solvents with a medium that is not adsorbed into the framework pores, and has a low enough melting point that it does not interfere with the SCO behaviour.

A metal dilution study of **Au**·{EtOH} has already demonstrated that an abrupt transition in this framework can be converted to a smooth, continuous transition, with the magnitude and temperature range of the thermal expansion behaviour dependent on the metal dilution concentration. Following on from this result, it would be interesting to investigate the properties of the *desolvated* framework when synthesised with a non-SCO metal dopant, to determine whether the abrupt volumetric negative thermal expansion that accompanies the spin transition may be modified to create a continuous effect. In a similar vein, it would be interesting to synthesise the framework using an octahedral transition metal that is not Fe(II), and investigate the lattice structural properties and guest dependence of such a non-SCO framework. As observed for the **Au** material, the anomalous thermal expansion behaviour is often independent of the spin transition, and it would be worth studying the influence of non-Fe(II) metal centres on the lattice compression properties. Such studies would enable more accurate understanding of the specific effect from the spin transition on the framework structure.

Similarly to the Hofmann series (**§6.1**), replacing the bpac ligand in this framework with other pillar ligands, such as that shown in **Figure 6-1**, would be expected to form frameworks with similar topologies, which may produce interesting magnetic and structural behaviour, and facilitate study of the role of lattice pore size on the guest effect. Pressure studies and Light-Induced Excited Spin State Trapping (LIESST) experiments may also yield interesting behaviours. Variable temperature IR/Raman spectroscopy may provide useful information on the cyanide stretching frequencies and ligand–metal orbital overlap, perhaps complementing the PXRD results regarding distortion of the M–CN–M′ linkers.

References

(1) Fellows, E. A. PhD Thesis, University of Sydney, 2011.
(2) Bartual-Murgui, C.; Salmon, L.; Akou, A.; Ortega-Villar, N. A.; Shepherd, H. J.; Muñoz, M. C.; Molnár, G.; Real, J. A.; Bousseksou, A. *Chem. Eur. J.* **2012**, *18*, 507.
(3) Muñoz-Lara, F. J.; Gaspar, A. B.; Muñoz, M. C.; Arai, M.; Kitagawa, S.; Ohba, M.; Real, J. A. *Chem. Eur. J.* **2012**, *18*, 8013.
(4) Muñoz Lara, F. J.; Gaspar, A. B.; Aravena, D.; Ruiz, E.; Muñoz, M. C.; Ohba, M.; Ohtani, R.; Kitagawa, S.; Real, J. A. *Chem. Comm.* **2012**, *48*, 4686.

Chapter 7: Experimental Methods and Techniques

Electron gun at the Australian Synchrotron, used to accelerate electrons before injecting them into a linear accelerator and on to the booster ring.

7.1 *General*

All precursor compounds and solvents were commercially available as reagent grade materials and used as received without further purification.

7.2 *Ligand Synthesis*

The syntheses of 1,2-dibromo-1,2-bis(4′-pyridyl)ethane and 1,2-bis(4′-pyridyl)acetylene (**Scheme 7-1**) were performed as described by Xina Hudson in her Honours thesis (University of Sydney, 2004), which were adapted from published methods[1-2] and reproduced here with the quantities used. The ligand synthesis was confirmed using ^{1}H NMR in *d*-chloroform.

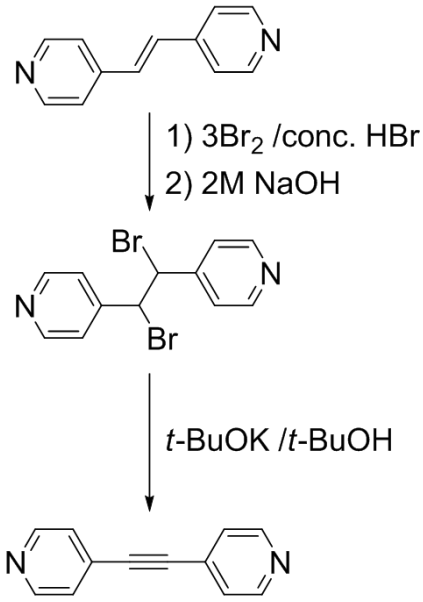

Scheme 7-1: Synthetic procedure to make 1,2-bis(4′-pyridyl)acetylene (bpac) from 1,2-bis(4′-pyridyl)ethylene (tvp), with 1,2-dibromo-1,2-bis(4′-pyridyl)ethane as an intermediate.

1,2-Dibromo-1,2-bis(4′-pyridyl)ethane

Trans-1,2-bis(4′-pyridyl)ethylene (tvp) (2.03 g, 11.0 mmol) was suspended in concentrated hydrobromic acid (48%, 20 mL) at 0 °C. Bromine (7.13 g, 44.6 mmol) was added to the suspension with stirring. The reaction mixture was heated at reflux for 1 hr, then cooled to 0 °C. The precipitate was isolated by filtration, then treated with NaOH (2 M, 4 × 20 mL), washed with water (3 × 15 mL) and dried. The solid was then dissolved in a mixture of

dichloromethane and chloroform (3:2, 200 mL), dried over anhydrous sodium sulfate and the solution filtered. The solvent was removed from the filtrate under reduced pressure to give 1,2-dibromo-1,2-bis(4′-pyridyl)ethane (3.66 g, 10.7 mmol, 97%) as a fine white powder. **^{1}H NMR** (300 MHz, $CDCl_3$): δ ppm 5.28 (2H, s, CHBr), 7.40 (4H, d, ^{3}J = 4.5 Hz, pyridyl H), 8.69 (4H, d, ^{3}J = 4.5 Hz, pyridyl H); **^{13}C NMR** (300 MHz, $CDCl_3$): δ ppm 150.47, 147.61, 122.56, 51.78.

1,2-Bis(4′-pyridyl)acetylene (bpac)

1,2-Dibromo-1,2-bis(4′-pyridyl)ethane (2.12 g, 6.20 mmol) was dissolved in *tert*-butanol (40 mL) and added dropwise to a solution of potassium *tert*-butoxide (2.8 g, 28 mmol) in *tert*-butanol (50 mL) at 110 °C. The reaction mixture was heated at reflux for 1 hr. Water (3 mL) was added and the solvent removed under reduced pressure. The crude product was extracted into diethyl ether (3 × 20 mL) from water (20 mL), dried over anhydrous sodium sulfate and filtered. The filtrate was evaporated to dryness and the resulting solid was recrystallised from hexane to give 1,2-bis(4′-pyridyl)acetylene (bpac) (0.559 g, 3.07 mmol, 50%) as pale yellow crystals; **^{1}H NMR** (300 MHz, $CDCl_3$): δ ppm 7.41 (4H, d, ^{3}J = 4.5 Hz, pyridyl H), 8.65 (4H, d, ^{3}J = 4.5 Hz, pyridyl H); **^{13}C NMR** (300 MHz, $CDCl_3$): δ ppm 150.34, 130.63, 125.99, 91.01; **mp** = 115–117 °C.

7.3 *Coordination Framework Syntheses*

7.3.1 *Bulk Framework Synthesis*

The $[Fe(bpac)M(CN)_4]\cdot 0.5(bpac)$ (M = Ni, Pd, Pt) frameworks were synthesised for bulk analysis using the following method: potassium tetracyanidometallate (0.14 mmol: Ni = 36 mg; Pd = 40 mg; Pt = 60 mg) and bpac (**Pd**, **Pt**: 100 mg, 0.56 mmol, 4 eqv; **Ni**: 75 mg, 0.42 mmol, 3 eqv) were dissolved in an EtOH/water mixture (1:1, 30 mL). $Fe(ClO_4)_2\cdot 9H_2O$ (58 mg, 0.14 mmol) dissolved in EtOH/water (1:1, 10 mL) was added, causing the rapid formation of an orange precipitate. This solution was stirred for 1 hr, then centrifuged, the solvent decanted and the solid washed with ethanol (2 × 10 mL), after which the solid became yellow. Yields were not obtained as the product was not dried, but stored under EtOH. **Ni** Anal. Calcd for $[Fe(bpac)Ni(CN)_4]\cdot 0.51(bpac)(H_2O)$, $C_{22.12}H_{14.08}FeNiN_{7.02}O$: Fe 11.0, Ni 11.5, C 52.2, H 2.79, N 19.3%. Found: Fe 11, Ni 11.5, C 52.54, H 2.74, N 18.81%. **Pd** Anal. Calcd. for $[Fe(bpac)Pd(CN)_4]\cdot 0.55(bpac)(H_2O)$, $C_{22.6}H_{14.4}FePdN_{7.1}O$:

Fe 9.9, C 48.16, H 2.57, N 17.6%. Found: Fe 10, C 48.69, H 2.46, N 17.45%. **Pt** Anal. Calcd. for $[Fe(bpac)Pt(CN)_4]\cdot 0.55(bpac)(H_2O)$, $C_{22.6}H_{14.4}FePtN_{7.1}O$: Fe 8.6, C 41.6, H 2.22, N 15.24%. Found: Fe 8.5, C 41.52, H 2.25, N 15.18%. When the synthesis of **Pd** is performed with one equivalent of bpac: Anal. Calcd. for $[Fe(bpac)Pd(CN)_4]\cdot 0.37(bpac)(H_2O)$, $C_{20.44}H_{12.96}FePdN_{6.74}O$: Fe 10.51, C 46.21, H 2.46, N 17.77%. Found: Fe 10.55, C 46.29, H 2.43, N 17.64%.

The $[Fe(bpac)(Au(CN)_2)_2]$ framework was synthesised in bulk using the following method: potassium dicyanidoaurate (81 mg, 0.28 mmol) and bpac (25 mg, 0.14 mmol) were dissolved in ethanol (30 mL). $Fe(ClO_4)_2\cdot 9H_2O$ (58 mg, 0.14 mmol) dissolved in ethanol (10 mL) was added, causing the rapid formation of a yellow precipitate. This solution was stirred for 1 hr, then centrifuged, the solvent decanted and the solid washed with water (2 × 10 mL) to remove precipitated potassium perchlorate, then washed with ethanol (2 × 10 mL). The product was stored under ethanol. Anal. Calcd. for $C_{16}H_8N_6FeAu_2$: Fe 7.61, Au 53.66, C 26.18, H 1.10, N 11.45%. Found: Fe 7.6, Au 53.9, C 25.8, H 1.2, N 11.1%.

7.3.2 *Growth of Single Crystals by Diffusion Techniques*

To grow diffraction quality single crystals of the frameworks studied, the slow liquid-liquid diffusion method was employed. This was carried out using the vial-in-vial technique or using H-cells of 30 mL capacity. Multiple diffusions were prepared for each framework, stoppered and left undisturbed for up to 2 months, until crystals of sufficient size had formed.

The single crystal diffusions were prepared as follows: $Fe(ClO_4)_2$ was placed in one arm of the H-cell, or the smaller vial in the vial-in-vial diffusions (A), while the cyanidometallate salt and organic ligand were placed in the other arm, or the larger vial (B). Solvent was then slowly layered on top of the reagents until it lay above the intersection of the two reagent depositories (**Figure 7-1**).

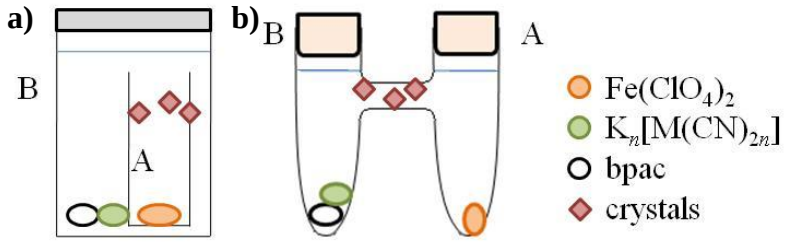

Figure 7-1: Experimental setup for: **a)** vial-in-vial diffusion; and **b)** H-cell diffusion. Crystals form where the metal salt, anion and ligand meet.

Diffusions of the $[Au(CN)_2]^-$ anion used a 2:1:2 mole ratio of the anion, Fe(II) and ligand reagents respectively with ethanol as the solvent. The diffusions with $[Ni(CN)_4]^{2-}$, $[Pd(CN)_4]^{2-}$ or $[Pt(CN)_4]^{2-}$ used an equimolar ratio of the reagents and a 1:1 ethanol/water mixture as solvent. Masses were calculated based on 15 mg of $Fe(ClO_4)_2$.

7.4 *Single Crystal X-ray Diffraction*

All single crystal X-ray diffraction analyses, including data processing and structural solution and refinement, were performed by Dr David Price.

Single crystal X-ray diffraction data for all materials were collected on a Bruker-Nonius FR591 Kappa APEX II using Mo-Kα (0.71073 Å) radiation and an Oxford Instruments nitrogen gas cryostream. Suitable crystals were selected under a polarising microscope and mounted on a mohair fibre in a thin film of paratone oil and quench cooled in a stream of cold nitrogen gas. Matrix collections were performed to determine unit cells and for complete structure determination, full spheres of data were collected over a range of incident angles. Data collection was performed using the *APEX2* software and unit cell refinement and data reduction were undertaken with *SAINT* v7.60A.[3] The structure was solved with *SHELXS-97*[4] using direct methods and refined using *SHELXL-97*,[5] through the *X-Seed* GUI, using the full-matrix least-squares on F^2 method.

All non-hydrogen framework atoms were modelled anisotropically, and hydrogen atoms were modelled using riding atom constraints. In the **Pd** and **Pt** frameworks, disordered guest atoms were modelled anisotropically, and they were modelled isotropically for the **Au** framework.

Solvent accessible volumes were calculated within *PLATON*.[6] Illustrations were produced using *POV-RAY*[7] and *Mercury*.[8] Crystallographic information files (CIF) for all structures

studied are provided on the accompanying CD-ROM and data tables are given in **Appendix A**.

7.5 *Powder X-ray Diffraction*

In-house powder X-ray diffraction (PXRD) patterns were collected on a PANalytical X'Pert PRO MPD diffractometer using Cu-Kα_1 (1.54059 Å) radiation and was equipped with an Oxford Cryostream 700. The application software was *X'Pert Data Collector* v2.2f,[9] and the instrument control software was *XPERT-PRO* v1.9E.[10]

Samples were packed in a glass capillary that was mounted and aligned on a goniometer, which was set to spin within the incident X-ray beam. Data were collected in the 2θ range 5–30° with a step size of 0.013°.

7.5.1 *Synchrotron Powder X-Ray Diffraction*

For high resolution powder diffraction experiments, the PD beamline at the Australian Synchrotron was used. The samples were prepared in the same way as for the in-house experiments, in sealed capillaries, under solvent and mounted on a spinning goniometer. The X-ray energy used for the diffraction experiments was 20.5035 keV (0.605384 Å). Data were collected on a strip detector from 1 to 81° in two sets separated by 0.5° to compensate for gaps in the detector, which were merged with the Australian Synchrotron in-house software, *DataPro* v2.6. Unless otherwise stated, all powder diffraction data presented in this thesis were obtained at the Australian Synchrotron.

For variable temperature studies, PXRD patterns were obtained at discrete points over a range of temperatures. Data were collected using the same parameters as the single-temperature collections, with angle ranges depending on the instrument as detailed above. The temperature was ramped at 120 K/hr (no overshoot) using an Oxford Instruments nitrogen gas cryostream.

7.5.2 *Fitting Rietveld and Le Bail Models*

To extract unit cell parameters a Le Bail model was fitted to the PXRD data, and the unit cell parameters were subsequently refined using *GSAS*[11] through the *EXPGUI*[12] interface. A histogram profile function with a pseudo-Voigt peak shape and a 4–10 term shifted

Chebyshev background function was used. Diffraction peak profile and unit cell parameters were refined.

For the variable temperature data collections, a sequential refinement was performed for each phase using a software script, in which the starting parameters from a refinement were taken from the parameters of the previously refined structure in the series. The first diffraction pattern of each phase was refined manually to the best obtainable fit. Where multiple phases were present, a refinement model that incorporated each phase was used if the data were of sufficient quality to fit them. With data of exceptionally high quality, Rietveld refinements were performed, and individual atomic positions were refined to as high a precision as possible within the data limitations.

7.6 *Magnetic Susceptibility Measurements*

Variable temperature magnetic susceptibility measurements were collected using an in-house Quantum Design PPMS magnetometer fitted with a Vibrating Sample Mount (VSM) attachment, with an applied magnetic field strength of 5000 Oe, measuring continuously at 1.5 K min^{-1} (no overshoot).

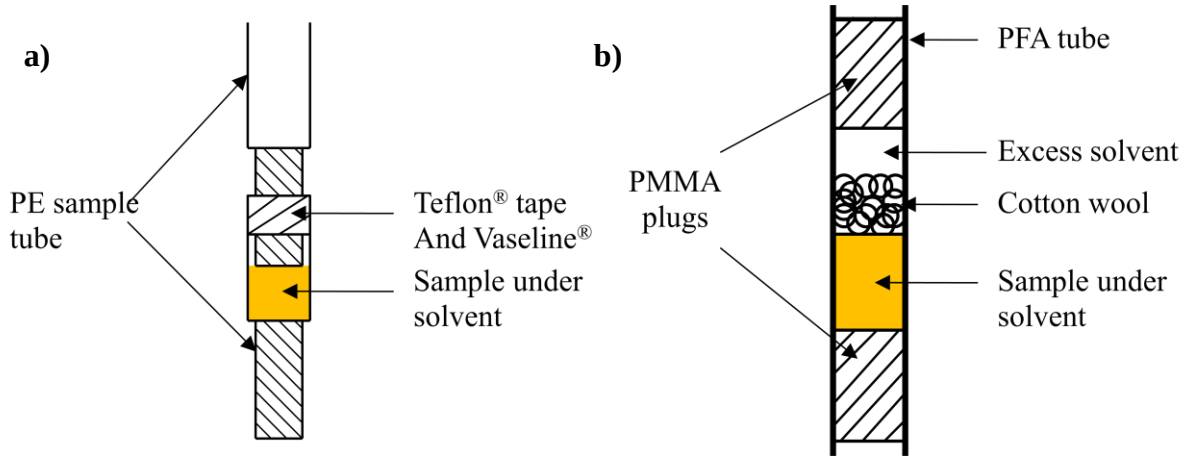

Figure 7-2: Sample preparation for PPMS magnetometry measurements: **a**) the traditional setup; and **b)** the sample containment technique developed to prevent desolvation.

The traditional sample containment method immobilised the sample under solvent between two specially designed polyethylene (PE) sample tubes, which were sealed using Teflon® and Vaseline® (shown in **Figure 7-2a**). Due to the pump/purge procedure used to prepare the PPMS for measurements, as well as the often prolonged time at relatively high temperatures

with volatile solvents, the prevention of desolvation proved difficult using the traditional sample holder. In order to combat this effect, a special sample preparation was devised by Dr Peter Southon, which involved the following: the solvated sample was loaded into a perfluoroalkoxy (PFA, a fluoropolymer) tube of 1/8" outer diameter and 1/16" inner diameter, which had been stoppered at one end with a PMMA (poly(methyl methacrylate)) plug. This was centrifuged such that the sample was firmly packed in the bottom of the container, most of the excess solvent was removed and a small amount of cotton wool was inserted in the top to ensure sufficient packing of the sample. The top of the tube was then trimmed to the desired length, closed by careful heating and insertion of a second PMMA plug in the top, which was again heat-sealed closed. The result is a fully sealed sample environment under solvent (**Figure 7-2b**). For the magnetism experiment, the sample tube was immobilised within a brass sample holder. Unless otherwise stated, all magnetic measurements described in this thesis were undertaken using the developed sample setup shown in **Figure 7-2b**.

Following correction for diamagnetic contributions of the sample and sample holder, the molar magnetic susceptibility in the systems studied can be determined using the Curie Law, $\chi = C/T$ (C = constant, T = temperature),[13] so χT is independent of temperature. The Fe(II) SCO materials studied have different numbers of unpaired electrons in the HS and LS states, and the resulting magnetic behaviour can be monitored to observe the behaviour of the spin transition.

The stoichiometric HS fraction of the spin centres at any point in a transition can be calculated using the generalised **Equation 7.1**. This involves the experimentally observed value at a given point (x), and the HS (a_{HS}) and LS (a_{LS}) values above and below the transition respectively. For magnetic measurements, the variable quantities in this equation are taken from the relevant magnetic susceptibility values.

$$\gamma_{HS} = (x - a_{LS})/(a_{HS} - a_{LS}) \quad (7.1)$$

7.7 *Gas and Vapour Adsorption*

7.7.1 *Nitrogen Adsorption*

The gas adsorption isotherm measurements were performed using an Accelerated Surface

Area & Porosimetry System (ASAP) 2020 supplied by Micromeritics Instruments Inc. The sample was placed in a pre-weighed sample tube with a Transeal cap to prevent intrusion of atmospheric gas during transfer and weighing. The sample was desolvated at 100 °C under high vacuum for 12 hr. The mass of the degassed sample was measured and the evacuated sample tube was transferred to the analysis port of the instrument. The warm and cold free space corrections were measured using high purity helium gas and the nitrogen adsorption and desorption isotherms were then measured at 77 K. The data were analysed using BET[14] and Langmuir[15-16] models to determine the surface area.

7.7.2 *Gravimetric Analysis*

The ethanol adsorption properties of $[Fe(bpac)Pd(CN)_4]\cdot 0.4(bpac)$ and their effect on the spin transition were studied over a range of temperatures, using an IGA-002 gravimetric adsorption instrument (Hiden-Isochema, UK). For each experiment, the sample was evacuated under high vacuum and heated to 78 °C for 90 h, after which time the sample mass was stable, indicating complete loss of solvent. Ethanol vapour was then introduced over a range of pressures, and the temperature controlled by inserting the glass container in which the sample was suspended into a thermally isolated water bath.

The SCO Pressure-Temperature phase diagram in **§3.4** was mapped out by a combination of isotherms and isobars:

Isotherms: During measurement of the isotherm the sample temperature was controlled within ±0.1 °C. At each pressure point the sample chamber was pressurised to a set pressure of ethanol vapour and allowed to equilibrate for one hour before moving to the next pressure point. Whenever the mass was not stable after this time, the equilibrium mass was extrapolated from the measured data using the Avrami equation.

Isobars: The pressure of ethanol vapour in the chamber was set and controlled to within 0.1 mbar. Starting at a temperature well below the LS-to-HS transition, the temperature was ramped at 0.1 °C/min to approximately 310 K, then cooled at the same rate. The slow rate of heating and cooling was intended to keep the sample adsorption at near-equilibrium conditions and avoid any kinetic effects.

References

(1) Hudson, X. BSc (Hons) Thesis, University of Sydney, 2004.
(2) Tanner, M.; Ludi, A. *Chimia* **1980**, *34*, 23.
(3) Bruker AXS Inc.: Madison, Wisconsin, USA, 1995.
(4) Sheldrick, G. M.; University of Gottingen: Gottingen, Germany, 1997.
(5) Sheldrick, G. M.; University of Gottingen: Gottingen, Germany, 1997.
(6) Spek, A. L.; Utrecht University: Utrecht, The Netherlands, 2007.
(7) Persistence of Vision Raytracer Pty. Ltd.: Williamstown, Victoria, Australia, 2004.
(8) Cambridge Crystallographic Data Centre: Cambridge, United Kingdom, 2001.
(9) PANAlytical B.V.: Almelo, The Netherlands, 2008.
(10) PANAlytical B.V.: Almelo, The Netherlands, 2008.
(11) Larson, A. C.; Dreele, R. B. V.; Los Alamos National Laboratory: 2000.
(12) Toby, B. H. *J. Appl. Crystallogr.* **2001**, *34*, 210.
(13) Kahn, O. *Molecular Magnetism*, Wiley.
(14) Brunauer, S.; Emmett, P. H.; Teller, E. *J. Am. Chem. Soc.* **1938**, *60*, 309.
(15) Langmuir, I. *J. Am. Chem. Soc.* **1916**, *38*, 2221.
(16) Langmuir, I. *J. Am. Chem. Soc.* **1918**, *40*, 1631.

Appendices

Appendix A: Crystallographic Information Files (CD-ROM)

The crystallographic information files (.cif) of the crystal structures presented in this thesis are given in the accompanying CD-ROM.

'Hofmann Structures' Folder

Within this folder are the files for the Hofmann-type frameworks, which had the general formula [Fe(bpac)M(CN)$_4$]·0.5(bpac){guest} (**M·0.5(bpac)**{guest}) (M = Ni, Pd, Pt).

File Name	Space Group	Compound	Temperature / K
Ni model	*Pmmm*	**Ni·0.5(bpac)**{EtOH}	250
Pd Pmmm	*Pmmm*	**Pd·0.5(bpac)**{EtOH/H_2O}	100
Pd P4ommm	*P4/mmm*	**Pd·0.5(bpac)**{EtOH/H_2O}	100
Pt	*Pmmm*	**Pt·0.5(bpac)**{EtOH/H_2O}	100

'Interpenetrated Structure' Folder

Within this folder are the files for the interpenetrated frameworks, which had the general formula [Fe(bpac)(Au(CN)$_2$)$_2$]·{guest} (**Au**·{guest}).

File Name	Space Group	Compound	Temperature / K
Au Cmma EtOH 100	*Cmma*	**Au**·{EtOH}	100
Au Cmma EtOH 190	*Cmma*	**Au**·{EtOH}	190
Au Cmma EtOH 240	*Cmma*	**Au**·{EtOH}	240
Au Cmma MeOH-EtOH 100	*Cmma*	**Au**·{MeOH/EtOH}	100
Au Cmma MeOH-EtOH 200	*Cmma*	**Au**·{MeOH/EtOH}	200
Au Cmma MeOH-EtOH 230	*Cmma*	**Au**·{MeOH/EtOH}	230
Au Pbaa EtOH 230	*Pbaa*	**Au**·{EtOH}	230

Appendix B: Further Crystal Structure Pictures

Asymmetric Units

Illustrations of the asymmetric units for structures presented in this thesis that were not already presented in the main body of the text, are presented below. The pictures were created using *POV-RAY*. In certain structures, hydrogens have been removed for clarity. Unless otherwise stated, all framework non-hydrogen atoms and guest bpac atoms were modelled anisotropically, and guest solvent molecules were modelled isotropically. Ellipsoids are shown at 50% probability.

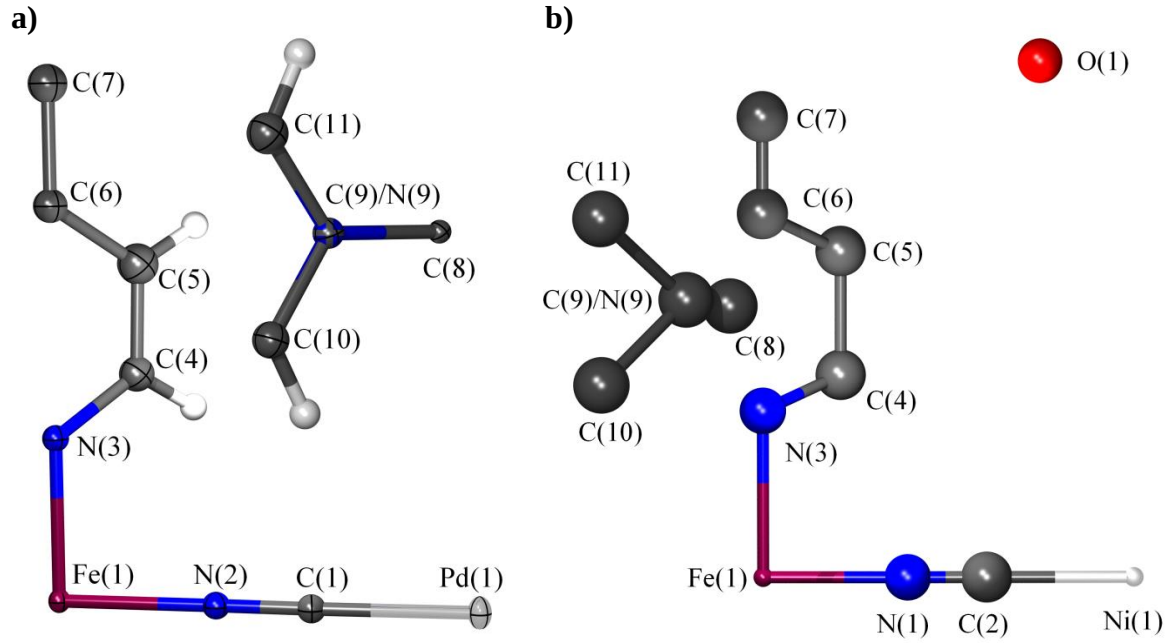

Figure B-1: Asymmetric Unit for **a) Pd -** $[Fe(bpac)Pd(CN)_4]\cdot 0.5(bpac)$, modelled from SCXRD data at 100 K; and **b) Ni -** $[Fe(bpac)Ni(CN)_4]\cdot 0.5(bpac)$, modelled using Reitveld methods on synchrotron powder X-ray diffraction data at 250 K. All atoms of the **Ni** structure were refined isotropically.

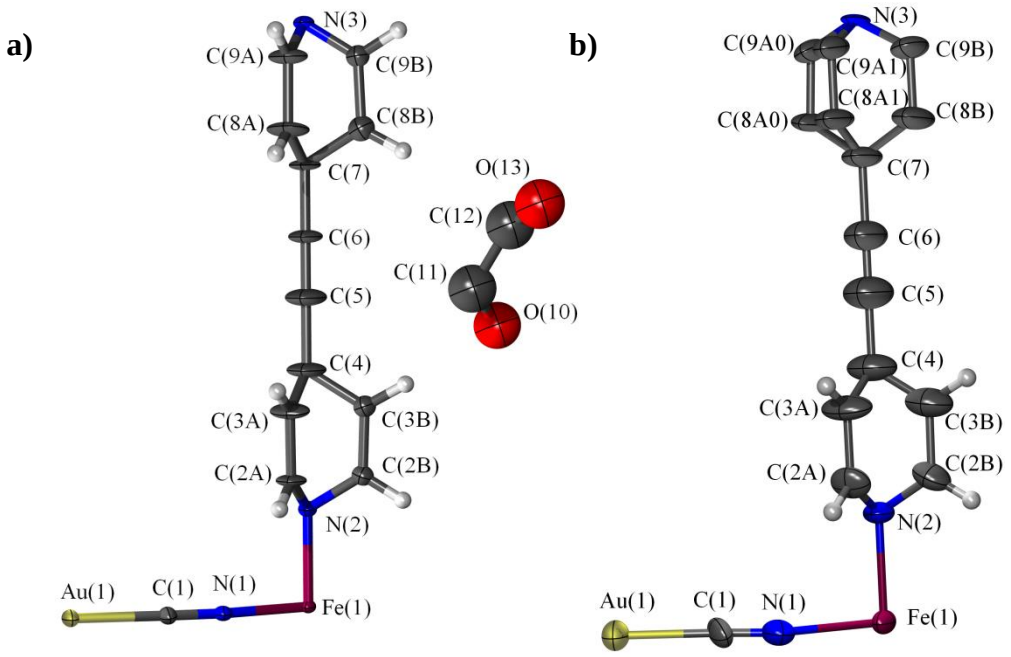

Figure B-2: Asymmetric Unit for [Fe(bpac)(Au(CN)$_2$)$_2$]·{EtOH}, **Au**·{EtOH}, at **a)** 100 K; and **b)** 240 K.

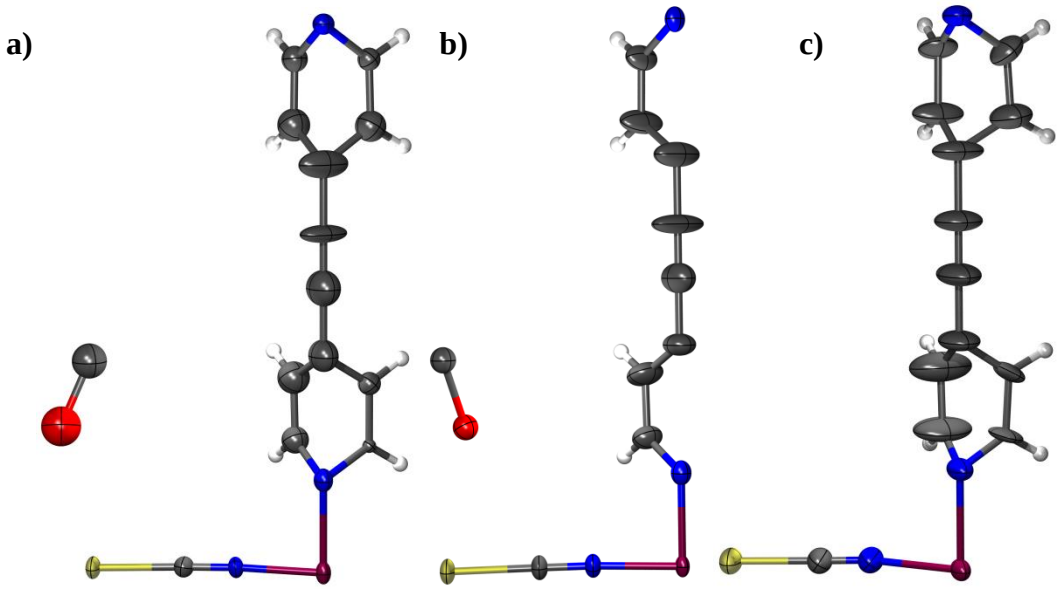

Figure B-3: Asymmetric Unit for **Au**·{1:1 MeOH/EtOH} in the *Cmma* space group at **a)** 100 K; **b)** 200 K and **c)** 230 K.

Other Crystal Structure Pictures

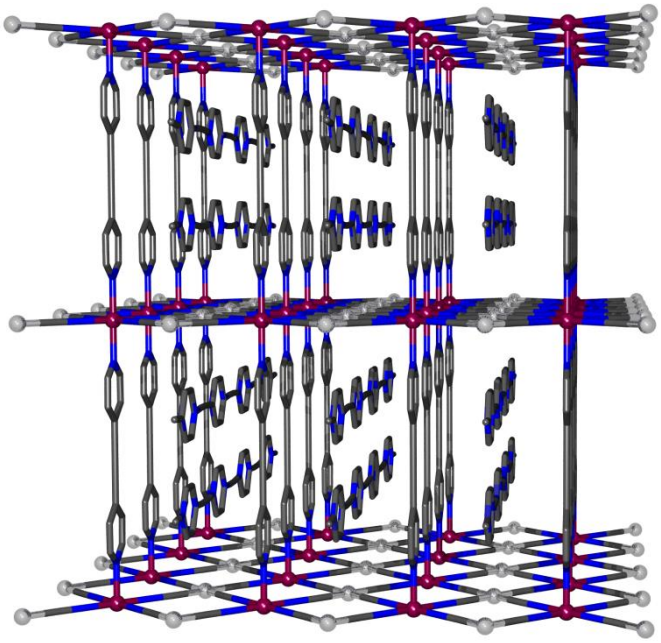

Figure B-4: Single crystal structure of **Pd** at 100 K. The framework structure is wholly analogous to the **Pt** framework.

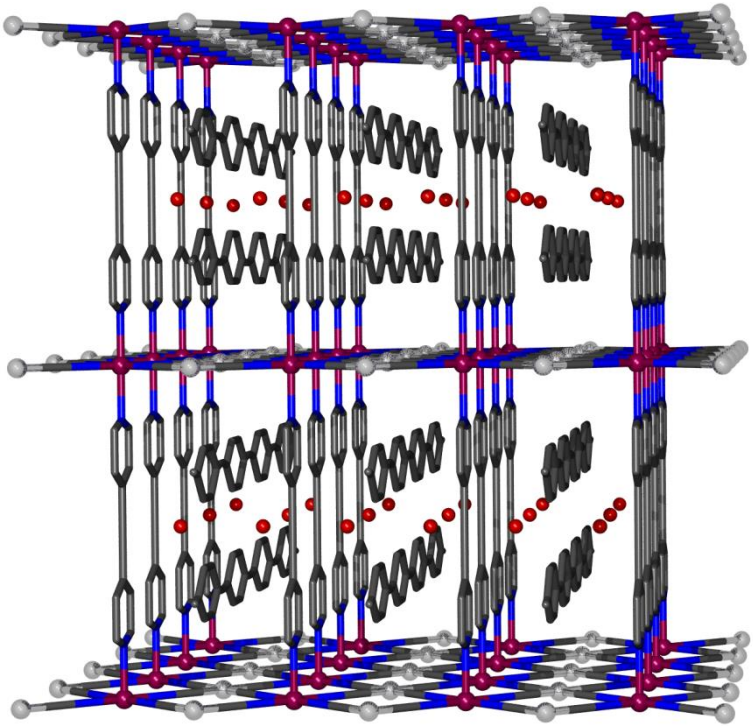

Figure B-5: Crystal structure of **Ni** at 250 K, as refined from synchrotron powder diffraction data and modelled based on the **Pt** single crystal structure using Reitveld refinement. The structure is fully analogous to **Pd** and **Pt**.

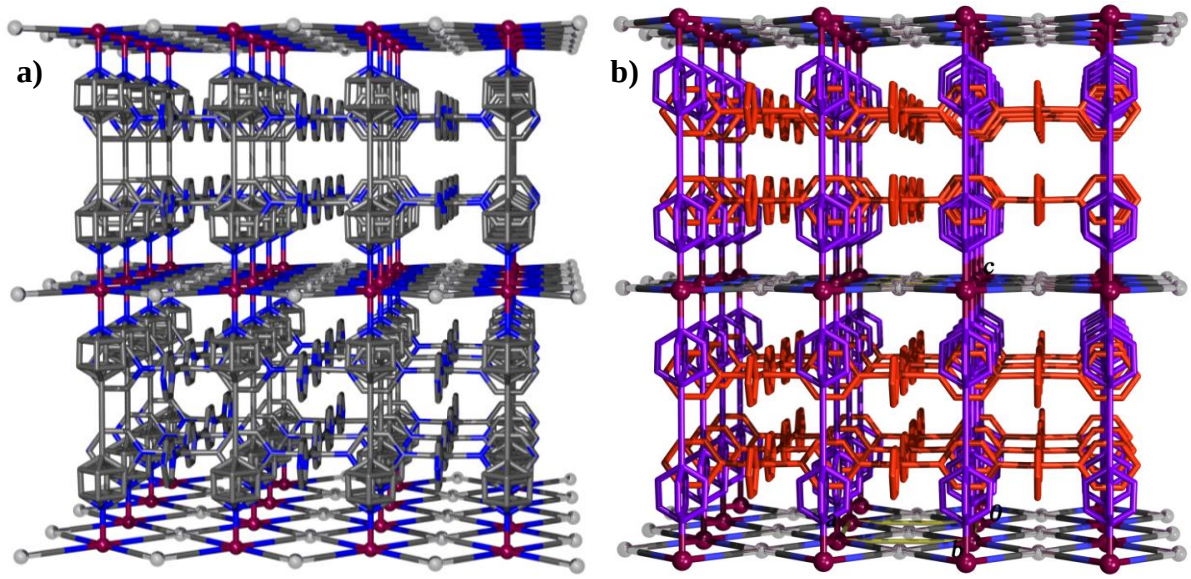

Figure B-6: a) Illustration of **Pd** when solved in the tetragonal space group *P*4/*mmm*. The bound and guest bpac molecules are disordered along the *a* and *b* axes; and **b)** the same illustration, with the ligand and bpac guest clearly shown in different colours.

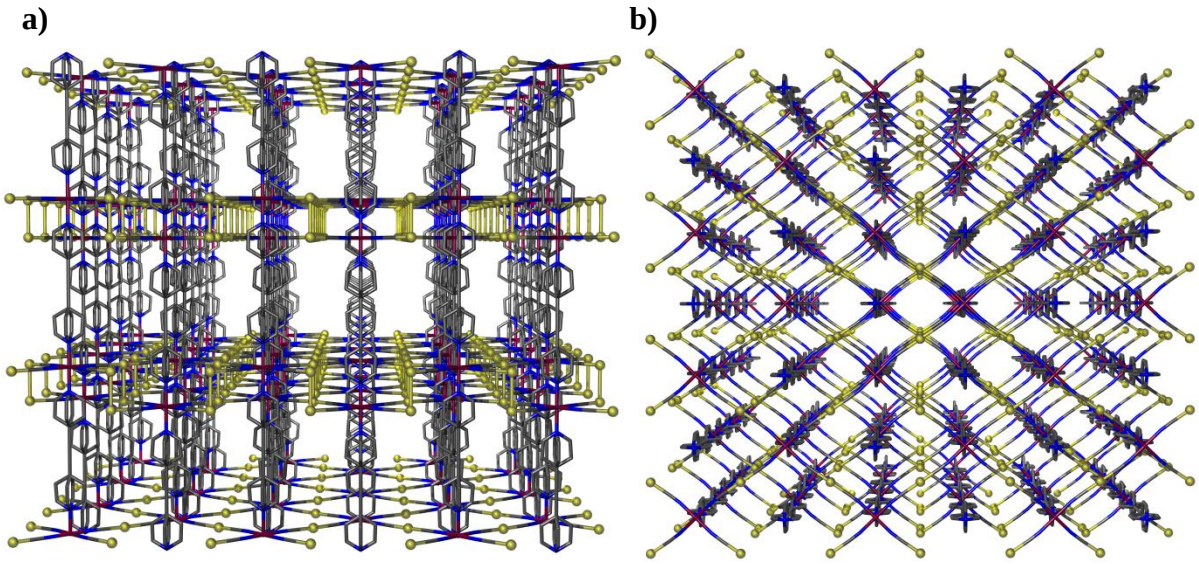

Figure B-7: Crystal structure of **Au**·{EtOH} in the orthorhombic *Cmma* space group at 190 K showing the aurophilic interactions between the interpenetrated nets, viewed **a)** through the structural pores; and **b)** through the cyanide grid.

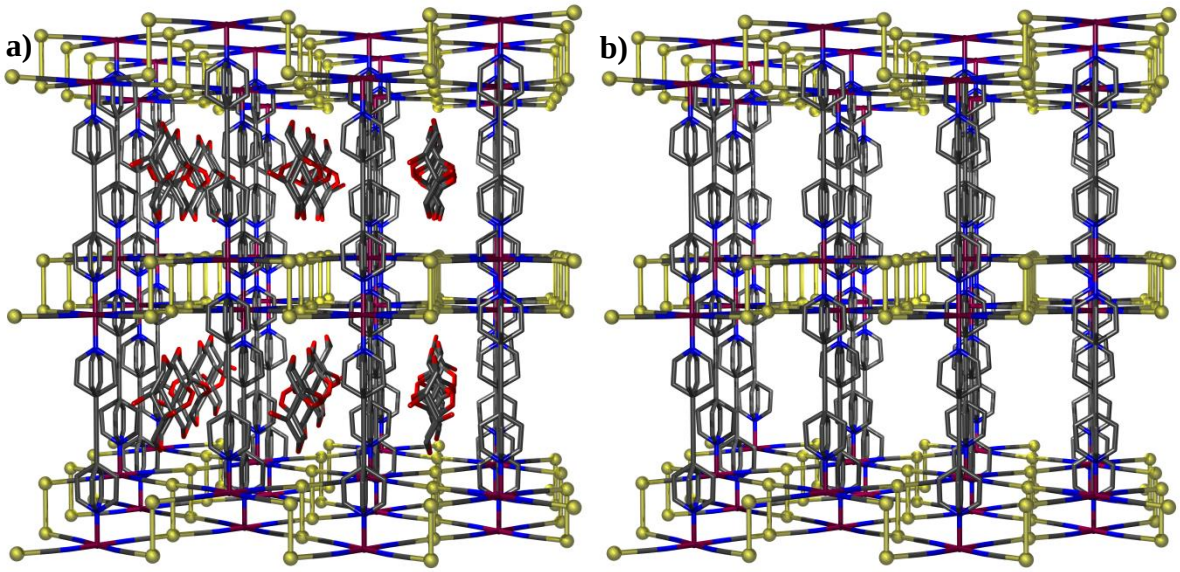

Figure B-8: Crystal structure of **Au**·{EtOH} in the *Cmma* space group at 190 K, comparing the structure when rendered **a)** with, and **b)** without solvent molecules. The occluded EtOH molecules in the pores form a disordered hydrogen-bonding chain.

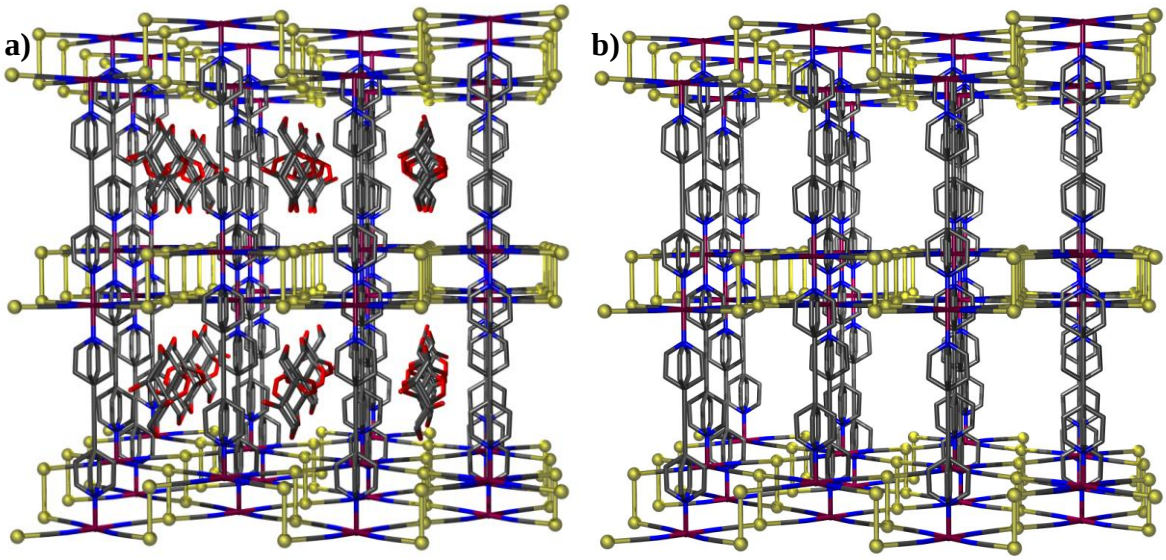

Figure B-9: Crystal structure of **Au**·{EtOH} in the *Cmma* space group at 100 K, comparing the structure when rendered **a)** with, and **b)** without solvent molecules.

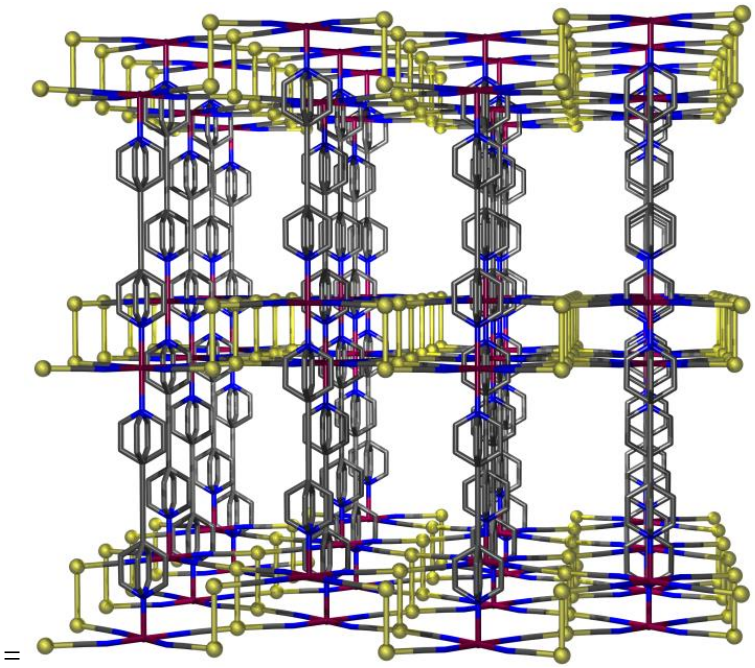

Figure B-10: Crystal structure of **Au**·{EtOH} in the *Cmma* space group at 240 K.

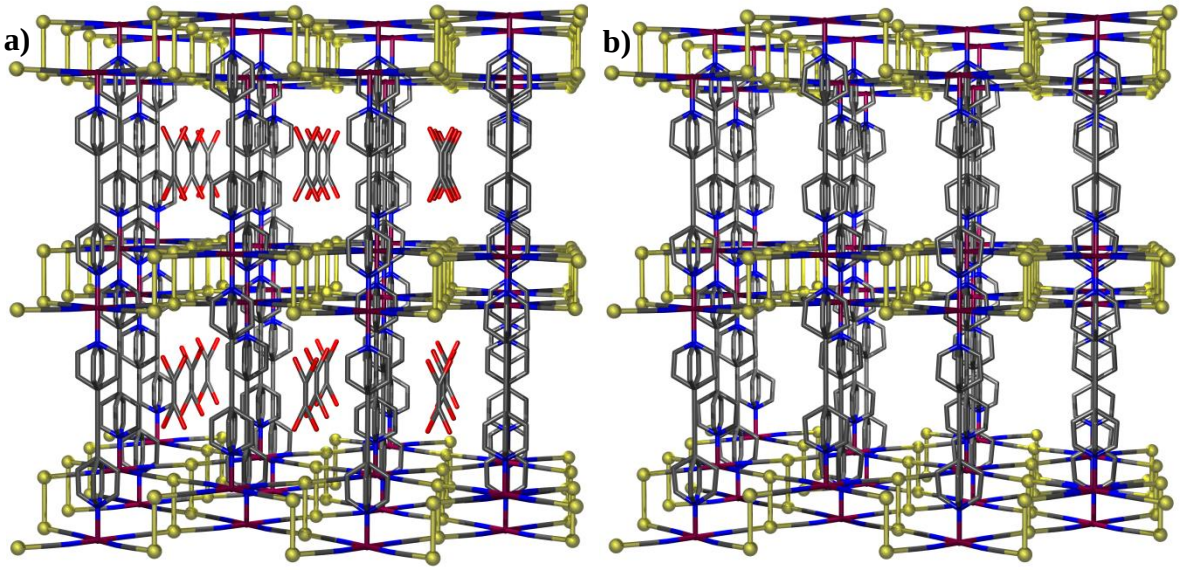

Figure B-11: Crystal structure of **Au**·{MeOH/EtOH} in the *Cmma* space group at 100 K **a)** with; and **b)** without solvent. Solvent was modelled as a disordered methanol/ethanol molecule.

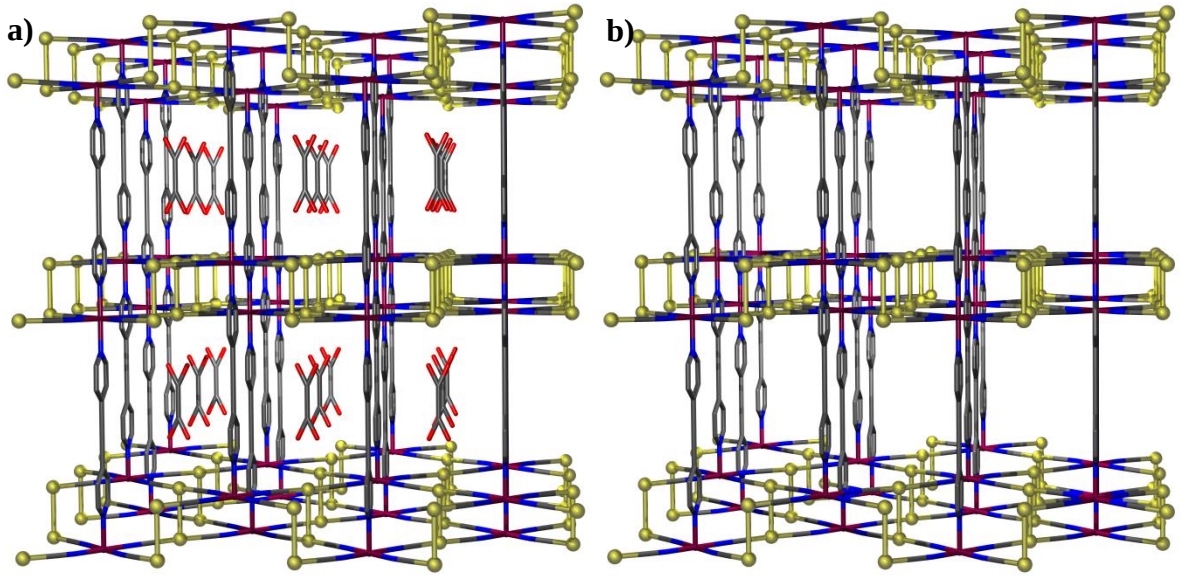

Figure B-12: Crystal structure of **Au**·{MeOH/EtOH} in the *Cmma* space group at 200 K **a)** with; and **b)** without solvent. Solvent was modelled as a disordered methanol/ethanol molecule.

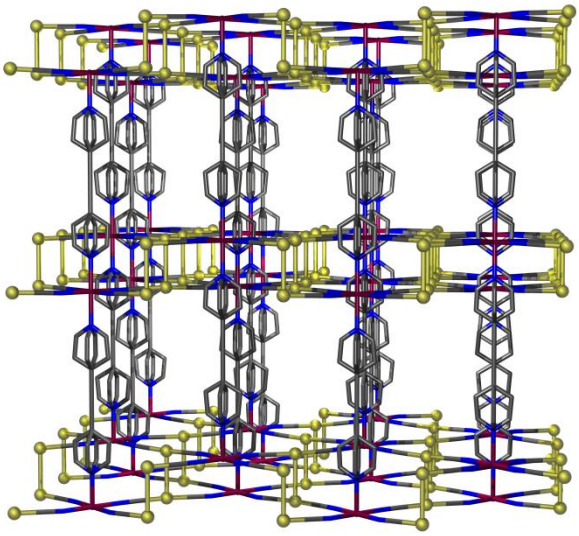

Figure B-13: Crystal structure of **Au**·{MeOH/EtOH} in the *Cmma* space group at 230 K.

Appendix C: Further Powder Diffraction Pictures

Note that in the graphs of Le Bail fits or Rietveld refinements, the data are represented by (×), the background by a green line, the model by a red line and the difference between the model and the data by a blue line. Only part of the powder patterns are displayed, for clarity.

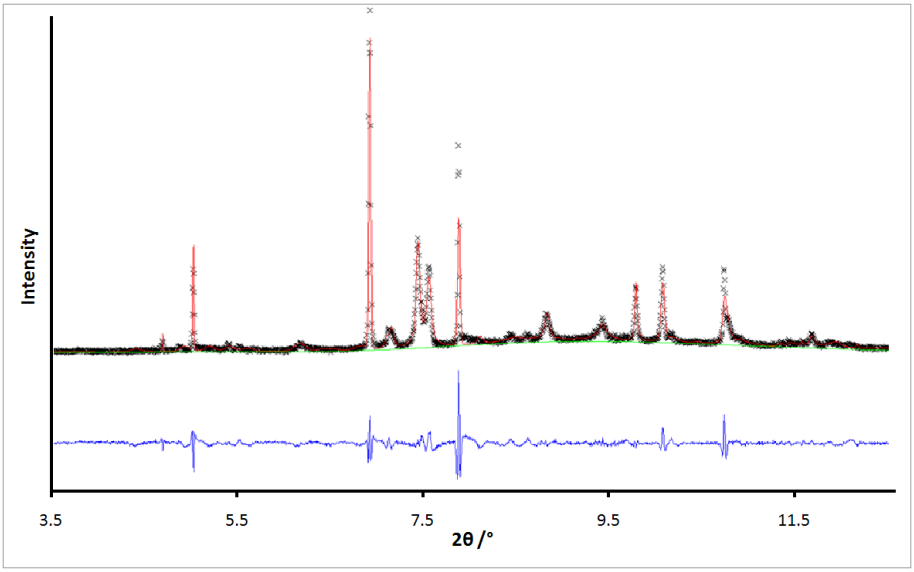

Figure C-1: Le Bail fit to the powder pattern for **Pd·0.5(bpac)**{EtOH} at 310 K (HS).

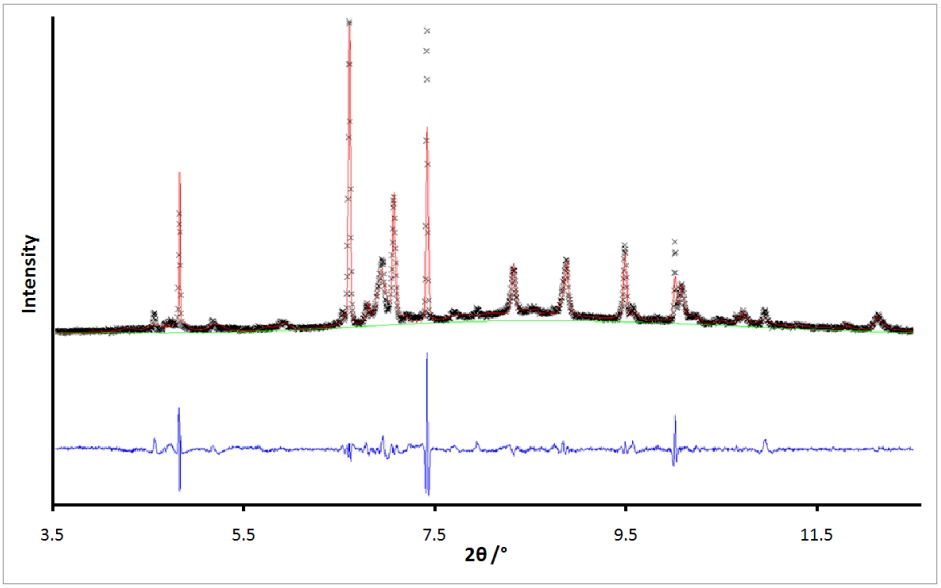

Figure C-2: Le Bail fit to the powder pattern for **Pd·0.5(bpac)**{EtOH} at 250 K (LS), solved in the orthorhombic space group *Pmmm*.

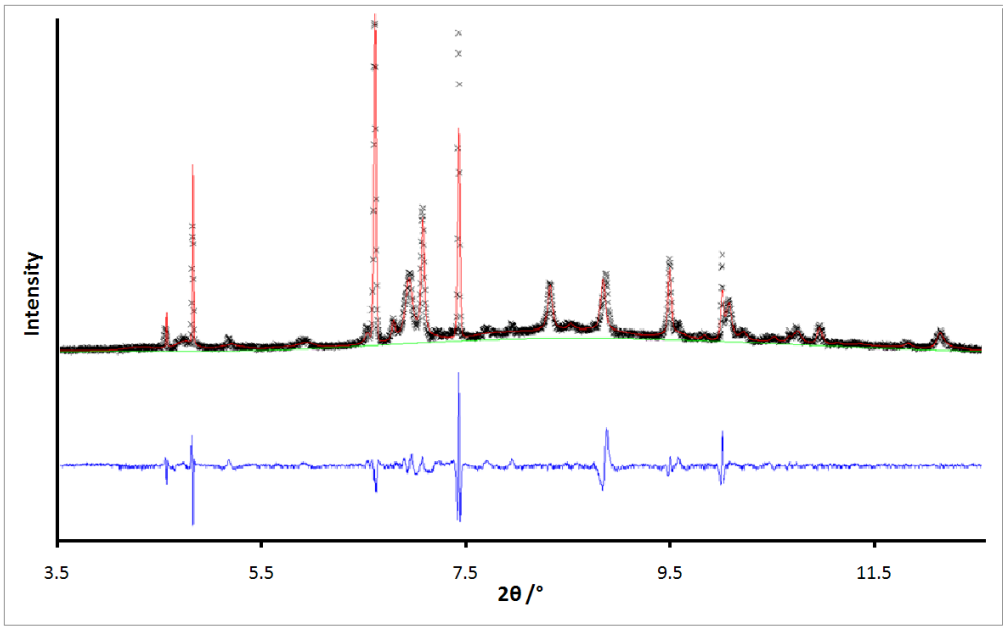

Figure C-3: Le Bail fit to the powder pattern for **Pd·0.5(bpac)**{EtOH} at 250 K (LS), solved in the tetragonal space group *P*4/*mmm*. The major difference between the fit of this model and that of the orthorhombic model in **Figure C-2** is that the (013) peak at *ca*. $2\theta = 9.05°$ is fit more poorly by this model.

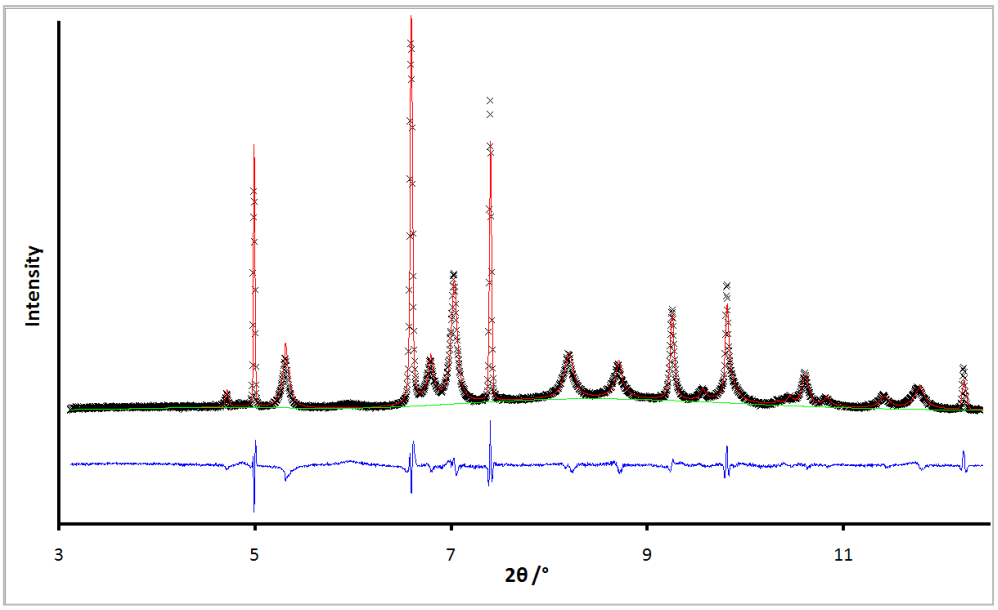

Figure C-4: Le Bail fit to the powder pattern for **Pt·0.5(bpac)**{EtOH} at 310 K (HS).

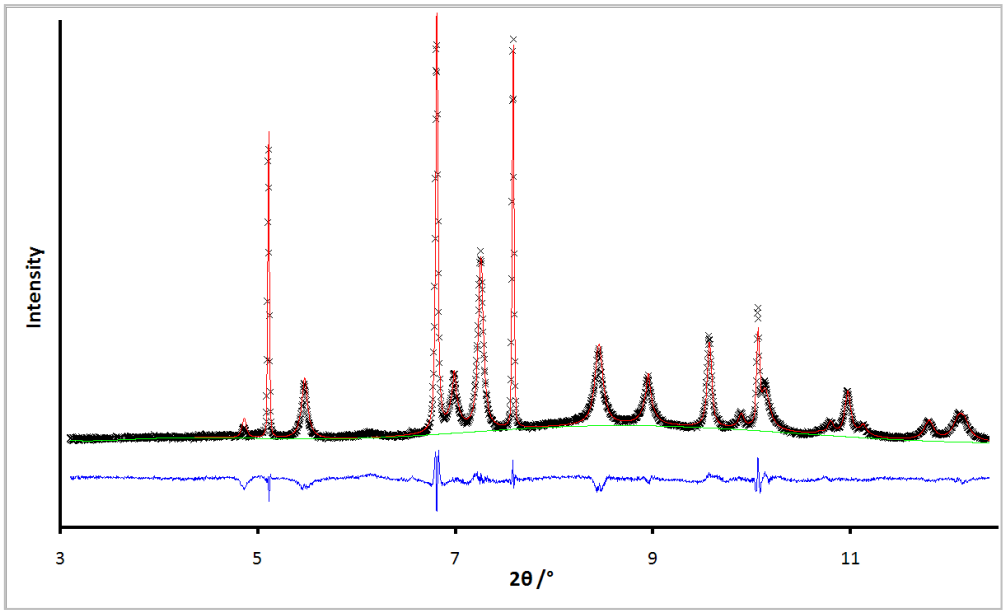

Figure C-5: Le Bail fit to the powder pattern for **Pt·0.5(bpac)**{EtOH} at 250 K (LS).

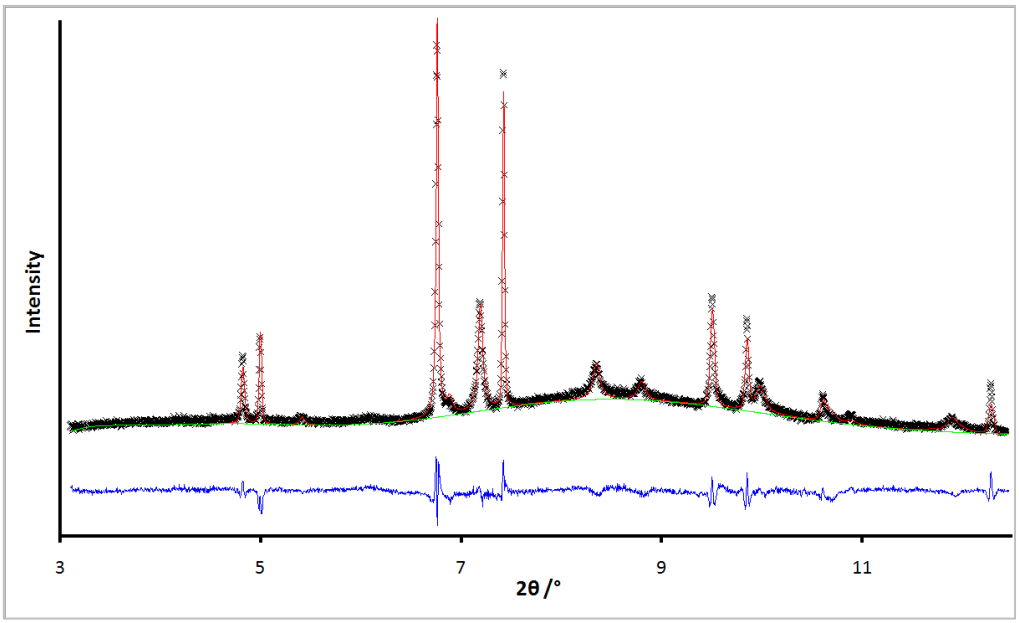

Figure C-6: Rietveld refinement fit to the powder pattern for **Ni·0.5(bpac)**{EtOH} at 310 K (HS).

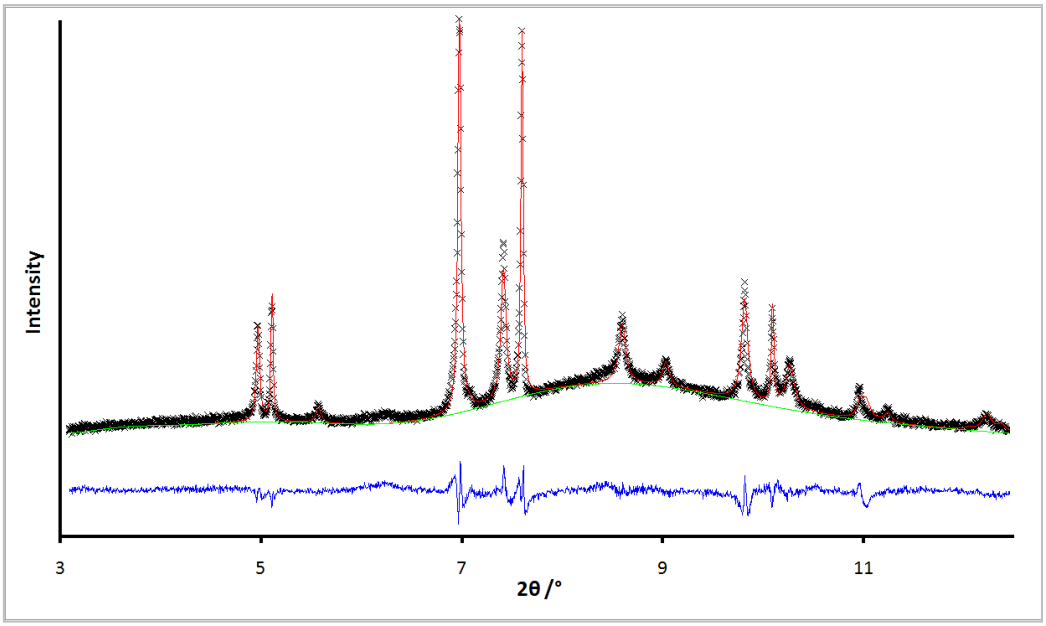

Figure C-7: Rietveld refinement fit to the powder pattern for **Ni·0.5(bpac)**{EtOH} at 250 K (LS).

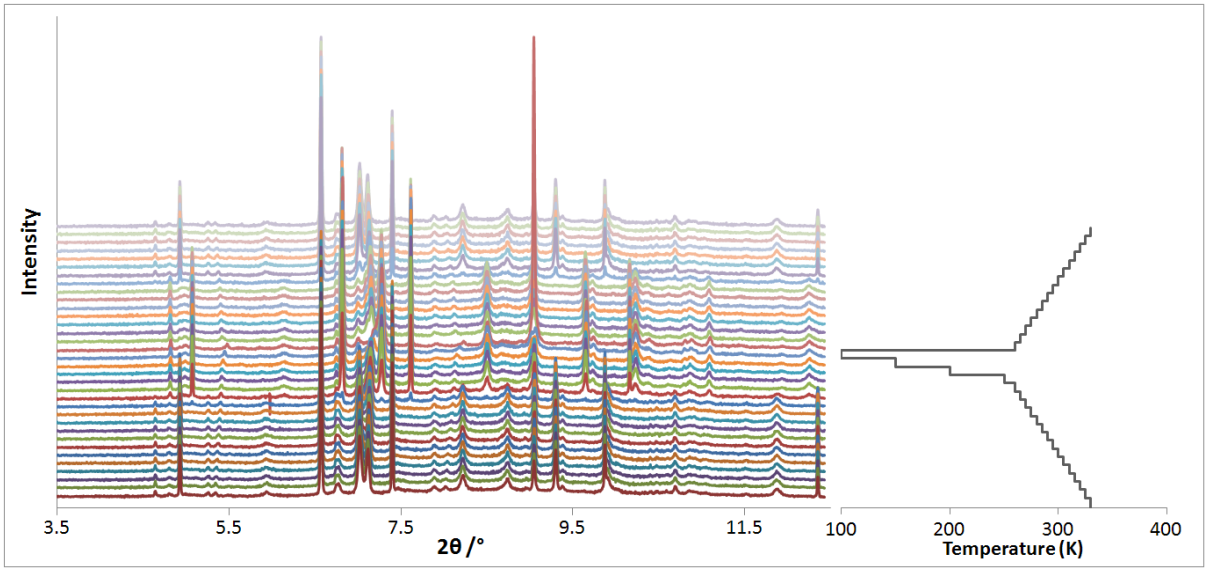

Figure C-8: A portion of the variable temperature powder X-ray diffraction patterns for **Pd·0.4(bpac)**{EtOH}. The structural transition is clearly seen as the sample is cooled from 330 to 100 K, then warmed back up to 330 K.

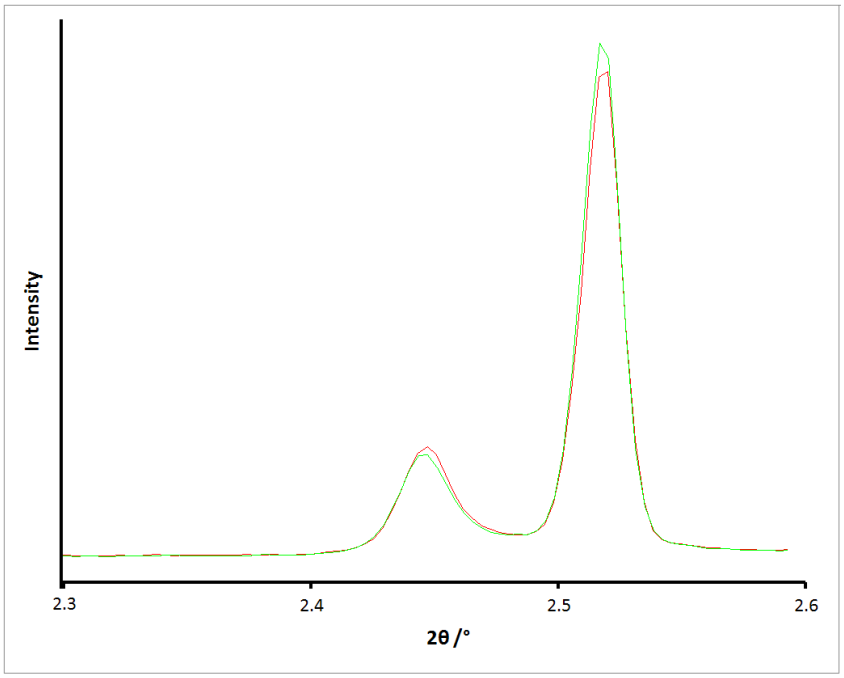

Figure C-9: Comparison of the powder patterns for **Pd·0.4(bpac)**{EtOH} at 260 K and 150 K. Between these two temperatures, some of the HS crystallites have undergone SCO, decreasing the HS fraction and increasing the LS fraction. The peak shown corresponds to the (001) reflection.

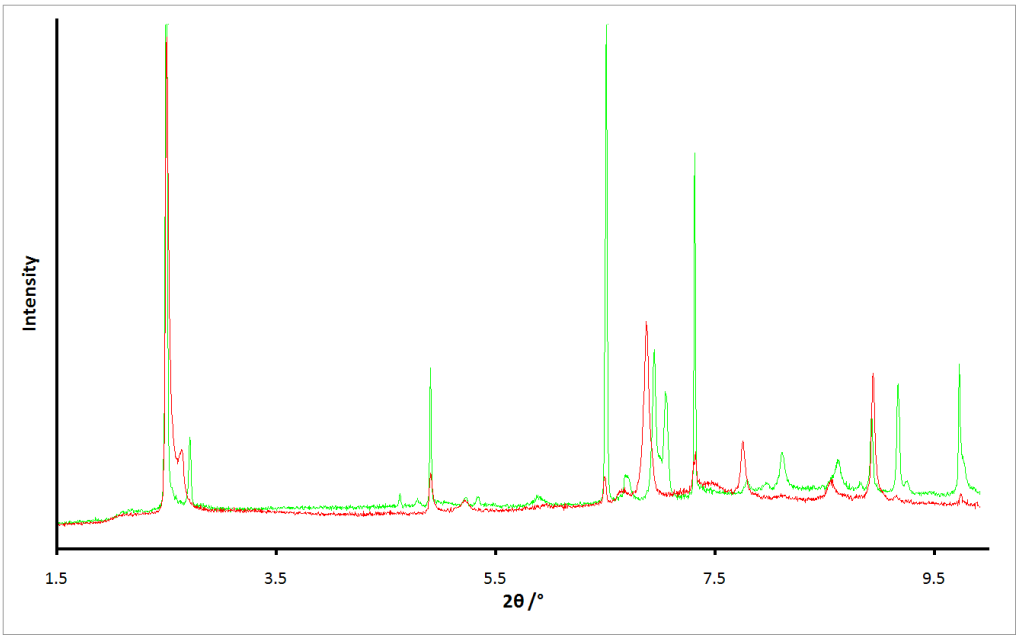

Figure C-10: Comparison of the powder patterns for **Pd·0.4(bpac)**{EtOH} at 300 K (HS) and **Pd·0.4(bpac)**{1-PnOH} at 300 K (HS). Although they are both in the HS state, the peak intensities and distribution are significantly different, implying the two samples have different unit cells and/or space groups.

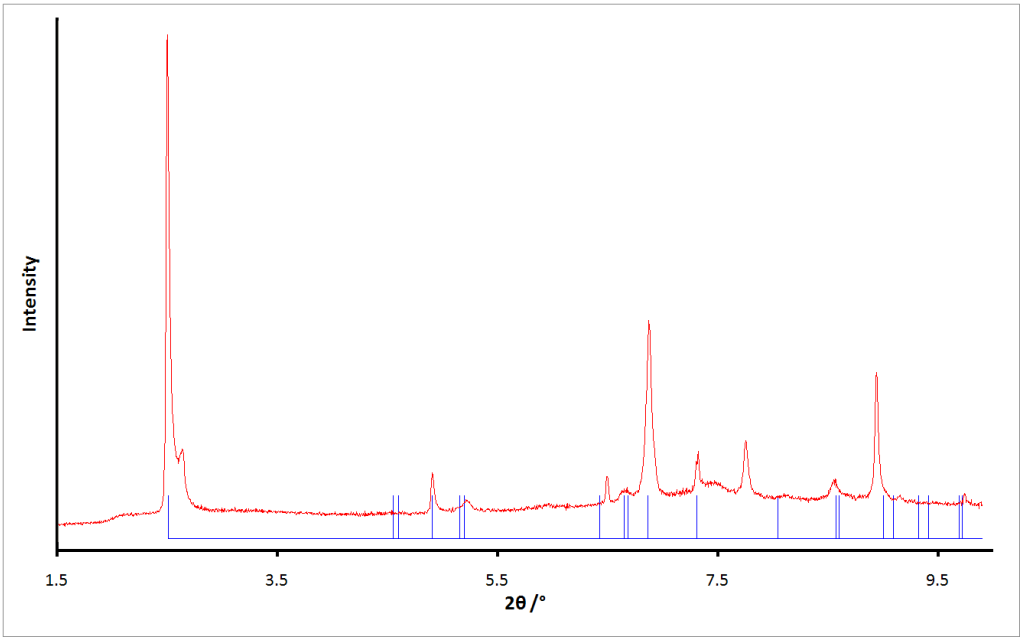

Figure C-11: the powder diffractogram of — **Pd·0.4(bpac)**{1-PnOH} at 300 K (HS), and — the peak distribution with the normal *Pmmm* unit cell. It is clear that important peaks are missed by this model.

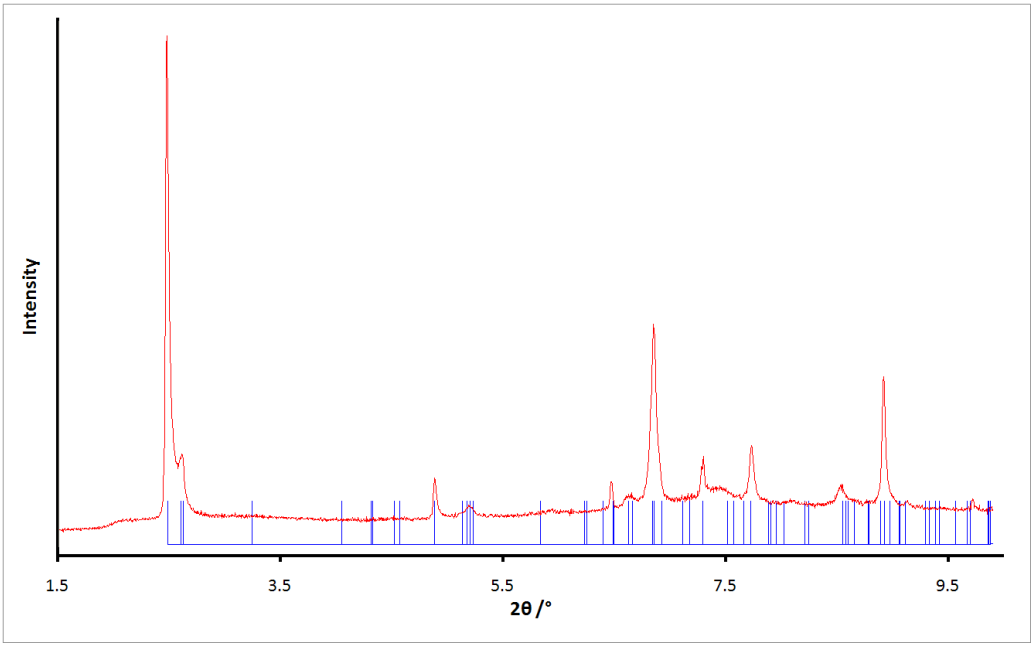

Figure C-12: the powder diffractogram of — **Pd·0.4(bpac)**{1-PnOH} at 300 K (HS), and — the peak distribution with the *Immm* unit cell, in which all three unit cell parameters are doubled compared to the normal *Pmmm* unit cell. All peaks are fit, though there are many other theoretical peaks shown which have no intensity in the experimental pattern, possibly due to pseudosymmetry.

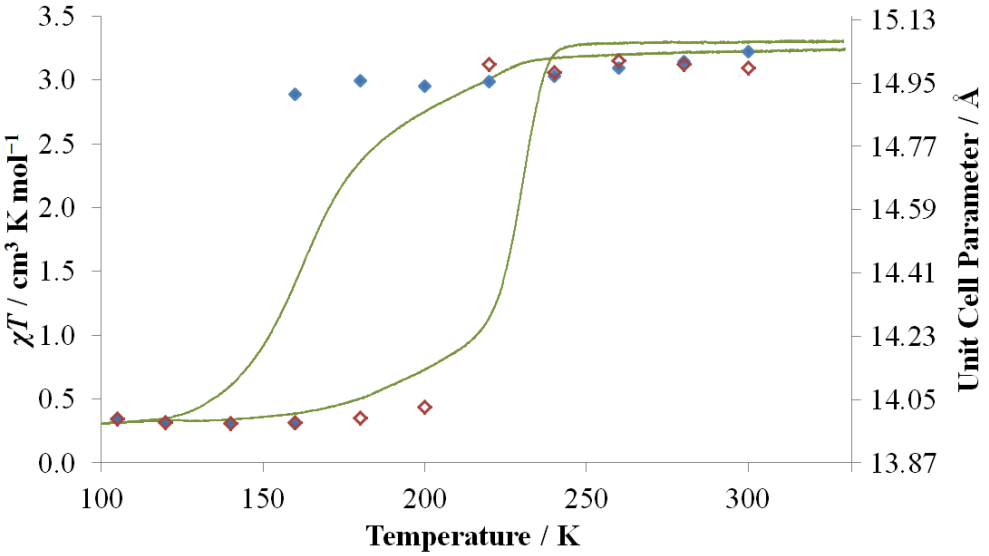

Figure C-13: Comparison of variable temperature data for **Pd·0.4(bpac)**{1-PnOH}: ▬ the magnetic susceptibility; and the *a*-parameter calculated using powder X-ray diffraction data upon ◆ cooling and ◇ warming

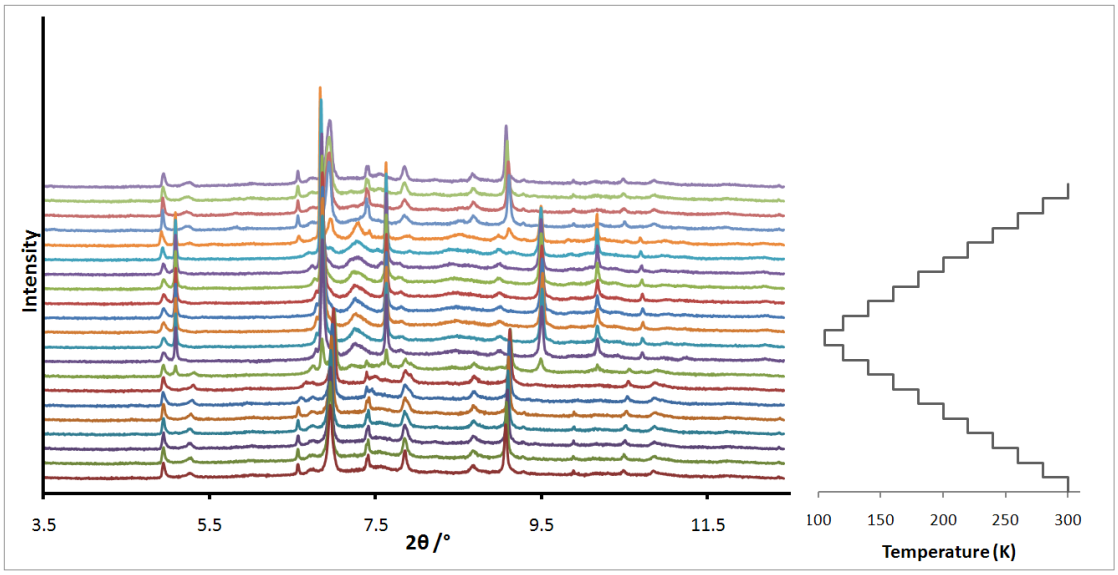

Figure C-14: A portion of the variable temperature powder X-ray diffraction patterns for **Pd·0.4(bpac)**{1-PnOH}. The structural transition is clearly seen as the sample is cooled from 300 to 105 K, then warmed back up to 300 K.

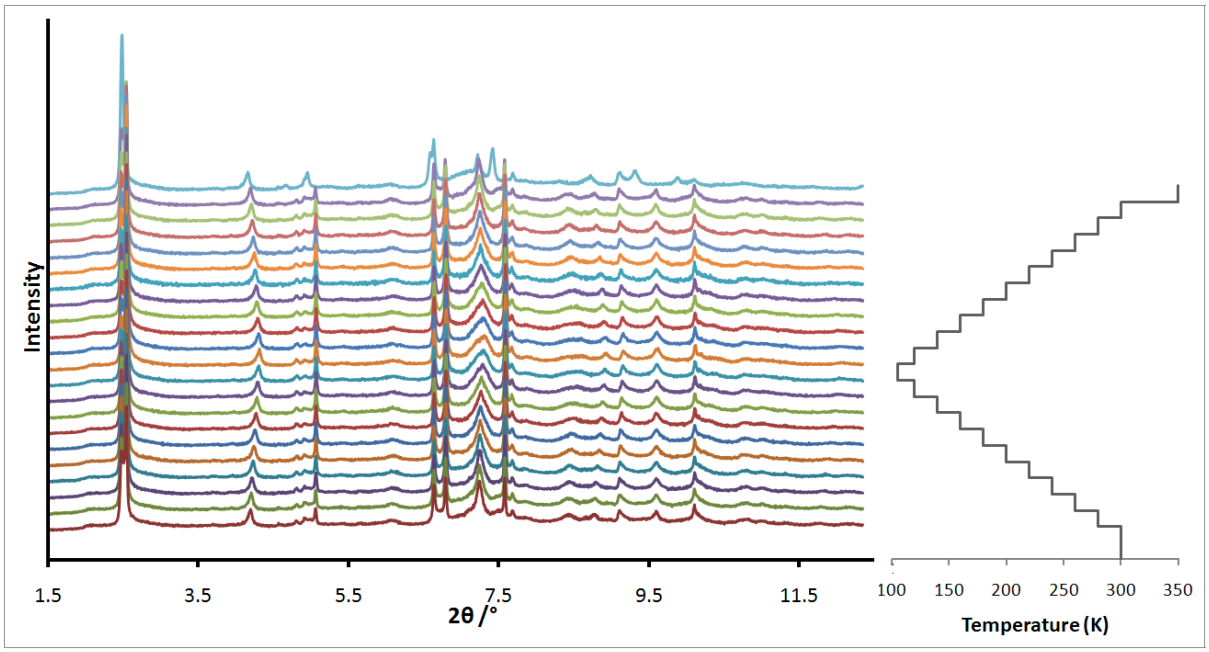

Figure C-15: A portion of the variable temperature powder X-ray diffraction patterns for **Pd·0.4(bpac)**{Ø}. The sample is cooled from 300 to 100 K, then warmed back up to 300 K with a further data point taken at 350 K.

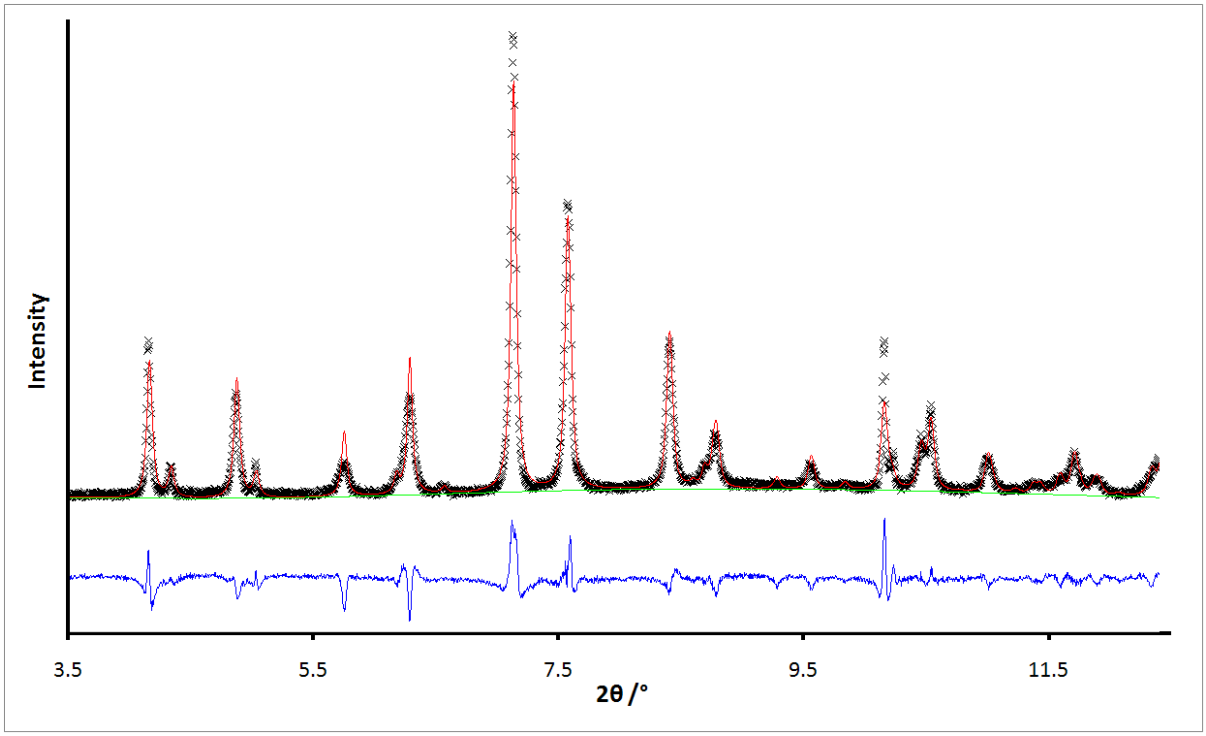

Figure C-16: Le Bail fit to the powder pattern for **Au**·{EtOH} at 240 K (HS).

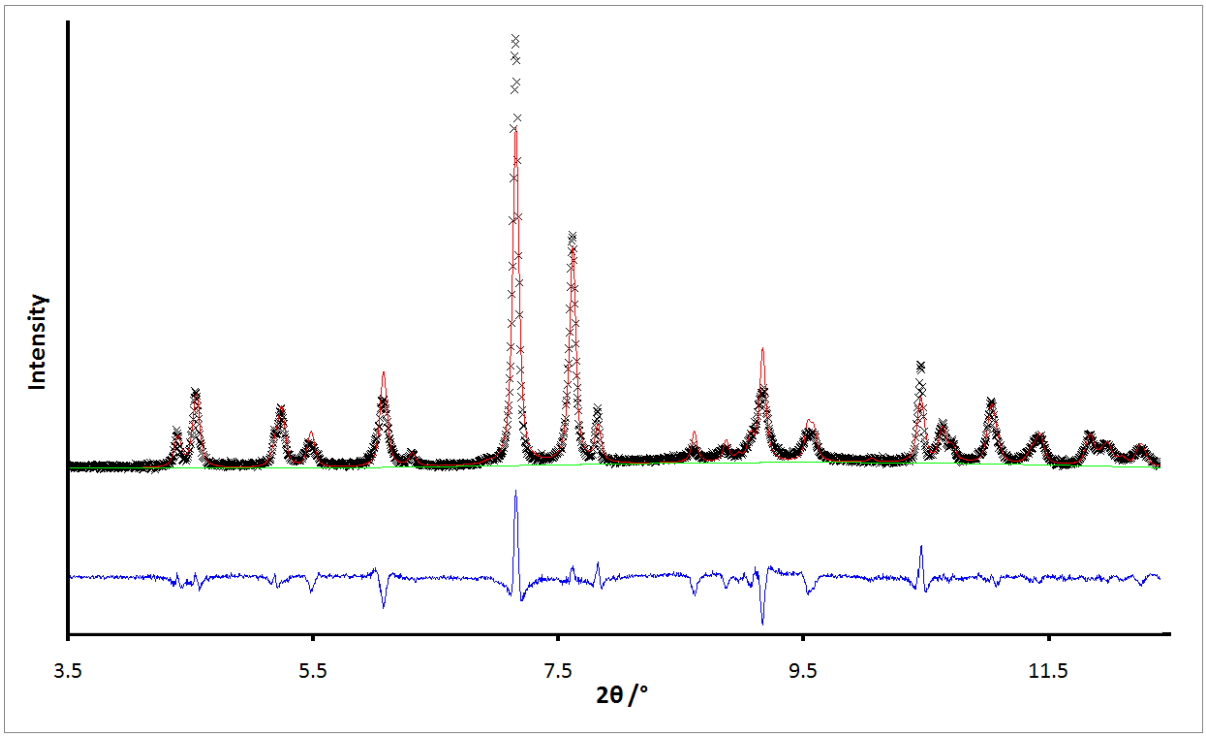

Figure C-17: Le Bail fit to the powder pattern for **Au**·{EtOH} at 190 K (LS).

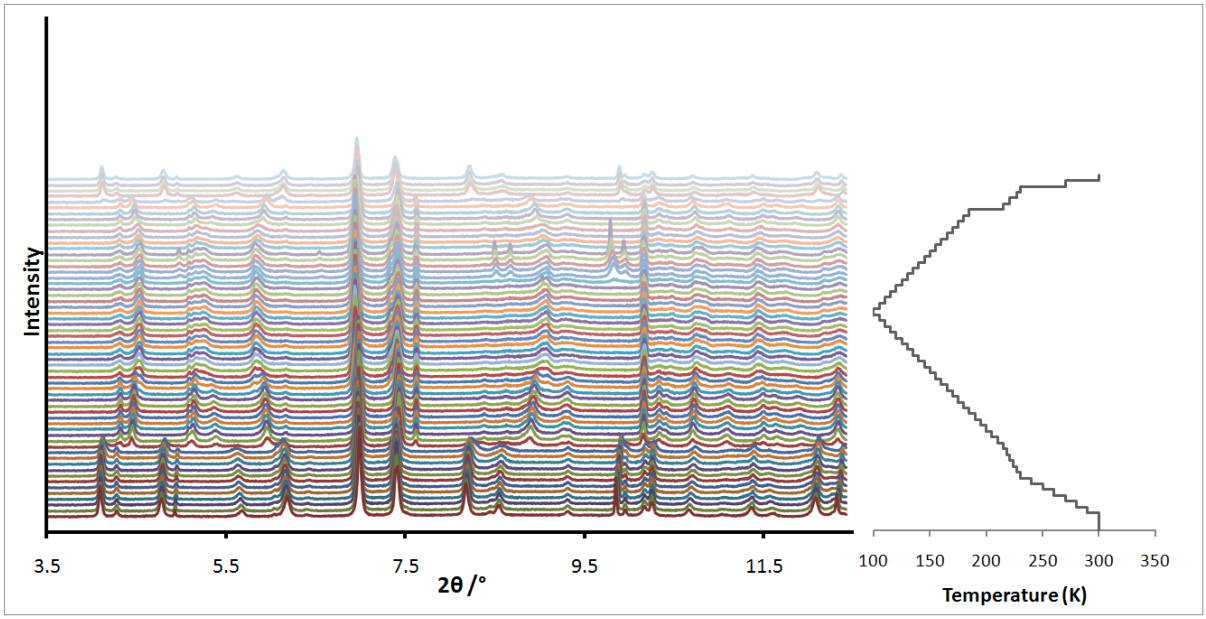

Figure C-18: A portion of the variable temperature powder X-ray diffraction patterns for **Au**·{EtOH}. The sample is cooled from 300 to 100 K, then warmed back up to 300 K over different temperature intervals. The unit cell parameter divergence can be clearly seen by the movement of the peaks. On warming at 130–150 K, a crystalline EtOH phase was also observed and refined with the framework phase.

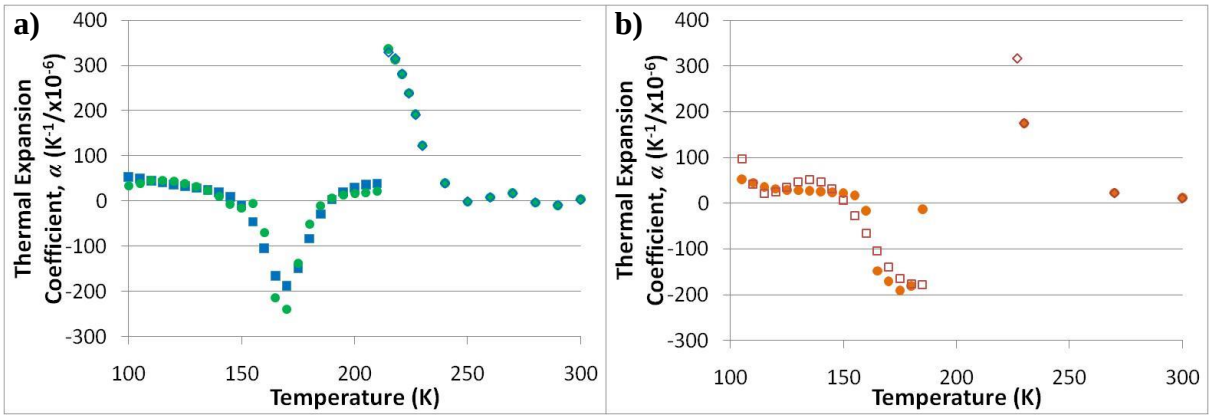

Figure C-19: Volumetric thermal expansion coefficients for **Au**·{EtOH} upon **a)** cooling and **b)** warming, as calculated using using **Equation 1.4** (circles) or by fitting a model to the data (squares and diamonds). The parameters show very high correlation above the spin transition, with moderate correlation below the spin transition, especially for the warming data.

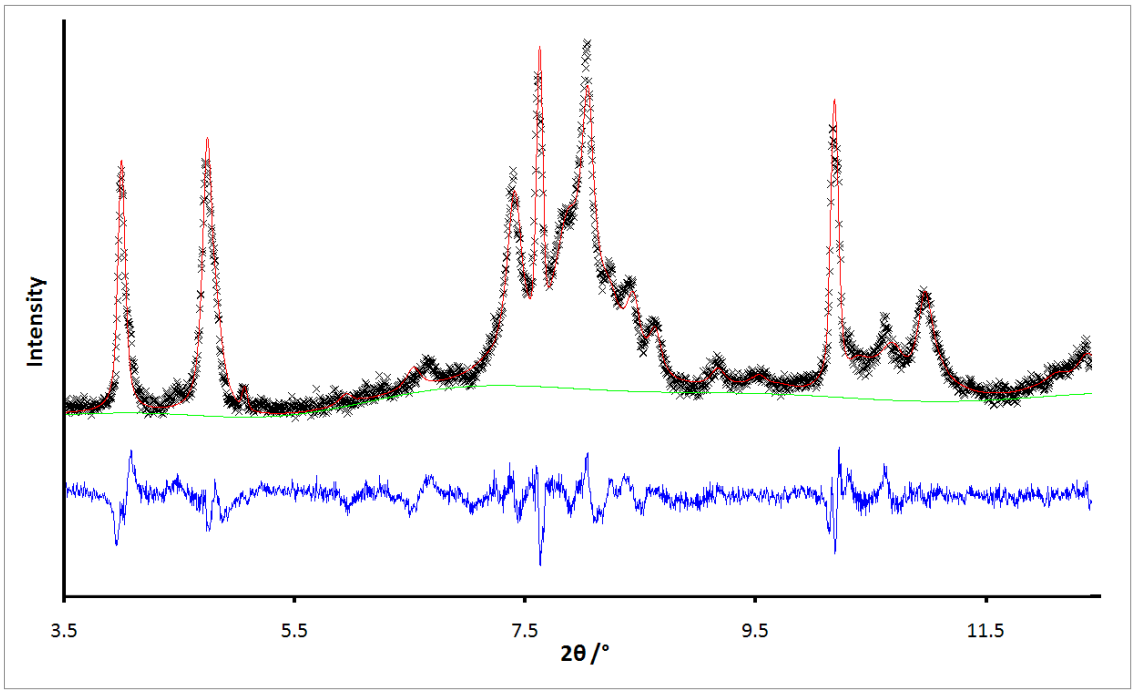

Figure C-20: Le Bail fit to the powder pattern for **Au**·{Ø} at 300 K (HS). The peaks are not fit very well due to a distribution of framework lattice parameters in the bulk.

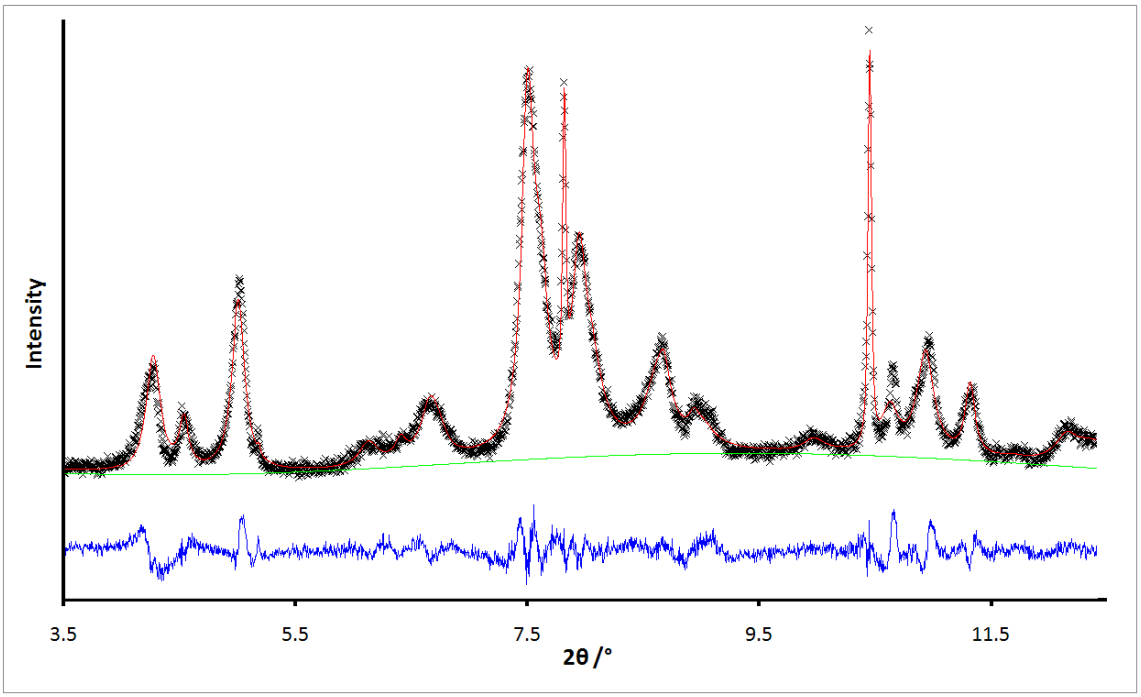

Figure C-21: Le Bail fit to the powder pattern for **Au**·{Ø} at 180 K (LS).

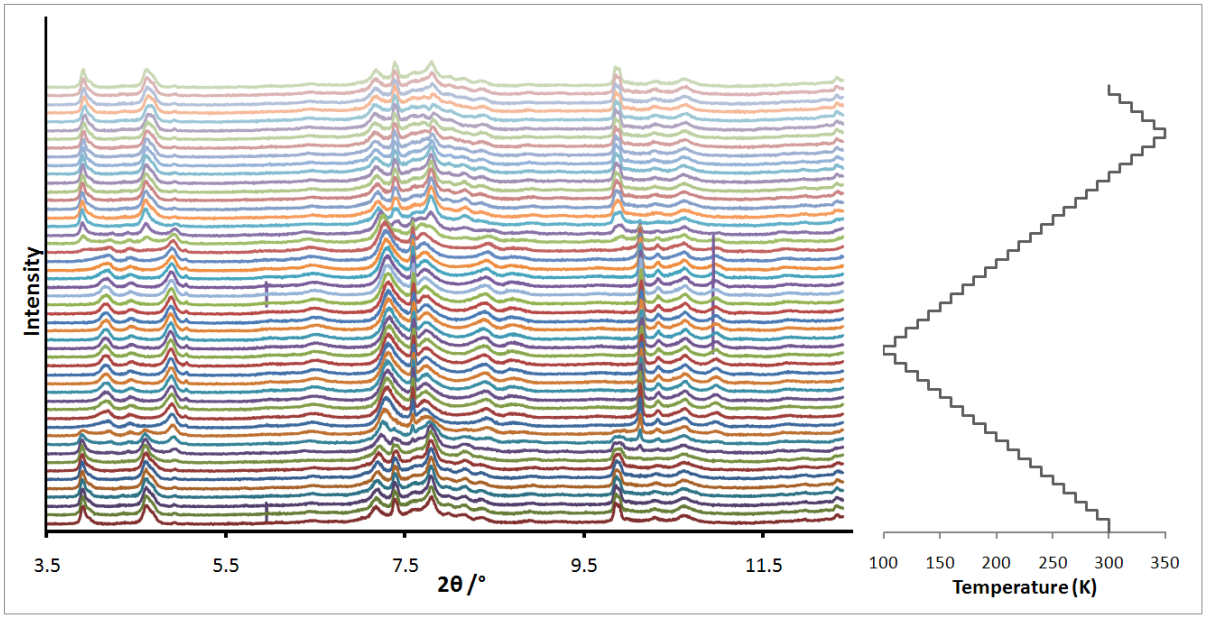

Figure C-22: A portion of the variable temperature powder X-ray diffraction patterns for **Au**·{Ø}. The sample is cooled from 300 to 100 K, then warmed up to 350 K, then back down again to 300 K at 10 K intervals. The paucity of useful data is clear when compared to the **Au**·{EtOH} powder patterns, shown in **Figure C-18**.

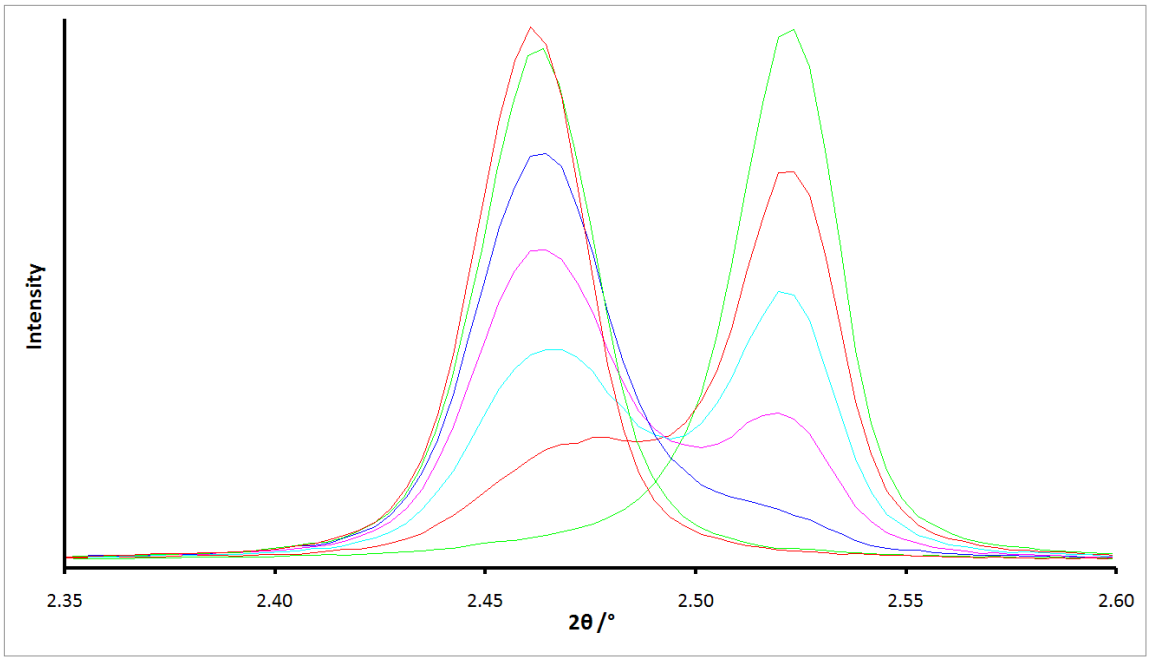

Figure C-23: Comparison of the (001) peak in the powder patterns for **Au**·{Ø} from 250 to 190 K. There are two distinct HS and LS phases observed over the spin transition, but there is still some movement of the two peaks as the fractions of the two phases increase or decrease, implying that some Fe(II) sites within the crystallites undergo spin transition independently of the rest of the crystallite.

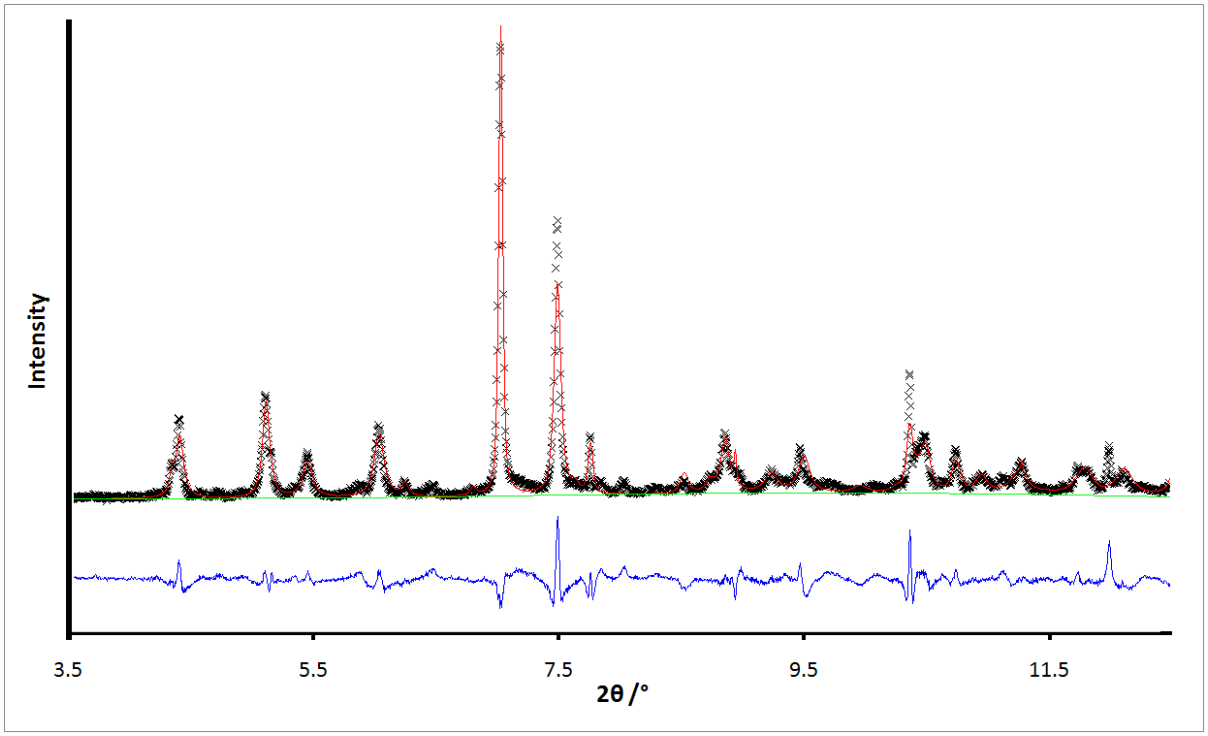

Figure C-24: Le Bail fit to the powder pattern for **Au**·{MeOH} at 270 K (HS), using the *Cmma* space group with the normal *c*-parameter. There are a few small peaks which are not fit at all, and many of the remaining peaks are fit poorly.

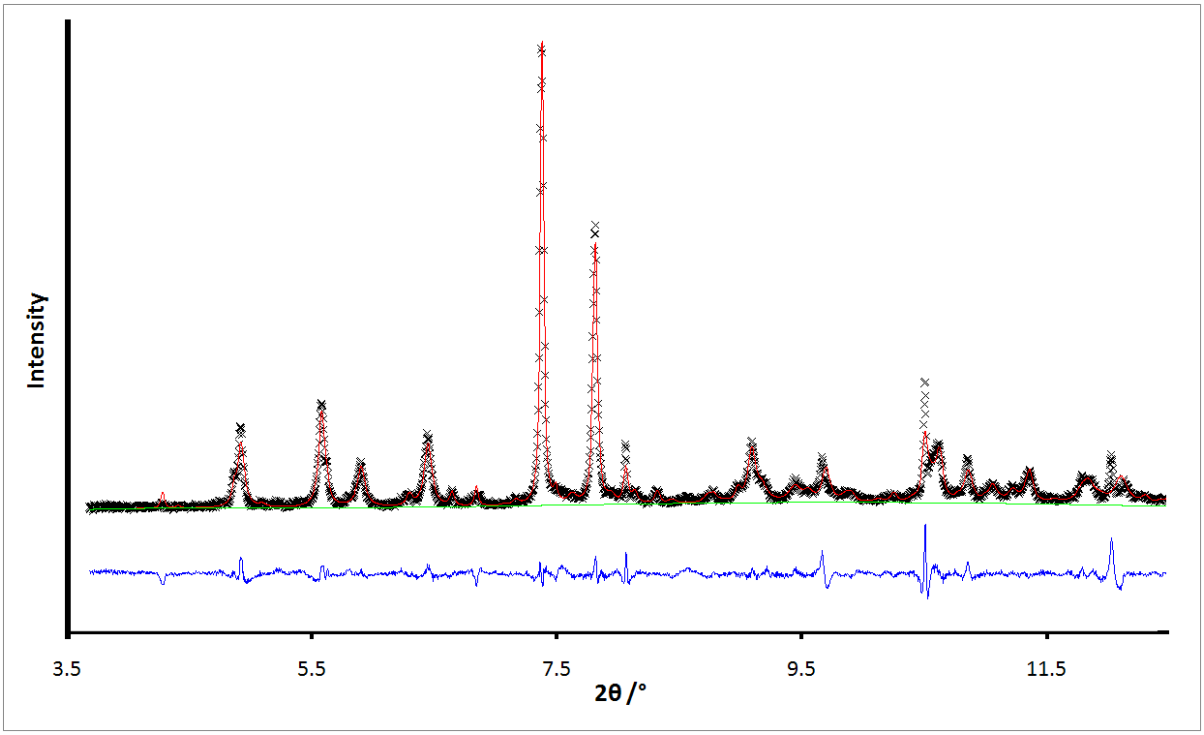

Figure C-25: Le Bail fit to the powder pattern for **Au**·{MeOH} at 270 K (HS), using the *Cmma* space group with a doubled *c*-parameter compared to normal. Nearly all observed peaks are fit reasonably well, with the exception of a small peak at *ca*. 2θ = 11.6°.

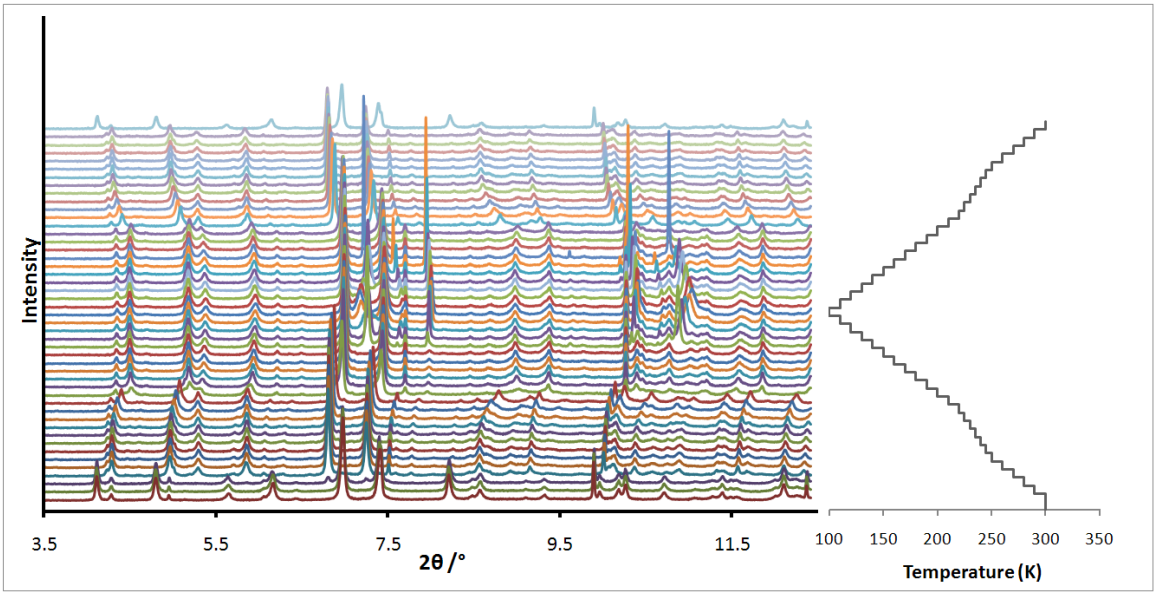

Figure C-26: A portion of the variable temperature powder X-ray diffraction patterns for **Au**·{MeOH}. The sample is cooled from 300 to 100 K, then warmed back up to 300 K at either 5 or 10 K intervals. Ice formed on the capillary at low temperature, and was refined as an additional phase with the framework between the 140 K cooling and 170 K warming data.

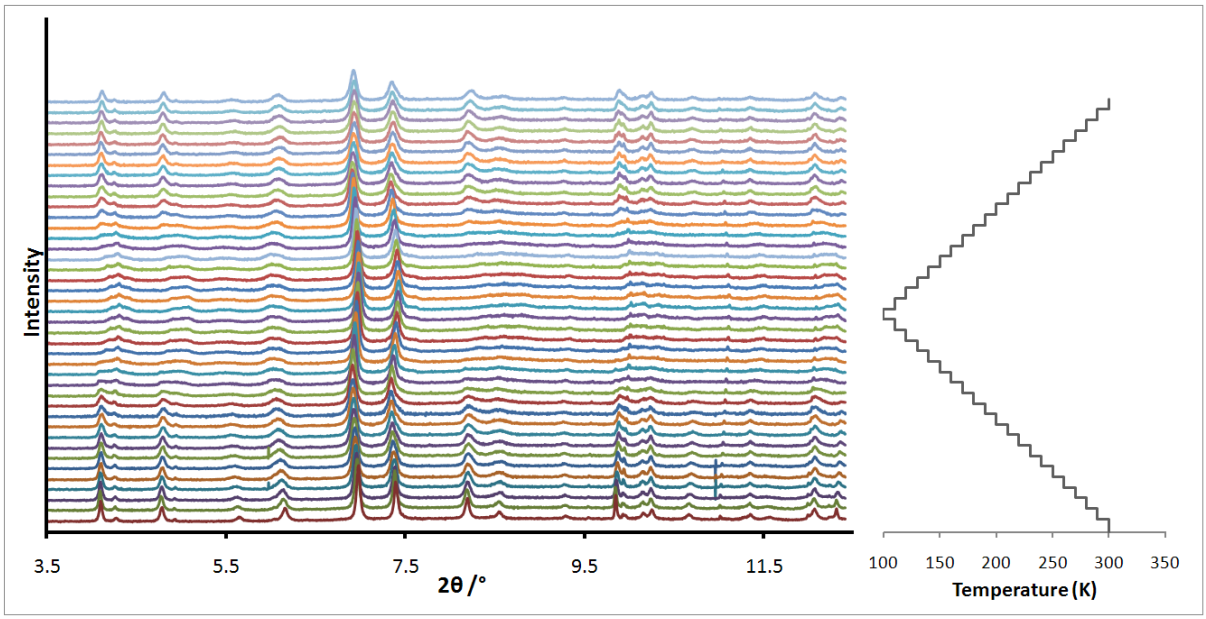

Figure C-27: A portion of the variable temperature powder X-ray diffraction patterns for **Au**·{1-PrOH}. The sample is cooled from 300 to 100 K, then warmed back up to 300 K at 10 K intervals. The peaks noticeably broaden as the material undergoes spin transition, due to a range of lattice parameters among the crystallites.

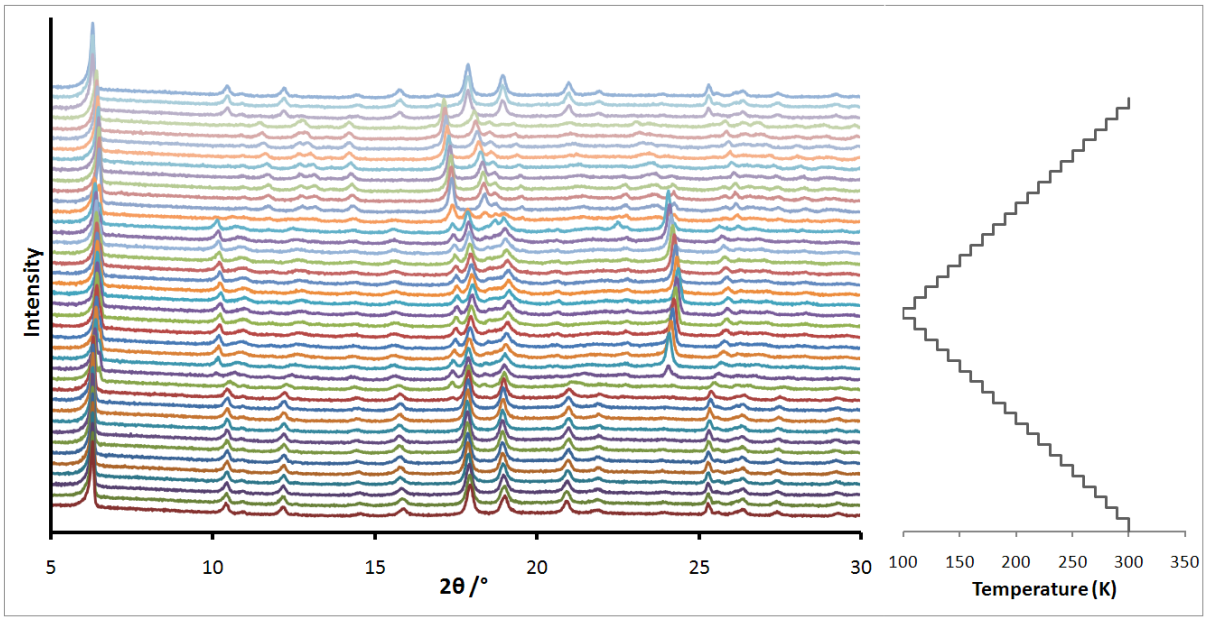

Figure C-28: The variable temperature powder X-ray diffraction patterns for **Au**·{1-BuOH}. The sample is cooled from 300 to 100 K, then warmed back up to 300 K at 10 K intervals. There are three distinct phases shown as the sample is warmed from 100 K.

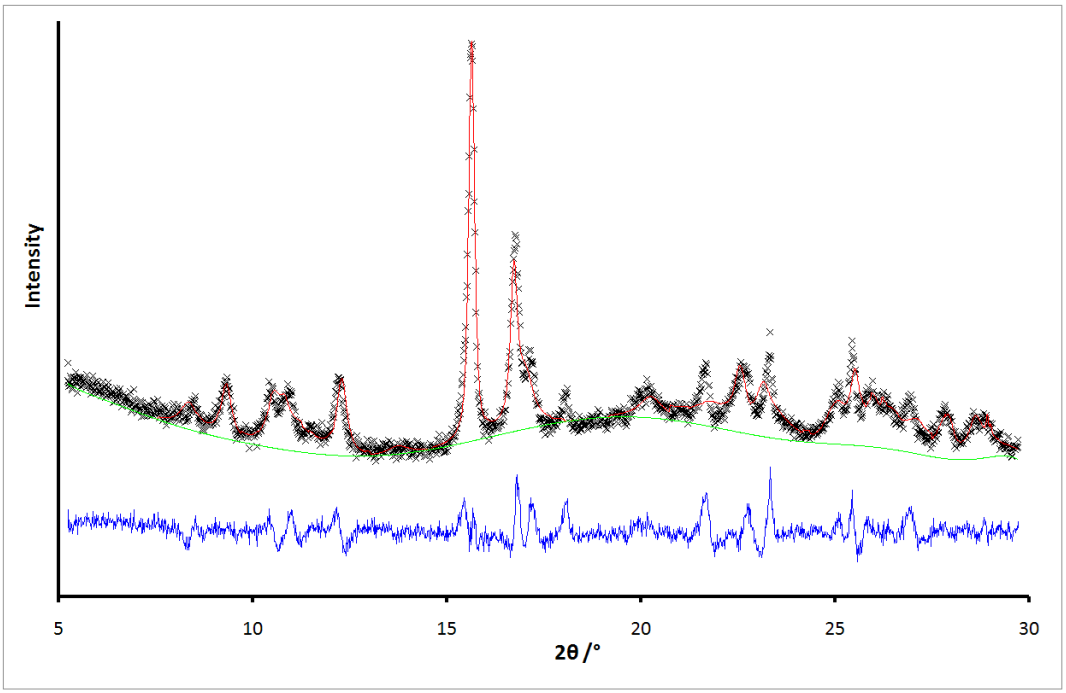

Figure C-29: Le Bail fit to the powder pattern for **Au**·{1-BuOH} at 200 K (decompressed phase), using the orthorhombic *Cmma* space group with a non-modified unit cell. The peaks are fit poorly.

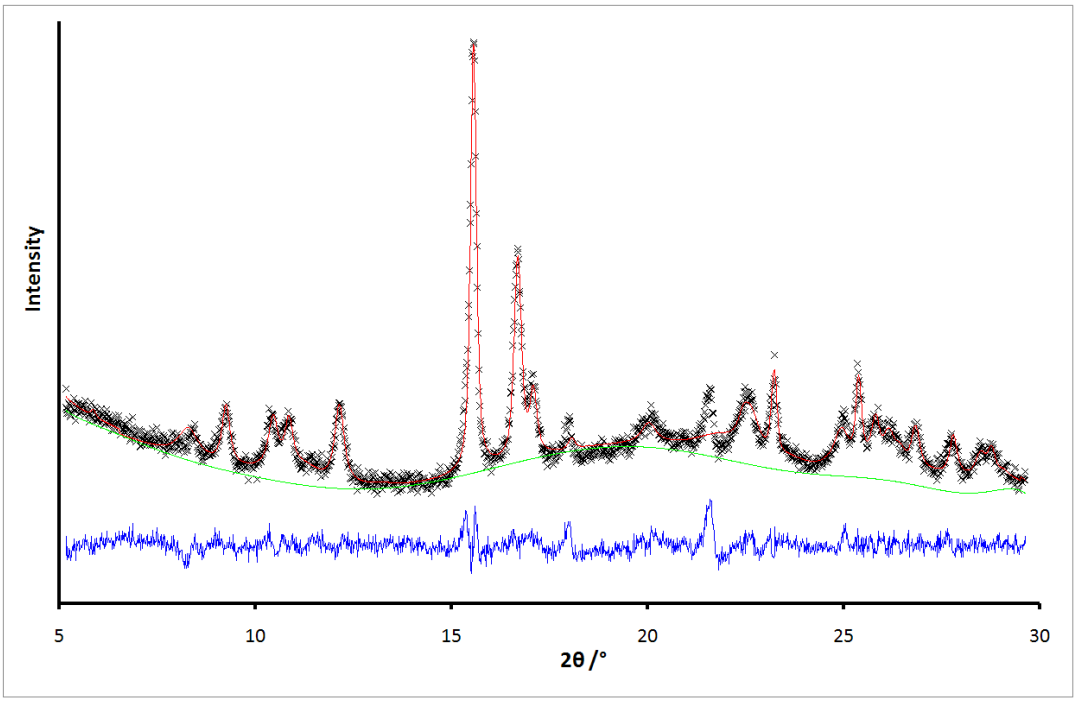

Figure C-30: Le Bail fit to the powder pattern for **Au**·{1-BuOH} at 200 K (decompressed phase), using the monoclinic *C*2/*m* space group with the unit cell (13.89, 15.10, 13.61, 92.32, 90, 90). The peaks are fit much better than in **Figure C-29**, with the notable exception of the reflection at 2θ = 23°, which is due to residual crystalline solvent.

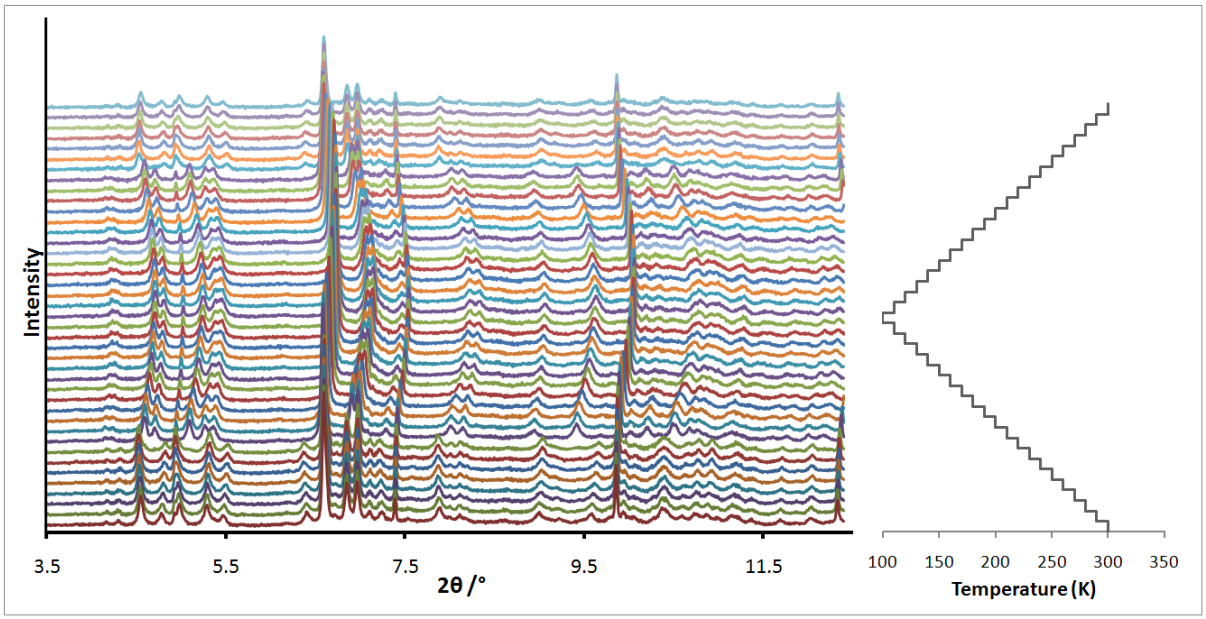

Figure C-31: The variable temperature powder X-ray diffraction patterns for **Au**·{2-BuOH}. The sample is cooled from 300 to 100 K, then warmed back up to 300 K at 10 K intervals. A phase change from a unit cell with a greater to lesser *c*-axis angle distortion is clearly observed in the partial convergence of some peaks (notably the split (2,−2,1) and (−2,−2,1) reflections at *ca*. $2\theta = 7.0°$).

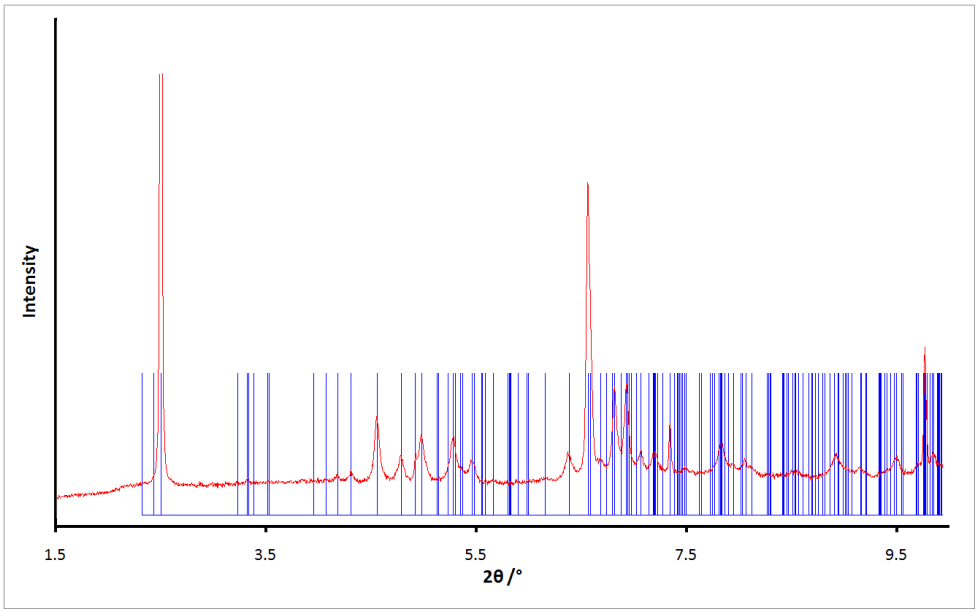

Figure C-32: The powder diffractogram of — **Au**·{2-BuOH} at 300 K (HS); and — the peak distribution with the triclinic *P*1 unit cell (14.43, 15.21, 14.08, 94.94, 92.46, 90). While all peaks are matched by a theoretical reflection, there are many reflections that are not observed.

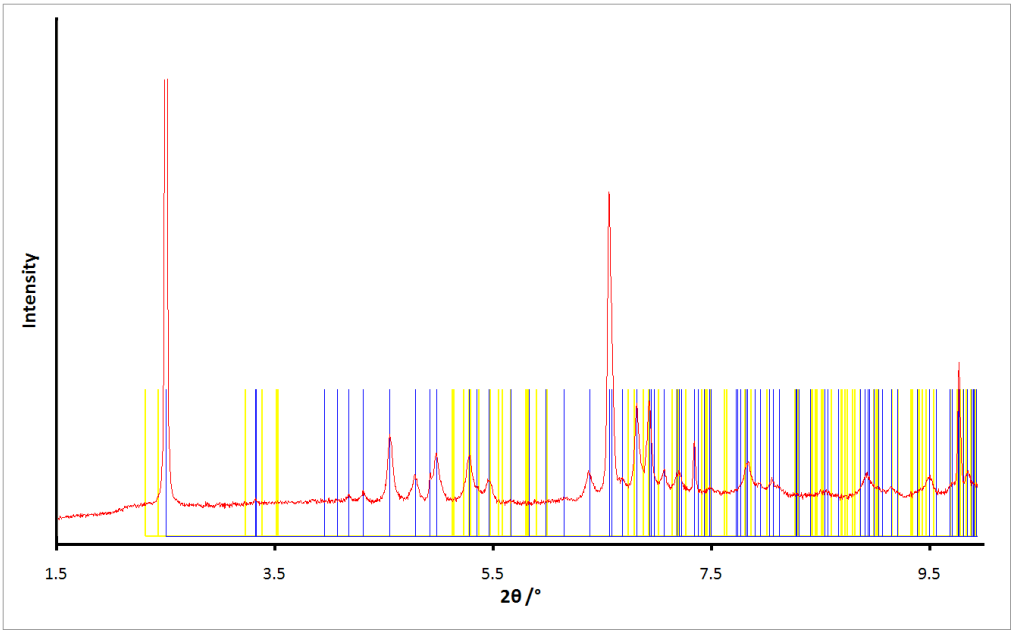

Figure C-33: The powder diffractogram of **Au**·{2-BuOH} at 300 K (HS), and the peak distribution with the triclinic unit cell (14.43, 15.21, 14.08, 94.94, 92.46, 90) and *C*2/*m* space group symmetry. In contrast to the *P*1 space group (**Figure C-32**), all peaks are matched by a reflection, but there are very few reflections without a peak.

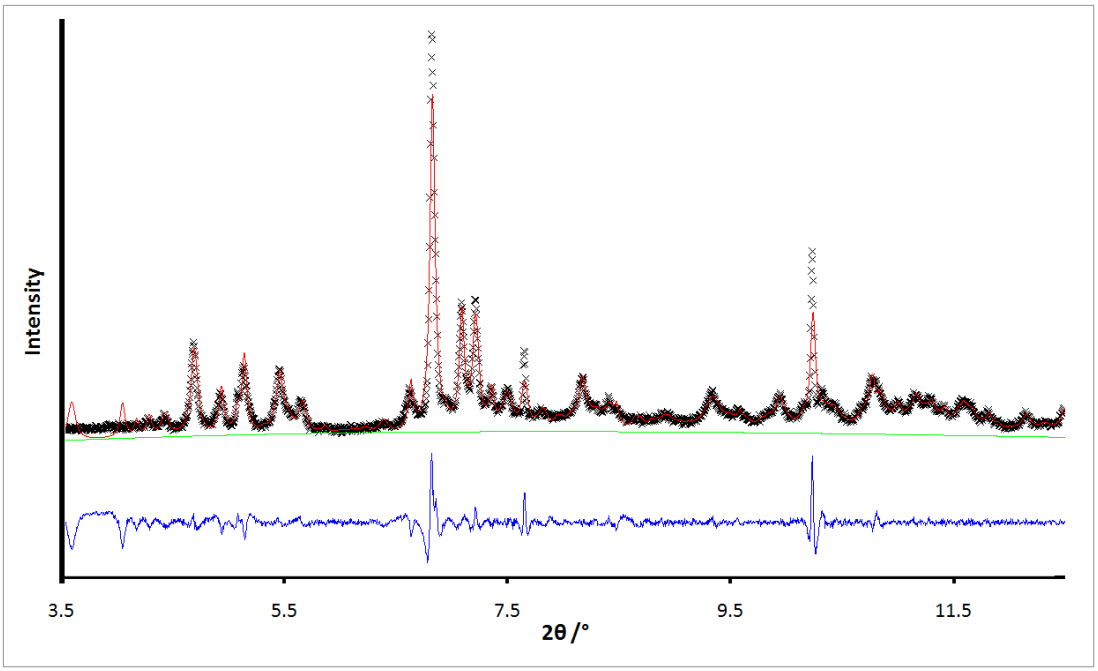

Figure C-34: Le Bail fit to the powder pattern for **Au**·{2-BuOH} at 300 K, using the triclinic *P*1 space group with the unit cell (14.43, 15.21, 14.08, 94.98, 92.55, 90). Every peak is matched by a model reflection, but due to the base-centred pseudosymmetry of the unit cell, there are many reflections that are absent in the diffractogram, and many of the observed peaks are not fit well.

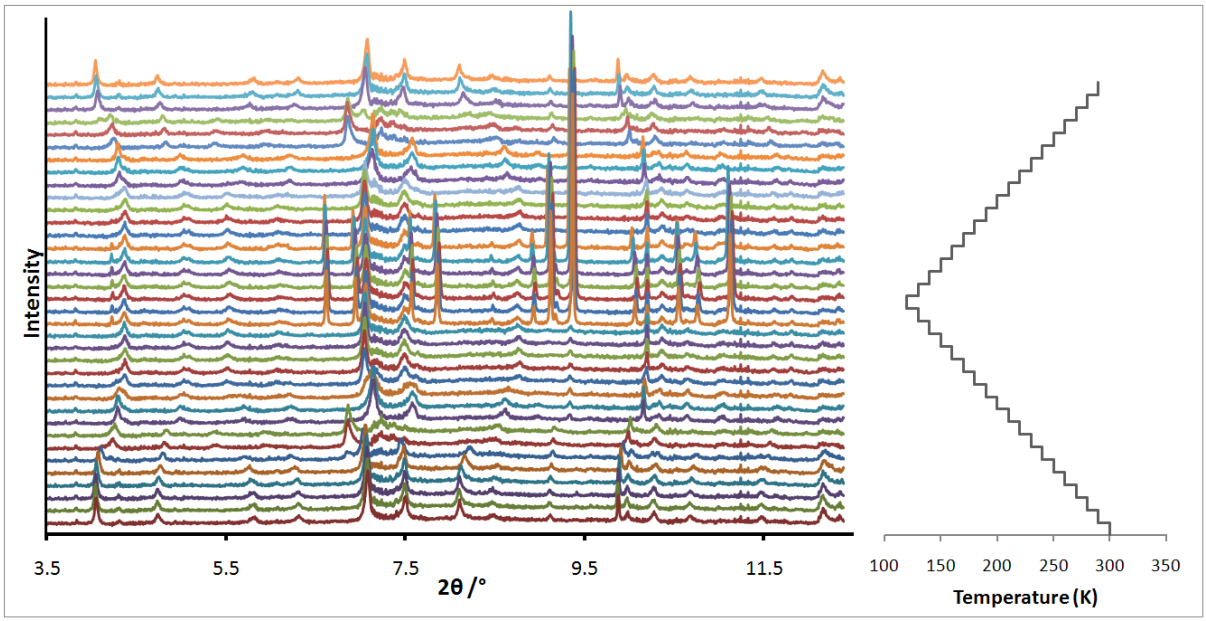

Figure C-35: The variable temperature powder X-ray diffraction patterns for **Au**·{1-PrBr}. The sample is cooled from 300 to 120 K, then warmed back up to 290 K at 10 K intervals. The sharp peaks present at low temperature are due to frozen 1-PrBr crystallites.

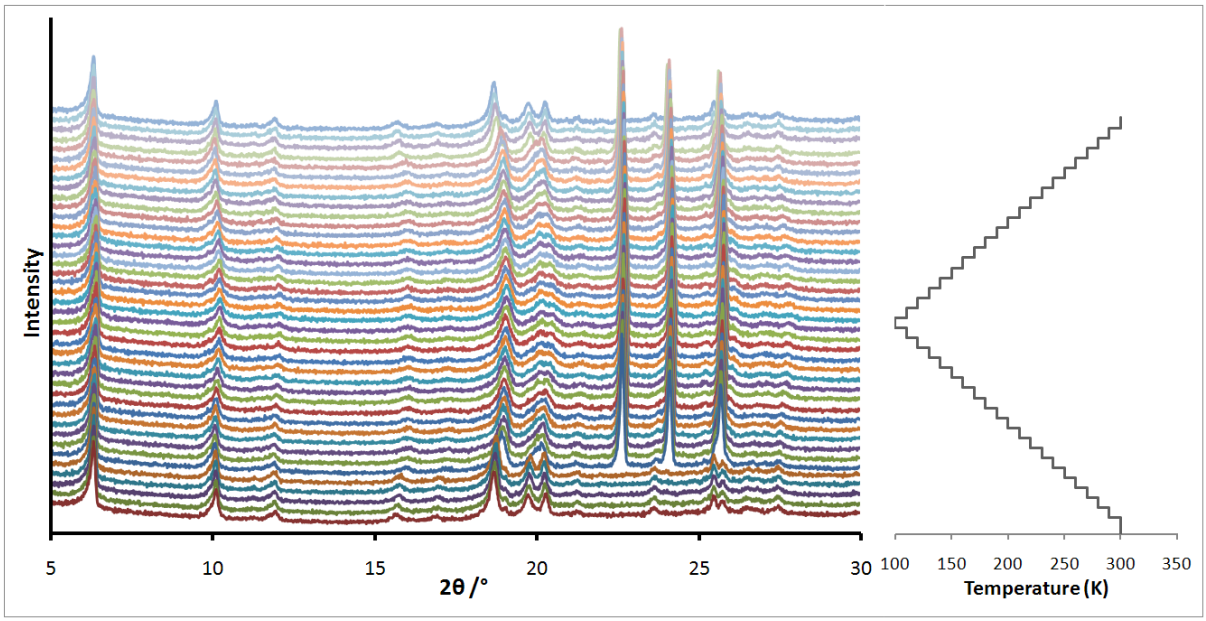

Figure C-36: The variable temperature powder X-ray diffraction patterns for **Au**·{H_2O}. The sample is cooled from 300 to 100 K, then warmed back up to 300 K at 10 K intervals. The split (221) peak at *ca.* $2\theta = 20°$ indicates that the structure has a similar unit cell distortion as was observed in the **Au**·{2-BuOH} sample. The sharp peaks present at low temperature are due to frozen H_2O crystallites.

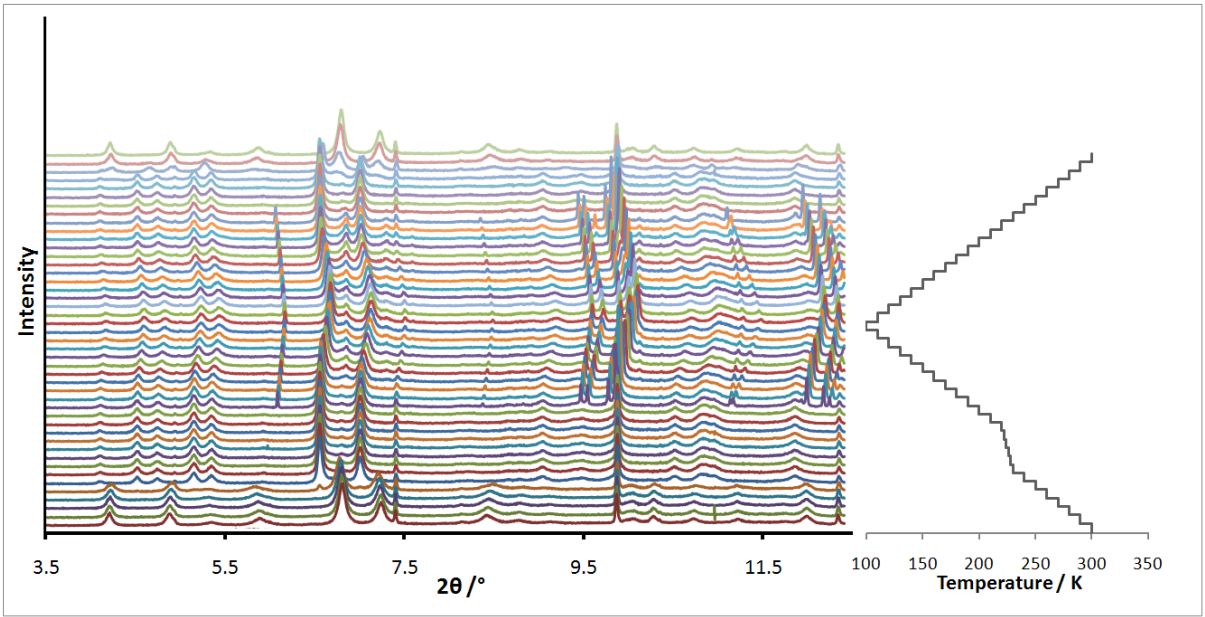

Figure C-37: The variable temperature powder X-ray diffraction patterns for **Au**·{MeCN}. The sample is cooled from 300 to 100 K, then warmed back up to 300 K. Crystalline frozen MeCN is observed below *ca*. 210 K, and a second minor framework phase is observed below 170 K in the cooling data, until 240 K in the warming data.

Appendix D: Solvent Physical Properties

This table provides the values for various physical properties of the solvents included as guests in the framework materials studied in this thesis. Values are given at atmospheric pressure. The density values were obtained at 20 °C (except for 1-PrOH, which is at 25 °C), and all viscosity values were obtained at 25 °C.[1] The molecular volumes were calculated using a software macro.[2]

Solvent	**MW / g mol^{-1}**	**MP / K**	**BP / K**	**Density / g ml^{-1}**	**viscosity / mPa s**	**Calc. Molecular Volume / Å^3**
MeOH	32.04	176	338	0.791	0.544	36.84
EtOH	46.07	159	351	0.789	1.074	53.73
1-PrOH	60.10	149	370	0.800	1.945	70.75
1-BuOH	74.12	185	391	0.810	2.544	87.74
2-BuOH	74.12	158[3]	373	0.806	3.096	87.81
1-PnOH	88.15	196	411	0.814	3.619	104.72
$MeCl_2$	84.93	176	313	1.327	0.413	56.33
MeBrCl	129.38	185	341	1.934	0.667[4]	60.69
EtBr	108.97	155	312	1.460	0.374	63.56
EtI	155.97	162	345	1.936	0.556	69.78
1,2-$EtCl_2$	98.96	237	357	1.245	0.779	73.30
1,2-$EtBr_2$	187.86	283	405	2.168	1.595	81.98
PrCl	78.54	150	320	0.890	0.334	76.20
PrBr	122.99	163	344	1.354	0.489	80.55
PrI	169.99	172	376	1.749	0.703	86.78
MeCN	41.05	229	355	0.786	0.369	44.87
H_2O	18.00	273	373	0.998	0.894	19.51
CS_2	76.14	161	319	1.263	0.352	53.70

References

(1) Lide, D. R. *CRC Handbook of Chemistry and Physics*; 84 ed.; CRC Press: Boca Raton, FL, USA, 2003-2004.
(2) Calculator Plugins were used for structure property prediction and calculation, Marvin v 5.9.4, **2012**, ChemAxon, http://www.chemicalize.org (accessed on May 14 2012)
(3) 2-butanol, http://webbook.nist.gov, **2012**, (accessed on July 30, 2012)
(4) Dreisbach, R. R. *Physical Properties of Chemical Compounds*; Am. Chem. Soc.: Washington, 1959.

Appendix E: Crystallographic Parameters Extracted from Variable Temperature Powder X-ray Diffraction

Included in each of the following tables are the *a*-, *b*- and *c*-parameters, unit cell volume and the calculated linear Fe–M–Fe distance. Values given are the raw values determined using the relevant unit cell model, and are not adjusted to be comparable with other datasets. In the **Au** framework structures, the calculated acute Au–Fe–Au angles are also presented. For the monoclinic and triclinic structures, the non-90° unit cell angles are also given. Where a structure was modelled in a single space group throughout, it is given in the table heading. Where the framework is modelled with different space groups in the same variable temperature run, the space group is given for the modelled phase(s) at each temperature.

Pd·{EtOH} (Pmmm)

#	Temp / K	Spin State	*a*-parameter / Å	*b*-parameter / Å	*c*-parameter / Å	Volume / Å^3	Fe–Pd–Fe Distance / Å
00	330	HS	7.4458(6)	7.4533(6)	14.03746(23)	779.0(3)	10.5353(8)
01	325	HS	7.4465(6)	7.4538(6)	14.03833(22)	779.2(2)	10.5361(8)
02	320	HS	7.4459(6)	7.4531(7)	14.03719(22)	779.0(3)	10.5352(9)
03	315	HS	7.4464(6)	7.4540(6)	14.03815(23)	779.2(3)	10.5362(8)
04	310	HS	7.4461(6)	7.4534(6)	14.03737(22)	779.1(2)	10.5355(8)
05	305	HS	7.4469(6)	7.4538(6)	14.03828(22)	779.2(2)	10.5364(8)

#	Temp / K	Spin State	*a*-parameter / Å	*b*-parameter / Å	*c*-parameter / Å	Volume / Å^3	Fe–Pd–Fe Distance / Å
06	300	HS	7.4477(8)	7.4520(8)	14.03688(21)	779.1(3)	10.5357(1)
07	295	HS	7.4472(6)	7.4539(6)	14.03831(21)	779.3(2)	10.5367(8)
08	290	HS	7.4469(6)	7.4534(6)	14.03690(21)	779.1(2)	10.5361(8)
09	285	HS	7.4475(6)	7.4535(6)	14.03727(21)	779.2(2)	10.5366(8)
10	280	HS	7.4495(6)	7.4503(6)	14.03614(20)	779.0(2)	10.5357(8)
11	275	HS	7.4472(5)	7.4541(6)	14.03739(21)	779.2(2)	10.5368(7)
12	270	HS	7.4407(4)	7.4691(4)	14.04170(18)	780.4(2)	10.5428(5)
13	265	HS	7.4283(4)	7.4820(9)	14.04850(15)	780.8(2)	10.1602(9)
13	265	LS	7.2619(7)	7.1060(6)	13.63992(20)	703.9(2)	10.5432(9)
14	260	LS	7.2558(6)	7.1105(5)	13.63840(19)	703.6(2)	10.1590(7)
15	250	LS	7.2579(6)	7.1077(6)	13.63861(18)	703.6(2)	10.1586(8)
16	200	LS	7.2508(6)	7.1081(5)	13.63688(17)	702.8(2)	10.1538(7)
17	150	LS	7.2548(6)	7.1027(6)	13.63913(17)	702.8(2)	10.1529(8)
18	100	LS	7.2534(4)	7.09941(32)	13.63772(18)	702.3(4)	10.1496(2)
19	260	LS	7.2531(6)	7.1128(6)	13.63884(21)	703.6(2)	10.1587(8)
20	265	LS	7.2493(5)	7.1166(5)	13.63815(19)	703.6(2)	10.1587(7)
21	270	LS	7.2512(5)	7.1174(5)	13.64029(20)	704.0(2)	10.1606(7)

#	Temp / K	Spin State	*a*-parameter / Å	*b*-parameter / Å	*c*-parameter / Å	Volume / Å^3	Fe–Pd–Fe Distance / Å
22	275	LS	7.2538(5)	7.1148(5)	13.63947(21)	703.9(2)	10.1606(7)
23	280	LS	7.2555(5)	7.1153(5)	13.64171(20)	704.3(2)	10.1622(7)
24	285	LS	7.2571(5)	7.1137(5)	13.64176(21)	704.3(2)	10.1622(7)
25	290	LS	7.2604(6)	7.1127(5)	13.64375(22)	704.6(2)	10.1639(7)
26	295	LS	7.2782(6)	7.0951(6)	13.64353(28)	704.5(3)	10.1643(8)
26	295	HS	7.4328(4)	7.4692(5)	14.03650(5)	779.3(1)	10.5373(6)
27	300	HS	7.4464(4)	7.4558(4)	14.03863(29)	779.4(2)	10.5374(5)
28	305	HS	7.4472(6)	7.4530(6)	14.03762(23)	779.1(3)	10.5360(8)
29	310	HS	7.4477(6)	7.4537(7)	14.03855(23)	779.3(3)	10.5369(9)
30	315	HS	7.4479(7)	7.4519(7)	14.03735(23)	779.1(3)	10.5357(9)
31	320	HS	7.4467(6)	7.4541(6)	14.03813(24)	779.2(3)	10.5365(8)
32	325	HS	7.4464(6)	7.4535(6)	14.03736(24)	779.1(3)	10.5358(8)
33	330	HS	7.4465(6)	7.4542(6)	14.03803(24)	779.2(3)	10.5364(8)

Pd·{1-PnOH} (Immm)

#	Temp / K	Spin State	*a*-parameter / Å	*b*-parameter / Å	*c*-parameter / Å	Volume / Å^3	Fe−Pd−Fe Distance / Å
00	300	HS	15.0459(12)	15.2088(15)	28.1318(31)	6437.4(18)	10.6968(10)
01	280	HS	15.0177(13)	15.2212(16)	28.1494(15)	6434.6(15)	10.6913(10)
02	260	HS	15.0006(13)	15.2239(16)	28.1416(15)	6426.6(15)	10.6863(10)
03	240	HS	14.9774(13)	15.2150(18)	28.1086(29)	6405.4(19)	10.6750(11)
04	220	HS	14.9610(12)	15.1883(18)	28.0949(29)	6384.1(19)	10.6597(10)
05	200	mixed	14.9485(12)	15.1547(18)	28.0836(32)	6362.1(19)	10.6433(10)
06	180	mixed	14.9643(16)	15.1070(28)	28.1199(34)	6356.9(26)	10.6319(15)
07	160	mixed	14.9249(8)	15.0776(8)	28.0251(27)	6306.5(12)	10.6076(6)
07	160	LS	13.9885(21)	14.603(18)	27.2741(27)	5571.4(20)	10.1110(13)
08	140	LS	13.9890(9)	14.5776(5)	27.2233(13)	5551.5(8)	10.1020(5)
09	120	LS	13.9908(9)	14.5691(5)	27.2226(14)	5548.9(8)	10.0995(5)
10	105	LS	14.0001(11)	14.5640(7)	27.2247(17)	5551.0(1)	10.1009(6)
11	120	LS	13.9905(9)	14.5678(6)	27.2221(15)	5548.2(8)	10.0989(5)
12	140	LS	13.9892(9)	14.5768(5)	27.2232(14)	5551.3(8)	10.1017(5)
13	160	LS	13.9911(8)	14.5848(5)	27.2218(12)	5554.8(7)	10.1053(5)

#	Temp / K	Spin State	*a*-parameter / Å	*b*-parameter / Å	*c*-parameter / Å	Volume / Å^3	Fe−Pd−Fe Distance / Å
14	180	LS	14.0039(8)	14.5888(5)	27.2183(12)	5560.7(7)	10.1112(5)
15	200	LS	14.0336(8)	14.5888(6)	27.2184(12)	5572.5(7)	10.1215(5)
16	220	HS	15.0101(17)	15.1849(7)	28.0663(25)	6397.1(15)	10.6757(8)
17	240	HS	14.9876(16)	15.2122(7)	28.0852(30)	6403.3(16)	10.6775(8)
18	260	HS	15.0219(10)	15.2218(7)	28.0759(32)	6419.8(14)	10.6930(6)
19	280	HS	15.0106(17)	15.2491(10)	28.090(4)	6429.7(12)	10.6988(10)
20	300	HS	15.0006(5)	15.2806(7)	28.1508(20)	6452.7(9)	10.7065(4)

Au·{EtOH} (Cmma)

#	Temp / K	Spin State	*a*-parameter / Å	*b*-parameter / Å	*c*-parameter / Å	Volume / Å^3	Fe–Au–Fe Distance / Å	Au–Fe–Au Angle / °
00	300	HS	12.2240(4)	16.9405(6)	14.0650(4)	2912.6(3)	10.4452(4)	71.627(4)
01	290	HS	12.2415(4)	16.9270(6)	14.0559(4)	2912.5(3)	10.4448(4)	71.748(4)
02	280	HS	12.2599(4)	16.9164(5)	14.0470(4)	2913.3(3)	10.4459(3)	71.864(3)
03	270	HS	12.2720(4)	16.9061(5)	14.0365(4)	2912.2(3)	10.4453(3)	71.951(3)
04	260	HS	12.2829(4)	16.9023(5)	14.0299(4)	2912.7(3)	10.447(3)	72.011(3)

#	Temp / K	Spin State	*a*-parameter / Å	*b*-parameter / Å	*c*-parameter / Å	Volume / Å^3	Fe–Au–Fe Distance / Å	Au–Fe–Au Angle / °
05	250	HS	12.2909(4)	16.8961(5)	14.0234(4)	2912.2(3)	10.4468(3)	72.067(3)
06	240	HS	12.2979(4)	16.8919(6)	14.0164(4)	2911.7(3)	10.4472(4)	72.111(4)
07	230	HS	12.3045(4)	16.8791(6)	14.0088(4)	2909.5(3)	10.4440(4)	72.182(4)
08	227	HS	12.3106(4)	16.8746(5)	14.0041(4)	2909.2(3)	10.4439(3)	72.224(3)
09	224	HS	12.3164(4)	16.8615(5)	13.9980(4)	2907.0(3)	10.4404(3)	72.292(3)
10	221	HS	12.3273(4)	16.8433(6)	13.9924(4)	2905.3(3)	10.4362(4)	72.399(4)
11	218	HS	12.3450(4)	16.8018(6)	13.9779(4)	2899.3(3)	10.4247(4)	72.612(4)
12	215	HS	12.4058(23)	16.7633(23)	13.9438(23)	2899.8(1)	10.4273(16)	73.007(17)
12	215	LS	12.8857(5)	15.5950(7)	13.6412(6)	2741.2(3)	10.1149(4)	79.131(5)
13	210	LS	12.8795(6)	15.5714(7)	13.6420(6)	2735.9(4)	10.1038(5)	79.19(5)
14	205	LS	12.8867(5)	15.5606(5)	13.6383(5)	2734.8(3)	10.1020(4)	79.260(4)
15	200	LS	12.8929(5)	15.5486(5)	13.6358(5)	2733.5(3)	10.0993(4)	79.331(4)
16	195	LS	12.9032(5)	15.5410(5)	13.6347(5)	2734.1(3)	10.0997(4)	79.403(4)
17	190	LS	12.9112(5)	15.5307(5)	13.6333(5)	2733.7(3)	10.0983(4)	79.475(4)
18	185	LS	12.9216(5)	15.5243(5)	13.6335(5)	2734.9(3)	10.0992(4)	79.544(4)
19	180	LS	12.931(5)	15.5131(6)	13.6324(5)	2734.7(3)	10.0979(4)	79.626(4)
20	175	LS	12.9462(5)	15.5032(6)	13.6327(5)	2736.2(3)	10.0989(4)	79.728(4)

#	Temp / K	Spin State	*a*-parameter / Å	*b*-parameter / Å	*c*-parameter / Å	Volume / Å^3	Fe–Au–Fe Distance / Å	Au–Fe–Au Angle / °
21	170	LS	12.9742(6)	15.4839(7)	13.6307(6)	2738.3(4)	10.1005(5)	79.920(5)
22	165	LS	13.0148(8)	15.4576(9)	13.6298(7)	2742.0(5)	10.1035(6)	80.192(7)
23	160	LS	13.0713(9)	15.4006(10)	13.6268(8)	2743.2(5)	10.1000(7)	80.646(8)
24	155	LS	13.1242(9)	15.3440(10)	13.6271(8)	2744.2(5)	10.0956(7)	81.082(8)
25	150	LS	13.1431(9)	15.3242(10)	13.6269(8)	2744.6(5)	10.0942(7)	81.237(8)
26	145	LS	13.1535(8)	15.3129(8)	13.6281(6)	2744.9(4)	10.0933(6)	81.323(6)
27	140	LS	13.1556(8)	15.3070(8)	13.6275(7)	2744.2(5)	10.0918(6)	81.354(6)
28	135	LS	13.1561(8)	15.3074(8)	13.6278(6)	2744.4(4)	10.0921(6)	81.355(6)
29	130	LS	13.1564(8)	15.2995(8)	13.6264(7)	2742.8(5)	10.0892(6)	81.386(6)
30	125	LS	13.1590(9)	15.3050(12)	13.6218(10)	2743.4(6)	10.0921(7)	81.376(8)
31	120		13.1567(9)	15.3038(12)	13.6202(11)	2742.4(6)	10.0909(7)	81.371(8)
32	115	LS	13.1567(9)	15.3038(12)	13.6202(11)	2742.4(6)	10.0909(7)	81.371(8)
33	110	LS	13.1545(10)	15.3026(13)	13.6200(11)	2741.7(7)	10.0897(8)	81.366(9)
34	105	LS	13.1624(7)	15.3037(9)	13.6277(7)	2745.1(4)	10.0927(6)	81.396(6)
35	100	LS	13.1467(13)	15.3043(18)	13.6175(15)	2739.9(9)	10.0878(11)	81.326(12)
36	105	LS	13.1537(8)	15.2949(8)	13.6286(7)	2741.9(5)	10.0865(6)	81.391(6)
37	110	LS	13.1483(8)	15.3035(8)	13.6284(7)	2742.2(5)	10.088(6)	81.336(6)

#	Temp / K	Spin State	*a*-parameter / Å	*b*-parameter / Å	*c*-parameter / Å	Volume / Å^3	Fe–Au–Fe Distance / Å	Au–Fe–Au Angle / °
38	115	LS	13.1612(11)	15.3084(14)	13.6284(13)	2745.8(7)	10.0941(9)	81.374(10)
39	120	LS	13.1456(8)	15.3150(8)	13.6292(7)	2743.9(5)	10.0915(6)	81.282(6)
40	125	LS	13.1612(8)	15.2968(9)	13.6295(7)	2743.9(5)	10.0897(6)	81.416(7)
41	130	LS	13.1638(10)	15.2976(12)	13.6250(9)	2743.7(6)	10.0909(8)	81.424(9)
42	135	LS	13.1666(10)	15.2991(11)	13.6266(9)	2744.9(6)	10.0923(7)	81.431(8)
43	140	LS	13.1674(10)	15.2967(12)	13.6256(9)	2744.4(6)	10.0917(8)	81.443(9)
44	145	LS	13.1743(10)	15.2993(12)	13.6275(10)	2746.7(6)	10.0949(8)	81.463(9)
45	150	LS	13.1797(12)	15.2925(13)	13.6265(12)	2746.4(7)	10.0941(9)	81.512(10)
46	155	LS	13.1535(10)	15.3232(12)	13.6244(9)	2746.0(6)	10.0972(8)	81.285(9)
47	160	LS	13.1446(10)	15.3312(12)	13.6240(9)	2745.5(6)	10.0974(8)	81.218(9)
48	165	LS	13.1427(10)	15.3325(12)	13.6229(9)	2745.2(6)	10.0972(8)	81.205(9)
49	170	LS	13.1166(11)	15.3488(12)	13.6239(9)	2742.8(6)	10.0949(8)	81.032(9)
50	175	LS	13.0267(11)	15.4395(13)	13.6266(9)	2740.7(6)	10.1004(9)	80.310(1)
51	180	LS	12.9754(10)	15.4811(12)	13.6269(9)	2737.3(6)	10.0998(8)	79.935(9)
52	185	LS	12.9543(9)	15.4995(11)	13.6286(9)	2736.4(6)	10.1001(7)	79.777(8)
53	215	LS	12.8908(9)	15.5712(11)	13.6373(9)	2737.4(6)	10.1074(7)	79.240(8)
54	221	LS	12.8857(5)	15.6080(8)	13.6453(6)	2744.3(4)	10.1199(5)	79.085(5)

#	Temp / K	Spin State	*a*-parameter / Å	*b*-parameter / Å	*c*-parameter / Å	Volume / Å^3	Fe–Au–Fe Distance / Å	Au–Fe–Au Angle / °
54	221	HS	12.4058(23)	16.7740(5)	13.8720(4)	2886.7(7)	10.4316(9)	72.972(11)
55	227	HS	12.3527(5)	16.8290(7)	13.9857(5)	2907.4(3)	10.4380(4)	72.558(4)
57	230	HS	12.3483(5)	16.8429(6)	13.9924(5)	2910.2(3)	10.4423(4)	72.493(4)
58	270	HS	12.3370(5)	16.8637(6)	14.0070(5)	2914.1(3)	10.4473(4)	72.376(4)
59	300	HS	12.3403(5)	16.8604(6)	14.0109(5)	2915.1(3)	10.447(4)	72.401(4)

Au·{Ø}

#	Temp / K	Space Group	Spin State	*a*-parameter / Å	*b*-parameter / Å	*c*-parameter / Å	Volume / Å^3	Fe–Au–Fe Distance / Å	Au–Fe–Au Angle / °
00	300	*Pbaa*	HS	10.013(5)	17.7499(23)	14.0306(11)	2493.7(13)	10.189(2)	58.86(3)
01	290	*Pbaa*	HS	10.028(4)	17.755(18)	14.0297(8)	2497.9(10)	10.1956(18)	58.92(2)
02	280	*Pbaa*	HS	10.0356(33)	17.7631(13)	14.0347(4)	2501.9(8)	10.201(14)	58.93(2)
03	270	*Pbaa*	HS	10.043(4)	17.7592(14)	14.028(7)	2502.1(9)	10.2011(16)	58.98(2)
04	260	*Pbaa*	HS	10.055(5)	17.7612(17)	14.0263(11)	2504.9(12)	10.2049(20)	59.03(3)
05	250	*Pbaa*	mixed	10.036(4)	17.7628(12)	14.0242(6)	2499.8(10)	10.201(15)	58.93(2)
06	240	*Pbaa*	mixed	10.008(20)	17.7661(5)	14.0208(8)	2497.5(12)	10.1955(7)	58.8(1)

#	Temp / K	Space Group	Spin State	*a*-parameter / Å	*b*-parameter / Å	*c*-parameter / Å	Volume / Å^3	Fe–Au–Fe Distance / Å	Au–Fe–Au Angle / °
07	230	*Pbaa*	mixed	10.01123(35)	17.72172(24)	14.0058(15)	2484.85(29)	10.177(10)	58.925(2)
08	220	*Pbaa*	mixed	9.9549(29)	17.6866(9)	13.9942(16)	2463.9(8)	10.1479(11)	58.746(17)
09	210	*Pbaa*	mixed	9.9473(14)	17.5331(34)	13.9999(20)	2441.7(7)	10.0792(18)	59.136(16)
09	210	*Cmma*	mixed	11.5581(24)	16.289(4)	13.5939(30)	2559.3(10)	9.9865(2)	70.72(2)
10	200	*Cmma*	mixed	11.6122(29)	16.425(5)	13.633(23)	2600.2(12)	10.057(3)	70.52(3)
11	190	*Cmma*	mixed	11.5763(19)	16.482(4)	13.6353(14)	2601.6(8)	10.070(2)	70.17(2)
12	180	*Cmma*	LS	11.5574(18)	16.4878(32)	13.6305(13)	2597.4(7)	10.0675(18)	70.058(19)
13	170	*Cmma*	LS	11.5507(18)	16.4948(33)	13.6296(13)	2596.8(7)	10.0685(19)	70.004(19)
14	160	*Cmma*	LS	11.545(20)	16.5002(34)	13.6277(13)	2596(7)	10.069(2)	69.96(2)
15	150	*Cmma*	LS	11.5381(20)	16.5004(34)	13.6242(13)	2593.8(7)	10.067(2)	69.93(2)
16	140	*Cmma*	LS	11.5286(21)	16.501(4)	13.6208(14)	2591.1(8)	10.064(2)	69.88(2)
17	130	*Cmma*	LS	11.5231(21)	16.508(4)	13.6198(14)	2590.9(8)	10.066(2)	69.83(2)
18	120	*Cmma*	LS	11.5134(22)	16.507(4)	13.6182(15)	2588.2(8)	10.062(2)	69.79(2)
19	110	*Cmma*	LS	11.5082(22)	16.511(4)	13.6163(15)	2587.2(8)	10.062(2)	69.75(2)
20	100	*Cmma*	LS	11.4992(22)	16.508(4)	13.6128(15)	2584.2(8)	10.059(2)	69.72(2)
21	110	*Cmma*	LS	11.506(22)	16.515(4)	13.6175(15)	2587.6(8)	10.064(2)	69.73(2)
22	120	*Cmma*	LS	11.5131(22)	16.516(4)	13.6199(14)	2589.8(8)	10.066(2)	69.76(2)

#	Temp / K	Space Group	Spin State	*a*-parameter / Å	*b*-parameter / Å	*c*-parameter / Å	Volume / Å^3	Fe–Au–Fe Distance / Å	Au–Fe–Au Angle / °
23	130	*Cmma*	LS	11.519(22)	16.504(4)	13.6183(14)	2589(8)	10.063(2)	69.83(2)
24	140	*Cmma*	LS	11.5266(21)	16.505(4)	13.6213(14)	2591.4(8)	10.065(2)	69.86(2)
25	150	*Cmma*	LS	11.5321(20)	16.5039(35)	13.6237(14)	2592.9(8)	10.066(2)	69.89(2)
26	160	*Cmma*	LS	11.541(20)	16.5038(35)	13.6266(13)	2595.5(7)	10.069(2)	69.93(2)
27	170	*Cmma*	LS	11.5566(21)	16.501(4)	13.6351(14)	2600.1(8)	10.072(2)	70.01(2)
28	180	*Cmma*	LS	11.5557(18)	16.49(33)	13.6303(13)	2597.3(7)	10.0679(19)	70.04(11)
29	190	*Cmma*	LS	11.5694(18)	16.4824(32)	13.6325(13)	2599.6(7)	10.0688(18)	70.131(19)
30	200	*Cmma*	LS	11.583(19)	16.477(4)	13.636(14)	2602.5(8)	10.070(2)	70.21(2)
31	210	*Cmma*	LS	11.6207(23)	16.446(5)	13.6392(18)	2606.6(10)	10.068(3)	70.49(3)
32	220	*Cmma*	LS	11.664(34)	16.356(6)	13.6296(27)	2600.3(14)	10.044(3)	70.99(4)
33	230	*Pbaa*	mixed	9.9821(29)	17.7129(10)	13.9946(15)	2509(6)	10.166(11)	58.806(17)
34	240	*Pbaa*	mixed	10.1227(22)	17.712(8)	13.994(10)	2509.3(6)	10.2003(9)	59.497(13)
35	250	*Pbaa*	mixed	10.061(6)	17.7623(21)	14.0219(16)	2505.7(15)	10.206(2)	59.06(4)
36	260	*Pbaa*	mixed	10.075(5)	17.7647(16)	14.025(11)	2510.2(13)	10.2114(19)	59.12(3)
37	270	*Pbaa*	mixed	10.04(5)	17.7646(16)	14.0283(10)	2502(13)	10.2027(19)	58.95(3)
38	280	*Pbaa*	mixed	10.03(7)	17.7663(26)	14.0305(17)	2500.1(18)	10.201(3)	58.89(4)
39	290	*Pbaa*	mixed	10.023(6)	17.7611(20)	14.0314(11)	2497.8(15)	10.197(2)	58.87(3)

#	Temp / K	Space Group	Spin State	*a*-parameter / Å	*b*-parameter / Å	*c*-parameter / Å	Volume / Å^3	Fe–Au–Fe Distance / Å	Au–Fe–Au Angle / °
40	300	*Pbaa*	mixed	10.006(4)	17.7577(14)	14.033(7)	2493.4(9)	10.1914(16)	58.8(2)
41	310	*Pbaa*	HS	9.994(5)	17.7456(21)	14.0336(15)	2489(13)	10.183(2)	58.77(3)
42	320	*Pbaa*	HS	9.985(8)	17.728(4)	14.0331(27)	2484.2(21)	10.173(4)	58.78(4)
43	330	*Pbaa*	HS	9.982(15)	17.705(9)	14.037(6)	2480.8(41)	10.162(8)	58.83(8)
44	340	*Pbaa*	HS	9.9785(33)	17.6859(20)	14.0334(10)	2476.6(9)	10.1533(17)	58.86(2)
45	350	*Pbaa*	HS	10.0197(30)	17.6535(18)	14.0299(9)	2481.6(8)	10.1494(15)	59.16(2)
46	340	*Pbaa*	HS	10.0007(28)	17.6315(16)	14.0311(8)	2474.1(8)	10.1351(14)	59.124(18)
47	330	*Pbaa*	HS	9.9753(28)	17.6554(18)	14.0316(7)	2471.2(8)	10.1393(15)	58.932(19)
48	320	*Pbaa*	HS	9.9493(29)	17.6836(17)	14.0333(7)	2469(8)	10.1452(15)	58.726(19)
49	310	*Pbaa*	HS	9.9278(20)	17.69791(20)	14.03576(7)	2466.1(5)	10.1461(6)	58.581(10)
50	300	*Pbaa*	HS	10.1289(31)	17.7368(19)	14.0278(6)	2520.2(8)	10.2126(16)	59.46(2)

Au·{N$_2$}

#	Temp / K	Space Group	Spin State	*a*-parameter / Å	*b*-parameter / Å	*c*-parameter / Å	Volume / Å^3	Fe–Au–Fe Distance / Å	Au–Fe–Au Angle / °
00	250	*Pbaa*	HS	10.20825(26)	17.7651(5)	14.06003(31)	2549.8(2)	10.2446(3)	59.765(3)

#	Temp / K	Space Group	Spin State	*a*-parameter / Å	*b*-parameter / Å	*c*-parameter / Å	Volume / Å^3	Fe–Au–Fe Distance / Å	Au–Fe–Au Angle / °
01	220	*Pbaa*	HS	10.16177(23)	17.7822(4)	14.06111(32)	2540.8(2)	10.2405(2)	59.492(2)
02	210	*Pbaa*	HS	10.1717(4)	17.7664(10)	14.0478(9)	2539(2)	10.2361(5)	59.584(5)
02	210	*Cmma*	LS	11.8481(4)	16.2195(5)	13.6359(4)	2620(1)	10.0430(3)	72.295(4)
03	200	*Pbaa*	HS	10.1733(4)	17.7644(10)	14.0439(9)	2538(2)	10.2356(5)	59.598(5)
03	200	*Cmma*	LS	11.8476(4)	16.2196(5)	13.6357(4)	2620(1)	10.0429(3)	72.292(4)
04	190	*Cmma*	LS	11.81349(30)	16.2439(4)	13.63835(31)	2617.2(2)	10.0427(2)	72.054(3)
05	180	*Cmma*	LS	11.77417(30)	16.2699(4)	13.63970(29)	2612.9(2)	10.0417(2)	71.785(3)
06	170	*Cmma*	LS	11.73789(30)	16.2976(4)	13.64029(29)	2609.4(2)	10.0423(2)	71.525(3)
07	160	*Cmma*	LS	11.70434(29)	16.3218(4)	13.64002(29)	2605.7(2)	10.0423(2)	71.289(3)
08	150	*Cmma*	LS	11.67662(30)	16.3444(4)	13.64032(29)	2603.2(2)	10.0434(2)	71.085(3)
09	140	*Cmma*	LS	11.68107(26)	16.3383(4)	13.64003(26)	2603.2(2)	10.0423(9)	71.126(3)
10	130	*Cmma*	LS	11.75577(35)	16.2928(4)	13.63418(30)	2611.4(2)	10.0456(12)	71.623(3)
11	120	*Cmma*	LS	12.4536(7)	15.7999(11)	13.5864(7)	2673(2)	10.0589(6)	76.491(7)
12	110	*Cmma*	LS	13.3989(4)	15.1244(5)	13.62718(28)	2761.6(2)	10.1029(3)	83.076(4)
13	100	*Cmma*	LS	13.3777(5)	15.1482(6)	13.6262(4)	2761(1)	10.1048(4)	82.897(4)
14	110	*Cmma*	LS	13.3851(5)	15.1369(7)	13.6287(4)	2761(1)	10.1031(4)	82.971(5)
15	120	*Cmma*	LS	13.4034(6)	15.1125(7)	13.6252(4)	2760(1)	10.1000(5)	83.140(5)

#	Temp / K	Space Group	Spin State	*a*-parameter / Å	*b*-parameter / Å	*c*-parameter / Å	Volume / Å^3	Fe–Au–Fe Distance / Å	Au–Fe–Au Angle / °
15	120	*Cmma*	LS	12.4940(4)	15.8000(7)	13.605(5)	2686(1)	10.0715(4)	76.671(4)
16	130	*Cmma*	LS	12.0441(10)	16.1079(11)	13.614(8)	2641(2)	10.0564(7)	73.572(8)
17	140	*Cmma*	LS	11.70992(30)	16.3238(4)	13.63925(28)	2607.1(2)	10.0448(10)	71.308(3)
18	150	*Cmma*	LS	11.69682(30)	16.3295(4)	13.64028(29)	2605.3(2)	10.0433(10)	71.228(3)
19	160	*Cmma*	LS	11.70825(31)	16.3204(4)	13.64021(30)	2606.4(2)	10.0429(11)	71.311(3)
20	170	*Cmma*	LS	11.73265(30)	16.3008(4)	13.63954(30)	2608.6(2)	10.0421(10)	71.490(3)
21	180	*Cmma*	LS	11.76650(31)	16.2765(4)	13.63973(29)	2612.2(2)	10.0421(11)	71.727(3)
22	190	*Cmma*	LS	11.80313(32)	16.2502(4)	13.63863(30)	2615.9(2)	10.0422(11)	71.985(3)
23	200	*Cmma*	LS	11.83946(31)	16.2270(4)	13.63664(31)	2619.9(2)	10.0435(11)	72.230(3)
24	210	*Cmma*	LS	11.87237(30)	16.2032(4)	13.63664(30)	2623.3(2)	10.0436(10)	72.462(3)
25	220	*Cmma*	LS	11.90745(30)	16.1799(4)	13.63812(30)	2627.5(2)	10.0446(11)	72.702(3)
26	230	*Cmma*	LS	11.93915(30)	16.1592(4)	13.63887(29)	2631.3(2)	10.0457(11)	72.917(3)
27	240	*Cmma*	LS	11.96891(30)	16.1408(4)	13.64079(28)	2635.2(2)	10.0471(11)	73.116(3)
28	250	*Pbaa*	HS	10.20470(26)	17.7632(4)	14.05914(30)	2548.5(2)	10.2429(8)	59.753(2)
29	260	*Pbaa*	HS	10.22276(31)	17.7566(5)	14.05937(30)	2552.1(2)	10.2445(10)	59.859(3)
30	270	*Pbaa*	HS	10.2419(4)	17.7523(6)	14.05923(31)	2556.2(2)	10.2474(4)	59.964(4)
31	280	*Pbaa*	HS	10.26382(33)	17.7406(6)	14.05806(31)	2559.8(2)	10.2479(11)	60.103(3)

Au·{MeOH} (Cmma)

#	Temp / K	Spin State	*a*-parameter / Å	*b*-parameter / Å	*c*-parameter / Å	Volume / Å^3	Fe–Au–Fe Distance / Å	Au–Fe–Au Angle / °
00	300	HS	12.2930(5)	16.8709(7)	14.0159(4)	2906.8(3)	10.4373(4)	72.158(4)
01	290	HS	12.2966(5)	16.8707(7)	14.0140(4)	2907.2(3)	10.4382(4)	72.174(4)
02	280	HS	12.3075(5)	16.8624(8)	14.0033(5)	2906.2(4)	10.4381(5)	72.249(5)
03	270	HS	13.0912(9)	16.1717(12)	27.6714(13)	5858.2(11)	10.4032(7)	77.981(8)
04	260	HS	13.0872(9)	16.1696(11)	27.6533(12)	5851.8(11)	10.4011(7)	77.971(8)
05	250	mixed	13.0820(8)	16.1678(11)	27.6369(12)	5845.4(10)	10.3988(7)	77.955(7)
06	245	mixed	13.0840(8)	16.1666(11)	27.6287(12)	5844.1(10)	10.3989(7)	77.968(7)
07	240	mixed	13.0874(9)	16.1536(11)	27.6157(12)	5838.2(11)	10.3949(7)	78.027(8)
08	235	mixed	13.0934(9)	16.1312(12)	27.5973(13)	5828.9(11)	10.3881(7)	78.131(8)
09	230	mixed	13.1102(8)	16.0776(12)	27.5690(12)	5811.0(10)	10.3726(7)	78.389(8)
10	225	mixed	13.1182(7)	16.0031(11)	27.5156(11)	5776.4(9)	10.3463(6)	78.684(7)
11	220	mixed	13.1217(6)	15.9220(9)	27.4520(10)	5735.4(8)	10.3161(5)	78.985(6)
12	210	mixed	13.1020(5)	15.7633(8)	27.3167(10)	5641.7(7)	10.2487(5)	79.464(5)
13	200	LS	13.083(18)	15.3499(27)	26.9823(32)	5418.7(23)	10.0844(1)	80.883(18)

#	Temp / K	Spin State	*a*-parameter / Å	*b*-parameter / Å	*c*-parameter / Å	Volume / Å^3	Fe–Au–Fe Distance / Å	Au–Fe–Au Angle / °
14	190	LS	12.9807(5)	15.3795(7)	26.9731(7)	5384.8(6)	10.0626(4)	80.330(5)
15	180	LS	12.9562(5)	15.3933(7)	26.9720(7)	5379.3(6)	10.0600(4)	80.173(5)
16	170	LS	12.9406(4)	15.3996(6)	26.9692(7)	5374.4(5)	10.0574(4)	80.082(4)
17	160	LS	12.9339(4)	15.4053(7)	26.9691(7)	5373.6(5)	10.0574(4)	80.031(4)
18	150	LS	12.9279(4)	15.4073(7)	26.9671(7)	5371.4(5)	10.0563(4)	79.998(4)
19	140	LS	12.9248(5)	15.4346(7)	26.9839(10)	5383.0(7)	10.0658(4)	79.885(5)
20	130	LS	12.917(5)	15.4339(7)	26.9803(11)	5378.8(7)	10.0630(4)	79.853(5)
21	120	LS	12.9097(4)	15.4389(6)	26.9773(11)	5376.9(6)	10.0626(4)	79.803(4)
22	110	LS	12.9046(5)	15.4319(7)	26.9699(12)	5370.9(7)	10.0582(4)	79.806(5)
23	100	LS	12.9001(5)	15.4275(7)	26.9706(13)	5367.6(7)	10.0551(4)	79.803(5)
24	110	LS	12.9031(4)	15.4302(6)	26.9682(12)	5369.3(6)	10.0571(4)	79.806(4)
25	120	LS	12.9098(5)	15.4371(6)	26.9748(12)	5375.8(7)	10.0619(4)	79.810(4)
26	130	LS	12.9144(4)	15.4392(6)	26.9823(10)	5379.9(6)	10.0642(4)	79.822(4)
27	140	LS	12.9234(5)	15.4375(7)	26.9847(11)	5383.6(7)	10.0664(4)	79.868(5)
28	150	LS	12.9333(5)	15.4223(7)	26.9250(11)	5370.5(7)	10.0638(4)	79.967(5)
29	160	LS	12.9405(5)	15.4209(7)	26.9625(8)	5380.5(6)	10.0655(4)	80.003(5)
30	170	LS	12.9519(5)	15.4167(7)	26.9710(9)	5385.4(6)	10.0676(4)	80.068(5)

#	Temp / K	Spin State	*a*-parameter / Å	*b*-parameter / Å	*c*-parameter / Å	Volume / Å^3	Fe–Au–Fe Distance / Å	Au–Fe–Au Angle / °
31	180	LS	12.9534(5)	15.3961(8)	26.9696(8)	5378.6(6)	10.0602(5)	80.150(5)
32	190	LS	12.9751(5)	15.3807(8)	26.9706(8)	5382.4(6)	10.0613(5)	80.301(5)
33	200	LS	13.0272(6)	15.3560(8)	26.9756(8)	5396.4(7)	10.0687(5)	80.618(6)
34	210	mixed	13.1037(6)	15.7308(9)	27.2903(11)	5625.4(8)	10.2368(5)	79.588(6)
35	220	mixed	13.1204(6)	15.8479(10)	27.3882(11)	5694.8(8)	10.2871(6)	79.242(6)
36	225	mixed	13.1267(7)	15.9410(11)	27.4659(12)	5747.3(10)	10.3250(6)	78.939(7)
37	230	mixed	13.1230(7)	16.0256(12)	27.5286(14)	5789.4(10)	10.3566(7)	78.626(7)
38	235	mixed	13.1146(8)	16.0851(12)	27.5690(15)	5815.7(11)	10.3769(7)	78.382(8)
39	240	mixed	13.1098(9)	16.1225(13)	27.5966(15)	5832.9(12)	10.3899(8)	78.231(8)
40	245	mixed	13.1025(9)	16.1442(12)	27.6119(16)	5840.7(12)	10.3960(7)	78.125(8)
41	250	mixed	13.1041(9)	16.1548(12)	27.6259(16)	5848.2(12)	10.4007(7)	78.095(8)
42	260	HS	13.1170(9)	16.1644(12)	27.6537(16)	5863.4(12)	10.4085(7)	78.116(8)
43	270	HS	13.1275(11)	16.1565(15)	27.6607(20)	5866.7(15)	10.4087(9)	78.189(10)
44	280	HS	13.1377(10)	16.1558(16)	27.6754(20)	5874.1(15)	10.4116(9)	78.235(10)
45	290	HS	13.1373(11)	16.1623(17)	27.6957(21)	5880.6(16)	10.4140(10)	78.210(11)
46	300	HS	12.3363(5)	16.8367(7)	13.9933(28)	2906.4(8)	10.4362(4)	72.460(4)

Au·{1-PrOH} (Cmma)

#	Temp / K	Spin State	*a*-parameter / Å	*b*-parameter / Å	*c*-parameter / Å	Volume / Å^3	Fe–Au–Fe Distance / Å	Au–Fe–Au Angle / °
00	300	HS	12.2718(6)	16.9124(7)	14.0872(5)	2923.7(4)	10.4478(5)	71.930(5)
01	290	HS	12.2930(6)	16.8986(8)	14.0768(5)	2924.2(4)	10.4485(5)	72.068(5)
02	280	HS	12.3200(6)	16.8801(8)	14.0585(5)	2923.6(4)	10.4489(5)	72.247(5)
03	270	HS	12.3435(7)	16.8708(8)	14.0523(5)	2926.3(4)	10.4521(5)	72.382(6)
04	260	HS	12.3623(7)	16.8631(8)	14.044(5)	2927.7(4)	10.4546(5)	72.490(6)
05	250	HS	12.3786(7)	16.8558(8)	14.0376(5)	2929.0(4)	10.4564(5)	72.585(6)
06	240	HS	12.3954(7)	16.8479(9)	14.0315(5)	2930.3(4)	10.4582(6)	72.685(6)
07	230	HS	12.4120(7)	16.8435(9)	14.0267(5)	2932.4(4)	10.4614(6)	72.773(6)
08	220	HS	12.4277(9)	16.8363(11)	14.0218(5)	2933.9(5)	10.4631(7)	72.865(8)
09	210	HS	12.4418(9)	16.8286(12)	14.0148(5)	2934.4(5)	10.4642(7)	72.952(8)
10	200	HS	12.4502(11)	16.8301(16)	14.0033(6)	2934.2(7)	10.4673(10)	72.985(10)
11	190	HS	12.4514(10)	16.8217(15)	13.9870(7)	2929.6(6)	10.4643(9)	73.017(9)
12	180	HS	12.4398(12)	16.8217(19)	13.9516(9)	2919.5(8)	10.4609(11)	72.966(11)
13	170	mixed	12.4236(14)	16.7955(25)	13.8962(12)	2899.6(10)	10.4455(14)	72.980(14)
14	160	mixed	12.4216(16)	16.7447(29)	13.8588(13)	2882.6(11)	10.4245(16)	73.137(17)

#	Temp / K	Spin State	*a*-parameter / Å	*b*-parameter / Å	*c*-parameter / Å	Volume / Å^3	Fe–Au–Fe Distance / Å	Au–Fe–Au Angle / °
15	150	mixed	12.4274(17)	16.6651(31)	13.8210(13)	2862.4(12)	10.3943(18)	73.424(18)
16	140	mixed	12.4597(14)	16.5414(28)	13.7928(12)	2842.7(10)	10.3545(15)	73.977(16)
17	130	mixed	12.4650(14)	16.4722(29)	13.7693(11)	2827.2(10)	10.3285(16)	74.231(16)
18	120	mixed	12.4635(14)	16.4359(29)	13.7535(11)	2817.4(10)	10.3136(16)	74.346(16)
19	110	mixed	12.4553(15)	16.4114(30)	13.7353(11)	2807.6(11)	10.3013(16)	74.392(17)
20	100	mixed	12.4509(15)	16.3903(31)	13.7267(11)	2801.3(11)	10.2916(17)	74.444(17)
21	110	mixed	12.4508(15)	16.4073(30)	13.7315(10)	2805.1(11)	10.2983(16)	74.386(17)
22	120	mixed	12.4624(15)	16.4299(30)	13.7486(11)	2815.1(11)	10.3108(16)	74.362(17)
23	130	mixed	12.4725(15)	16.4500(30)	13.7641(11)	2824.0(11)	10.3219(16)	74.339(17)
24	140	mixed	12.4710(15)	16.5071(30)	13.7859(12)	2838.0(11)	10.3442(16)	74.141(17)
25	150	mixed	12.4929(15)	16.5095(30)	13.7967(12)	2845.6(11)	10.3518(16)	74.230(17)
26	160	mixed	12.5101(15)	16.5402(29)	13.8253(12)	2860.7(11)	10.3692(16)	74.203(16)
27	170	mixed	12.5018(16)	16.6166(31)	13.8574(12)	2878.7(12)	10.3972(17)	73.913(17)
28	180	HS	12.4543(14)	16.7748(24)	13.9104(11)	2906.1(10)	10.4463(14)	73.183(14)
29	190	HS	12.4619(11)	16.8049(17)	13.9607(9)	2923.7(7)	10.4607(10)	73.118(10)
30	200	HS	12.4650(11)	16.8167(16)	13.9965(6)	2933.9(7)	10.4663(10)	73.093(10)
31	210	HS	12.4537(11)	16.8238(14)	14.0082(6)	2935.0(6)	10.4658(9)	73.020(9)

#	Temp / K	Spin State	*a*-parameter / Å	*b*-parameter / Å	*c*-parameter / Å	Volume / Å^3	Fe–Au–Fe Distance / Å	Au–Fe–Au Angle / °
32	220	HS	12.4403(10)	16.8327(13)	14.0214(5)	2936.1(6)	10.4654(8)	72.932(9)
33	230	HS	12.4249(11)	16.8380(13)	14.0236(5)	2933.9(6)	10.4630(8)	72.847(9)
34	240	HS	12.4127(11)	16.8484(13)	14.0316(5)	2934.5(6)	10.4636(8)	72.760(9)
35	250	HS	12.3989(11)	16.8462(13)	14.0304(5)	2930.6(6)	10.4586(8)	72.706(9)
36	260	HS	12.3929(11)	16.8523(13)	14.0362(5)	2931.4(6)	10.4593(8)	72.660(9)
37	270	HS	12.3984(11)	16.8417(13)	14.0313(5)	2929.9(6)	10.4566(8)	72.719(9)
38	280	HS	12.4052(9)	16.8331(10)	14.0334(6)	2930.4(5)	10.4552(7)	72.776(7)
39	290	HS	12.4199(9)	16.8182(10)	14.0261(6)	2929.8(5)	10.4535(7)	72.890(7)
40	300	HS	12.4373(11)	16.8069(14)	14.0246(6)	2931.6(6)	10.4542(9)	73.003(9)

Au·{1-BuOH}

#	Temp / K	Space Group	Spin State	*a*-parameter / Å	*b*-parameter / Å	*c*-parameter / Å	*α*-angle / °	Volume / Å^3	Fe–Au–Fe Distance / Å	Au–Fe–Au Angle / °
00	300	*Cmma*	HS	12.1683(15)	17.005(4)	14.0936(13)	90	2916.3(13)	10.455(2)	71.17(2)
01	290	*Cmma*	HS	12.1781(16)	17.001(4)	14.0946(13)	90	2918.1(13)	10.456(2)	71.22(2)
02	280	*Cmma*	HS	12.2011(15)	16.985(4)	14.0919(13)	90	2920.3(13)	10.456(2)	71.38(2)

#	Temp / K	Space Group	Spin State	*a*-parameter / Å	*b*-parameter / Å	*c*-parameter / Å	*α*-angle / °	Volume / Å^3	Fe–Au–Fe Distance / Å	Au–Fe–Au Angle / °
03	270	*Cmma*	HS	12.2308(14)	16.954(4)	14.0882(13)	90	2921.3(13)	10.452(2)	71.61(2)
04	260	*Cmma*	HS	12.2465(14)	16.946(4)	14.0861(13)	90	2923.3(13)	10.454(2)	71.70(2)
05	250	*Cmma*	HS	12.2587(15)	16.940(4)	14.0831(13)	90	2925.5(13)	10.455(2)	71.78(2)
06	240	*Cmma*	HS	12.2647(16)	16.933(4)	14.077(14)	90	2923.5(14)	10.454(2)	71.83(2)
07	230	*Cmma*	HS	12.268(17)	16.924(4)	14.0719(14)	90	2921.7(14)	10.451(2)	71.87(9)
08	220	*Cmma*	HS	12.2694(16)	16.936(4)	14.0688(14)	90	2923.4(14)	10.456(2)	71.84(2)
09	210	*Cmma*	HS	12.2614(17)	16.942(4)	14.0614(15)	90	2921.0(14)	10.456(2)	71.78(2)
10	200	*Cmma*	HS	12.250(4)	16.940(9)	14.0471(25)	90	2915(3)	10.452(5)	71.74(5)
11	190	*Cmma*	HS	12.2504(23)	16.926(5)	14.0412(13)	90	2911.4(17)	10.447(3)	71.79(3)
12	180	*Cmma*	mixed	12.2960(4)	16.767(8)	14.0075(17)	90	2888(3)	10.396(4)	72.50(4)
13	170	*Cmma*	mixed	12.3765(35)	16.595(8)	13.969(10)	90	2869(10)	10.351(4)	73.43(4)
14	160	*Cmma*	mixed	12.399(4)	16.503(9)	13.953(11)	90	2855(3)	10.320(5)	73.83(5)
15	150	*Cmma*	mixed	12.359(4)	16.533(10)	13.954(10)	90	2851(3)	10.320(5)	73.55(5)
16	140	*Cmma*	mixed	12.324(4)	16.558(10)	13.949(9)	90	2846(3)	10.320(5)	73.32(5)
17	130	*Cmma*	mixed	12.299(4)	16.57(10)	13.94(8)	90	2841(3)	10.317(5)	73.16(5)
18	120	*Cmma*	mixed	12.280(4)	16.577(11)	13.924(8)	90	2834(3)	10.315(6)	73.06(5)

#	Temp / K	Space Group	Spin State	*a*-parameter / Å	*b*-parameter / Å	*c*-parameter / Å	*α*-angle / °	Volume / Å^3	Fe–Au–Fe Distance / Å	Au–Fe–Au Angle / °
19	110	*Cmma*	mixed	12.250(4)	16.601(10)	13.908(7)	90	2828(3)	10.315(5)	72.84(5)
20	100	*Cmma*	mixed	12.238(4)	16.587(10)	13.904(7)	90	2822(3)	10.306(5)	72.84(5)
21	110	*Cmma*	mixed	12.252(4)	16.59(10)	13.9(7)	90	2825(3)	10.311(5)	72.89(5)
22	120	*Cmma*	mixed	12.266(4)	16.6(10)	13.918(7)	90	2834(3)	10.320(5)	72.92(5)
23	130	*Cmma*	mixed	12.292(4)	16.583(10)	13.930(8)	90	2839(3)	10.321(5)	73.09(5)
24	140	*Cmma*	mixed	12.322(4)	16.563(10)	13.936(9)	90	2844(3)	10.321(5)	73.29(5)
25	150	*Cmma*	mixed	12.354(4)	16.547(10)	13.939(9)	90	2849(3)	10.325(5)	73.49(5)
26	160	*Cmma*	mixed	12.39(4)	16.520(9)	13.921(10)	90	2849(3)	10.325(5)	73.73(5)
27	170	*Cmma*	mixed	12.407(5)	16.553(10)	13.963(15)	90	2868(3)	10.343(6)	73.70(6)
28	190	*C*2/*m*	mixed	13.8701(19)	15.1126(22)	13.642(12)	92.33(4)	2857(3)	10.2563(15)	85.090(16)
29	200	*C*2/*m*	mixed	13.8839(19)	15.1202(22)	13.676(14)	92.30(4)	2869(3)	10.2638(15)	85.118(16)
30	210	*C*2/*m*	mixed	13.9017(20)	15.1261(23)	13.71(14)	92.31(4)	2881(3)	10.272(15)	85.169(17)
31	220	*C*2/*m*	mixed	13.9191(19)	15.1456(22)	13.736(14)	92.37(4)	2893(3)	10.2851(15)	85.167(16)
32	230	*C*2/*m*	mixed	13.9497(18)	15.184(21)	13.728(13)	92.63(4)	2905(3)	10.3096(14)	85.148(15)
33	240	*C*2/*m*	mixed	13.9753(17)	15.2403(20)	13.758(14)	92.82(4)	2927(3)	10.339(13)	85.041(14)
34	250	*C*2/*m*	mixed	13.9785(17)	15.3035(20)	13.817(16)	92.92(4)	2952(3)	10.3633(13)	84.818(14)

#	Temp / K	Space Group	Spin State	*a*-parameter / Å	*b*-parameter / Å	*c*-parameter / Å	*α*-angle / °	Volume / Å^3	Fe–Au–Fe Distance / Å	Au–Fe–Au Angle / °
35	260	*C*2/*m*	mixed	13.9843(17)	15.3634(20)	13.826(17)	93.13(4)	2966(4)	10.3874(13)	84.619(14)
36	270	*C*2/*m*	mixed	13.9816(21)	15.4252(25)	13.887(21)	93.30(6)	2990(5)	10.4094(16)	84.379(18)
37	280	*Cmma*	HS	12.288(11)	16.898(24)	14.058(5)	90	2919(7)	10.4467(12)	72.04(12)
38	290	*Cmma*	HS	12.259(18)	16.941(4)	14.0764(16)	90	2923(5)	10.455(7)	71.78(9)
39	300	*Cmma*	HS	12.2616(24)	16.935(5)	14.0758(19)	90	2922.8(18)	10.454(3)	71.81(3)

Au·{2-BuOH}

#	Temp / K	Space Group	Spin State	*a*-parameter / Å	*b*-parameter / Å	*c*-parameter / Å	*α*-angle / °	*β*-angle / °	Volume / Å^3	Fe–Au–Fe Distance / Å	Au–Fe–Au Angle / °
00	300	*P*1	HS	14.4331(17)	15.2108(18)	14.0810(14)	94.944(9)	92.457(9)	3078.3(4)	10.4843(12)	86.994(14)
01	290	*P*1	HS	14.4165(10)	15.2352(11)	14.0822(11)	94.981(9)	92.54(9)	3077.0(4)	10.4875(7)	86.836(8)
02	280	*P*1	HS	14.4063(10)	15.2447(11)	14.0786(12)	95.015(9)	92.569(10)	3077.5(4)	10.4874(7)	86.760(8)
03	270	*P*1	HS	14.4002(7)	15.2538(10)	14.0803(11)	95.111(8)	92.544(8)	3077.2(4)	10.4886(6)	86.702(7)
04	260	*P*1	HS	14.3917(7)	15.2607(11)	14.0826(12)	95.165(8)	92.523(9)	3078.6(4)	10.4882(6)	86.642(7)
05	250	*P*1	HS	14.3856(8)	15.2719(10)	14.0858(13)	95.195(9)	92.628(9)	3074.2(4)	10.4902(6)	86.576(7)
06	240	*P*1	HS	14.3533(11)	15.2863(9)	14.0861(13)	95.234(8)	92.737(8)	3070.4(4)	10.4844(7)	86.394(8)

#	Temp / K	Space Group	Spin State	*a*-parameter / Å	*b*-parameter / Å	*c*-parameter / Å	*α*-angle / °	*β*-angle / °	Volume / Å^3	Fe–Au–Fe Distance / Å	Au–Fe–Au Angle / °
07	230	*P*1	HS	14.3362(10)	15.2928(9)	14.0804(13)	95.263(8)	92.75(7)	3072.3(5)	10.4809(7)	86.301(7)
08	220	*C*2/*m*	HS	14.6358(17)	15.0216(21)	13.9857(10)	93.266(10)	90	3069.8(6)	10.4864(13)	88.509(15)
09	210	*C*2/*m*	mixed	14.6262(17)	14.9960(22)	13.9703(11)	93.270(10)	90	3059.2(6)	10.4738(14)	88.569(15)
10	200	*C*2/*m*	mixed	14.6115(17)	14.9719(21)	13.954(11)	93.256(10)	90	3047.7(6)	10.4601(13)	88.604(15)
11	190	*C*2/*m*	mixed	14.5822(19)	14.9310(22)	13.9291(11)	93.234(9)	90	3027.9(6)	10.4352(15)	88.645(16)
12	180	*C*2/*m*	mixed	14.5293(20)	14.8579(24)	13.8859(12)	93.172(10)	90	2993.0(7)	10.3906(16)	88.718(17)
13	170	*C*2/*m*	mixed	14.4882(21)	14.8133(24)	13.8544(13)	92.948(13)	90	2969.5(7)	10.3603(16)	88.728(18)
14	160	*C*2/*m*	mixed	14.4559(19)	14.7839(22)	13.8288(12)	92.631(11)	90	2952.3(6)	10.3385(15)	88.714(16)
15	150	*C*2/*m*	mixed	14.4353(17)	14.7590(20)	13.8116(11)	92.556(9)	90	2939.7(6)	10.3224(13)	88.729(15)
16	140	*C*2/*m*	mixed	14.4159(18)	14.7323(20)	13.7943(11)	92.500(9)	90	2926.8(6)	10.3061(13)	88.756(15)
17	130	*C*2/*m*	mixed	14.3878(21)	14.7046(24)	13.7769(13)	92.451(11)	90	2912.1(7)	10.2863(16)	88.752(18)
18	120	*C*2/*m*	mixed	14.3711(17)	14.6767(19)	13.7596(10)	92.477(7)	90	2899.5(5)	10.2705(13)	88.794(14)
19	110	*C*2/*m*	mixed	14.3648(18)	14.6706(20)	13.7549(11)	92.404(9)	90	2896.2(6)	10.2661(13)	88.793(15)
20	100	*C*2/*m*	mixed	14.3525(18)	14.6632(20)	13.7473(11)	92.369(9)	90	2890.7(6)	10.2592(13)	88.773(15)
21	110	*C*2/*m*	mixed	14.3616(18)	14.6659(21)	13.7521(11)	92.370(10)	90	2894.1(6)	10.2633(14)	88.798(15)
22	120	*C*2/*m*	mixed	14.3676(19)	14.6694(22)	13.7555(12)	92.385(10)	90	2896.7(6)	10.2667(15)	88.809(16)
23	130	*C*2/*m*	mixed	14.3844(18)	14.6925(21)	13.7703(12)	92.44(10)	90	2907.6(6)	10.2808(14)	88.785(15)

#	Temp / K	Space Group	Spin State	*a*-parameter / Å	*b*-parameter / Å	*c*-parameter / Å	*α*-angle / °	*β*-angle / °	Volume / Å^3	Fe–Au–Fe Distance / Å	Au–Fe–Au Angle / °
24	140	*C*2/*m*	mixed	14.4077(18)	14.7207(21)	13.7884(12)	92.472(10)	90	2921.7(6)	10.2990(14)	88.768(15)
25	150	*C*2/*m*	mixed	14.4277(18)	14.7488(21)	13.8042(11)	92.506(10)	90	2934.6(6)	10.3161(14)	88.738(15)
26	160	*C*2/*m*	mixed	14.4457(18)	14.7743(21)	13.8206(12)	92.572(10)	90	2946.7(6)	10.3315(14)	88.711(15)
27	170	*C*2/*m*	mixed	14.4688(18)	14.7970(21)	13.8389(12)	92.696(10)	90	2959.5(6)	10.3477(14)	88.715(15)
28	180	*C*2/*m*	mixed	14.4995(20)	14.8323(24)	13.8653(13)	92.893(11)	90	2978.1(7)	10.3710(16)	88.699(17)
29	190	*C*2/*m*	mixed	14.5401(18)	14.8897(22)	13.9014(12)	92.998(10)	90	3005.5(6)	10.4057(14)	88.638(16)
30	200	*C*2/*m*	mixed	14.5870(18)	14.9532(23)	13.9391(11)	93.169(10)	90	3035.8(7)	10.4448(15)	88.579(16)
31	210	*C*2/*m*	mixed	14.6162(18)	14.9905(23)	13.9620(11)	93.243(10)	90	3054.3(6)	10.4684(15)	88.551(16)
32	220	*C*2/*m*	HS	14.6318(18)	15.0113(22)	13.9754(11)	93.274(9)	90	3064.6(6)	10.4813(14)	88.533(15)
33	230	*C*2/*m*	HS	14.6306(17)	15.0266(21)	13.9844(10)	93.251(10)	90	3069.5(6)	10.4863(13)	88.470(15)
34	240	*P*1	HS	14.3716(17)	15.2893(16)	14.0756(19)	95.239(10)	92.627(10)	3076.6(6)	10.4917(12)	86.455(13)
35	250	*P*1	HS	14.3816(16)	15.2985(16)	14.0927(18)	95.143(9)	92.61(10)	3084.9(6)	10.4985(11)	86.461(12)
36	260	*P*1	HS	14.3963(15)	15.3001(15)	14.0985(18)	95.108(9)	92.585(10)	3089.9(6)	10.5041(11)	86.513(12)
37	270	*P*1	HS	14.4057(15)	15.2986(17)	14.0980(18)	95.089(9)	92.536(10)	3091.7(6)	10.5068(11)	86.556(12)
38	280	*P*1	HS	14.4108(20)	15.2855(23)	14.0939(20)	95.106(11)	92.532(13)	3089.2(8)	10.5038(15)	86.625(17)
39	290	*P*1	HS	14.4248(15)	15.2364(15)	14.0762(17)	94.966(12)	92.447(13)	3079.3(6)	10.4907(11)	86.865(12)
40	300	*P*1	HS	14.4350(17)	15.2203(16)	14.0740(17)	94.934(13)	92.412(14)	3077.9(6)	10.4884(12)	86.966(13)

Au·{PrBr}

#	Temp / K	Space Group	Spin State	*a*-parameter / Å	*b*-parameter / Å	*c*-parameter / Å	*α*-angle / °	Volume / Å^3	Fe–Au–Fe Distance / Å	Au–Fe–Au Angle / °
00	300	*Cmma*	HS	11.8973(20)	17.0410(17)	13.9945(16)	90	2837(4)	10.3916(13)	69.842(14)
01	290	*Cmma*	HS	11.8994(17)	17.0391(12)	13.9911(12)	90	2837(3)	10.3914(10)	69.857(11)
02	280	*Cmma*	HS	11.9108(16)	17.0400(10)	13.9879(10)	90	2839(2)	10.3951(9)	69.906(10)
03	270	*Cmma*	mixed	11.9416(15)	17.0256(12)	13.9811(11)	90	2843(3)	10.3980(9)	70.090(11)
04	260	*Cmma*	mixed	12.0136(16)	17.0016(7)	13.9727(11)	90	2853.9(18)	10.4089(7)	70.491(9)
05	250	*Cmma*	mixed	12.338(3)	16.764(4)	13.8803(27)	90	2870.9(20)	10.407(26)	72.703(16)
06	240	*C*2/*m*	mixed	12.818(5)	16.349(4)	13.853(4)	92.618(27)	2900.1(16)	10.39(3)	76.194(4)
07	230	*C*2/*m*	mixed	12.837(4)	16.250(4)	13.816(5)	92.691(30)	2878.9(15)	10.354(27)	76.614(17)
08	220	*Cmma*	LS	12.0997(17)	16.0399(21)	13.6113(7)	90	2642(4)	10.0459(14)	74.058(15)
09	210	*Cmma*	LS	12.1075(26)	16.025(4)	13.6044(8)	90	2639.6(14)	10.0423(9)	74.144(13)
10	200	*Cmma*	LS	12.1715(30)	15.970(5)	13.588(8)	90	2641.2(16)	10.040(2)	74.625(15)
11	190	*Cmma*	LS	12.4625(35)	15.780(5)	13.5719(9)	90	2669.0(18)	10.054(3)	76.600(17)
12	180	*Cmma*	LS	12.4893(34)	15.751(5)	13.5608(9)	90	2667.7(18)	10.051(3)	76.823(17)
13	170	*Cmma*	LS	12.4941(22)	15.7471(33)	13.5567(7)	90	2667(6)	10.0508(20)	76.858(22)
14	160	*Cmma*	LS	12.4855(17)	15.7436(24)	13.5510(6)	90	2664(5)	10.0467(15)	76.832(16)

#	Temp / K	Space Group	Spin State	*a*-parameter / Å	*b*-parameter / Å	*c*-parameter / Å	*α*-angle / °	Volume / Å^3	Fe–Au–Fe Distance / Å	Au–Fe–Au Angle / °
15	150	*Cmma*	LS	12.4701(17)	15.7574(24)	13.5530(7)	90	2663(5)	10.0474(15)	76.714(16)
16	140	*Cmma*	LS	12.4434(23)	15.790(4)	13.5595(21)	90	2664.2(16)	10.0519(23)	76.480(12)
17	130	*Cmma*	LS	12.4291(24)	15.797(4)	13.5569(21)	90	2661.8(16)	10.0502(23)	76.391(12)
18	120	*Cmma*	LS	12.4198(24)	15.793(4)	13.5506(22)	90	2657.9(16)	10.0458(23)	76.363(12)
19	130	*Cmma*	LS	12.4211(23)	15.806(4)	13.5525(21)	90	2660.7(16)	10.0513(23)	76.323(12)
20	140	*Cmma*	LS	12.4399(24)	15.796(4)	13.5591(21)	90	2664.4(16)	10.0532(23)	76.443(12)
21	150	*Cmma*	LS	12.4574(24)	15.782(4)	13.5577(21)	90	2665.5(16)	10.0531(23)	76.571(12)
22	160	*Cmma*	LS	12.4714(24)	15.777(4)	13.5606(23)	90	2668.2(16)	10.0555(23)	76.651(12)
23	170	*Cmma*	LS	12.4914(20)	15.7457(30)	13.5538(7)	90	2666(6)	10.0494(18)	76.851(20)
24	180	*Cmma*	LS	12.4991(19)	15.7390(26)	13.5534(7)	90	2666(5)	10.0492(16)	76.909(18)
25	190	*Cmma*	LS	12.4994(19)	15.7438(25)	13.5628(8)	90	2669(5)	10.0511(16)	76.893(17)
26	200	*Cmma*	LS	12.4620(25)	15.7598(29)	13.5707(8)	90	2665(6)	10.0458(19)	76.670(21)
27	210	*Cmma*	LS	12.1749(24)	15.974(29)	13.5918(7)	90	2643(5)	10.0424(19)	74.627(21)
28	220	*Cmma*	LS	12.1193(17)	16.0201(21)	13.6001(6)	90	2640(4)	10.0439(14)	74.215(15)
29	230	*Cmma*	LS	12.1171(19)	16.0396(24)	13.6228(10)	90	2648(5)	10.051(15)	74.138(17)
30	240	*C*2/*m*	mixed	12.823(3)	16.288(4)	13.847(5)	92.529(26)	2889.3(15)	10.37(3)	76.424(16)
31	250	*C*2/*m*	mixed	12.796(4)	16.388(4)	13.872(5)	92.443(24)	2906.4(15)	10.40(3)	75.97(3)

#	Temp / K	Space Group	Spin State	*a*-parameter / Å	*b*-parameter / Å	*c*-parameter / Å	*α*-angle / °	Volume / Å^3	Fe–Au–Fe Distance / Å	Au–Fe–Au Angle / °
32	260	*C*2/*m*	mixed	12.764(4)	16.422(4)	13.890(5)	92.641(24)	2908.6(16)	10.40(3)	75.71(3)
33	270	*Cmma*	HS	12.0072(18)	16.9877(10)	13.9722(13)	90	2850(2)	10.4014(9)	70.506(11)
34	280	*Cmma*	HS	11.9258(17)	17.0006(6)	13.9724(12)	90	2832.8(16)	10.3832(7)	70.098(10)
35	290	*Cmma*	HS	11.8921(17)	17.0063(8)	13.9746(12)	90	2826(2)	10.3759(8)	69.928(10)

*Au·{H_2O} (Cmma)**

#	Temp / K	Spin State	*a*-parameter / Å	*b*-parameter / Å	*c*-parameter / Å	Volume / Å^3	Fe–Au–Fe Distance / Å	Au–Fe–Au Angle / °
00	300	HS	11.3077(15)	17.5415(24)	13.9846(25)	2773(5)	10.435(1)	65.61(1)
01	290	HS	11.2826(17)	17.5716(35)	13.9820(26)	2772(6)	10.441(2)	65.41(2)
02	280	HS	11.2624(15)	17.5966(34)	13.9854(24)	2771(6)	10.446(2)	65.24(2)
03	270	HS	11.2507(16)	17.5940(34)	13.9892(28)	2769(6)	10.442(2)	65.19(2)
04	260	HS	11.2376(15)	17.6014(31)	13.9885(28)	2766(6)	10.441(2)	65.11(2)
07	230	mixed	11.108(4)	17.6127(33)	13.998(4)	2738(7)	10.411(2)	64.48(3)
08	220	mixed	11.0986(34)	17.5993(34)	13.999(4)	2734(7)	10.403(2)	64.47(3)
09	210	mixed	11.086(4)	17.581(4)	14.000(5)	2728(8)	10.392(3)	64.47(3)

#	Temp / K	Spin State	*a*-parameter / Å	*b*-parameter / Å	*c*-parameter / Å	Volume / Å^3	Fe–Au–Fe Distance / Å	Au–Fe–Au Angle / °
10	200	mixed	11.082(6)	17.560(4)	13.999(6)	2724(9)	10.382(3)	64.51(4)
11	190	mixed	11.088(6)	17.538(5)	13.998(5)	2722(10)	10.375(4)	64.60(4)
12	180	mixed	11.092(4)	17.515(5)	13.980(4)	2716(10)	10.366(3)	64.69(3)
13	170	mixed	11.0884(34)	17.495(5)	13.970(4)	2710(9)	10.356(3)	64.73(3)
14	160	mixed	11.0844(33)	17.471(5)	13.959(5)	2703(10)	10.345(3)	64.79(3)
15	150	mixed	11.076(29)	17.446(5)	13.936(6)	2692(10)	10.332(3)	64.82(3)
16	140	mixed	11.0643(26)	17.422(5)	13.918(8)	2682(10)	10.319(3)	64.84(3)
17	130	mixed	11.0581(24)	17.416(5)	13.908(11)	2678(8)	10.315(3)	64.83(3)
18	120	mixed	11.0577(25)	17.394(5)	13.897(7)	2672(10)	10.306(3)	64.89(3)
19	110	mixed	11.0531(27)	17.377(5)	13.892(9)	2668(10)	10.297(3)	64.92(3)
20	100	mixed	11.0517(27)	17.372(6)	13.887(7)	2666(11)	10.295(3)	64.93(3)
21	110	mixed	11.0535(27)	17.386(6)	13.889(7)	2669(11)	10.301(3)	64.89(3)
22	120	mixed	11.0592(25)	17.395(6)	13.898(7)	2673(11)	10.306(3)	64.89(3)
23	130	mixed	11.0644(32)	17.404(6)	13.902(7)	2677(11)	10.312(3)	64.89(3)
24	140	mixed	11.0693(26)	17.416(5)	13.907(7)	2681(10)	10.318(3)	64.88(3)
25	150	mixed	11.0745(27)	17.443(5)	13.929(6)	2690(10)	10.331(3)	64.82(3)
26	160	mixed	11.0748(30)	17.449(5)	13.956(5)	2696(9)	10.333(3)	64.81(3)

#	Temp / K	Spin State	*a*-parameter / Å	*b*-parameter / Å	*c*-parameter / Å	Volume / Å^3	Fe–Au–Fe Distance / Å	Au–Fe–Au Angle / °
27	170	mixed	11.0836(31)	17.473(5)	13.963(5)	2704(9)	10.346(3)	64.78(3)
28	180	mixed	11.084(4)	17.495(5)	13.979(5)	2710(10)	10.355(3)	64.71(3)
29	190	mixed	11.090(4)	17.513(5)	13.982(5)	2715(10)	10.365(3)	64.69(3)
30	200	mixed	11.093(4)	17.532(5)	13.995(5)	2721(10)	10.373(3)	64.65(3)
31	210	mixed	11.094(4)	17.561(4)	13.998(5)	2727(8)	10.386(3)	64.56(3)
32	220	mixed	11.0930(35)	17.5821(32)	14.004(5)	2731(7)	10.395(2)	64.50(3)
38	280	HS	11.256(17)	17.600(4)	13.9879(29)	2771(7)	10.446(2)	65.20(2)
39	290	HS	11.2727(17)	17.592(4)	13.9832(29)	2773(7)	10.447(2)	65.30(2)
40	300	HS	11.2986(18)	17.560(4)	13.9822(24)	2774(7)	10.440(2)	65.52(2)

* Note that the *Cmma* space group was used as a best approximation considering the quality of the data. The true space group is more likely to be triclinic, with a base-centred pseudosymmetry in a similar manner to the **Au**·{2-BuOH} sample.

Au·{MeCN} (Cmma)

#	Temp / K	Spin State	*a*-parameter / Å	*b*-parameter / Å	*c*-parameter / Å	Volume / Å^3	Fe–Au–Fe Distance / Å	Au–Fe–Au Angle / °
00	300	HS	12.9488(8)	16.4224(12)	14.0230(7)	2982(3)	10.4567(7)	76.510(8)
01	290	HS	12.9618(8)	16.4154(12)	14.0212(7)	2983(3)	10.4579(7)	76.590(8)
02	280	HS	12.9919(8)	16.3954(11)	14.0200(7)	2986(2)	10.4594(7)	76.787(7)

#	Temp / K	Spin State	*a*-parameter / Å	*b*-parameter / Å	*c*-parameter / Å	Volume / Å^3	Fe–Au–Fe Distance / Å	Au–Fe–Au Angle / °
03	270	HS	13.0218(9)	16.3786(12)	14.0160(7)	2989(3)	10.4621(7)	76.972(8)
04	260	HS	13.0994(11)	16.3247(17)	14.0392(16)	3002(4)	10.4653(10)	77.489(11)
05	250	HS	14.5727(11)	15.2944(12)	14.0171(7)	3124(3)	10.5627(8)	87.231(9)
06	240	HS	14.5716(9)	15.2953(10)	14.0137(6)	3123(2)	10.5626(7)	87.223(7)
07	230	HS	14.5730(9)	15.2946(9)	14.0134(5)	3123(2)	10.5629(6)	87.232(7)
08	220	HS	14.5721(9)	15.2946(10)	14.0134(5)	3123(2)	10.5626(7)	87.228(7)
09	210	HS	14.5698(9)	15.2957(9)	14.0128(5)	3123(2)	10.5622(6)	87.215(7)
10	200	HS	14.5680(8)	15.2967(9)	14.0124(5)	3123(2)	10.5619(6)	87.204(7)
11	190	mixed	14.5681(8)	15.2976(9)	14.0130(5)	3123(2)	10.5623(6)	87.201(7)
12	180	mixed	14.5700(8)	15.2965(9)	14.0125(5)	3123(2)	10.5625(6)	87.213(7)
13	170	mixed	14.5642(8)	15.2943(9)	14.0109(5)	3121(2)	10.5597(6)	87.198(7)
14	160	mixed	14.5551(9)	15.2962(10)	14.0127(8)	3120(2)	10.5573(7)	87.155(7)
15	150	mixed	14.5442(13)	15.2875(14)	14.0070(10)	3114(3)	10.5504(10)	87.145(10)
16	140	mixed	14.5346(10)	15.2809(11)	14.0046(10)	3110(3)	10.5447(7)	87.132(8)
17	130	mixed	14.5094(12)	15.2671(12)	13.9831(5)	3097(3)	10.5310(8)	87.084(9)
18	120	mixed	14.4729(12)	15.2272(13)	13.9559(5)	3076(3)	10.5040(9)	87.090(10)
19	110	mixed	14.4211(13)	15.1813(13)	13.9169(5)	3047(3)	10.4695(9)	87.057(10)

#	Temp / K	Spin State	*a*-parameter / Å	*b*-parameter / Å	*c*-parameter / Å	Volume / Å^3	Fe–Au–Fe Distance / Å	Au–Fe–Au Angle / °
20	100	mixed	14.3859(12)	15.1475(13)	13.8914(5)	3027(3)	10.4451(9)	87.045(10)
21	110	mixed	14.3537(12)	15.1180(14)	13.8643(5)	3009(3)	10.4233(9)	87.028(10)
22	120	mixed	14.3254(12)	15.0814(14)	13.8445(5)	2991(3)	10.4003(9)	87.054(10)
23	130	mixed	14.2851(10)	15.0738(11)	13.8342(7)	2979(3)	10.3837(7)	86.922(8)
24	140	mixed	14.2731(11)	15.0660(11)	13.8282(7)	2974(3)	10.3767(8)	86.903(9)
25	150	mixed	14.2947(12)	15.0617(15)	13.8228(5)	2976(3)	10.3826(10)	87.006(11)
26	160	mixed	14.3151(12)	15.0661(15)	13.8355(5)	2984(3)	10.3912(10)	87.071(10)
27	170	mixed	14.3343(12)	15.0874(15)	13.8484(5)	2995(3)	10.4055(10)	87.067(10)
28	180	mixed	14.3696(13)	15.1304(15)	13.8756(5)	3017(3)	10.4333(10)	87.045(11)
29	190	mixed	14.3979(14)	15.1622(16)	13.8977(5)	3034(4)	10.4546(11)	87.037(12)
30	200	HS	14.4449(14)	15.2058(15)	13.9306(6)	3060(3)	10.4866(10)	87.060(11)
31	210	HS	14.4789(17)	15.2604(15)	13.9719(7)	3087(4)	10.5181(11)	86.989(12)
32	220	HS	14.5134(18)	15.2887(17)	13.9983(8)	3106(4)	10.5402(12)	87.019(13)
33	230	HS	14.528(18)	15.3006(17)	14.0084(8)	3114(4)	10.5495(12)	87.032(13)
34	240	HS	14.5347(18)	15.3116(17)	14.0191(8)	3120(4)	10.5558(12)	87.017(13)
35	250	HS	14.5385(18)	15.3172(18)	14.0217(7)	3122(4)	10.5592(13)	87.011(14)
36	260	HS	14.5638(11)	15.2986(13)	14.0195(9)	3124(3)	10.5611(9)	87.180(9)

#	Temp / K	Spin State	*a*-parameter / Å	*b*-parameter / Å	*c*-parameter / Å	Volume / Å^3	Fe–Au–Fe Distance / Å	Au–Fe–Au Angle / °
37	270	HS	14.5742(9)	15.2913(10)	14.0132(6)	3123(2)	10.5621(7)	87.249(7)
38	280	HS	14.5811(9)	15.2914(10)	14.0236(7)	3127(2)	10.5645(7)	87.275(7)
39	290	HS	14.5823(9)	15.2898(10)	14.0138(6)	3125(2)	10.5643(7)	87.286(7)
40	300	HS	14.5858(9)	15.2864(10)	14.0148(5)	3125(2)	10.5643(7)	87.312(7)